

Bioinspired Engineering of Nanomaterials for Electrocatalytic Sensing of Heavy Metals and Organic Analytes

Thesis Submitted in Partial Fulfilment of the Requirements
for the Award of the Degree of

DOCTOR OF PHILOSOPHY

by

SMRUTI RANJAN DASH



Centre for the Environment
Indian Institute of Technology Guwahati
Assam-781039, INDIA
September 2021



The logo of the Indian Institute of Technology Guwahati is a circular emblem. It features a central stylized figure with three rounded protrusions, resembling a traditional Indian motif. The figure is surrounded by a circular border containing text in both Hindi and English. The Hindi text at the top reads 'भारतीय प्रौद्योगिकी संस्थान गुवाहाटी' and the English text at the bottom reads 'Indian Institute of Technology Guwahati'.

***Dedicated to Mom and Dad, for always loving and
supporting me
&
Paulomi my partner in crime***





Centre for the Environment
Indian Institute of Technology Guwahati
Guwahati -781 039
Assam, India

DECLARATION

I, hereby declare that the content embodied in this thesis entitled **“Bioinspired Engineering of Nanomaterials for Electrocatalytic Sensing of Heavy Metals and Organic Analytes”** is the result of investigations carried out by me at the Indian Institute of Technology Guwahati, Guwahati – 781 039, Assam, under the supervision of Prof. Animes K Golder, Department of Chemical Engineering, IIT Guwahati, and Prof. Subhendu Sekhar Bag, Department of Chemistry, IIT Guwahati, and is submitted to the Indian Institute of Technology Guwahati, for the award of the degree of Doctor of Philosophy.

In keeping with the general practice of reporting scientific observations, due acknowledgements have been made wherever the work described is based on the findings of other investigators.

Smruti Ranjan Dash

Roll No. 146152008

Centre for the Environment

Indian Institute of Technology Guwahati





Centre for the Environment
Indian Institute of Technology Guwahati
Guwahati -781 039
Assam, India

CERTIFICATE

This is to certify that the thesis entitled “**Bioinspired Engineering of Nanomaterials for Electrocatalytic Sensing of Heavy Metals and Organic Analytes**”, being submitted by **Mr. Smruti Ranjan Dash**, to the Indian Institute of Technology Guwahati, India, for the degree of Doctor of Philosophy, has been carried out by him under our guidance and supervision and this work has not been submitted elsewhere for the award of any degree.

Dr. Animes K. Golder
(Thesis Supervisor)
Professor
Department of Chemical Engineering
Indian Institute of Technology Guwahati
Guwahati-781 039
Assam, India

Dr. Subhendu Sekhar bag
(Thesis Supervisor)
Professor
Department of Chemistry
Indian Institute of Technology Guwahati
Guwahati- 781 039
Assam, India



Acknowledgement

It is a pleasure to acknowledge the roles of several individuals who were instrumental in completing my PhD research.

First of all, I would like to express my gratitude to Prof. Animes K Golder, who encouraged me to pursue this project and guided me through my research work and gave me the freedom to explore independently. His insightful comments and constructive criticisms at different stages of my research were thought-provoking and they helped me focus my ideas.

My sincere gratitude is extended towards Prof. Subhendu Sekhar Bag for his constant support; his unwavering enthusiasm for science kept me constantly engaged with my research. His generosity at difficult times helped a lot and made my PhD stress free.

I have been amazingly fortunate to have a great panel of Doctoral Committee members comprising Prof. Kaustubha Mohanty, Prof. Kannan Pakshirajan, Prof. Ajay Kalamdhad and Prof. Chandan Das who helped me time to time for the continual evaluation, at the same time their guidance to recover when my steps faltered.

I thank Head Centre for the Environment Prof. Utpal Bora for providing all research facilities at the centre. My appreciation also extends to our former Heads of Centre Prof. Gopal Das, Prof. Vikas Kumar Dubey, Prof. Mihir Kumar Purkait and all staff members of Centre for the Environment, Department of Chemical Engineering and Central Instrument Facility at IIT Guwahati to provide me with a conducive work environment and facilities to conduct my research. My sincere thanks go to Dr. Deepmoni Deka, Mr. Partha P. Bakal, Mr. Kaustubh Rakshit, Mr. Rajiv Gogoi and Mr. Mridul Das for helping me in all possible ways and made themselves available when in need. Help extended by Central Instruments Facilities of IIT Guwahati in providing me with some of the world-class instrumentation facilities is deeply accredited without which this work would not have been possible. A huge shout out to all the Research Scholars of Centre for the environment whose presence in the lab always kept the atmosphere lively for research.

I would also thank Commonwealth Commission, UK, for providing me with the Commonwealth Split-site Fellowship-2019. My great appreciation goes to Dr. Aruna Ivaturi for accepting the proposal for hosting me as a Commonwealth Scholar in her lab. I thank all the lab members of the SMaRDT group at the University of Strathclyde for making my stay at Glasgow pleasant. A special mention goes to Dr. Varun Saxena, Mr. Aquib Jawed and Mr. Mano Balaji Gandhi to be my constant mental support and made the stay in Glasgow stress-free and enjoyable .even during the lockdown due to the Covid-19 pandemic.

I am immensely thankful to my lab seniors Dr. Vihangraj V Kulkarni, Dr. Raj Kumar Das and Dr. Venkatnarasimha Rao Chelli for sharing their experiences and helping with various lab activities. A special thanks goes to my lab mates (Mr. Anirban Chowdhury, Mr.

Ravi and Mr. Chandrabhan) for being so nice and understanding that helped me to conduct my lab activities with ease.

This long journey would not have completed without the blessings, endless love, and support from my family. I dedicate my every accomplishment to my father (Shri Madan Mohan Dash), my mother (Smt. Sudhanshubala Dash) and my in-laws; Shri Tapan Kumar Basu and Smt. Jhanjha Basu. Their constant blessings, support and sacrifice for me every single day made my life cheerful.

A special mention to my wife Dr. Paulomi Bose without whose love and support I would not be where I am today. Her constant support and belief in me have made me stronger and provided me with the zeal and enthusiasm for completing my research.

Above all, I thank the Almighty God, for bestowing me with the wonderful life and appropriate environment in which I could flourish and enhance my vistas of learning. I thank Lord Jagannath for giving me the power to rise whenever I tumble. I thank almighty for blessing me with a lovely family and a bunch of well-wishers and friends.

*Smruti Ranjan Dash
Centre for the Environment
IIT Guwahati
September 2021*

Abstract

Development of bioinspired routes for the synthesis of nanostructured materials is a prudent area of research for their applications to engineer the electrocatalytic activity for sensing of wide variants of organic and inorganic analytes and to produce a device that is reproducible, stable, low-cost, and must have practical applicability. It is also important to further study and design approaches for the successful implementation of nanoparticles-based systems for the development of novel electrocatalytic sensors. This would help in achieving two primary sustainability goals, i.e., ensuring the availability of clean drinking water and achieving proper health and wellbeing for the masses. The phytochemicals present in *Psidium guajava* (guava) leaves extract have been exploited in this doctoral study for the formation of engineered metal nanoparticles, and the leftover biomass residue was used for the synthesis of carbon dots for electrocatalytic sensing of heavy metal ions and organic analytes.

To harness the potential of nanotechnology, the synthesis of nanoparticles needs to be controlled and modified as per the requirements. With these aims in mind, the doctoral work is segregated into various parts based on the synthesis of different nanoparticles and their applications in developing electrochemical sensors.

In the first part, one-pot synthesis of AgNPs is carried out by using the analytes present in the aqueous extract of *Psidium guajava* leaves (284 ascorbic acid equivalent/100 g fresh leaves), where the synthesis reaction was synergised by microwave (MW). The synergy between the MW input powers and the disintegration of capping agents leading to particle aggregation was explored. The modified electrode (AgNPs (pH9.5)/GPE, graphite paste electrode) exhibited a reduction in charge transfer resistance from 3.2 to 0.453 K Ω . A single electron reaction (Tafel slope 103 mV/decade, $\alpha=0.57$) of ascorbic acid (AA, 0.380 V vs. Ag/AgCl) was found in a phosphate buffer media (pH 7.2) and, AA oxidation was diffusion control at AA \leq 150 μ M and activation control at 150 \leq AA \leq 2000 μ M. Dopamine and uric acid couldn't interfere with the response current of the chronoamperometric test of AgNPs(pH9.5)/GPE, and the (peak)separation potential of 0.272 and 1.114 V was found for AA-dopamine and AA-uric acid. The limit of detection and sensitivities of AgNPs(pH9.5)/GPE were estimated as 14.63 μ M and, 0.719 (diffusion control) and 0.390 (activation control) μ A/cm². μ M. The concentration of AA in *S. edule* and *Z. mauritiana* extract

was determined using AgNPs(pH9.5)/GPE well-matched with high-performance liquid chromatography.

Synthesis of tailor-made nanostructures in bio- and bio-inspired routes is a challenge of decades. Therefore, the focus of this study moved a step further, and the synthesis of highly crystalline and ordered Ag@PtNPs core-shell nanoparticles (NPs) under a short exposure of microwave (900 W and 300 s) using the analytes present in the aqueous extract of *Psidium guajava* leaves was introduced. A thorough characterization of Ag@PtNPs and their single metal counterparts (AgNPs and PtNPs synthesized using the same bio-extract) was performed using UV-vis, XRD, FETEM, EDX, particle size, and zeta-potential analysis. The graphite support electrode was surface-modified by these NPs for electrocatalytic sensing of Pb(II) by square wave anodic stripping voltammetry. The electron transfer resistance was reduced by 1.2, 26, and 2.9 folds, respectively, for PtNPs, AgNPs and Ag@PtNPs modified graphite electrodes in comparison to the bare graphite electrode, and the constant phase element and solution resistance were almost invariant. The sensitivity of Ag@PtNPs/graphite electrode for Pb(II) sensing calculated against the electroactive area was about 4.5 and 20.20 folds higher than PtNPs/graphite and AgNPs/graphite electrodes at -0.43 V. vs. Ag/AgCl (3 M KCl) and pH 5 with a deposition potential of -1.2 V vs. Ag/AgCl (3 M KCl) for 300 s, and the limit of detection was as low as 0.8 nM. The response of the sensor (max. 1.98% variation in peak current) was almost invariant in the presence of co-ions (Cd(II), Cu(II), and Hg(II) from 0.25-10 μ M), and it could effectively determine Pb(II) (with and without spiking) from environmental water samples collected from the river, domestic supply and sewage treatment plant (max. 6.3% variation in comparison of atomic absorption spectroscopy).

Noble metal nanoparticles could impart an enhanced electrocatalytic activity of various redox reactions by improving the electron transfer kinetics. Taking keynotes from those facts, herein, facile bioinspired synthesis of PtNPs and their integration for the formation of PtNPs/graphene nanocomposite using *Psidium guajava* (guava) leaves extract was carried out. Graphene used in nanocomposite formulation was synthesized by exfoliation of graphite in water/acetone (25:75 v/v) mixture followed by mechanical shearing using ultrasonication and microwave irradiation. PtNPs/graphene nanocomposite was drop-cast onto a glassy carbon electrode (GCE, 3 mm dia). The electrocatalytic activity of PtNPs/graphene nanocomposite was tested in a three-electrode system for sensing metabolic products of dipyrone (DIP) formed through $1 e^-$ and $2 e^-$ transfer reactions. The modified electrode exhibited an almost 50% reduction in electrode resistance. The limit of detection was found to be 0.142 μ M with

sensitivities of 0.820 and 0.445 $\mu\text{A} \cdot \mu\text{M}^{-1} \text{cm}^{-2}$ for DIP concentration below and above 100 μM , respectively, using square wave voltammetry. The signal of sensing of metabolites of DIP was almost invariant in the presence of glucose, dopamine, uric acid, and ciprofloxacin; however, the response current was decayed by 20% within the 10th cycle. The sensing of DIP spiked in treated sewage-water and running tap-water samples was ~100% recoverable and comparable with HPLC.

The bioinspired synthesis of the novel metal nanoparticles could generate a substantial amount of *Psidium guajava* leaves residue. This study aimed at the synthesis of carbon dots (CDs) using leftover biomass residue. The hydrothermal method was used for the synthesis of CDs. These CDs were then decorated on the glassy carbon electrode (GCE) for the electrochemical sensing of chlorpyrifos (an organophosphate pesticide) in an aqueous ethanolic solution. CDs were characterized by FETEM, XRD, FTIR, and photoluminescence spectroscopy. Monodispersed CDs of average particle size of 3.7 nm were obtained at 200°C for a reaction time of 10 h. Square wave voltammetric technique was employed for the sensing and quantification of chlorpyrifos and for the determination of fundamental electro-kinetic parameters. The reduction of chlorpyrifos involved an irreversible two electron process with a heterogeneous reaction rate constant (k°) of 1.21 s^{-1} and a formal potential (E°) of 1.34 V vs. Ag/AgCl, respectively. The modified GCE exhibited a smooth noise-free peak-current response along with its good repeatability (RSD 4.7%, n=10), reproducibility (RSD 1.17%, n=3), and sensitivity ($1.27 \text{ mA} \cdot \mu\text{M}^{-1} \cdot \text{cm}^{-2}$) towards the target analyte. The limit of chlorpyrifos determination and quantification was found to be 1.5 nM and 4.5 nM, respectively, with a linear range of 0.1-1 μM .

Finally, the fabrication of fluorine-doped tin oxide (FTO) based miniaturized device using Cu nanorods (CuNRs) and Cu@Ag nanorods (Cu@AgNRs), which were used as electrocatalysts for the detection of Zn(II), Cd(II), Pb(II), and Hg(II) ions present in various environmental samples was performed. An automatic laser engraver-based patterning of the FTO sheet was carried out to draw an etched pattern providing a miniaturized three-electrode system (1.5×2.5 cm). A layer of Ag/AgCl ink was coated by doctor blading on a section of the FTO sheet to develop the reference electrode. CuNRs and Cu@AgNRs synthesized by using ascorbic acid (a major component in the bio-extract) were drop-casted to develop the working electrode section (CuNRs/FTO or Cu@AgNRs/FTO) on the patterned FTO sheet. The bare FTO surface worked as the counter electrode. Ag was deposited on CuNRs by partial galvanic displacement of Cu to form Cu@AgNRs. The electroactive surface areas of the prepared

devices were respectively 0.026, 0.093, and 0.125 cm² for bare FTO, CuNRs/FTO, and Cu@AgNRs/FTO. The Cu@AgNRs/FTO showed the peak separation by 0.40, 0.25, and 0.51 V between Zn(II)-Cd(II), Cd(II)-Pb(II), and Pb(II)-Hg(II), respectively. The limit of detection for Cu@AgNRs/FTO was found to be 0.005, 0.003, 0.002, and 0.0025 μM, respectively for Zn(II), Cd(II), Pb(II), and Hg(II), whereas CuNRs/FTO was unable to sense Zn(II) and Hg(II) ions till its initial concentration of 3 μM. It was observed that the current response for the devices remained invariant up to 4 consecutive cycles.

Keywords: Phenolic analytes; Metal nanoparticles synthesis; Bioinspired route; Rate acceleration; Particles aggregation; Core-shell nanoparticles; Bioinspired nanocomposite; Carbon dots; Electrocatalysis; Anodic stripping voltammetry; Square wave voltammetry; Ascorbic acid sensing; Heavy metal sensing; Dipyrone sensing; Chlorpyrifos sensing; FTO substrates; Miniaturized sensing device

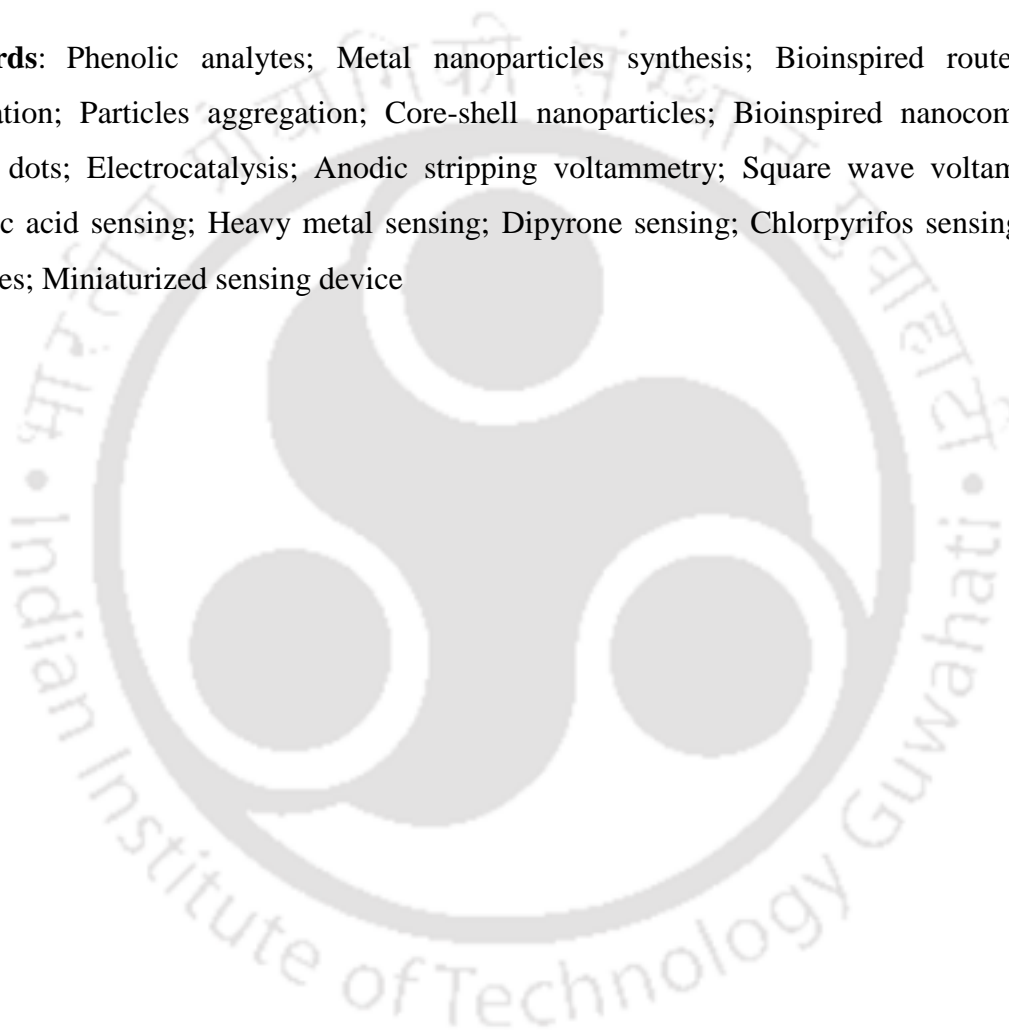


Table of Contents

Declaration	i
Certificate	iii
Acknowledgement	v
Abstract	vii
Table of Contents	xi
List of Table Captions	xvii
List of Figure Captions	xix

Chapter 1: Introduction, Literature Review and Research Objectives

1.1	Nanotechnology: History and background	2
1.1.1	History of nanotechnology	2
1.1.2	Background of nanotechnology and nanomaterials	2
1.2	Nanoparticles and their classifications	4
1.2.1	Ceramic nanoparticles	4
1.2.2	Polymeric nanoparticles	5
1.2.3	Semiconductor nanoparticles	5
1.2.4	Lipid-based nanoparticles	6
1.2.5	Carbon-based nanoparticles	6
1.2.6	Metal nanoparticles	7
1.2.6.1	Catalytic activities of metal nanoparticles	7
1.2.6.2	Antimicrobial activity of MNPs	8
1.2.6.3	Medicinal and therapeutic uses of MNPs	10
1.3	Approaches of MNPs synthesis	11
1.3.1	Top-down approach	12
1.3.1.1	Flame spray pyrolysis	12
1.3.1.2	Attrition	13
1.3.1.3	Exploding wire	14
1.3.1.4	Laser ablation	15
1.3.2	Bottom-up approach	16
1.3.2.1	Co-precipitation technique	16
1.3.2.2	Sol-gel process	17
1.3.2.3	Solvothermal method	18
1.3.2.4	Micro-emulsions mediated synthesis	19
1.3.2.5	Chemical vapour deposition	21
1.4	Bioinspired synthesis of MNPs	22
1.4.1	MNPs synthesis using bacteria	23
1.4.2	MNPs synthesis using Fungi	24
1.4.3	MNPs synthesis using plant-based extracts	25
1.5	Synthesis of tailored MNPs	27
1.6	Analytical tools and techniques	28
1.6.1	Conventional techniques for detection of an analyte	28
1.6.1.1	UV-vis spectrophotometric techniques	28
1.6.1.2	Chromatographic techniques	29
1.6.1.3	Mass spectrometric techniques	29
1.6.1.4	Fluorescence techniques	30
1.6.2	Sensor-based techniques in analyte detection	30
1.6.2.1	Biochemical sensors	31
1.6.2.2	Optical sensors	31

1.6.2.3	Electrochemical sensing catalyzed by MNPs	32
1.6.3	Tailoring MNPs in bioinspired routes and electrocatalytic activity	37
1.7	Fabrication of MNPs based miniaturized sensing device	39
1.8	Indian scenario for synthesis and implications of bioinspired MNPs	42
1.9	Knowledge gap and thesis objectives	43
1.10	Organization of the thesis	44
	References	47

Chapter 2: Materials and Methodology

2.1	Reagents and chemicals	74
2.1.1	Analytical reagents	74
2.1.2	Preparation of buffer solutions	75
2.1.2.1	Phosphate buffer solution	75
2.1.2.2	Acetate buffer	75
2.1.2.3	Britton-Robinson (B-R) buffer solution	76
2.1.3	Target analytes for electrochemical sensing	76
2.2	Biomass and bio-extract	76
2.2.1	Selection of <i>Psidium guajava</i> leaves extract	76
2.2.2	Preparation of <i>Psidium guajava</i> leaves extract	77
2.2.3	DPPH assay of bio-extract	78
2.3	Methodologies of electrocatalysts syntheses	78
2.3.1	Microwave-assisted bioinspired synthesis of AgNPs	78
2.3.2	Microwave-assisted bioinspired synthesis of PtNPs	79
2.3.3	Bio-inspired synthesis of Ag@PtNPs	79
2.3.4	Bioinspired synthesis of PtNPs/graphene nanocomposite	80
2.3.4.1	Synthesis of graphene	80
2.3.4.2	Synthesis of PtNPs/graphene nanocomposite	81
2.3.5	Synthesis of carbon dots (CDs) from <i>P. guajava</i> waste biomass	82
2.3.6	Synthesis of Cu and Cu@Ag nanorods	83
2.4	Characterizations of electrocatalysts	85
2.4.1	UV-vis spectroscopy	85
2.4.2	High performance liquid chromatography	85
2.4.3	Fourier transform infrared spectroscopy	86
2.4.4	High resolution mass spectrometry	86
2.4.5	X-ray diffraction	87
2.4.6	Field emission scanning electron microscopy	87
2.4.7	Field emission transmission electron microscopy	88
2.4.8	Energy-dispersive X-ray spectroscopy	88
2.4.9	Atomic absorption spectroscopy	88
2.4.10	Raman spectroscopy	89
2.4.11	Thermogravimetric analysis	89
2.5	Electroanalytical techniques of sensing	89
2.5.1	Three-electrode system for electrochemical sensing studies	89
2.5.2	Fabrication of working electrodes	92
2.5.3	Cyclic voltammetry	94
2.5.4	Chronoamperometry	94
2.5.5	Square wave voltammetry	95
2.5.6	Square wave anode stripping voltammetry	96
2.5.7	Electrochemical impedance spectroscopy	98

2.5.8	Determination of electrochemical surface area	99
2.5.9	Fabrication of miniaturized three-electrode sensing device	100
2.6	Electrochemical sensing of analytes	101
2.6.1	Electrochemical studies and AA determination	101
2.6.2	Electrochemical studies and HMIs detection	101
2.6.3	Electrocatalytic sensing of DIP and its metabolites	102
2.6.4	Electrochemical studies and chlorpyrifos sensing	103
2.6.5	Sensing of heavy metal ions using miniaturized device	104
	References	106

Chapter 3: Synergizing AgNPs Synthesis in a Bioinspired Route using Microwave and Studies on Electrocatalytic Sensing of Ascorbic Acid from Biological Entities

3.1	Background and executive motivation	110
3.2	Results and Discussions	112
3.2.1	Physiochemical attributes of AgNPs	112
3.2.1.1	AgNPs synthesis kinetics and particles sizes	112
3.2.1.2	Crystalline nature of AgNPs	122
3.2.1.3	Proposed mechanism of AgNPs formation using <i>P. guajava</i> leaves extract	124
3.2.1.4	Transmission electron micrographs of AgNPs	127
3.2.1.5	FTIR spectrum of AgNPs	128
3.2.1.6	Characterizations of AgNPs(pH9.5)/GPE nanocomposite	128
3.2.2	Electrochemical behaviour of AgNPs(pH9.5)/GPE	130
3.2.2.1	Electrochemical impedance spectroscopy (EIS)	130
3.2.2.2	Cyclic voltammetric and amperometric responses	131
3.2.3	Analysis of AA in biological entities	136
3.3	Major findings	137
	References	139

Chapter 4: Bioinspired Synthesis of Highly Structured Spherical Ag@Pt Core-shell Nanoparticles for Electrocatalytic Pb(II) Sensing

4.1	Background and executive motivation	148
4.2	Results and Discussions	150
4.2.1	Characterizations of prepared nanostructures	150
4.2.1.1	Formation of Ag-core (AgNPs) and PtNPs	150
4.2.1.2	UV-Vis spectra of AgNPs, PtNPs and Ag@PtNPs	152
4.2.1.3	Electron microscopic characterizations of synthesized Ag@Pt NPs	153
4.2.1.4	Crystal structure of synthesized nanoparticles	156
4.2.2	Characterizations of fabricated electrodes	158
4.2.2.1	Elemental analysis of prepared Ag@Pt/GPE electrode surface	158
4.2.2.2	Electrochemical characterization of electrodes	159
4.2.3	Pb(II) pre-concentration on electrode prior to its sensing	161
4.2.3.1	Determination of Pb(II) deposition potential	161
4.2.3.2	Optimization of Pb(II) deposition time	162
4.2.4	Pb(II) detection and determination by stripping from electrode surface	163

4.2.4.1	Optimal pH of Pb(II) sensing	163
4.2.4.2	Pb(II) determination in absence of co-ions interference	164
4.2.4.3	Co-ions interference on Pb(II) detection	169
4.2.4.4	Pb(II) determination in real sample	171
4.3	Major finding	173
	References	174

Chapter 5: Bioinspired Synthesis of PtNPs/graphene Nanocomposites for Electrocatalytic Sensing of Metabolites of Dipyrone

5.1	Background and executive motivation	182
5.2	Results and Discussions	184
5.2.1	Characterization of PtNPs/graphene nanocomposites	184
5.2.1.1	Morphology study of PtNPs/graphene nanocomposites	184
5.2.1.2	Crystallinity analysis of PtNPs/graphene nanocomposites	187
5.2.1.3	Raman analysis of graphene nanosheet	187
5.2.2	EIS of PtNPs/graphene/GCE	189
5.2.3	Electrocatalytic DIP sensing at PtNPs/graphene/GCE	192
5.2.3.1	Determination of electrokinetic parameters	192
5.2.3.2	Electrode stability and interference studies	200
5.2.3.3	Analysis of DIP spiked with environmental water samples	202
5.3	Major findings	205
	References	206

Chapter 6: Electrocatalytic Sensing of Chlorpyrifos using Carbon Dots Derived from Waste *Psidium guajava* Leaves Biomass

6.1	Background and executive motivation	216
6.2	Results and Discussion	218
6.2.1	Synthesis and characterization of CDs	218
6.2.1.1	Optimization of reaction temperature	218
6.2.1.2	Physiochemical attributes of synthesized CDs	219
6.2.2	Characterization of working electrodes	221
6.2.2.1	Electroactive surface area of WE	221
6.2.2.2	Electrochemical impedance studies (EIS) of WE	222
6.2.3	Electrochemical sensing of Chlorpyrifos	223
6.2.3.1	Optimization of electrochemical sensing parameters	223
6.2.3.2	Electrochemical attributes of CHL	225
6.2.3.3	Repeatability and reproducibility of CHL sensing	229
6.2.3.4	Electrochemical quantification of CHL in agriculture sample	230
6.3	Major findings	233
	References	234

Chapter 7: Fabrication of a Miniaturized Electrochemical Sensing Device using Cu and Cu@Ag Nanorods for Heavy Metals Sensing

7.1	Background and executive motivation	240
7.2	Results and discussions	241

7.2.1	Synthesis and characterizations of CuNRs and Cu@AgNRs	241
7.2.1.1	Progressive formation of CuNRs and Cu@AgNRs	241
7.2.1.2	Spectral absorbance of CuNRs and Cu@AgNRs	242
7.2.1.3	Nature of crystallinity of CuNRs and Cu@AgNRs	243
7.2.1.4	FTIR spectra of CuNRs and Cu@AgNRs	243
7.2.1.5	FETEM and EDX analysis of CuNRs and Cu@AgNRs	245
7.2.2	Electrochemical characterization of the fabricated electrodes	246
7.2.2.1	Electrochemical impedance spectroscopy (EIS)	246
7.2.2.2	Determination of electro-active surface area	247
7.2.3	Electrochemical sensing of HMs	248
7.2.3.1	CuNRs/FTO in electrochemical sensing of single HM	248
7.2.3.2	Cu@AgNRs/FTO in electrochemical sensing of single HM	250
7.2.3.3	Simultaneous electrochemical sensing of HMs	252
7.2.3.4	Reproducibility and repeatability of fabricated devices	256
7.2.3.5	Cu@AgNRs/FTO device in environmental sample analysis	257
7.3	Major finding	260
	References	261

Chapter 8: Conclusions and Scopes for Future Studies

8.1	Overall conclusions	268
8.2	Scopes for future studies	270
	Annexure-I	271
	Research Outcomes	275
	Curriculum Vitae	277



List of Table Captions

Table 1.1: Nanoparticles and their size-dependent antimicrobial activities.	10
Table 1.2: Use of metal nanoparticles as highly sensitive electrochemical sensors.	34
Table 1.3: Nanomaterials of varying sizes and shapes and their effects on electrochemical sensing of HMIs.	37
Table 2.1: List of chemicals and reagents used in this doctoral work.	74
Table 3.1: Abundance of active compounds/analytes present in fresh <i>P. guajava</i> leaves.	121
Table 3.2: XRD parameters of AgNPs synthesized at pH 9.5.	122
Table 4.1: Calculated performance parameters of the electrochemical sensors for determining Pb(II) ions.	166
Table 4.2: Electrochemical determination of Pb(II) in NPs catalysed system: Present work versus earlier reports.	171
Table 4.3: Performance of Ag@PtNPs/GPE electrochemical sensors for Pb(II) determination from real water sample and its comparison with atomic absorption spectrophotometry (AAS).	172
Table 5.1: Electrokinetic parameters of sensing of DIP and its metabolites at different oxidation peaks using PtNPs/graphene/GCE.	194
Table 5.2: Comparison between electrochemical performances of the proposed method and other studies extracted from the literature for dipyrone determination.	196
Table 5.3: Peaks obtained from mass spectroscopy and their identification before reaction.	199
Table 5.4: Peaks obtained from mass spectroscopy and their identification after reaction.	199
Table 5.5: Determination of DIP spiked in different real environmental water samples using PtNPs/graphene/GCE and HPLC.	203
Table 5.6: Physico-chemical characterization of water samples.	203
Table 6.1: Performance comparison for CHL determination by electrochemical sensing at GCE/CDs and by HPLC.	233
Table 7.1: Fabricated sensor performance parameters for individual HM detection using CuNRs/FTO.	250
Table 7.2: Fabricated sensor performance parameters for individual HM detection using Cu@AgNRs/FTO.	251
Table 7.3: Fabricated sensor performance parameters for simultaneous HMs detection.	256
Table 7.4: Performance of Cu@AgNRs/FTO device for HMs determination from environmental water samples.	259



List of Figure Captions

Figure 1.1:	Mechanism of antimicrobial activity of nanoparticles (adapted from Palza (2015) with permission from mdpi.com).	9
Figure 1.2:	Typical methods for the fabrication of nanoparticles.	11
Figure 1.3:	(a) Image showing the experimental setup for the synthesis of the nanoparticles using double nozzle flame spray pyrolysis, and (b-d) TEM and High-angle annular dark-field (HAADF) STEM images of Pt doped TiO ₂ nanoparticles. Reprinted from Grossmann et al. (2015) with prior permission. Copyright 2015 Springer Nature.	13
Figure 1.4:	(a) Schematic diagram of attrition process, and (b & c) Hexagonal wurtzite ZnO nanoparticles of average size of 15 nm. Figures 1.4b & 1.4c reprinted from Chen et al. (2012) with prior permission. Copyright 2012 Elsevier.	13
Figure 1.5:	(a) SEM image of starting graphite material, (b) Ball milled particles, and (c) Particle size distribution of nitrogen-doped carbon nanoparticles prepared by high energy attrition process showing a wide range of particle size distribution. Reprinted from Xing et al. (2013) with prior permission.	14
Figure 1.6:	Images showing the nanoparticles (Pb/Cu) size with different degree of superheating (W_m): (a) $W_m=1.1$ average particle size of 95 nm, (b) $W_m=1.6$ average particle size of 92 nm and, and (c) $W_m=2.4$ average particle size of 72 nm. Reprinted from Lerner et al. (2015) with prior permission. Copyright 2015 Elsevier.	15
Figure 1.7:	Au nano-colloid synthesis by laser ablation method. Reprinted from Wagener et al. (2011) with prior permission. Copyright 2011 Royal Society of Chemistry.	16
Figure 1.8:	Doped zinc oxide nanoparticles synthesized by co-precipitation method: (a) 5% Co, and (b) 1% Co (scale 100 nm). Reprinted from Oves et al. (2015) with prior permission. Copyright 2015 Elsevier.	17
Figure 1.9:	Schematic representation of a typical sol-gel process (Samiey et al., 2014).	18
Figure 1.10:	(a) Schematic representation of solvothermal growth of nanoparticles, and (b) Image of CIGS nanoparticles synthesized by this process. Reprinted from Mousavi et al. (2016) with prior permission. Copyright 2016 Elsevier.	19
Figure 1.11:	Schematic diagram for microemulsion techniques. Reprinted from Sanchez-Dominguez et al. (2012) with prior permission. Copyright 2012 Elsevier.	20
Figure 1.12:	Size dependence of Au nanoparticles on the surfactants used for the templating microemulsion: (a) Dioctyl sodium sulfosuccinate (AOT) mediated synthesis, (b) Dodecyl-dimethyl-ammonium bromide (DDAB), and (c) Cetyl trimethyl ammonium bromide (CTAB). Reprinted from Latsuzbaia et al. (2015) with prior permission. Copyright 2015 Elsevier.	21
Figure 1.13:	Diagram of chemical vapour deposition setup for FeS ₂ nanofilms synthesis. Reprinted from Samad et al. (2015) with prior permission. Copyright 2015 American Chemical Society.	22
Figure 1.14:	Prerequisites for the bioinspired synthesis of stable nanoparticles.	23
Figure 1.15:	TEM micrographs of bioinspired metal and metal oxide nanoparticles: (a) Ag nanoparticles (Mishra et al., 2015), (b) SnO ₂	26

	nanoparticles (Vidhu et al., 2015), (c) Au nanoparticles (Patra et al., 2015), and (d) ZnO nanoparticles (Sangeetha et al., 2011). Reprinted with prior permission. Copyright 2015 Elsevier (Figures 1.15a-1.15c) and Copyright 2011 Elsevier (Figure 1.15d).	
Figure 1.16:	Images showing reaction of silver nanoparticles towards different concentrations of cysteine. Reprinted from Borase et al. (2015) with prior permission. Copyright 2015 Springer-Nature.	32
Figure 1.17:	Schematic representation of working of electrochemical sensor developed by Radhakrishnan et al. (2014). Reprinted with prior permission. Copyright 2015 Elsevier.	34
Figure 1.18:	Schematic pictures of the different structures of core-shell nanoparticles: (A) Core-shell nanoparticles, (B) Core double-shell particles or core multi-shell nanoparticle, (C) Polyhedral core/shell nanoparticles, (D) Core porous-shell nanoparticles, (E) Hollow-core shell nanoparticles or single-shell nanoparticles, (F) Hollow-core double-shell nanoparticles, (G) Moveable core-shell nanoparticles, (H) Multi-core shell nanoparticles, (I) Irregular shape core shell nanoparticles, and (J) Rod core-shell nanoparticles. Reprinted from Khatami et al. (2018) with permission from mdpi.com.	38
Figure 1.19:	(A) Scheme for screen-printing of silver/carbon screen-printed electrode (S/C-SPE)- (a) polyester substrate, (b) silver track, (c) carbon layer, (d) silver/silver chloride track and (e) insulating layer; (B) Screen-printed silver/carbon screen-printed electrode(S/C-SPE); and (C) Modified screen printed electrodes as electrochemical tongue for simultaneous detection of HMIs in a mixed matrix of 4 HMIs and two interferences. Herein (i) denotes connectors to potentiostat, (ii) are three working electrodes, (iii) is the Ag/AgCl electrode and (iv) a blank SPE working as counter electrode. Figures 1.19A and B are reprinted from Jadav et al. (2018) with prior permission. Copyright 2018 Elsevier; Figure 1.19C is reprinted from Pérez-Ràfols et al. (2017) with prior permission. Copyright 2017 Elsevier.	41
Figure 2.1:	Chemical structures: (a) Ascorbic acid [(R)-3,4-Dihydroxy-5-((S)-1,2-dihydroxyethyl)furan-2(5H)-one], (b) Dipyron drug [(2,3-dihydro- 1,5-dimethyl- 3-oxo- 2-phenyl-1-pyrazol-4-yl) methyl amino], and (c) Chlorpyrifos [O,O-Diethyl O-3,5,6-trichloropyridin-2-yl phosphorothioate].	76
Figure 2.2:	Preparation of <i>P. guajava</i> leaf extract: (a) <i>P. guajava</i> leaves at the source, (b) Chopped leaves, (c) Ground leaves with required amount of water (20 g leaves per 100 mL deionized water), (d) Bio-extract after filtration using a muslin cloth, and (e) Clarified bio-extract after centrifugation at 10000 rpm for 15 min.	77
Figure 2.3:	Determination of ascorbic acid equivalent of prepared <i>P. guajava</i> leaf extract using DPPH assay.	78
Figure 2.4:	Schematic diagram depicting the steps of the bioinspired synthesis of Ag@Pt core@shell NPs.	80
Figure 2.5:	Schematic representation of the preparation of graphene solution.	81
Figure 2.6:	Digital images showing different stages of preparation of bioinspired PtNPs/graphene nanocomposite.	82

Figure 2.7:	Schematic representation of the synthesis of CDs from <i>P. guajava</i> leaves using hydrothermal method.	83
Figure 2.8:	Schematic representation of the step-by-step synthesis of CuNRs and Cu@AgNRs.	84
Figure 2.9:	Conversion graph between different reference electrodes.	90
Figure 2.10:	Effect of the positioning of the electrodes on resistances in a three-electrode system.	91
Figure 2.11:	Experimental setup for the three-electrode electrochemical system used for electrochemical sensing of various analytes displaying all the major components for conducting the experiments.	92
Figure 2.12:	Step by step method for the preparation of the working electrode.	93
Figure 2.13:	Potential vs. time waveform for an anodic stripping voltammetry experiment displaying ‘a’ constant potential applied during deposition step, ‘b’ quiescence stage, and ‘c’ ramping applied potential during stripping phase.	98
Figure 2.14:	(a) Sample Nyquist plot showing the resistance developed at the fabricated device, and (b) Corresponding equivalent circuit diagram of working electrode.	99
Figure 2.15:	Step by step method to fabricate the compact three-electrode system for targeted sensing of HMIs.	100
Figure 2.16:	Image of the fabricated miniaturized FTO based three-electrode sensing device. The black connector corresponds to the counter electrode, the red connector corresponds to the working electrode and the blue connector refers to the reference electrode (Ag/AgCl).	105
Figure 3.1:	UV-vis spectra of AgNPs dispersed in the reaction mixture at different bio-extract concentrations with a total reaction volume of 250 mL (remnant 0.3 mM AgNO ₃). Reaction conditions: pH 9.5, microwave power 1200W, Ag ⁺ concentration 0.3 mM and reaction time 300 s.	113
Figure 3.2:	Digital image of showing the formation of AgNPs at different irradiation time at MW power of 960 W. Experimental conditions: reaction volume 250 mL, water to leaves ratio 500, initial Ag ⁺ concentration 0.3 mM and pH 9.5.	113
Figure 3.3:	UV-vis spectra of AgNPs at different time of irradiation and MW power at pH 11. Experimental conditions: reaction volume 250 mL, water to leaves ratio 500 and initial Ag ⁺ concentration 0.3 mM.	114
Figure 3.4:	UV-vis absorption spectra of AgNPs at different time of irradiation and MW power at pH 9.5. Experimental conditions: reaction volume 250 mL, water to leaves ratio 50 and initial Ag ⁺ concentration 0.3 mM.	115
Figure 3.5:	Transition from blue shift to red shift at peak position (λ_{\max}) from optical absorbance with time of irradiation at different MW power and (a) pH 9.5 and (b) pH 11. Experimental conditions: reaction volume 250 mL, water to leaves ratio 500 and initial Ag ⁺ concentration 0.3 mM.	116
Figure 3.6:	Particle size distribution of AgNPs obtained after 300 s of MW irradiation at varying input power at (a) pH 9.5 and (b) pH 11.	117
Figure 3.7:	TGA analysis of AgNPs. Experimental conditions of AgNPs synthesis: pH 9.5, reaction volume 250 mL and MW 960 W.	118

Figure 3.8:	Zeta-potential obtained after 300 s of irradiation at varying MW power. Experimental conditions: reaction volume 250 mL, water to leaves ratio 500 and Ag ⁺ concentration 0.3 mM.	119
Figure 3.9:	Control experiment at 25±5°C without irradiation showing variation of spectral absorbance ($\lambda_{\max} = 410$ nm) with the time of reaction at different pH.	120
Figure 3.10:	Mass spectra of <i>P. guajava</i> leaf extract showing different bio-constituents present in the extract.	120
Figure 3.11:	UV-vis spectral absorbance at λ_{\max} of AgNPs at different time of irradiation and microwave power at (a) pH 11 and (b) pH 9.5. Experimental conditions: reaction volume 250 mL, water to leaves ratio 500 and initial Ag ⁺ concentration 0.3 mM.	121
Figure 3.12:	XRD patterns of AgNPs synthesized at (a) pH 9.5 and (b) pH 11.	123
Figure 3.13:	Schematic diagram showing the participation of various significant reducing agents for the bio-mediated AgNPs formation along with their important oxidation products.	124
Figure 3.14:	Proposed mechanism for the synthesis of AgNPs using <i>P. guajava</i> leaves extract. Reactions involved in Ag ⁺ reduction forming AgNPs by (a) Chlorogenic acid, (b) D-glucose and (c) Quercetin are shown.	126
Figure 3.15:	FETEM, HRTEM/SAED micrographic results, and particle size distribution of AgNPs at 960 W and pH 9.5 (a, b, c: for AgNPs formed at 90 s of MW irradiation and d, e, f: for AgNPs formed at 300 s of MW irradiation).	127
Figure 3.16:	FTIR spectrum of AgNPs synthesised at pH 9.5. Experimental conditions: reaction volume 250 mL, water to leaves ratio 500, Ag ⁺ concentration 0.3 mM, MW power 960 W and irradiation time 300 s.	128
Figure 3.17:	XRD patterns of (a) AgNPs(pH9.5)/GPE, and (b) bare GPE.	129
Figure 3.18:	Morphology and EDX analysis of AgNPs(pH9.5)/GPE: (a) Cross-sectional view showing the active surface area of bare GPE, (b) Cross-sectional view showing the active surface area of AgNP(pH9.5)/GPE, (c) Elemental analysis of AgNPs(pH9.5)/GPE nanocomposite, (d) FESEM micrograph of drop coated AgNPs(pH9.5)/GPE and (e) Elemental EDX mapping of AgNPs(pH9.5)/GPE nanocomposite.	130
Figure 3.19:	Nyquist plots for EIS measurements (0.5 mM K ₃ [Fe(CN)] ₆) at (a) bare GPE and AgNPs(pH9.5)/GPE, (b) equivalent circuit diagram of GPE and (c) equivalent circuit diagram of AgNPs(pH9.5)/GPE showing resistance of working electrodes.	131
Figure 3.20:	(a) Cyclic voltamograms recorded with AgNPs(pH9.5)/GPE at different AA concentration (25 to 1000 μ M). Inset: CV obtained with similar experimental conditions using 700 μ M AA and GPE in place of AgNPs(pH9.5)/GPE, (b) Cyclic voltamograms recorded at different scan rates at AgNPs(pH9.5)/GPE, (c) Variation of peak current (I_p) with $v^{1/2}$ (v : 10 to 100 $\text{mV}\cdot\text{s}^{-1}$), (d) Variation of E_p and $\log(v)$ (v : 10 to 100 $\text{mV}\cdot\text{s}^{-1}$) with 100 μ M AA in 0.1 M.	133
Figure 3.21:	Chronoamperometric profile with step-wise addition of AA along with intermediate addition of dopamine (DA) and uric acid (UA) as interferants at AgNPs(pH9.5)/GPE. Inset: shows calibration curves for the variation of cell (steady) current with AA concentration at	134

	AgNPs(pH9.5)/GPE. Experimental conditions: $E_{\text{anode}} = 0.380$ V vs. Ag/AgCl, pH 7.2 and PBS 100 mL.	
Figure 3.22:	Square wave voltammogram obtained with AgNPs(pH9.5)/GPE for a mixture of 1 mM of AA and 0.5 mM of DA, and UA. Experimental conditions: scan rate $50 \text{ mV} \cdot \text{s}^{-1}$, pH 7.2 and 100 mL PBS.	135
Figure 3.23:	Calibration curves for the variation of cell (steady) current with AA concentration at AgNPs(pH9.5)/GPE. Experimental conditions: $E_{\text{anode}} = 0.380$ V vs. Ag/AgCl, pH 7.2 and PBS 100 mL.	136
Figure 4.1:	Effect of washing on the synthesized AgNPs. (a) TEM image of AgNPs before washing, (b) TEM image of after washing, (c) Particle size distribution before washing and (d) Particle size distribution after washing. Reaction condition: 0.3 mM AgNO_3 , pH 9.5, water to leaves ratio 50, and microwave irradiation of 960 W for 300 s.	151
Figure 4.2:	TEM image of synthesized PtNPs at different magnifications (a) 50 nm scale, (b) 10 nm scale and (c) particle size distribution of the synthesized PtNPs. Reaction conditions: H_2PtCl_6 0.3 mM, water to leaves ratio 50, pH 9.5, and microwave irradiation of 960 W for 300 s.	152
Figure 4.3:	(a) UV-Vis spectra of bimetallic Ag@PtNPs showing the decrease in the SPR response with time, and (b) Digital photograph of the nanoparticle suspension: (i) AgNPs core (precursor salt 0.3 mM, water to leaves (v/w) ratio 50, pH 9.5, microwave 960 W and 300 s), (ii) Ag@PtNPs after 30 s (iii) Ag@PtNPs after 120 s and (iv) Ag@PtNPs after 240 s (seed concentration 0.8 mg/mL, H_2PtCl_6 1 mM, pH 9.5, microwave 700 W and 240 s), and (v) PtNPs (precursor salt 0.3 mM, water to leaves ratio (v/w) 50, pH 9.5, 960 W and 300 s).	153
Figure 4.4:	(a, b, and c) TEM micrographs of Ag@PtNPs at different magnifications, (d) SAED micrograph of Ag@PtNPs, (e) IFFT profile of Ag-crystalline region of Ag@PtNPs, (f) IFFT profile of Pt-crystalline region of Ag@PtNPs showing distance between crystal lattices, and (g) EDX spectra showing the elemental composition of Ag@PtNPs. Reaction condition: water to leaves ratio 50 (v/w), pH 9.5, chloroplatinic acid 1 mM and Ag-core 50 mL, microwave 720 W and microwave time 240 s.	155
Figure 4.5:	Schematic representation of the mechanisms involved in the formation of Ag@PtNPs.	156
Figure 4.6:	Calculation of lattice strain of (a) AgNPs, (b) PtNPs and (c) Ag@PtNPs using Williamson-Hall analysis.	157
Figure 4.7:	X-ray diffraction patterns of AgNPs, PtNPs, and Ag@PtNPs. Reaction condition: water to leaves ratio 50 (v/w), pH 9.5, chloroplatinic acid 1 mM and Ag-core 50 mL, microwave 720 W and microwave time 240 s.	158
Figure 4.8:	Surface morphology of Ag@PtNPs modified graphite-support electrode. (a) FESEM micrograph, (b) Distribution of Pt metal on electrode surface, (c) Distribution of Ag metal on electrode, (d) Overlay mapping image of the electrode surface, and (e) Elemental composition at the electrode surface.	159
Figure 4.9:	Equivalent circuit diagram for (a) GPE, (b) AgNPs/GPE, (c) PtNPs/GPE, and (d) Ag@PtNPs/GPE systems.	161

- Figure 4.10:** (a) EIS spectra, and (b) Peak current vs. square root of scan rate (5-100 $\text{mV}\cdot\text{s}^{-1}$) of different prepared electrodes. Reaction conditions: $\text{K}_3(\text{Fe}[\text{CN}]_6)$ 1 mM in 100 mL of 0.05M KCl at ambient temperature. 161
- Figure 4.11:** (a) Pb(II) stripping current in SWASV captured at varying deposition potential from -0.4 to -1.6 V and (b) Peak current at different deposition potentials. Deposition time 300 s and Pb(II) concentration 5 μM in 100 mL acetate buffer (0.1 M) at pH 5. 162
- Figure 4.12:** (a) Pb(II) stripping current in SWASV captured at varying deposition time from 30 to 360 s, and (b) Peak current at different deposition time and corresponding residual Pb(II) conc. In solution. Deposition potential -1.2 V, Pb(II) concentration of 5 μM in 100 mL acetate buffer at pH 5. 163
- Figure 4.13:** (a) SWASV of Pb(II) sensing at different pH for Ag@PtNPs/GPE (b) Variation of peak current with electrolyte media pH. Experimental conditions: Reaction volume 100 mL, Pb(II) concentration of 5 μM in acetate buffer at different pH adjusted using 1 M HCl and 1 M NaOH. 164
- Figure 4.14:** Influence of initial concentration of Pb(II) on its detection and determination in SWASV at (a) AgNPs/GPE, (b) PtNPs/GPE (c) Ag@PtNPs/GPE and (d) Variation of I_p with Pb(II) concentration in the absence co-ions. Experimental condition: Deposition potential -1.2 V, deposition time 300 s, Pb(II) concentration of 0.25 to 10 μM in 100 mL acetate buffer at pH 5. 167
- Figure 4.15:** Schematic representation of the factors enhancing the electrocatalytic properties of Ag@PtNPs. 168
- Figure 4.16:** Peak current response of Pb(II) ions for different electrodes. Reaction conditions: Acetate buffer pH 5 and Pb(II) concentration 10 μM . 168
- Figure 4.17:** Variation of peak current of Pb(II) sensing at Ag@PtNPs/GPE at pH 5 and Pb(II) of 5 μM , (a) After 90 days of storage at room temperature, (b) Repeatability of Pb(II) sensing using the same electrode in 5 different Pb(II) solutions of same concentration (5 μM) and (c) Reproducibility of Pb(II) sensing using three different fresh Ag@PtNPs/GPE fabricated using the optimized protocol. 169
- Figure 4.18:** Influence of co-HM ions at different concentration on SWASV current response at fixed Pb(II) concentration. (a) Pb(II) of 0.25 μM , (b) Pb(II) of 1 μM , and (c) Peak current response at Ag@PtNPs/GPE at varying interfering HM concentration (0.25-10 μM). Experimental condition: SWASV pulse amplitude 0.025 V, frequency 15 Hz, step potential 4 mV, deposition potential -1.2 V and deposition time 300 s in 100 mL acetate buffer at pH 5. 170
- Figure 4.19:** Ion chromatographs of (a) river water, (b), tap water, and (c) sewage water samples showing the anionic constituents present in the samples. 172
- Figure 5.1:** (a) TEM micrograph of graphene sheet (inset: SAED of graphene), (b) HRTEM micrograph of graphene, (c) FETEM micrograph of PtNPs, (d) HRTEM micrograph of PtNPs/graphene nanocomposite highlighted circles showing PtNPs (inset: SAED of PtNPs/graphene nanocomposite), (e) IFFT image of PtNPs on graphene sheet showing the characteristic fringe distance of 0.227 nm, (f) elemental 185

mapping showing the distribution of Pt element on PtNPs/graphene nanocomposite, and (g) EDX spectra of PtNPs/graphene nanocomposite.

- Figure 5.2:** (a) FESEM image of bare graphene, and (b) FESEM image of PtNPs/graphene nanocomposites. 186
- Figure 5.3:** (a) Particles size distribution of PtNPs and (b) PtNPs/graphene nanocomposite. 186
- Figure 5.4:** X-ray diffraction patterns of (a) bare graphite, (b) graphene nanosheet, and (c) PtNPs/graphene nanocomposite. 187
- Figure 5.5:** Raman spectra of bare graphite and synthesized graphene. 188
- Figure 5.6:** Nyquist plot with 0.1 mM DIP in 0.5 M KCl electrolyte at pH 7 within a frequency range of 10^{-2} to 10^6 Hz and 0.01 V vs. Ag/AgCl at open circuit potential. 190
- Figure 5.7:** Equivalent circuit diagrams of (a) bare GCE (support), (b) PtNPs/GCE, and (c) PtNPs/graphene/GCE. 190
- Figure 5.8:** Square wave response of DIP sensed using different working electrodes. DIP concentration of 50 μ M using 0.5 M KCl as supporting electrolyte. Square wave parameters: Initial potential 0.00 V and end potential 1.10 V, step potential 0.002 V, and amplitude 0.05 V vs. Ag/AgCl. 191
- Figure 5.9:** Cyclic voltammetry of (a) bare/GCE and (b) PtNPs/graphene/GCE at various scan rates from 5-200 $\text{mV}\cdot\text{s}^{-1}$ and (c) Peak current vs. square root of scan rate (25-1000 mV/s) using GCE and PtNPs/graphene/GCE. Reaction conditions: 1 mM $[\text{Ru}(\text{NH}_3)_6]\text{Cl}_3$ as redox probe in 100 mL of 0.1 M KCl as supporting electrolyte at ambient temperature. 192
- Figure 5.10:** (a) Square wave response at different pH using PtNPs/graphene/GCE, and (b) E_p vs. pH (peak 1). Reaction conditions: DIP concentration of 50 μ M in 0.5 M KCl supporting electrolyte. Square wave parameters: Initial potential 0.00 V, end potential 1.10 V, step potential 0.002 V, and amplitude 0.05 V vs. Ag/AgCl. 193
- Figure 5.11:** (a) Cyclic voltammogram recorded at different scan rates at PtNPs/graphene/GCE, (b) Variation of peak current (I_p) with $v^{1/2}$ (v : 5 to 200 mV/s), (c) Variation of E_p with $\log(v)$ (v : 5 to 200 mV/s) with 100 μ M DIP in 0.5 M 100 mL KCl at pH 7, (d) SWV profile recorded with PtNPs/graphene/GCE at different DIP concentration (1 to 300 μ M), (e) Calibration curve for DIP sensing, and (f) CV of DIP in a smaller electrochemical window (0.2 -0.8 V vs. Ag/AgCl) (black line) and wider electrochemical window (0.2 -1.2 V vs. Ag/AgCl) (red line) at the scan rate of 50 $\text{mV}\cdot\text{s}^{-1}$. 197
- Figure 5.12:** HPLC chromatograms (a) before and (b) after DIP sensing reaction. [An HPLC (Make: Agilent; 1260 Infinity II) equipped with UV detector was used for the chromatographic analysis of DIP. The detection was done at 214 nm using a UV detector. 198
- Figure 5.13:** Mass spectra recorded (a) before and (b) after DIP sensing. Experimental conditions: DIP concentration 100 μ M, reaction volume 100 mL, pH 7.0 and KCl 0.5 M. Mass spectra was taken after appropriate dilution using acetonitrile. 199
- Figure 5.14:** Schematic representation of the oxidation pathway of dipyrone. 200

- Figure 5.15:** Square wave voltammetry (SWV) of PtNPs/graphene/GCE for 10 consecutive cycles using the same electrode to obtain the electrode stability. Experimental conditions: Reaction volume 100 mL, pH 7.0, KCl 0.5 M and DIP 15 μM . SWV parameters: step potential 4 mV pulse amplitude 25 mV, pulse frequency 15 Hz, scan rate of 60 $\text{mV}\cdot\text{s}^{-1}$, and scanning potential 0-1.2 V. 201
- Figure 5.16:** (a) Repeatability of DIP sensing using PtNPs/graphene/GCE in 10 different DIP solutions at the same concentration of 15 μM , and (b) Chronoamperometric profile showing the current response of DIP sensing in the presence of different interfering compounds (1 μM) at the set potential of 0.51 V vs. Ag/AgCl using 0.5 M KCl at pH 7. 202
- Figure 5.17:** Ion-chromatographs of (a) Sewage water (filtered) and (b) Tap water used to prepare the samples spiked with DIP. 204
- Figure 5.18:** Mass spectra analysis of DIP in water exposed to environment for (A) 0 h, (B) 6 h, (C) 12 h, (D) 24 and (E) 24 h with an initial DIP concentration of 0.5 μM . 204
- Figure 6.1:** TEM micrographs of CDs formed from dried *P. guajava* leaves after a hydrothermal reaction for 10 h at different temperatures of (a) 160°C, (b) 180°C and (c) 200°C. 219
- Figure 6.2:** (a) Photoluminescence (PL) spectra and (b) FTIR spectra, of synthesized CDs. Synthesis time 10 h and temperature 200°C. 220
- Figure 6.3:** XRD pattern of synthesized CDs. Synthesis time 10 h and temperature 200°C. 220
- Figure 6.4:** (a) HRTEM micrograph, (b) SAED, and (c) Particle size analysis of synthesized CDs. Synthesis time 10 h and temperature 200°C. 221
- Figure 6.5:** Cyclic voltammetry plots at different scan rates for (a) Bare GCE, (b) GCE/CDs and (c) Peak current vs. square root of scan rate. Reaction conditions: $\text{K}_3\text{Fe}[\text{CN}]_6$ 1 mM in 100 mL of 0.05 M KCl at ambient temperature. 222
- Figure 6.6:** (a) Nyquist plot obtained with bare GCE and GCE/CDs in a 1 mM $\text{K}_3[\text{Fe}(\text{CN})_6]$ solution containing 0.1 M KCl against the electrochemical circuit diagrams for (b) bare GCE, and (c) GCE/CDs. 223
- Figure 6.7:** (a) Effect of deposition potential (E_{DEP}) on the square wave response of CHL, (b) Peak current vs. E_{DEP} , (c) Effect of deposition time (t_{DEP}) on the square wave response of CHL, and (d) Peak current vs. t_{DEP} . Reaction conditions: 0.5 μM CHL in B-R buffer (100 mL) at pH 7. 224
- Figure 6.8:** (a) HPLC analysis of 10 μM analytical grade (standard) CHL dissolved in ethanol, showing the retention time at 8.36 min and (b) HPLC analysis of 10 μM diluted (in acetonitrile) agriculture grade CHL (20% v/v) showing the presence of various additives that elute out at different retention times. 224
- Figure 6.9:** (a) SWV response recorded using GCE/CDs during electrochemical sensing of CHL (0.25 μM) with different electrolytes at pH 7, (b) Effect of pH variation on CHL sensing in B-R buffer system (0.5 μM CHL), and (c) Linear fitting of variation of peak potential as a function of pH. Reaction conditions: 0.1 M 100 mL B-R buffer, $E_{\text{DEP}} = -0.40$ V and $t_{\text{DEP}} = 60$ s. 226
- Figure 6.10:** Electrochemical reduction reaction of CHL molecule at GCE/CDs. 227

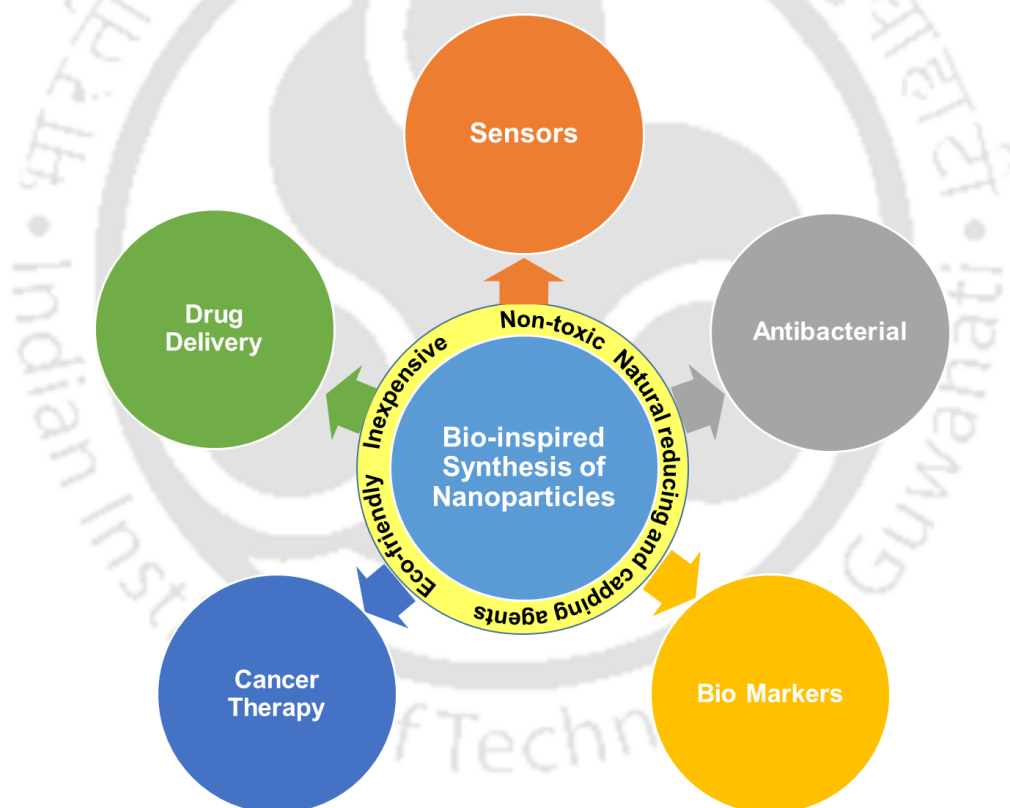
Figure 6.11:	Mass spectra analysis of (a) chlorpyrifos before reaction and (b) after 20 min chronoamperometry run at -1.40 V vs. Ag/AgCl using CDs/GCE as working electrode. The insets of Figures 6.9a and 6.9b show the corresponding simulated MS spectra using m/z calculator software from Integrative Omics, PNNL, USA.	227
Figure 6.12:	Square wave voltammograms recorded at different scan rates at GCE/CDs, (b) Variation of peak current (I_p) with $v^{1/2}$ (v : 5 to 150 $\text{mV}\cdot\text{s}^{-1}$), and (c) Variation of E_p with $\log(v)$ (v : 5 to 150 $\text{mV}\cdot\text{s}^{-1}$) with 0.5 μM CHL in 0.1 M 100 mL B-R buffer at pH 7, $E_{\text{DEP}} = -0.40$ V and $t_{\text{DEP}} = 60$ s.	228
Figure 6.13:	(a) Square wave voltammetric profiles recorded with CDs/GCE at different CHL concentration (0.1 to 10 μM), and (b) Calibration curve of CHL sensing. Reaction conditions: 0.1 M 100 mL B-R buffer at pH 7, scan rate 0.1 $\text{V}\cdot\text{s}^{-1}$, $E_{\text{DEP}} = -0.40$ V and $t_{\text{DEP}} = 60$ s.	229
Figure 6.14:	(a) SWV profile recorded with GCE/CDs, and (b) The corresponding trend in the current response in 10 consecutive sensing cycles. Reaction conditions: 0.5 μM CHL in 0.1 M 100 mL B-R buffer at pH 7, scan rate 0.1 $\text{V}\cdot\text{s}^{-1}$, $E_{\text{DEP}} = -0.40$ V and $t_{\text{DEP}} = 60$ s.	230
Figure 6.15:	SWV analysis of commercial pesticides (20% EC) in B-R buffer (pH 7) using GCE/CDs. Reaction conditions: 0.1 M 100 mL B-R buffer at pH 7, $E_{\text{DEP}} = -0.4$ V and $t_{\text{DEP}} = 60$ s.	231
Figure 6.16:	SWV analysis of CHL in river water (pH 7) using GCE/CDs. Reaction conditions: 0.1 M 100 mL B-R buffer at pH 7, $E_{\text{DEP}} = -0.4$ V and $t_{\text{DEP}} = 60$ s.	232
Figure 6.17:	Ion Chromatography (IC) analysis of river water showing various anions present in the water sample. Operating conditions: Run time of 30 min using an eluent containing a mixture of 1.0 mM NaHCO_3 and 3.3 mM Na_2CO_3 in DI water at a flow rate of 0.7 $\text{mL}\cdot\text{min}^{-1}$. The IC column used was 6.1006.530 Metrosep A Supp 5-250 Make: Metrohm.	232
Figure 7.1:	Digital photographs showing various stages of the progression of CuNRs synthesis: (a) Initial solution (60 mL), (b) 15 min, (c) 1 h, (d) 3 h, (e) 5 h, (f) 7 h, (g) 24h of reaction time, and (h) cleaned CuNRs suspended in water. Reaction conditions: CuCl_2 0.1 M, NaCl 0.35 M, AA 1.5 M and PVP 2.4 wt%, reaction volume 30 mL, pH 3.5 and reaction temperature 80°C .	242
Figure 7.2:	UV-vis spectroscopy analysis of the synthesized CuNRs and Cu@AgNRs.	243
Figure 7.3:	XRD analysis of the synthesized (a) CuNRs, (b) Cu@AgNRs, and (c) Corresponding JCPDS card.	244
Figure 7.4:	FTIR spectra of (a) CuNRs and (b) Cu@AgNRs showing various functional groups present on the nanomaterial surface.	244
Figure 7.5:	TEM micrographs of (a) CuNRs, (b and c) Cu@AgNRs, (d) HRTEM micrograph, (e) Elemental mapping, and Elemental distribution of (f) Copper, (g) Silver, and (h) EDX spectra and the elemental composition of Cu@AgNRs.	245
Figure 7.6:	(a) FETEM micrograph of CuNRs showing the growth of various crystalline faces and (b) SAED image of CuNRs showing various diffraction rings.	246

- Figure 7.7:** (a) Nyquist plot showing the change in resistance due to surface modifications of the FTO, (b) Bare FTO, (c) CuNRs/FTO, and (d) Cu@AgNRs/FTO showing the corresponding equivalent circuits. 247
- Figure 7.8:** Cyclic voltammograms with different electrodes: (a) Bare FTO, (b) CuNRs/FTO and (c) Cu@AgNRs/FTO at various scan rates (10-200 $\text{mV}\cdot\text{s}^{-1}$) and (d) Variation of peak current with square root of scan rate. Reaction conditions: $\text{K}_3(\text{Fe}[\text{CN}]_6)$ (1 mM) in 100 mL of 0.1 M KCl at ambient temperature. 248
- Figure 7.9:** Square wave voltammograms recorded with different HM ions: (a) Zn(II), (b) Cd(II), (c) Pb(II), (d) Hg(II), and (e) Corresponding calibration curves using CuNRs/FTO based miniature device. Reaction conditions HMs concentration 0.1-10 μM in acetate buffer at pH 5. The frequency was set at 15 Hz and amplitude 0.02 V, deposition time 90 s and conditioning time 30 s. 249
- Figure 7.10:** Square wave voltammograms captured with different HMs ions: (a) Zn(II), (b) Cd(II), (c) Pb(II), and (d) Hg(II) using Cu@AgNR/FTO based miniature device. Reaction conditions HMs concentration 0.1-10 μM in acetate buffer at pH 5. The frequency was set at 15 Hz and amplitude 0.02 V, deposition time 90 s, and conditioning time 30 s. 251
- Figure 7.11:** Simultaneous electrochemical sensing of Zn(II), Cd(II), Pb(II), and Hg(II) with various modified FTO based devices. Reaction conditions: HMs concentration 10 μM , in acetate buffer at pH 5.0. The frequency was set at 15 Hz and amplitude 0.02 V, deposition time 90 s, and conditioning time 30 s. 254
- Figure 7.12:** Squarewave voltammograms for simultaneous electrochemical sensing of Zn(II), Cd(II), Pb(II) and Hg(II) using (a) CuNRs/FTO and (b) Cu@AgNRs/FTO based devices, (c) Calibration curve with CuNRs/FTO, and (d) Calibration curves with Cu@AgNRs/FTO. Reaction conditions: HMs concentration 0.25-10 μM in acetate buffer at pH 5.0. The frequency was set at 15 Hz and amplitude 0.02 V, deposition time 90 s and conditioning time 30 s. 255
- Figure 7.13:** Square wave anodic stripping voltammetric profiles for simultaneous sensing of Zn(II), Cd(II), Pb(II), and Hg(II) using the fabricated miniaturized electrochemical device for seven different cycles at the (a) CuNRs/FTO and (b) Cu@AgNRs/FTO. Experimental conditions: Heavy metals concentration 10 μM , acetate buffer (pH 5.0), square wave frequency 15 Hz, amplitude 0.02 V, deposition time 90 s, deposition potential -0.5 V, and conditioning time 30 s. 257
- Figure 7.14:** Repeatability of the peak current of sensing of heavy metal ions using (a) CuNRs/FTO and (b) Cu@AgNRs/FTO. Experimental conditions: HMs concentration 10 μM , acetate buffer (pH 5.0), square wave frequency 15 Hz, amplitude 0.02 V, deposition time 90 s, deposition potential -0.5 V, and conditioning time 30 s. 257
- Figure 7.15:** Square wave voltammetry signal for HMs in environmental water samples. Reaction conditions: The frequency was set at 15 Hz and amplitude 0.02 V, deposition time 90 s, and conditioning time 30 s at pH 5. 259
- Figure 7.16:** Ion-chromatographs of (a) River water and (b) Tap water used to prepare the samples spiked with HMs. 259

CHAPTER 1

Introduction, Literature Review and Research Objectives

This chapter presents the general introductory information about the metal nanoparticles, various synthesis approaches and catalytic properties. A concise review of the bioinspired approaches of metal nanoparticles synthesis and application in electrochemical sensing of various organic and inorganic pollutants is presented in this chapter.



1.1. Nanotechnology: History and background

1.1.1 History of nanotechnology

The use of Nanotechnology dates way back to 4th Century AD with the famous example of “The Lycurgus Cup” developed by the Romans. The cup was made up of glass embedded with gold and silver alloy nanoparticles that changed colours depending on the lighting conditions. During 9th-17th century, various coloured ceramics and glass panes have been found to contain nanoparticles like gold, silver, copper and alloys of them. In 1857, Michel Faraday was the one who demonstrated the peculiar optical and electronic properties of gold colloids in one of his famous publications in the Philosophical transactions, that showed that gold colloids exhibited different coloured solutions at different lighting conditions (Faraday, 1857). In the Modern Era, Sir Richard Adolf Zsigmondy, an Austrian-Hungarian Chemist, one of the pioneers who worked exclusively on colloids proved the heterogeneous nature of colloidal solutions, for which he was awarded Nobel prize in chemistry in the year 1925. He coined the word ‘Nanometer’ explicitly to describe the size of the particles he observed in gold colloids using the slit-ultra microscope which he developed in collaboration with Siedentopf in the 1900s. The concept of nanotechnology was first introduced by the American physicist and Nobel Prize laureate Richard Feynman in 1959 which was further elaborated by the eminent Japanese scientist Norio Taniguchi in the year 1974. He defined Nanotechnology as “Nanotechnology mainly consists of the processing, separation, consolidation, and deformation of materials by one atom or one molecule” (Bayda et al., 2020).

1.1.2 Background of nanotechnology and nanomaterials

Nanotechnology primarily focuses on the synthesis of nanostructured materials by manipulating individual atoms and molecules to build complicated structures as per the requirement for a specific application. The particles behave much differently when their size is close to the range of their constituent atomic dimensions. Nanotechnology could play an important role for the betterment of broad societal goals and improved understanding of nature, increased productivity, better healthcare, and extending the limits of sustainable development. Nanotechnology opens up a broad prospect in health, electronics, agriculture, energy and the environment.

The particle sizes within 1 to 100 nm range by virtue of possessing a large surface to volume ratio come under the periphery of nanomaterials or nanoparticles. To harness the

potential of nanotechnology, we need to control the synthesis of nanoparticles, modify them as per our requirement and study their effect on the environment, health and largely on our society.

Nanotechnology can play an essential role in addressing the challenges posed by the shortage of energy, potable water and agriculture. It has revolutionized the energy sectors with the development of photovoltaic cells (Günes et al., 2007) and organic light-emitting devices based on quantum dots (Pal et al., 2020) as well as carbon nanotubes in composite film coatings for solar cells, increasing their efficiency by two folds (Kongkanand et al., 2007). In the area of hydrogen fuel, nanocatalysts for hydrogen generation (Jiang et al., 2015), novel hydrogen storage systems based on carbon nanomaterials (Jordá-Beneyto et al., 2007) and other applications of nanotechnology have the potential to reduce the energy loads. The safe and efficient ways to store hydrogen, as well as improvements in batteries and supercapacitors, could also be made possible using nanomaterials (Darkrim et al., 2002).

The improvement of quality and carrying capacity of ecosystems, including water in surface bodies, aquifers and soil profile and arresting degradation of natural resources have been made one of the prime schemes incorporated into the Ministry of Rural Development (MoRD), Government of India, in the 12th five-year plan.

In India, the introduction of National Rural Drinking Water Programme (NRDWP) in the 12th plan has proposed the availability of safe drinking water to 55% of rural households at 55 L per capita per day. This program also includes the monitoring and treatment of water to minimize contamination and ensure the potable water supply to all rural households (Greening Rural Development Report MoRD, 2012). It also emphasizes the use of sustainable and renewable methods and sources for water purification.

The key pollutants deteriorating the water quality include microbial contaminants, heavy metals, salinity, endemic and anthropogenic contaminants. Nanotechnology could play an important role in evading these problems with the development and applications like nanomaterial-based sensors for the detection of various contaminants (Wang and Hu, 2009), antimicrobial components based on nanoparticles (Pérez-Díaz et al., 2015), nanoporous catalysts for the degradation of micropollutants like pesticides (Shi et al., 2015), herbicides (Santacruz-chávez et al., 2015) and nanoparticles in water purification systems (Kunduru et al., 2017).

Agriculture in India plays an essential part in the economic wellbeing of our society. Nano fertilizers have been developed that slowly release the nutrients and help in the

efficient use of water and fertilizers by plants (Naderi and Danesh-Shahraki, 2013). Nanostructured pesticides for targeted release of anti-pest components without much affecting the environment have been developed and have shown greater efficiency than conventional pesticides (Kah, 2015). Nanosensors for soil quality detection and plant health monitoring have also been developed (Kar et al., 2012).

To address the goals of achieving sustainable development of the society by using nanoparticles, it is vital to explore and devise techniques for their synthesis, characterization and applications. It is crucial to further study and design strategies for successfully implementing nanoparticles in the development of sensors, biological and medicinal applications, or applications in electrochemical catalysis. The following sections shall describe the various synthesis techniques of nanoparticles, their applications and strategies used by researchers to find out knowledge gaps and set objectives to further research.

1.2. Nanoparticles and their classifications

Nanoparticles are classified based on their size, morphology, chemical and physical properties. The various types of nanoparticles are briefly described in the following sections.

1.2.1 Ceramic nanoparticles

Ceramic nanoparticles are oxides, carbides, carbonates and phosphates of various inorganic elements. These nanoparticles are known to possess great thermal resistance and are inert against most chemicals. Ceramic nanoparticles have been applied in photocatalysis (Baaloudj et al., 2021), photo-degradation of dyes (Mortazavi-derazkola et al., 2015), drug delivery (Moreno-Vega et al., 2012), and imaging (Zako et al., 2015). They perform as a good drug delivery agent by slight tweaking of their size, morphology and surface to volume ratio (Moreno-Vega et al., 2012). These nanoparticles are used successfully in drug delivery systems for the treatment of diseases like cancer and bacterial infections, etc. Mesoporous silica nanoparticles decorated with magnetite nanoparticles are used for the targeted delivery of anticancer drug doxorubicin (J. E. Lee et al., 2010). However, the synthesis requires toxic chemicals and reagents and a few reports have shown concern on the cytotoxic properties of these nanoparticles (Singh et al., 2016).

1.2.2 Polymeric nanoparticles

Polymers nanoparticles are organic nanoparticles forming nanocapsules or nanospheres by virtue of their synthesis processes. A nanosphere has a matrix-like form where the active compounds and the polymer are uniformly dispersed. Whereas in the case of nanocapsules, it possesses a core-shell structure with the active compounds bound within the polymer shell in the core.

Polymeric nanoparticles have the advantages of controlled release and protection of drug molecules as compared to ceramic nanoparticles. The ability to combine therapy and imaging towards specific targeting makes polymer nanoparticles preferably more attractive than ceramic nanoparticles. The polymeric nanoparticles being biocompatible and biodegradable provides a sustainable alternative to ceramic nanoparticles towards drug delivery. These nanoparticles have limited applications confining specifically to drug and gene delivery (Li et al., 2013). A small change in temperature can trigger morphological changes in the polymeric nanoparticles and this property is harnessed for targeted drug delivery in a diseased body (Bawa et al., 2009). The disadvantages of these polymeric nanoparticles are the monomers are generally toxic, and the degradation of such polymers sometimes generates toxic end products (Lockman et al., 2002).

1.2.3 Semiconductor nanoparticles

Semiconductor nanoparticles having properties of both metals and non-metals can be found in groups II-VI, III-V or IV-VI of the periodic table. The large bandgaps of these nanoparticles can be tuned easily to perform various applications based on our requirements. They are used in photocatalysis (Pascariu et al., 2018), photo-optics (Born et al., 2016) and water splitting applications (Sathish et al., 2006). Gallium nitride (GaN), gallium phosphide (GaP), indium phosphide (InP), indium arsenate (InAs) from Group III-V, zinc oxide (ZnO), zinc sulphide (ZnS), cadmium sulphide (CdS), cadmium selenide (CdSe), cadmium telluride (CdTe) are II-VI semiconductors, and silicon and germanium from Group IV are few of the examples of semiconductor nanoparticles being used extensively. Organic semiconductor heterojunction nanoparticles have been used for photocatalytic hydrogen evolution reactions. The photocatalysts showed very high H₂ evolution rate of over 60,000 $\mu\text{mol}\cdot\text{h}^{-1}\cdot\text{g}^{-1}$ under visible light (Kosco et al., 2020). ZnS nanoparticles with amine functional groups on the surface have been synthesized and applied for the fluorescence sensing of 2,4,6-trinitrotoluene (TNT) (Wang et al., 2012). The

process of synthesis of these nanoparticles often requires costly, toxic reagents and harsh lab conditions.

1.2.4 Lipid-based nanoparticles

Lipid nanoparticles are usually spherical in shape with a diameter of between 10 and 100 nm. It consists of a rigid centre composed of lipids and other soluble lipophilic molecules that constitute the nanoparticles matrix. This matrix is then stabilized by using suitable surfactants and emulsifiers for the intended use in the biomedical field as a drug transporter, transmission and release of RNA in cancer therapy and as a contrast enhancer in molecular imaging (García-Pinel et al., 2019; Li and Szoka, 2007; Mulder et al., 2006). Paclitaxel/Epigallocatechin gallate loaded lipid nanoparticles of average diameter 130 nm were used to deliver the drugs to the cancer cells (Ramadass et al., 2015). Similarly, Oliveira et al. (2018) developed magnetic solid lipid nanoparticles and demonstrated the triggered release of Paclitaxel at the affected location with the magnetic induction of hyperthermia at the affected location.

These nanoparticles are highly unstable and a slight change in the surrounding may lead to particle aggregation and change in size (Hanumanaik et al., 2013). They are seldom used in electrochemical sensors due to mechanical instability and low tolerance to a dynamic environment.

1.2.5 Carbon-based nanoparticles

Carbon-based nanoparticles include carbon nanotubes (CNTs), fullerenes and carbon dots (CDs). CNTs are sheets of graphene folded into a tube. These materials being 100 times stronger than steel, are most often used as structural supports. CNTs may be categorized as single-walled carbon nanotubes (SWCNTs) and multi-walled carbon nanotubes (MWCNTs). CNTs are thermally conductive along the length and non-conductive around the tube. Fullerenes, on the other hand, are a hollow cage structure of sixty or more carbon atoms. They have commercial applications due to their high electrical conductivity and mechanical stability. The use of harmful reagents demands sophisticated lab installations for the synthesis of these materials.

CDs, on the other hand, can be synthesized sustainably from organic biomass wastes (Zhou et al., 2012) and other sustainable sources and comparatively milder reaction conditions and do not require any harmful chemical for its synthesis (Silva et al., 2011). This has drawn the attention of researchers to explore the properties and applications of

CDs in various fields like bio-imaging (Sun et al., 2006), fluorescence sensors (Wang et al., 2009), etc. This special class of carbon structure presents a great potential to be used in electrochemical sensing applications. First, CDs can have a huge surface area providing ample active sites for analytes to adsorb. Second, CDs can be conveniently synthesized in a simple path, with cheap raw materials, and without the use of sophisticated equipment. More specifically, because the prepared CDs-based substance already has a mass of hydrophilic functional groups, no specific alteration is needed to impart hydrophilic properties to the CDs. This is a major benefit, since these functional groups may be the reason why CDs adsorb pollutants (Zhang et al., 2019). CDs modified GCE have shown successful electrochemical sensing of adrenaline with very high selectivity and sensitivity. They concluded the presence of hydroxyl functional groups imparted a negative charge to the electrode surface that allowed the adsorption of cationic adrenaline hence increasing the sensitivity of the sensor (Shankar et al., 2019). Similarly, screen-printed electrodes (SPEs) modified with CDs could successfully detect Fe(II) ions with an LoD of 0.44 mg/L (Tan et al., 2017). Ghorbani-Bidkorbbeh et al. (2010) modified GCE with CDs to detect naltrexone (NAL) with an LoD of 0.1 μM by using differential pulse voltammetry (DPV). Though CDs are well known for their applications in fluorescence sensors, recently people are exploring the applicability of CDs in electrochemical sensing.

1.2.6 Metal nanoparticles

1.2.6.1 Catalytic activities of metal nanoparticles

Metal nanoparticles (MNPs) are known to function as catalysts for different types of chemical reactions. The catalytic sites are mostly situated on the surface atoms of MNPs. The ratio of surface atoms increases with the decreasing particle size. In other words, the smaller the particle size greater is its catalytic activity of the MNPs (Zhou et al., 2010). MNPs need to be stabilized. Otherwise, they could coagulate easily and form aggregates that are less effective in catalyzing a reaction. Advantages of using MNPs as catalysts are the following:

- MNPs dispersed in solution generally catalyze reactions at temperatures below the boiling point of the solvent.
- MNPs are transparent to light; hence if dispersed in solutions can be used as photocatalysts effectively.

- A slight modification in the reaction conditions could produce MNPs with a plethora of sizes and shapes as per the catalytic requirements for a given reaction.
- MNPs immobilized on solid supports could catalyze the reactions even involving the gaseous reactants.
- Bimetallic and alloy MNPs also can be easily prepared by modifying the structures and compositions.

1.2.6.2 Antimicrobial activity of MNPs

Many metals and metal oxide nanoparticles possess antimicrobial activities. Silver exhibits excellent antimicrobial activities by inhibiting enzymatic systems of the respiratory chain and by altering the DNA replication process (Hernández-Sierra et al., 2008). ZnO nanoparticles also show antibacterial effects against various types of bacteria. It has also been found that, in the presence of AgNPs, the antimicrobial activity of many commercially available antibiotics increases against both gram-positive and gram-negative bacteria (Hernández-Sierra et al., 2008).

Similarly, low-cost metal oxide nanoparticles of ZnO, SnO₂, CuO, NiO, and Fe₂O₃ have also been found to be potent for antimicrobial applications (Li et al., 2008; Meena Kumari and Philip, 2015; Talebian and Zavvare, 2014). Talebian and Zavvare (2014) showed the effectiveness of solvo-thermally synthesized SnO₂ nanoparticles against *E. coli* at different lighting and ambient conditions.

Researchers have also shown the antimicrobial activity of bimetallic nanoparticles (Banerjee et al., 2011; Malika et al., 2016; Valodkar et al., 2011). Banerjee et al. (2011) synthesized bimetallic Au-Ag core-shell nanoparticles. They reported a better antimicrobial activity against both gram-positive and gram-negative bacteria as compared to the individual nanoparticles. However, basic research and exploration of antimicrobial activity of bimetallic or mixed metal oxide nanoparticles need to be done to obtain an effective formula of nanoparticles. The antibacterial activity of different metal and metal oxide nanoparticles is summarized in Table 1.1.

Metals are highly toxic to many bacteria and fungus at low concentrations. Based on the nature and property of the metal, the antibacterial mechanism depends on its reducing potential and the metal donor atom selectivity (Palza, 2015). A metal could generate reactive oxygen species within the cell membrane that could damage the cell genomic material and hamper the protein synthesis. Some metal nanoparticles trigger the

Fenton reaction and produce reactive free hydroxyl radicals that interfere in the enzymatic process of the cell. Figure 1.1 describes the possible mechanisms of antimicrobial behaviour. In the case of CuO nanoparticles, the bactericidal activity mostly depends on the soluble ion release within the cell membrane that causes cytotoxicity by interacting with the metalloprotein complexes (Gunawan et al., 2011).

Possible routes of antimicrobial activity of nanoparticles are adhesion of nanoparticles onto the bacterial cell surface and acting as catalytic cofactors in either generating or catalyzing reactive oxygen species (ROS). The formation of free radicals within the cell and the release of metal ions by nanoparticles within the cell acts by attacking the genomic DNA or by interfering with the activities of the signalling protein cascades, and metal oxides react by the release of metal ions or by forming complexes with polypeptides.

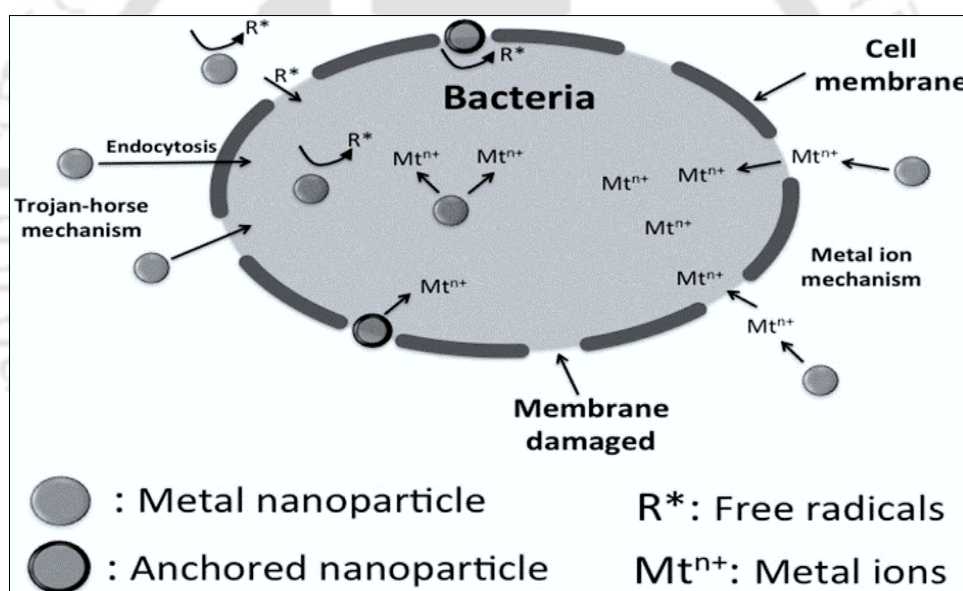


Figure 1.1: Mechanism of antimicrobial activity of nanoparticles (adapted from Palza (2015) with permission from mdpi.com).

Table 1.1: Nanoparticles and their size-dependent antimicrobial activities.

Nanoparticle	Synthesis Technique	*Size (nm)	Antimicrobial stains	Remarks	Sources
Ag	Biosynthesis	13.4	<i>E. coli, S. aureus</i>	MIC for <i>E. coli</i> is 6.6 nM and MIC for <i>S. aureus</i> is 33 nM	Kim et al., 2007
Au	Biosynthesis	18-56	<i>E. coli, S. aureus, S. epidermidis</i>	21.51% inhibition at 0.2 mM AuNP and 52.98% inhibition at 1 mM concentration	Sreekanth et al., 2014
Pd	Pyrolysis	2 - 3	<i>E. coli, S. aureus</i>	10 ⁻⁹ M of PdNPs shows microbial inhibition and more effective against <i>S. aureus</i>	Adams et al., 2014
Al ₂ O ₃	Biosynthesis	34.5	<i>P. aeruginosa (MDR strain)</i>	MIC at 1600 µg/mL and complete inhibition at >2000 µg/mL	Ansari et al., 2015
ZnO	Biosynthesis	25	<i>E. coli, S. mutans</i>	1 mm inhibition zone for <i>E. coli</i> and 3.2 mm for <i>S. mutans</i> (10 µg/mL)	Issa et al., 2015
MgO	Hydro-thermal	Nano wires 6-8 nm dia	<i>E. coli, Basillus spp.</i>	Gram positive bacterial less susceptible than gram negative bacteria	Al-Hazmi et al., 2012
SnO ₂	Biosynthesis	2.1-4.1	<i>E. coli</i>	Positive inhibitory effect on <i>E. coli</i>	Vidhu and Philip, 2015
CuO	Biosynthesis	6-8	<i>E. coli, K. aerogenes, P. desmolyticum, S. aureus</i>	IC ₅₀ of CuO NP is 566 µg/mL	Udayabhannu et al., 2015
Fe ₂ O ₃	Biosynthesis (Fungus mediated)	80	<i>D. congelesis</i>	MIC observed at >2000 µg/mL	Atef et al., 2016
TiO ₂	Enzyme assisted	25-50	<i>E. coli, S. aureus</i>	MIC for both strains 62.5 µg/mL	Ahmad et al., 2014

*Particles are usually spherical in nature except for the study by Al-Hazmi et al. (2012)

From Table 1.1, it can be observed that the antimicrobial activity of different metal and metal oxide nanoparticles mainly depends on two factors that is the size of the nanoparticles and the reducing potential of the parent metal element in consideration.

1.2.6.3 Medicinal and therapeutic uses of MNPs

Nanoparticles are extensively tested in drug delivery because of their unique property of solubility, drug release capability and immunogenicity. Many materials ranging from biodegradable polymeric nanoparticles (Soppimath et al., 2001), mesoporous silica (Gary-Bobo et al., 2012; Slowing et al., 2008), noble metal nanoparticles (Ghosh et al., 2008) and chitosan-based nanocarriers (Agnihotri et al., 2004) have successfully been used as the medium for drug delivery and cancer therapeutics. Silver nanoparticles synthesized by photocatalytic reduction of Ag⁺ ions have been used to formulate an antimicrobial and

antifungal gel (Jain et al., 2009). Kunjachan et al. (2015) developed Au nanoparticles modified with PEG and tagged with near-infrared imaging agent (AF647) that specifically attach themselves to tumor cells and, the affected area could be identified using IR imaging for radiation therapy. Yang et al. (2006) developed magnetic poly ethyl-2-cyanoacrylate (PECA) nanoparticles of size 250 ± 15 nm that could successfully deliver anticancer drug Ciplastin to a point target under controlled mobility induced by external magnetic fields.

1.3 Approaches of MNPs synthesis

Nanoparticles often show diverse physical, chemical and biochemical characteristics compared to their bulk counterparts (Vidhu and Philip, 2015). There are many established techniques for the fabrication of nanoparticles that are used based on the quality and characteristics required for their end applications. The size, stability, morphology and characteristics of nanoparticles strongly depend on the preparation methods and experimental conditions (Yin et al., 2003). The so-called techniques of nanoparticle fabrication are summarized in Figure 1.2. A brief description of the techniques commonly used to synthesize nanoparticles is described in the subsequent sections.

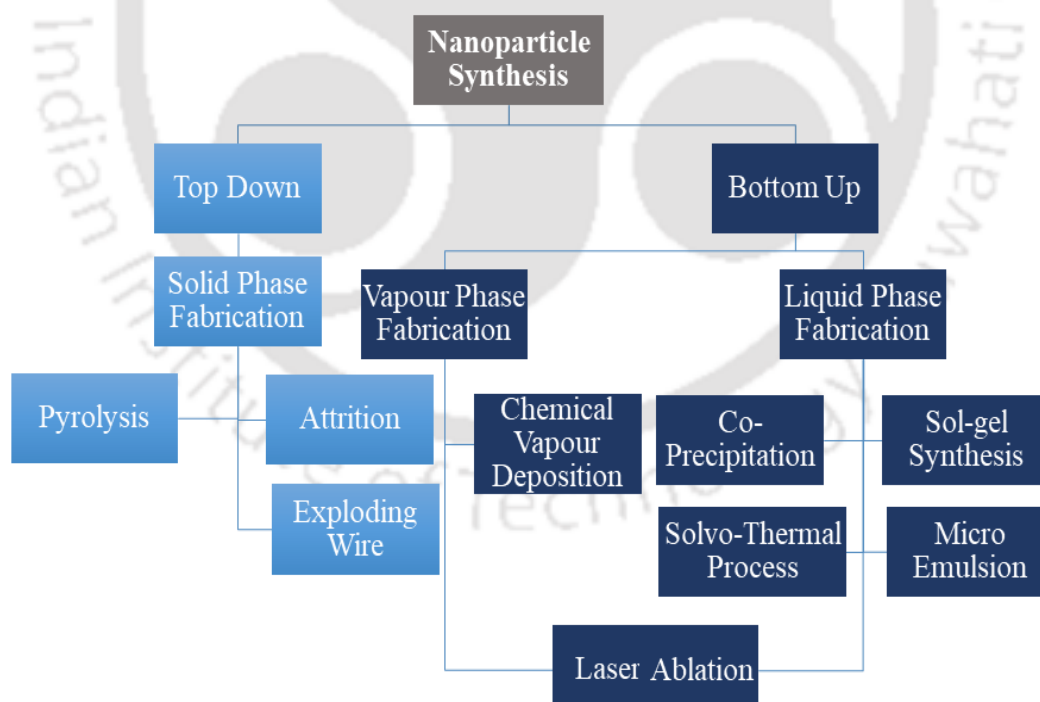


Figure 1.2: Typical methods for the fabrication of nanoparticles.

1.3.1 Top-down approach

1.3.1.1 Flame spray pyrolysis

Liquid feed-flame spray pyrolysis (LF-FSP) is one of the most recent developments in flame spray pyrolysis (FSP) technology. In FSP, nano metal oxide powders could be produced by oxidizing highly volatile gaseous metal chlorides in an oxygen-hydrogen flame. FSP can be used to produce a wide array of high purity nano-powders ranging from single metal oxides such as alumina or titania to more complex mixed oxides and catalysts. The technique is first developed by a research group of Sotiris E. Pratsinis at ETH Zurich, Switzerland (Strobel and Pratsinis, 2007).

There are two flame pyrolysis methods practiced in the laboratory scale, i.e., flame aerosol synthesis (FAS) and flame spray pyrolysis (FSP). In FAS, metal precursors are dissolved in an appropriate solvent, and the solvent vapour is carried into the flame environment by a carrier gas followed by gas to particle conversion. FSP, on the other hand, is more versatile as it uses liquid precursors producing particles of more complex compositions.

Grossmann et al. (2015) synthesized Pt doped TiO₂ particles by slight modification in the pyrolysis reactor using the double nozzle spray method, as shown in the image (Figure 1.3a). They were also able to produce various heterogeneous nanoparticles by using this double spray pyrolysis method. Images of few synthesized nanoparticles by this method are depicted in Figures 1.3b to 1.3d.

Many types of nanomaterials have successfully been synthesized by this process and also been reported for their applications in different fields like the use of copper oxide nanoparticles formed by FSP for the photo-electrochemical splitting of water to produce hydrogen (Chiang et al., 2012), calcium phosphate nanoparticles and their use in the enhancing the osteogenic differentiation in stem cells (Ataol et al., 2015), defluorination of water using Al₂O₃ nanoparticles synthesized by FSP (Tangsir et al., 2016), and the use of titania nanoparticles in solar and photo-electrochemical catalysis (Tantis et al., 2016). This method though shows promising results in the large scale production of nanoparticles but, the method is fairly expensive and requires a lot of energy inputs.

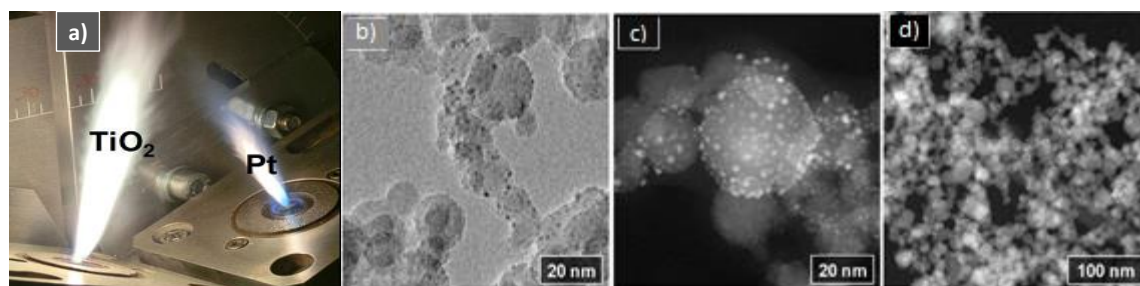


Figure 1.3: (a) Image showing the experimental setup for the synthesis of the nanoparticles using double nozzle flame spray pyrolysis, and (b-d) TEM and High-angle annular dark-field (HAADF) STEM images of Pt doped TiO₂ nanoparticles. Reprinted from Grossmann et al. (2015) with prior permission. Copyright 2015 Springer Nature.

1.3.1.2 Attrition

It is a top-down process of synthesis of nanoparticles. In this process, the bulk material is taken and is crushed in high-energy ball mills to downsize the particles into nanostructures. The kinetic energy of the grinding medium like steel or tungsten carbide ball beads is transferred into the coarse particles whose nanomaterials are desired. The sample is placed in a drum with a controlled atmospheric environment which rotates at a very high rpm imparting its kinetic energy to the material through the grinding medium (Figure 1.4a).

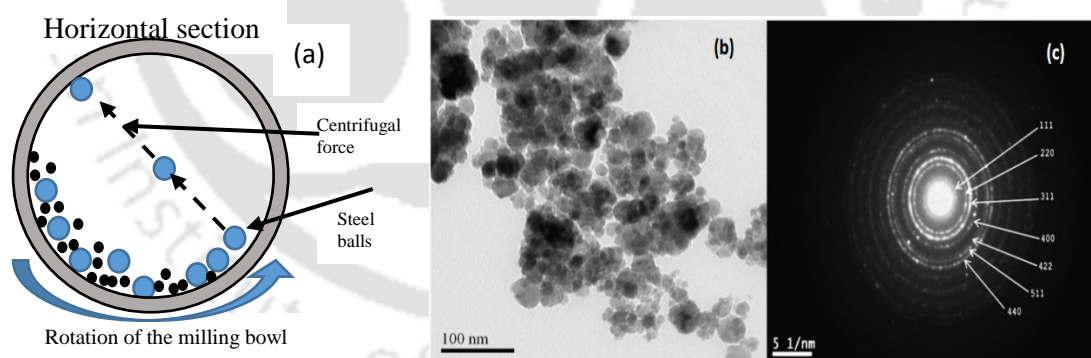


Figure 1.4: (a) Schematic diagram of attrition process, and (b & c) Hexagonal wurtzite ZnO nanoparticles of average size of 15 nm. Figures 1.4b & 1.4c reprinted from Chen et al. (2012) with prior permission. Copyright 2012 Elsevier.

The bulk production of nanoparticles can easily be achieved through this approach. The process is comparatively more straightforward and can be used effectively where high purity of nanoparticles is not required. Chakka et al. (2006) fabricated Fe, Co and FeCo bimetallic nanoparticles using high energy ball milling with the assistance of surfactants to

obtain 30 nm nanoparticles with a very narrow particle size distribution. Zhang et al. (2014) obtained Ni ferrite nanoparticles of wide size distribution. Chen et al. (2013) found MnFe_2O_4 nanoparticles with an average diameter of 20 nm using high-energy microwave-assisted ball milling (Figures 1.4b-1.4c). Hexagonal wurtzite ZnO nanoparticles of an average size of 15 nm were prepared by microwave-assisted ball milling, and it was used in photocatalytic applications (Chen et al., 2012).

This process has certain drawbacks, such as there could be a significant variation in the particle size distribution (Figure 1.5). There is a chance of contamination of the product with various components. During the ball milling process, severe plastic deformation of the sample material leads to the formation of defects and dislocations in the structure of nanoparticles as well (Valiev et al., 1996).

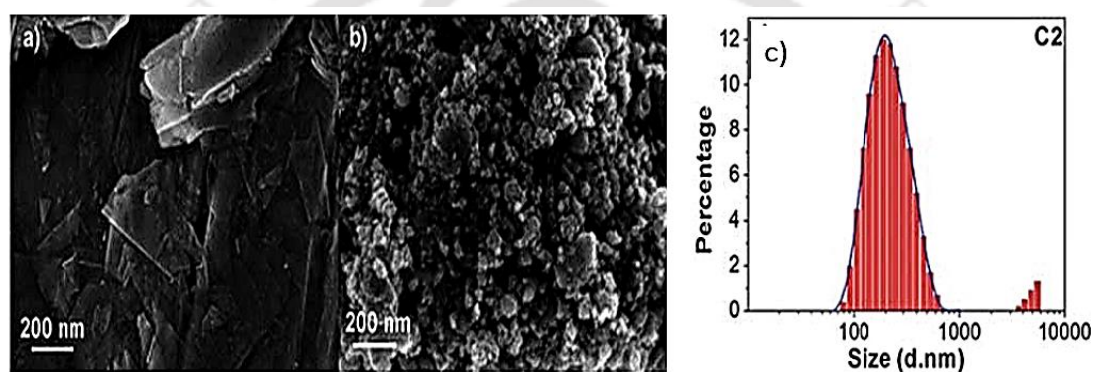


Figure 1.5: (a) SEM image of starting graphite material, (b) Ball milled particles, and (c) Particle size distribution of nitrogen-doped carbon nanoparticles prepared by high energy attrition process showing a wide range of particle size distribution. Reprinted from Xing et al. (2013) with prior permission.

1.3.1.3 Exploding wire

In this process, high-density current is passed through the metal wire such that the energy exceeds the binding energy of the metal atoms, and the wire explodes, giving rise to a vapour of the metal wire. This method is highly productive, and nanoparticles up to 200 g/h with particle sizes ranging from 20 to 100 nm have successfully been demonstrated (Kotov, 2003). This technique is employed for fabrications of Ag, Fe, Cu and Al metal nano-powders. Sato et al. (2015) showed the effect of carrier gases in the process while fabricating Pd nanoparticles. They found that Ar as a carrier gas produces the smallest particle with the size of 16 nm followed by N_2 and He gases. Lerner et al. (2016) synthesized bimetallic nanoparticles of Ag-Cu, Al-Pb and Cu-Pb using twisted metal wires and obtained core-shell type bimetallic nanoparticles with different degrees of superheating

of wires. The images of nanoparticles obtained by the exploding of Pd/Cu wires are given in Figure 1.6. The main advantage of this technique is that high purity nanoparticles can be produced, but the process is highly energy extensive and requires energy as high as 25 kWh/kg. The synthesized metal vapour is pyrophorous in nature and immediately oxidizes with a minute contact with air. Hence, it needs to be stored in an inert gas environment which adds to the running cost of the process (Kotov, 2003).

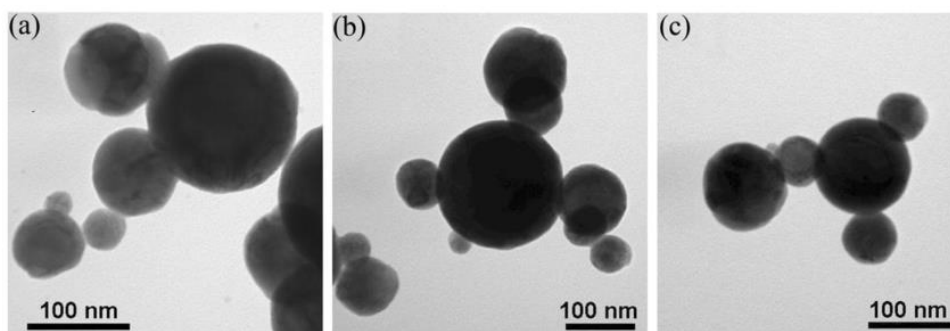


Figure 1.6: Images showing the nanoparticles (Pb/Cu) size with different degree of superheating (W_m): (a) $W_m=1.1$ average particle size of 95 nm, (b) $W_m=1.6$ average particle size of 92 nm and, and (c) $W_m=2.4$ average particle size of 72 nm. Reprinted from Lerner et al. (2015) with prior permission. Copyright 2015 Elsevier.

1.3.1.4 Laser ablation

This is an alternative bottom-up approach for the synthesis of nanoparticles in which a bulk metal target is vaporized by using a high-intensity laser beam. The vapour is then condensed to obtain the nanoparticles. The target metal is immersed in a solvent, and it directly produces nano colloids. If the metal is placed in an inert air chamber, the process follows the principle of chemical vapour deposition (CVD). The rapid formation of Au colloids by the pulsed laser ablation method has been successfully demonstrated by Wagener et al. (2011). The experimental images, as depicted in Figure 1.7, show the progress of real-time nano gold formation. The effect of different solvents on the Pd nanoparticles produced by laser ablation has been studied by Cristoforetti et al. (2012). The nanoparticles obtained are smaller in the case of acetone and alcohol (3-5 nm) than that of water (6.7 nm). However, the nanoparticles produced in toluene and 2-propanol were unstable, and 50-60% of the nanoparticles were degraded within one month. The main advantage of this system is that it doesn't require any metal precursor solution and produces bare nanoparticles without any surface ligands. The continuous gas phase laser ablation

process suffers from rapid agglomeration that limits its applications in many processes (Werner et al., 2008).

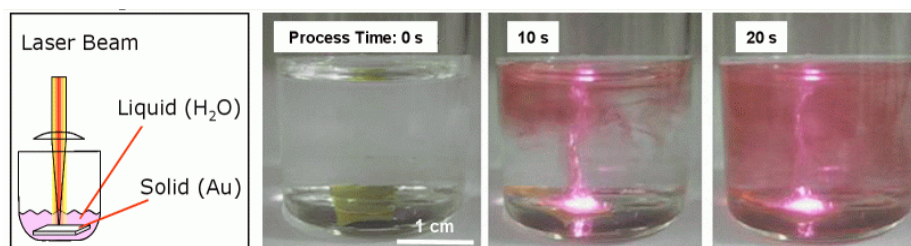


Figure 1.7: Au nano-colloid synthesis by laser ablation method. Reprinted from Wagener et al. (2011) with prior permission. Copyright 2011 Royal Society of Chemistry.

1.3.2 Bottom-up approach

1.3.2.1 Co-precipitation technique

Co-precipitation is a phenomenon where a solute typically remains dissolved, is precipitated out on a carrier and tends to bind together rather than remaining dispersed. The reaction also leads to agglomeration and crystalline growth during calcination (Vichery et al., 2013). Wang et al. (2002) synthesized NiO, ZnO and SnO₂ nanoparticles via the co-precipitation method using metal chloride salts in aqueous solutions. Gaikwad et al. (2005) prepared pure ultrafine single-phase SrBi₂Nb₂O₉ nanoparticles by co-precipitation method. Ammonium hydroxide and ammonium oxalate are used to precipitate Sr²⁺, Bi³⁺ and Nb⁵⁺ simultaneously. This method is used for the commercial production of various nanoparticles. Elhalil et al. (2016) demonstrated the efficiency of fluoride removal using double-layered magnesium and aluminium oxide nanoparticles prepared by the co-precipitation method. They also confirmed that the enhanced adsorptive capacity shown by the use of sonication could assist the co-precipitation process. Oves et al. (2015) synthesized cobalt doped zinc oxide nanoparticles by this method using ZnCl₂ and CoCl₂ as precursors at pH 1.5. They obtained the particles of size ranging between 20 and 55 nm (Figure 1.8). The size of the ZnO nanoparticles decreases with increased Co dosage and shows an increase in antimicrobial activity with increased cobalt dose.

This is a simple technique where homogenous mixing of reactants is possible, and the reaction typically occurs at lower temperatures. Particles formed by this process are generally lower in purity and do not work well if the reactants have different solubility and precipitation rates (Xu et al., 2006). In most cases, the calcination of the prepared nanoparticles is required before using them.

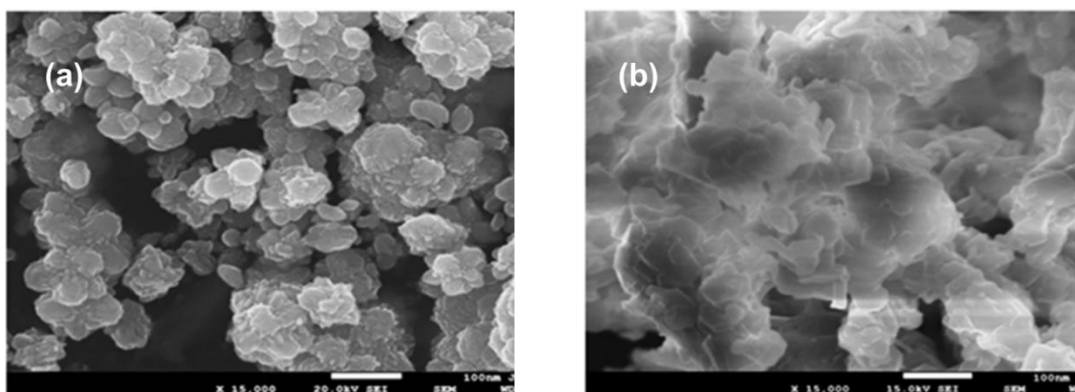


Figure 1.8: Doped zinc oxide nanoparticles synthesized by co-precipitation method: (a) 5% Co, and (b) 1% Co (scale 100 nm). Reprinted from Oves et al. (2015) with prior permission. Copyright 2015 Elsevier.

1.3.2.2 Sol-gel process

The sol-gel process can be defined as the hydrolysis and condensation of a liquid precursor on a solid support. This method is used for the production of metal oxides, mainly the oxides of silicon and titanium. It involves both physical and chemical processes, i.e., hydrolysis, polymerization, gelation, condensation, drying and densification (Brinker and Scherer, 1990).

The sol-gel process is similar to that of co-precipitation. The main difference is the formation of a polymer precipitate instead of fine-grained powders obtained by co-precipitation. As the pH of the solution increases, the repulsive force between particles reduces, which leads to spontaneous coagulation of particulate gels. The hydrolysis and condensation reactions are generally catalyzed by the addition of acids or bases like HCl, CH₃COOH, HF, NH₃, KOH, etc.

The schematic representation of all available routes of nanoparticle synthesis by this process has been well described by Samiey et al. (2014) in their published review paper on different synthesis techniques of organic and inorganic hybrid polymers (Figure 1.9).

Alagiri et al. (2012) published a paper describing the detailed procedure for the synthesis of NiO nanoparticles by using the sol-gel process with polysaccharide agarose as the gelling agent. NiO nanoparticles are of the size of around 3 nm. Other nanoparticles like magnetic oxide nanoparticles of homogenous size as low as 8 nm have successfully been synthesized by sol-gel method (Alagiri et al., 2012). The use of the non-hydrolytic sol-gel process for the synthesis of TiO₂ nanocrystals for the utilization of solar photocatalyst has been demonstrated by Leong et al. (2014). 2,4-Dichlorophenol is

degraded under natural sunlight using these synthesized nanoparticles. This process produces uniform-sized nanoparticles with lower size ranges at a lower calcination temperature. The main disadvantage of sol-gel routes is that the processes are costly with low yields. It also requires the use of surfactants and coordinating solvents as stabilizing ligands which prevents agglomeration of nanoparticles within themselves. The uses of ligands can also help in controlling the surface properties of the nanoparticles.

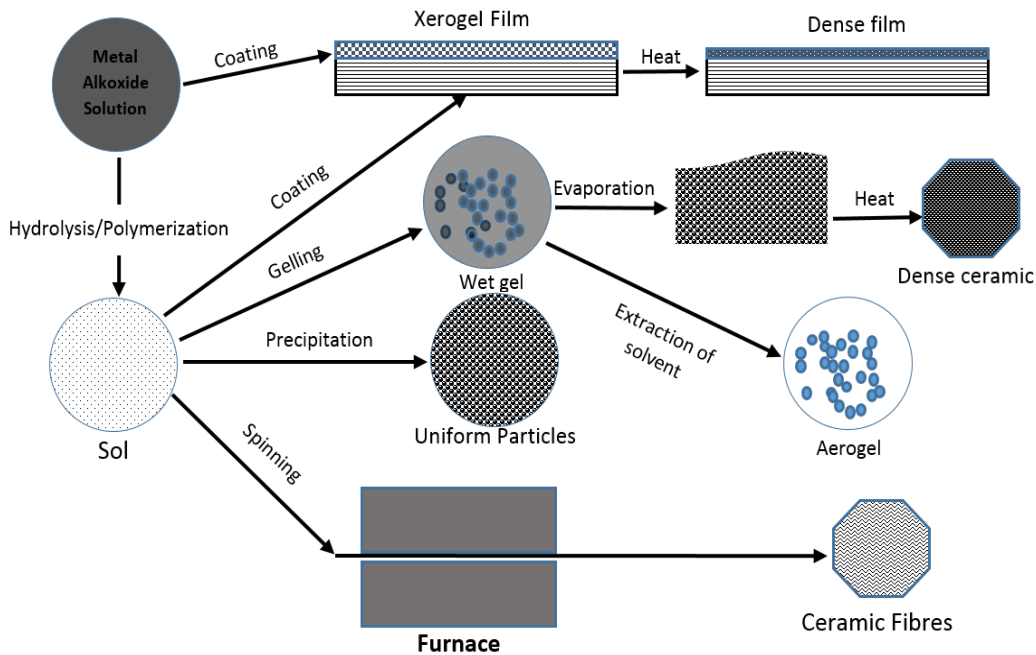


Figure 1.9: Schematic representation of a typical sol-gel process (Samiey et al., 2014).

1.3.2.3 Solvothermal method

Typically, the solvothermal method uses solvents like ethanol, toluene and water for the synthesis of zeolites, inorganic open frame structures and other solid materials (Figure 1.10a). The synthesis reaction is carried out under moderate to high pressure ranging between 1 and 10,000 atm and temperature 100-1000°C (Iwamoto and Inoue, 2008). In hydrothermal synthesis, water is used a solvent, and the synthesis is usually performed below the supercritical temperature of water (374°C). The properties of the solvent, such as density, viscosity and diffusion coefficient, is changed radically under solvo(hydro)thermal conditions with a little variation in the temperature or pressure, and the solvent behaves much differently from what is expected under ambient conditions. The process is used to prepare thin films, bulk nano-powders and single nanocrystals. Akhtar et al. (2010) have successfully fabricated PbS nanoparticles by solvothermal methods using oleyl amine as a solvent. The complex nanocomposite materials like copper indium gallium

diselenide (CGIS) of size ranging from 20 to 100 nm (Figure 1.10b) have also been synthesized at a faster rate as compared to other processes (Mousavi et al., 2016). Khayatian et al. (2016) successfully prepared Al-doped ZnO nanoparticles over graphene oxide nanoparticles. They found that there is a decrease in the ZnO nanoparticles size with an increase in Al concentration.

The main advantage of this process is that calcination is not required, and the starting material can be inexpensive oxides, hydroxides, chlorides or nitrates. The products obtained from this process are generally crystalline anhydrous with controlled particle size, shape and stoichiometry. The main disadvantages of this process is the use of stabilizing surfactants and maintaining a high temperature, often in the supercritical range of the solvent makes the process very tedious and expensive.

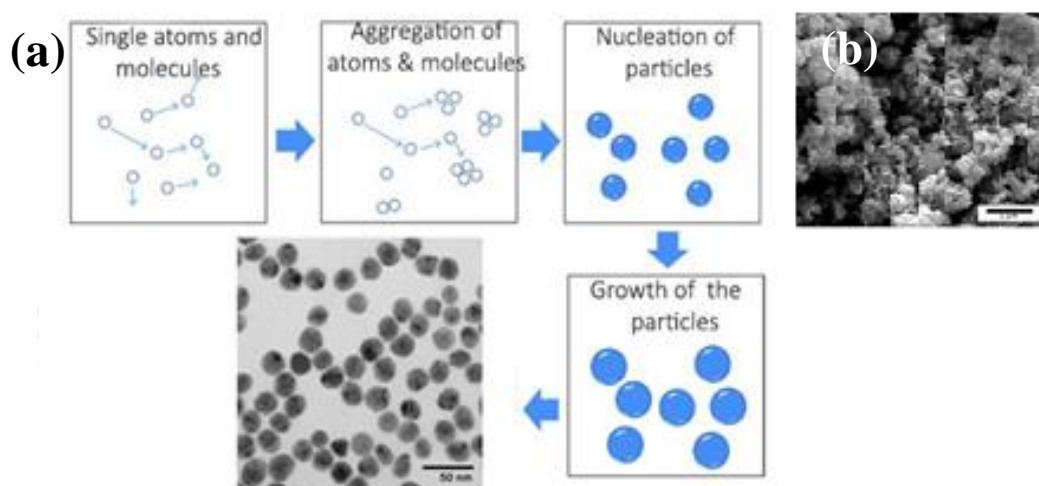


Figure 1.10: (a) Schematic representation of solvothermal growth of nanoparticles, and (b) Image of CIGS nanoparticles synthesized by this process. Reprinted from Mousavi et al. (2016) with prior permission. Copyright 2016 Elsevier.

1.3.2.4 Micro-emulsions mediated synthesis

With the addition of surfactant to a mixture of water and oil, spherical aggregates with the polar heads orienting towards the center are formed known as ‘reverse micelles’ (Figure 1.11). These micelles could act as small reactors that are loaded with ionic metal salts solutions at the hydrophobic core. These micelles thus formed collide with each other due to Brownian motion and could fuse to exchange contents and the nanomaterial synthesis takes place within the core. Now the addition of organically soluble reagents could release the nanoparticles from the micelles and size control synthesis of nanoparticles depends on the intra micellar particle growth (Eastoe and Ellis, 2007).

Pileni and Lisiecki (1993) successfully fabricated Cu and Ag nanoparticles using microemulsion techniques. It is comparatively a greener approach to produce nanoparticles. It is used for the production of a variety of metal and metal oxide nanoparticles and complex ceramic nanomaterials (Sanchez-dominguez et al., 2015). Micro-emulsion is a single phase of all three components, water, oil and surfactant. Sanchez-dominguez et al. (2015) fabricated Zn doped TiO₂ nanoparticles of size less than 20 nm for the enhanced photocatalytic degradation of phenol.

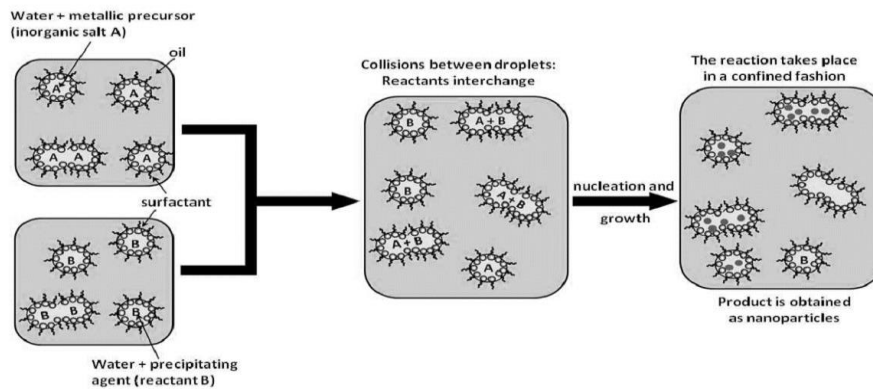


Figure 1.11: Schematic diagram for microemulsion techniques. Reprinted from Sanchez-Dominguez et al. (2012) with prior permission. Copyright 2012 Elsevier.

The maintenance of proper surfactant to water ratio is a crucial parameter in determining the nanoparticles' size and quality (Granata et al., 2015). Hence, there is a control over the particle size and can easily be modified as per the requirements. Latsuzbaia et al. (2015) showed the effect of different surfactants on the particle size for Au and Pt nanoparticles. A typical example for micro-emulsions mediated synthesis of Au nanoparticles is depicted in Figure 1.12. It shows the HRTEM images and the particle size distribution of Au nanoparticles with various surfactants. In the case of Au nanoparticles, the reaction time controls the particle size, but for Pt nanoparticles, the surfactant type governs the particle size. The disadvantage of this process is productivity is quite low, and it is very difficult to separate out the nanoparticles from a biphasic system.

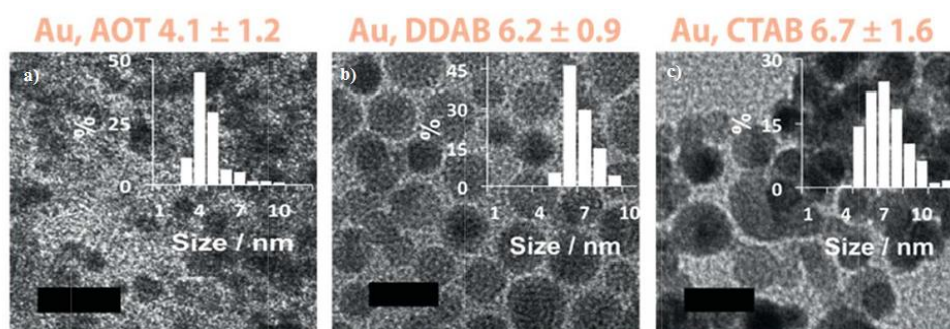


Figure 1.12: Size dependence of Au nanoparticles on the surfactants used for the templating microemulsion: (a) Dioctyl sodium sulfosuccinate (AOT) mediated synthesis, (b) Dodecyl-dimethyl-ammonium bromide (DDAB), and (c) Cetyl trimethyl ammonium bromide (CTAB). Reprinted from Latsuzbaia et al. (2015) with prior permission. Copyright 2015 Elsevier.

1.3.2.5 Chemical vapour deposition

The majority of chemical vapour deposition (CVD) applications involve coatings on solid thin-film surfaces. In this process, the thermal decomposition of a hydrocarbon vapour is carried out in the presence of a metal catalyst. A precursor gas or gases passes into a chamber over the heated object(s) to be coated. Chemical reactions occur on and near the hot surfaces depositing a thin film on the surface. The temperature typically ranges from 200 to 1600°C. Iron nanotubes of diameter ranging from 9.5 to 31 nm supported on magnesia are produced by CVD by Barbinta-Patrascu et al. (2014). Colomer et al. (2000) showed the potential of this process in the large-scale production of single-walled carbon nanotubes by catalytic decomposition of methane gas at 1000°C over well-dispersed metal (Fe, Co, Ni) supported on MgO particles. n-Type doping of thin layer graphene sheets was possible to produce electrically modified graphene sheets (Wei et al., 2009). Pure iron pyrite (FeS_2) layers of nanoparticles are synthesized for application in solar panels as a non-toxic semiconductor material (Samad et al., 2015). The experimental setup used in CVD of FeS_2 is illustrated below in Figure 1.13.

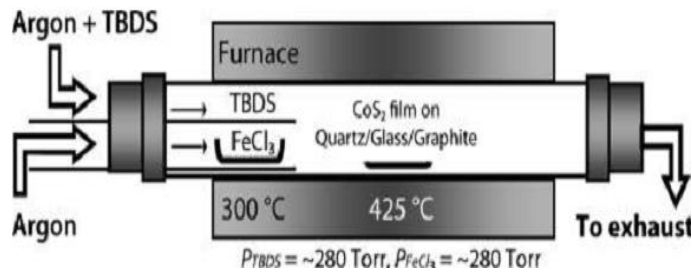


Figure 1.13: Diagram of chemical vapour deposition setup for FeS_2 nanofilms synthesis. Reprinted from Samad et al. (2015) with prior permission. Copyright 2015 American Chemical Society.

The methodology employed in the bioinspired synthesis of nanoparticles comes under the genesis of bottom-up approaches. This work primarily focuses on the implications of bioinspired MNPs in electrochemical sensing of heavy metals ions and selected organic analytes. The state-of-the-art literature survey on the bioinspired synthesis of MNPs and their functionality is outlined in the following sections.

1.4 Bioinspired synthesis of MNPs

Physical and chemical methods mainly involve the use of toxic chemicals, and the process could be expensive as well (Narayanan and Sakthivel, 2010). On the other hand, the biological synthesis of stabilized metal nanoparticles could be achieved by simply utilizing electron-donor analytes present in plant and plant biomasses.

The biosynthesis of nanoparticles can be both intracellular and extracellular. The intracellular synthesis of nanoparticles involves an additional step for the release of nanoparticles from the cell interior to the bulk solution so that they can be recovered for further applications. However, this additional step is not required in the case of extracellular synthesis of nanoparticles. The prerequisites for the bioinspired synthesis (extracellular synthesis) of nanoparticles are shown in Figure 1.14.

A number of research initiatives have been put in the recent past to investigate the bio-reduction efficiency for the synthesis of a variety of metal nanoparticles (MNPs), namely, Ag, Au, Pd, and Pt. It mostly involves the exploration of the reduction capability of bio-chemicals and enzymes present in bacteria, fungi, plant and plant organs. Yong et al. (2002) showed that sulfate-reducing bacteria *D. desulfuricans* are able to synthesize Pd nanoparticles with the help of intracellular enzymes like the formate hydrogenaselyase complex. The nanoparticles they obtained were stable and could act as a catalyst for various

chemical reactions. Fungi-mediated nanoparticle synthesis was reported by Bhainsa and D'Souza (2006). They successfully synthesized extracellularly silver nanoparticles of size ranging from 5-25 nm using fungus *Aspergillus fumigatus* cell extract. Dujardin et al. (2003) used tobacco mosaic virus as organic templates to synthesize various noble metal nanoparticles of Au, Ag and Pt. In addition, the bio-extracts contain natural capping agents that could obstruct the aggregation of particles. Likewise, it could provide better size and shape control of the resulting metal nanoparticles (Shankar et al., 2004), an essential criterion for producing application-specific particles.



Figure 1.14: Prerequisites for the bioinspired synthesis of stable nanoparticles.

1.4.1 MNPs synthesis using bacteria

Green synthesis of MNPs has stepped to be a reliable, cost-effective and environmentally friendly manufacturing method. Nanomaterial applications rely heavily on their particle size. The exploration of the underlying molecular mechanism of MNPs formation is important for controlling the synthesis process for specific applications. Although the underlying MNPs formulation mechanisms have been presented in many studies (Ali et al., 2019), nitrate reductase is typically seen as the primary agent for reduction. The function of catalytic proteins and stabilizers will undoubtedly play an important role in controlling the morphology and crystallinity of nanomaterials.

MNPs can be produced by bacteria either intracellularly by utilizing various intracellular enzymes as reducing and stabilizing agents or extracellularly by releasing

various proteins and radicals to the reaction medium. *Bacillus subtilis* reduced water-soluble Au(III) ions to Au⁰, which produced octahedral AuNPs of 5–25 nm inside the cell walls (Beveridge and Murray, 1980; Southam and Beveridge, 1994). Interestingly, heterotrophic sulfate-reducing bacterial (SRB) found in gold mines could efficiently form AuNPs (<10 nm) in which the reduction of the gold(I)-thiosulphate complex (Au(S₂O₃)₂³⁻) took place into the bacterial envelope. H₂S is released as a metabolic byproduct during AuNPs formation (Lengke and Southam, 2006). It has been reported that *Escherichia coli* DH5 α mediated bioreduction of chloroauric acid to AuNPs, which produced mainly spherical with a small portion being triangular and quasi-hexagon shape (Du et al., 2007). For the synthesis of more than one nanoparticle and bimetallic alloys, a few bacteria have been identified. *Lactobacillus sp.* was found by Nair and Pradeep (2002) to synthesize crystals of microscopic gold, silver and gold–silver alloy in buttermilk without hampering their viability. They produced intracellular hexagonal and triangular shapes of AuNPs and AgNPs and clusters of gold crystals of size between 20 and 50 nm.

Extracellular nanoparticle production has broader applications in optoelectronic, mechanical, bio-imaging and sensor technology in comparison to intracellular formation. *Rhodospseudomonas capsulata*, a prokaryotic cellular organism, was used successfully to reduce Au(III) to Au⁰, with spherical AuNPs mainly in size range of 10–20 nm at pH 7.0 and room temperature (He et al., 2007). However, different types of particles and sizes could be created by adjusting the pH of the solution. Triangular nanoparticles and spherical nanoparticles appeared at pH 4.0. The triangular nanoparticles were 50–400 nm in size and spherical particles 10–50 nm in size. However, the mechanisms and pH-dependent shape and size variation of the synthesized nanoparticles could not be deciphered.

Tedious purification processes and ambiguity of the mechanisms involved in the MNPs synthesis are the major disadvantages associated with the biosynthesis of NPs using bacteria. The key challenges in MNPs biosynthesis often lie in regulating the particle size and shape and in attaining the monodispersity of particles. It seems as if a range of significant technical problems have to be solved before a viable and competitive alternative to this green bio-based approach for industrial MNPs synthesis using bacteria as a tool.

1.4.2 MNPs synthesis using Fungi

Biosynthesis of nanoparticles using Fungi have a greater advantage due to their high tolerance to metal, greater metal-binding capabilities, and intracellular metal uptakes capabilities as compared with other microorganisms such as bacteria (Zhan et al., 2018).

They possess high growth rates and are easier to harvest with low production requirements. In comparison with other microorganisms nanoparticles that are synthesized by fungus are fairly monodispersed and stable (Feroze et al., 2020). Fungi have the ability to secrete large amounts of secondary metabolites, which have the ability to reduce metal ions to metal nanoparticles. Recently, vast fungal flora got the significant interest of research to synthesize biocompatible AgNPs are *Trichoderma resei* (Tomah et al., 2020), *Aspergillus niger* (Farrag et al., 2020), *Fusarium oxysporum* (Dutta et al., 2020). AgNPs were synthesized by using an endophytic fungus *Botryosphaeria rhodina* isolated from the medicinal plant, *Catharanthus roseus* (Linn.). The fungi could produce spherical AgNPs with a particle size distribution of 2-50 nm. These were successfully used as anti-cancer agent against A-549 cell line (Akther et al., 2019).

1.4.3 MNPs synthesis using plant-based extracts

Recent studies in plant-extract-based biosynthesis have excavated a new era of quick and sustainable methods for the manufacture of nanoparticles. MNPs synthesis using plant-based extracts present a plethora of advantages over the use of bacteria and fungi. The extracellularly synthesized nanoparticles using plant extracts are found to be more stable, and the rate of synthesis of nanoparticles is much quicker than that by the microorganisms (Iravani et al., 2011).

Mishra et al. (2015) used *Averrhoa carambola* leaf extract for the formation of stable Ag nanoparticles of size 14 nm (Figure 1.15a). They compared the nanoparticle growth kinetics with dried and fresh leaf extracts, which showed the quicker formation of nanoparticles in fresh leaf extracts. SnO₂ nanoparticles (Figure 1.15b), produced by *S. indica* flower extract exhibited an excellent antimicrobial and antioxidant activity against the particle size variation from 13.1 to 2.1 nm (Vidhu et al., 2015). Patra et al. (2015) demonstrated the production of Au nanoparticles using *B. monosperma* leaf extract (Figure 1.15 c). They obtained a well-dispersed Au nanoparticle of various shapes and sizes (10-30 nm). The crystalline ZnO nanoparticles (Figure 1.15 d) have been synthesized using fresh aloe vera leaf extracts to obtain ZnO with an average particle size of 35 nm (Sangeetha et al., 2011).

Though extensive works have been done in the field of bioinspired synthesis of nanoparticles using plant extracts, a few works have been reported on the synthesis of tailored MNPs. The potential of this method of producing tailored MNPs was demonstrated long back in the year of 2004. Bioinspired synthesis of Ag-Au core-shell nanoparticles

using neem leaves broth (*A. indica*) by co-reduction method was reported. This method produced spherical core-shell nanoparticles that remained stable in solution for 4 weeks. It was proposed that reducing sugars and terpenoids present in the neem leaves broth helped to reduce the Ag and Au precursor salts (Shankar et al., 2004). Similarly, silver nanorods (AgNRs) were successfully synthesized using *Euphorbia prostrata* leaves extract measuring 25-80 nm, with an average length of 52.4 nm (Zahir and Rahuman, 2012). Cubic AgNPs were synthesized by using *Iresine herbstii* leaves extract. However, the reaction took 7 days to complete at room temperature in the dark (Dipankar and Murugan, 2012).

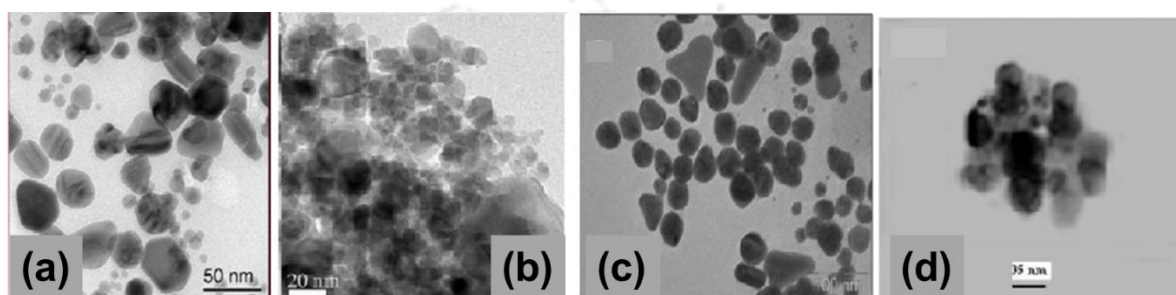


Figure 1.15: TEM micrographs of bioinspired metal and metal oxide nanoparticles: (a) Ag nanoparticles (Mishra et al., 2015), (b) SnO₂ nanoparticles (Vidhu et al., 2015), (c) Au nanoparticles (Patra et al., 2015), and (d) ZnO nanoparticles (Sangeetha et al., 2011). Reprinted with prior permission. Copyright 2015 Elsevier (Figures 1.15a-1.15c) and Copyright 2011 Elsevier (Figure 1.15d).

Though the bioinspired synthesis methods are very sustainable for the production of MNPs, the process is relatively slow and primarily produces polydispersed particles. Therefore, inherent improvements are desired to make the synthesis process faster and to produce nanoparticles with comparable quality as with the chemical counterparts. The parameters, such as pH and synthesis temperature, are tweaked to increase the rate of nanoparticles synthesis (Chelli and Golder, 2016). Microwave (MW) assisted synthesis of nanoparticles has been quite efficient in increasing nanoparticle synthesis rates while confirming with the eco-friendly synthesis strategies.

Furthermore, with MW-assisted methods, the reaction mixture receives homogenous heating with a reduced thermal gradient. This creates a reliable nucleation and growth environment that leads to the formation of nanoparticles with a uniform size distribution (Kumar et al., 2020). Kumar et al. (2020) outlined the advantages of the use of MW in comparison to conventional heating. MW increases the reaction rates, product yield, less production of undesirable secondary compounds, high purity of

materials and high reproducibility. MW-assisted method to prepare silica-covered gold nanoparticles has been reported by Bahadur et al. (2011). In this method, colloidal AuNPs with a uniform SiO₂ coating using the silane capping reagent were formed. Applying sodium citrate as a reducing agent, monodispersed AuNPs (average particle size of 16 nm) were first prepared that acted as the core. Silica was coated on them by using tetraethoxysilane (TEOS) to synthesize Au@SiO₂ core-shell suspension under MW conditions. The development of a sustainable and clean MW-assisted bioinspired synthesis could be of low cost and high productivity method. This could take the advantages of both bioinspired and rapid MW synthesis, bridging the gap between chemical synthesis and bioinspired synthesis of nanoparticles.

1.5 Synthesis of tailored MNPs

Tailored MNPs are a special kind of nanoparticles. It can be synthesized in conventional as well as in bioinspired routes for targeted applications with enhanced functionalities. In comparison with their monometallic counterparts, bimetallic nanostructures could have well-defined morphology and distinct catalytic characteristics. In addition, to minimize the use of precious metals, bimetal electro catalysts can boost the functionality and durability of catalysts. In recent years, several bimetallic nanocrystals have been identified. The activity of tailored MNPs is researched for electrochemical catalytic reactions such as oxygen reduction reactions and alcohol oxidation (Santoveña-Urbe et al., 2021; Yang et al., 2020; Zhang et al., 2017). Owing to their special structures, tailored nanoparticles have received extensive attention compared to monometallic. Tailored MNPs can be synthesized by pulverizing bulk metals (physical method) and particle growth from molecular precursors (chemical method). The chemical methods are better than the physical methods because the MNPs size and stability can easily be tailored according to the requirement.

The tailored MNPs have been synthesized by various methods, including the microwave (Cabello et al., 2017; Njoki et al., 2020), co-precipitation (de Mello et al., 2019), hydrothermal (Liao et al., 2006), ultrasonic (Ghanbari et al., 2017) and microemulsion (Zhang and Chan, 2003), etc. The microwave (MW) dielectric heating is very advantageous for the synthesis of MNPs as the structural aspect can be tailored by controlling the reaction conditions. The catalytic characteristics of the resulting nanoparticles can be greatly enhanced by bimetalization, which is not attainable by using monometallic catalysts. The

electronic effect plays an important role in bimetallic catalysts that defines the charge transfer. The alloying of the constituent elements can lead to morphological modifications in bimetallic nanoparticles, which introduces an extra level of freedom as compared to their monometallic counterparts (Sharma et al., 2015). Yu and He (2015) have shown an enhanced catalytic activity using bimetallic Au-Ag dendritic nanoparticles by chemiluminescent detection of D-glucose through sensing of H₂O₂ produced by the enzymatic activity of glucose oxidase enzyme. Similarly, Ag@Pt core@shell bimetallic nanoparticles have shown an enhanced electrochemical detection of adenine as compared to its individual counterparts (Karthikeyan and Murugavelu, 2012). The incorporation of Sn (24% w/w) into Ni (75% w/w) to form bimetallic alloy nanoparticles shown an elevated chemical reduction of 2-nitroaniline even at mild ambient temperature conditions that was not possible by using Ni nanoparticles alone (Shah et al., 2015).

1.6 Analytical tools and techniques

1.6.1 Conventional techniques for detection of an analyte

Agricultural waste production, industrial sewage, livestock and anthropogenic activities affect clean water, which leads to the reduction in the supply of potable water. Water ecology offers services such as food processing, nutrient cycling and improving soil quality. Infectious diseases are initiated mostly by biological and chemical pollutants present in tap and drinking water. Thus, it is important to develop fast and responsive detection techniques for timely detection and removal of contaminants. This section describes the conventional techniques that are available for the detection of water pollutants and other analytes.

1.6.1.1 UV-vis spectrophotometric techniques

Spectrophotometry is a method where a substance present in the sample is detected by comparing the colour change that arises due to some specific chemical reactions of the analytes or in the presence of some dyes. Generally, the colouration developed is compared with the sample standard to quantify the components. The change in the surface properties of nanomaterials could cause a noticeable change in their apparent colour due to the Surface plasmon resonance (SPR). Many metal ions can cause the aggregation and dispersion state transition of the nanogold probe solution. As a result, the absorbance and colour of the mixed solution can be changed by varying the metal ion concentration (Wu et al., 2015).

The SPR peak position obtained from UV-vis analysis of nanoparticles basically depends on the size of the nanoparticles formed. Bhui et al. (2009) showed that the SPR band of AgNPs at 411 nm after 2 h of reaction is shifted to 460 nm after 6 h of reaction. The SPR peak of AgNPs was directly correlated with the nanoparticle sizes. In our work, UV-vis spectrophotometry was extensively used to study the formation of AgNPs, PtNPs and other MNPs described in various chapters based on their SPR response.

1.6.1.2 Chromatographic techniques

Chromatography is a separation technique in which the sample is separated into its individual components by distribution between two phases, i.e., a stationary phase (solid/liquid) and a mobile phase (liquid/gas). A continuous supply of the mobile phase helps to transport the sample through the stationary phase. As the sample passes through the mobile phase, individual components in the sample get separated based on the relative affinity, molecular structure and intramolecular forces. Chromatography is always done at a condition that is close to the equilibrium or rapid equilibrium. At these conditions, the distribution condition of the analytes solely depends on the molecular structure, the two phases and the temperature. It is a robust analytical tool that is used for the detection of various organic analytes such as toxic organophosphates (Sud et al., 2021), organic acids (Shui and Leong, 2002), pharmaceutical components (Pugajeva et al., 2017) and toxic heavy metal ions (Rekhi et al., 2017).

The main drawback of this technique is that the separation and detection of individual components are possible only if the two components have a separate partition coefficient. In such cases, the desired degree of separation could be achieved by tweaking the mobile phase or the temperature by a trial and error approach.

1.6.1.3 Mass spectrometric techniques

Mass spectrometry (MS) is an effective analytical tool for quantifying known compounds and identifying unknown compounds in a specimen. The technique is also extremely useful in finding out the structure and chemical properties of various molecules. In this process, the samples are converted into gaseous ions, which are then characterized based on their mass-to-charge ratio (m/z) and relative abundances. A mass spectrometer produces several ions from the studied sample, separates them according to their particular m/z ratio, and records the relative abundance of each type of ion. The first step is the generation of gas-phase ions, primarily by electron ionization. The ions are isolated by a

mass spectrometer and detected in proportion to their m/z ratio. The combination of chromatography with mass spectroscopy is a great analytical tool that could detect individual components of analytes to the molecular level. Many emerging contaminants could be detected using the combination of liquid chromatography (LC) and MS systems like pesticides (Liu et al., 2020), polycyclic aromatic hydrocarbons (PAHs) (Baroudi et al., 2020), pharmaceutical compounds (Kachhawaha et al., 2021), etc. However, these instruments are very costly and often involve pre-preparation of samples before analysis. This poses a great problem in the on-field applications of this equipment.

1.6.1.4 Fluorescence techniques

Fluorescence is caused by photons exciting a molecule and elevating it to an excited electronic configuration. In this process, high-energy photons are bombarded on a molecule, and electrons are transferred to the excited singlet states. The aroused molecule then emits a photon of different intensity, and the wavelength is longer than the absorbed photon.

Fluorescence spectroscopy has been used for the detection of microbial contamination (Sorensen et al., 2018), pesticides (Lin et al., 2020) and other emerging pollutants (Ryu et al., 2020; Wasswa et al., 2019). If more than one excited electronic state is present, the only downside of this is often that the studied sample comprises a combination of fluorescing molecules. In addition, due to different local conditions or molecular transitions, different excited species could be produced, which makes the analysis more complicated as these analytes are difficult to interpret.

1.6.2 Sensor-based techniques in analyte detection

The unique optical, electrochemical, and other physical properties of nanoparticles have driven researchers to use nanoparticles for numerous applications like environmental pollutant detection (Chen et al., 2012; Kaur and Gupta, 2009; Wang and Yu, 2013), medicine (Fortina et al., 2007; Salata, 2004), fabrication of semiconductor devices (Schaadt et al., 2005) and photovoltaic or photocatalytic devices (Schaadt et al., 2005). Nanoparticles have several applications because of their unique properties that are quite different from their bulk metals, such as enhanced surface area and many enhanced biocidal properties such as antibacterial, antifungal and even antiviral properties (Bhuyan et al., 2015). This antibiotic property of some metal and metal oxide nanoparticles shows potential for their applications in the field of water and wastewater treatment. Nanoparticles are well known

for their applications in the fabrication of highly sensitive optical, biochemical and electrochemical sensors.

1.6.2.1 Biochemical sensors

Nanotechnology plays an important role in the development of biochemical sensors or simply biosensors by introducing a new group of materials with high stability and reproducibility. The biosensors mainly involve the use of biological entities such as DNA, peptides or proteins, enzymes, and other bio-components for the detection of low molecular weight compounds such as drug or risk chemicals with the nanomaterials acting as matrices for the immobilization of biomolecules and controlling the properties of transducers.

Many biosensors have been developed for the determination of components in body fluids which have revolutionized the identification and treatment of various anomalies. Casero et al. (2014) developed a biochemical sensor-based on bio-nano composites using TiO₂ and lactate oxidase enzyme on graphene oxide nanosheets to determine lactate, which showed a determination limit of 0.6 μ M. Similarly, NiO-modified carbon paste electrodes have also been used for the determination of Nicotinamide adenine dinucleotide hydrogen (NADH), which imparts an improved sensitivity of 0.009 μ M from 0.03 μ M as in conventional carbon paste electrodes (Karimi-Maleh et al., 2014a). Nanomaterials have successfully been used in biosensors for the detection of organophosphorous based pesticides accumulated in the organisms (Zhang and Fang, 2010). Hence, the introduction of nanomaterials into the field of sensing has enabled us to develop better, low-cost and reliable sensors.

1.6.2.2 Optical sensors

Nanoparticles have an amazing property showing the Localized surface plasmon resonance (LSPR) and enhanced Raman effect by scattering light from surface known as Surface Enhanced Raman Scattering (SERS). The optical nanosensors utilize the LSPR that is unique for various metal nanoparticles, and the shift in the LSPR due to interaction with contaminants present in the test sample is detected (Haes et al., 2004). These properties of nanoparticles are exploited to fabricate various optical devices or sensors (Shipway et al., 2000). Weissman et al. (1996) initially developed a crystalline colloidal array that could enable to sense Pb⁺ ions in a solution with a concentration as low as 40 μ g/L to give a change in colour of solution that can be detected by the naked eye. ZnO and TiO₂ nanoparticles have the property to absorb UV light; hence they are used in cosmetics and

UV protecting films on glasses (Kruis et al., 1998). Optical detection of Hg^{2+} ions in liquid samples has successfully been demonstrated using silver nanoparticles with a limit of detection (LoD) of $10 \mu\text{M}$ (Roy et al., 2015). As shown in the images (Figure 1.16), Borase et al. (2015), with an objective to develop low-cost, rapid, sensitive and reliable optical sensors, have successfully used biosynthesized silver nanoparticles for the detection of cysteine in blood plasma, and few other biological samples. They obtained a selective LoD as low as 100 nM .

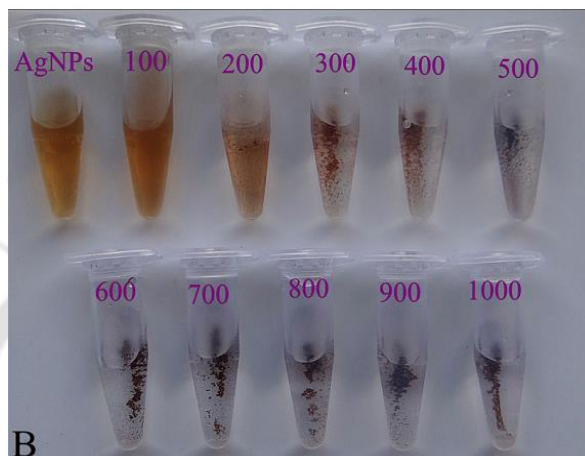


Figure 1.16: Images showing reaction of silver nanoparticles towards different concentrations of cysteine. Reprinted from Borase et al. (2015) with prior permission. Copyright 2015 Springer-Nature.

1.6.2.3 Electrochemical sensing catalyzed by MNPs

The integration of nanotechnology with biology and electrochemistry can create wonders in the field of electrochemical sensors. Metal or semiconductor nanoparticles could be deposited on the working electrode surface by physical adsorption, electro-deposition, or chemical covalent bonding. These modified electrodes help in the deposition of contaminants and lead to specific interactions with the substrate. The advantage of using nanomaterials as components for electrochemical sensors is that nanoparticles decrease the overpotential of some important reactions in the electrochemical analysis. It can also provide reversibility to redox reactions that are not possible in bulk electrodes (Katz and Wang, 2004). The main advantages are: (i) The high surface to volume ratio produces high roughened surface area after they are immobilized onto electrodes (Wang et al., 2010), (ii) Nanoparticles provide the flexibility of tailoring their surfaces according to the properties of the analytes and could be used in developing an electrochemical sensor (Guo and Wang, 2007), (iii) Nanoparticles being structurally robust and highly conductive, enable the design

of electrochemical sensors with controlled electrochemical functions, and (iv) Finally, the specific target binding properties of nanoparticles act as an effective label for electrochemical analysis at infinitesimally low concentration of analytes making the system highly sensitive (Lee et al., 2007).

Ju et al. (2002) used Au nanoparticles doped carbon paste electrodes as a microenvironment that could affect direct electron transfer in redox enzymes for the reduction of H_2O_2 so that it can be detected. Wang and Lin (2005) devised Pt-Fe(III) nanoparticles film for the detection of NO gas without any effect in the presence of many cations and anions. The detection level is as low as 3.5×10^{-5} M NO. Hence, it can be used for NO detection in the field without much difficulty. Similarly, indium SnO_2 films were successfully used as H_2O_2 detector with enzymes immobilized on Au-chitosan nanoparticles (J. Wang et al., 2009). Graphene-ZnO nanocomposites synthesized by rapid microwave irradiation were tested for the preparation of capacitors that show very high capacitance with a very high recycling capacity with a capacitance value of 146 F/g (Lu et al., 2011). Meng et al. (2015) constructed modified Glassy carbon electrodes (GCE) doped with SnO_2 nanoparticles for the detection of Hg^+ ions in the water samples with LOD of 0.001 $\mu\text{g/L}$. Radhakrishnan et al. (2014) tested the use of Fe_2O_3 nanoparticles doped onto graphene sheets to prepare a highly sensitive sensor that can be used for the rapid detection of nitrite from the raw field samples (Figure 1.17).

The biosynthesized metal and metal oxide nanoparticles have also shown their potential in the fabrication of highly sensitive and selective electrochemical sensors. Wang et al. (2010) synthesized Se nanoparticles using *Bacillus subtilis* and obtained nanoparticles with sizes ranging from 50-400 nm. They used these nanoparticles for developing electrochemical sensors for the detection of H_2O_2 . The LoD of the sensor was found to be 8×10^{-8} M. Vidya et al. (2016) synthesized microwave-assisted AgNPs using Banyan leaf extract as reducing agents and used them to develop a sensor for the detection of dopamine in the presence of ascorbic acid and uric acid. The detection limits for dopamine was found to be 0.085 μM .

Nanoparticles show great potential in their application in the field of electrochemical sensors that are more dependable and simple. Table 1.2 highlights the potential use of nanoparticles synthesized in various bottom-up approaches and tested them as sensor components.



Figure 1.17: Schematic representation of working of electrochemical sensor developed by Radhakrishnan et al. (2014). Reprinted with prior permission. Copyright 2015 Elsevier.

Table 1.2: Use of metal nanoparticles as highly sensitive electrochemical sensors.

Nanoparticles	Synthesis technique	Analytes	Performance Analysis	Dynamic range (μM)	LoD (μM)	Sources
Au	Co-precipitation	H ₂ O ₂	<ul style="list-style-type: none"> Stable after three weeks of storage at 4°C, Response time <20 s 	50-30600	20	Zhu et al., 2006
Ag	Sol-gel	H ₂ O ₂	<ul style="list-style-type: none"> Linear range from 1 μM to 1 mM Signal to noise ratio 3 Michaelis-Menten constant of the sensor to H₂O₂ was 1.2 mM, showing a high affinity 	1 - 1000	0.4	Xu et al., 2004
Pd	Electro-deposition	Glucose	<ul style="list-style-type: none"> Relative deviation of determination of glucose (5 mM) was 5% after 14 days Stability loss was 40% after 50 days of storage 	12000	150	Lim et al., 2005
Pt	Co-precipitation	Glucose	<ul style="list-style-type: none"> Response time of 3 s Exhibited a linearity from 0.5 to 5 mM Sensitivity of 2.11 $\mu\text{A}/\text{mM}$ of glucose 	0.5-5000	0.5	Hrapovic et al., 2004
Ni/NiO/Ni(OH) ₂	Pyrolysis/Sputtering	Sugar	<ul style="list-style-type: none"> High sensitivity towards determination of both monosaccharides and disaccharides Excellent electro-catalytic ability and stability at 0.8% Ni as compared to bulk Ni electrode Good reproducibility for 40 consecutive injections of sugar with standard deviation of 1.75% 	Glucose: 0.05-500 Fructose: 0.05-500 Sucrose: 0.10-250 Lactose: 0.08-250	Glucose: 20 Fructose: 25 Sucrose: 50 Lactose: 37	You et al., 2003

Cu	Electro-deposition	Nitrate	<ul style="list-style-type: none"> Linear range of 10-200 μM Sensitivity of 0.085 per M Loses its activity if exposed to air, (might be due to formation of oxide layer of copper that inhibits the nitrate detection) 	10-200	1.5	Welch et al., 2005
ZnO/CNT	Co-precipitation	Hydrazine and Phenol	<ul style="list-style-type: none"> Sensitivity towards the oxidation of hydrazine in the absence of phenol was 18.4860 $\mu\text{A}/\mu\text{M}$ In the presence of phenol was 18.5210 $\mu\text{A}/\mu\text{M}$ Sensitivity of electrode towards the oxidation of phenol in the of hydrazine 0.0565 In presence of hydrazine was 0.0567 $\mu\text{A}/\mu\text{M}$ 	Hydrazine: 0.02-0.7 Phenol: 1.0 -750	Hydrazine: 0.009 Phenol: 0.5	Karimi-Maleh et al., 2014b
SnO ₂ / Graphene oxide	Wet chemical synthesis	Cu, Hg, Pb and Cd	<ul style="list-style-type: none"> Simultaneous and selective detection of analytes could be achieved Minimum response time was 20 s but the optimum was kept at 120 s Sensitivity was better during simultaneous determination as compared to individual determination of analytes 	ND	Cu: 0.00011 Hg: 0.000034 Pb: 0.00018 Cd: 0.000010	Wei et al., 2012

It is evident from the above studies that the size of the nanoparticles and their distribution over the medium is one of the most important characteristics of the nanoparticles in designing electrochemical sensors. The nature of the voltammetric responses depends on the particle size, and by controlling the particle size, the sensing response can be tuned. Table 1.3 describes the functionality of metal and metal oxide nanoparticles with their sizes and shapes for electrochemical sensing of various heavy metal ions (HMIs). The shift in using mercury drop electrodes for HMIs sensing encouraged the use of the less toxic bismuth nanoparticles (BiNPs) modified working electrodes. BiNPs were used for the detection of a wide range of HMIs in different environmental samples. Gold nanoparticles (AuNPs) of different sizes are generally used for the electrochemical sensing of Hg(II) owing to the property of Hg forming amalgam with Au (Tang et al., 2016). The use of AuNPs modified electrodes also helped in reducing the memory effects and enhanced the sensitivity and repeatability of the electrodes (Tonelli et al., 2019). Other noble metal nanoparticles were also successfully used for the electrochemical sensing of HMIs. Biosynthesized silver nanoparticles (AgNPs) were found

to be effective against Pb(II), Cd(II), As(III), Hg(II), etc. Spherical AgNPs with size ranges between 20 and 50 nm have shown better sensing ability due to increased surface area and uniform coverage on the working electrode surface (Table 1.3).

The nanoparticles can also aggregate to increase the effective particle size. It is a well-known fact that larger particles tend to have less catalytic activity compared to smaller monodispersed nanoparticles (Kempahanumakkagari et al., 2017). Therefore, it is desirable to minimize aggregation via functionalization of the NPs, which, in turn, also provides stability to the NPs dispersions. Improved sensitivity and selectivity were shown in the Bi nanoparticle-modified electrode with the decrease in particle size for the electrochemical sensing of Pb(II), Cd(II) and Zn(II), which was attributed to a higher electroactive surface area (G. J. Lee et al., 2010).

A short introduction and literature survey emphasizing the functionality of bioinspired metal nanoparticles for sensing applications is also provided in Chapter 3.

Quantum dots (QDs) have been known to be applied in optical methods of HMIs sensing for few decades (Chini et al., 2019; Liu et al., 2019; Raj et al., 2020). Recently, QDs have also attracted attention towards electrochemical sensing owing to their ability to interact with different HMIs because of their innate ability to surface and edge adsorptions (Li et al., 2018). The high sensitivity and specificity of QDs have attracted attention for HMIs detection. QDs with specific modifications could function for targeted sensing of HMIs. Carbon dots have shown enhanced adsorption of hydrated Cd(II) and Pb(II) ions with the unsaturated carbon atoms at the edges (Subramaniam et al., 2019). This enhanced adsorption of HMIs onto QDs can be harnessed to pre-concentrate HMIs on the electrode surface for an enhanced electrochemical response. The direct use of QDs as electrochemical sensors is limited. However, the use of QDs as signal enhancers has been reported in numerous electrochemical and electroluminescence biosensors (Li et al., 2018; Zhang et al., 2014). Recently, nitrogen-doped graphene QDs (NGQDs) decorated indium tin oxide (ITO) glass substrate was used successfully for the direct electrochemical sensing of Hg(II) ion and obtained an LoD of 10 $\mu\text{g/L}$ (Fu et al., 2020). A concise survey of literature on the synthesis of carbon dots for electrochemical sensing of Chlorpyrifos (CHL) is also added in Chapter 6.

Table 1.3: Nanomaterials of varying sizes and shapes and their effects on electrochemical sensing of HMIs.

NPs	Particle size (nm)	Particle shape	Analytes	LOD ($\mu\text{g.L}^{-1}$)	Electrochemical technique	Reference
BiNPs	100	Spherical	Pb(II) Cd(II) Ni(II)	0.81 0.65 5.47	*SWASV (pH 4.5)	Niu et al., 2015
	50	Spherical	Pb(II) Cd(II)	0.07 0.15	*ASV (pH 5.0)	Lee et al., 2007
AuNPs	20-30	Spherical	Cr(VI)	103.9	Cyclic voltammetry	Tsai and Chen, 2008
	30	Spherical	Hg	0.008	SWASV (pH 5.0)	Gong et al., 2010a
	41	Star	Pb(II) Hg(II) As(III)	20.55 11.08 3.57	SWASV	Dutta et al., 2019
AgNPs	12.2	Spherical	Pb(II) Cd(II)	3.3 3.7	*DPASV (pH 4.5)	Torres-Rivero et al., 2019
	20.4	Prism	Pb(II) Cd(II)	3.4 2.1	DPASV (pH 4.5)	Torres-Rivero et al., 2019
	25.7	Spherical	Pb(II)	2.6	SWASV (pH 5.0)	Dash et al., 2020
	51.1	Spherical	As(III)	0.06	SWASV (pH 5.3)	Dar et al., 2014
	100-300	Oval (nano-nuts)	Pb(II) Cd(II)	0.15 0.10	DPASV	Prakash and Shahi, 2011
PtNPs		Spherical	As(III)	5.68	Cyclic voltammetry	Sanlloriente-Méndez et al., 2009
	4.55	Spherical	Pb(II)	0.45	SWASV (pH 5.0)	Dash et al., 2020
Fe ₃ O ₄ NPs	10-12	Spherical	Hg(II)	20.1	SWASV (pH 5.0)	Deshmukh et al., 2017
	10-12	Spherical	Pb(II)	10.4		
	10-12	Spherical	Cd(II)	1.1		
Ag@PtNPs	24.5	Spherical (Core-shell)	Pb(II)	0.16	SWASV (pH 5.0)	Dash et al., 2020
BiSn@C	20	Spherical	Cd(II)	0.33	SWASV (pH 4.5)	Chen et al., 2019
AuNPs/TiO ₂	10	Spherical	Cr(Vi)	1.6	Amperometry	Jin et al., 2014
AuPtNPs	120	Spherical	Hg(II)	0.1	SWASV	Gong et al., 2010b

*SWASV: Squarewave anode stripping Voltammetry; ASV: Anode stripping voltammetry; DPASV: Differential pulse anode stripping voltammetry

1.6.3 Tailoring MNPs in bioinspired routes and electrocatalytic activity

Many forms of nanoparticles have been used extensively in electrochemical sensors and bio-sensors, including metal nanoparticles, oxide nanoparticles, semiconductor nanoparticles, and even composite nanoparticles. Although these nanoparticles play various roles based on their special properties, the fundamental features of nanoparticles

are primarily classified as (1) biomolecules immobilization-improves sensor stability, (2) electrochemical reaction catalysis-improves sensitivity and selectivity, (3) increased electron transfers kinetics-improves sensitivity, (4) biomolecules labeling-improves sensitivity by indirect detection of electrochemically inert analytes, and (5) acting as an efficient reactant by providing an increased surface area and new reaction mechanism. Tailoring a structure of MNPs mostly falls into the following categories for bimetallic: (i) core-shell nanoparticles, (ii) movable core-shell nanoparticles, (iii) alloy nanoparticles, etc. Figure 1.18 shows various tailored nanoparticles.

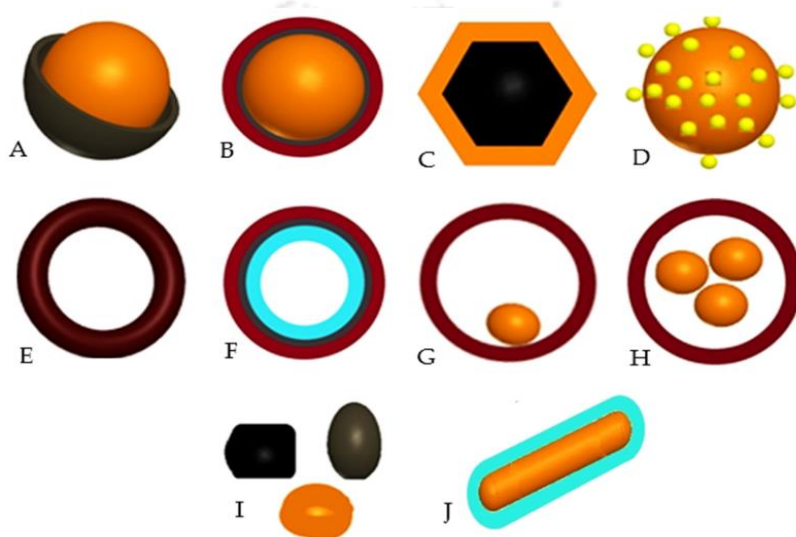


Figure 1.18: Schematic pictures of the different structures of core-shell nanoparticles: (A) Core-shell nanoparticles, (B) Core double-shell particles or core multi-shell nanoparticle, (C) Polyhedral core/shell nanoparticles, (D) Core porous-shell nanoparticles, (E) Hollow-core shell nanoparticles or single-shell nanoparticles, (F) Hollow-core double-shell nanoparticles, (G) Moveable core-shell nanoparticles, (H) Multi-core shell nanoparticles, (I) Irregular shape core shell nanoparticles, and (J) Rod core-shell nanoparticles. Reprinted from Khatami et al. (2018) with permission from mdpi.com.

Bimetallic nanoparticles are expected to exhibit enhanced optical, electronic and chemical or biological properties due to the bi-functional or synergistic effects of both metal constituents. Bimetallic Au@Ag core-shell nanoparticles of 10-60 nm were synthesized using *Antigonon leptopus* extract (Ganaie et al., 2016). Similarly, *Stigmaphyllon ovatum* leaf extract, and *Dovyalis caffra* fruit extract, could successfully synthesize bimetallic Au-Ag nanoparticles that showed effective anticancer effects (Adeyemi et al., 2019; Elemike et al., 2019). Devi and Ahmaruzzaman (2017) used *Momordica charantia* leaves extract to

successfully synthesize complex spherical Au@Ag@AgCl core@double shell nanoparticles and used them to degrade ibuprofen and clofibrac acid present in water.

Though the bioinspired methods are reported in the literature for the synthesis of tailor-made nanoparticles, the reports on their performance in electrochemical sensing are scanty. A brief introduction and underlying literature reviews on the synthesis of tailor-made nanoparticles and composite nanostructures are included at the beginning of Chapter 4 and Chapter 5.

1.7 Fabrication of MNPs based miniaturized sensing device

The analytical techniques, namely, atomic absorption spectrometry (AAS), mass spectrometry (MS), inductively coupled plasma MS (ICP-MS), atomic emission spectrometry (AES), X-ray fluorescence (XRF), etc. are used widely for contaminants analyses and assays. However, there is a need for in-situ analysis of contaminants for better and reproducible results. For example, currently, commercially available heavy metal ions (HMIs) detector kits provide high sensitivity but require image processing (colourimetric analysis using microfluidic paper-based devices) (Morbioli et al., 2017) or the use of molecular recognition probes (Ullah et al., 2018). The sophistication and expense of these commercial kits make them incompetent for in-situ environmental monitoring on a global scale in real-time. On the other hand, the electrochemical methods can be considered as one of the most appropriate methods for in-situ analyses of HMIs primarily due to small instrument size, quick operation, low cost, convenient sample preparation, and ability to perform multi-element detection. There has been much growth in recent years in miniaturization and improved portability of potentiostat units. Beach et al. (2005) developed an implantable and dynamically configurable potentiostat for remote monitoring. Ainla et al. (2018) have recently rationalized potentiostat by developing an open-source universal battery-powered and Bluetooth-connected potentiostat (UWED) capable of providing ample potential ranges for most electrochemical analysis in aqueous solutions. With the availability of portable potentiostats, it is now necessary to develop miniaturized three-electrode electrochemical sensing platforms to detect various water contaminants such as HMIs ions and analytes.

Disposable screen-printed electrodes (SPEs) integrates conventional three electrodes on a non-conducting substrate (like polyethylene terephthalate, polyvinylchloride and ceramic), making it portable, inexpensive, and easy to operate

(Dorledo de Faria et al., 2019). Conductive ink such as graphene (Randviir et al., 2014), gold ink (Määttä et al., 2012), conductive carbon ink (Liao et al., 2019), silver ink (Ghosale et al., 2018), etc. is used to screenprint precisely controlling the layer thickness and the desired computer-generated design of the electrodes to obtain the screen printed electrodes. Various SPEs and other chemically modified SPEs are discussed in detail in the review by Barton et al. (2016). Figures 1.19A and 1.19B describe the process of the fabrication of SPE for HMIs sensing applications. The controlled electrode size enables the use of small sample volumes, and the precise placing of electrodes reduces the signal-to-noise ratio and improves the mass transfer of ions during the deposition phase by using Anodic stripping voltammetry (ASV) for HMIs analysis. SPEs allow fast detection and do not require pretreatment steps like electrode polishing which is usually required in the traditional three-electrode system.

The use of carbon fibre-based SPEs has been extensively used in the determination of HMIs. Figure 1.19C describes the use of various modified SPEs to simultaneously detect an array of HMIs present in a complex matrix. The SPEs were modified with cysteine, antimony and glutathione to detect different HMIs like Pb(II), Cd(II), Tl(I), Bi(II), In(III) and Zn(II). The antimony modified SPEs gave the best results for Zn(II), Cd(II), and Bi(II) with the limit of detection (LoD) of 4.5, 3.2 and 5.2 $\mu\text{g/L}$, respectively. Similarly, LoD of 3.1 $\mu\text{g/L}$ was obtained for Pb(II) using cysteine modified SPEs. However, In(III) and Tl(I) showed the best results with the unmodified commercially available carbon fibre-based SPEs. The obtained LoDs were 3.0 and 6.5 $\mu\text{g/L}$, respectively (Pérez-Ràfols et al., 2017). The method is a very innovative method, but it generates a lot of used SPEs as waste.

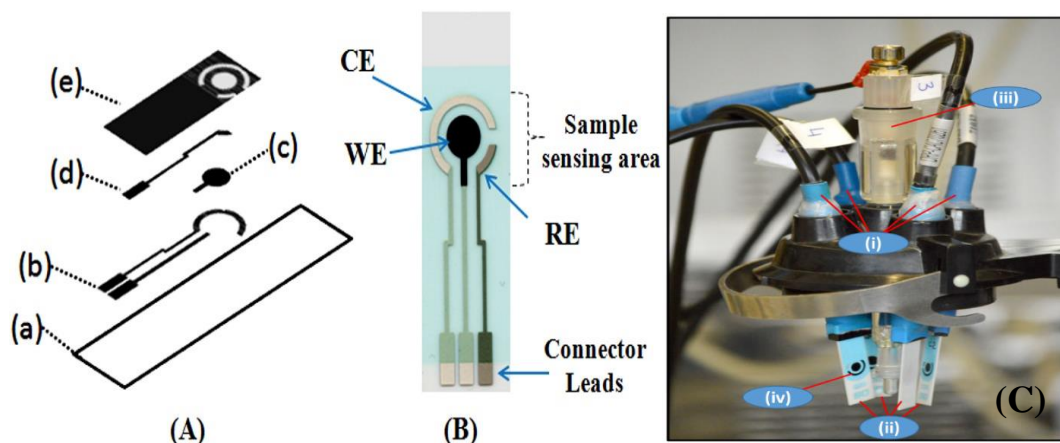


Figure 1.19: (A) Scheme for screen-printing of silver/carbon screen-printed electrode (S/C-SPE)- (a) polyester substrate, (b) silver track, (c) carbon layer, (d) silver/silver chloride track and (e) insulating layer; (B) Screen-printed silver/carbon screen-printed electrode(S/C-SPE); and (C) Modified screen printed electrodes as electrochemical tongue for simultaneous detection of HMIs in a mixed matrix of 4 HMIs and two interferences. Herein (i) denotes connectors to potentiostat, (ii) are three working electrodes, (iii) is the Ag/AgCl electrode and (iv) a blank SPE working as counter electrode. Figures 1.19A and B are reprinted from Jadav et al. (2018) with prior permission. Copyright 2018 Elsevier; Figure 1.19C is reprinted from Pérez-Ràfols et al. (2017) with prior permission. Copyright 2017 Elsevier.

The use of various MNPs modified miniaturized three-electrode systems are known to be successfully used for contaminant detections. MNPs are also capable of tracking other analytes, paving the way for new applications. PtNPs are capable of catalyzing the degradation of small organic molecules, such as ethanol and formaldehyde. Hence PtNPs based SPEs were used for a successful sensing platform for evaluating the quality of wines and beers (Pereira Silva Neves et al., 2017). The affinity of sulfur towards gold provides the prospect of direct identification of sulfur compounds, acquisition of instruments capable of detecting sulfite in beverages (Chen et al., 2016) and free sulfide in tap water (Molinero-Abad et al., 2013), carbofuran in food materials (Jirasirichote et al., 2017), or trazodone (Salama et al., 2018).

The majority of the studies found in the literature provide sensing platforms capable of reaching the permissible LoDs. However, expensive electrode materials are required that can only be found in a research laboratory and it also suffers from multi-elemental interference. Another major problem with the commercial SPEs is that they are generally single-use devices and can produce huge amounts of solid wastes during an extensive in-

situ application. It is therefore essential that research should concentrate on developing portable and cost-effective electrochemical sensing devices to allow for easy, cheap and fast in-field contaminant detection and allowing a fair bit of reusability of the substrate and repeatability of the device.

An introductory section and also a short literature review by emphasizing the fabrication of miniaturized electrochemical sensing devices for MHIs sensing is provided in Chapter 7.

1.8 Indian scenario for synthesis and implications of bioinspired MNPs

The geographical location and favourable climatic conditions have bestowed India with vivid biodiversity. The tropical plants that thrive in India are a rich source of organic acids, polyphenols, flavonoids, amino, vitamins, etc. The availability of these biomolecules in plenty unlocks the hidden potential of them being harnessed for the bioinspired synthesis of various MNPs and other carbon-based nanomaterials like carbon dots that can be synthesized from biomass or biomass wastes. The advantages of plant extract-mediated synthesis of MNPs in India was quickly realized following the first demonstration of synthesis of AuNPs back in the year 1999 using the extract from alfalfa biomass (Gardea-Torresdey et al., 1999). Prof. Murali Sastry and group in National Chemical Laboratory, Pune got themselves involved in the plant-mediated bioinspired synthesis of noble MNPs like AuNPs and AgNPs between the year 2003-2006 using plant extracts like geranium leaves (Shankar et al., 2003) and *Emblica officinalis* fruit extracts (Ankamwar et al., 2005). Further, they could successfully demonstrate the synthesis of Ag-Au bimetallic nanoparticles synthesis and AuNPs with various shapes (Ankamwar et al., 2005; Chandran et al., 2006; Shankar et al., 2005). They also proved that the yield of Au nanotriangles was superior using lemongrass extract compared to chemical synthesis (Shankar et al., 2005). These early demonstrations in India further escalated the bioinspired synthesis of MNPs, and reports of various tailor-made bioinspired nanoparticles started to pop up at various research laboratories in India. AuNPs of triangular, spherical, truncated triangular shapes were reported using coriander leaves extract (Narayanan and Sakthivel, 2008). Au-Ag Bi-metallic alloy nanoparticles using *Spirulina* extract (Govindaraju et al., 2008). Apart from Ag and Au NPs, researchers now started to venture into the synthesis of other MNPs. The synthesis of PdNPs using coffee and tea extracts was reported by Nadagouda and Varma (2008). Similarly, bioinspired synthesis using plant extract has traveled a long way, and

now a synthesis of complex and tailored nanomaterials like core-shell nanoparticles can be achieved possible (Kaur et al., 2018).

1.9 Knowledge gap and thesis objectives

In India, with 1.3 billion people, the demand for clean drinking water is always increasing. Limited availability of clean drinking water and increased industrialization has led to increased ecological demand for the environment. Depletion of groundwater, degradation of the environment and pollution of water bodies due to increased industrialization has created a crisis for the supply of contaminant-free clean water. The increasing population and increased demand for food have led to the excessive use of chemical pesticides, insecticides, and fertilizers that end up in the water bodies and contaminate them with heavy metals like Hg, Cd, Pb, Cu, etc. This creates a threat to the guaranteed availability of safe drinking water to the people. According to a study conducted by the Ministry of Water Resource, India (River Data Directorate Planning & Development Organisation, 2018), 57 stations out of 414 stations at important river basins were identified to contain two or more toxic metals beyond the permissible limit. Water collected from 168, 19, 4, 7 and 63 monitoring stations were considered to be unfit for drinking purposes due to the presence of, respectively, Fe, Cd, Cu, Cr, and Pb beyond the permissible limit. Therefore, it is high time to develop and promote low-cost heavy metal sensing devices that could be used directly by the people to monitor the in-situ water quality and educate the authorities to take proper actions.

The abundance of nanoparticles currently used in electrochemical sensing of contaminants is clear from the available library of reports. However, more focuses need to be drawn towards novel and sustainable approaches for the fabrication of these nanoparticles. A number of studies are reported on the physicochemical and mechanical processes of nanoparticle synthesis and their applications in electrochemical sensing. However, very few approaches show the use of bio-synthesized metal nanoparticles and their applications in electrochemical sensors. The application of such particles in developing electrochemical sensing devices will become increasingly predominant as the pollution control criteria are becoming stringent day by day. The functionalized nanoparticles create an excellent tool in electroanalytical applications for the sensing of the majority of the contaminants. It is vital to capture the analytes of interest before catalyzing its detection. The main challenges faced in electro-analysis are developing a procedure for

the production of nanoparticles in a sustainable way and decorating the working electrode uniformly with those nanoparticles for efficient activity, reproducibility and stability, and must have practical applicability. Herein, this is proposed to be achieved using biosynthesized nanoparticles for the development of electrochemical sensors for quick and effective detection of organic and inorganic analytes.

There are several tropical plants in the Northeastern states of India. The organs of many of such plants are known to have loads of ascorbic acid, polyphenols, flavonoids and other enzymes that could help in reducing the metal ions to their corresponding nanoparticles (Chelli and Golder, 2016; Rao and Golder, 2016; Chakraborty et al., 2017; Das and Golder, 2017). Therefore, the following objectives are taken into consideration in this doctoral work.

- Microwave irradiation to synergize the rate of bioinspired synthesis of silver nanoparticles using *Psidium guajava* leaves extract and electrocatalytic sensing of ascorbic acid
- Bioinspired tailoring toward the synthesis of Ag@Pt core-shell nanoparticles and sensing of Pb(II) with high selectivity
- One-pot bioinspired synthesis of platinum-nanoparticles/graphene nanocomposites and sensing of dipyrone and its metabolic compounds
- Hydrothermal synthesis of carbon dots using *Psidium guajava* leaves biomass for enhanced electrocatalytic sensing of chlorpyrifos organophosphate insecticide
- Fabrication of a miniaturized electrocatalytic sensing platform by depositing silver-coated copper nanorods on fluorine-doped tin oxide for the quantification of heavy metals

1.10 Organization of the thesis

CHAPTER 1: Introduction and background of the work

This chapter presents the general introductory information about the metal nanoparticles, various approaches of their synthesis, catalytic properties, and a review on the bioinspired approaches of metal nanoparticles synthesis and their application in electrochemical sensing of various organic and inorganic pollutants and analytes.

CHAPTER 2: Materials and methodology

This chapter describes the experimental methods, the reagents used, and the equipment employed to characterize and analyze the catalysts and the target analytes, respectively. This chapter also describes the general theory and detailed instructions of all the electrochemical experiments involved in this study.

CHAPTER 3: Synergizing AgNPs synthesis in a bioinspired route using microwave and studies on electrocatalytic sensing of ascorbic acid from biological entities

In this chapter, one-pot synthesis of AgNPs is carried out by using the analytes present in the aqueous extract of *Psidium guajava* leaves. The synthesis reaction was synergized by microwave (MW). The synergy between the MW input powers and the disintegration of capping agents leading to particle aggregation was explored. A fast and reliable method for the bioinspired synthesis of AgNPs was developed to electrocatalyze the sensing of ascorbic acid (AA) found in different biological entities like *Zizhipus maritima* leaves extract and *Sechium edule* fruit extracts.

CHAPTER 4: Bioinspired synthesis of highly structured spherical Ag@Pt core-shell nanoparticles for electrocatalytic Pb(II) sensing

This chapter focuses on the synthesis of highly crystalline and ordered Ag@PtNPs core-shell nanoparticles (NPs) under a short exposure of microwave using the analytes present in the aqueous extract of *Psidium guajava* leaves. The nanoparticles were used for the electrochemical sensing of Pb(II). In the presence of co-ions (Cd(II), Cu(II) and Hg(II) from 0.25-10 μ M), it could effectively determine Pb(II) (with and without spiking) from environmental water samples collected from the river, domestic supply and sewage treatment plant. The effectiveness of the core-shell nanoparticle was compared with their individual counterparts.

CHAPTER 5: Bioinspired synthesis of PtNPs/graphene nanocomposites for electrocatalytic sensing of metabolites of dipyrone

Facile bioinspired synthesis of PtNPs/graphene nanocomposites is performed in this chapter. Graphene used in nanocomposite formulation was synthesized by exfoliation of graphite in water/acetone mixture followed by mechanical shearing using ultrasonication and microwave irradiation. A procedure for the one-pot bioinspired synthesis of

PtNPs/graphene nanocomposites was developed, and the sensing of metabolites of dipyrone was conducted in this chapter.

CHAPTER 6: Electrocatalytic sensing of chlorpyrifos using carbon dots derived from waste *Psidium guajava* leaves biomass

Chlorpyrifos is an organophosphate pesticide. In this study, biocompatible carbon dots (CDs) were synthesized using the hydrothermal method and decorated on the glassy carbon electrode (GCE) for the electrochemical sensing of chlorpyrifos in an aqueous ethanolic solution. A square-wave voltammetric technique was employed for the sensing and quantification of chlorpyrifos, and the fundamental electro-kinetic parameters were determined. The effectiveness of the sensor was tested in various environmental water samples collected from sewage treatment plants and river beds.

CHAPTER 7: Fabrication of a miniaturized electrochemical sensing device using Cu and Cu@Ag nanorods for heavy metals sensing

Chapter 7 reports on the fabrication of fluorine-doped tin oxide (FTO) based miniaturized device using Cu nanorods (CuNRs) and Cu@Ag nanorods (Cu@AgNRs), which were used as electrocatalysts for the detection of Zn(II), Cd(II), Pb(II), and Hg(II) ions present in various environmental samples. The performance of the device was reproducible, and the LoDs were well within the permissible limits.

CHAPTER 8: Conclusions and scopes for future studies

This chapter outlines the salient outcomes of the overall work. The suggestion and recommendations of future work direction are also included based on the experience from the present study.

References

- Adams, C.P., Walker, K.A., Obare, S.O., Docherty, K.M., 2014. Size-dependent antimicrobial effects of novel palladium nanoparticles. *PLoS One* 9. <https://doi.org/10.1371/journal.pone.0085981>
- Adeyemi, J.O., Elemike, E.E., Onwudiwe, D.C., Singh, M., 2019. Bio-inspired synthesis and cytotoxic evaluation of silver-gold bimetallic nanoparticles using Kei-Apple (*Dovyalis caffra*) fruits. *Inorg. Chem. Commun.* 109, 107569. <https://doi.org/10.1016/j.inoche.2019.107569>
- Agnihotri, S.A., Mallikarjuna, N.N., Aminabhavi, T.M., 2004. Recent advances on chitosan-based micro- and nanoparticles in drug delivery. *J. Control. Release* 100, 5–28. <https://doi.org/10.1016/j.jconrel.2004.08.010>
- Ahmad, R., Mohsin, M., Ahmad, T., Sardar, M., 2014. Alpha amylase assisted synthesis of TiO₂ nanoparticles: Structural characterization and application as antibacterial agents. *J. Hazard. Mater.* 283, 171–177. <https://doi.org/10.1016/j.jhazmat.2014.08.073>
- Ainla, A., Mousavi, M.P.S., Tsaloglou, M.N., Redston, J., Bell, J.G., Fernández-Abedul, M.T., Whitesides, G.M., 2018. Open-Source Potentiostat for Wireless Electrochemical Detection with Smartphones. *Anal. Chem.* 90, 6240–6246. <https://doi.org/10.1021/acs.analchem.8b00850>
- Akhtar, J., Malik, M.A., O'Brien, P., Helliwell, M., 2010. Controlled synthesis of PbS nanoparticles and the deposition of thin films by Aerosol-Assisted Chemical Vapour Deposition (AACVD). *J. Mater. Chem.* 20, 6116–6124. <https://doi.org/10.1039/c0jm00830c>
- Akther, T., Mathipi, V., Kumar, N.S., Davoodbasha, M., Srinivasan, H., 2019. Fungal-mediated synthesis of pharmaceutically active silver nanoparticles and anticancer property against A549 cells through apoptosis. *Environ. Sci. Pollut. Res.* 26, 13649–13657. <https://doi.org/10.1007/s11356-019-04718-w>
- Al-Hazmi, F., Alnowaiser, F., Al-Ghamdi, A.A., Al-Ghamdi, Attieh A., Aly, M.M., Al-Tuwirqi, R.M., El-Tantawy, F., 2012. A new large – Scale synthesis of magnesium oxide nanowires: Structural and antibacterial properties. *Superlattices Microstruct.* 52, 200–209. <https://doi.org/10.1016/j.spmi.2012.04.013>
- Alagiri, M., Ponnusamy, S., Muthamizhchelvan, C., 2012. Synthesis and characterization of NiO nanoparticles by sol–gel method. *J. Mater. Sci. Mater. Electron.* 23, 728–732. <https://doi.org/10.1007/s10854-011-0479-6>

- Ali, J., Ali, N., Wang, L., Waseem, H., Pan, G., 2019. Revisiting the mechanistic pathways for bacterial mediated synthesis of noble metal nanoparticles. *J. Microbiol. Methods* 159, 18–25. <https://doi.org/10.1016/j.mimet.2019.02.010>
- Ankamwar, B., Damle, C., Ahmad, A., Sastry, M., 2005. Biosynthesis of gold and silver nanoparticles using *Emblica Officinalis* fruit extract, their phase transfer and transmetallation in an organic solution. *J. Nanosci. Nanotechnol.* 5, 1665–1671. <https://doi.org/10.1166/jnn.2005.184>
- Ansari, M. a, Khan, H.M., Alzohairy, M. a, Jalal, M., Ali, S.G., Pal, R., Musarrat, J., 2015. Green synthesis of Al₂O₃ nanoparticles and their bactericidal potential against clinical isolates of multi-drug resistant *Pseudomonas aeruginosa*. *World J. Microbiol. Biotechnol.* 31, 153–64. <https://doi.org/10.1007/s11274-014-1757-2>
- Ataol, S., Tezcaner, A., Duygulu, O., Keskin, D., Machin, N.E., 2015. Synthesis and characterization of nanosized calcium phosphates by flame spray pyrolysis, and their effect on osteogenic differentiation of stem cells. *J. Nanoparticle Res.* 17, 95. <https://doi.org/10.1007/s11051-015-2901-0>
- Atef, A., Mahmoud, H.K., Hesham, T., El, R.M.H.S., 2016. Herbal Biosynthesis of Zinc Nanoparticles and Evaluation of Their Antifungal and Antibacterial Effect for Buffaloes Skin. *Int. J. Curr. Res.* 7, 24338–24349. <https://doi.org/http://www.journalcra.com>
- Baaloudj, O., Nasrallah, N., Kebir, M., Khezami, L., Amrane, A., Assadi, A.A., 2021. A comparative study of ceramic nanoparticles synthesized for antibiotic removal: catalysis characterization and photocatalytic performance modeling. *Environ. Sci. Pollut. Res.* 28, 13900–13912. <https://doi.org/10.1007/s11356-020-11616-z>
- Bahadur, N.M., Watanabe, S., Furusawa, T., Sato, M., Kurayama, F., Siddiquey, I.A., Kobayashi, Y., Suzuki, N., 2011. Rapid one-step synthesis, characterization and functionalization of silica coated gold nanoparticles. *Colloids Surfaces A Physicochem. Eng. Asp.* 392, 137–144. <https://doi.org/10.1016/j.colsurfa.2011.09.046>
- Banerjee, M., Sharma, S., Chattopadhyay, A., Ghosh, S.S., 2011. Enhanced antibacterial activity of bimetallic gold-silver core-shell nanoparticles at low silver concentration. *Nanoscale* 3, 5120. <https://doi.org/10.1039/c1nr10703h>
- Barbinta-Patrascu, M.E., Ungureanu, C., Iordache, S.M., Bunghez, I.R., Badea, N., Rau, I., 2014. Green silver nanobioarchitectures with amplified antioxidant and antimicrobial properties. *J. Mater. Chem. B* 2, 3221–3231. <https://doi.org/10.1039/c4tb00262h>

- Baroudi, F., Al-Alam, J., Chimjarn, S., Delhomme, O., Fajloun, Z., Millet, M., 2020. Conifers as environmental biomonitors: A multi-residue method for the concomitant quantification of pesticides, polycyclic aromatic hydrocarbons and polychlorinated biphenyls by LC-MS/MS and GC-MS/MS. *Microchem. J.* 154, 104593. <https://doi.org/10.1016/j.microc.2019.104593>
- Barton, J., García, M.B.G., Santos, D.H., Fanjul-Bolado, P., Ribotti, A., McCaul, M., Diamond, D., Magni, P., 2016. Screen-printed electrodes for environmental monitoring of heavy metal ions: a review. *Microchim. Acta* 183, 503–517. <https://doi.org/10.1007/s00604-015-1651-0>
- Bawa, P., Pillay, V., Choonara, Y.E., du Toit, L.C., 2009. Stimuli-responsive polymers and their applications in drug delivery. *Biomed. Mater.* 4, 022001. <https://doi.org/10.1088/1748-6041/4/2/022001>
- Bayda, S., Adeel, M., Tuccinardi, T., Cordani, M., Rizzolio, F., 2020. The history of nanoscience and nanotechnology: From chemical-physical applications to nanomedicine. *Molecules* 25, 1–15. <https://doi.org/10.3390/molecules25010112>
- Beach, R.D., Conlan, R.W., Godwin, M.C., Moussy, F., 2005. Towards a miniature implantable in vivo telemetry monitoring system dynamically configurable as a potentiostat or galvanostat for two- and three-electrode biosensors. *IEEE Trans. Instrum. Meas.* 54, 61–72. <https://doi.org/10.1109/TIM.2004.839757>
- Beveridge, T.J., Murray, R.G.E., 1980. Sites of metal deposition in the cell wall of *Bacillus subtilis*. *J. Bacteriol.* 141, 876–887. <https://doi.org/10.1128/jb.141.2.876-887.1980>
- Bhainsa, K.C., D'Souza, S.F., 2006. Extracellular biosynthesis of silver nanoparticles using the fungus *Aspergillus fumigatus*. *Colloids Surfaces B Biointerfaces* 47, 160–164. <https://doi.org/10.1016/j.colsurfb.2005.11.026>
- Bhui, D.K., Bar, H., Sarkar, P., Sahoo, G.P., De, S.P., Misra, A., 2009. Synthesis and UV-vis spectroscopic study of silver nanoparticles in aqueous SDS solution. *J. Mol. Liq.* 145, 33–37. <https://doi.org/10.1016/j.molliq.2008.11.014>
- Bhuyan, T., Mishra, K., Khanuja, M., Prasad, R., Varma, A., 2015. Biosynthesis of zinc oxide nanoparticles from *Azadirachta indica* for antibacterial and photocatalytic applications. *Mater. Sci. Semicond. Process.* 32, 55–61. <https://doi.org/10.1016/j.mssp.2014.12.053>
- Borase, H.P., Patil, C.D., Salunkhe, R.B., Suryawanshi, R.K., Kim, B.S., Bapat, V. a., Patil, S. V., 2015. Bio-Functionalized Silver Nanoparticles: a Novel Colorimetric Probe for Cysteine Detection. *Appl. Biochem. Biotechnol.* 3479–3493.

<https://doi.org/10.1007/s12010-015-1519-0>

- Born, B., Geoffroy-Gagnon, S., Holzman, J.F., 2016. An investigation of semiconductor nanoparticles for application to all-optical switching, in: Betz, M., Elezzabi, A.Y. (Eds.), SPIE 9746, Ultrafast Phenomena and Nanophotonics XX., p. 97460E. <https://doi.org/10.1117/12.2208638>
- Cabello, G., Davoglio, R.A., Hartl, F.W., Marco, J.F., Pereira, E.C., Biaggio, S.R., Varela, H., Cuesta, A., 2017. Microwave-Assisted Synthesis of Pt-Au Nanoparticles with Enhanced Electrocatalytic Activity for the Oxidation of Formic Acid. *Electrochim. Acta* 224, 56–63. <https://doi.org/10.1016/j.electacta.2016.12.022>
- Casero, E., Alonso, C., Petit-Domínguez, M.D., Vázquez, L., Parra-Alfambra, A.M., Merino, P., Álvarez-García, S., de Andrés, A., Suárez, E., Pariente, F., Lorenzo, E., 2014. Lactate biosensor based on a bionanocomposite composed of titanium oxide nanoparticles, photocatalytically reduced graphene, and lactate oxidase. *Microchim. Acta* 181, 79–87. <https://doi.org/10.1007/s00604-013-1070-z>
- Chakka, V.M., Altuncevahir, B., Jin, Z.Q., Li, Y., Liu, J.P., 2006. Magnetic nanoparticles produced by surfactant-assisted ball milling. *J. Appl. Phys.* 99. <https://doi.org/10.1063/1.2170593>
- Chakraborty, S., Chelli, V.R., Das, R.K., Giri, A.S., Golder, A.K., 2017. Bio-mediated silver nanoparticle synthesis: mechanism and microbial inactivation. *Toxicol. Environ. Chem.* 99, 434–447. <https://doi.org/10.1080/02772248.2016.1214271>
- Chandran, S.P., Chaudhary, M., Pasricha, R., Ahmad, A., Sastry, M., 2006. Synthesis of gold nanotriangles and silver nanoparticles using Aloe vera plant extract. *Biotechnol. Prog.* 22, 577–583. <https://doi.org/10.1021/bp0501423>
- Chelli, V.R., Golder, A.K., 2016. pH dependent size control, formation mechanism and antimicrobial functionality of bio-inspired AgNPs. *RSC Adv.* 6, 95483–95493. <https://doi.org/10.1039/C6RA16475G>
- Chen, D., Zhang, Y., Kang, Z., 2013. A low temperature synthesis of MnFe₂O₄ nanocrystals by microwave-assisted ball-milling. *Chem. Eng. J.* 215–216, 235–239. <https://doi.org/10.1016/j.cej.2012.10.061>
- Chen, D., Zhang, Y., Tu, C., 2012. Preparation of high saturation magnetic MgFe₂O₄ nanoparticles by microwave-assisted ball milling. *Mater. Lett.* 82, 10–12. <https://doi.org/10.1016/j.matlet.2012.05.034>
- Chen, L., Xie, H., Li, J., 2012. Electrochemical glucose biosensor based on silver nanoparticles/multiwalled carbon nanotubes modified electrode. *J. Solid State*

- Electrochem. 16, 3323–3329. <https://doi.org/10.1007/s10008-012-1773-9>
- Chen, Y., Zhang, D., Wang, D., Lu, L., Wang, X., Guo, G., 2019. A carbon-supported BiSn nanoparticles based novel sensor for sensitive electrochemical determination of Cd (II) ions. *Talanta* 202, 27–33. <https://doi.org/10.1016/j.talanta.2019.04.066>
- Chen, Y.H., Kirankumar, R., Kao, C.L., Chen, P.Y., 2016. Electrodeposited Ag, Au, and AuAg nanoparticles on graphene oxide-modified screen-printed carbon electrodes for the voltammetric determination of free sulfide in alkaline solutions. *Electrochim. Acta* 205, 124–131. <https://doi.org/10.1016/j.electacta.2016.04.111>
- Chini, M.K., Kumar, V., Javed, A., Satapathi, S., 2019. Graphene quantum dots and carbon nano dots for the FRET based detection of heavy metal ions. *Nano-Structures and Nano-Objects* 19, 100347. <https://doi.org/10.1016/j.nanoso.2019.100347>
- Colomer, J.F., Stephan, C., Lefrant, S., Van Tendeloo, G., Willems, I., Kónya, Z., Fonseca, A., Laurent, C., Nagy, J.B., 2000. Large-scale synthesis of single-wall carbon nanotubes by catalytic chemical vapor deposition (CCVD) method. *Chem. Phys. Lett.* 317, 83–89. [https://doi.org/http://dx.doi.org/10.1016/S0009-2614\(99\)01338-X](https://doi.org/http://dx.doi.org/10.1016/S0009-2614(99)01338-X)
- Cristoforetti, G., Pitzalis, E., Spiniello, R., Ishak, R., Giammanco, F., Muniz-Miranda, M., Caporali, S., 2012. Physico-chemical properties of Pd nanoparticles produced by Pulsed Laser Ablation in different organic solvents. *Appl. Surf. Sci.* 258, 3289–3297. <https://doi.org/10.1016/j.apsusc.2011.11.084>
- Dar, R.A., Khare, N.G., Cole, D.P., Karna, S.P., Srivastava, A.K., 2014. Green synthesis of a silver nanoparticle-graphene oxide composite and its application for As(III) detection. *RSC Adv.* 4, 14432–14440. <https://doi.org/10.1039/c4ra00934g>
- Darkrim, F.L., Malbrunot, P., Tartaglia, G.P., 2002. Review of hydrogen storage by adsorption in carbon nanotubes. *Int. J. Hydrogen Energy* 27, 193–202. [https://doi.org/10.1016/S0360-3199\(01\)00103-3](https://doi.org/10.1016/S0360-3199(01)00103-3)
- Das, R.K., Golder, A.K., 2017. Co₃O₄ spinel nanoparticles decorated graphite electrode: Bio-mediated synthesis and electrochemical H₂O₂ sensing. *Electrochim. Acta* 251, 415–426. <https://doi.org/10.1016/j.electacta.2017.08.122>
- Dash, S.R., Bag, S.S., Golder, A.K., 2020. Synthesis of highly structured spherical Ag@Pt core-shell NPs using bio-analytes for electrocatalytic Pb(II) sensing. *Sensors Actuators, B Chem.* 314, 128062. <https://doi.org/10.1016/j.snb.2020.128062>
- de Mello, L.B., Varanda, L.C., Sigoli, F.A., Mazali, I.O., 2019. Co-precipitation synthesis of (Zn-Mn)-co-doped magnetite nanoparticles and their application in magnetic hyperthermia. *J. Alloys Compd.* 779, 698–705.

<https://doi.org/10.1016/j.jallcom.2018.11.280>

- Deshmukh, S., Kandasamy, G., Upadhyay, R.K., Bhattacharya, G., Banerjee, D., Maity, D., Deshusses, M.A., Roy, S.S., 2017. Terephthalic acid capped iron oxide nanoparticles for sensitive electrochemical detection of heavy metal ions in water. *J. Electroanal. Chem.* 788, 91–98. <https://doi.org/10.1016/j.jelechem.2017.01.064>
- Devi, T.B., Ahmaruzzaman, M., 2017. Bio-inspired facile and green fabrication of Au@Ag@AgCl core–double shells nanoparticles and their potential applications for elimination of toxic emerging pollutants: A green and efficient approach for wastewater treatment. *Chem. Eng. J.* 317, 726–741. <https://doi.org/10.1016/j.cej.2017.02.082>
- Dipankar, C., Murugan, S., 2012. The green synthesis, characterization and evaluation of the biological activities of silver nanoparticles synthesized from *Iresine herbstii* leaf aqueous extracts. *Colloids Surfaces B Biointerfaces* 98, 112–119. <https://doi.org/10.1016/j.colsurfb.2012.04.006>
- Dorledo de Faria, R.A., Messaddeq, Y., Heneine, G.D., Matencio, T., 2019. Application of screen-printed carbon electrode as an electrochemical transducer in biosensors. *Int. J. Biosens. Bioelectron.* 5, 9–10. <https://doi.org/10.15406/ijbsbe.2019.05.00143>
- Du, L., Jiang, H., Liu, X., Wang, E., 2007. Biosynthesis of gold nanoparticles assisted by *Escherichia coli* DH5 α and its application on direct electrochemistry of hemoglobin. *Electrochem. commun.* 9, 1165–1170. <https://doi.org/10.1016/j.elecom.2007.01.007>
- Dujardin, E., Peet, C., Stubbs, G., Culver, J.N., Mann, S., 2003. Organization of metallic nanoparticles using tobacco mosaic virus templates. *Nano Lett.* 3, 413–417. <https://doi.org/10.1021/nl034004o>
- Dutta, P., Kumari, J., Borah, P., Baruah, P., Kaman, P.K., Das, G., Kumari, A., Saikia, B., 2020. Synthesis of fungus mediate silver nanoparticles (AgNP) its characterization and study the efficacy against inoculum, biomass and protein content of *Fusarium oxysporum*. *Int. J. Chem. Stud.* 8, 2619–2625. <https://doi.org/10.22271/chemi.2020.v8.i4ae.10029>
- Dutta, S., Strack, G., Kurup, P., 2019. Gold nanostar electrodes for heavy metal detection. *Sensors Actuators, B Chem.* <https://doi.org/10.1016/j.snb.2018.10.111>
- Eastoe, J., Ellis, C., 2007. De-gassed water and surfactant-free emulsions: History, controversy, and possible applications 135, 89–95. <https://doi.org/10.1016/j.cis.2007.04.017>
- Elemike, E.E., Onwudiwe, D.C., Nundkumar, N., Singh, M., Iyekowa, O., 2019. Green

- synthesis of Ag, Au and Ag-Au bimetallic nanoparticles using *Stigmaphyllon ovatum* leaf extract and their in vitro anticancer potential. *Mater. Lett.* 243, 148–152. <https://doi.org/10.1016/j.matlet.2019.02.049>
- Elhalil, A., Qourzal, S., Mahjoubi, F.Z., Elmoubarki, R., Farnane, M., Tounsadi, H., Sadiq, M., Abdennouri, M., Barka, N., 2016. Defluoridation of groundwater by calcined Mg/Al layered double hydroxide. *Emerg. Contam.* 2, 42–48. <https://doi.org/10.1016/j.emcon.2016.03.002>
- Faraday, M., 1857. Experimental Relations of Gold (and other Metals) to Light. *Phil. Trans. R. Soc.* 147, 145–181.
- Farrag, H.M.M., Mostafa, F.A.A.M., Mohamed, M.E., Huseein, E.A.M., 2020. Green biosynthesis of silver nanoparticles by *Aspergillus niger* and its antiamoebic effect against *Allovalbancampylopusis* trophozoite and cyst. *Exp. Parasitol.* 219, 108031. <https://doi.org/10.1016/j.exppara.2020.108031>
- Feroze, N., Arshad, B., Younas, M., Afridi, M.I., Saqib, S., Ayaz, A., 2020. Fungal mediated synthesis of silver nanoparticles and evaluation of antibacterial activity. *Microsc. Res. Tech.* 83, 72–80. <https://doi.org/10.1002/jemt.23390>
- Fortina, P., Kricka, L.J., Graves, D.J., Park, J., Hyslop, T., Tam, F., Halas, N., Surrey, S., Waldman, S.A., 2007. Applications of nanoparticles to diagnostics and therapeutics in colorectal cancer. *Trends Biotechnol.* 25, 145–52. <https://doi.org/10.1016/j.tibtech.2007.02.005>
- Fu, C.C., Hsieh, C. Te, Juang, R.S., Gu, S., Ashraf Gandomi, Y., Kelly, R.E., Kihm, K.D., 2020. Electrochemical sensing of mercury ions in electrolyte solutions by nitrogen-doped graphene quantum dot electrodes at ultralow concentrations. *J. Mol. Liq.* 302, 112593. <https://doi.org/10.1016/j.molliq.2020.112593>
- Gaikwad, S., Dhage, S., Potdar, H., Samuel, V., Ravi, V., 2005. Co-precipitation method for the preparation of nanocrystalline ferroelectric SrBi₂Nb₂O₉ ceramics. *J. Electroceramics* 14, 83–87. <https://doi.org/10.1007/s10832-005-6588-y>
- Ganaie, S.U., Abbasi, T., Abbasi, S.A., 2016. Rapid and green synthesis of bimetallic Au–Ag nanoparticles using an otherwise worthless weed *Antigonon leptopus*. *J. Exp. Nanosci.* 11, 395–417. <https://doi.org/10.1080/17458080.2015.1070311>
- García-Pinel, B., Porrás-Alcalá, C., Ortega-Rodríguez, A., Sarabia, F., Prados, J., Melguizo, C., López-Romero, J.M., 2019. Lipid-Based Nanoparticles: Application and Recent Advances in Cancer Treatment. *Nanomaterials* 9, 638. <https://doi.org/10.3390/nano9040638>

- Gardea-Torresdey, J.L., Tiemann, K.J., Gamez, G., Dokken, K., Tehuacanero, S., José-Yacamán, M., 1999. Gold nanoparticles obtained by bio-precipitation from gold(III) solutions. *J. Nanoparticle Res.* 1, 397–404. <https://doi.org/10.1023/A:1010008915465>
- Gary-Bobo, M., Hocine, O., Brevet, D., Maynadier, M., Raehm, L., Richeter, S., Charasson, V., Loock, B., Morère, A., Maillard, P., Garcia, M., Durand, J.O., 2012. Cancer therapy improvement with mesoporous silica nanoparticles combining targeting, drug delivery and PDT. *Int. J. Pharm.* 423, 509–515. <https://doi.org/10.1016/j.ijpharm.2011.11.045>
- Ghanbari, N., Hoseini, S.J., Bahrami, M., 2017. Ultrasonic assisted synthesis of palladium-nickel/iron oxide core-shell nanoalloys as effective catalyst for Suzuki-Miyaura and p-nitrophenol reduction reactions. *Ultrason. Sonochem.* 39, 467–477. <https://doi.org/10.1016/j.ultsonch.2017.05.015>
- Ghorbani-Bidkorbeh, F., Shahrokhian, S., Mohammadi, A., Dinarvand, R., 2010. Electrochemical determination of naltrexone on the surface of glassy carbon electrode modified with Nafion-doped carbon nanoparticles: Application to determinations in pharmaceutical and clinical preparations. *J. Electroanal. Chem.* 638, 212–217. <https://doi.org/10.1016/j.jelechem.2009.11.012>
- Ghosale, A., Shrivastava, K., Deb, M.K., Ganesan, V., Karbhal, I., Bajpai, P.K., Shankar, R., 2018. A low-cost screen printed glass electrode with silver nano-ink for electrochemical detection of H₂O₂. *Anal. Methods* 10, 3248–3255. <https://doi.org/10.1039/c8ay00652k>
- Ghosh, P., Han, G., De, M., Kim, C.K., Rotello, V.M., 2008. Gold nanoparticles in delivery applications. *Adv. Drug Deliv. Rev.* 60, 1307–1315. <https://doi.org/10.1016/j.addr.2008.03.016>
- Gong, J., Zhou, T., Song, D., Zhang, L., 2010a. Monodispersed Au nanoparticles decorated graphene as an enhanced sensing platform for ultrasensitive stripping voltammetric detection of mercury(II). *Sensors Actuators, B Chem.* 150, 491–497. <https://doi.org/10.1016/j.snb.2010.09.014>
- Gong, J., Zhou, T., Song, D., Zhang, L., Hu, X., 2010b. Stripping voltammetric detection of mercury(II) based on a bimetallic Au-Pt inorganic-organic hybrid nanocomposite modified glassy carbon electrode. *Anal. Chem.* 82, 567–573. <https://doi.org/10.1021/ac901846a>
- Govindaraju, K., Basha, S.K., Kumar, V.G., Singaravelu, G., 2008. Silver, gold and bimetallic nanoparticles production using single-cell protein (*Spirulina platensis*)

- Geitler, J. *Mater. Sci.* 43, 5115–5122. <https://doi.org/10.1007/s10853-008-2745-4>
- Granata, G., Pagnanelli, F., Nishio-Hamane, D., Sasaki, T., 2015. Effect of surfactant/water ratio and reagents' concentration on size distribution of manganese carbonate nanoparticles synthesized by microemulsion mediated route. *Appl. Surf. Sci.* 331, 463–471. <https://doi.org/10.1016/j.apsusc.2015.01.101>
- Grossmann, H.K., Grieb, T., Meierhofer, F., Hodapp, M.J., Noriler, D., Gröhn, A., Meier, H.F., Fritsching, U., Wegner, K., Mädler, L., 2015. Nanoscale mixing during double-flame spray synthesis of heterostructured nanoparticles. *J. Nanoparticle Res.* 17, 174. <https://doi.org/10.1007/s11051-015-2975-8>
- Gunawan, C., Teoh, W.Y., Marquis, C.P., Amal, R., 2011. Cytotoxic Origin of Copper (II) Oxide Nanoparticles : Comparative Studies and Metal Salts. *ACS Nano* 5, 7214–7225. <https://doi.org/10.1021/nn2020248>
- Günes, S., Neugebauer, H., Sariciftci, N.S., 2007. Conjugated polymer-based organic solar cells. *Chem. Rev.* 107, 1324–38. <https://doi.org/10.1021/cr050149z>
- Guo, S., Wang, E., 2007. Synthesis and electrochemical applications of gold nanoparticles. *Anal. Chim. Acta* 598, 181–192. <https://doi.org/10.1016/j.aca.2007.07.054>
- Haes, a J., Zou, S.L., Schatz, G.C., Van Duyne, R.P., 2004. A nanoscale optical biosensor: The long range distance dependence of the localized surface plasmon resonance of noble metal nanoparticles. *J. Phys. Chem. B* 108, 109–116. <https://doi.org/10.1021/jp0361327>
- Hanumanaik, M., Patel, S.K., Sree, K.R., 2013. Solid Lipid Nanoparticles; A Review. *Int. J. Pharm. Sci. Res.* 928–940. [https://doi.org/10.13040/IJPSR.0975-8232.4\(3\).928-40](https://doi.org/10.13040/IJPSR.0975-8232.4(3).928-40)
- He, S., Guo, Z., Zhang, Y., Zhang, S., Wang, J., Gu, N., 2007. Biosynthesis of gold nanoparticles using the bacteria *Rhodospseudomonas capsulata*. *Mater. Lett.* 61, 3984–3987. <https://doi.org/10.1016/j.matlet.2007.01.018>
- Hernández-Sierra, J.F., Ruiz, F., Cruz Pena, D.C., Martínez-Gutiérrez, F., Martínez, A.E., de Jesús Pozos Guillén, A., Tapia-Pérez, H., Martínez Castañón, G., 2008. The antimicrobial sensitivity of *Streptococcus mutans* to nanoparticles of silver, zinc oxide, and gold. *Nanomedicine Nanotechnology, Biol. Med.* 4, 237–240. <https://doi.org/10.1016/j.nano.2008.04.005>
- Hrapovic, S., Liu, Y., Male, K.B., Luong, J.H.T., 2004. Electrochemical Biosensing Platforms Using Platinum Nanoparticles and Carbon Nanotubes. *Anal. Chem.* 76, 1083–1088. <https://doi.org/10.1021/ac035143t>
- Issa, Z.I., Kadhim, J.F., Asimuddin, M., Acharya, N.P., Jamil, K., 2015. Biosynthesis of

- zinc oxide nanoparticles and its characterization for antibacterial and anticancer properties. *World J. Pharm. Pharm. Sci.* 4, 1002–1018. <https://doi.org/www.wjpps.com>
- Iwamoto, S., Inoue, M., 2008. Solvothermal synthesis of inorganic materials and their performance as catalysts. *J. Japan Pet. Inst.* 51, 143–156. <https://doi.org/10.1627/jpi.51.143>
- Jadav, J.K., Umrana, V. V., Rathod, K.J., Golakiya, B.A., 2018. Development of silver/carbon screen-printed electrode for rapid determination of vitamin C from fruit juices. *LWT - Food Sci. Technol.* 88, 152–158. <https://doi.org/10.1016/j.lwt.2017.10.005>
- Jain, J., Arora, S., Rajwade, J.M., Omray, P., Khandelwal, S., Paknikar, K.M., 2009. Silver nanoparticles in therapeutics: Development of an antimicrobial gel formulation for topical use. *Mol. Pharm.* 6, 1388–1401. <https://doi.org/10.1021/mp900056g>
- Jin, W., Wu, G., Chen, A., 2014. Sensitive and selective electrochemical detection of chromium(VI) based on gold nanoparticle-decorated titania nanotube arrays. *Analyst* 139, 235–241. <https://doi.org/10.1039/c3an01614e>
- Jirasirichote, A., Punrat, E., Suea-Ngam, A., Chailapakul, O., Chuanuwatanakul, S., 2017. Voltammetric detection of carbofuran determination using screen-printed carbon electrodes modified with gold nanoparticles and graphene oxide. *Talanta* 175, 331–337. <https://doi.org/10.1016/j.talanta.2017.07.050>
- Jordá-Beneyto, M., Suárez-García, F., Lozano-Castelló, D., Cazorla-Amorós, D., Linares-Solano, A., 2007. Hydrogen storage on chemically activated carbons and carbon nanomaterials at high pressures. *Carbon N. Y.* 45, 293–303. <https://doi.org/10.1016/j.carbon.2006.09.022>
- Ju, H., Liu, S., Ge, B., Lisdat, F., Scheller, F.W., 2002. Electrochemistry of cytochrome c immobilized on colloidal gold modified carbon paste electrodes and its electrocatalytic activity. *Electroanalysis* 14, 141–147. [https://doi.org/10.1002/1521-4109\(200201\)14:2](https://doi.org/10.1002/1521-4109(200201)14:2)
- Kachhawaha, A.S., Nagarnaik, P.M., Labhasetwar, P., Banerjee, K., 2021. A review of recently developed LC–MS/MS methods for the analysis of pharmaceuticals and personal care products in water. *J. AOAC Int.* 103, 9–22. <https://doi.org/10.5740/jaoacint.19-0209>
- Kah, M., 2015. Nanopesticides and Nanofertilizers: Emerging Contaminants or Opportunities for Risk Mitigation? *Front. Chem.* 3, 1–6.

<https://doi.org/10.3389/fchem.2015.00064>

- Kar, S., Bindal, R.C., Tewari, P.K., 2012. Carbon nanotube membranes for desalination and water purification: Challenges and opportunities. *Nano Today* 7, 385–389. <https://doi.org/10.1016/j.nantod.2012.09.002>
- Karimi-Maleh, H., Moazampour, M., Ensafi, A. a, Mallakpour, S., Hatami, M., 2014a. An electrochemical nanocomposite modified carbon paste electrode as a sensor for simultaneous determination of hydrazine and phenol in water and wastewater samples. *Environ. Sci. Pollut. Res. Int.* 21, 5879–88. <https://doi.org/10.1007/s11356-014-2529-0>
- Karimi-Maleh, H., Sanati, A.L., Gupta, V.K., Yoosefian, M., Asif, M., Bahari, A., 2014b. A voltammetric biosensor based on ionic liquid/NiO nanoparticle modified carbon paste electrode for the determination of nicotinamide adenine dinucleotide (NADH). *Sensors Actuators B Chem.* 204, 647–654. <https://doi.org/10.1016/j.snb.2014.08.037>
- Karthikeyan, B., Murugavelu, M., 2012. Nano bimetallic Ag/Pt system as efficient opto and electrochemical sensing platform towards adenine. *Sensors Actuators, B Chem.* 163, 216–223. <https://doi.org/10.1016/j.snb.2012.01.039>
- Katz E, W.L., Wang, J., 2004. Electroanalytical and bioelectroanalytical systems based on metal and semiconductor nanoparticles. *Electroanalysis* 16, 19–44. <https://doi.org/10.1002/elan.200302930>
- Kaur, A., Gupta, U., 2009. A review on applications of nanoparticles for the preconcentration of environmental pollutants. *J. Mater. Chem.* 19, 8279. <https://doi.org/10.1039/b901933b>
- Kaur, P., Thakur, R., Malwal, H., Manuja, A., Chaudhury, A., 2018. Biosynthesis of biocompatible and recyclable silver/iron and gold/iron core-shell nanoparticles for water purification technology. *Biocatal. Agric. Biotechnol.* 14, 189–197. <https://doi.org/10.1016/j.bcab.2018.03.002>
- Kempahanumakkagari, S., Deep, A., Kim, K.H., Kumar Kailasa, S., Yoon, H.O., 2017. Nanomaterial-based electrochemical sensors for arsenic - A review. *Biosens. Bioelectron.* <https://doi.org/10.1016/j.bios.2017.04.013>
- Khatami, M., Alijani, H., Nejad, M., Varma, R., 2018. Core@shell Nanoparticles: Greener Synthesis Using Natural Plant Products. *Appl. Sci.* 8, 411. <https://doi.org/10.3390/app8030411>
- Khayatian, S.A., Kompany, A., Shahtahmassebi, N., Zak, A.K., 2016. Preparation and characterization of Al doped ZnO NPs/graphene nanocomposites synthesized by a

- facile one-step solvothermal method. *Ceram. Int.* 42, 110–115. <https://doi.org/10.1016/j.ceramint.2015.08.008>
- Kim, J.S., Kuk, E., Yu, K.N., Kim, J.H., Park, S.J., Lee, H.J., Kim, S.H., Park, Y.K., Park, Y.H., Hwang, C.Y., Kim, Y.K., Lee, Y.S., Jeong, D.H., Cho, M.H., 2007. Antimicrobial effects of silver nanoparticles. *Nanomedicine Nanotechnology, Biol. Med.* 3, 95–101. <https://doi.org/10.1016/j.nano.2006.12.001>
- Kongkanand, A., MartinezDominguez, R., Kamat, P. V., 2007. Single Wall Carbon Nanotube Scaffolds for Photoelectrochemical Solar Cells. Capture and Transport of Photogenerated Electrons. *Nano Lett.* 7, 676–680. <https://doi.org/10.1021/nl0627238>
- Kosco, J., Bidwell, M., Cha, H., Martin, T., Howells, C.T., Sachs, M., Anjum, D.H., Gonzalez Lopez, S., Zou, L., Wadsworth, A., Zhang, W., Zhang, L., Tellam, J., Sougrat, R., Laquai, F., DeLongchamp, D.M., Durrant, J.R., McCulloch, I., 2020. Enhanced photocatalytic hydrogen evolution from organic semiconductor heterojunction nanoparticles. *Nat. Mater.* 19, 559–565. <https://doi.org/10.1038/s41563-019-0591-1>
- Kotov, Y.A., 2003. Electric explosion of wires as a method for preparation of nanopowders. *J. Nanoparticle Res.* 5, 539–550. <https://doi.org/10.1023/B:NANO.0000006069.45073.0b>
- Kruis, F.E., Fissan, H., Peled, A., 1998. Synthesis of nanoparticles in the gas phase for electronic, optical and magnetic applications—a review. *J. Aerosol Sci.* 29, 511–535. [https://doi.org/10.1016/S0021-8502\(97\)10032-5](https://doi.org/10.1016/S0021-8502(97)10032-5)
- Kumar, A., Kuang, Y., Liang, Z., Sun, X., 2020. Microwave chemistry, recent advancements, and eco-friendly microwave-assisted synthesis of nanoarchitectures and their applications: a review. *Mater. Today Nano* 11, 100076. <https://doi.org/10.1016/j.mtnano.2020.100076>
- Kunduru, K.R., Nazarkovsky, M., Farah, S., Pawar, R.P., Basu, A., Domb, A.J., 2017. Nanotechnology for water purification: applications of nanotechnology methods in wastewater treatment, *Water Purification*. <https://doi.org/10.1016/b978-0-12-804300-4.00002-2>
- Kunjachan, S., Detappe, A., Kumar, R., Ireland, T., Cameron, L., Biancur, D.E., Motto-Ros, V., Sancey, L., Sridhar, S., Makrigiorgos, G.M., Berbeco, R.I., 2015. Nanoparticle Mediated Tumor Vascular Disruption: A Novel Strategy in Radiation Therapy. *Nano Lett.* 15, 7488–7496. <https://doi.org/10.1021/acs.nanolett.5b03073>
- Latsuzbaia, R., Negro, E., Koper, G., 2015. Bicontinuous microemulsions for high yield,

- wet synthesis of ultrafine nanoparticles: a general approach. *Faraday Discuss.* 00, 1–12. <https://doi.org/10.1039/C5FD00004A>
- Lee, G.-J., Lee, H.-M., Rhee, C.-K., 2007. Bismuth nano-powder electrode for trace analysis of heavy metals using anodic stripping voltammetry. *Electrochem. commun.* 9, 2514–2518. <https://doi.org/10.1016/j.elecom.2007.07.030>
- Lee, G.J., Kim, C.K., Lee, M.K., Rhee, C.K., 2010. Simultaneous voltammetric determination of Zn, Cd and Pb at bismuth nanopowder electrodes with various particle size distributions. *Electroanalysis* 22, 530–535. <https://doi.org/10.1002/elan.200900356>
- Lee, J.E., Lee, N., Kim, H., Kim, J., Choi, S.H., Kim, J.H., Kim, T., Song, I.C., Park, S.P., Moon, W.K., Hyeon, T., 2010. Uniform mesoporous dye-doped silica nanoparticles decorated with multiple magnetite nanocrystals for simultaneous enhanced magnetic resonance imaging, fluorescence imaging, and drug delivery. *J. Am. Chem. Soc.* 132, 552–557. <https://doi.org/10.1021/ja905793q>
- Lengke, M., Southam, G., 2006. Bioaccumulation of gold by sulfate-reducing bacteria cultured in the presence of gold(I)-thiosulfate complex. *Geochim. Cosmochim. Acta* 70, 3646–3661. <https://doi.org/10.1016/j.gca.2006.04.018>
- Leong, K.H., Monash, P., Ibrahim, S., Saravanan, P., 2014. Solar photocatalytic activity of anatase TiO₂ nanocrystals synthesized by non-hydrolitic sol–gel method. *Sol. Energy* 101, 321–332. <https://doi.org/10.1016/j.solener.2014.01.006>
- Lerner, M.I., Pervikov, A. V., Glazkova, E.A., Svarovskaya, N. V., Lozhkomoev, A.S., Psakhie, S.G., 2016. Structures of binary metallic nanoparticles produced by electrical explosion of two wires from immiscible elements. *Powder Technol.* 288, 371–378. <https://doi.org/10.1016/j.powtec.2015.11.037>
- Li, L., Liu, D., Shi, A., You, T., 2018. Simultaneous stripping determination of cadmium and lead ions based on the N-doped carbon quantum dots-graphene oxide hybrid. *Sensors Actuators, B Chem.* 255, 1762–1770. <https://doi.org/10.1016/j.snb.2017.08.190>
- Li, Q., Mahendra, S., Lyon, D.Y., Brunet, L., Liga, M. V., Li, D., Alvarez, P.J.J., 2008. Antimicrobial nanomaterials for water disinfection and microbial control: Potential applications and implications. *Water Res.* 42, 4591–4602. <https://doi.org/10.1016/j.watres.2008.08.015>
- Li, W., Szoka, F.C., 2007. Lipid-based Nanoparticles for Nucleic Acid Delivery. *Pharm. Res.* 24, 438–449. <https://doi.org/10.1007/s11095-006-9180-5>

- Li, Y., Gao, G.H., Lee, D.S., 2013. Stimulus-Sensitive Polymeric Nanoparticles and Their Applications as Drug and Gene Carriers. *Adv. Healthc. Mater.* 2, 388–417. <https://doi.org/10.1002/adhm.201200313>
- Liao, Q., Tannenbaum, R., Wang, Z.L., 2006. Synthesis of FeNi₃ alloyed nanoparticles by hydrothermal reduction. *J. Phys. Chem. B* 110, 14262–14265. <https://doi.org/10.1021/jp0625154>
- Liao, Y., Zhang, R., Wang, H., Ye, S., Zhou, Y., Ma, T., Zhu, J., Pfefferle, L.D., Qian, J., 2019. Highly conductive carbon-based aqueous inks toward electroluminescent devices, printed capacitive sensors and flexible wearable electronics. *RSC Adv.* 9, 15184–15189. <https://doi.org/10.1039/c9ra01721f>
- Lim, S.H., Wei, J., Lin, J., Li, Q., KuaYou, J., 2005. A glucose biosensor based on electrodeposition of palladium nanoparticles and glucose oxidase onto Nafion-solubilized carbon nanotube electrode. *Biosens. Bioelectron.* 20, 2341–2346. <https://doi.org/10.1016/j.bios.2004.08.005>
- Lin, G., Ji, R., Yao, H., Chen, R., Yu, Y., Wang, X., Yang, X., Zhu, T., Bian, H., 2020. Fluorescence detection of multiple kinds of pesticides with multi hidden layers neural network algorithm. *Optik (Stuttg.)* 211, 164632. <https://doi.org/10.1016/j.ijleo.2020.164632>
- Liu, J., Zhang, Q., Xue, W., Zhang, H., Bai, Y., Wu, L., Zhai, Z., Jin, G., 2019. Fluorescence characteristics of aqueous synthesized tin oxide quantum dots for the detection of heavy metal ions in contaminated water. *Nanomaterials* 9. <https://doi.org/10.3390/nano9091294>
- Liu, Z., Qi, P., Wang, J., Wang, Z., Di, S., Xu, H., Zhao, H., Wang, Q., Wang, Xinquan, Wang, Xinhong, 2020. Development, validation, comparison, and implementation of a highly efficient and effective method using magnetic solid-phase extraction with hydrophilic-lipophilic-balanced materials for LC-MS/MS analysis of pesticides in seawater. *Sci. Total Environ.* 708, 135221. <https://doi.org/10.1016/j.scitotenv.2019.135221>
- Lockman, P.R., Mumper, R.J., Khan, M.A., Allen, D.D., 2002. Nanoparticle Technology for Drug Delivery Across the Blood-Brain Barrier. *Drug Dev. Ind. Pharm.* 28, 1–13. <https://doi.org/10.1081/DDC-120001481>
- Lu, T., Pan, L., Li, H., Zhu, G., Lv, T., Liu, X., Sun, Z., Chen, T., Chua, D.H.C., 2011. Microwave-assisted synthesis of graphene-ZnO nanocomposite for electrochemical supercapacitors. *J. Alloys Compd.* 509, 5488–5492.

- <https://doi.org/10.1016/j.jallcom.2011.02.136>
- Määttänen, A., Ihalainen, P., Pulkkinen, P., Wang, S., Tenhu, H., Peltonen, J., 2012. Inkjet-printed gold electrodes on paper: Characterization and functionalization. *ACS Appl. Mater. Interfaces* 4, 955–964. <https://doi.org/10.1021/am201609w>
- Malika, M., Rao, C.V., Das, R.K., Giri, A.S., Golder, A.K., 2016. Evaluation of bimetal doped TiO₂ in dye fragmentation and its comparison to mono-metal doped and bare catalysts. *Appl. Surf. Sci.* 368, 316–324. <https://doi.org/10.1016/j.apsusc.2016.01.230>
- Meena Kumari, M., Philip, D., 2015. Synthesis of biogenic SnO₂ nanoparticles and evaluation of thermal, rheological, antibacterial and antioxidant activities. *Powder Technol.* 270, 312–319. <https://doi.org/10.1016/j.powtec.2014.10.034>
- Meng, H., Yang, W., Yan, X., Zhang, Y., Feng, L., Guan, Y., 2015. A highly sensitive and fast responsive semiconductor metal oxide detector based on In₂O₃ nanoparticle film for portable gas chromatograph. *Sensors Actuators B Chem.* 216, 511–517. <https://doi.org/10.1016/j.snb.2015.04.068>
- Mishra, P.M., Kumar Sahoo, S., Kumar Naik, G., Parida, K., 2015. Biomimetic synthesis, characterization and mechanism of formation of stable silver nanoparticles using *Averrhoa carambola* L. leaf extract. *Mater. Lett.* 160, 566–571. <https://doi.org/10.1016/j.matlet.2015.08.048>
- Molinero-Abad, B., Alonso-Lomillo, M.A., Domínguez-Renedo, O., Arcos-Martínez, M.J., 2013. Amperometric determination of sulfite using screen-printed electrodes modified with metallic nanoparticles. *Microchim. Acta* 180, 1351–1355. <https://doi.org/10.1007/s00604-013-1074-8>
- Morbioli, G.G., Mazzu-Nascimento, T., Stockton, A.M., Carrilho, E., 2017. Technical aspects and challenges of colorimetric detection with microfluidic paper-based analytical devices (μPADs) - A review. *Anal. Chim. Acta* 970, 1–22. <https://doi.org/10.1016/j.aca.2017.03.037>
- Moreno-Vega, A.-I., Gómez-Quintero, T., Nuñez-Anita, R.-E., Acosta-Torres, L.-S., Castaño, V., 2012. Polymeric and Ceramic Nanoparticles in Biomedical Applications. *J. Nanotechnol.* 2012, 1–10. <https://doi.org/10.1155/2012/936041>
- Mortazavi-derazkola, S., Zinatloo-ajabshir, S., Salavati-niasari, M., 2015. Novel simple solvent-less preparation, characterization and degradation of the cationic dye over holmium oxide ceramic nanostructures. *Ceram. Int.* 41, 9593–9601. <https://doi.org/10.1016/j.ceramint.2015.04.021>
- Mousavi, S.H., Müller, T.S., Karos, R., de Oliveira, P.W., 2016. Faster synthesis of CIGS

- nanoparticles using a modified solvothermal method. *J. Alloys Compd.* 659, 178–183. <https://doi.org/10.1016/j.jallcom.2015.10.261>
- Mulder, W.J.M., Strijkers, G.J., Tilborg, G.A.F. Van, Griffioen, A.W., Nicolay, K., 2006. Lipid-based nanoparticles for contrast-enhanced MRI and molecular imaging 142–164. <https://doi.org/10.1002/nbm.1011>
- Nadagouda, M.N., Varma, R.S., 2008. Green synthesis of silver and palladium nanoparticles at room temperature using coffee and tea extract. *Green Chem.* 10, 859–86. <https://doi.org/10.1039/b804703k>
- Naderi, M.R., Danesh-Shahraki, 2013. Nanofertilizers and their roles in sustainable agriculture. *Int. J. Agric. Crop Sci. IJACS/2013*, 2229–2232. <https://doi.org/www.ijagcs.com IJACS/2013/5-19/2229-2232>
- Narayanan, K.B., Sakthivel, N., 2010. Biological synthesis of metal nanoparticles by microbes. *Adv. Colloid Interface Sci.* <https://doi.org/10.1016/j.cis.2010.02.001>
- Narayanan, K.B., Sakthivel, N., 2008. Coriander leaf mediated biosynthesis of gold nanoparticles. *Mater. Lett.* 62, 4588–4590. <https://doi.org/10.1016/j.matlet.2008.08.044>
- Niu, P., Fernández-Sánchez, C., Gich, M., Ayora, C., Roig, A., 2015. Electroanalytical assessment of heavy metals in waters with bismuth nanoparticle-porous carbon paste electrodes. *Electrochim. Acta* 165, 155–161. <https://doi.org/10.1016/j.electacta.2015.03.001>
- Njoki, P.N., Rhoades, A.E., Barnes, J.I., 2020. Microwave-Assisted synthesis of Anisotropic copper–silver nanoparticles. *Mater. Chem. Phys.* 241, 122348. <https://doi.org/10.1016/j.matchemphys.2019.122348>
- Oliveira, R.R., Carrião, M.S., Pacheco, M.T., Branquinho, L.C., de Souza, A.L.R., Bakuzis, A.F., Lima, E.M., 2018. Triggered release of paclitaxel from magnetic solid lipid nanoparticles by magnetic hyperthermia. *Mater. Sci. Eng. C* 92, 547–553. <https://doi.org/10.1016/j.msec.2018.07.011>
- Oves, M., Arshad, M., Khan, M.S., Ahmed, A.S., Azam, A., Ismail, I.M.I., 2015. Antimicrobial activity of cobalt doped zinc oxide nanoparticles: Targeting water borne bacteria. *J. Saudi Chem. Soc.* <https://doi.org/10.1016/j.jscs.2015.05.003>
- Pal, A., Sk, M.P., Chattopadhyay, A., 2020. Recent advances in crystalline carbon dots for superior application potential. *Mater. Adv.* 1, 525–553. <https://doi.org/10.1039/d0ma00108b>
- Palza, H., 2015. Antimicrobial Polymers with Metal Nanoparticles. *Int. J. Mol. Sci.* 16,

- 2099–2116. <https://doi.org/10.3390/ijms16012099>
- Pascariu, P., Tudose, I.V., Sucheai, M., Koudoumas, E., Fifere, N., Airinei, A., 2018. Preparation and characterization of Ni, Co doped ZnO nanoparticles for photocatalytic applications. *Appl. Surf. Sci.* 448, 481–488. <https://doi.org/10.1016/j.apsusc.2018.04.124>
- Pereira Silva Neves, M.M., González-García, M.B., Bobes-Limenes, P., Pérez-Junquera, A., Hernández-Santos, D., Vidal-Iglesias, F.J., Solla-Gullón, J., Fanjul-Bolado, P., 2017. A non-enzymatic ethanol sensor based on a nanostructured catalytic disposable electrode. *Anal. Methods* 9, 5108–5114. <https://doi.org/10.1039/c7ay01078h>
- Pérez-Díaz, M.A., Boegli, L., James, G., Velasquillo, C., Sánchez-Sánchez, R., Martínez-Martínez, R.-E., Martínez-Castañón, G.A., Martínez-Gutierrez, F., 2015. Silver nanoparticles with antimicrobial activities against *Streptococcus mutans* and their cytotoxic effect. *Mater. Sci. Eng. C* 55, 360–366. <https://doi.org/10.1016/j.msec.2015.05.036>
- Pérez-Ràfols, C., Serrano, N., Díaz-Cruz, J.M., Ariño, C., Esteban, M., 2017. A screen-printed voltammetric electronic tongue for the analysis of complex mixtures of metal ions. *Sensors Actuators, B Chem.* 250, 393–401. <https://doi.org/10.1016/j.snb.2017.04.165>
- Pileni, M.P., Lisiecki, I., 1993. Nanometer metallic copper particle synthesis in reverse micelles. *Colloids Surfaces A Physicochem. Eng. Asp.* 80, 63–68. [https://doi.org/10.1016/0927-7757\(93\)80224-3](https://doi.org/10.1016/0927-7757(93)80224-3)
- Prakash, S., Shahi, V.K., 2011. Improved sensitive detection of Pb²⁺ and Cd²⁺ in water samples at electrodeposited silver nanonuts on a glassy carbon electrode. *Anal. Methods* 3, 2134–2139. <https://doi.org/10.1039/c1ay05265a>
- Pugajeva, I., Rusko, J., Perkons, I., Lundanes, E., Bartkevics, V., 2017. Determination of pharmaceutical residues in wastewater using high performance liquid chromatography coupled to quadrupole-Orbitrap mass spectrometry. *J. Pharm. Biomed. Anal.* 133, 64–74. <https://doi.org/10.1016/j.jpba.2016.11.008>
- Radhakrishnan, S., Krishnamoorthy, K., Sekar, C., Wilson, J., Kim, S.J., 2014. A highly sensitive electrochemical sensor for nitrite detection based on Fe₂O₃ nanoparticles decorated reduced graphene oxide nanosheets. *Appl. Catal. B Environ.* 148–149, 22–28. <https://doi.org/10.1016/j.apcatb.2013.10.044>
- Raj, S.K., Yadav, V., Bhadu, G.R., Patidar, R., Kumar, M., Kulshrestha, V., 2020. Synthesis of highly fluorescent and water soluble graphene quantum dots for detection

- of heavy metal ions in aqueous media. *Environ. Sci. Pollut. Res.* <https://doi.org/10.1007/s11356-020-07891-5>
- Ramadass, S.K., Anantharaman, N.V., Subramanian, S., Sivasubramanian, S., Madhan, B., 2015. Paclitaxel/Epigallocatechin gallate coloaded liposome: A synergistic delivery to control the invasiveness of MDA-MB-231 breast cancer cells. *Colloids Surfaces B Biointerfaces* 125, 65–72. <https://doi.org/10.1016/j.colsurfb.2014.11.005>
- Randviir, E.P., Brownson, D.A.C., Metters, J.P., Kadara, R.O., Banks, C.E., 2014. The fabrication, characterisation and electrochemical investigation of screen-printed graphene electrodes. *Phys. Chem. Chem. Phys.* 16, 4598–4611. <https://doi.org/10.1039/c3cp55435j>
- Rao, C.V., Golder, A.K., 2016. Development of a bio-mediated technique of silver-doping on titania. *Colloids Surfaces A Physicochem. Eng. Asp.* 506, 557–565. <https://doi.org/10.1016/j.colsurfa.2016.07.031>
- Rekhi, H., Rani, S., Sharma, N., Malik, A.K., 2017. A Review on Recent Applications of High-Performance Liquid Chromatography in Metal Determination and Speciation Analysis. *Crit. Rev. Anal. Chem.* 47, 524–537. <https://doi.org/10.1080/10408347.2017.1343659>
- River Data Directorate Planning & Development Organisation, 2018. Status of Trace and Toxic Metals in Indian Rivers, Central Water Commission.
- Roy, K., Sarkar, C.K., Ghosh, C.K., 2015. Rapid colorimetric detection of Hg²⁺ ion by green silver nanoparticles synthesized using *Dahlia pinnata* leaf extract. *Green Process. Synth.* 4, 455–461. <https://doi.org/10.1515/gps-2015-0052>
- Ryu, H., Li, B., De Guise, S., McCutcheon, J., Lei, Y., 2020. Recent progress in the detection of emerging contaminants PFASs. *J. Hazard. Mater.* 408, 124437. <https://doi.org/10.1016/j.jhazmat.2020.124437>
- Salama, F.M., Attia, K.A., Said, R.A., El-Olemy, A., Abdel-Raouf, A.M., 2018. Disposable gold nanoparticle functionalized and bare screen-printed electrodes for potentiometric determination of trazodone hydrochloride in pure form and pharmaceutical preparations. *RSC Adv.* 8, 11517–11527. <https://doi.org/10.1039/c8ra00745d>
- Salata, O., 2004. Applications of nanoparticles in biology and medicine. *J. Nanobiotechnology* 2, 3. <https://doi.org/10.1186/1477-3155-2-3>
- Samad, L., Caba, M., Shearer, M.J., Park, K., Hamers, R.J., 2015. Direct Chemical Vapor Deposition Synthesis of Phase-Pure Iron Pyrite (FeS₂) Thin Films. <https://doi.org/10.1021/acs.chemmater.5b00664>

- Samiey, B., Cheng, C.H., Wu, J., 2014. Organic-inorganic hybrid polymers as adsorbents for removal of heavy metal ions from solutions: A review. *Materials (Basel)*. 7, 673–726. <https://doi.org/10.3390/ma7020673>
- Sanchez-dominguez, M., Morales-mendoza, G., Rodriguez-vargas, M.J., Ibarra-malo, C.C., Rodriguez-rodriguez, A.A., Vela-gonzalez, A. V, Perez-garcia, S.A., Gomez, R., 2015. Synthesis of Zn-doped TiO₂ nanoparticles by the novel oil-in-water (O/W) microemulsion method and their use for the photocatalytic degradation of phenol. *J. Environ. Chem. Eng.* 3, 3037–3047. <https://doi.org/http://dx.doi.org/10.1016/j.jece.2015.03.010>
- Sanchez-Dominguez, M., Pemartin, K., Boutonnet, M., 2012. Preparation of inorganic nanoparticles in oil-in-water microemulsions: A soft and versatile approach. *Curr. Opin. Colloid Interface Sci.* 17, 297–305. <https://doi.org/10.1016/j.cocis.2012.06.007>
- Sanlloriente-Méndez, S., Domínguez-Renedo, O., Arcos-Martínez, M.J., 2009. Determination of arsenic(III) using platinum nanoparticle-modified screen-printed carbon-based electrodes. *Electroanalysis* 21, 635–639. <https://doi.org/10.1002/elan.200804389>
- Santacruz-chávez, J.A., Oros-ruiz, S., Prado, B., Zanella, R., 2015. Journal of Environmental Chemical Engineering Photocatalytic degradation of atrazine using TiO₂ super efficiently modified with metallic nanoparticles 3, 1–7. <https://doi.org/10.1016/j.jece.2015.04.025>
- Santoveña-Urbe, A., Maya-Cornejo, J., Bahena, D., Ledesma, J., Pérez, R., Esparza, R., 2021. Synthesis and Characterization of AgPd Bimetallic Nanoparticles as Efficient Electrocatalysts for Oxygen Reduction Reaction. *Electrocatalysis* 11, 536–545. <https://doi.org/10.1007/s12678-020-00613-y>
- Sathish, M., Viswanathan, B., Viswanath, R.P., 2006. Alternate synthetic strategy for the preparation of CdS nanoparticles and its exploitation for water splitting. *Int. J. Hydrogen Energy* 31, 891–898. <https://doi.org/10.1016/j.ijhydene.2005.08.002>
- Sato, Y., Suematsu, H., Sarathi, R., Kikuchi, T., Sasaki, T., Tokoi, Y., Suzuki, T., Nakayama, T., Niihara, K., 2015. Preparation of palladium nanoparticles and a grain-size determining equation of pulsed wire discharge in N₂, Ar, and He ambient gasses. *Jpn. J. Appl. Phys.* 54. <https://doi.org/10.7567/JJAP.54.045002>
- Schaadt, D.M., Feng, B., Yu, E.T., 2005. Enhanced semiconductor optical absorption via surface plasmon excitation in metal nanoparticles. *Appl. Phys. Lett.* 86, 1–3. <https://doi.org/10.1063/1.1855423>

- Shah, M., Guo, Q.X., Fu, Y., 2015. The colloidal synthesis of unsupported nickel-tin bimetallic nanoparticles with tunable composition that have high activity for the reduction of nitroarenes. *Catal. Commun.* 65, 85–90. <https://doi.org/10.1016/j.catcom.2015.02.026>
- Shankar, S.S., Ahmad, A., Sastry, M., 2003. Geranium Leaf Assisted Biosynthesis of Silver Nanoparticles. *Biotechnol. Prog.* 19, 1627–1631. <https://doi.org/10.1021/bp034070w>
- Shankar, S.S., Rai, A., Ahmad, A., Sastry, M., 2005. Controlling the optical properties of lemongrass extract synthesized gold nanotriangles and potential application in infrared-absorbing optical coatings. *Chem. Mater.* 17, 566–572. <https://doi.org/10.1021/cm048292g>
- Shankar, S.S., Rai, A., Ahmad, A., Sastry, M., 2004. Rapid synthesis of Au, Ag, and bimetallic Au core-Ag shell nanoparticles using Neem (*Azadirachta indica*) leaf broth. *J. Colloid Interface Sci.* 275, 496–502. <https://doi.org/10.1016/j.jcis.2004.03.003>
- Shankar, S.S., Shereema, R.M., Ramachandran, V., Sruthi, T. V., Kumar, V.B.S., Rakhi, R.B., 2019. Carbon Quantum Dot-Modified Carbon Paste Electrode-Based Sensor for Selective and Sensitive Determination of Adrenaline. *ACS Omega* 4, 7903–7910. <https://doi.org/10.1021/acsomega.9b00230>
- Sharma, G., Naushad, M., Kumar, A., Devi, S., Khan, M.R., 2015. Lanthanum/Cadmium/Polyaniline bimetallic nanocomposite for the photodegradation of organic pollutant. *Iran. Polym. J. (English Ed.)* 24, 1003–1013. <https://doi.org/10.1007/s13726-015-0388-2>
- Shi, H., Wang, R., Yang, J., Ren, H., Liu, S., Guo, T., 2015. Novel imprinted nanocapsule with highly enhanced hydrolytic activity for organophosphorus pesticide degradation and elimination. *Eur. Polym. J.* 72, 190–201. <https://doi.org/10.1016/j.eurpolymj.2015.09.016>
- Shipway, A.N., Katz, E., Willner, I., 2000. Nanoparticle Arrays on Surfaces for Electronic, Optical, and Sensor Applications. *ChemPhysChem* 1, 18–52. <https://doi.org/10.1002/1439-7641>
- Shui, G., Leong, L.P., 2002. Separation and determination of organic acids and phenolic compounds in fruit juices and drinks by high-performance liquid chromatography. *J. Chromatogr. A* 977, 89–96. [https://doi.org/10.1016/S0021-9673\(02\)01345-6](https://doi.org/10.1016/S0021-9673(02)01345-6)
- Silva, E. da, C.G., J., Gonçalves, M.R., H., 2011. Analytical and bioanalytical applications of carbon dots. *TrAC Trends Anal. Chem.* 30, 1327–1336. <https://doi.org/10.1016/j.trac.2011.04.009>

- Singh, D., Singh, S., Sahu, J., Srivastava, S., Singh, M.R., 2016. Ceramic nanoparticles: Recompense, cellular uptake and toxicity concerns. *Artif. Cells, Nanomedicine, Biotechnol.* 44, 401–409. <https://doi.org/10.3109/21691401.2014.955106>
- Slowing, I.I., Vivero-Escoto, J.L., Wu, C.-W., Lin, V.S.-Y., 2008. Mesoporous silica nanoparticles as controlled release drug delivery and gene transfection carriers. *Adv. Drug Deliv. Rev.* 60, 1278–88. <https://doi.org/10.1016/j.addr.2008.03.012>
- Soppimath, K.S., Aminabhavi, T.M., Kulkarni, a R., Rudzinski, W.E., 2001. Biodegradable polymeric nanoparticles as drug delivery devices. *J. Control. Release* 70, 1–20. [https://doi.org/10.1016/S0168-3659\(00\)00339-4](https://doi.org/10.1016/S0168-3659(00)00339-4)
- Sorensen, J.P.R., Vivanco, A., Ascott, M.J., Goody, D.C., Lapworth, D.J., Read, D.S., Rushworth, C.M., Bucknall, J., Herbert, K., Karapanos, I., Gumm, L.P., Taylor, R.G., 2018. Online fluorescence spectroscopy for the real-time evaluation of the microbial quality of drinking water. *Water Res.* 137, 301–309. <https://doi.org/10.1016/j.watres.2018.03.001>
- Southam, G., Beveridge, T.J., 1994. The in vitro formation of placer gold by bacteria, *Geochimica et Cosmochimica Acta.* [https://doi.org/10.1016/0016-7037\(94\)90355-7](https://doi.org/10.1016/0016-7037(94)90355-7)
- Sreekanth, T.V.M., Nagajyothi, P.C., Supraja, N., Prasad, T.N.V.K. V, 2014. Evaluation of the antimicrobial activity and cytotoxicity of phytogenic gold nanoparticles. *Appl. Nanosci.* 595–602. <https://doi.org/10.1007/s13204-014-0354-x>
- Strobel, R., Pratsinis, S.E., 2007. Flame aerosol synthesis of smart nanostructured materials. *J. Mater. Chem.* 17, 4743. <https://doi.org/10.1039/b711652g>
- Subramaniam, M.N., Goh, P.S., Lau, W.J., Ismail, A.F., 2019. The roles of nanomaterials in conventional and emerging technologies for heavy metal removal: A state-of-the-art review. *Nanomaterials* 9. <https://doi.org/10.3390/nano9040625>
- Sud, D., Kaur, P., Bansal, P., 2021. High-performance liquid chromatographic techniques for determination of organophosphate pesticides in complex matrices, in: *Green Sustainable Process for Chemical and Environmental Engineering and Science.* pp. 175–196. <https://doi.org/10.1016/b978-0-12-821883-9.00006-0>
- Sun, Y., Zhou, B., Lin, Y., Wang, W., Fernando, K.A.S., Pathak, P., Mezziani, M.J., Harruff, B.A., Wang, X., Wang, H., Luo, P.G., Yang, H., Kose, M.E., Chen, B., Veca, L.M., Xie, S., 2006. Quantum-Sized Carbon Dots for Bright and Colorful Photoluminescence. *J. Am. Chem. Soc.* 128, 7756–7757. <https://doi.org/10.1021/ja062677d>
- Talebian, N., Zavvare, H.S.H., 2014. Enhanced bactericidal action of SnO₂ nanostructures

- having different morphologies under visible light: Influence of surfactant. *J. Photochem. Photobiol. B Biol.* 130, 132–139. <https://doi.org/10.1016/j.jphotobiol.2013.10.018>
- Tan, S.C., Chin, S.F., Pang, S.C., 2017. Disposable carbon dots modified screen printed carbon electrode electrochemical sensor strip for selective detection of ferric ions. *J. Sensors* 2017, 1–8. <https://doi.org/10.1155/2017/7576345>
- Tang, J., Huang, Y., Zhang, C., Liu, H., Tang, D., 2016. DNA-based electrochemical determination of mercury(II) by exploiting the catalytic formation of gold amalgam and of silver nanoparticles. *Microchim. Acta* 183, 1805–1812. <https://doi.org/10.1007/s00604-016-1813-8>
- Tangsir, S., Hafshejani, L.D., Lähde, A., Maljanen, M., Hooshmand, A., Naseri, A.A., Moazed, H., Jokiniemi, J., Bhatnagar, A., 2016. Water defluoridation using Al₂O₃ nanoparticles synthesized by flame spray pyrolysis (FSP) method. *Chem. Eng. J.* 288, 198–206. <https://doi.org/http://dx.doi.org/10.1016/j.cej.2015.11.097>
- Tantis, I., Dozzi, M.V., Bettini, L.G., Chiarello, G.L., Dracopoulos, V., Selli, E., Lianos, P., 2016. Highly functional titania nanoparticles produced by flame spray pyrolysis. Photoelectrochemical and solar cell applications. *Appl. Catal. B Environ.* 182, 369–374. <https://doi.org/10.1016/j.apcatb.2015.09.040>
- Tomah, A.A., Alamer, I.S.A., Li, B., Zhang, J.Z., 2020. Mycosynthesis of silver nanoparticles using screened trichoderma isolates and their antifungal activity against sclerotinia sclerotiorum. *Nanomaterials* 10, 1–15. <https://doi.org/10.3390/nano10101955>
- Tonelli, D., Scavetta, E., Gualandi, I., 2019. Electrochemical deposition of nanomaterials for electrochemical sensing. *Sensors (Switzerland)* 19. <https://doi.org/10.3390/s19051186>
- Torres-Rivero, K., Torralba-Cadena, L., Espriu-Gascon, A., Casas, I., Bastos-Arrieta, J., Florido, A., 2019. Strategies for surface modification with ag-shaped nanoparticles: Electrocatalytic enhancement of screen-printed electrodes for the detection of heavy metals. *Sensors (Switzerland)* 19, 1–14. <https://doi.org/10.3390/s19194249>
- Tsai, M.C., Chen, P.Y., 2008. Voltammetric study and electrochemical detection of hexavalent chromium at gold nanoparticle-electrodeposited indium tin oxide (ITO) electrodes in acidic media. *Talanta* 76, 533–539. <https://doi.org/10.1016/j.talanta.2008.03.043>
- Udayabhanu, Nethravathi, P.C., Pavan Kumar, M.A., Suresh, D., Lingaraju, K., Rajanaika,

- H., Nagabhushana, H., Sharma, S.C., 2015. Tinospora cordifolia mediated facile green synthesis of cupric oxide nanoparticles and their photocatalytic, antioxidant and antibacterial properties. *Mater. Sci. Semicond. Process.* 33, 81–88. <https://doi.org/10.1016/j.mssp.2015.01.034>
- Ullah, N., Mansha, M., Khan, I., Qurashi, A., 2018. Nanomaterial-based optical chemical sensors for the detection of heavy metals in water: Recent advances and challenges. *TrAC - Trends Anal. Chem.* 100, 155–166. <https://doi.org/10.1016/j.trac.2018.01.002>
- Valodkar, M., Modi, S., Pal, A., Thakore, S., 2011. Synthesis and anti-bacterial activity of Cu, Ag and Cu–Ag alloy nanoparticles: A green approach. *Mater. Res. Bull.* 46, 384–389. <https://doi.org/10.1016/j.materresbull.2010.12.001>
- Venkatanarasimha Rao Chelli, Subhendu Sekhar Bag, A.K.G., 2017. A Biosynthesis Route to Nearly Spherical AgNPs Using Chayote Fruit Extract. *Environ. Prog. Sustain. Energy* 36, 192–199. <https://doi.org/10.1002/ep.12440>
- Vichery, C., Maurin, I., Proux, O., Kieffer, I., Hazemann, J.L., Cortès, R., Boilot, J.P., Gacoin, T., 2013. Introduction of cobalt ions in γ -Fe₂O₃ nanoparticles by direct coprecipitation or postsynthesis adsorption: Dopant localization and magnetic anisotropy. *J. Phys. Chem. C* 117, 19672–19683. <https://doi.org/10.1021/jp405450p>
- Vidhu, V.K., Philip, D., 2015. Biogenic synthesis of SnO₂ nanoparticles: Evaluation of antibacterial and antioxidant activities. *Spectrochim. Acta - Part A Mol. Biomol. Spectrosc.* 134, 372–379. <https://doi.org/10.1016/j.saa.2014.06.131>
- Vidya, H., Kumara Swamy, B.E., Schell, M., 2016. One step facile synthesis of silver nanoparticles for the simultaneous electrochemical determination of dopamine and ascorbic acid. *J. Mol. Liq.* 214, 298–305. <https://doi.org/10.1016/j.molliq.2015.12.025>
- Wagener, P., Brandes, G., Schwenke, A., Barcikowski, S., 2011. Impact of in situ polymer coating on particle dispersion into solid laser-generated nanocomposites. *Phys. Chem. Chem. Phys.* 13, 5120–6. <https://doi.org/10.1039/c0cp02262d>
- Wang, C., Yu, C., 2013. Detection of chemical pollutants in water using gold nanoparticles as sensors: a review. *Rev. Anal. Chem.* 32, 1–14. <https://doi.org/10.1515/revac-2012-0023>
- Wang, F., Hu, S., 2009. Electrochemical sensors based on metal and semiconductor nanoparticles. *Microchim. Acta* 165, 1–22. <https://doi.org/10.1007/s00604-009-0136-4>
- Wang, J., Wang, L., Di, J., Tu, Y., 2009. Electrodeposition of gold nanoparticles on indium/tin oxide electrode for fabrication of a disposable hydrogen peroxide

- biosensor. *Talanta* 77, 1454–1459. <https://doi.org/10.1016/j.talanta.2008.09.034>
- Wang, L., Ma, W., Xu, L., Chen, W., Zhu, Y., Xu, C., Kotov, N. a., 2010. Nanoparticle-based environmental sensors. *Mater. Sci. Eng. R Reports* 70, 265–274. <https://doi.org/10.1016/j.mser.2010.06.012>
- Wang, S., Lin, X., 2005. Electrodeposition of Pt-Fe(III) nanoparticle on glassy carbon electrode for electrochemical nitric oxide sensor. *Electrochim. Acta* 50, 2887–2891. <https://doi.org/10.1016/j.electacta.2004.11.037>
- Wang, T., Yang, L., Zhang, B., Liu, J., 2010. Extracellular biosynthesis and transformation of selenium nanoparticles and application in H₂O₂ biosensor. *Colloids Surfaces B Biointerfaces* 80, 94–102. <https://doi.org/10.1016/j.colsurfb.2010.05.041>
- Wang, X., Cao, L., Lu, F., Meziari, M.J., Li, H., Qi, G., Zhou, B., Harruff, B.A., Kermarrec, F., Sun, Y., 2009. Photoinduced electron transfers with carbon dots. *Chem. Commun.* 3774. <https://doi.org/10.1039/b906252a>
- Wang, X., Xie, Z., Huang, H., Liu, Z., Chen, D., Shen, G., 2012. Gas sensors, thermistor and photodetector based on ZnS nanowires. *J. Mater. Chem.* 22, 6845. <https://doi.org/10.1039/c2jm16523f>
- Wasswa, J., Mladenov, N., Pearce, W., 2019. Assessing the potential of fluorescence spectroscopy to monitor contaminants in source waters and water reuse systems. *Environ. Sci. Water Res. Technol.* 5, 370–382. <https://doi.org/10.1039/c8ew00472b>
- Wei, D., Liu, Y., Wang, Y., Zhang, H., Huang, L., Yu, G., 2009. Synthesis of n-doped graphene by chemical vapor deposition and its electrical properties. *Nano Lett.* 9, 1752–1758. <https://doi.org/10.1021/nl803279t>
- Wei, Y., Gao, C., Meng, F., Li, H., Wang, L., Liu, J., Huang, X., 2012. SnO₂ / Reduced Graphene Oxide Nanocomposite for the Simultaneous Electrochemical Detection of Cadmium (II), Lead (II), Copper (II), and Mercury (II): An Interesting Favorable Mutual Interference. *J. Phys. Chem. C* 116, 1034–1041. <https://doi.org/dx.doi.org/10.1021/jp209805c>
- Weissman, J.M., Sunkara, H.B., Tse, A.S., Asher, S.A., 1996. Thermally switchable periodicities and diffraction from mesoscopically ordered materials. *Science* (80-.). 274, 959–960. <https://doi.org/10.1126/science.274.5289.959>
- Welch, C.M., Hyde, M.E., Banks, C.E., Compton, R.G., 2005. The detection of nitrate using in-situ copper nanoparticle deposition at a boron doped diamond electrode. *Anal. Sci.* 21, 1421–1430. <https://doi.org/10.2116/analsci.21.1421>
- Werner, D., Hashimoto, S., Tomita, T., Matsuo, S., Makita, Y., 2008. In-situ spectroscopic

- measurements of laser ablation-induced splitting and agglomeration of metal nanoparticles in solution. *J. Phys. Chem. C* 112, 16801–16808. <https://doi.org/10.1021/jp804647a>
- Wu, B., Xu, L., Wang, S., Wang, Y., Zhang, W., 2015. A PEGylated colorimetric and turn-on fluorescent sensor based on BODIPY for Hg(II) detection in water. *Polym. Chem.* 6, 4279–4289. <https://doi.org/10.1039/c5py00390c>
- Xing, T., Sunarso, J., Yang, W., Yin, Y., Glushenkov, A.M., Li, L.H., Howlett, P.C., Chen, Y., 2013. Ball milling: a green mechanochemical approach for synthesis of nitrogen doped carbon nanoparticles. *Nanoscale* 5, 7970. <https://doi.org/10.1039/c3nr02328a>
- Xu, G., Zhang, X., He, W., Liu, H., Li, H., Boughton, R.I., 2006. Preparation of highly dispersed YAG nano-sized powder by co-precipitation method. *Mater. Lett.* 60, 962–965. <https://doi.org/10.1016/j.matlet.2005.10.052>
- Xu, J.Z., Zhang, Y., Li, G.X., Zhu, J.J., 2004. An electrochemical biosensor constructed by nanosized silver particles doped sol-gel film. *Mater. Sci. Eng. C* 24, 833–836. <https://doi.org/10.1016/j.msec.2004.08.028>
- Yang, H., Wang, K., Tang, Z., Liu, Z., Chen, S., 2020. Bimetallic PdZn nanoparticles for oxygen reduction reaction in alkaline medium: The effects of surface structure. *J. Catal.* 382, 181–191. <https://doi.org/10.1016/j.jcat.2019.12.018>
- Yang, J., Lee, H., Hyung, W., Park, S.B., Haam, S., 2006. Magnetic PECA nanoparticles as drug carriers for targeted delivery: Synthesis and release characteristics. *J. Microencapsul.* 23, 203–212. <https://doi.org/10.1080/02652040500435444>
- Yin, B., Ma, H., Wang, S., Chen, S., 2003. Electrochemical synthesis of silver nanoparticles under protection of poly(N-vinylpyrrolidone). *J. Phys. Chem. B* 107, 8898–8904. <https://doi.org/10.1021/jp0349031>
- Yong, P., Rowson, N.A., Farr, J.P.G., Harris, I.R., Macaskie, L.E., 2002. Bioreduction and biocrystallization of palladium by *Desulfovibrio desulfuricans* NCIMB 8307. *Biotechnol. Bioeng.* 80, 369–379. <https://doi.org/10.1002/bit.10369>
- You, T., Niwa, O., Chen, Z., Hayashi, K., Tomita, M., 2003. An Amperometric Detector Formed of Highly Dispersed Ni Nanoparticles Embedded in a Graphite-like Carbon Film Electrode for Sugar Determination. *Anal. Chem.* 75, 5191–5196. <https://doi.org/10.1021/ac034204k>
- Zahir, A.A., Rahuman, A.A., 2012. Evaluation of different extracts and synthesised silver nanoparticles from leaves of *Euphorbia prostrata* against *Haemaphysalis bispinosa* and *Hippobosca maculata*. *Vet. Parasitol.* 187, 511–520.

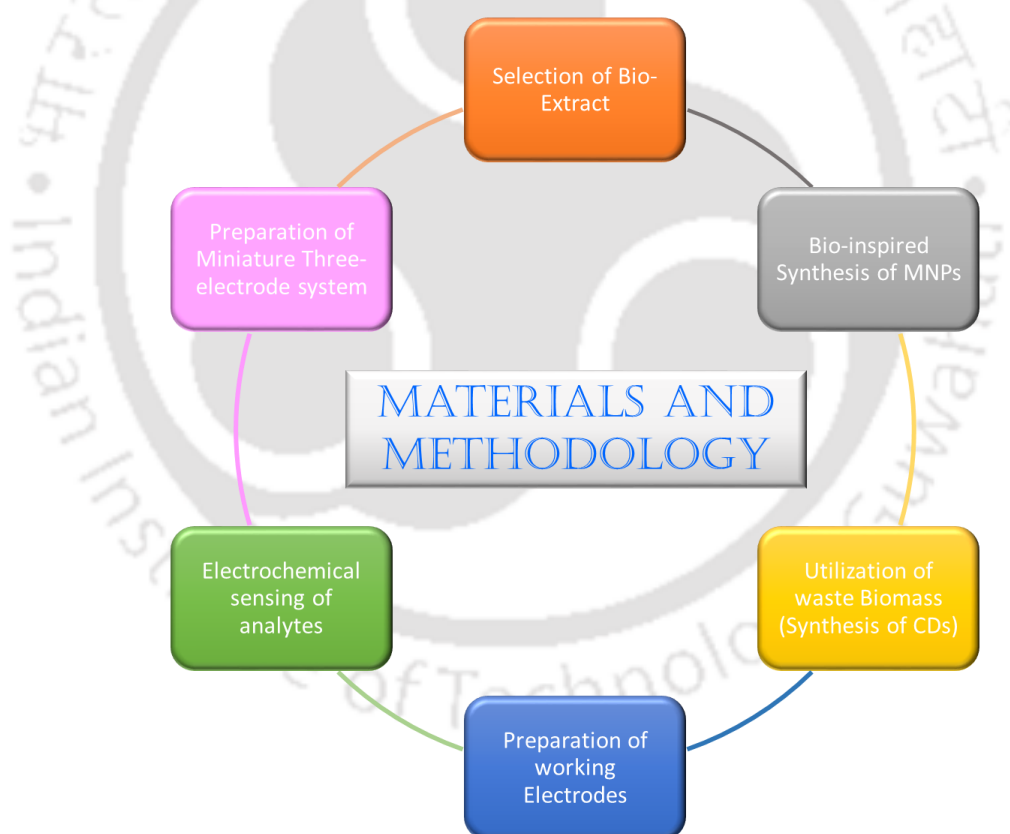
<https://doi.org/10.1016/j.vetpar.2012.02.001>

- Zako, T., Yoshimoto, M., Hyodo, H., Kishimoto, H., Ito, M., Kaneko, K., Soga, K., Maeda, M., 2015. Cancer-targeted near infrared imaging using rare earth ion-doped ceramic nanoparticles. *Biomater. Sci.* 3, 59–64. <https://doi.org/10.1039/C4BM00232F>
- Zhan, F., Wang, T., Iradukunda, L., Zhan, J., 2018. A gold nanoparticle-based lateral flow biosensor for sensitive visual detection of the potato late blight pathogen, *Phytophthora infestans*. *Anal. Chim. Acta* 1036, 153–161. <https://doi.org/10.1016/j.aca.2018.06.083>
- Zhang, J., Wang, M., Yao, X., Deng, A., Li, J., 2014. Highly sensitive electroluminescence immunoassay for Hg(II) ions based on the use of CdSe quantum dots, the methylmercury-6-mercaptopnicotinic acid-ovalbumin conjugate, and a specific monoclonal antibody. *Microchim. Acta* 182, 469–477. <https://doi.org/10.1007/s00604-014-1343-1>
- Zhang, L., Fang, M., 2010. Nanomaterials in pollution trace detection and environmental improvement. *Nano Today* 5, 128–142. <https://doi.org/10.1016/j.nantod.2010.03.002>
- Zhang, N., Chen, F., Wu, X., Wang, Q., Qaseem, A., Xia, Z., 2017. The activity origin of core-shell and alloy AgCu bimetallic nanoparticles for the oxygen reduction reaction. *J. Mater. Chem. A* 5, 7043–7054. <https://doi.org/10.1039/C6TA10948A>
- Zhang, X., Chan, K.Y., 2003. Water-in-oil microemulsion synthesis of platinum-ruthenium nanoparticles, their characterization and electrocatalytic properties. *Chem. Mater.* 15, 451–459. <https://doi.org/10.1021/cm0203868>
- Zhang, Y.N., Niu, Q., Gu, X., Yang, N., Zhao, G., 2019. Recent progress on carbon nanomaterials for the electrochemical detection and removal of environmental pollutants. *Nanoscale* 11, 11992–12014. <https://doi.org/10.1039/c9nr02935d>
- Zhou, J., Sheng, Z., Han, H., Zou, M., Li, C., 2012. Facile synthesis of fluorescent carbon dots using watermelon peel as a carbon source. *Mater. Lett.* 66, 222–224. <https://doi.org/10.1016/j.matlet.2011.08.081>
- Zhou, X., Xu, W., Liu, G., Panda, D., Chen, P., 2010. Size-dependent catalytic activity and dynamics of gold nanoparticles at the single-molecule level. *J. Am. Chem. Soc.* 132, 138–146. <https://doi.org/10.1021/ja904307n>
- Zhu, Q., Yuan, R., Chai, Y., Zhuo, Y., Zhang, Y., Li, X., Wang, N., 2006. A Novel Amperometric Biosensor for Determination of Hydrogen Peroxide Based on Nafion and Polythionine as Well as Gold Nanoparticles and Gelatin as Matrixes. *Anal. Lett.* 39, 483–494. <https://doi.org/10.1080/00032710500535956>

CHAPTER 2

MATERIALS AND METHODOLOGY

This chapter describes the experimental methods, the reagents used, and the equipment employed to characterize and analyze the catalysts and the target analytes. This chapter also describes the general theory and detailed instructions of all the electrochemical experiments involved in this study. Any specific change or deviation from what is outlined herein is mentioned in the respective Chapter.



2.1 Reagents and chemicals

2.1.1 Analytical reagents

Chemicals, reagents, and materials were used as received without further purification unless otherwise mentioned. All solutions were prepared using Milli-Q water (resistance $\geq 18.2 \text{ M}\Omega\cdot\text{cm}$ at 25°C) (Millipore, USA).

Table 2.1: List of chemicals and reagents used in this doctoral work.

Reagents/chemicals	Purity (%)	Grade	CAS/ Catalogue no.	Make
Ethanol (C ₂ H ₅ OH)	99.9	AR	GB678-90	TEDIA High Purity Solvents, USA
Nafion D-521 [®] (dispersion in water and 1-propanol)	5% w/w	-	-	Alfa Aesar, USA
Hexaammineruthenium(III) chloride	>98	AR	14282-91-8	
L(+)-Ascorbic acid (C ₆ H ₈ O ₆)	99.8	AR	50-81-7	SRL, India
Acetic acid	99.9	HPLC	64-19-7	
2,2-diphenyl-1-picrylhydrazyl (DPPH) (C ₁₈ H ₁₂ N ₅ O ₆)	99	AR	1898-66-4	
Acetonitrile (C ₂ H ₃ N)	99	HPLC	75-05-8	Merck (India/UK)
Acetone (C ₃ H ₆ O)	99	HPLC	67-64-1	
Boric Acid (H ₃ BO ₃)	99	AR	10043-35-3	
Cadmium chloride (CdCl ₂),	99.9	AR	233-296-7	
Copper sulfate (CuSO ₄ ·5H ₂ O)	99	AR	7758-98-7	
Copper chloride anhydrous (CuCl ₂)	99	AR	7447-39-4	
Hydrochloric acid	36.5	AR	7647-01-0	
Isopropyl alcohol (C ₃ H ₈ O)	99.5	AR	71-23-8	
Lead nitrate (Pb(NO ₃) ₂)	99	EMSURE	10099-74-8	
Mercuric nitrate (HgNO ₃)	98.5	AR	7783-34-8	
Nitric acid (HNO ₃)	69	EMSURE	7697-37-2	
Phosphoric acid (H ₃ PO ₄)	85	EMSURE	7664-38-2	
Potassium bromide (KBr)	99.5	GR	03-02-7758	
Potassium chloride (KCl)	99.5	AR	7447-40-7	
Potassium ferricyanide (K ₃ [Fe(CN) ₆])	99	AR	13746-66-2	
Polyvinylpyrrolidone (PVP-40000) (C ₆ H ₉ NO) _n	99	AR	9003-39-8	
Paraffin wax	99.95	AR	7778-50-9	
Sodium acetate (CH ₃ COONa)	99	AR	6131-90-4	
Sodium chloride (NaCl)	99.5	GR	7647-14-5	

Sodium citrate tribasic (Na ₃ C ₆ H ₅ O ₇)	99	AR	6132-04-3	Sigma Aldrich (Bangalore, India)
Sodium dihydrogen phosphate dihydrate (NaH ₂ PO ₄ ·2H ₂ O)	99	AR	7558-80-7	
Sodium hydroxide (NaOH)	97	AR	1310-73-2	
Disodium hydrogen phosphate (Na ₂ HPO ₄)	99	AR	7558-79-4	
Silver nitrate (AgNO ₃)	99	AR	7761-88-8	
Sulphuric acid (H ₂ SO ₄)	98	AR	7664-93-9	
Zinc nitrate (ZnNO ₃ ·6H ₂ O)	99	AR	19154-63-3	
Chloroplatinic acid (H ₂ PtCl ₆)	8	AR	16941-12-1	
Dipyron (C ₁₃ H ₁₇ N ₃ O ₄ S)	99.8	HPLC	68-89-3	
Chlorpyrifos (C ₉ H ₁₁ C ₁₃ NO ₃ PS)	99	AR	69-52-3	
Graphite powder (spherical <20 μm size)	99.9	Synthetic	7782-42-5	
Uric acid (C ₅ H ₄ N ₄ O ₃)	≥99	AR	69-93-2	
Dopamine hydrochloride ((HO) ₂ C ₆ H ₃ CH ₂ CH ₂ NH ₂ ·HCl)	≥98	AR	62-31-7	

2.1.2 Preparation of buffer solutions

2.1.2.1 Phosphate buffer solution

For the preparation of phosphate buffer solution (PBS) of 0.1 M ionic strength of pH 7.2, 0.1 M of sodium dihydrogen phosphate dihydrate (purity 99% AR grade) and 0.1 M of disodium hydrogen phosphate (purity 99%, AR grade) were mixed in a volumetric ratio of 28:72 (v/v). PBS of required strength was freshly prepared before the experiments by diluting 1 M stock solutions of the above reagents. PBS was used as a supporting electrolyte for the electrochemical sensing of ascorbic acid (Chapter 3).

2.1.2.2 Acetate buffer

Acetate buffer of ionic strength 0.1 M pH 5.0 was used as an electrolyte for all heavy metal sensing experiments. The concentration of 0.1 M of acetic acid (HPLC grade) and sodium acetate (purity 99% AR grade) was made by mixing an appropriate amount of the reagents in deionized (DI) water. A volume of 141 mL of 0.1 M sodium acetate and 59 mL of acetic acid were mixed together to obtain the buffer of required strength and pH. It was used as a supporting electrolyte for the electrochemical sensing of heavy metal ions (Chapter 4 and Chapter 7).

2.1.2.3 Britton-Robinson (B-R) buffer solution

The buffer was prepared by mixing equal volumes of 0.04 M H_3BO_3 (2.04 g / 100 mL), 0.04 M H_3PO_4 (2.8 mL of 85% H_3PO_4 / 100 mL) and 0.04 M CH_3COOH (2.3 mL of glacial CH_3COOH / 100 mL). The pH of this solution was adjusted to the desired value using 0.2 M NaOH. A required amount of KCl was added to obtain an effective ionic strength of 0.1 M, which was taken from the buffer table prepared by Mongay and Cerdrá, 1974. B-R buffer was used as a supporting electrolyte for the electrochemical sensing of chlorpyrifos (Chapter-6).

2.1.3 Target analytes for electrochemical sensing

Ascorbic acid (purity > 99.8 %), Dipyron drug (purity > 99.8 % w/w) and Chlorpyrifos PESTANAL® (Organophosphate pesticide) (purity > 99 % w/w) were procured from Sigma-Aldrich, Bangalore, India. The chemical structures of the targeted organic analytes are depicted in Figure 2.1. Apart from the organic analytes, the electrochemical sensing of heavy metals ions (HMIs) such as Pb(II) ($\text{Pb}(\text{NO}_3)_2$), Cd(II) (CdCl_2), Hg(II) (HgNO_3), Cu(II) (CuNO_3) and Zn(II) (ZnNO_3) was also conducted. All precursor salts mentioned above were of analytical grade obtained from Merck, Mumbai, India, or Merck, Gillingham, UK.

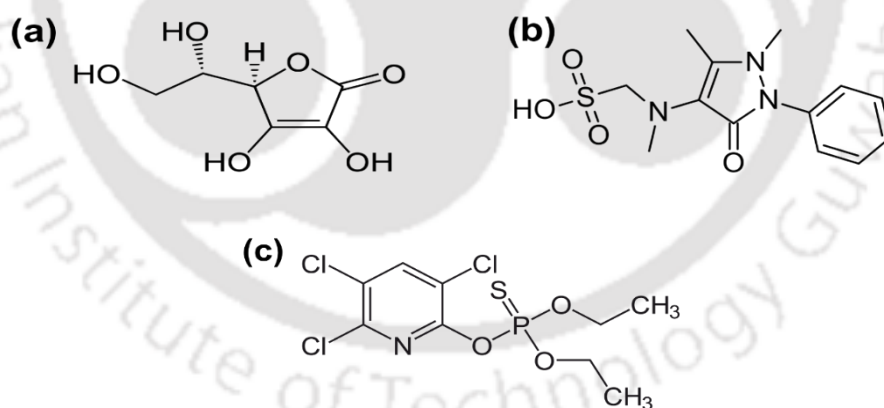


Figure 2.1: Chemical structures: (a) Ascorbic acid [(R)-3,4-Dihydroxy-5-((S)- 1,2-dihydroxyethyl)furan-2(5H)-one], (b) Dipyron drug [(2,3-dihydro- 1,5-dimethyl- 3-oxo-2-phenyl-1-pyrazol-4-yl) methyl amino], and (c) Chlorpyrifos [O,O-Diethyl O-3,5,6-trichloropyridin-2-yl phosphorothioate].

2.2 Biomass and bio-extract

2.2.1 Selection of *Psidium guajava* leaves extract

The fresh and mature *Psidium guajava* (mentioned as *P. guajava* afterward) leaves (Figure 2.2a) were collected from the plants naturally grown at Indian Institute Technology

Guwahati Campus, Assam, India. The abundance of active chemical compounds present in *P. guajava* leaves from different geographical locations and also identified in the mass spectra. *P. guajava* leaf is a rich source of various potential reducing analytes such as quercetin (10.15 mg/g), catechin (4.94 mg/g), caffeic acid (4.30 mg/g), chlorogenic acid (4.23 mg/g), rutin (3.52 mg/g), and ascorbic acid (AA) (0.9 mg/g) (Barbalho, 2012). Citric acid, a common capping agent is also abundant in *P. guajava* leaves along with other organic acids like maleic acid, malonic acid, and acetic acid (Kim et al., 2012).

Three group of plants were initially investigated for their suitability for nanoparticles synthesis. One is a shrub (*S. trilobata*), second is a fern (*D. esculentum*) and third is a group of two higher plants (*Z. maritima* and *P. guajava*). The detailed work and the results are presented in Annexure I of the thesis.

2.2.2 Preparation of *Psidium guajava* leaves extract

An amount 20 g of *Psidium guajava* (*P. guajava*) leaves (Figure 2.2a) were washed several times with running tap water followed by deionized (DI) water to get rid of any dust particles or contaminants. The cleaned leaves were chopped into small pieces (Figure 2.2b) and a paste was made (Figure 2.2c) with 100 mL water (5 mL DI water per g fresh leaves) using a mortar and pestle. The paste was squeezed manually using a muslin cloth to obtain the (crude) extract from the leaves (Figure 2.2d). This extract was then centrifuged at 10000 rpm (R-24, REMI, Mumbai, India) for 15 min to obtain the clear bio-extract (pH 5.86) (Figure 2.2e), which was used in the synthesis of various nanomaterials.

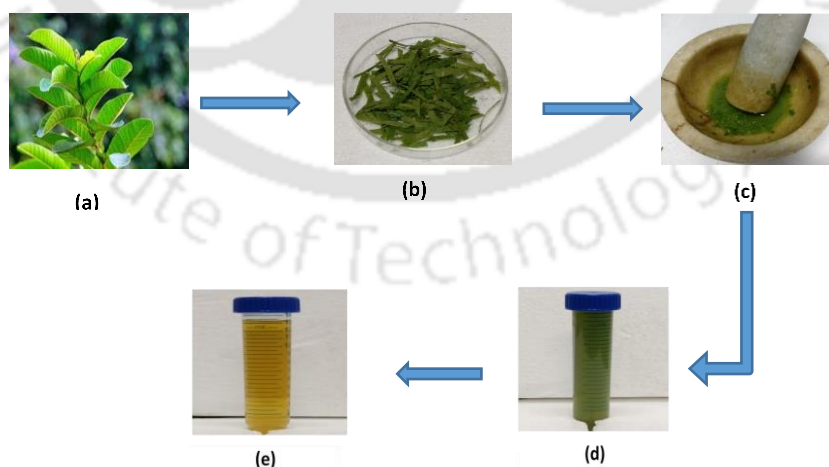


Figure 2.2: Preparation of *P. guajava* leaf extract: (a) *P. guajava* leaves at the source, (b) Chopped leaves, (c) Ground leaves with required amount of water (20 g leaves per 100 mL deionized water), (d) Bio-extract after filtration using a muslin cloth, and (e) Clarified bio-extract after centrifugation at 10000 rpm for 15 min.

2.2.3 DPPH assay of bio-extract

For the 2,2-diphenyl-1-picrylhydrazyl (DPPH) assay, 200 μM (7.9 mg DPPH in 100 mL ethanol) reagent was prepared and stored in a refrigerator in dark condition. A standard calibration curve of ascorbic acid (AA) was prepared by mixing 1 mL of AA of known concentration to 1 mL of DPPH reagent and was allowed to react for 30 min at room temperature in dark condition. The absorbance of the reaction mixture was taken at 517 nm against 1:1 (v/v) ethanol: water as the blank and plotted against the [AA] to obtain the calibration curve (Figure 2.3). A control reaction was made by replacing AA with DI water. Similarly, the absorbance value of the bio-extract was determined and the AA equivalent of the sample was estimated from the straight line (Thaipong et al., 2006; Ramaley and Krause, 1969).

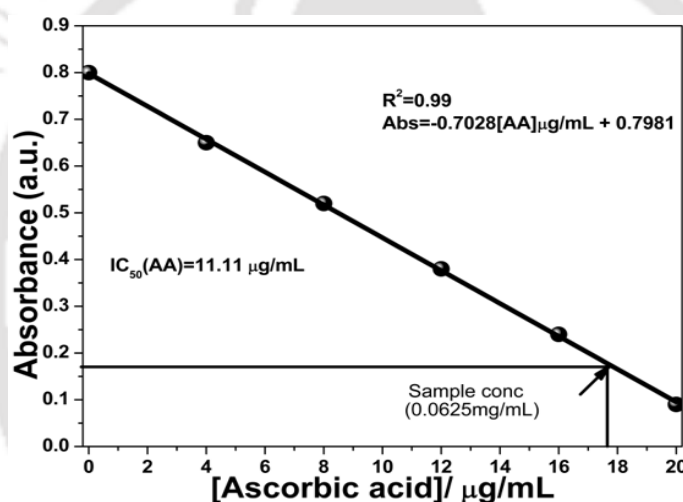


Figure 2.3: Determination of ascorbic acid equivalent of prepared *P. guajava* leaf extract using DPPH assay.

2.3 Methodologies of electrocatalysts syntheses

2.3.1 Microwave-assisted bioinspired synthesis of AgNPs

A reaction volume of 250 mL was maintained with 2.5 mL of as-prepared bio-extract and the remnant amount of 0.3 mM AgNO_3 solution. The ratio of AgNO_3 solution and bio-extract was selected based on the trial runs to maximize the yield of AgNPs. The silver nanoparticles (AgNPs) synthesis pH was maintained either at 9.5 or 11 which was adopted from the results obtained in the earlier studies (Chelli and Golder, 2016; Rao and Golder, 2016). pH of the precursor solution was adjusted using 1 M NaOH before the addition of bio-extract as it could not alter the pH of the reaction mixture (only 2.5 mL bio-

extract/ 250 mL precursor solution). It was then subjected to microwave irradiation up to 300 s at different power inputs of 240, 480, 720, 960 and 1200 W. UV-Vis spectra of the intermediate samples were recorded to study the kinetics and nature of AgNPs formed. AgNPs thus formed were centrifuged at 14000 rpm for 20 min and washed with an ethanol-water mixture (1:1 v/v) followed by DI water. AgNPs were then dried in a hot air oven at 106°C and, it was used for the detailed characterizations and fabrication of modified electrode. These AgNPs were used to modify graphite paste electrodes for the electrochemical sensing of ascorbic acid (Chapter 3) and Pb(II) ions (Chapter 4).

2.3.2 Microwave-assisted bioinspired synthesis of PtNPs

A reaction volume of 250 mL was maintained with 2.5 mL of as-prepared bio-extract and the remnant amount of 0.3 mM chloroplatinic acid solution. The platinum nanoparticles (PtNPs) synthesis pH was maintained at 9.5. The pH of the precursor solution was adjusted using 1 M NaOH before the addition of bio-extract as it could not alter the pH of the reaction mixture (only 2.5 mL bio-extract/ 250 mL precursor solution). It was then subjected to microwave irradiation up to 300 s at 960 W. PtNPs thus formed was centrifuged at 14000 rpm for 20 min and washed with an ethanol-water mixture (1:1 v/v) followed by DI water. PtNPs were then dried in a hot air oven at 106°C and, it was used for the detailed characterizations and fabrication of modified electrode. The PtNPs thus synthesized were used for electrochemical sensing of Pb (II) ions (Chapter 4).

2.3.3 Bio-inspired synthesis of Ag@PtNPs

A two-step seed-mediated method was employed for the synthesis of bimetallic Ag@Pt core-shell NPs (Figure 2.4). The formation of seed/Ag-core was carried out at pH 9.5. Briefly, a volume of 50 mL of 0.3 mM of AgNO₃ and bio-extract (water to leaves ratio 50) were subjected to 300 s microwave (MW) irradiation at 960 W. The so formed Ag-core/AgNPs were centrifuged at 14000 rpm for 15 min to separate the nanoparticles from the reaction media. The AgNPs thus obtained were washed twice using ethanol and deionized water (1:1 v/v at pH 9.5 adjusted using 1 M NaOH) to remove any un-coordinated compounds. It was again re-dispersed in 50 mL water (0.8 mg/mL) at pH 9.5. The suspension was sonicated for 10 min to disperse AgNPs aggregate, if any. This Ag-core was then used for the synthesis of Ag@PtNPs.

The formation of the Pt-shell on the Ag-core was also facilitated by the use of microwave but a lower input power. This was done by reducing 1 mM H_2PtCl_6 (2.5 mL of 20 mM stock) at pH 9.5 in the presence of 50 mL Ag-core suspension and *P. guajava* leaf extract (5 mL/ 250 mL). The reaction was carried out for 240 s at 760 W of microwave power with an off period of 10 s after every 30 s of irradiation. These bio-inspired Ag@PtNPs were used for the electrochemical sensing of Pb(II) ions in various environmental water samples (Chapter 4), and the results were compared with individual AgNPs and PtNPs as described in previous sections (Sections 2.3.1 and 2.3.2) (Chapter 2).

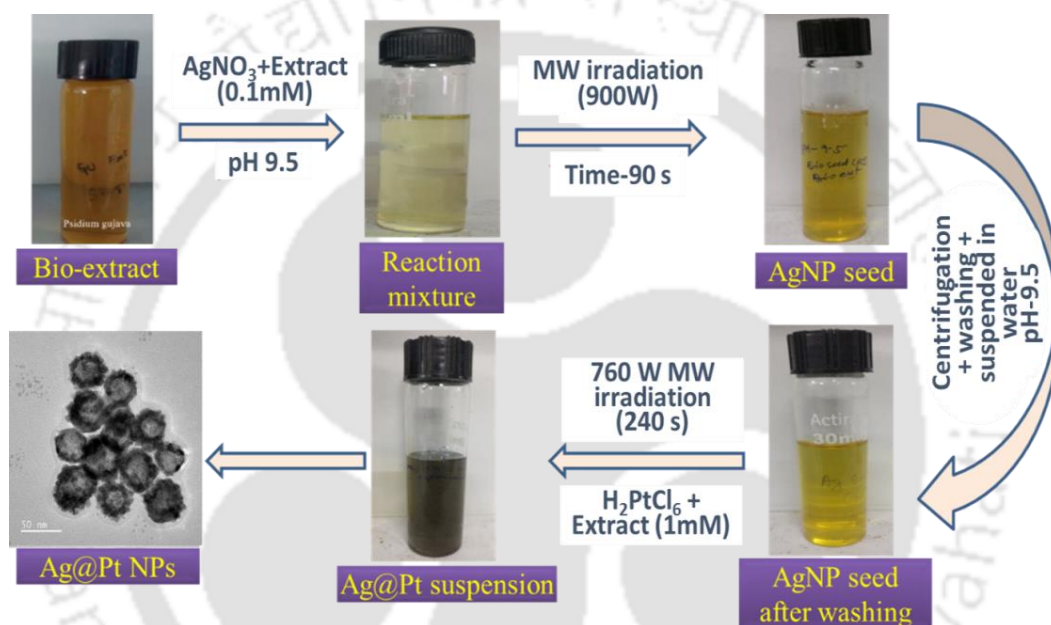


Figure 2.4: Schematic diagram depicting the steps of the bioinspired synthesis of Ag@Pt core@shell NPs.

2.3.4 Bioinspired synthesis of PtNPs/graphene nanocomposite

2.3.4.1 Synthesis of graphene

Graphene was synthesized following the method, an alternative to modified Hummer's method, as described by Yi and coworkers (Yi et al., 2013) with a little modification. Briefly, an amount of 300 mg of graphite powder (<20 μm) was taken in 100 mL acetone: water (75:25 v/v) and kept under ultrasonication (40 Hz) for 4 h. The temperature of the sonicator bath was maintained at $\sim 25^\circ\text{C}$ through icy water circulation. The obtained solution was centrifuged at 1000 rpm for 20 min to separate the larger graphitic particles from graphene. The yield of graphene was about 0.8 mg/mL of acetone-

water solution. It was further subjected to microwave irradiation for 3 min at 700 W to exfoliate graphene layers and re-sonicated for 1 h in the acetone-water mixture. The final solution with a concentration of 0.5 mg/mL (prepared by diluting using the required amount of DI water) was used for further experiments. The steps involved in the synthesis of graphene are schematized in Figure 2.5.

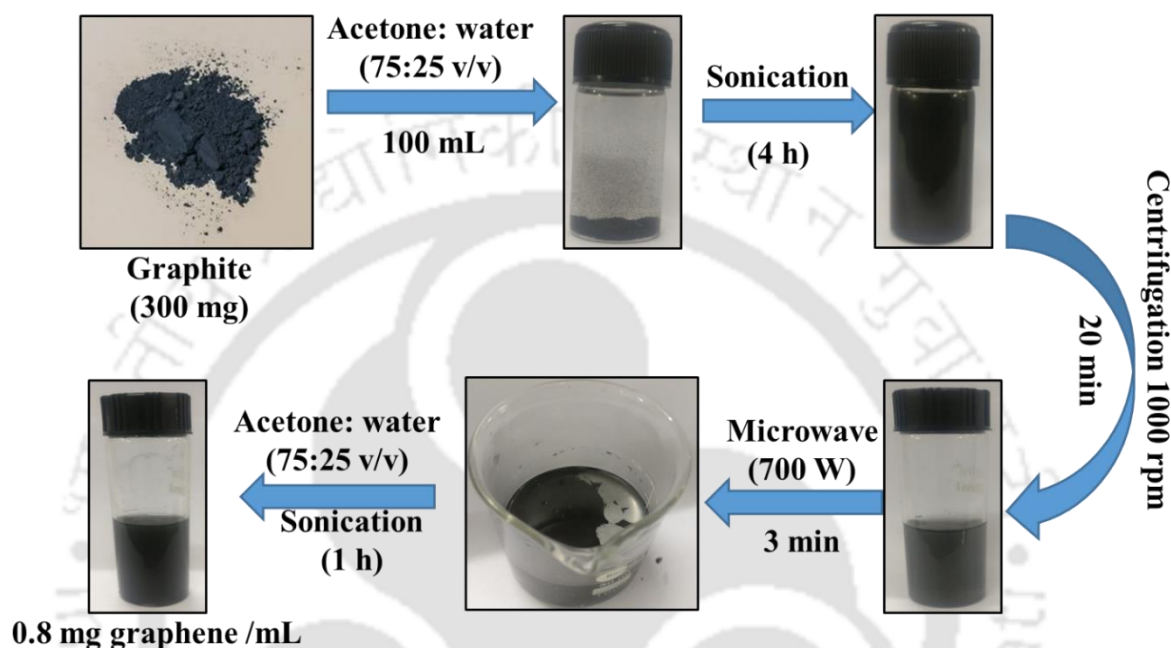


Figure 2.5: Schematic representation of the preparation of graphene solution.

2.3.4.2 Synthesis of PtNPs/graphene nanocomposite

In the preparation of *P. guajava* leaves extract, an amount of 20 g of fresh matured leaves were crushed in 150 mL of distilled water using a mortar and pestle, and a slurry was formed. The slurry was then vacuum filtered through a 0.2 μm nylon filter paper to get a clarified bio-extract, and it was then stored at 4 $^{\circ}\text{C}$. A reaction mix containing 750 μL of 20 mM stock of H_2PtCl_6 (final concentration 0.3 mM), graphene (0.5 mg/mL) and 6.5 mL of bio-extract (water to leaves ratio 50) with a total volume of 50 mL was taken in a 250 mL borosilicate glass beaker. The pH of the reaction mixture was maintained at 9.5 using 1M NaOH (200 μL). The mixture was then exposed to the microwave (MW) irradiation at 900 W for a duration of 300 s. By that time, the colour of the mixture was turned from yellowish-brown to dark brown (Figure 2.6). After that, it was allowed to cool to room temperature, and the PtNPs/graphene mixture was collected by centrifugation (14000 rpm, 30 min). The supernatant containing bio-residuals was discarded. The PtNPs/graphene

nanocomposites obtained in this way were re-dispersed in 1:1 ethanol-water (v/v) and collected further by centrifugation. The rinsed PtNPs/graphene nanocomposite was dried and re-dispersed in DI water with a concentration of 0.5 mg/mL for further use. The step-by-step method for the synthesis of PtNPs/graphene nanocomposites is depicted in Figure 2.6. The synthesized PtNPs/graphene nanocomposites were used for the electrochemical sensing of dipyrone drug (Chapter 5).

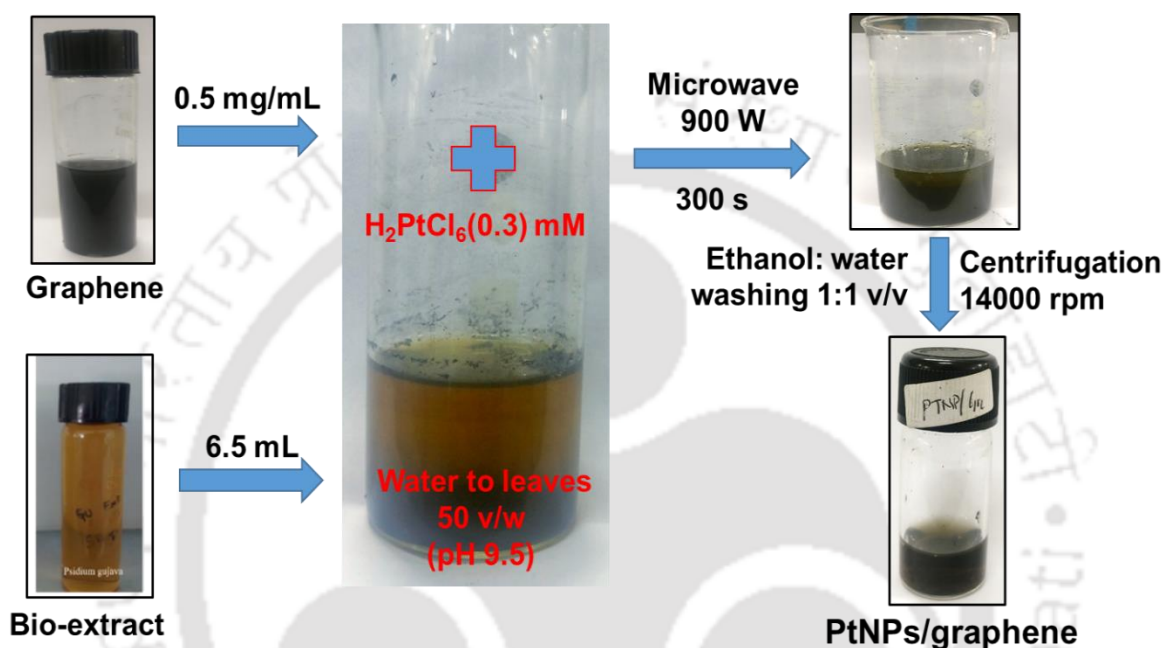


Figure 2.6: Digital images showing different stages of preparation of bioinspired PtNPs/graphene nanocomposite.

2.3.5 Synthesis of carbon dots (CDs) from *P. guajava* waste biomass

The carbon dots (CDs) were synthesized by hydrothermal degradation of dried *P. guajava* leaves powder. The fresh *P. guajava* leaves were first cut into small pieces and made into a paste using 150 mL of DI water per 20 g of leaves (Figure 2.2). The paste was then squeezed through a muslin cloth to separate the bio-extract from the leaves biomass that was used in the bioinspired synthesis of PtNPs, AgNPs and Ag@PtNPs core-shell nanoparticles in my previous studies (Sections 2.3.1-2.3.4, Chapter 2). The leaves residue left behind after the bio-extract separation was dried overnight at 80°C in a hot air oven. The dried powder was then pulverized using a domestic blender and used for further reactions.

An amount of 1 g of the prepared *P. guajava* leaves powder was taken in 60 mL DI water in a Teflon lined hydrothermal reactor of 100 mL capacity and was put in a hot air oven for 10 h (Yuan et al., 2015; Zhang et al., 2019; Lai et al., 2020) at different temperatures (160–200 °C). The obtained brownish-yellow liquid was then vacuum filtered through a 0.2 µm Nylon filter, and the filtrate containing CDs was stored for further use. Figure 2.7 gives a schematic description of the processes involved in CDs synthesis. CDs thus synthesized were used to modify the glassy carbon electrode (GCE) for the electrochemical sensing of Chlorpyrifos (Chapter 6).

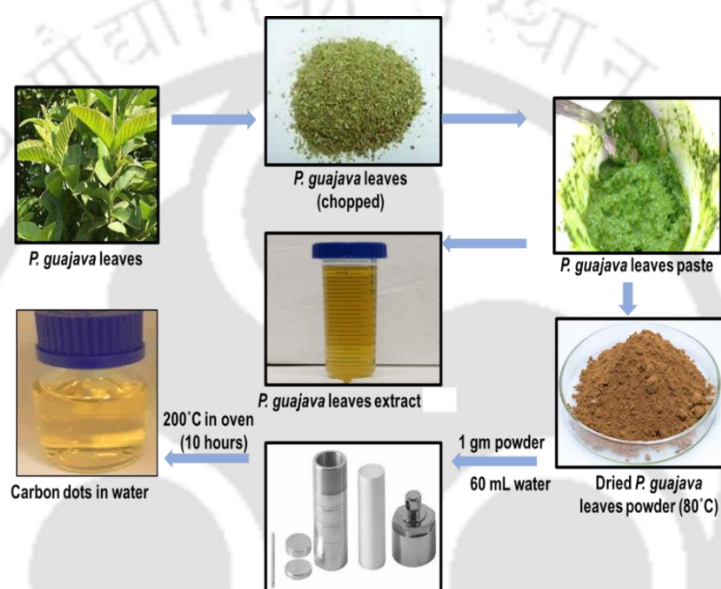


Figure 2.7: Schematic representation of the synthesis of CDs from *P. guajava* leaves using hydrothermal method.

2.3.6 Synthesis of Cu and Cu@Ag nanorods

This work was initiated at the University of Strathclyde, Glasgow (UK) under the Commonwealth Slit-Fellowship Programme, and it was completed at my parent Institution (IIT Guwahati). Copper nanorods (CuNRs) were synthesized using a method previously described with slight modifications (Yokoyama et al., 2018). All chemicals used in this study were of analytical grade obtained from Sigma Aldrich/Merck, UK. Deionized water (18.2 MΩ) obtained from a Milli Q water purifier system (Make: Millipore Ltd., model: IQ 7000, Watford, UK) was used in all experiments. CuNRs were synthesized using CuCl₂ as the source of Cu, sodium chloride (NaCl) as an additive, polyvinylpyrrolidone (PVP K40) as a capping agent, and L(+)-ascorbic acid as a reducing agent. CuCl₂ and AA solutions were prepared separately by dissolving 0.806 g anhydrous CuCl₂ (0.1 M) and AA (1.5 M)

in deionized water under ultrasonication for 0.5 h. PVP K40 1.44 g (2.4 wt %) and NaCl 1.22 g (0.35 M) were also added into the AA solution in a glass vial (100 mL capacity) under stirring. The CuCl_2 solution was then poured into the glass vial. The solution pH was adjusted to 3.5 by adding 4 M NaOH (~2 mL), and the final reaction volume was adjusted to 60 mL. The solution was equally divided into two identical vials of 30 mL each. The reaction temperature was controlled at 80°C using a water bath (Make: Clifton, model: NE4-HT, North Somerset, UK) with intermittent shaking, and the reaction was continued for 24 h. The prepared nanomaterials were washed thrice using 1:1 (v/v) ethanol and water, and it was stored in a storage solution comprising of 1 M AA and 2.4 wt% PVP K40 in water with a nanomaterial concentration of 1 mg/mL. Before further using the synthesized CuNRs, it was thoroughly washed with DI water to remove the AA and PVP K40 in the storage solution (Stewart et al., 2015). For the synthesis of Cu@AgNRs, 0.5 mL of 0.025 M AgNO_3 solution was pipetted into the CuNRs solution (1 mg/mL) stored in the storage solution of 10 mL and vigorously shaken to get a uniform mixture. It was then allowed to stand undisturbed for 2 h for the reaction to complete (Stewart et al., 2015). Figure 2.8 shows the schematic of the step-by-step method for the synthesis of CuNRs and Cu@AgNRs. These synthesized nanorods were used for the fabrication of miniaturized Fluorine-doped tin oxide (FTO) based sensing device for the determination of heavy metal ions (HMIs), namely Zn(II), Hg(II), Cd(II) and Pb(II) (Chapter 7).

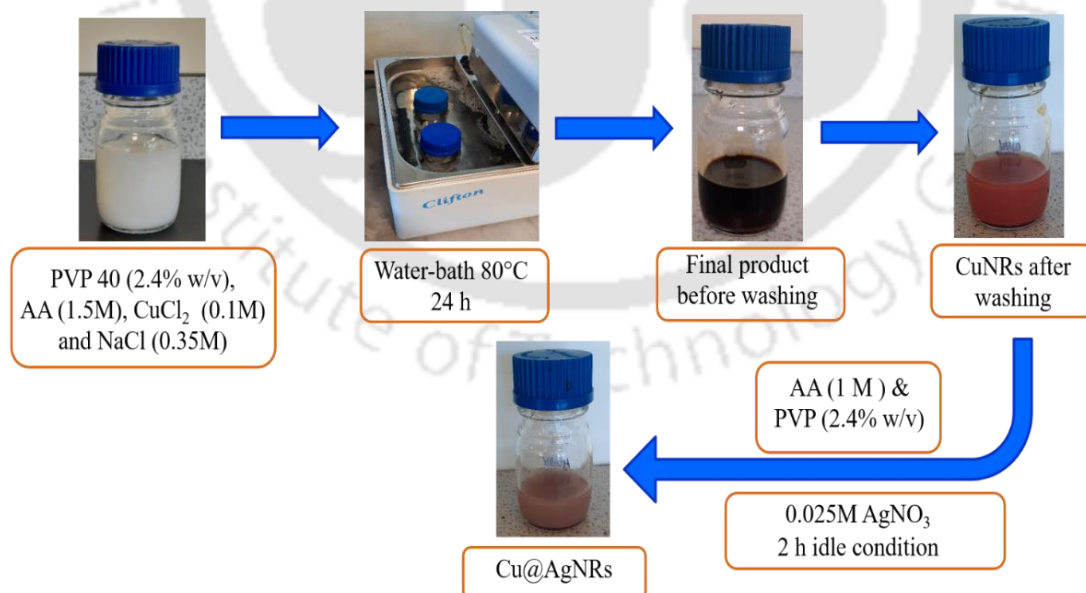


Figure 2.8: Schematic representation of the step-by-step synthesis of CuNRs and Cu@AgNRs.

2.4 Characterizations of electrocatalysts

2.4.1 UV-vis spectroscopy

The optical absorbance spectra of AgNPs and PtNPs dispersions formed at different experimental conditions were recorded using a UV-Vis spectrophotometer (Cary-100, Agilent, USA) with 10 mm quartz cuvettes. It was used to detect the Surface plasmon resonance (SPR) in typical nanoparticles that could tentatively provide us with the structural and morphological details. The absorbance was recorded by scanning the wavelength of the incident light from 350-800 nm depending on the experiments.

2.4.2 High performance liquid chromatography

High performance liquid chromatography (HPLC) was performed using a 1200 series HPLC from Agilent Technologies, Sunnyvale (CA) equipped with a C₁₈ analytical column of dimensions 250 mm × 4.6 mm. A UV detector at the required wavelength was used for the detection of various analytes. The solution was first passed through a syringe filter of pore size 0.22 μm to clear out any suspended particles. It was then transferred into HPLC vial of 2 mL capacity for the analysis. The sample injection volume was kept constant at 20 μL.

For the detection of ascorbic acid (AA), the mobile phase used was acetic acid (0.05%) and acetonitrile (99.9%) at a ratio of 80:20 (v/v). A flow rate of 1 mL.min⁻¹ was applied. The detection was done using a UV detector at 254 nm wavelength (Chapter 3).

The analysis of dipyrone (DIP) was done using the mobile phase of a mixture of 15:85 (v/v) orthophosphoric acid (0.0 M, 15%) and acetonitrile (85%). The mobile phase was clarified using a 0.2 μm filter paper and degassed for 1 h using a sonicator (Chemtech; 40 Hz). The flow rate was maintained at 1.0 mL.min⁻¹, and the detection was done at 214 nm using a UV detector (Belal et al., 2014) (Chapter 5).

HPLC analysis for chlorpyrifos (CHL) was done by the method described in literature with slight modifications (Mauldin et al., 2006). The agriculture grade samples were briefly diluted using acetonitrile (HPLC grade, ≥99.9 %) to the required concentrations by vigorous shaking using the vortex shaker to obtain a clear pale yellow solution. The mobile phase (a mixture of acetonitrile (90%) and phosphate buffer (10% v/v pH 4.5)) was set at a flow rate of 0.7 mL.min⁻¹. The detection was done at 230 nm using a UV detector (Chapter 6).

2.4.3 Fourier transform infrared spectroscopy

Infrared (IR spectrum) emission or absorption of samples was recorded using Fourier transform infrared (FTIR) spectroscopy. The sample absorbs a certain amount of infrared radiation and transmits a certain amount of radiation based on the types of functional groups present in the sample. The FTIR spectra of the bioinspired nanoparticles and bio-extract were captured to determine the presence of various surface functional groups in the specimens. The samples were properly mixed with approximately 10-15 mg KBr to create the pellet. The background spectrum was taken first, and the percentage of the transmission in the presence of the sample was recorded by comparing it with the background spectrum. The FTIR analysis of the sample was conducted in a Fourier transform infrared spectrometer (Make: Perkin Elmer, model: Spectrum two, Waltham, USA) to detect the functional groups present in the synthesized electrocatalysts. The FTIR analysis of the liquid samples such as bio-extract was done using a demountable liquid cell made up of KBr. These cells were equipped with thin Teflon spacers to create a minute gap for the liquid samples to form a thin film over the KBr. This cell was then placed in the instrument perpendicular to the incident IR beam using a cell holder provided by the manufacturer. The transmission spectra of the electrocatalysts were recorded in the spectral range of 400-4000 cm^{-1} .

2.4.4 High resolution mass spectrometry

Mass spectrometry (MS) is an analytical technique that is used to detect the chemical identity or structure of various molecules. During the analysis, the samples are transformed into gaseous ions by bombarding them with electrons. These will help the molecules either become charged or break into charged ions which can then be detected with the use of a magnetic field according to their mass to charge (m/z) ratio and finally provide the spectral peaks. In this study, the mass spectra of the solid samples were recorded. The samples were at first solubilized in acetonitrile and then it was injected into the mass analyzer. The mass spectra of the analyte were obtained through the high-resolution mass spectrometer (HR-MS) (Make: Agilent, model: 6520, Santa Clara, USA). The obtained peaks were used to identify the molecular mass of the sample. This helped us in deriving various electrochemical reaction mechanisms. The active anti-oxidants present in the *P. guajava* leaves extract were analyzed using this technique (Chapter 3), reaction mechanism and analysis of various electro-oxidation products of Dipyrone (Chapter 5) and Chlorpyrifos (Chapter 6).

2.4.5 X-ray diffraction

X-ray diffraction (XRD) analysis is an analytical technique that is used to identify the phase of the crystalline materials. X-ray diffraction results from the constructive interference between X-rays and electrons of the sample materials. X-rays generated from a cathode ray tube are filtered and monochromatic radiation is produced, which is then assimilated to concentrate before pointing on the sample. The diffraction occurs only when the Bragg's law is satisfied with the constructive interference from the crystal planes with spacing d (Eq. 2.1).

$$n\lambda = 2d \sin\theta \quad (2.1)$$

Where, λ is the wavelength, d is the spacing between the two crystal planes, and θ is the Bragg's angle, which is the angle between the incident and reflected beam. After that, the diffracted X-rays are detected, processed and recorded. This phenomenon helps to identify the substance present in the sample, and the bioinspired nanocatalysts and nanocomposites were characterized by using this method. Briefly, 20 mg of dried sample was placed in the sample holder and then the XRD patterns were recorded between 10 and 90° 2θ angle. The X-ray diffraction analysis was carried out in an advanced X-ray diffractometer (Make: Bruker, model: D8 Advance, Karlsruhe, Germany) with $\lambda = 0.15406$ nm of $\text{CuK}\alpha$ radiation at 5° per min scan rate.

2.4.6 Field emission scanning electron microscopy

Field emission scanning electron microscopy (FESEM) is used to study the surface topography and morphology of a specimen. This technique helps researchers to examine minute structures on a nanometer scale. FESEM's high electron energy beam is generated using a field emission cathode. FESEM can magnify the samples higher than the 10 KX range. At first, the synthesized catalysts were dispersed properly in an appropriate solvent (HPLC grade ethanol) and sonicated to make complete homogenized dispersion. A glass slide covered with aluminum foil was used as the base in which a drop of the prepared dispersion was poured and dried in the oven. After drying, the glass slide was then kept on the metal stub covered with conductive carbon tape in an electron microscope. In this work, FESEM (Make: Zeiss, model: Sigma, Jena, Germany) was done to study the morphology of the nanoparticles, dispersion of the nanocatalysts and nanocomposites on the working electrode surface, and decoration of PtNPs on the prepared graphene nanosheets.

2.4.7 Field emission transmission electron microscopy

In Field emission transmission electron microscopy (FETEM), the electron beam is projected on the sample and the transmitted electrons from the samples are then used to generate two-dimensional images. In the case of FETEM, as the electrons pass through the samples, the internal structure of the sample could be distinguished based on the contrast due to the variation in atomic densities. The sample was prepared by dispersing about 1 mg sample in 1 mL ethanol-water solution (1:1). Then the sample was drop cast over a TEM grid made of copper. The sample was then dried in an oven and the grid was placed in the sample holder and the TEM analysis was carried out (Make: JEOL, model: JEM 2100F, Tokyo, Japan). The TEM analysis provided us minute details and insights of the nanocatalysts like its fringe width, crystallinity (from SAED data) and Inverse Fast Fourier Transform (IFFT) images that helped in establishing the proper synthesis of the nanomaterials.

2.4.8 Energy-dispersive X-ray spectroscopy

Energy-dispersive X-ray spectroscopy (EDX) is an analytical technique used for the elemental analysis or chemical characterization of a sample. In this technique, a beam of X-rays is focused and penetrates on the sample and after interacting with it, the X-rays are emitted. The emitted X-rays are then detected by the energy dispersive detector. The preparation of the sample is similar to that of the preparation in FESEM/FETEM analyses depending on the parent equipment used. The EDX spectra, elemental mapping of the electrocatalysts and electrodes coated with the nanoparticles/catalysts, and the percentage elemental compositions of the catalysts were investigated. The EDX spectra of the catalysts were obtained either using FESEM (Make: Zeiss, model: Sigma, Jena, Germany) or TEM (Make: JEOL, model: JEM 2100F, Tokyo, Japan).

2.4.9 Atomic absorption spectroscopy

Atomic absorption spectroscopy (AAS) is a spectroscopic method that determines the percentage of chemical elements using the absorption of optical radiation (light) by the free atoms in those elements in a gaseous state. At first, the molecules are exposed to a high temperature in a flame or graphite furnace. This is done using an atomizer and the role of it is to separate the particles into various individual molecules and then into atoms. The free atoms generated in the atomizer can absorb the radiation at a specific frequency and thus makes transitions to higher electronic energy levels. The concentration is then calculated from the amount of spectral absorption. In this study, AAS was used to compare the results

obtained from the electrochemical sensing of HMIs. (Make: Varian, model: AA240FS, Mulgrave, Australia). The calibration curve was obtained in the range of 1 to 10 mg·L⁻¹ for all metal ions separately, and calibration samples were prepared each time before the analyses.

2.4.10 Raman spectroscopy

The Raman spectra were done to characterize the synthesized graphene nanocomposites (Chapter 5). The analysis was done by Laser Micro Raman System (Make: Horiba Jobin, model: LabRam HR, Vyon, USA) in the Raman shift range of 100-3000 cm⁻¹.

2.4.11 Thermogravimetric analysis

The mass losses of bioinspired AgNPs with the temperature were studied by the Thermogravimetric analysis (TGA) (Make: Netzsch, model: TG 209 F1 Libra, Selb, Germany). A 10 mg sample was used for the analysis at the temperature range of 30 to 800°C. A heating rate of 10°C/min with an N₂ flow rate of 20 mL/min was applied (Rao and Golder, 2016b).

2.5 Electroanalytical techniques of sensing

2.5.1 Three-electrode system for electrochemical sensing studies

The three-electrode electrochemical sensor system comprises the working electrode (WE) or sensing electrode, the counter electrode (CE) or auxiliary electrode and the reference electrode (RE). The WE is the one on which the intended electrochemical reaction takes place. The WE surface is generally modified, and the electrode material is chosen based on the application of the electrochemical sensor.

All electrochemical sensors require an external potential difference between the electrodes. Hence, it is expected to have a fluctuating potential at the sensing electrode due to the continuous electrochemical reaction-taking place at the surface, which could lead to a continuous change at the electrode surface. So, to maintain a stable electrode performance of the sensor over extended periods, it becomes quite necessary to have a stable and constant potential at the sensing electrode. A reference electrode is placed at close proximity with the sensing electrode to maintain the applied value of the voltage to the actual voltage at the sensing electrode (Chauliya and Prasad, 2016). No current flows to or

from the reference electrode. The analytes react at the sensing electrode and the current flow between the sensing and the counter electrode is measured. The value of the voltage applied to the sensing electrode makes the sensor specific to the target HMIs or analytes. Various reference electrodes like standard hydrogen electrode (SHE) or normal hydrogen electrode (NHE), standard calomel electrode (SCE), $\text{Fe}^{3+}/\text{Fe}^{2+}$, Ag/AgCl electrode with varying KCl concentrations as supporting electrolytes are used for this purpose. The potential applied can easily be converted from one reference to another to enable uniformity in all the reactions irrespective of the reference electrodes used. A conversion table from one reference electrode to another is provided in Figure 2.9.

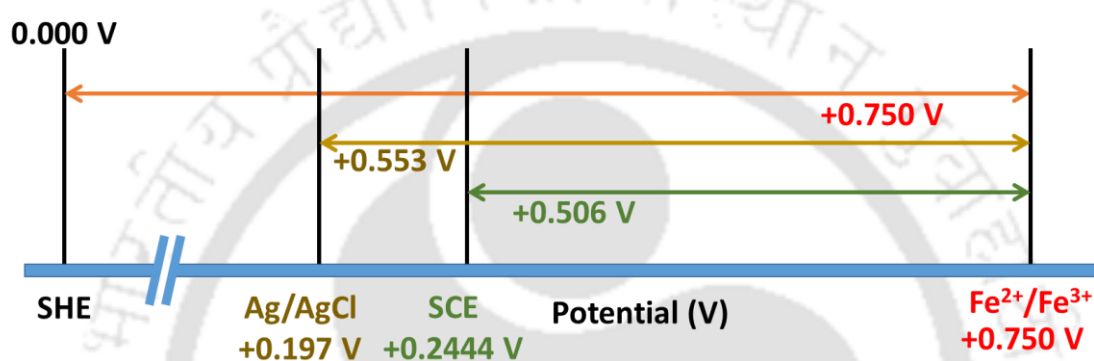


Figure 2.9: Conversion graph between different reference electrodes.

The surface area of a working electrode plays a paramount role in enhancing the electrochemical signal towards the sensing of target analytes or MHIs. High surface provides plenty of active sites for the docking of analytes. This helps in pre-concentrating the analytes onto the electrode surface and thereby providing a chance of increased electrochemical reactions.

In a three-electrode system, the counter electrode and the working electrodes provide a circuit over which either oxidation or reduction occurs depending on the positive or negative applied potential to the working electrode. The counter electrode generally supplies the electrochemical system with electrons during oxidation reactions or acts as an electron quencher during reduction reactions. Therefore, it is necessary that the counter electrode can suffice the electron neutrality to the electrochemical cell. The uninterrupted electrochemical reaction is assured by providing a large surface area of the counter electrode.

In order to avoid the iR drop across the electrodes, it is vital to align the electrodes correctly. In a three-electrode system, it is preferred to place the reference electrode as close

as possible to the working electrode and the counter electrode with a maximum distance of twice that of the diameter of the capillary tube of the reference electrode to avoid the drop in the iR_{cell} . The effect of the iR drop is depicted in Figure 2.10. The uncompensated resistance (iR_u) between the WE and RE is difficult to remove; hence, it is necessary to confirm that RE is always at constant potential and no current passes through it to avoid potential shifts (Britz and Brocke, 1975).

All electrochemical experiments in this work were conducted using Potentiostat/Galvanostat (Make: Metrohm Model: PGSTAT 302 N, Kanaalweg, The Neatherlands). The three-electrode system included a platinum wire (1 mm dia) as the counter electrode (CE), Ag/AgCl/3 M KCl) as the reference electrode (RE), and the fabricated graphite paste electrode (GPE, bare or modified) as the working electrode (WE) (Chapters 3 and 4), modified Glassy carbon electrode (3 mm dia) (Chapters 5 and 6). The image of the electrochemical setup with all the working electrodes is provided in (Figure 2.11). A miniaturized three-electrode system was also fabricated based on FTO for electrochemical sensing of HMIs. The detailed fabrication process of all the WEs is provided in the following sections.

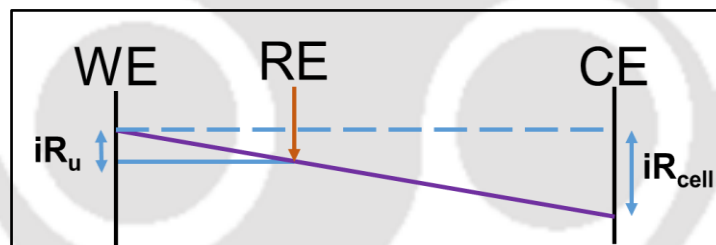


Figure 2.10: Effect of the positioning of the electrodes on resistances in a three-electrode system.

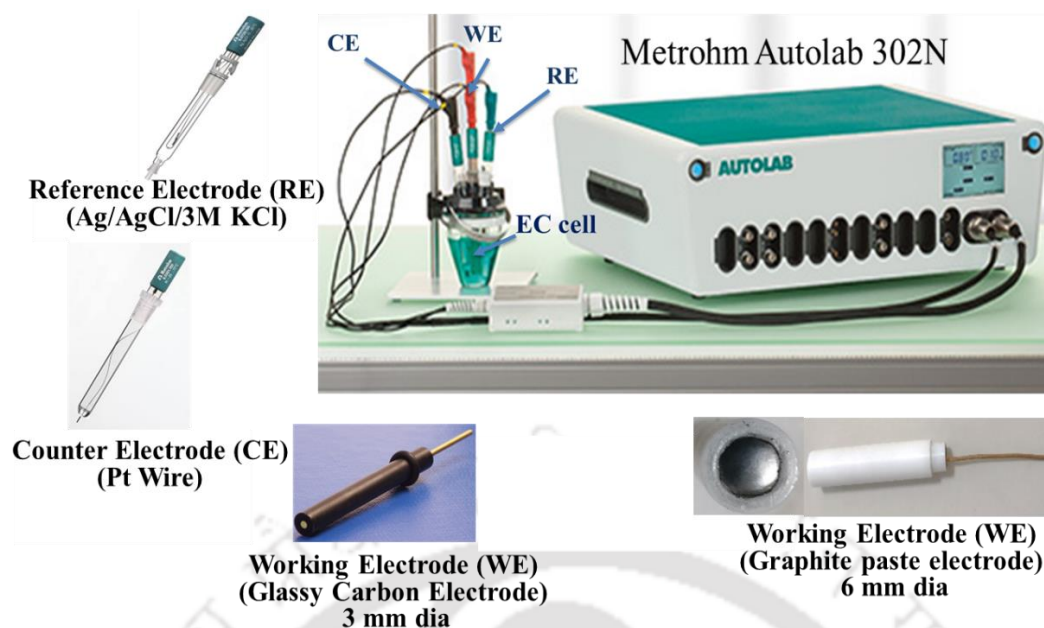


Figure 2.11: Experimental setup for the three-electrode electrochemical system used for electrochemical sensing of various analytes displaying all the major components for conducting the experiments.

2.5.2 Fabrication of working electrodes

An amount of 650 mg graphite powder and 350 mg paraffin wax mixed thoroughly and heated at about 60 °C to obtain a homogeneous mixture of about 1 g (Jayasri and Narayanan, 2007). The resulting mixture was packed into a Teflon tube of 6 mm in diameter and 50 mm in length. A copper wire of 18 gauge (1.02 mm) was inserted at one end for the electrical connection. The electrode was kept in a dust-free container and allowed to gradually cool to room temperature for solidification. The support electrode surface was smoothed by polishing on a piece of 75 gsm A4 sheet before use. It was carefully cleaned using 5% nitric acid solution followed by profuse washing with DI water and dried at room temperature in a vacuum desiccator (150 mm diameter). This support electrode is mentioned as the graphite paste electrode (GPE) (Figure 2.12). The as-prepared GPE was drop-coated (40 μ L) with a mixture containing the required amount of nanomaterials in 1 mL 0.5% Nafion solution and allowed to dry at room temperature in the vacuum desiccator. This process was repeated two times to obtain the modified GPE. This GPE modified with AgNPs was used for the electrochemical sensing of ascorbic acid (Chapter 3) and modified with Ag@PtNPs, PtNPs and AgNPs for the electrochemical sensing of Pb(II) ions (Chapter 4)

The commercial glassy carbon electrodes (GCEs) were modified with nanomaterials by drop-casting 40-60 μL of nanomaterials + Nafion solution (0.5%) and used as the WEs for the sensing of Dipyrone (Chapter 5) and Chlorpyrifos (Chapter 6). The GCE (3 mm dia) was first polished with 0.5 μm alumina powder to get a shiny mirror finish. It was after that dip-washed by using 5% nitric acid (v/v) and ultrasonic cleaner (40 Hz) for 5 min followed by a thorough rinse with a profuse amount of acetone and DI water. GCE was then dried at $25\pm 2^\circ\text{C}$ in a vacuum desiccator. PtNPs/graphene ($0.5\text{ mg}\cdot\text{mL}^{-1}$) was dispersed in 0.5% Nafion solution in isopropanol (0.5 mg PtNPs/graphene added to 1 mL Nafion dispersion), and 40 μL of the prepared mixture (2 mL) was then drop-casted onto the polished and clean GCE. The modified electrode (denoted as PtNPs/graphene/GCE) was allowed to dry at room temperature. This was used for the electrocatalytic sensing of dipyrone (DIP) (Chapter 5).

Similarly, carbon dots (CDs $0.35\text{ mg}\cdot\text{mL}^{-1}$) was dispersed in 0.5% Nafion solution in isopropanol, and 60 μL of the prepared mixture (2 mL) was then drop-casted onto the polished and clean GCE. The modified electrode (GCE/CDs) was allowed to dry at room temperature and used in the electrochemical sensing of chlorpyrifos (CHL) (Chapter 6).



Figure 2.12: Step by step method for the preparation of the working electrode.

2.5.3 Cyclic voltammetry

Cyclic voltammetry (CV) is a typical electroanalytical measurement technique. In this technique, the working electrode potential is ramped linearly with time. When the set potential is reached in a CV experiment, the working electrode potential is ramped in the opposite direction to return to the initial potential. These cycles of possible ramps can be done as many times as required. The current (I) at the working electrode is plotted against the applied voltage (E) (that is, the working electrode's potential) to map the cyclic voltammogram. CV is a flexible tool for scientific investigation and advancement due to the fact that most chemical processes involve electron transfer, which allows them to be analyzed by this technique. CV has long been important in many areas facilitating research as an analytical method. The technique provides scientists with an insight into various electrochemical processes, reaction mechanism, quantitative analyses and electron transfer process. The manner in which the analyte passes its electrical responses to the surrounding environment allows scientists to observe the behavior, thus determining their characteristics. In addition, due to the ease of operation, the technique is convenient and cheaper.

In this work, CV has been extensively used for the determination of electrochemical behavior of various analytes, determination of reaction mechanisms, deduction of electrochemical kinetics and electrochemical characterization of the working electrodes (Section 2.5.8). In Chapter 3, the CV tests were performed at room temperature. The scanning rate of AA was varied from 10 to 100 $\text{mV}\cdot\text{s}^{-1}$ and 1 to 2000 μM , respectively. Phosphate buffer solution (PBS 0.1 M, pH 7.2) of 100 mL in a 150 mL capacity electrochemical cell (Metrohm, cat. no. 6.1418.250) was used as the supporting electrolyte to avoid AA decomposition at higher pH. Similarly, in Chapters 5, CV was performed using PtNPs/graphene/GCE at different scan rates ($5\text{-}200\text{ mV}\cdot\text{s}^{-1}$) from 0-1.2 V vs. Ag/AgCl and KCl as the supporting electrolyte (pH 7) to derive the fundamental electrokinetic parameters and also to understand the redox pathway of Dipyrone (DIP) sensing.

2.5.4 Chronoamperometry

Chronoamperometry is a versatile technique that, in conjugation with the CV technique, is an excellent tool to investigate any electrochemical reactions. In this technique, the potential of the working electrode is stepped based on the redox peaks obtained from the CV experiments. The functional relationship between the current response and time is measured after applying a single or double potential step to the

working electrode of the electrochemical system. The current generated (I) at the working electrode (at the set potential E) is plotted against time (t). This technique is used by the researchers to track the Faradaic current of an electrochemical reaction and let them know the live status of an ongoing reaction. This technique is used for electrochemical conversion reactions in detecting any side reactions that are taking place, determining electrode/catalyst stability and sensitivity of an electrocatalyst for a specific analyte.

In this doctoral work, this technique is used for preparing calibration curves, interfering agent detection and the sensitivity of the working electrodes. The chronoamperometry tests were performed at 0.380 V vs. Ag/AgCl using AgNPs/GPE as the working electrode with the successive addition of AA from 25 to 100 μM in an interval of 30 s up to the AA concentration of 2000 μM , and the variation in current was recorded (Chapter 3). In Chapter 5, chronoamperometry was utilized to evaluate the selectivity of the PtNPs/graphene/GCE towards DIP sensing. The experiment was conducted through sequential addition of DIP, and the current response was recorded at 0.51 V vs. Ag/AgCl. A probable interference of different organic molecules, including a pharmaceutical drug, on DIP sensing, was done by adding 1 μM of each of the interfering molecules at an interval of 10 s.

2.5.5 Square wave voltammetry

In square-wave voltammetry (SWV), the current at a (usually stationary) WE is determined while the potential between the WE and the RE is measured linearly over time. The potential waveform can be seen as a superposition of a regular square wave on the underlying staircase; in this sense, SWV can be considered a modification of the voltammetry of the staircase voltammetry (Ramaley and Krause, 1969).

The current is sampled at two points - once at the end of the forward potential pulse and again at the end of the reverse potential pulse just before the potential direction is reversed. As a result of this current sampling technique, the contribution to the current signal from the non-Faradaic current is minimized. Two current waveforms are collected because of having current sampling at two different instances per square-wave cycle resembling the forward and reverse current waveforms of a cyclic voltammogram. In SWV, the potentiostat software plots the differential current waveform derived by subtracting the reverse current waveform from the forward current waveform against the applied potential. The peaks in the plot are indicative of redox processes involved in the electrochemical

reaction, and the magnitudes of the peaks in this plot are proportional to the concentrations of the various redox-active species.

In this study, SWV was used extensively to study various redox processes involved during the electrochemical sensing of various analytes and in deriving various electrochemical reaction mechanisms. In Chapter 3, SWV was performed to evaluate the interference of uric acid and dopamine at a concentration of 50 μM during sensing of AA. The wave frequency of 25 Hz, amplitude of 0.02 V and the scan rate of 50 $\text{mV}\cdot\text{s}^{-1}$ was used for this experiment. For the electrochemical sensing of DIP, SWV tests were conducted using PtNPs/graphene/GCE in 0.5 M KCl solution with a potential range of 0 to 1.2 V vs. Ag/AgCl/3 M KCl. The step potential and the pulse amplitude were maintained at 4 mV and 25 mV, respectively. The frequency was kept at 15 Hz providing a scan rate of 60 $\text{mV}\cdot\text{s}^{-1}$ (Chapter 5). Similarly, in Chapter 6 for the sensing of chlorpyrifos, SWV experiments were done at a frequency of 20 Hz. The step amplitude and potential were maintained at 25 mV and 5 mV, respectively. The effective scan rate obtained was 100 $\text{mV}\cdot\text{s}^{-1}$. A deposition period of 60 s at -0.40 V vs. Ag/AgCl was provided before each run to allow the interaction of functional groups on CDs surfaces with CHL molecules.

2.5.6 Square wave anode stripping voltammetry

Square wave anode stripping voltammetry (SWASV) is a modified version of the square wave voltammetry analysis. It is normally used for the electrochemical sensing of non-complex and inorganic analytes, such as ultra-trace amounts of heavy metal ions (HMIs). In this case, the deposition/accumulation/pre-concentration potential labeled 'a' in Figure 2.12 is applied at a more negative potential than the E^0 of the target HMIs. If the analysis is done for a mixture of HMIs, the applied deposition potential should be more negative than the reduction potential obtained from cyclic voltammetry of the mixture. The reduction reaction, indicating the deposition of metal ions (denoted by M) on the WE, is shown below (Eq. 2.2).



The duration of the deposition step should be longer for a low concentration of analytes to enable proper deposition on the WE. The solution containing the analyte is kept in continuous stirring during this step to ensure faster mass transport to the electrode by breaking the hydrodynamic barrier. The interval indicated by 'b' Figure 2.13 is the quiet time. During this period, the potential is still applied but the stirring is stopped for few seconds prior to stripping analysis so that the agitated electrolyte can be stabilized and

ensure a noise-free stripping potential. In the region (labeled 'c' in Figure 2.13), the potential is scanned towards more positive potentials to oxidize the metal back to its ionic state. The following electrode reactions take place at the WE (Eq. 2.3).



The resulting plot of current versus the potential for this oxidation process is called a voltammogram. The observed peak current is proportional to the analyte concentration, and the peak position depends on the oxidation potential of the analytes present in the sample as in SWV analysis.

SWASV tests were performed at room temperature at a fixed scan rate of $60 \text{ mV} \cdot \text{s}^{-1}$. The deposition potential and deposition time were first optimized, and the WE was conditioned for 60 s before every run at +1.0 V to ensure the removal of the residual effect of HMIs from previous runs (Chapter 4). The stripping potential was varied from -1.2 to $+0.75$ V with a step potential of 4 mV and pulse amplitude of 25 mV at a frequency of 15 Hz. The solution was mixed (stirring at 500 rpm) throughout the conditioning and deposition processes to overcome the bulk diffusion resistance of the analytes. N_2 purging ($1.2 \text{ L} \cdot \text{min}^{-1}$) was continued from 5 min before the start of voltammetry experiments to eliminate dissolved oxygen from the electrolyte. In Chapter 7, the electrochemical sensing of Zn(II), Cd(II), Pb(II), and Hg(II) ions were performed using SWASV in the potential range of -1.4 to 0.5 V vs. Ag/AgCl/3M KCl (ink) with an amplitude of 0.02 V and pulse width of 0.05 s. The CuNRs and Cu@AgNRs modified FTO was flooded with 250 μL of 0.1 M acetate buffer solution at pH 5 and the target metal ions at the desired concentrations. These were then pre-concentrated onto the WE surface at -0.4 V for 90 s and subsequently stripped off from the electrode surface into the electrolytic solution by varying the potential in the opposite direction within the said potential range.

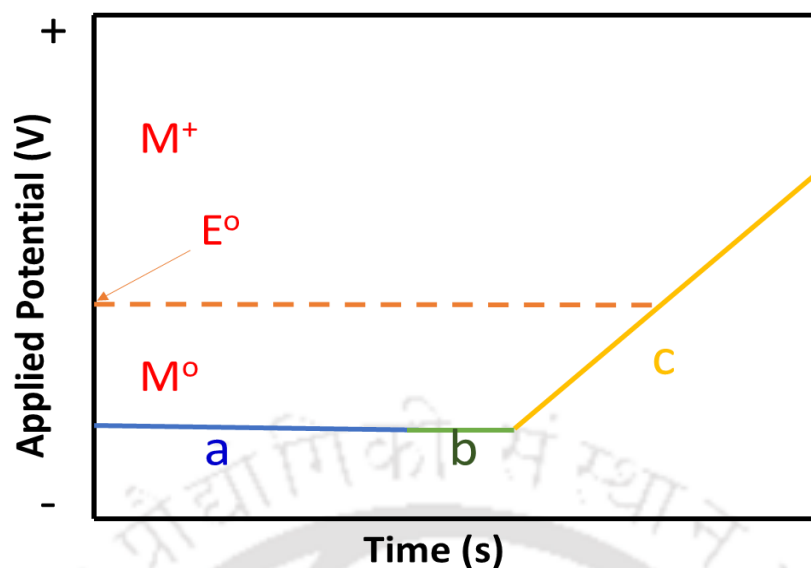


Figure 2.13: Potential vs. time waveform for an anodic stripping voltammetry experiment displaying ‘a’ constant potential applied during deposition step, ‘b’ quiescence stage, and ‘c’ ramping applied potential during stripping phase.

2.5.7 Electrochemical impedance spectroscopy

A Randles circuit is an equivalent electrical circuit that consists of an active electrolyte resistance (R_s) in series with the parallel combination of the double-layer capacitance (C_{dl}) and an impedance of a Faradaic reaction. It is commonly used in Electrochemical impedance spectroscopy (EIS) for interpretation of impedance spectra, often with a Constant phase element (CPE) replacing the double layer capacitance, C_{dl} . The Randles equivalent circuit is one of the simplest possible models describing the processes at the electrochemical interface. In this doctoral work, EIS was used to find out the effect of WE modification on the electrode resistances and determining the proper parameters for the fabrication of the WEs. Figure 2.14a shows a typical Nyquist plot using a modified glassy carbon electrode (GCE) simulated at the parameters given in Figure 2.14b. The Warburg element (W) manifests itself in EIS spectra by a line with an angle of 45 degrees in the low-frequency region. The values of the charge transfer resistance and Warburg coefficient depend on the physicochemical parameters of a system under investigation. The charge transfer resistance (denoted as R_{ct} or R_p) provides the actual resistance generated at the WE and electrolyte interface.

In order to study the effect of electrode modifications on the charge transfer rate, EIS was conducted in the presence of 100 mL of 0.5 mM $K_3[FeCN]_6$ as an analyte probe in

0.1 M KCl solution at room temperature. The electrode spacing between the working and counter electrodes was fixed at 20 mm and that of between the working and reference electrodes was fixed at 10 mm (centre to centre). The frequency was varied from 10^{-2} to 10^6 Hz, and the reading was captured at an open circuit potential of the electrodes.

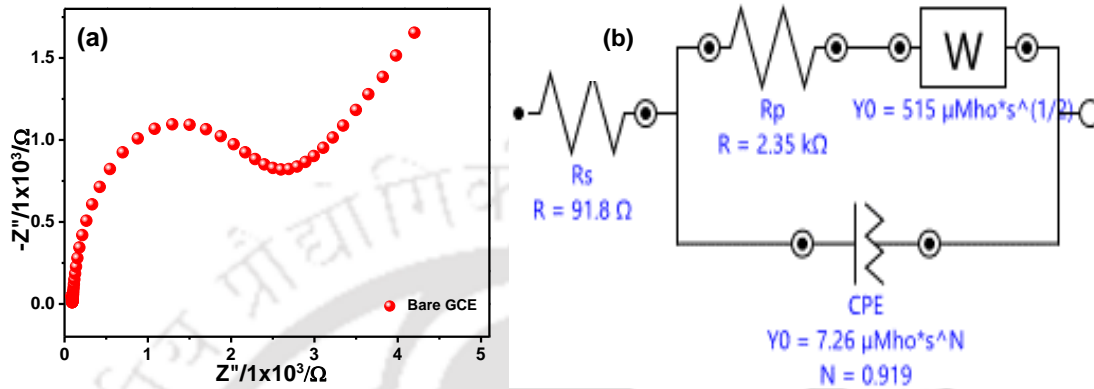


Figure 2.14: (a) Sample Nyquist plot showing the resistance developed at the fabricated device, and (b) Corresponding equivalent circuit diagram of working electrode.

2.5.8 Determination of electrochemical surface area

It is important to determine the physical parameter of the WE before the sensing experiments. The effective area of the WE (A_{eff}) was calculated for determining the sensitivity of the WE towards a given analyte. This area is often different from the geometrical surface area of the electrode. A known standard redox probe such as $K_2[Fe(CN)_6]$ or $[Ru(NH_3)_6]Cl_3$ of known concentration is generally used, which have a known diffusion coefficient (D). CV experiments were conducted at various scan rates, and the peak currents were obtained. Then, A_{eff} of the prepared/modified WEs is calculated using the Randles-Sevcik equation (Eq. 2.4) (Bin Hamzah et al., 2018).

$$I_{Pa} = (2.69 \times 10^5) n^{0.66} A_{\text{eff}} D^{0.5} v^{0.5} C_0 \quad (2.4)$$

Where, n , v , D and C_0 are the number of electrons involved in the electrochemical reaction, scan rate in $V \cdot s^{-1}$, diffusion coefficient in $cm \cdot s^{-1}$ and bulk concentration in M of the redox probe $K_3[Fe(CN)_6]$ or $[Ru(NH_3)_6]Cl_3$, respectively. From the plot of I_{Pa} vs. $v^{0.5}$ and equating the slope values by considering D for $K_2[Fe(CN)_6]$ as $7.6 \times 10^{-6} cm^2 \cdot s^{-1}$ or D for $[Ru(NH_3)_6]Cl_3$ as $8.43 \times 10^{-6} cm^2 \cdot s^{-1}$ ($n = 1$), A_{eff} was calculated.

2.5.9 Fabrication of miniaturized three-electrode sensing device

A miniaturized three-electrode sensing device was fabricated at the later stage of this doctoral work. To start with, a laser engraver (Make: Epilog Laser engraver, model: Helix Clavedon, UK) was used for the patterning of the Fluorine-doped tin oxide (FTO) sheet with a square resistance of 7Ω (TEC 7). The etching was done based on the pattern and parameters developed using AutoCAD software (Figure 2.15). The etching parameters were set at 85% laser power with a frequency of 5000 Hz. The scanning speed was maintained at 20% of the maximum capacity. A layer of Ag/AgCl ink (≈ 0.5 mm thick) (ASL Co., Japan) was coated by the doctor blading method on one of the sections of the FTO that acts as the reference electrode. The other part of the electrodes was masked using two layers of scotch that prevent the smudging of the Ag/AgCl ink onto other sections of the patterned FTO. It also acts as a guide for the layer thickness for the coating. Similarly, in the next step, the nanocatalyst (washed and suspended in DI water) was added by drop casting of $60 \mu\text{L}$ of nanocatalysts solution and dried at 60°C in a hot air oven. A layer of Nafion 0.5% solution (in iso-propanaol) of $100 \mu\text{L}$ was added on the top of it and dried to prepare the required modified miniature three-electrode system.

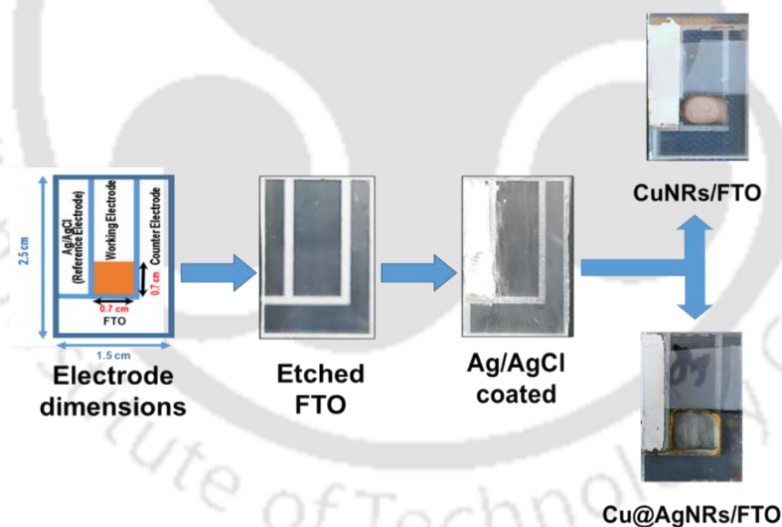


Figure 2.15: Step by step method to fabricate the compact three-electrode system for targeted sensing of HMIs.

2.6 Electrochemical sensing of analytes

2.6.1 Electrochemical studies and AA determination

In order to study the effect of electrode modifications on the charge transfer rate, electrochemical impedance spectroscopy was conducted using GPE and AgNPs/GPE as the working electrodes with 100 mL of 0.5 mM $K_3[FeCN]_6$ as an analyte probe in 1M KCl solution at room temperature (Mamuru et al., 2010). The electrode spacing between the working and counter electrodes was fixed at 20 mm and that of between the working and reference electrodes was fixed at 10 mm (centre to centre). The frequency was varied from 10^{-2} to 106 Hz and, the reading was captured at an open circuit potential of 0.079 V.

The cyclic voltammetry (CV) and square wave voltammetry (SWV) tests were also performed with the same electrochemical system at room temperature. The scanning rate and the analyte concentration (here AA) were varied from 10 to 100 $mV.s^{-1}$ and 1 to 2000 μM , respectively. Phosphate buffer solution (PBS 0.1M, pH 7.2) of 100 mL in a 150 mL capacity electrochemical cell was used as the supporting electrolyte to avoid AA decomposition at higher pH.

The chronoamperometric test was performed at $E_{anode}=0.380$ V vs. Ag/AgCl using AgNPs/GPE as the working electrode with the successive addition of AA from 25 to 100 μM in an interval of 30 s up to the AA concentration of 2000 μM . Two close-electroactive species, namely, UA and DA are generally found in biological entities along with AA (Dinesh et al., 2017). They also could interfere with the selectivity of AA during the chronoamperometric analysis. The interference of both the compounds at a concentration of 50 μM was studied by SWV with a frequency of 25 Hz, amplitude of 0.02 V, and scan rate of 50 $mV.s^{-1}$.

2.6.2 Electrochemical studies and HMIs detection

SWASV tests were performed at room temperature at a fixed scan rate of 60 $mV.s^{-1}$. The deposition potential and deposition time were first optimized, and the working electrode was conditioned for 60 s before every run at +1.0 V to ensure the removal of residual effect of HMIs (also denoted as MHs) from previous runs. The stripping potential was varied from -1.2 to +0.75 V with a step potential of 4 mV and pulse amplitude of 25 mV at a frequency of 15 Hz. The solution was mixed (stirring at 500 rpm) throughout the conditioning and deposition processes to overcome the bulk diffusion resistance of the

analytes. N₂ purging (1.2 L.min⁻¹) was continued from 5 min before the start of voltammetry experiments to eliminate dissolved oxygen from the electrolyte. The data was recorded in a desktop PC using NOVA 1.11 software. The analyte concentration (here HMIs) was varied from 0.1 to 10 μM in an acetate buffer at pH 5 to generate a calibration curve as the highest peak current (-425 mV vs. Ag/AgCl/3 M KCl) of Pb(II) sensing was noted at pH 5. The quantum of analyte was 100 mL in a 150 mL capacity electrochemical cell.

2.6.3 Electrocatalytic sensing of DIP and its metabolites

To study the electrochemical interactions and surface reactions of the analyte (DIP) molecules, EIS spectra were recorded using 100 μM DIP (100 mL) in 0.5M KCl solution. The scanning frequency was ranged from 10⁻² to 10⁶ Hz in the case of all three working electrodes (GCE, PtNPs/GCE, and PtNPs/graphene/GCE). The charge transfers resistance (R_p) of the electrodes were determined by fitting the experimental frequency response analysis (FRA) data with the Randles equivalent circuit diagram using NOVA 1.11 software. The effective surface area (A_{eff}) of the prepared electrodes was also determined using the Randles-Sevcik equation by using K₃[FeCN]₆ as a standard analyte probe. KCl of 0.1M was used as the electrolyte solution. The detailed experimental procedure is described in Section 2.5.8 of this chapter.

Square wave voltammetry (SWV) tests were conducted using PtNPs/graphene/GCE in 0.5M KCl solution with a potential range of 0 to 1.2 V vs. Ag/AgCl/3 M KCl. The step potential and the pulse amplitude were maintained at 4 mV and 25 mV, respectively. The frequency was kept at 15 Hz providing a scan rate of 60 mV.s⁻¹. The pH of the electrolyte medium was optimized by conducting the SWV tests at different pH values from 3 to 11. The calibration curve was generated by varying the concentration of the analyte from 0.1 to 300 μM (pH 7.0). The total volume of electrolyte was 100 mL in a 150 mL electrochemical cell.

Cyclic voltammetry was performed using PtNPs/graphene/GCE at different scan rates (5-200 mV.s⁻¹) from 0-1.2 V vs. Ag/AgCl and KCl as the supporting electrolyte (pH 7) to derive the fundamental electrokinetic parameters and also to understand the redox pathway of DIP sensing.

To study the stability of the PtNPs/graphene/GCE and reproducibility of DIP sensing, three fresh PtNPs/graphene/GCEs were fabricated following the same procedure stated earlier and applied for DIP sensing. SWV runs were conducted between the potential

window of 0-1.2 V vs. Ag/AgCl, and the peak current responses were analyzed for 10 consecutive cycles in the presence of 15 μM DIP. Similarly, SWV was conducted with the environmental samples replacing the DI water in the electrolyte at the optimized condition.

It is highly likely that DIP is present in real water samples in association with other interfering redox compounds. Therefore, the interference studies were conducted using close electroactive molecules such as glucose (GLU), dopamine (DA), uric acid (UA), and ciprofloxacin (CIP) using chronoamperometric tests at 0.51 V vs. Ag/AgCl in the presence of 1 μM of each interfering substance to the electrolyte at the optimized condition. The required amount of interfering agents was injected in a chronological manner to check for the spike in current at the testing potential. An intermittent injection of DIP was also done to observe any change in the current response.

In order to check the performance of the PtNPs/graphene/GCE for the sensing of DIP present in real samples, DIP (1-100 μM) was spiked with the effluent samples of the sewage treatment plant and domestic tap-water available at Indian Institute of Technology Guwahati Campus. The effluent samples were filtered through a 0.2 μm Nylon filter to remove suspended materials. KCl at 0.5 M was added as the supporting electrolyte at pH 7, which was adjusted using 0.1 M HCl/NaOH before conducting the SWV experiments in the potential range of 0-1.2V.

2.6.4 Electrochemical studies and chlorpyrifos sensing

Square wave voltammetry (SWV) experiments were done at a frequency of 20 Hz. The step amplitude and potential were maintained at 25 mV and 5 mV, respectively. The effective scan rate obtained was 100 $\text{mV}\cdot\text{s}^{-1}$. A deposition period of 60 s at -0.40 V vs. Ag/AgCl was provided before each run to allow the surface interaction of functional groups on CDs surface with chlorpyrifos (CHL) molecules. The electro-kinetics studies were done by varying the scan rate, and the Laviron equation was used to deduce the formal potential (E°) and heterogeneous electron transfer rate constant k° (Ghiasi et al., 2021). The calibration curve was generated by varying the concentration of CHL from 0.1-10 μM , and the detection and quantification limits were calculated. All electrochemical experiments were conducted with a volume of 100 mL electrolyte at ambient temperature. The working electrode and the Ag/AgCl reference electrode were placed at a proximity of 5 mm, and the counter electrode was placed at a distance of 10 mm from the working electrode.

2.6.5 Sensing of heavy metal ions using miniaturized device

All electrochemical measurements were performed on PGSTAT 302N Potentiostat/Galvanostat (Metrohm, Herisau, Switzerland) at room temperature using the fabricated miniaturized three-electrode system where CuNRs and Cu@AgNRs modified FTO served as a working electrode, bare FTO as an auxiliary electrode and Ag/AgCl ink as a reference electrode (Figure 2.15). The connecting wires are modified to work with the FTO based devices. A pictorial view of the sensing system is provided in Figure 2.16.

Electrochemical sensing of Zn(II), Cd(II), Pb(II), and Hg(II) ions were performed using square wave anodic stripping voltammetry (SWASV) in the potential range of -1.4 to 0.5 V vs. Ag/AgCl (ink) with an amplitude of 0.02 V and pulse width of 0.05 s. The CuNRs and Cu@AgNRs modified FTO was flooded with 250 μ L of 0.1 M acetate buffer solution at pH 5 and the target metal ions at the desired concentrations. These were then pre-concentrated onto working electrode surface at -0.4 V for 90 s and subsequently stripped off from the electrode surface into the electrolytic solution by varying the potential in the opposite direction within the predetermined potential range.

The investigation of the viability of the fabricated electrochemical sensing system, HMIs analysis was done on environmental samples collected from Clyde River, Glasgow (UK) and supplied tap water from the University of Strathclyde Campus. The collected water samples were stored in a refrigerator at 4°C to preserve the characteristics of the collected water samples and were used without any pretreatment. The anions (chloride, fluoride, nitrate, sulphate and phosphate) concentrations in the collected samples were determined. The effect of the presence of these anions on the simultaneous electrochemical sensing of HMIs was determined by preparing the electrolyte using the collected water samples instead of DI water. It was then spiked with the required concentration of HMIs, and the sensing performance was evaluated by obtaining the square wave voltammograms with the optimized sensing parameters.



Figure 2.16: Image of the fabricated miniaturized FTO based three-electrode sensing device. The black connector corresponds to the counter electrode, the red connector corresponds to the working electrode and the blue connector refers to the reference electrode (Ag/AgCl).



References

- Barbalho, S.M., 2012. Psidium Guajava (Guava): A Plant of Multipurpose Medicinal Applications. *Med. Aromat. Plants* 01, 1–6. <https://doi.org/10.4172/2167-0412.1000104>
- Belal, T.S., Khamis, E.F., El Yazbi, F.A., Hamdy, M.M.A., 2014. High performance liquid chromatographic determination of the ternary mixture of caffeine, dipyrone and drotaverine hydrochloride in tablets dosage form. *J. Appl. Pharm. Sci.* 4, 033–039. <https://doi.org/10.7324/JAPS.2014.40605>
- Bin Hamzah, H.H., Keattch, O., Covill, D., Patel, B.A., 2018. The effects of printing orientation on the electrochemical behaviour of 3D printed acrylonitrile butadiene styrene (ABS)/carbon black electrodes. *Sci. Rep.* 8, 1–8. <https://doi.org/10.1038/s41598-018-27188-5>
- Britz, D., Brocke, W.A., 1975. Elimination of iR-drop in electrochemical cells by the use of a current-interruption potentiostat. *J. Electroanal. Chem. Interfacial Electrochem.* 58, 301–311. [https://doi.org/10.1016/S0022-0728\(75\)80088-X](https://doi.org/10.1016/S0022-0728(75)80088-X)
- Chauliya, S., Prasad, G., 2016. *Sensing and Monitoring Technologies for Mines and Hazardous Areas*, 1st ed. Elsevier.
- Chelli, V.R., Golder, A.K., 2016. pH dependent size control, formation mechanism and antimicrobial functionality of bio-inspired AgNPs. *RSC Adv.* 6, 95483–95493. <https://doi.org/10.1039/C6RA16475G>
- Dinesh, B., Saraswathi, R., Kumar, A.S., 2017. Water based homogenous carbon ink modified electrode as an efficient sensor system for simultaneous detection of ascorbic acid, dopamine and uric acid. *Electrochim. Acta* 233, 92–104. <https://doi.org/10.1016/j.electacta.2017.02.139>
- Ghiasi, T., Ahmadi, S., Ahmadi, E., Bavi Olyai, M.R.T., Khodadadi, Z., 2021. Novel electrochemical sensor based on modified glassy carbon electrode with graphene quantum dots, chitosan and nickel molybdate nanocomposites for diazinon and optimal design by the Taguchi method. *Microchem. J.* 160, 105628. <https://doi.org/10.1016/j.microc.2020.105628>
- Jayasri, D., Narayanan, S.S., 2007. Amperometric determination of hydrazine at manganese hexacyanoferrate modified graphite-wax composite electrode. *J. Hazard. Mater.* 144, 348–354. <https://doi.org/10.1016/j.jhazmat.2006.10.038>
- Kim, D.K., Jeong, S.C., Gorinstein, S., Chon, S.U., 2012. Total Polyphenols, Antioxidant and Antiproliferative Activities of Different Extracts in Mungbean Seeds and Sprouts. *Plant Foods Hum. Nutr.* 67, 71–75. <https://doi.org/10.1007/s11130-011-0273-x>
- Lai, X., Liu, C., He, H., Li, J., Wang, L., Long, Q., Zhang, P., Huang, Y., 2020. Hydrothermal synthesis and characterization of nitrogen-doped fluorescent carbon quantum dots from citric acid and urea. *Ferroelectrics* 566, 116–123. <https://doi.org/10.1080/00150193.2020.1762435>

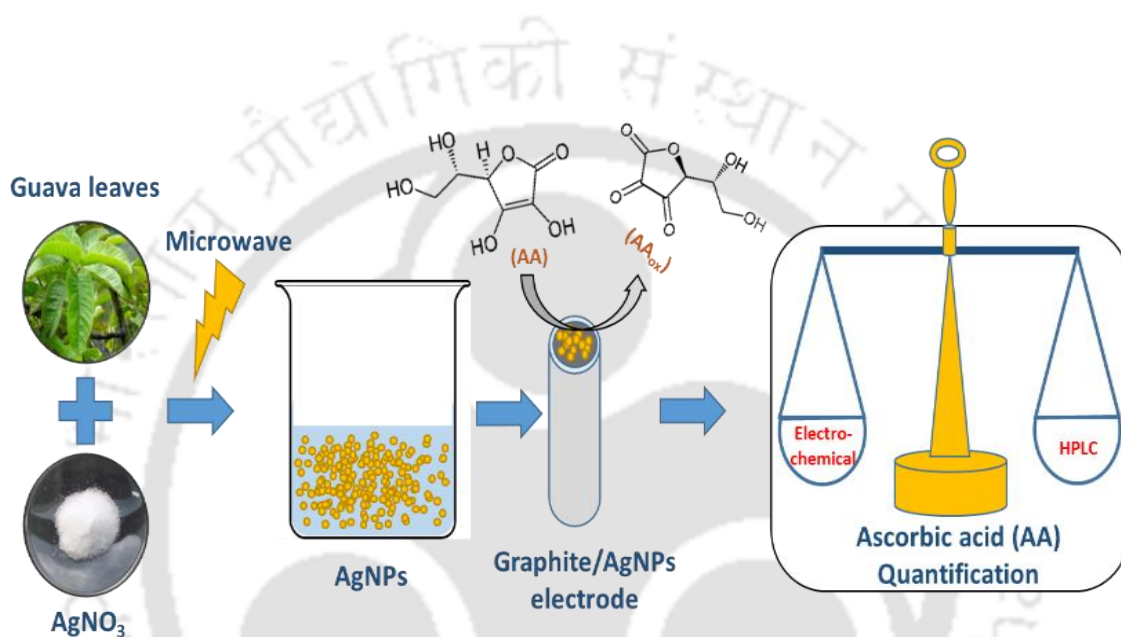
- Mamuru, S.A., Ozoemena, K.I., Fukuda, T., Kobayashi, N., Nyokong, T., 2010. Studies on the heterogeneous electron transport and oxygen reduction reaction at metal (Co, Fe) octabutylsulphonylphthalocyanines supported on multi-walled carbon nanotube modified graphite electrode. *Electrochim. Acta* 55, 6367–6375.
<https://doi.org/10.1016/j.electacta.2010.06.056>
- Mauldin, R.E., Primus, T.M., Buettgenbach, T.A., Johnston, J.J., Linz, G.M., 2006. A simple HPLC method for the determination of chlorpyrifos in black oil sunflower seeds. *J. Liq. Chromatogr. Relat. Technol.* 29, 339–348. <https://doi.org/10.1080/10826070500451863>
- Mongay, C., Cerdrá, V., 1974. A Britton-Robinson buffer of known ionic strength. *Ann. Chim.* 64, 5.
- Ramaley, L., Krause, M.S., 1969. Theory of Square Wave Voltammetry. *Anal. Chem.* 41, 1362–1365. <https://doi.org/10.1021/ac60280a005>
- Rao, C.V., Golder, A.K., 2016. Development of a bio-mediated technique of silver-doping on titania. *Colloids Surfaces A Physicochem. Eng. Asp.* 506, 557–565.
<https://doi.org/10.1016/j.colsurfa.2016.07.031>
- Stewart, I.E., Ye, S., Chen, Z., Flowers, P.F., Wiley, B.J., 2015. Synthesis of Cu-Ag, Cu-Au, and Cu-Pt Core-Shell Nanowires and Their Use in Transparent Conducting Films. *Chem. Mater.* 27, 7788–7794. <https://doi.org/10.1021/acs.chemmater.5b03709>
- Thaipong, K., Boonprakob, U., Crosby, K., Cisneros-Zevallos, L., Hawkins Byrne, D., 2006. Comparison of ABTS, DPPH, FRAP, and ORAC assays for estimating antioxidant activity from guava fruit extracts. *J. Food Compos. Anal.* 19, 669–675.
<https://doi.org/10.1016/j.jfca.2006.01.003>
- Yi, M., Shen, Z., Zhang, X., Ma, S., 2013. Achieving concentrated graphene dispersions in water/acetone mixtures by the strategy of tailoring Hansen solubility parameters. *J. Phys. D. Appl. Phys.* 46. <https://doi.org/10.1088/0022-3727/46/2/025301>
- Yokoyama, S., Motomiya, K., Jeyadevan, B., Tohji, K., 2018. Environmentally friendly synthesis and formation mechanism of copper nanowires with controlled aspect ratios from aqueous solution with ascorbic acid. *J. Colloid Interface Sci.* 531, 109–118.
<https://doi.org/10.1016/j.jcis.2018.07.036>
- Yuan, M., Zhong, R., Gao, H., Li, W., Yun, X., Liu, J., Zhao, X., Zhao, G., Zhang, F., 2015. One-step, green, and economic synthesis of water-soluble photoluminescent carbon dots by hydrothermal treatment of wheat straw, and their bio-applications in labeling, imaging, and sensing. *Appl. Surf. Sci.* 355, 1136–1144. <https://doi.org/10.1016/j.apsusc.2015.07.095>
- Zhang, Q., Zhang, X., Bao, L., Wu, Y., Jiang, L., Zheng, Y., Wang, Y., Chen, Y., 2019. The application of green-synthesis-derived carbon quantum dots to bioimaging and the analysis of mercury(II). *J. Anal. Methods Chem.* 2019. <https://doi.org/10.1155/2019/8183134>



This page is intentionally left blank

CHAPTER 3

Synergizing AgNPs Synthesis in a Bioinspired Route using Microwave and Studies on Electrocatalytic Sensing of Ascorbic Acid from Biological Entities



Highlights

- ◆ Microwave irradiation decreased AgNPs synthesis time to 90 s from 10 h at pH 9.5 using *Psidium guajava* leaves extract
- ◆ Microwave overexposure led to AgNPs aggregation with 5 times particle size increase
- ◆ AgNPs electrocatalyzed selective ascorbic acid sensing in phosphate media with a low detection limit (14.63 μ M)
- ◆ AgNPs catalyzed ascorbic acid sensing in biological entities was comparable with HPLC (variation $\leq 5\%$)

3.1 Background and executive motivation

Silver nanoparticles (AgNPs) possess several important properties such as chemical stability, good conductivity, excellent catalytic activity and unique optoelectronic properties in comparison to the bulk materials and, further these properties could be improved through the alteration of its size and shape at the nanoscale (Khan et al., 2017). AgNPs have found many important applications in catalysis (Joshi et al., 2016), sensor development (Sun et al., 2015), drug delivery (Sridhar et al., 2015), optics (Haes et al., 2004), etc. The chemical processes are the most popular for the synthesis of AgNPs because of its simplicity in operation and easy to control the size and morphology (Abbasi et al., 2016). The rate of the synthesis reaction is also quite fast and could be completed within a couple of minutes (Lokanathan et al., 2014). This process involves the use of many environmentally aggressive reducing agents such as sodium borohydride (1-5 mM) (Agnihotri et al., 2004), hydrazine hydrate (2-12 mM) (Lee et al., 2010), ethylene glycol as a solvent (99%) (Shambharkar and Chowdhury, 2016), and capping agents such as tri-sodium citrate (1-4.28 mM) (Agnihotri et al., 2004), poly vinyl pyrrolidone (8 mM) (Mitzel and Tufenkji, 2014) and dodecyl amine (0.08 mM) (Mathew and Kuriakose, 2013), etc.

Therefore, it is necessary to develop environmentally sustainable processes for the synthesis of AgNPs, especially on a large scale within a shorter reaction time (<5 min). The biological and bio-mediated methods could eliminate the use of such chemicals (both reducing and capping agents) for the synthesis of noble metal (Chelli and Golder, 2016; Dauthal and Mukhopadhyay, 2016) and transition metal nanoparticles (Das and Golder, 2017). Though the stability of particles (up to 4 months at 25°C) can be achieved in this method, the rate of synthesis is slow, and it can take from 30 min even up to 124 h (Thakkar et al., 2010). The time of AgNPs synthesis can be reduced by 20 folds by performing the reaction at an elevated temperature of 90°C from 20°C (Khan et al., 2013). pH of the synthesis medium also could help for the faster synthesis, but it could degrade the (bio-) analytes and deteriorate the nanoparticles quality and purity (Chelli et al., 2017). The microwave-assisted processes are considered as the less energy intensive processes than conventional convecting heating methods. It also offers a rapid and uniform heating which helps for the uniform nucleation and growth of nanoparticles (Liu et al., 2011).

Therefore, the first objective of this doctoral work is framed as “Microwave irradiation to synergize the rate of bioinspired synthesis of silver nanoparticles using *Psidium guajava* leaves extract and electrocatalytic sensing of ascorbic acid”. *P. guajava* (common name is guava) leaves was used as the source of the (bio-) analytes rich in quercetin, D-glucose, rutin, chlorogenic acid, ascorbic acid (AA), etc. (Güçlü et al., 2005; Liu et al., 2016) for AgNPs synthesis in the absence of (external) capping agents which need to be spiked in a chemical synthesis process. The possible mechanistic routes for the formation of AgNPs were elucidated which is one of the serious shortcomings of most of the earlier studies on the bio-inspired processes for the synthesis of metal nanostructures. The physiochemical attributes of synthesised AgNPs were investigated and, then these nanoparticles were tested in catalysing the electrochemical analysis of AA present in the synthetic medium and also in the (real) bio-extracts along with other analytes which is a step forward for designing of a miniaturised electrochemical sensor catalysed by AgNPs. The selectivity of AA determination was also investigated by the square wave voltammetry (SWV) through the addition of dopamine (DA) hydrochloride and uric acid (UA) (Lykkesfeldt, 2000). The high purity graphite was employed as the electrode support and AgNPs were decorated over it using Nafion (5% w/w) as a binder. The performance of the amperometric method determining AA at graphite/AgNPs anode was also compared with the high-performance liquid chromatography (HPLC).

AA is an essential vitamin for humans, and it is known to be effective for the prevention and treatment of the common cold, mental illness, infertility, and diseases like scurvy and cancer (Lee et al., 1997). Several techniques like spectroscopic (Bagheri et al., 2017), chromatographic (Filik et al., 2016), enzymatic (Tashkhourian et al., 2009), and electrochemical (Morais-Braga et al., 2016) are in use for the determination of AA. The advantages of the electrochemical technique are the high sensitivity ($0.25\text{-}0.5 \mu\text{A}\cdot\text{mM}^{-1}$ of AA) and selectivity for the detection and determination of AA even at a low concentration ($1\text{-}5 \mu\text{g}\cdot\text{L}^{-1}$) even in the presence of close electro-active species like dopamine, uric acid, tryptophan, etc. (Iamjud et al., 2014). In particular, AgNPs modified electrodes exhibit high electrocatalytic activities towards the compounds such as AA which have a slow redox process and higher overpotential (0.4 V) at the bare electrodes (Barbalho, 2012).

3.2 Results and Discussions

3.2.1 Physiochemical attributes of AgNPs

3.2.1.1 AgNPs synthesis kinetics and particles sizes

The optimum bio-extract and precursor ratio was first determined by varying the volume of bio-extract from 0.5-5.0 mL in 250 mL of reaction volume. The precursor concentration was kept constant at 0.3 mM. It was observed from the preliminary study that the spectral absorbance peak due to the localized surface plasma resonance effect of AgNPs was maximum with a water to leaves ratio (w/w) of 500 in 300 s of microwave (MW) irradiation (Figure 3.1). Therefore, the water to leaves ratio of 500 was selected for further studies.

The progress of the formation of AgNPs was monitored by acquiring the change in the spectral absorbance during the reaction. The optimal MW power requirement for the synthesis of AgNPs was determined at two different values of pH of 9.5 and 11. The variation of the colour of the reaction mixture is also indicative of the progress of formation of AgNPs (Figure 3.2). On exposure to MW, the initially translucent reaction mixture was gradually turned to intense yellow coloration. The formation of AgNPs was almost instantaneous irrespective of the MW power input and reaction pH (Figures 3.3 and 3.4). An absorbance peak in the visible wavelength (406-420 nm) was identified due to the resonance between the electromagnetic field and coherent electron motion of AgNPs which is known as surface plasmon resonance (SPR) effect (Dinesh et al., 2017). The peak intensity was significant even within 60 s of MW irradiation at 240 W at pH 9.5 and, it increased gradually with the synthesis time (Figure 3.4). The rate of reaction was faster at a higher MW power (≤ 1200 W) and, the formation of AgNPs was complete within 300, 240, 180, 150, and 120 s for an input MW power starting from 240 to 1200 W at pH 9.5 as there was no appreciable change in the peak intensities (Figure 3.4). The rate of AgNPs formation seems to be even faster at a higher pH of 11 and, the AgNPs formation was completed by 180, 150, 120, 90, and 60 s (Figure 3.3) at the same MW power as at pH 9.5.

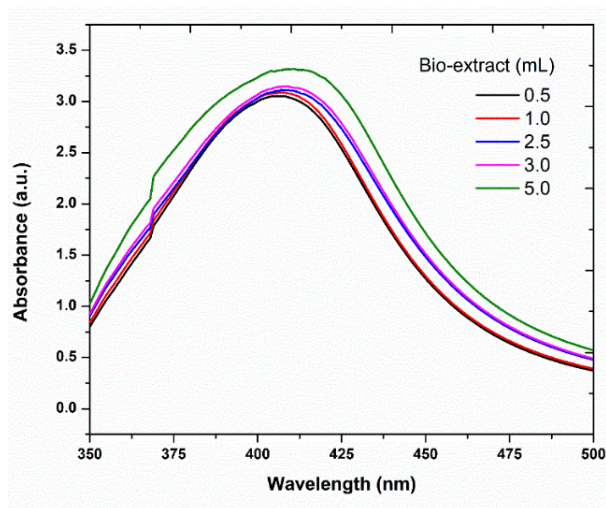


Figure 3.1: UV-vis spectra of AgNPs dispersed in the reaction mixture at different bio-extract concentrations with a total reaction volume of 250 mL (remenant 0.3 mM AgNO_3). Reaction conditions: pH 9.5, microwave power 1200W, Ag^+ concentration 0.3 mM and reaction time 300 s.

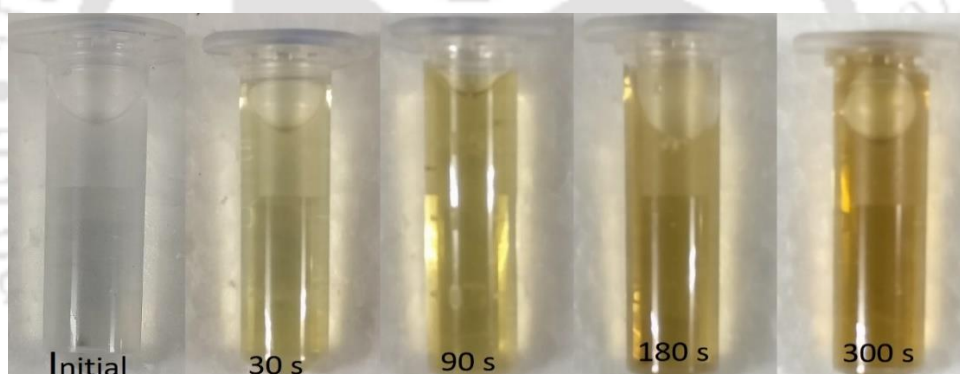


Figure 3.2: Digital image of showing the formation of AgNPs at different irradiation time at MW power of 960 W. Experimental conditions: reaction volume 250 mL, water to leaves ratio 500, initial Ag^+ concentration 0.3 mM and pH 9.5.

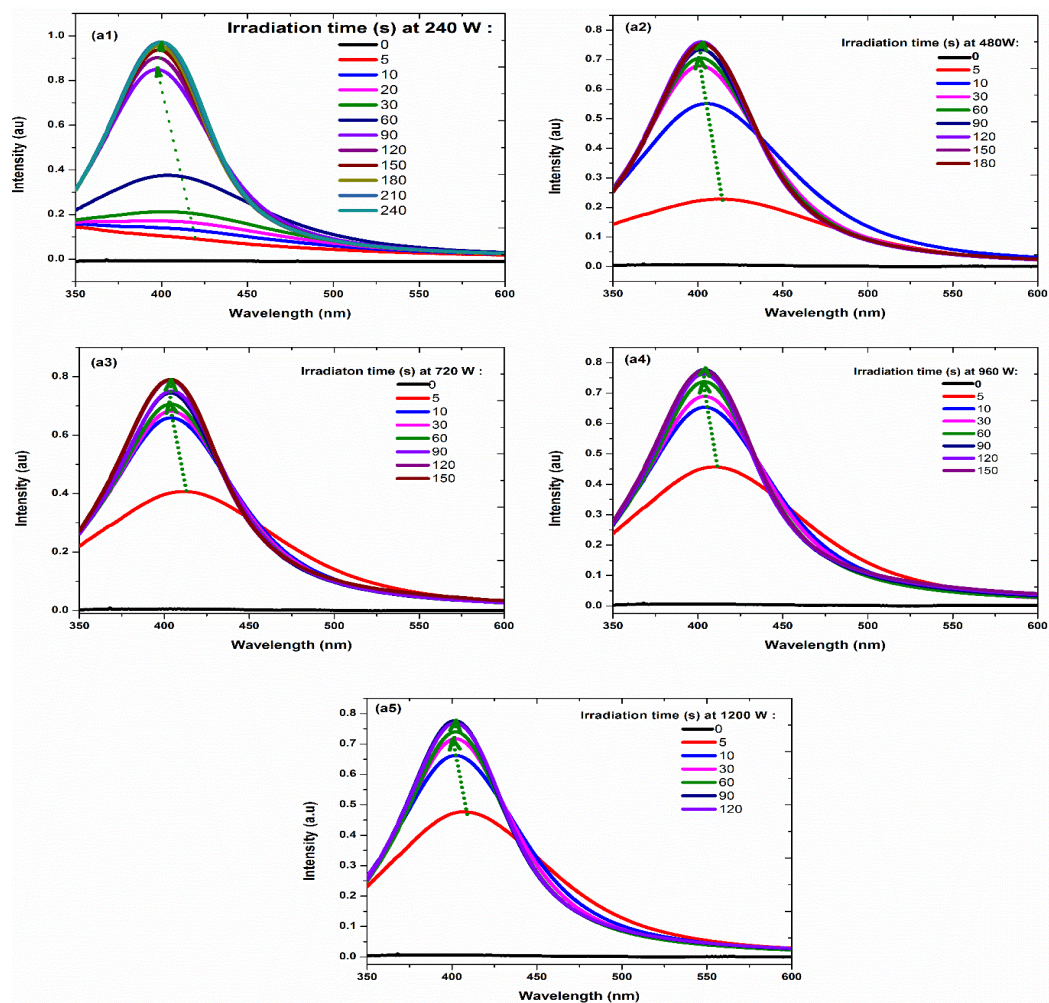


Figure 3.3: UV-vis spectra of AgNPs at different time of irradiation and MW power at pH 11. Experimental conditions: reaction volume 250 mL, water to leaves ratio 50 and initial Ag^+ concentration 0.3 mM.

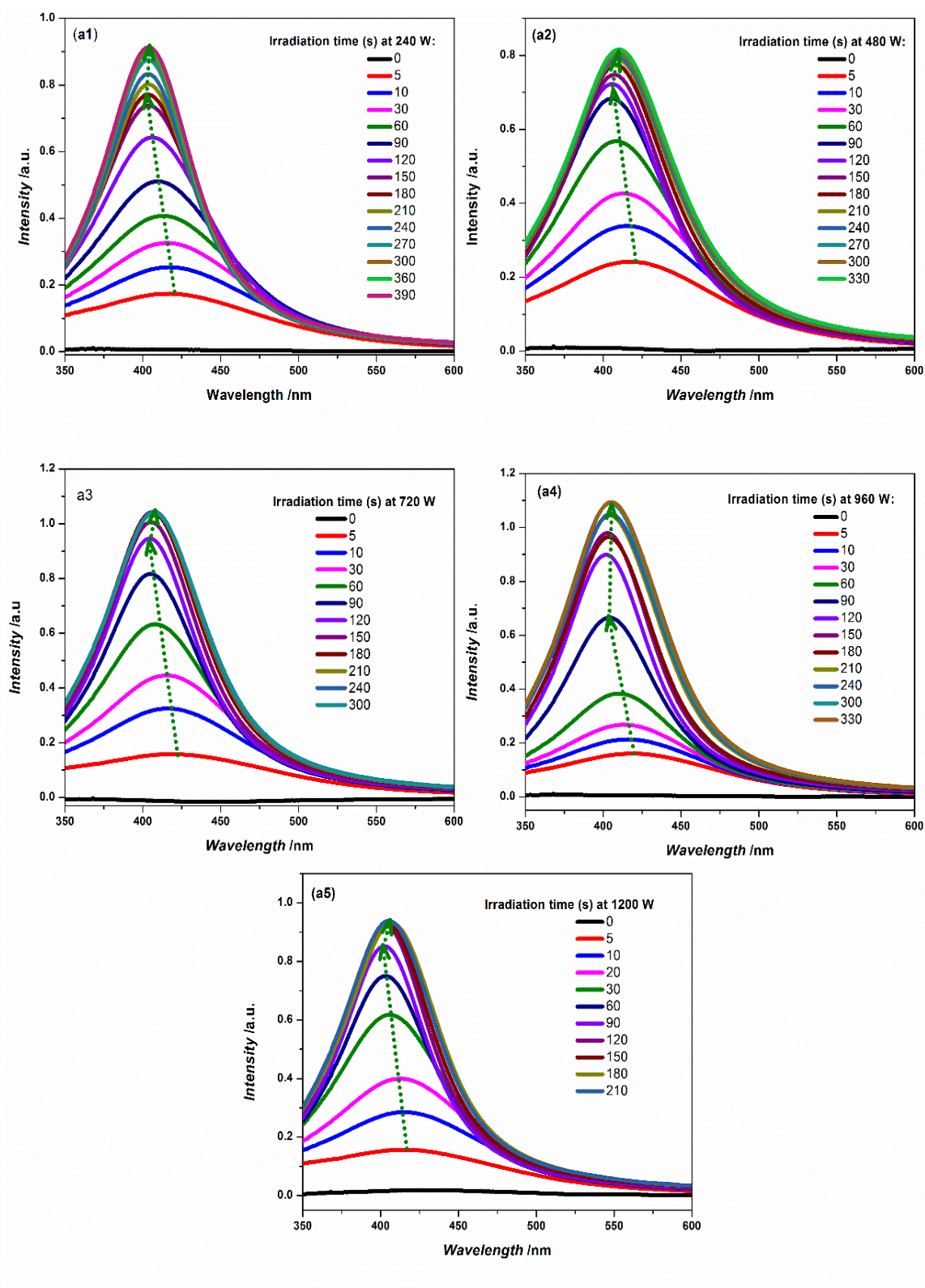


Figure 3.4: UV-vis absorption spectra of AgNPs at different time of irradiation and MW power at pH 9.5. Experimental conditions: reaction volume 250 mL, water to leaves ratio 50 and initial Ag^+ concentration 0.3 mM.

It was noticed that there was a blue shift up to a certain period of MW irradiation followed by a redshift. For an example, a blue shift was observed up to 180 s at 240 W and pH 9.5 indicating the formation of small size stabilised AgNPs. The corresponding peak position was skewed from 420 to 402 nm and, it was then moved to a slightly higher wavelength (402 to 405 nm at >180 s) (Figure 3.5a). A faster nucleation rate could hinder the capping process at a higher temperature. So, larger particles were produced due to aggregation. Further, the agglomeration of AgNPs may also occur due to the removal of the capping materials at a higher exposure time by forming localised hotspots from the differential MW heating for Ag^+ ions and H_2O molecule (Irfan et al., 2017). The frictional stress developed on the AgNPs surface due to the constant alignment of the polar H_2O molecules to the alternating electric field generated by MW may also wear away the capping molecules out of the AgNPs surface inducing agglomeration. Similar results were obtained at pH 11 with the variation of MW power, but in a shorter reaction time (Figure 3.5b).

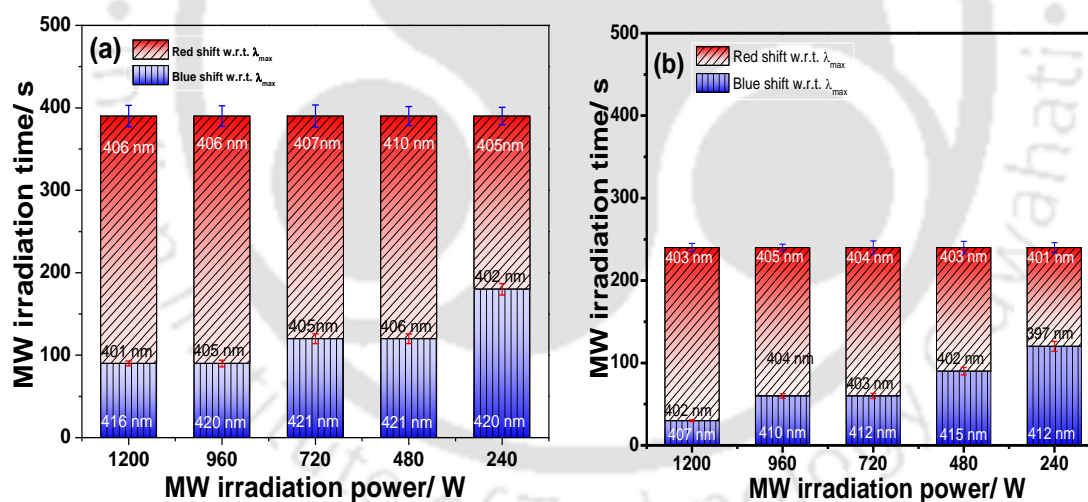


Figure 3.5: Transition from blue shift to red shift at peak position (λ_{max}) from optical absorbance with time of irradiation at different MW power and (a) pH 9.5 and (b) pH 11. Experimental conditions: reaction volume 250 mL, water to leaves ratio 500 and initial Ag^+ concentration 0.3 mM.

The size of AgNPs was determined at the end of the reaction (Figures 3.3 and 3.4) and, the results both at pH 9.5 and 11 are shown in Figures 3.6a and 3.6b. The hydrodynamic particle size distributions revealed a gradual decrease in average

diameter with the increase in MW power up to 960 W at the end of the reaction. It can be observed that at both pH 9.5 and 11, a very narrow particle size distribution between 20-50 nm and 10-18 nm were obtained at 960 W. A high localised temperature induced rapid nucleation and reduction of Ag^+ ions at a rate faster than the rate of stabilisation of AgNPs leading to the formation of larger particles at 1200 W (Irfan et al., 2017).

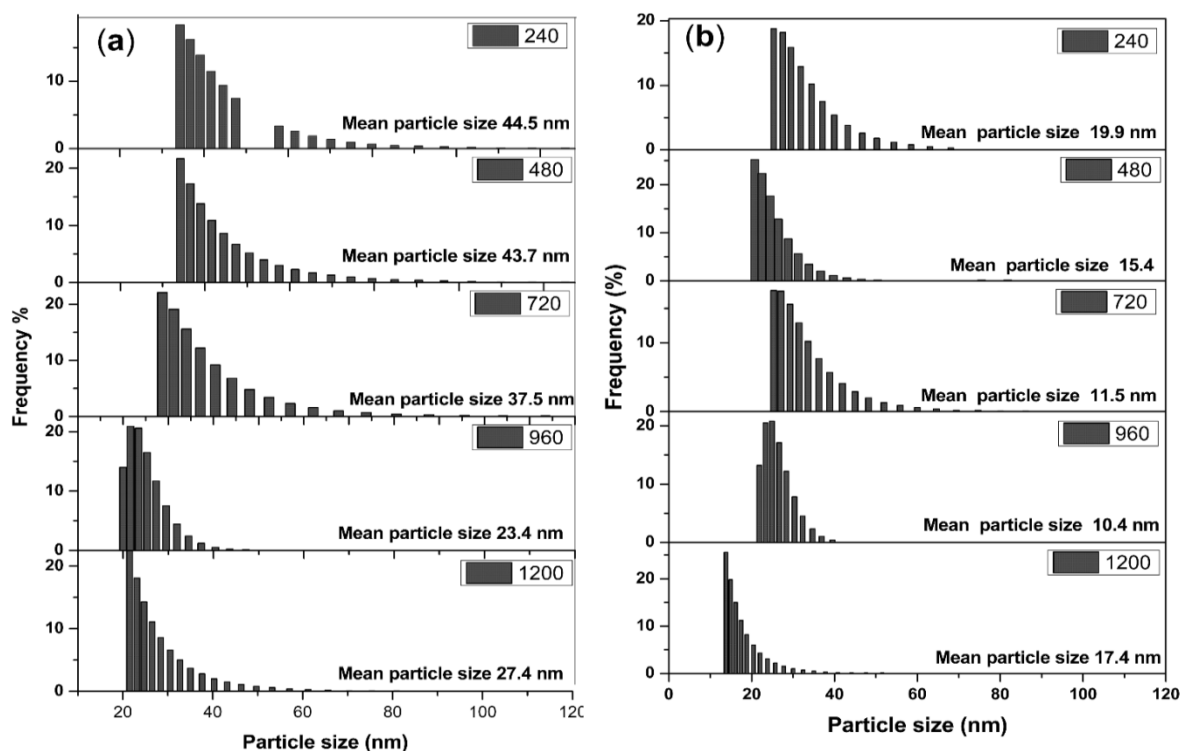


Figure 3.6: Particle size distribution of AgNPs obtained after 300 s of MW irradiation at varying input power at (a) pH 9.5 and (b) pH 11.

Thermogravimetric analysis (TGA) would provide a gross determination of the quantity of organic constituents adsorbed on AgNPs. Figure 3.7 shows the thermograms of AgNPs formed at 90 and 300 s of MW irradiation at 960 W with an incremental heating from 25 to 700°C. It can be observed that mass losses mostly took place in three-step. For AgNPs obtained at 90 s, moisture was first removed and only 0.5 % mass loss was found up to 100°C. The mass loss of 7.5% was for the decomposition of organic constituents like carbohydrates and lignin molecules between 100 and 300°C (Gan et al., 2012). A steady mass loss of 8% was observed at $\geq 300^\circ\text{C}$. The degradation of carbonates and thermos-resistive organic compounds usually occurred at a higher temperature (Carballo et al., 2008). But in comparison

to AgNPs synthesised at 90 s, there was a steady decrease in the mass loss less for AgNPs produced at 300 s of MW irradiation (Figure 3.7). So, it is highly likely that the decrease in the mass loss found with the prolonged irradiation time was for the disintegration of organic constituents/capping agents.

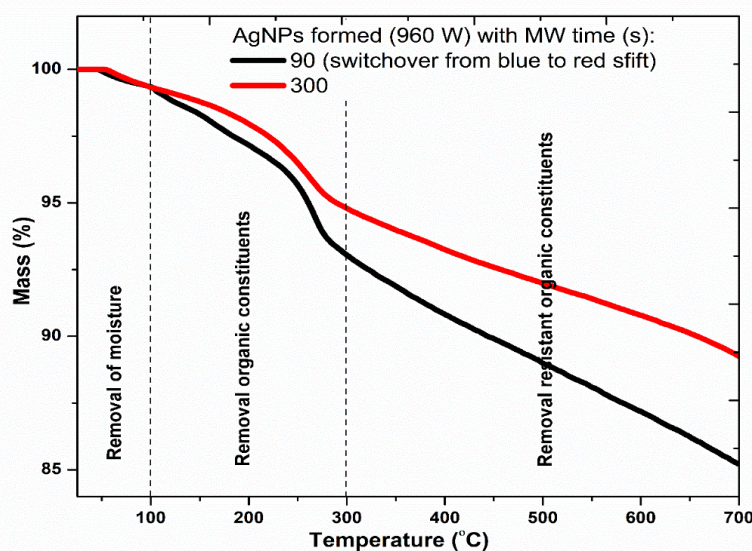


Figure 3.7: TGA analysis of AgNPs. Experimental conditions of AgNPs synthesis: pH 9.5, reaction volume 250 mL and MW 960 W.

Zeta-potential has a significant role in maintaining the size of AgNPs. Even though the synthesis reaction was carried out at the same pH but there was a gradual decrease in zeta-potential. At pH 9.5, it decreased from -31.3 mV at 240 W to -33.3 mV at 1200 W. It was even lower at pH 11 (-33.5 mV at 240 W and -34.2 mV at 1200 W). The adsorbed biomolecules usually helped for the intense negative charge development on the surface by forming an organic layer (Chelli et al., 2017) and, it was likely disintegrated at a higher MW heating rate (Darmanin et al., 2012). So, it lowered the particle size (Figure 3.6) at a higher negative zeta-potential (Figure 3.8).

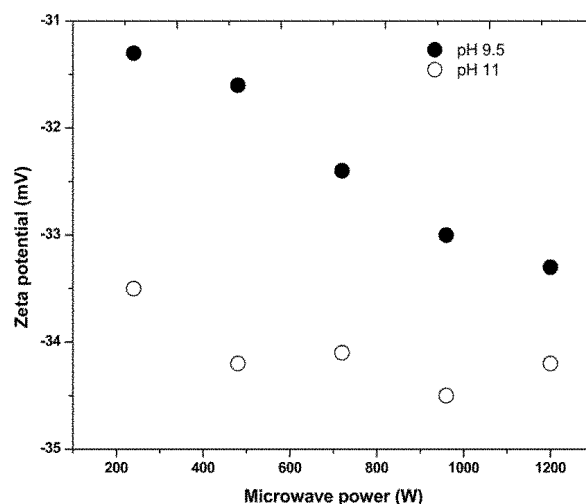


Figure 3.8: Zeta-potential obtained after 300 s of irradiation at varying MW power. Experimental conditions: reaction volume 250 mL, water to leaves ratio 500 and Ag⁺ concentration 0.3 mM.

A control experiment without MW was conducted at room temperature by varying the solution pH from 4 to 12. Rate retardation for the formation of AgNPs was observed at $\text{pH} \leq 7$. About 88-90% AgNPs formation was complete by 10 h of reaction both at pH 9.5 and 12 (Figure 3.9) which was determined by analysing the residual Ag⁺ ion concentration. However, a higher pH (>9.5) is usually avoided as the resulting AgNPs could be laden with Ag₂O (Rao and Golder, 2016). The deprotonated forms ($\text{pH} < 10.5$) of polyphenolic compounds (Table 3.1) usually had a higher affinity towards Ag⁺ ions and accelerated the formation of smaller sized AgNPs due to a faster nucleation rate (Iravani and Zolfaghari, 2013). The mass spectra (Figure 3.10) and the detailed components identified in the bio-extract from the mass spectra analysis are summarized in Table 3.1. For chayote fruit extract, the room temperature formation of AgNPs took 12 h at pH 12.5 to achieve the similar extent of AgNPs yield (Rao and Golder, 2016). AgNPs synthesis was complete for the fresh *A. carambola* leaves within 6 h (Mishra et al., 2015) and even a prolonged reaction time was usually needed for a bio-inspired process of AgNPs synthesis (Ahmed et al., 2016).

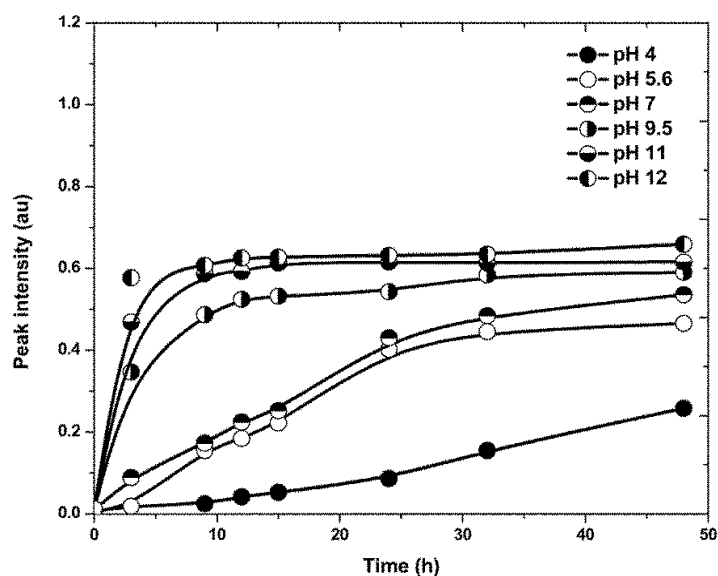


Figure 3.9: Control experiment at $25 \pm 5^\circ\text{C}$ without irradiation showing variation of spectral absorbance ($\lambda_{\text{max}} = 410 \text{ nm}$) with the time of reaction at different pH.

For MW assisted AgNPs synthesis, the variation of SPR peak intensity with irradiation is illustrated in Figure 3.11. Both localised and bulk heating is faster at a higher MW power leading to a quick AgNPs formation. Ag₂O particles were identified at pH 11 (Figure 3.12). The irreversible degradation of polyphenolic compounds (Table 3.1) also took place at $\text{pH} > 10.5$ (Friedman and Jürgens, 2000).

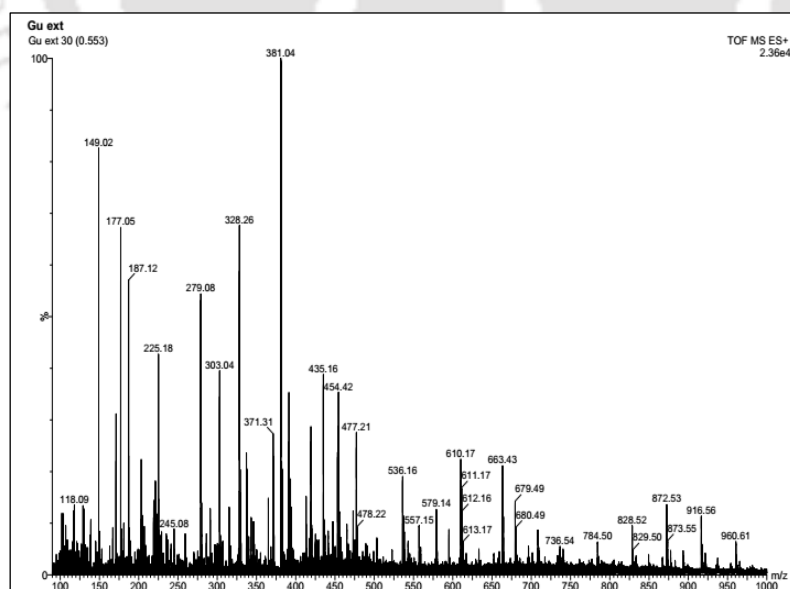


Figure 3.10: Mass spectra of *P. guajava* leaf extract showing different bio-constituents present in the extract.

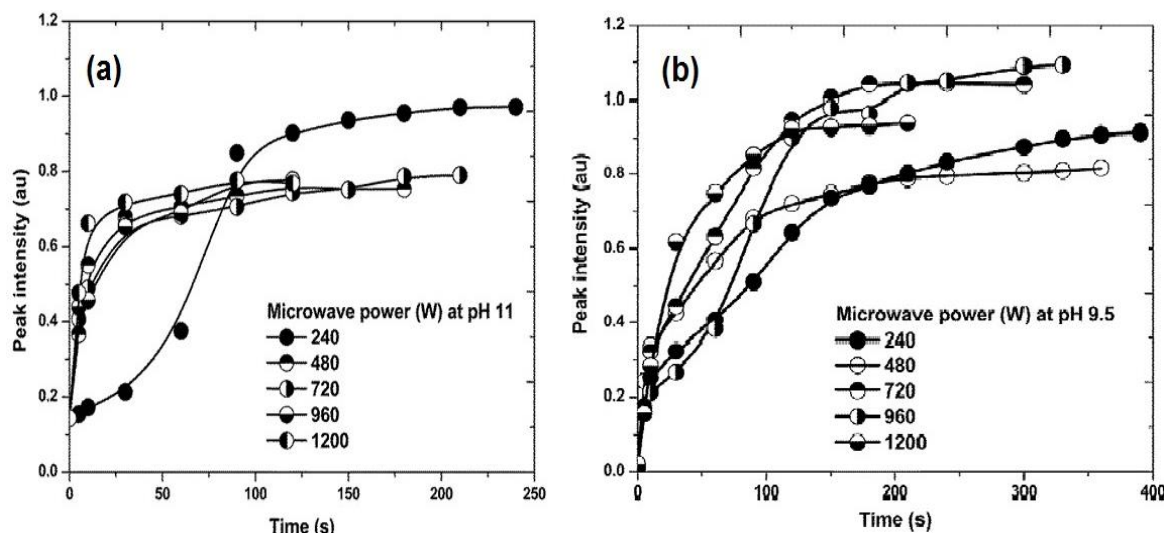


Figure 3.11: UV-vis spectral absorbance at λ_{\max} of AgNPs at different time of irradiation and microwave power at (a) pH 11 and (b) pH 9.5. Experimental conditions: reaction volume 250 mL, water to leaves ratio 500 and initial Ag^+ concentration 0.3 mM.

Table 3.1: Abundance of active compounds/analytes present in fresh *P. guajava* leaves.

Compounds	Chemical structure	Identified in mass spectra, m/z	Abundance (mg/g leaves)	Source
Rutin		610.17	3.52	Morais-Braga et al., 2016
Quercetin		303.03	10.15	
Chlorogenic acid (derivatives)		381.04	4.23	
Caffeic acid		187.12	4.30	
Naringenin		477.21	0.941	Díaz-de-Cerio et al., 2016
Ascorbic acid		177.05	0.90	Iamjud et al., 2014

3.2.1.2 Crystalline nature of AgNPs

The XRD pattern obtained AgNPs at pH 9.5 and 11 are shown in Figure 3.12. The dominant peaks at 38, 44, 65, 78, and 82° 2θ angles were the characteristics for face-centred cubic (fcc) AgNPs crystal for the diffraction from the (111), (200), (220), (311), and (222) planes, respectively (Jayaprakash et al., 2017). However, at pH 11, two distinct peaks corresponding to the presence of Ag₂O (110) and Ag₂O (111) were identified at 2θ = 29 and 32°, respectively (Rao and Golder, 2016). It implies that too high pH was detrimental for the formation AgNPs in such a bio-inspired route as the synthesised particles could be laden with Ag₂O impurities. Hence, AgNPs synthesis was performed at pH 9.5 and are used to decorate GPE (AgNPs(9.5)/GPE) to be used as the working electrode. Here, GPE denotes graphite paste electrode.

The crystalline size of AgNPs was calculated using the Scherrer's formula (Eq. 3.1) for crystalline powder materials (Sandeep et al., 2016).

$$D = k\lambda/(\beta\cos(\theta)) \quad (3.1)$$

Where, D is the average crystallite size perpendicular to the refraction plane, k is a shape factor (0.94 for spherical nanoparticles), λ is the wavelength of X-ray used (0.154 nm), θ is the diffraction angle (2θ/2), and β is the full-width half maxima (FWHM, radian). The results are summarised in Table 3.2. The average crystallite size was found to be 15.67 nm.

Table 3.2: XRD parameters of AgNPs synthesized at pH 9.5.

Sl. No	2θ (degrees)	Miller indices (hkl)	FWHM	Crystallite size D (nm)	Average crystallite D (nm)
1	38.33	111	0.4259	18.38	15.67
2	44.48	200	0.5182	14.80	
3	64.64	220	0.4468	15.68	
4	77.63	311	0.5058	12.77	
5	81.77	222	0.3750	16.71	

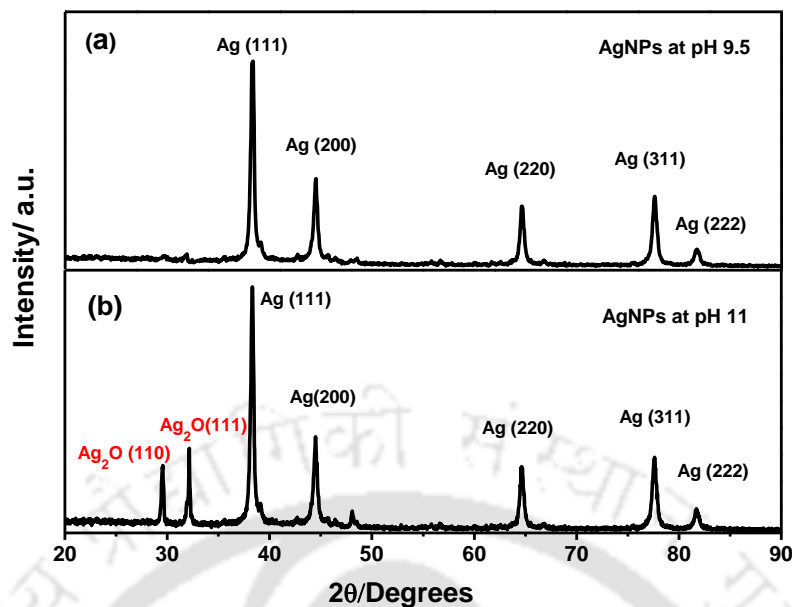


Figure 3.12: XRD patterns of AgNPs synthesized at (a) pH 9.5 and (b) pH 11.

P. guajava leaves are laden with Ag^+ reducing analytes (Figure 3.10) such as chlorogenic acid derivative (dimethoxy cinnamoylquinic acid), D-glucose, quercetin, and AA (Gu et al., 2009). Ag^+ is reduced to Ag^0 forming silver nuclei (Figure 3.13) which coalesce and AgNPs are formed. Quercetin and chlorogenic acid were oxidised to carboxylic derivatives and quinic acid (Figure 3.10) during the reduction Ag^+ . Epoxide derivatives and dehydroascorbic acid appeared in the mass spectra after the formation of AgNPs which were most likely formed from glucose and AA (Figure 3.10). The detailed mechanisms are outlined in Figures 3.14a to 3.14c.

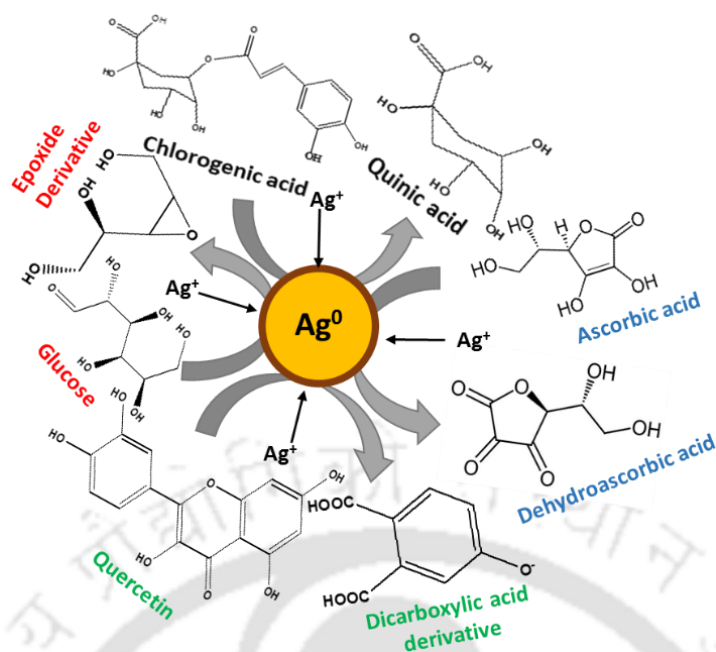


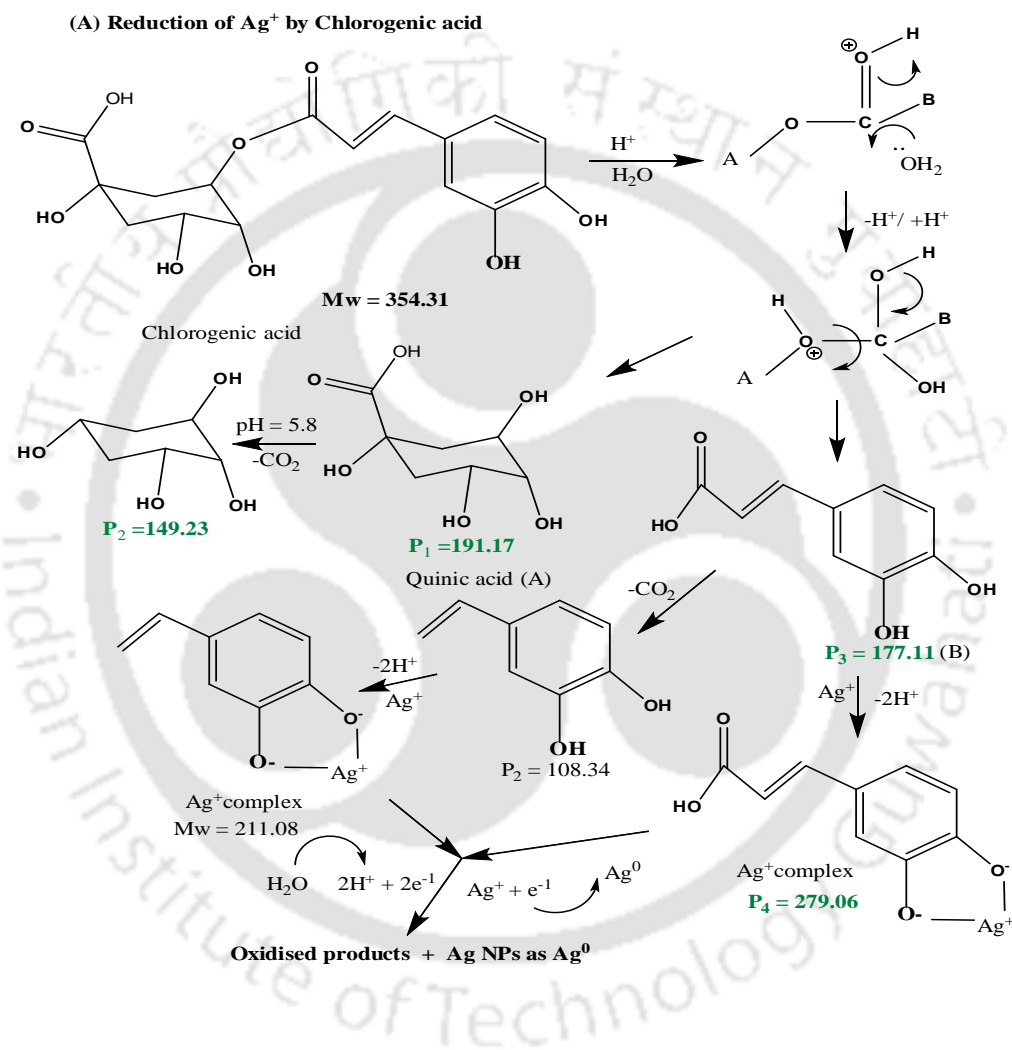
Figure 3.13: Schematic diagram showing the participation of various significant reducing agents for the bio-mediated AgNPs formation along with their important oxidation products.

3.2.1.3 Proposed mechanism of AgNPs formation using *P. guajava* leaves extract

Chlorogenic acid could reduce Ag^+ to Ag^0 , and itself is oxidised forming P₁ to P₄ products with a mass number of 191.17, 149.25, 177.11, and 279.06, respectively (Figure 3.14). All these four fragments were formed through protonation, followed by ester hydrolysis (Figure 3.14a). P₂ compound is originated by decarboxylation ($-\text{CO}_2$) reaction from P₁. Both the ester linkage ($-\text{COOR}$) cleavage and CO_2 removal are facilitated in the acidic media (Sykes, 2005). P₃ is formed from chlorogenic acid by acid catalysed ester hydrolysis reaction and forms a coordinate complex with Ag^+ ions, which is reduced to Ag^0 along with the formation of P₄ molecules (279.06). An intermediate Ag^+ -complex with a mass number of 211.08 (didn't appear in mass spectra) reduces Ag^+ and increases the rate of formation of AgNPs at a higher pH.

Glucose molecule (Mw = 180.00) also could take part in the formation of AgNPs, and P₅ (118.20) is formed (Figure 3.14b). Ag^+ forms a complex with a molar mass of 283.09 with deprotonated glucose molecule (β -D-glucoopyranoside) in an alkaline medium (pH = 9.5) (Chakraborty et al., 2017), and it is oxidised to an acid (197.03) which forms P₅ molecule through a decarboxylation reaction. Quercetin (Mw = 302.23) is identified in the mass spectra and reduces Ag^+ forming AgNPs. In these reactions, P₆ and P₇ molecules are

originated (Figure 3.14c). P₆ molecule is formed due to protonation followed by nucleophilic addition of water molecule at more electrophilic carbonyl centre -C=O group in quercetin molecule. The carbonyl centre acts as an electron deficient hole having a significant difference in electronegativity between carbon and oxygen atoms (Sykes, 2005). P₇ is yielded from Ag⁺-complex which is formed from an intermediate with a mass number of 146.07. The mechanism of Ag⁺ reduction forming AgNPs using AA present in the bio-extract is already outlined by the authors in the earlier study (Chelli and Golder, 2016).



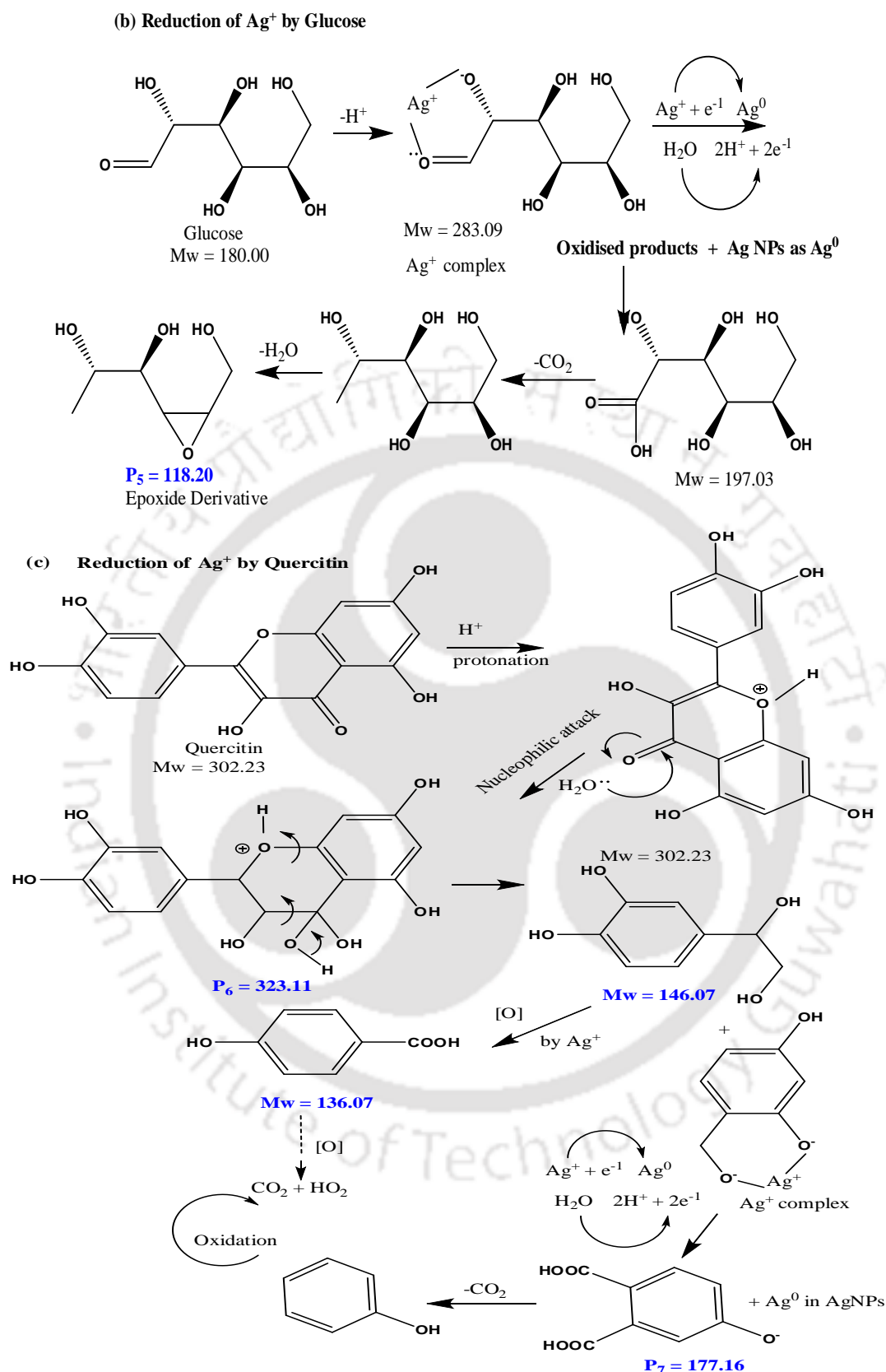


Figure 3.14: Proposed mechanism for the synthesis of AgNPs using *P. guajava* leaves extract. Reactions involved in Ag⁺ reduction forming AgNPs by (a) Chlorogenic acid, (b) D-glucose and (c) Quercetin are shown.

3.2.1.4 Transmission electron micrographs of AgNPs

The TEM micrographs illustrate the structural morphology, shape, and size of AgNPs. The particles were found to be irregular in shape at 90 s of irradiation (Figure 3.15a). The d-spacing was 0.234 nm from the HRTEM micrograph (Figure 3.15b) which is a characteristic dimension of AgNPs (Parveen et al., 2016). Four distinct diffraction rings from the SAED pattern indicated the reflection from the (111), (200), (220), and (311) planes of fcc AgNPs crystals (Inset of Figure 3.15b). The diameter of AgNPs ranged from 1 to 9 nm with an average size of 4.36 ± 1.6 nm (Figure 3.15c). The particles were grown big with the irradiation time and, the distinct irregular shapes were seen (Figure 3.15d). The particles were aggregated with the extended irradiation which is in accordance with the transition from blue shift to a redshift at 90 s for 960 W input power (Figure 3.5b). But, the crystallinity of particles was unaffected by the irradiation time (Figure 3.15e). The particle sizes were varied from 10 to 65 nm and, there was a 5-times increase in mean diameter after 300 s of MW heating (Figure 3.15f) (Parveen et al., 2016).

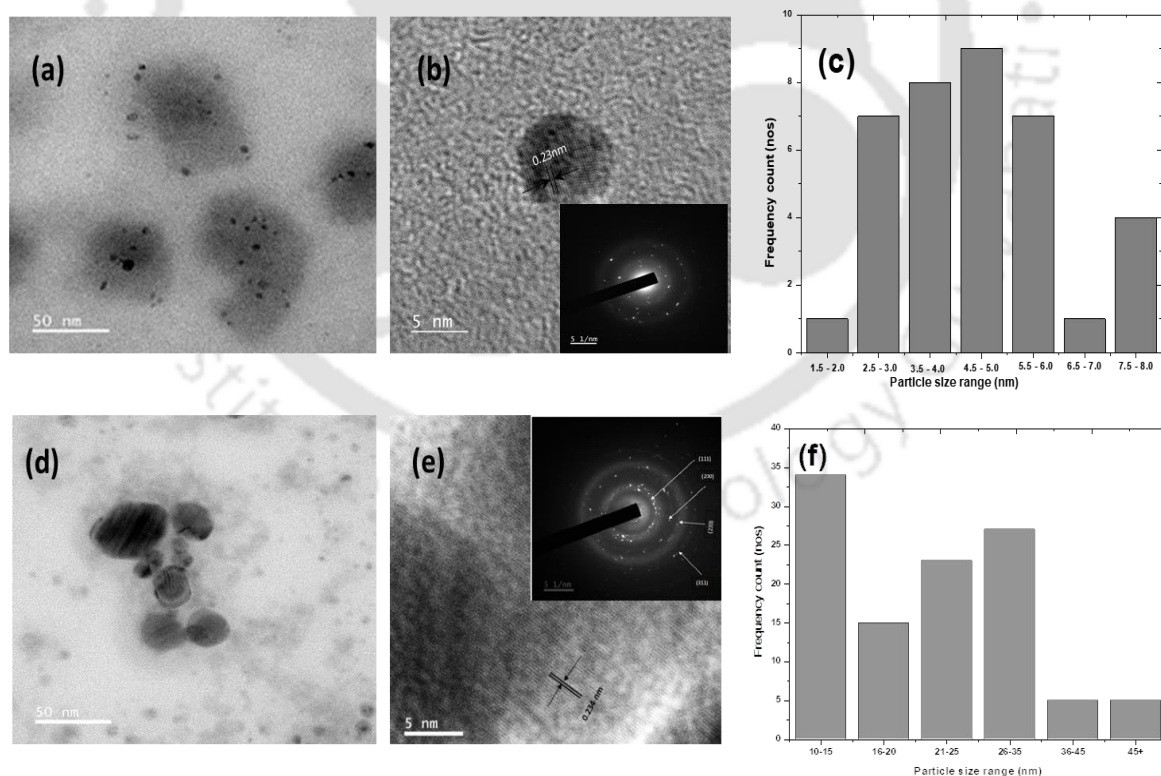


Figure 3.15: FETEM, HRTEM/SAED micrographic results, and particle size distribution of AgNPs at 960 W and pH 9.5 (a, b, c: for AgNPs formed at 90 s of MW irradiation and d, e, f: for AgNPs formed at 300 s of MW irradiation).

3.2.1.5 FTIR spectrum of AgNPs

The FTIR spectrum of AgNPs is illustrated in Figure 3.16. The intense broad absorption band around 3435 cm^{-1} is the typical characteristic of the -OH groups which is existent in different phenolic compounds such as quercetin, catechin, kaempferol, etc. The presence of a sharp peak at 2918 cm^{-1} was for the C-H stretching vibration. The strong absorption peak at 1638 cm^{-1} could be assigned to the stretching vibration of -C=O groups (El-naggar et al., 2017) and amide groups (e.g. -CONH₂) in the protein molecules that bind to AgNPs and help them stabilised. The absorption peak at 1381 cm^{-1} is attributable to C-C and C-N stretching bonds. The peak appeared at 1083 cm^{-1} was for the ether linkages (C-O-C) that are easily adsorbed on the surface of AgNPs (Shankar et al., 2004).

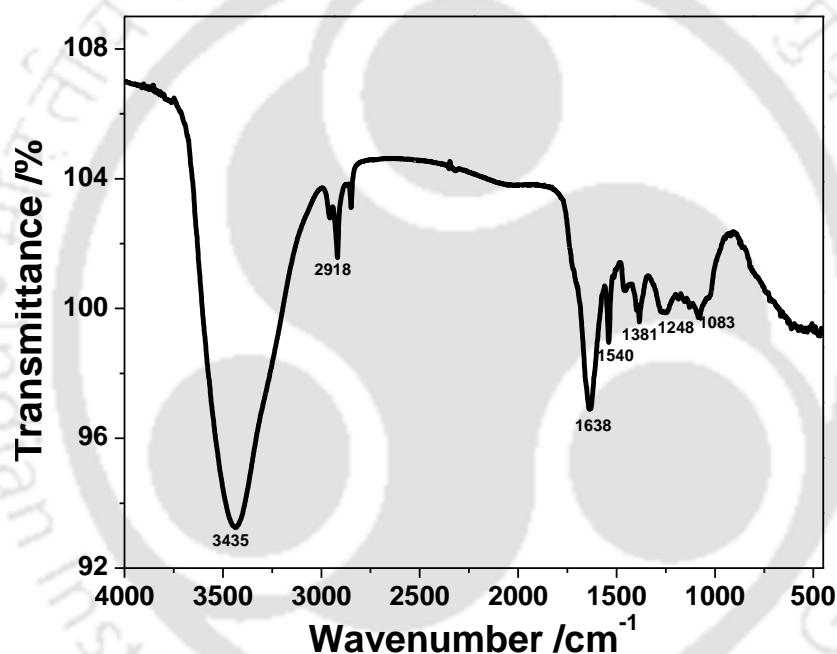


Figure 3.16: FTIR spectrum of AgNPs synthesised at pH 9.5. Experimental conditions: reaction volume 250 mL, water to leaves ratio 500, Ag⁺ concentration 0.3 mM, MW power 960 W and irradiation time 300 s.

3.2.1.6 Characterizations of AgNPs(pH9.5)/GPE nanocomposite

The XRD pattern of AgNPs(pH9.5)/GPE) and bare GPE are presented in Figure 3.17. A dominant peak at $2\theta = 26.5^\circ$ for the reflection from the (002) plane was for the existent of bulk graphite (Shankar et al., 2004) which was consistent with the XRD pattern of bare GPE (Figure 3.17b). Two lean peaks at $2\theta = 38$ and 44° corresponded for the diffraction from (111) and (200) planes for AgNPs traces in

nanocomposite (Figure 3.17a) (Rao and Golder, 2016). The peaks at 2θ values lower than C-002 are attributed to the C-110 and C-200 of carbon in paraffin wax that was used in the manufacture of the GPE (Rao and Zhang, 2011).

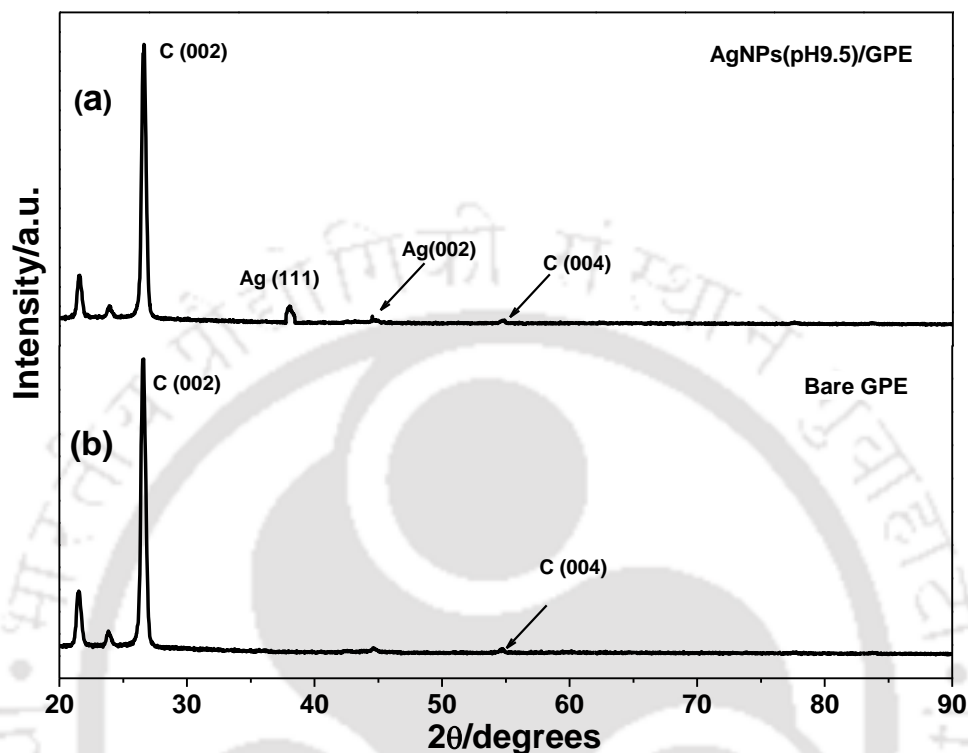


Figure 3.17: XRD patterns of (a) AgNPs(pH9.5)/GPE, and (b) bare GPE.

The fabricated AgNPs(pH9.5)/GPE electrode was polished by a plain A4 sheet. A digital image of the cross section of this electrode is depicted in Figure 3.18a and Figure 3.18b after coating. The electrode surface seemed to be smooth on the macroscopic scale. AgNPs(pH9.5)/GPE nanocomposite contained about 7.6% Ag (Figure 3.18c). The source of carbon (45.2%), fluorine (46%), and sulphur (1.2%) was the graphite and Nafion used as a binder of AgNPs on the bare GPE. A low magnification SEM micrograph of the electrode surface clearly revealed the formation of a Nafion film on the GPE (Figure 3.18d). A high dispersity of Ag on the electrode surface was also evident from the elemental image-mapping (green dots for Ag, (Figure 3.18) which was highly desirable for an increased sensitivity for AA detection.

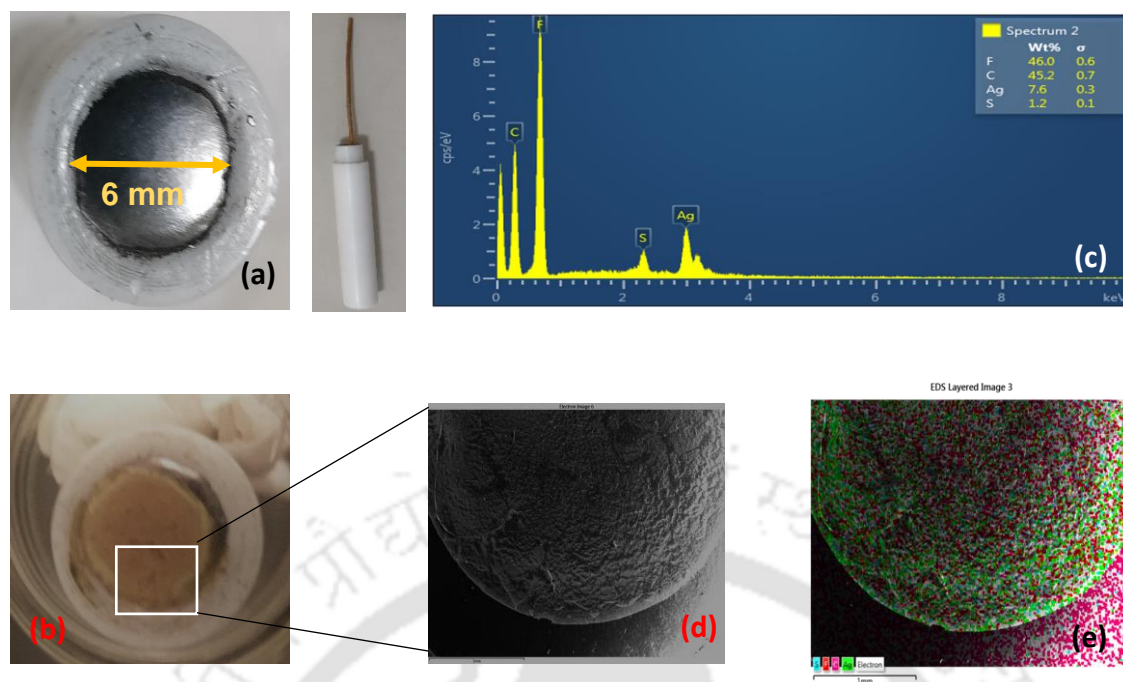


Figure 3.18: Morphology and EDX analysis of AgNPs(pH9.5)/GPE: (a) Cross-sectional view showing the active surface area of bare GPE, (b) Cross-sectional view showing the active surface area of AgNP(pH9.5)/GPE, (c) Elemental analysis of AgNPs(pH9.5)/GPE nanocomposite, (d) FESEM micrograph of drop coated AgNPs(pH9.5)/GPE and (e) Elemental EDX mapping of AgNPs(pH9.5)/GPE nanocomposite.

3.2.2 Electrochemical behaviour of AgNPs(pH9.5)/GPE

3.2.2.1 Electrochemical impedance spectroscopy (EIS)

The EIS spectra obtained with the bare GPE and AgNPs(pH9.5)/GPE are illustrated in Figure 3.19a. A truncated semicircle with a large diameter was observed for the GPE in the frequency range from 10^{-2} to 10^6 Hz and, the diameter of the semicircle was lower for AgNPs(pH9.5)/GPE. The charge transfers resistance (R_p) values for $K_3[Fe(CN)_6]/K_4[Fe(CN)_6]$ (0.5 mM) at the GPE and AgNPs(pH9.5)/GPE were found as 3.2 and 0.453 K Ω , respectively, which was obtained from the fitting and simulation of experiment data using NOVA 1.11 software against the values of solution resistance (R_s) and constant phase elements (CPE) as depicted in Figures 3.19b and 3.19c. The results implied that the charge transfer resistance of the electrode decreased with the AgNPs(pH9.5) decoration on the GPE and made it more sensitive towards the analyte. Similar results were also obtained using AgNPs for the modification of the glassy carbon electrode by drop coating of AgNPs/carbon nanotubes (Chen et al., 2012). Baek et al. (2016) also

showed a reduction in charge transfer resistance from 60 to 30 ohms in silicon nanowires by the introduction of AgNPs on its surface (Baek et al., 2016) (Baek et al., 2016). The reduction in charge transfer resistance was for the increase in the active surface area of the electrode and electrical conductivity in the presence of AgNPs.

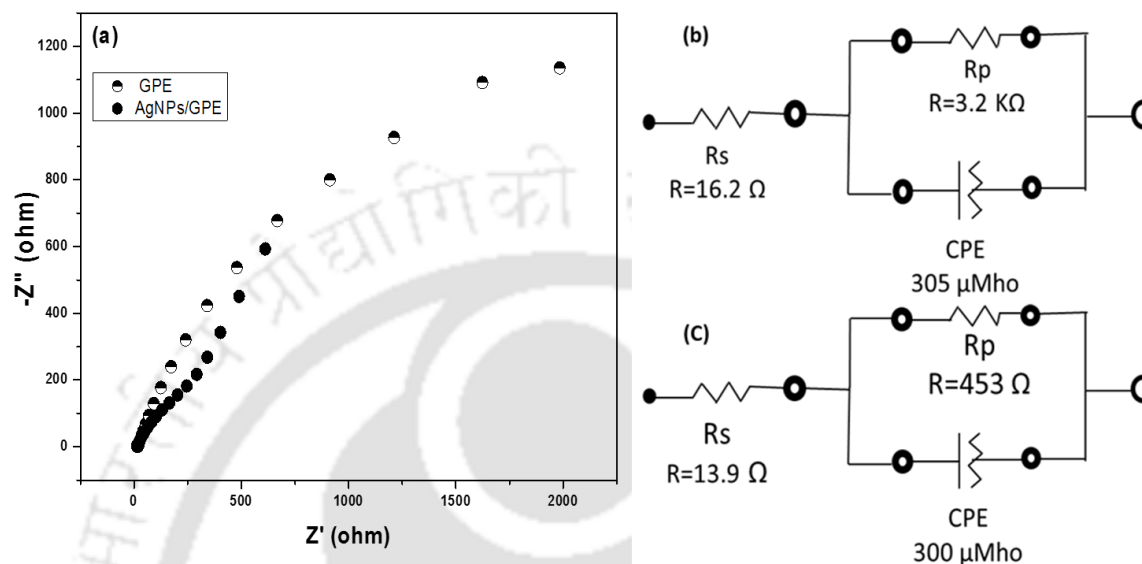


Figure 3.19: Nyquist plots for EIS measurements ($0.5 \text{ mM K}_3[\text{Fe}(\text{CN})_6]$) at (a) bare GPE and AgNPs(pH9.5)/GPE, (b) equivalent circuit diagram of GPE and (c) equivalent circuit diagram of AgNPs(pH9.5)/GPE showing resistance of working electrodes.

3.2.2.2 Cyclic voltammetric and amperometric responses

The cyclic voltammograms (CVs) with the GPE and AgNPs(pH9.5)/GPE are illustrated in Figure 3.20a. In the presence of $700 \mu\text{M AA}$, no oxidation peak was observed at GPE. AgNPs(pH9.5)/GPE showed a sharp peak at $E_{\text{anode}} = 0.402 \text{ V vs. Ag/AgCl}$ with a peak current of $90 \mu\text{A}$ at the same analyte concentration (Khalilzadeh and Borzoo, 2016). The maximum current density of $387.09 \mu\text{A}\cdot\text{cm}^{-2}$ was found with $1000 \mu\text{M AA}$ and 0.282 cm^2 working electrode area.

The CVs at variant AA concentration at AgNPs(pH9.5)/GPE is also depicted in Figure 3.20a. The peak potential was gradually shifted to a higher value with increasing AA concentration. The peak potential, $E_{\text{anode}} = 0.380 \text{ V vs. Ag/AgCl}$ at $25 \mu\text{M AA}$ was increased to 0.406 V at $1000 \mu\text{M}$ with a scan rate of $25 \text{ mV}\cdot\text{s}^{-1}$. At a lower analyte concentration, diffusion occurred in an uninterrupted way (Khalilzadeh and Borzoo, 2016). However, the analyte flux to the electrode surface was more at its higher concentration. Hence, a layer of dehydroascorbic acid was

formed at the onset of oxidation of AA which disrupted the mass transfer process. It implied that AgNPs catalysed a favourable AA oxidation at its lower concentration.

The scan rate with the AgNPs(pH9.5)/GPE was varied from 10 to 100 $\text{mV}\cdot\text{s}^{-1}$ for the kinetic studies. The results obtained are shown in Figure 3.20b. A faster scan rate (v) increased the oxidation peak current (I_P) due to a higher analyte flux toward the electrode (Hsu et al., 2017; Khalilzadeh and Borzoo, 2016; Rasappa et al., 2015). A linear variant ($R^2 = 0.989$) between I_P and $v^{1/2}$ was observed (Figure 3.20c). It indicated that AA oxidation at AgNPs(pH9.5)/GPE was in the diffusion controlled range with an AA concentration of 100 μM (Malinauskas et al., 2004). Figure 3.20d shows the variation of E_P vs. Ag/AgCl with $\log(v)$ and, the slope of the best fit line was related to the equation (Eq. 3.2) Laviron equation for a diffusion controlled process (Kaur et al., 2013).

$$E_P = E^0 + \frac{2.303RT}{\alpha nF} \log \frac{RTk^0}{\alpha nF} + \frac{2.303RT}{\alpha nF} \log v \quad (3.2)$$

Where, α is the anodic charge transfer coefficient, n is the number of electrons transferred, R is the universal gas constant ($8.314 \text{ J}\cdot\text{mol}^{-1}\cdot\text{K}^{-1}$), F is Faraday's constant ($96485 \text{ C}\cdot\text{mol}^{-1}$), T is the temperature in K and v is the scan rate in $\text{V}\cdot\text{s}^{-1}$. The value of the Tafel slope (Figure 3.20c) was found as $103 \text{ mV}\cdot\text{decade}^{-1}$. It implied only a single-step one electron transfer reaction which determined the rate of AA oxidation (Hsu et al., 2017). First and second deprotonation of AA exhibits the pK_a values of 4.17 and 11.57, respectively. AA existed as dehydro-AA in the PBS of pH 7.2 (Ensafi et al., 2016). So, the overall reaction involved a single-step single-electron transfer process as evident from the Tafel plot. The value of α was found as 0.57 with $n = 1$ which was close to the theoretical value of 0.5 for a completely irreversible process (Ensafi et al., 2016).

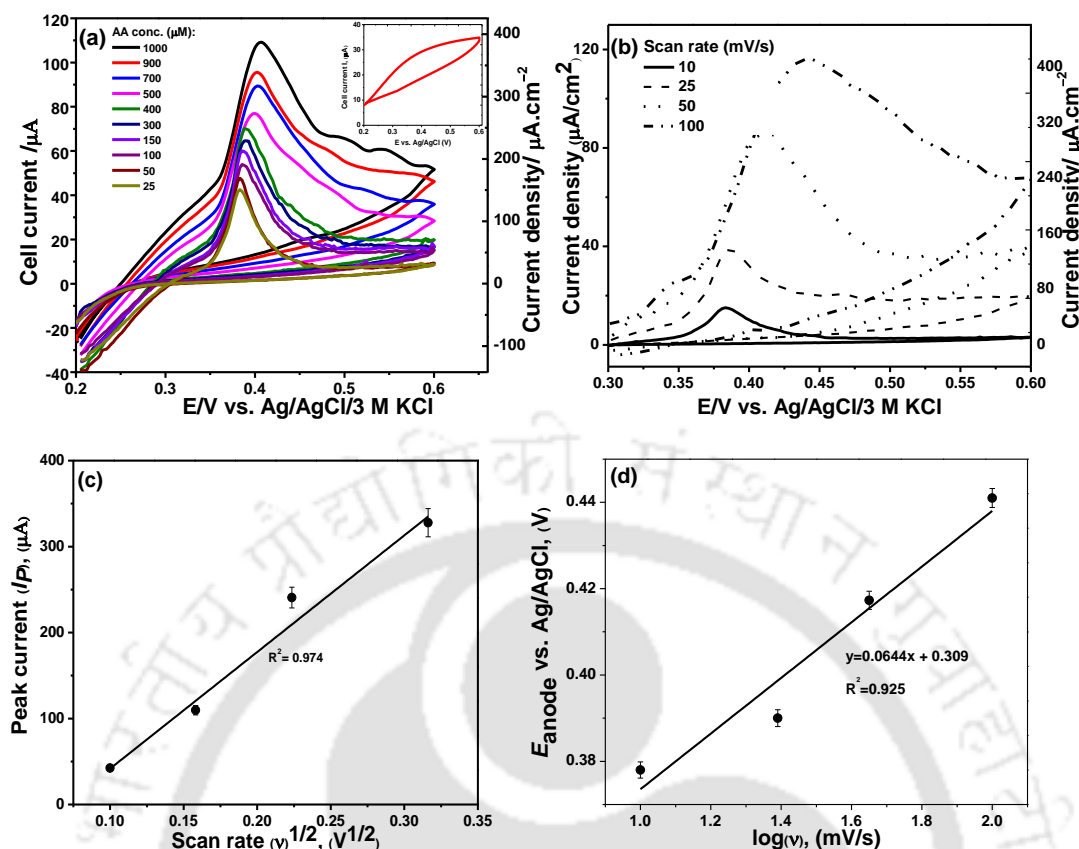


Figure 3.20: (a) Cyclic voltammograms recorded with AgNPs(pH9.5)/GPE at different AA concentration (25 to 1000 μM). Inset: CV obtained with similar experimental conditions using 700 μM AA and GPE in place of AgNPs(pH9.5)/GPE, (b) Cyclic voltammograms recorded at different scan rates at AgNPs(pH9.5)/GPE, (c) Variation of peak current (I_p) with $v^{1/2}$ (v : 10 to 100 $\text{mV}\cdot\text{s}^{-1}$), (d) Variation of E_p and $\log(v)$ (v : 10 to 100 $\text{mV}\cdot\text{s}^{-1}$) with 100 μM AA in 0.1 M.

The chronoamperometric experiment was performed with the addition of a different quantity of AA starting from 25 to 2000 μM at 0.380 V vs. Ag/AgCl with a signal to noise ratio of 3. Momentarily, there was a jump in the response current (Figure 3.21) after AA addition as AA having a strong affinity to be adsorbed on the AgNPs/graphite nanocomposite (Nguyen et al., 2016). The cell current with the AA addition was stabilised very quickly and, a steady current was reached by 5 s.

During the chronoamperometric test, the intermediate addition of DA and UA as interferants did not show an appreciable change in the response current (Figure 3.22). The calibration plot (Inset of Figure 3.21) shows that AgNPs(pH9.5)/GPE displayed a fairly linear relationship between AA and current response on the successive addition of AA. The influence of DA and UA during AA detection was

further studied by SWV with 1000 μM AA and 500 μM of each of DA and UA by varying the square wave potential from 0.5 to 1.25 V vs. Ag/AgCl. Three distinct peaks appeared at 0.397, 0.669, and 1.511 V vs. Ag/AgCl (Figure 3.22) for the oxidation AA, DA, and UA, respectively. So, it gave decent AA-DA and AA-UA separation (peak) potentials of 0.272 and 1.114 V, respectively. It implied a high selectivity of AgNPs(pH9.5)/GPE for the AA detection in the PBS. Shankar et al. obtained a separation potential of 0.196 V for AA-DA using tetraoctyl ammonium bromide modified carbon paste electrode for AA detection (Chang et al., 2017). In fact, two linear regions were noted for 25 to 150 μM with a slope of $2.03 \times 10^{-3} \mu\text{A} \cdot \mu\text{M}^{-1}$ AA and for 150 to 2000 μM with a slope of $1.1 \times 10^{-3} \mu\text{A} / \mu\text{M}$ AA, respectively with a reasonably good regression coefficient (>0.99). The abundance of AA molecules at the electrode vicinity at a higher concentration shifted the electrochemical reaction from the diffusion controlled to the surface-controlled domain. So, two separate linearity ranges were observed (Arabali et al., 2016).

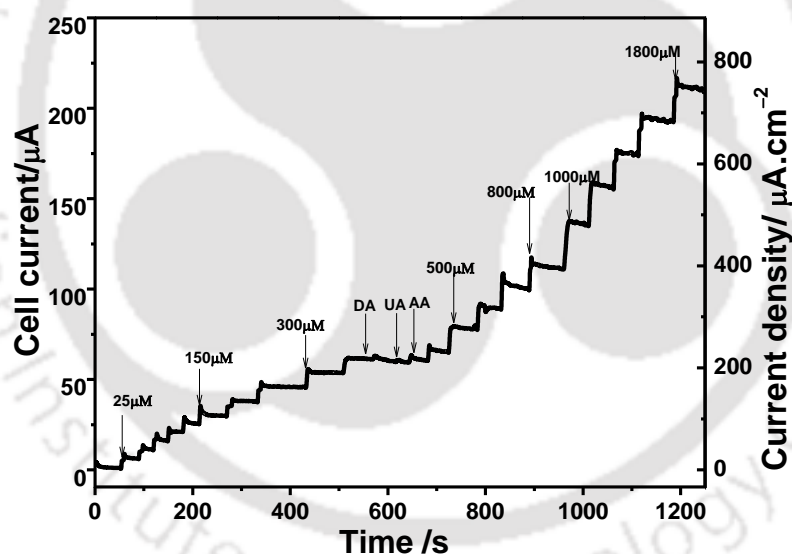


Figure 3.21: Chronoamperometric profile with step-wise addition of AA along with intermediate addition of dopamine (DA) and uric acid (UA) as interferants at AgNPs(pH9.5)/GPE. Inset: shows calibration curves for the variation of cell (steady) current with AA concentration at AgNPs(pH9.5)/GPE. Experimental conditions: $E_{\text{anode}} = 0.380$ V vs. Ag/AgCl, pH 7.2 and PBS 100 mL.

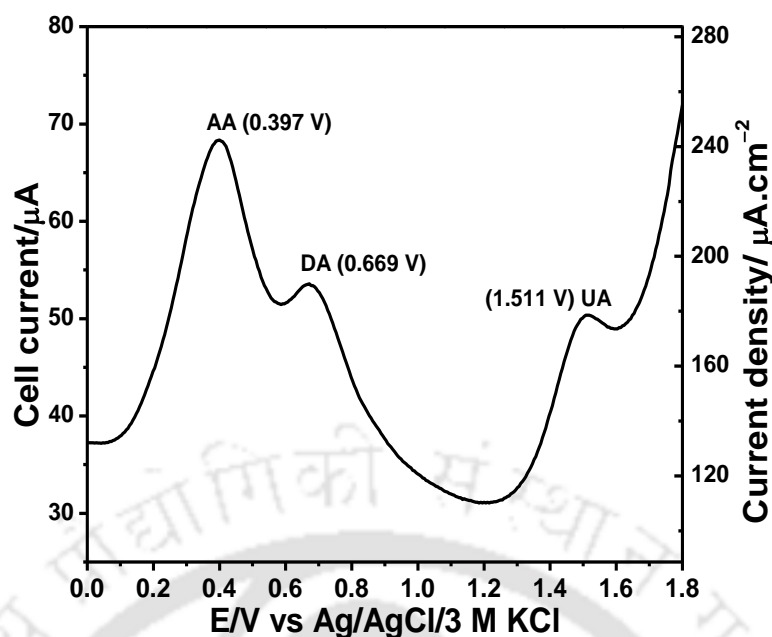


Figure 3.22: Square wave voltammogram obtained with AgNPs(pH9.5)/GPE for a mixture of 1 mM of AA and 0.5 mM of DA, and UA. Experimental conditions: scan rate 50 mV .s⁻¹, pH 7.2 and 100 mL PBS.

The limit of detection (LOD, Eq. 3.3) and limit of quantification (LOQ, Eq. 3.4) were calculated by its deviation from the standard deviation in the absence of analytes (Das and Golder, 2017).

$$\text{LOD} = (3S_b)/m \quad (3.3)$$

$$\text{LOQ} = (10S_b)/m \quad (3.4)$$

Where, S_b is the standard deviation without analyte (blank) and m is the slope of the calibration curve. LOD and LOQ were found to be 14.63 and 48.71 μM for $\text{AA} \leq 2000 \mu\text{M}$. These results were comparable with AgNPs (Chang et al., 2017) and AuNPs (Filik et al., 2016) catalysed AA detection at reduced graphene oxide and carbon paste electrodes, respectively. The sensitivity of AgNPs(pH9.5)/GPE was determined by Eq. 3.5 (Pisoschi et al., 2011).

$$S = b/A \quad (3.5)$$

Where, A is the active area of AgNPs(pH9.5)/GPE (0.282 cm^2) and b is the slope of the calibration curve (Figure 3.23). The sensitivity of the electrode was found to be $0.719 \mu\text{A} \cdot \mu\text{M} \cdot \text{cm}^{-2}$ for AA concentration $\leq 150 \mu\text{M}$ and $0.390 \mu\text{A} \cdot \mu\text{M} \cdot \text{cm}^{-2}$ for AA concentration between 150 and 2000 μM . It suggested that AgNPs catalysed AA determination from a trace of AA at least up to 2000 μM .

Similar results were obtained for the detection of AA and DA at ionic liquid modified electrodes/CdO nanoparticles cyclodextrin/AuNPs/graphene modified carbon electrodes (Loizzo et al., 2016; Zhang et al., 2016). Kaur et al. reported a sensitivity of $0.460 \mu\text{A} \cdot \mu\text{M}^{-1}$ on AgNPs/glassy carbon electrode (Kaur et al., 2013).

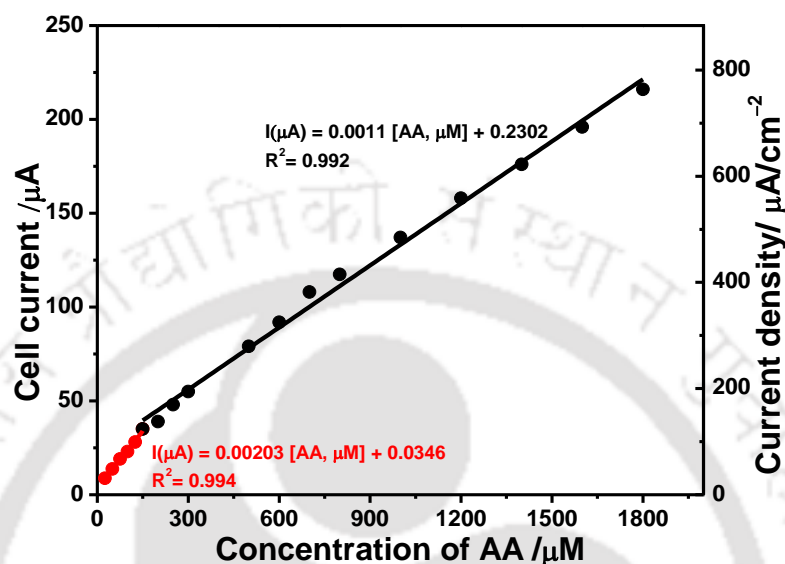


Figure 3.23: Calibration curves for the variation of cell (steady) current with AA concentration at AgNPs(pH9.5)/GPE. Experimental conditions: $E_{\text{anode}} = 0.380 \text{ V}$ vs. Ag/AgCl, pH 7.2 and PBS 100 mL.

Three freshly prepared AgNPs(pH9.5)/GPEs were employed in order to check the reproducibility of steady current response. The amperometric signal was captured after 300 s at 0.380 V vs. Ag/AgCl with 1000 μM AA. An average cell current of 116, 120, and 121 μA was achieved with these electrodes. It gave a relative standard deviation (rsd) of 2.64% which was well within a typical tolerance limit of 4% (Zhang et al., 2016). The amperometric tests were repeated for 10 times and, an average rsd of 1.95% was obtained.

3.2.3 Analysis of AA in biological entities

The AgNPs(pH9.5)/GPE was further tested for the detection of AA present in the bio-extract of *Z. mauritiana* and *S. edule* leaves being the good sources of AA. The *S. edule* extract was prepared following the method described by (Chelli and Golder, 2016), and *Z. mauritiana* extract was prepared in the same manner as for the preparation of *P. guajava* leaves extract. The bio-extracts thus obtained were diluted

using 0.1 M PBS and, the triplicated concentration of AA at $E_{\text{anode}} = 0.380 \text{ V}$ vs. Ag/AgCl is shown in Table 3.2. The concentration of AA was determined at two different dilutions which enabled us the use of both the calibration curves as shown in Figure 3.23. These results were remarkably comparable with the HPLC analyses and, the deviations were $<5\%$ in all the analyses (Pisoschi et al., 2011). Based on these results, the AA content per g of *S. edule* and *Z. mauritiana* leaf were estimated as 0.057 and 1.3 mg which was close to the earlier reports (Loizzo et al., 2016; Zhang et al., 2016).

Table 3.2: Determination of AA in two naturally obtained bio-extracts at AgNPs(pH9.5)/GPE and its comparison with HPLC measurements.

Specimen	[AA] by electrochemical method, (μM)	[AA] by HPLC, (μM)	Deviation, (%)
<i>Z. mauritiana</i> leaf extract	119 \pm 0.07	125 \pm 0.13	4.8
	176 \pm 0.13	182 \pm 2.3	3.2
<i>S. edule</i> fruit extract	49 \pm 0.03	51 \pm 3.8	3.9

3.3 Major findings

A microwave-assisted bio-inspired route of AgNPs synthesis to overcome the prolong time requirement for a typical bio-mediated process is successfully achieved. The reaction time of 10 h for AgNPs formation (up to 90%) without MW was decreased to 90 s at pH 9.5 with an average particle size of 19.6 nm for 960 W MW input power. The increase in MW exposure time and MW input power increased the AgNPs size without affecting the crystallinity of the particles. On the other hand, a higher reaction pH assisted for the formation of small-sized AgNPs (average diameter of 10.6 nm at pH 11) but the particles quality was sacrificed by the presence of remnant Ag₂O.

AgNPs was successfully drop-coated on the graphite paste electrode (GPE) and improved the electron transferability with a reduction of charge transfer resistance by 7 folds. AgNPs(pH9.5)/GPE was highly selective for AA sensing catalysed by AgNPs and the coexistence of dopamine and uric acid couldn't alter the oxidation potential (0.380 V vs. Ag/AgCl) of AA. The sensing of AA up to 150 μM was governed by its diffusion, but AA also could be sensed at a higher concentration ($150 \leq \text{AA} \leq 2000 \mu\text{M}$) under activation control and the corresponding sensitivities of

AgNPs(pH9.5)/GPE were found to be 0.719 and 0.390 $\mu\text{A}\cdot\mu\text{M}^{-1}\cdot\text{cm}^{-2}$. AgNPs(pH9.5)/GPE achieved a low limit of detection and limit of quantification as 14.63 and 48.71 μM , and the electrode response was reproducibility with a relative standard deviation of 2.64%. AgNPs(pH9.5)/GPE was also successful for analysing AA concentration in two biological entities, namely, *Z. mauritiana* and *S. edule*, and the results were comparable with HPLC (max 5% deviation).



References

- Abbasi, E., Milani, M., Aval, S.F., Kouhi, M., Akbarzadeh, A., Nasrabadi, H.T., Nikasa, P., Joo, S.W., Hanifehpour, Y., Nejati-Koshki, K., Samiei, M., 2016. Silver nanoparticles: Synthesis methods, bio-applications and properties. *Crit. Rev. Microbiol.* 42, 173–180. <https://doi.org/10.3109/1040841X.2014.912200>
- Agnihotri, S.A., Mallikarjuna, N.N., Aminabhavi, T.M., 2004. Recent advances on chitosan-based micro- and nanoparticles in drug delivery. *J. Control. Release* 100, 5–28. <https://doi.org/10.1016/j.jconrel.2004.08.010>
- Ahmed, S., Ahmad, M., Swami, B.L., Ikram, S., 2016. A review on plants extract mediated synthesis of silver nanoparticles for antimicrobial applications: A green expertise. *J. Adv. Res.* 7, 17–28. <https://doi.org/10.1016/j.jare.2015.02.007>
- Arabali, V., Ebrahimi, M., Abbasghorbani, M., Gupta, V.K., Farsi, M., Ganjali, M.R., Karimi, F., 2016. Electrochemical determination of vitamin C in the presence of NADH using a CdO nanoparticle/ionic liquid modified carbon paste electrode as a sensor. *J. Mol. Liq.* 213, 312–316. <https://doi.org/10.1016/j.molliq.2015.10.001>
- Baek, S.H., Park, J.S., Jeong, Y.M., Kim, J.H., 2016. Facile synthesis of Ag-coated silicon nanowires as anode materials for high-performance rechargeable lithium battery. *J. Alloys Compd.* 660, 387–391. <https://doi.org/10.1016/j.jallcom.2015.11.131>
- Bagheri, H., Pajooheshpour, N., Jamali, B., Amidi, S., Hajian, A., Khoshshafar, H., 2017. A novel electrochemical platform for sensitive and simultaneous determination of dopamine, uric acid and ascorbic acid based on Fe₃O₄SnO₂Gr ternary nanocomposite. *Microchem. J.* 131, 120–129. <https://doi.org/10.1016/j.microc.2016.12.006>
- Barbalho, S.M., 2012. Psidium Guajava (Guava): A Plant of Multipurpose Medicinal Applications. *Med. Aromat. Plants* 01, 1–6. <https://doi.org/10.4172/2167-0412.1000104>
- Carballo, T., Gil, M.V., Gómez, X., González-Andrés, F., Morán, A., 2008. Characterization of different compost extracts using Fourier-transform infrared spectroscopy (FTIR) and thermal analysis. *Biodegradation* 19, 815–830. <https://doi.org/10.1007/s10532-008-9184-4>
- Chakraborty, S., Chelli, V.R., Das, R.K., Giri, A.S., Golder, A.K., 2017. Bio-mediated silver nanoparticle synthesis: mechanism and microbial inactivation. *Toxicol. Environ. Chem.* 99, 434–447. <https://doi.org/10.1080/02772248.2016.1214271>

- Chang, Z., Zhou, Y., Hao, L., Hao, Y., Zhu, X., Xu, M., 2017. Simultaneous determination of dopamine and ascorbic acid using B-cyclodextrin/Au nanoparticles/graphene-modified electrodes. *RSC Anal. Methods* 9, 664–671. <https://doi.org/10.1039/C6AY03013K>
- Chelli, V.R., Bag, S.S., Golder, A.K., 2017. A biosynthesis route to nearly spherical AgNPs using chayote fruit extract. *Environ. Prog. Sustain. Energy* 36, 192–199. <https://doi.org/10.1002/ep.12440>
- Chelli, V.R., Golder, A.K., 2016. pH dependent size control, formation mechanism and antimicrobial functionality of bio-inspired AgNPs. *RSC Adv.* 6, 95483–95493. <https://doi.org/10.1039/C6RA16475G>
- Chen, L., Xie, H., Li, J., 2012. Electrochemical glucose biosensor based on silver nanoparticles/multiwalled carbon nanotubes modified electrode. *J. Solid State Electrochem.* 16, 3323–3329. <https://doi.org/10.1007/s10008-012-1773-9>
- Darmanin, T., Nativo, P., Gilliland, D., Ceccone, G., Pascual, C., De Berardis, B., Guittard, F., Rossi, F., 2012. Microwave-assisted synthesis of silver nanoprisms/nanoplates using a “modified polyol process.” *Colloids Surfaces A Physicochem. Eng. Asp.* 395, 145–151. <https://doi.org/10.1016/j.colsurfa.2011.12.020>
- Das, R.K., Golder, A.K., 2017. Co₃O₄ spinel nanoparticles decorated graphite electrode: Bio-mediated synthesis and electrochemical H₂O₂ sensing. *Electrochim. Acta* 251, 415–426. <https://doi.org/10.1016/j.electacta.2017.08.122>
- Dauthal, P., Mukhopadhyay, M., 2016. Noble Metal Nanoparticles: Plant-Mediated Synthesis, Mechanistic Aspects of Synthesis, and Applications. *Ind. Eng. Chem. Res.* 55, 9557–9577. <https://doi.org/10.1021/acs.iecr.6b00861>
- Díaz-de-Cerio, E., Gómez-Caravaca, A.M., Verardo, V., Fernández-Gutiérrez, A., Segura-Carretero, A., 2016. Determination of guava (*Psidium guajava* L.) leaf phenolic compounds using HPLC-DAD-QTOF-MS. *J. Funct. Foods* 22, 376–388. <https://doi.org/10.1016/j.jff.2016.01.040>
- Dinesh, B., Saraswathi, R., Kumar, A.S., 2017. Water based homogenous carbon ink modified electrode as an efficient sensor system for simultaneous detection of ascorbic acid, dopamine and uric acid. *Electrochim. Acta* 233, 92–104. <https://doi.org/10.1016/j.electacta.2017.02.139>
- El-naggar, N.E., Hussein, M.H., El-sawah, A.A., 2017. Bio-fabrication of silver nanoparticles by phycocyanin, characterization, in vitro anticancer activity against breast cancer cell line and in vivo cytotoxicity. *Sci. Rep.* 1–20.

<https://doi.org/10.1038/s41598-017-11121-3>

- Ensafi, A.A., Rezaei, B., Ghiaci, M., Chermahini, M.E., Moshiri, P., 2016. Non-enzymatic glucose electrochemical sensor based on silver nanoparticle decorated organic functionalized multiwall carbon nanotubes. *RSC Adv.* 65, 60926–60932. <https://doi.org/10.1039/C6RA10698F>
- Filik, H., Avan, A.A., Aydar, S., 2016. Simultaneous detection of ascorbic acid, dopamine, uric acid and tryptophan with Azure A-interlinked multi-walled carbon nanotube / gold nanoparticles composite modified electrode. *Arab. J. Chem.* 9, 471–480. <https://doi.org/10.1016/j.arabjc.2015.01.014>
- Friedman, M., Jürgens, H.S., 2000. Effect of pH on the stability of plant phenolic compounds. *J. Agric. Food Chem.* 48, 2101–2110. <https://doi.org/10.1021/jf990489j>
- Gan, P.P., Ng, S.H., Huang, Y., Fong, S., Li, Y., 2012. Bioresource Technology Green synthesis of gold nanoparticles using palm oil mill effluent (POME): A low-cost and eco-friendly viable approach. *Bioresour. Technol.* 113, 132–135. <https://doi.org/10.1016/j.biortech.2012.01.015>
- Gu, C., Cheng, C., Huang, H., Wong, T., Wang, N., Zhang, T.-Y., 2009. Growth and Photocatalytic Activity of Dendrite-like ZnO@Ag Heterostructure Nanocrystals. *Cryst. Growth Des.* 9, 3278–3285. <https://doi.org/10.1021/cg900043k>
- Güçlü, K., Sözgen, K., Tütem, E., Özyürek, M., Apak, R., 2005. Spectrophotometric determination of ascorbic acid using copper(II)-neocuproine reagent in beverages and pharmaceuticals. *Talanta* 65, 1226–1232. <https://doi.org/10.1016/j.talanta.2004.08.048>
- Haes, a J., Zou, S.L., Schatz, G.C., Van Duyne, R.P., 2004. A nanoscale optical biosensor: The long range distance dependence of the localized surface plasmon resonance of noble metal nanoparticles. *J. Phys. Chem. B* 108, 109–116. <https://doi.org/10.1021/jp0361327>
- Hsu, S.C., Cheng, H.T., Wu, P.X., Weng, C.J., Santiago, K.S., Yeh, J.M., 2017. Electrochemical Sensor Constructed Using a Carbon Paste Electrode Modified with Mesoporous Silica Encapsulating PANI Chains Decorated with GNPs for Detection of Ascorbic Acid. *Electrochim. Acta* 238, 246–256. <https://doi.org/10.1016/j.electacta.2017.04.021>
- Iamjud, K., Banyen, N., Boonprakob, U., Thaipong, K., 2014. Ascorbic acid, total phenolics and antioxidant activity of guava leaf extracts. *Acta Hort.* 1024, 367–372.

<https://doi.org/10.17660/ActaHortic.2014.1024.50>

- Iravani, S., Zolfaghari, B., 2013. Green Synthesis of Silver Nanoparticles Using Pinus eldarica Bark Extract. Biomed Res. Int. 2013, 1–5. <https://doi.org/10.1155/2013/639725>
- Irfan, M., Moniruzzaman, M., Ahmad, T., Chandra, P., Abdullah, B., Bhattacharjee, S., 2017. Growth kinetic study of ionic liquid mediated synthesis of gold nanoparticles using Elaeis guineensis (oil palm) kernels extract under microwave irradiation. Arab. J. Chem. <https://doi.org/10.1016/j.arabjc.2017.07.005>
- Jayaprakash, N., Vijaya, J.J., Kaviyarasu, K., Kombaiyah, K., Kennedy, L.J., Ramalingam, R.J., Munusamy, M.A., Al-Lohedan, H.A., 2017. Green synthesis of Ag nanoparticles using Tamarind fruit extract for the antibacterial studies. J. Photochem. Photobiol. B Biol. 169, 178–185. <https://doi.org/10.1016/j.jphotobiol.2017.03.013>
- Joshi, U., Lee, J., Giordano, C., Malkhandi, S., Yeo, B.S., 2016. Enhanced catalysis of the electrochemical hydrogen evolution reaction using composites of molybdenum-based compounds, gold nanoparticles and carbon. Phys. Chem. Chem. Phys. 18, 21548–21553. <https://doi.org/10.1039/C6CP02828D>
- Kaur, B., Pandiyan, T., Satpati, B., Srivastava, R., 2013. Simultaneous and sensitive determination of ascorbic acid, dopamine, uric acid, and tryptophan with silver nanoparticles-decorated reduced graphene oxide modified electrode. Colloids Surfaces B Biointerfaces 111, 97–106. <https://doi.org/10.1016/j.colsurfb.2013.05.023>
- Khalilzadeh, M.A., Borzoo, M., 2016. ScienceDirect Green synthesis of silver nanoparticles using onion extract and their application for the preparation of a modified electrode for determination of ascorbic acid. J. Food Drug Anal. 24, 796–803. <https://doi.org/10.1016/j.jfda.2016.05.004>
- Khan, Ibrahim, Saeed, K., Khan, Idrees, 2017. Nanoparticles: Properties, applications and toxicities. Arab. J. Chem. <https://doi.org/10.1016/j.arabjc.2017.05.011>
- Khan, Mujeeb, Khan, Merajuddin, Adil, S.F., Tahir, M.N., Tremel, W., Alkathlan, H.Z., Al-Warthan, A., Siddiqui, M.R.H., 2013. Green synthesis of silver nanoparticles mediated by Pulicaria glutinosa extract. Int. J. Nanomedicine 8, 1507–1516. <https://doi.org/10.2147/IJN.S43309>
- Lee, S.M., Song, K.C., Lee, B.S., 2010. Antibacterial activity of silver nanoparticles prepared by a chemical reduction method. Korean J. Chem. Eng. 27, 688–692. <https://doi.org/10.2478/s11814-010-0067-0>
- Lee, W., Roberts, S.M., Labbe, R.F., 1997. Ascorbic acid determination with an automated

- enzymatic procedure. *Clin. Chem.* 43, 154–157.
- Liu, J., Chen, Y., Wang, W., Feng, J., Liang, M., Ma, S., Chen, X., 2016. “Switch-On” Fluorescent Sensing of Ascorbic Acid in Food Samples Based on Carbon Quantum Dots–MnO₂ Probe. *J. Agric. Food Chem.* 64, 371–380. <https://doi.org/10.17660/ActaHortic.2014.1024.50>
- Liu, S., Tian, J., Wang, L., Sun, X., 2011. Microwave-assisted rapid synthesis of Ag nanoparticles/graphene nanosheet composites and their application for hydrogen peroxide detection. *J. Nanoparticle Res.* 13, 4539–4548. <https://doi.org/10.1007/s11051-011-0410-3>
- Loizzo, M.R., Bonesi, M., Menichini, F., Tenuta, M.C., Leporini, M., Tundis, R., 2016. Antioxidant and Carbohydrate-Hydrolysing Enzymes Potential of *Sechium edule* (Jacq.) Swartz (Cucurbitaceae) Peel, Leaves and Pulp Fresh and Processed. *Plant Foods Hum. Nutr.* 71, 381–387. <https://doi.org/10.1007/s11130-016-0571-4>
- Lokanathan, A.R., Uddin, K.M.A., Rojas, O.J., Laine, J., 2014. Cellulose nanocrystal-mediated synthesis of silver nanoparticles: Role of sulfate groups in nucleation phenomena. *Biomacromolecules* 15, 373–379. <https://doi.org/10.1021/bm401613h>
- Lykkesfeldt, J., 2000. Determination of Ascorbic Acid and Dehydroascorbic Acid in Biological Samples by High-Performance Liquid Chromatography Using Subtraction Methods: Reliable Reduction with Tris[2-carboxyethyl]phosphine Hydrochloride. *Anal. Biochem.* 282, 89–93. <https://doi.org/10.1006/abio.2000.4592>
- Malinauskas, A., Garjonyte, R., Mažeikiene, R., Jurevičiute, I., 2004. Electrochemical response of ascorbic acid at conducting and electrogenerated polymer modified electrodes for electroanalytical applications: A review. *Talanta* 64, 121–129. <https://doi.org/10.1016/j.talanta.2004.02.010>
- Manjari Mishra, P., Kumar Sahoo, S., Kumar Naik, G., Parida, K., 2015. Biomimetic synthesis, characterization and mechanism of formation of stable silver nanoparticles using *Averrhoa carambola* L. leaf extract. *Mater. Lett.* MLBLUED1500848. <https://doi.org/10.1016/j.matlet.2015.08.048>
- Mathew, T. V., Kuriakose, S., 2013. Photochemical and antimicrobial properties of silver nanoparticle- encapsulated chitosan functionalized with photoactive groups. *Mater. Sci. Eng. C* 33, 4409–4415. <https://doi.org/10.1016/j.msec.2013.06.037>
- Mitzel, M.R., Tufenkji, N., 2014. Transport of industrial PVP-stabilized silver nanoparticles in saturated quartz sand coated with *Pseudomonas aeruginosa* PAO1

- biofilm of variable age. *Environ. Sci. Technol.* 48, 2715–2723. <https://doi.org/10.1021/es404598v>
- Morais-Braga, M.F.B., Sales, D.L., Carneiro, J.N.P., Machado, A.J.T., dos Santos, A.T.L., de Freitas, M.A., Martins, G.M. de A.B., Leite, N.F., de Matos, Y.M.L.S., Tintino, S.R., Souza, D.S.L., Menezes, I.R.A., Ribeiro-Filho, J., Costa, J.G.M., Coutinho, H.D.M., 2016. *Psidium guajava* L. and *Psidium brownianum* Mart ex DC.: Chemical composition and anti - *Candida* effect in association with fluconazole. *Microb. Pathog.* 95, 200–207. <https://doi.org/10.1016/j.micpath.2016.04.013>
- Nguyen, T., Thuy, T., Tseng, T.T., 2016. A Micro-PlatinumWire Biosensor for Fast and Selective Detection of Alanine Aminotransferase. *Sensors* 6, 767. <https://doi.org/10.3390/s16060767>
- Parveen, M., Ahmad, F., Mohammed, A., Shaista, M., 2016. Microwave-assisted green synthesis of silver nanoparticles from *Fraxinus excelsior* leaf extract and its antioxidant assay. *Appl. Nanosci.* 267–276. <https://doi.org/10.1007/s13204-015-0433-7>
- Pisoschi, Aurelia, Pop, A., Negulescu, G.P., Pisoschi, Aurel, 2011. Determination of Ascorbic Acid Content of Some Fruit Juices and Wine by Voltammetry Performed at Pt and Carbon Paste Electrodes. *Molecules* 16, 1349–1365. <https://doi.org/10.3390/molecules16021349>
- Rao, C.V., Golder, A.K., 2016. Development of a bio-mediated technique of silver-doping on titania. *Colloids Surfaces A Physicochem. Eng. Asp.* 506, 557–565. <https://doi.org/10.1016/j.colsurfa.2016.07.031>
- Rao, Z.H., Zhang, G.Q., 2011. Thermal properties of paraffin wax-based composites containing graphite. *Energy Sources, Part A Recover. Util. Environ. Eff.* 33, 587–593. <https://doi.org/10.1080/15567030903117679>
- Rasappa, S., Ghoshal, T., Borah, D., Senthamarai kanna n, R., Holmes, J.D., Morris, M.A., 2015. A Highly Efficient Sensor Platform Using Simply Manufactured Nanodot Patterned Substrates. *Sci. Rep.* 5, 1–11. <https://doi.org/10.1038/srep13270>
- Sandeep, S., Santhosh, A.S., Swamy, N.K., Suresh, G.S., Melo, J.S., Mallu, P., 2016. Biosynthesis of silver nanoparticles using *Convolvulus pluricaulis* leaf extract and assessment of their catalytic, electrocatalytic and phenol remediation properties. *Adv. Mater. Lett.* 7, 383–389. <https://doi.org/10.5185/amlett.2016.6067>
- Shambharkar, B.H., Chowdhury, A.P., 2016. Ethylene glycol mediated synthesis of Ag₈SnS₆ nanoparticles and their exploitation in the degradation of eosin yellow and

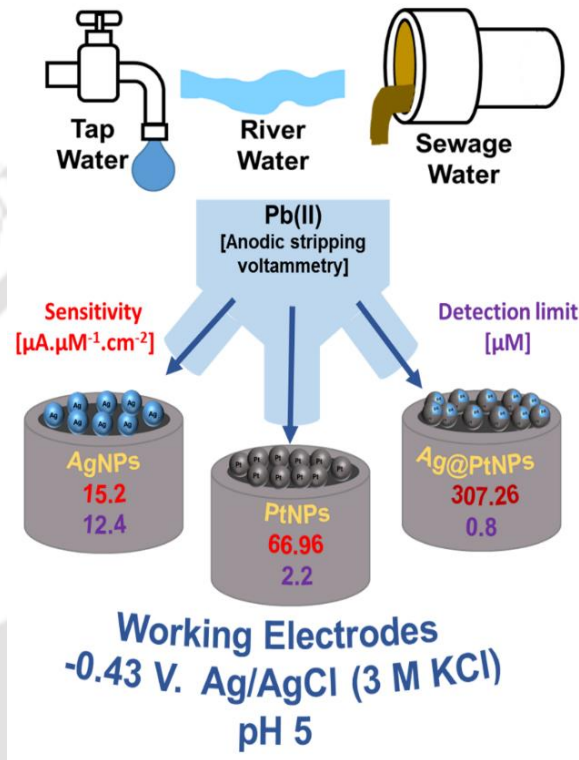
- brilliant green. RSC Adv. 6, 10513–10519. <https://doi.org/10.1039/C5RA25051J>
- Shankar, S.S., Rai, A., Ahmad, A., Sastry, M., 2004. Rapid synthesis of Au, Ag, and bimetallic Au core-Ag shell nanoparticles using Neem (*Azadirachta indica*) leaf broth. *J. Colloid Interface Sci.* 275, 496–502. <https://doi.org/10.1016/j.jcis.2004.03.003>
- Sridhar, R., Lakshminarayanan, R., Madhaiyan, K., Amutha Barathi, V., Lim, K.H.C., Ramakrishna, S., 2015. Electrospayed nanoparticles and electrospun nanofibers based on natural materials: applications in tissue regeneration, drug delivery and pharmaceuticals. *Chem. Soc. Rev.* 44, 790–814. <https://doi.org/10.1039/C4CS00226A>
- Sun, Y., He, K., Zhang, Z., Zhou, A., Duan, H., 2015. Real-time electrochemical detection of hydrogen peroxide secretion in live cells by Pt nanoparticles decorated graphene-carbon nanotube hybrid paper electrode. *Biosens. Bioelectron.* 68, 358–364. <https://doi.org/10.1016/j.bios.2015.01.017>
- Sykes, P., 2005. *A guidebook to mechanism in organic chemistry*, 6th ed, John Wiley & Sons. Fellow of Christ's College: Cambridge, U.K., Cambridge, UK.
- Tashkhourian, J., Nezhad, M.R.H., Khodavesi, J., Javadi, S., 2009. Silver nanoparticles modified carbon nanotube paste electrode for simultaneous determination of dopamine and ascorbic acid. *J. Electroanal. Chem.* 633, 85–91. <https://doi.org/10.1016/j.jelechem.2009.04.028>
- Thakkar, N., Mhatre, S., Parikh, Y., 2010. Biological synthesis of metallic nanoparticles. *Nanomedicine.*
- Zhang, C., Huang, J., Li, X., 2016. Transcriptomic Analysis Reveals the Metabolic Mechanism of L-Ascorbic Acid in *Ziziphus jujuba* Mill. *Front. Plant Sci.* 7, 1–11. <https://doi.org/10.3389/fpls.2016.00122>



This page is intentionally left blank

CHAPTER 4

Bioinspired Synthesis of Highly Structured Spherical Ag@Pt Core-shell Nanoparticles for Electrocatalytic Pb(II) Sensing



Highlights

- ◆ Development of a bio-inspired route for the synthesis of highly structured and stable Ag@Pt core-shell NPs
- ◆ Ag@PtNPs catalyzed electrochemical Pb(II) sensing from tap water, river water and sewage water
- ◆ Sensitivity and limit of Pb(II) detection showed clear superiority over AgNPs and PtNPs catalyzed system
- ◆ Response of Pb(II) sensor was almost invariant in the presence of Cu(II), Cd(II) and Hg(II) co-ions

4.1 Background and executive motivation

Heavy metals (HMs) contamination affects both aquatic and terrestrial environments (Schulz et al., 2015). The main sources of HMs in the environment include uncontrolled anthropogenic activities like industrial (Tchounwou et al., 2012), mining (Musilova et al., 2016), and agricultural (Mohammed et al., 2011). HMs such as cadmium (Cd), lead (Pb), mercury (Hg), chromium (Cr), arsenic (As), etc. are known to bioaccumulate in living organisms, and in humans it causes many metabolic disorders related to the central nervous system, kidney, gastro-intestinal, bones, etc. (Musilova et al., 2016; Sanders et al., 2009) even at a minute concentration.

HMs are considered as most dreadful contaminants, and they are very strictly regulated by authorities, namely World Health Organization (WHO), United States Environmental Protection Agency (USEPA) and Bureau of Indian Standards (BIS). They have set down the maximum permissible limit of Pb(II) in drinking water as 48, 72, and 48 nM, respectively (BIS, 2012; Dao et al., 2013). The adherence to the permissible limits necessitates the requirement of highly sensitive, selective, and reliable methods for the detection of HMs (at ppb level) in water, wastewater, soil, biological samples, and food, etc.

The sophisticated techniques such as Atomic Absorption Spectrometry (AAS), X-Ray Fluorescence (XRF) (Jaswal et al., 2019), Inductively Coupled Plasma-Mass Spectroscopy (ICP-MS) (Xing et al., 2019; Yamini and Safari, 2018), etc. require heavy and expensive installations, trained manpower, and complex sample-preparation procedures (Bansod et al., 2017). Among these, ICP-MS could determine a metal ion at an extremely low concentration over AAS and XRF.

On the other hand, electrochemical methods are rather simple, inexpensive, and sensitive. Most importantly, they are portable and can be utilized in and on-field applications, and could eliminate the inconvenience of storage and handling of samples (Lu et al., 2018). However, the sensitivity of HMs detection in electrochemical techniques using bulk electrodes is usually lower ($0.00948\text{--}0.0314 \mu\text{A} \cdot \mu\text{g} \cdot \text{L}^{-1}$) and the response is also sluggish (Mouhamed et al., 2018). The modification of the electrode composition using nanostructured materials could endow a rapid and accurate detection of HMs with high sensitivity (Lu et al., 2018).

Nanocatalysts such as carbon nanoparticles (NPs) (Simpson et al., 2018), carbon nanotubes (Xiao et al., 2008), nanowires (Aragay and Merkoçi, 2012), graphene-based

materials (Thirupathi et al., 2017), noble metal nanoparticles (Pérez-Ràfols et al., 2017), etc. have been extensively used in modifying conventional electrodes like glassy carbon electrodes, graphite paste electrodes or metal electrodes to increase their specificity and sensitivity towards the target metal ions. NPs are known to eliminate the memory effect and help increase the selectivity of the electrode towards a specific HM ions when it is present in a mixture of interfering HMs (Li et al., 2013). Moreover, NPs modified electrodes are known to show an improved limit of detection (LOD) (Salimi et al., 2008).

Bio-inspired methods for the synthesis of metal nanoparticles minimize the use of environmentally aggressive chemicals, and it directly employs the electron donor analytes which is extracted in a suitable solvent (mostly water) from plant (Lakshmanan et al., 2018), plant organs (Bäckström, 2003), fungi (Kobashigawa et al., 2019), algae (Sayadi et al., 2018), etc. However, it suffers from being a slow process; the structure and the size of the particles are also not uniform as discussed in Chapter 2 and Chapter 3 of the thesis. These are the main challenges for the application of bio-inspired processes for the synthesis of tailor-made nanoparticles such as core@shell structures (Khatami et al., 2018). Biomolecules could easily cap (i.e. 7-10% w/w of NPs) on the surface of the preformed core, and it hinders the formation of the shell on the top of the core metal.

Psidium guajava (guava) leaves extract exhibit a high ascorbic acid equivalent (AA equivalent 284 per 100 g fresh leaves) (Section 2.2.3, Chapter 2), and it could successfully form highly crystalline AgNPs (Chapter 3). Moreover, the bio-extracts are merited with self-stabilization of NPs (Bose and Chatterjee, 2016; Raghunandan et al., 2011). In this chapter, the potential of the bio-extract is explored for the synthesis of highly structured Ag@Pt core-shell NPs which is reported first time as long as the synthesis protocol and the application are concerned. So, the objective of this chapter is aimed at “Bioinspired tailoring toward synthesis of Ag@Pt core-shell nanoparticles and sensing of Pb(II) with high selectivity”.

The rate of the reaction for the formation of NPs is accelerated by the microwave irradiation. A protocol is devised for the partial removal of the capping layer from the top of the Ag-core without significant particles aggregation. Subsequently, a Pt-shell is formed on the Ag-core using the same bio-analytes. These Ag@Pt core-shell NPs are surface embedded in the graphite support electrode for the electrocatalytic Pb(II) determination. AgNPs and PtNPs synthesized in a single step bio-inspired process were also tested to understand the catalytic activity of Ag@PtNPs for Pb(II) determination, and the

mechanism of enhanced Pb(II) sensing catalysed by Ag@PtNPs over its pure metal NPs counterparts is also explored.

Square wave anode stripping voltammetry (SWASV) technique was employed for the detection of ultra-trace Pb(II) ions. In SWASV, Pb(II) was first electrodeposited in an acetate buffer (pH 5) at the optimized deposition potential and time (Lu et al., 2018). The optimal condition for the stripping of Pb from the working electrode was then found out for the determination of Pb(II) in pure and mixed matrix water samples. Furthermore, the interference of co-existing Cd(II), Cu(II), and Hg(II) were studied in details.

4.2 Results and Discussions

4.2.1 Characterizations of prepared nanostructures

4.2.1.1 Formation of Ag-core (AgNPs) and PtNPs

The formation of seed/Ag-core was carried out at pH 9.5 as described in details in Section 2.3.2 of Chapter 2. The so formed Ag-core (AgNPs) had an average diameter of 24.5 nm and zeta-potential of -31.3 mV (Figures 4.1a and 4.1b). The corresponding particles size distributions are shown in Figures 4.1c and 4.1d. After the formation of Ag-core, it was centrifuged at 14000 rpm for 15 min to separate out the nanoparticles from the reaction media and washed as per the procedure described in Chapter 2. This Ag-core now (25.7 nm average diameter and -29.1 mV zeta-potential) was then used for the synthesis of Ag@PtNPs (Section 2.3.3 of Chapter 2). A slight decrease (7%) in zeta potential value before and after washing could be due to the partial removal of the capping agents and the average size of the Ag-core also did not show much increase (4.7%). Figure 4.2 show the TEM images and the particle size distribution of the synthesized PtNPs, respectively.

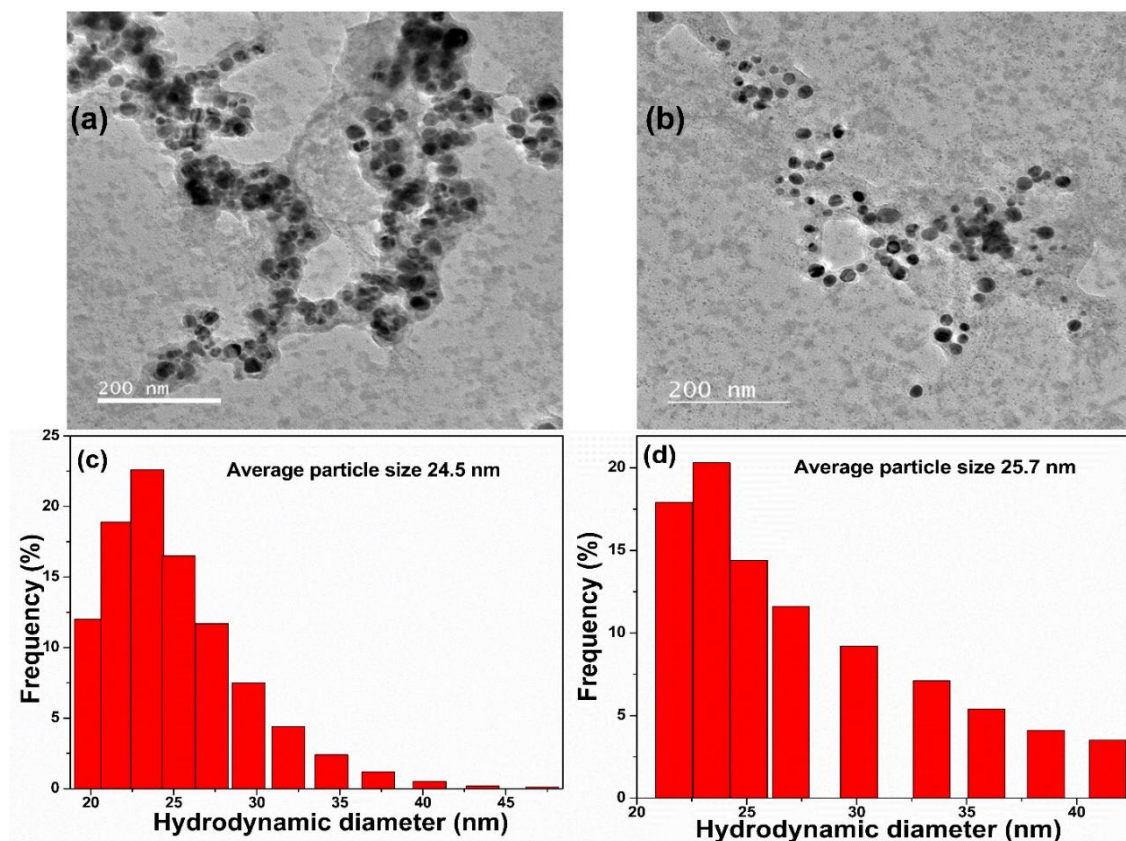


Figure 4.1: Effect of washing on the synthesized AgNPs. (a) TEM image of AgNPs before washing, (b) TEM image of after washing, (c) Particle size distribution before washing and (d) Particle size distribution after washing. Reaction condition: 0.3 mM AgNO₃, pH 9.5, water to leaves ratio 50, and microwave irradiation of 960 W for 300 s.

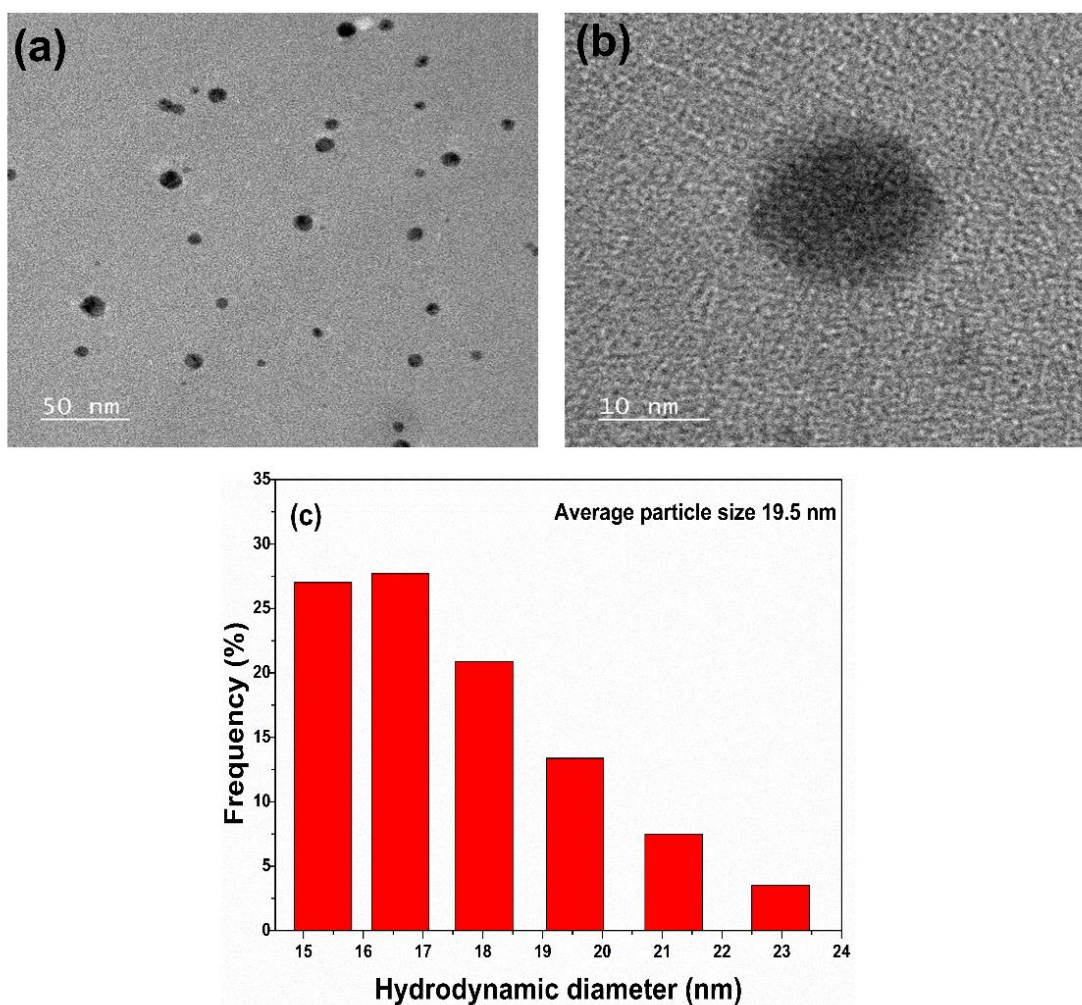


Figure 4.2: TEM image of synthesized PtNPs at different magnifications (a) 50 nm scale, (b) 10 nm scale and (c) particle size distribution of the synthesized PtNPs. Reaction conditions: H_2PtCl_6 0.3 mM, water to leaves ratio 50, pH 9.5, and microwave irradiation of 960 W for 300 s.

4.2.1.2 UV-Vis spectra of AgNPs, PtNPs and Ag@PtNPs

Ag-core, or simply AgNPs at the beginning just before the addition of Pt-precursor, showed a strong absorption peak at around 408 nm due to the well known surface plasmon resonance (SPR) effect of these NPs (Figure 4.3a). At the end of the reaction, the spectral response became almost similar to that of the pure PtNPs solution ensuring proper surface coverage of AgNPs by PtNPs. In case of Ag@PtNPs, with the development of Pt-shell, a blue shift (381 nm) was observed (Figure 4.3a), and the SPR peak intensity was also decreased in comparison to pure Ag-core. Finally, the SPR peak was diminished after 240 s of reaction. The gradual decrease in SPR peak intensity was caused by the increasing shielding-effect of higher electronegativity (2.28) Pt-shell resulting in the decrease of

surface electron density and electron transfer in the Ag-core (electronegativity 1.83) (Westsson and Koper, 2014) .

These observations are also supported by the colour of AgNPs core, (Figure 4.3b(i)), Ag@PtNPs for 30, 120 and 240 s of microwave irradiation (Figures 4.3b(ii), 4.3b(iii) and 4.3b(iv)), and PtNPs (Figure 4.3b(v)) visualized during the reaction. The colour of Ag@PtNPs turns dark brown from the typical yellow colour of Ag-core with the progressive development of Pt-shell on the core-particle.

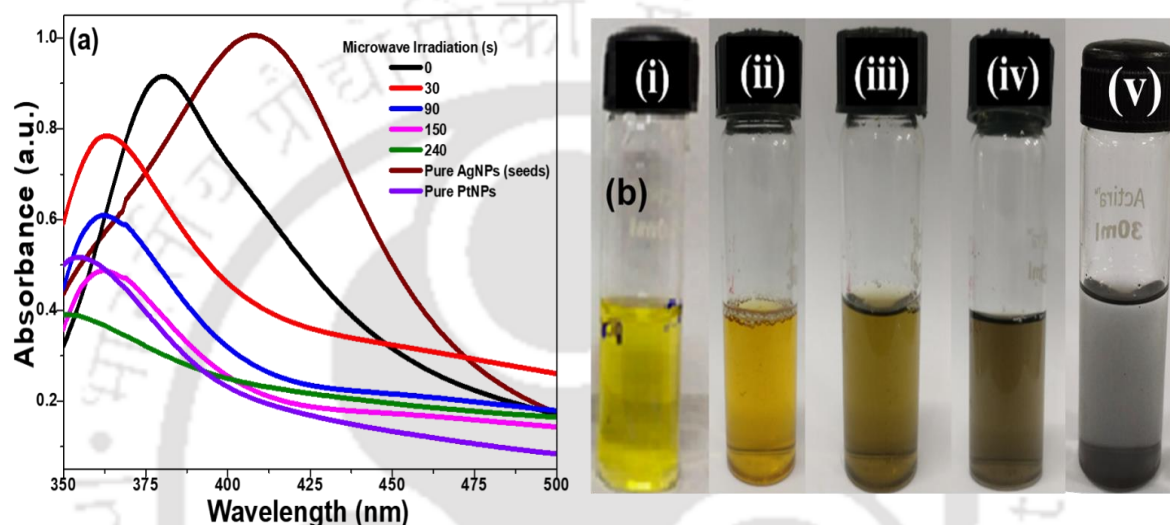


Figure 4.3: (a) UV-Vis spectra of bimetallic Ag@PtNPs showing the decrease in the SPR response with time, and (b) Digital photograph of the nanoparticle suspension: (i) AgNPs core (precursor salt 0.3 mM, water to leaves (v/w) ratio 50, pH 9.5, microwave 960 W and 300 s), (ii) Ag@PtNPs after 30 s (iii) Ag@PtNPs after 120 s and (iv) Ag@PtNPs after 240 s (seed concentration 0.8 mg/mL, H₂PtCl₆ 1 mM, pH 9.5, microwave 700 W and 240 s), and (v) PtNPs (precursor salt 0.3 mM, water to leaves ratio (v/w) 50, pH 9.5, 960 W and 300 s).

4.2.1.3 Electron microscopic characterizations of synthesized Ag@Pt NPs

TEM micrographs of Ag@PtNPs at different magnifications are illustrated in Figures 4.4a to 4.4c. The average diameter of Ag@Pt nanoparticles was found to be 23.5 nm. The layer of the Pt-shell was about 4.55 nm thick, and the Ag-core was 14.55 nm in diameter. In fact, the shell-layer was not uniform in thickness, and it exhibited a porous structure, which may be due to the non-uniform nucleation and growth process following a Stranski-Krastanov type growth mode (Peng et al., 2010). A PtNPs shell was formed very quickly by reacting with the electron donor bio-analytes with a high ascorbic acid

equivalent (Figure 2.3, Chapter 2). The formation of Ag@PtNPs is also mediated by the galvanic exchange between Ag^+ ($E^0 = +0.799$ V vs. SHE) and Pt^{2+} ($E^0 = +1.18$ V vs. SHE) leading to the formation of Pt nuclei on the AgNPs surface resulting in the dissolution of Ag-core (Betts et al., 2005). This explains the reason for the decrease in the Ag-core size from 24.5 nm (Figure 4.1) to 14.55 nm (Figures 4.4a-4.4c) in Ag@PtNPs (Betts et al., 2005) under the control pH (9.5), and Pt precursor and bio-analytes (capping agent) concentrations (Miyakawa et al., 2014). Figure 4.4d shows the SAED image of Ag@PtNPs, and an obvious light core and a dark shell can be seen. The lattice spacing of Ag@PtNPs was about 0.251 nm as calculated from the Inverse Fast Fourier Transform (IFFT) analysis. It corresponds to face-centred cubic (FCC) crystal structure of AgNPs (Figure 4.4e) at the core region, and it was 0.217 nm (Figure 4.4f) for the Pt-shell region. The lattice parameter for Ag alone is 0.232 nm, whereas that of Pt is 0.392 nm (Qi et al., 2009). The increase in the lattice space could be attributed from the development of the lattice strain in AgNPs as Pt atoms squeeze themselves into the lattice space of AgNPs, creating a compressive strain throughout the particles. Moreover, this squeezing of Pt atoms leads to the reduction in lattice parameter in Pt. This lattice strain effect is also known to enhance the catalytic activity of core-shell NPs (Wu et al., 2017). EDX spectrum showed Pt abundantly over Ag as the interaction of X-ray with Ag-core was followed by Pt-shell which subsequently affected the energy dispersion from the specimen (Figure 4.4g) (Tisdale et al., 2018). A schematic diagram showing mechanistic steps for the synthesis of Ag@PtNPs is depicted in Figure 4.5.

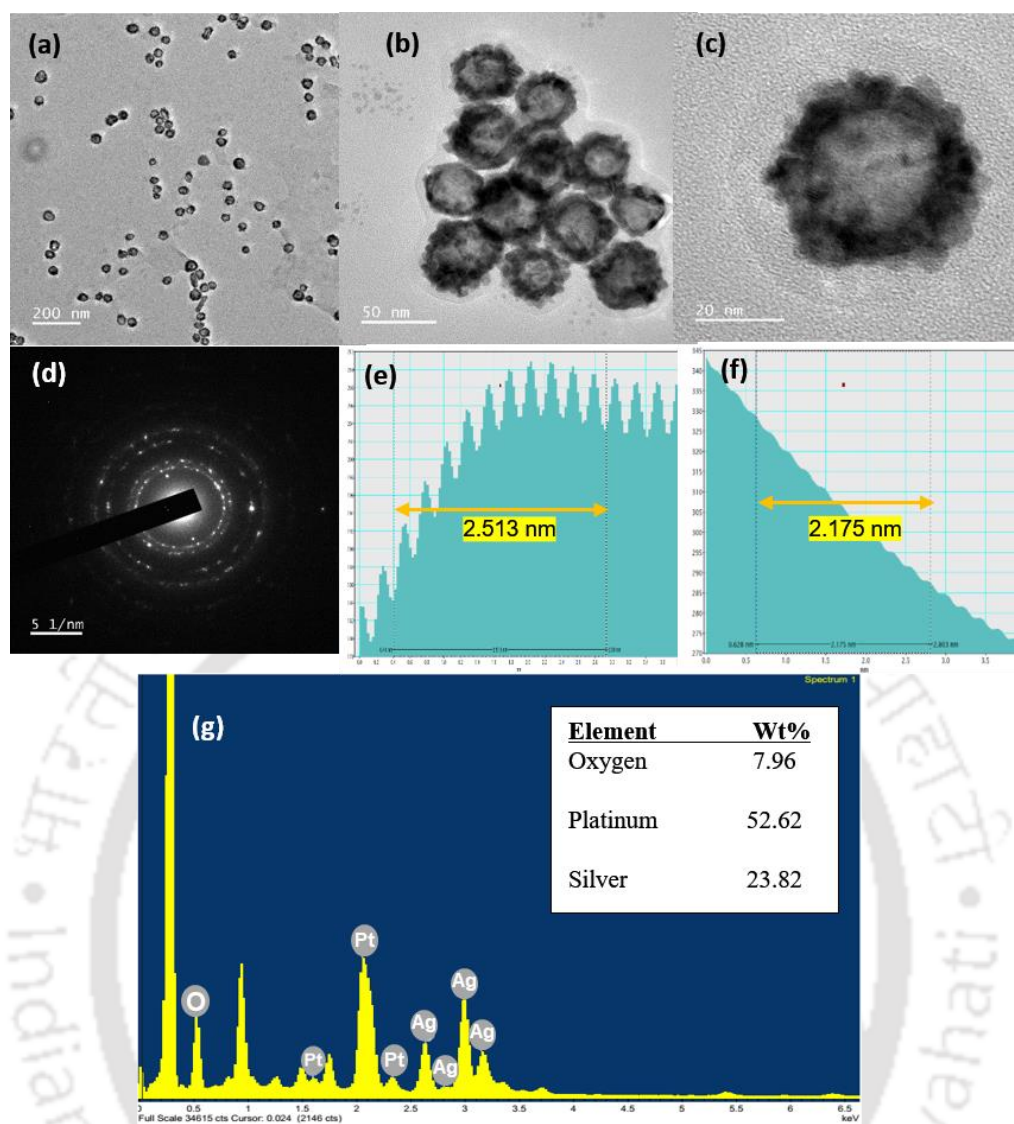


Figure 4.4: (a, b, and c) TEM micrographs of Ag@PtNPs at different magnifications, (d) SAED micrograph of Ag@PtNPs, (e) IFFT profile of Ag-crystalline region of Ag@PtNPs, (f) IFFT profile of Pt-crystalline region of Ag@PtNPs showing distance between crystal lattices, and (g) EDX spectra showing the elemental composition of Ag@PtNPs. Reaction condition: water to leaves ratio 50 (v/w), pH 9.5, chloroplatinic acid 1 mM and Ag-core 50 mL, microwave 720 W and microwave time 240 s.

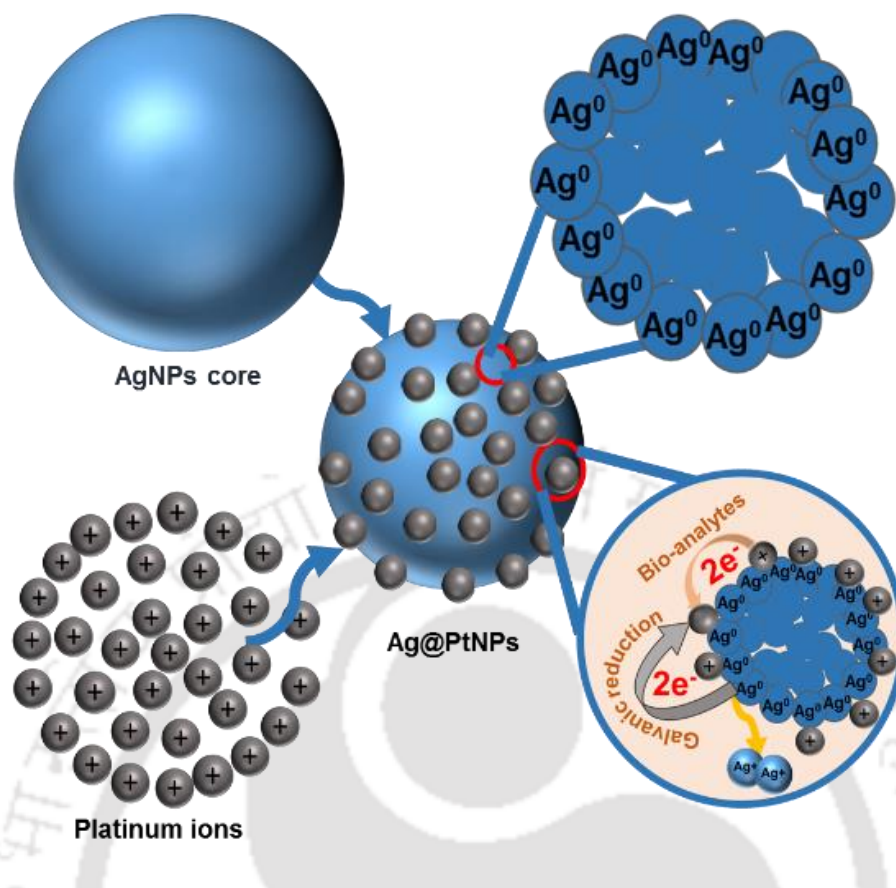


Figure 4.5: Schematic representation of the mechanisms involved in the formation of Ag@PtNPs.

4.2.1.4 Crystal structure of synthesized nanoparticles

Figure 4.6 shows the lattice strain to be 0.0014, -0.0027 and 0.0136 for AgNPs, PtNPs and Ag@PtNPs, respectively. The maximum shear lattice strain was observed in the Ag@PtNPs, which could be due to the deformities in lattice created by the alloying of Ag and Pt atoms at the interface of the core-shell structure (Esfandiari and Kazemini, 2018). It further supports the decrease in lattice spacings of Ag and Pt crystals in Ag@PtNPs (Figures 4.4e and 4.4f). The negative lattice strain for PtNPs suggests that the particles are under compressive strain due to their comparatively smaller crystallite size (Shao et al., 2011).

Figure 4.7 shows the XRD patterns of AgNPs, PtNPs, and Ag@PtNPs. Four diffraction peaks were observed for AgNPs at about 39.6° , 45.9° , 66.8° , and 80.6° 2θ angles (Figure 4.7a) which was for the diffraction from (111), (200), (220), and (311) planes of FCC AgNPs structure (JCPDS No. 089-3722). The diffraction peaks corresponding to those lattice planes were found at 40° , 46.7° , 67.5° , 82° , and 84.5° 2θ for PtNPs (JCPDS No. 04-0802) (Figure 4.7b). For Ag@PtNPs, the diffraction peaks of Ag-core and Pt-shell

counter were mostly overlapped (Liu et al., 2016). Nevertheless, the peak intensity for the diffraction from the Ag-core was less than the Pt-shell (Figure 4.7c). A layer (4.55 nm) of Pt-shell was coated over the Ag-core, that dampens the diffracted X-rays from AgNPs (Esfandiari and Kazemeini, 2018). The lattice strain for all nanoparticles was calculated using Williamson-Hall analysis (Eq. 4.1).

$$\beta \cos \theta = \frac{k\lambda}{D} + 4\varepsilon \sin \theta \quad (4.1)$$

Where, β = FWHM of the diffraction peaks, k = shape factor, λ = wavelength of incident X-ray, and ε = lattice strain.

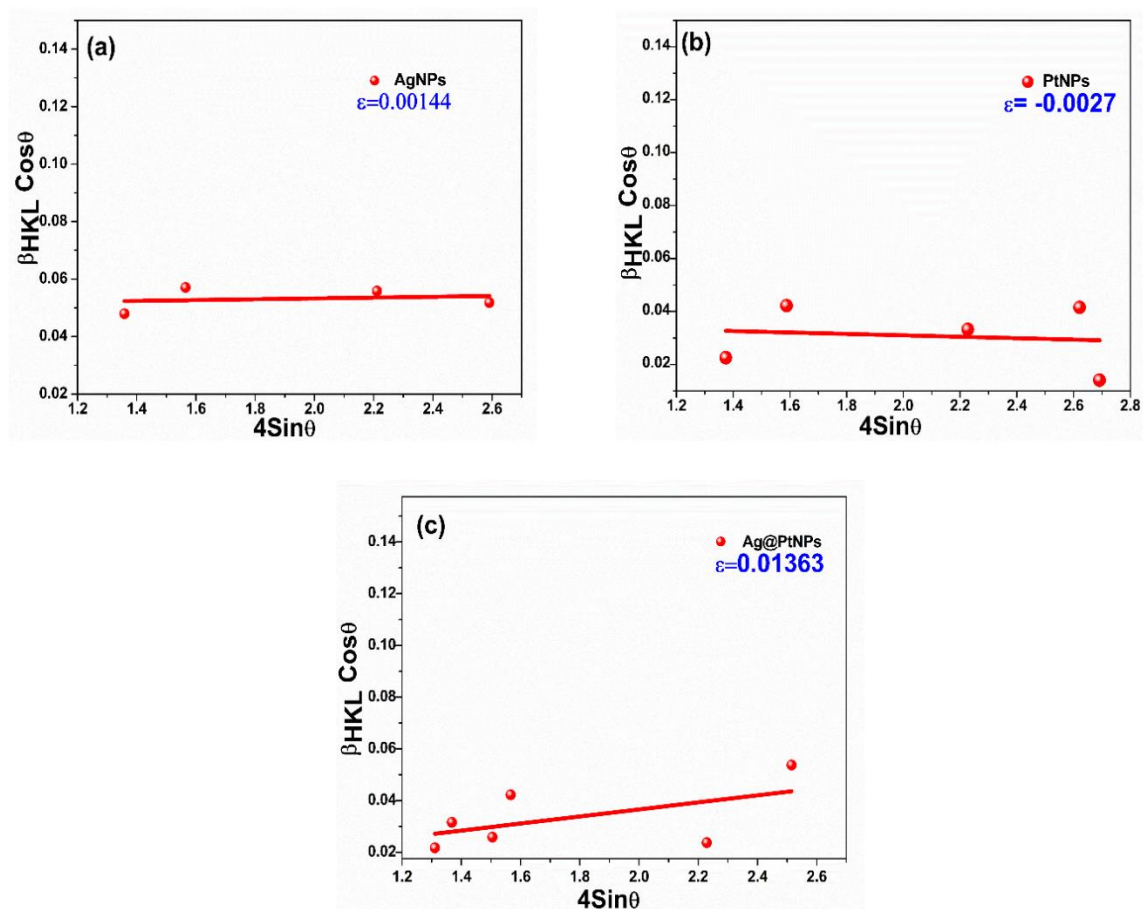


Figure 4.6: Calculation of lattice strain of (a) AgNPs, (b) PtNPs and (c) Ag@PtNPs using Williamson-Hall analysis.

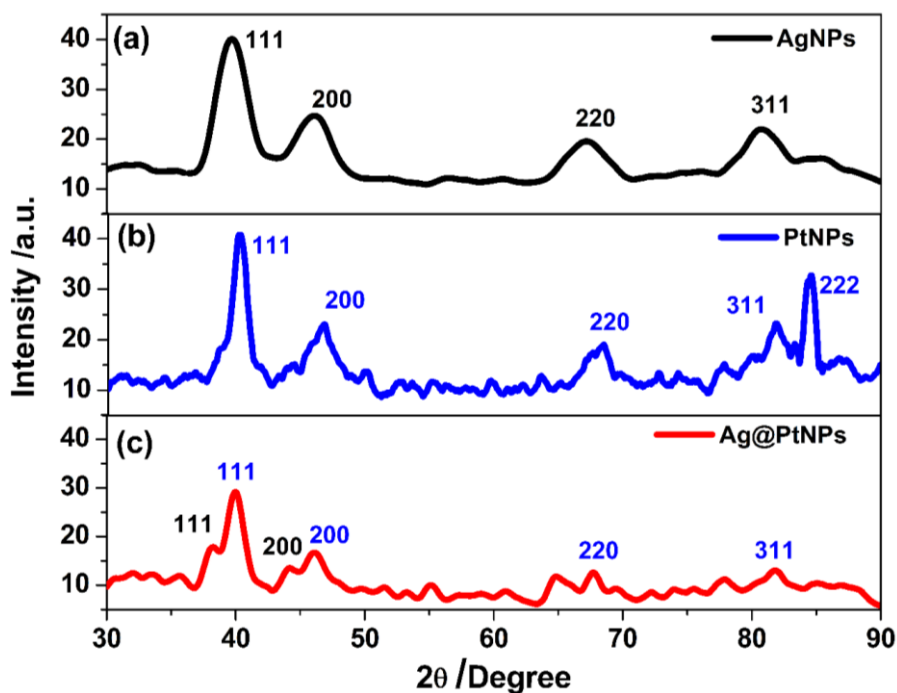


Figure 4.7: X-ray diffraction patterns of AgNPs, PtNPs, and Ag@PtNPs. Reaction condition: water to leaves ratio 50 (v/w), pH 9.5, chloroplatinic acid 1 mM and Ag-core 50 mL, microwave 720 W and microwave time 240 s.

4.2.2 Characterizations of fabricated electrodes

4.2.2.1 Elemental analysis of prepared Ag@Pt/GPE electrode surface

FESEM micrographs and EDX mapping of Ag@Pt/GPE electrode are shown in Figures 4.8a to 4.8d. The embedded Ag@PtNPs on the graphite support are protruded quite uniformly. However, the density of Ag element was lower than Pt as the Pt-shell covered on the Ag-core (Figures 4.8b-4.8d). This is also supported by the elemental analysis of Ag and Pt (Figure 4.8e).

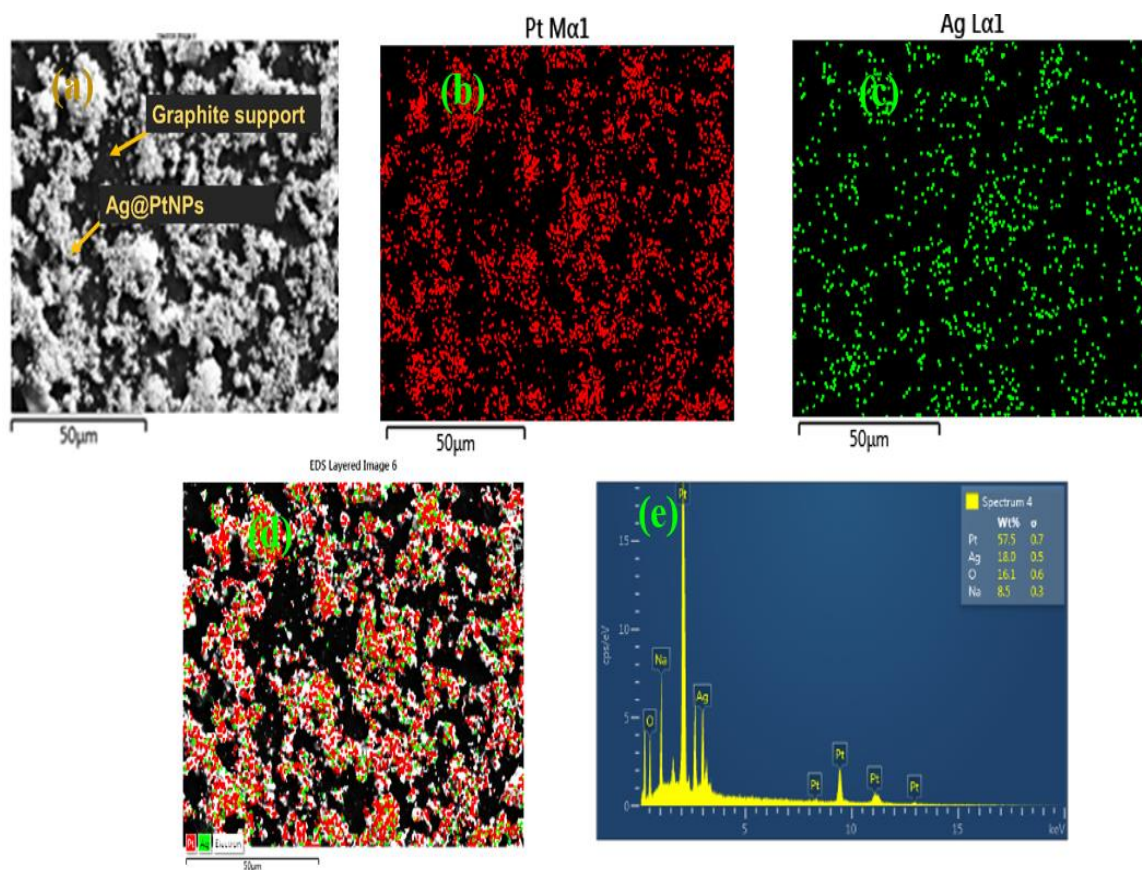


Figure 4.8: Surface morphology of Ag@PtNPs modified graphite-support electrode. (a) FESEM micrograph, (b) Distribution of Pt metal on electrode surface, (c) Distribution of Ag metal on electrode, (d) Overlay mapping image of the electrode surface, and (e) Elemental composition at the electrode surface.

4.2.2.2 Electrochemical characterization of electrodes

The electrical parameters of the WEs was determined by Electrochemical impedance spectrometry (EIS) by the procedure described in (Section 2.5.7 of Chapter 2). The charge transfers resistance (R_p) for each modified electrode was determined by performing a simulation using NOVA V 1.11 software, and the equivalent circuit diagrams are depicted in Figure 4.9. The electroactive surface area was also determined using the Randles-Sevcik equation by using standard electro analyte $K_3[FeCN]_6$ in 0.05M KCl as electrolyte solution (Bin Hamzah et al., 2018) as described in (Section 2.5.8 of Chapter 2).

Figure 4.10a shows the EIS spectra of the electrodes. The bare GPE had the largest diameter of the semicircle, and it showed a high electron transfer resistance (R_p , 42 k Ω) in $[Fe(CN)_6]^{4-/3-}$ redox system (0.5 mM) in the presence of 1 M KCl solution (Mamuru et al., 2010). There was a reduction in R_p (17%) for PtNPs/GPE (~1.4 mg PtNPs/cm² electrode surface). AgNPs/GPE gave the lowest R_p (1.5 k Ω) due to faster electron transfer resulted

from high electrical conductivity of AgNPs (Li et al., 2005). R_p is the key electrical parameters to determine the change in impedance for the analysis of the system kinetics required to observe the change in dielectric properties of the medium due to the presence of analytes. At a given analyte concentration, the variation in R_p occurs due to the interaction of the analyte molecules with the electrocatalyst on the electrode solution interface, thereby determining the electrocatalytic efficiency of the system (Li et al., 2005). The redox probe also could easily interact with the surface of the modified electrodes, and the attractive electrostatic force between them could increase which otherwise could be blocked by the presence of hydrophobic paraffin wax used in GPE fabrication (Yang et al., 2014). In the case of Ag@PtNPs/GPE, the presence of Ag-core decreased the value of R_p by 58% in comparison to PtNPs/GPE (Liu et al., 2016). From the equivalent circuit diagram (Figure 4.9), it can be seen that the solution resistance R_s remains fairly constant (12.6-13.8 Ω) and the constant phase element (CPE) value varied from 299-308 μMho . This minor variation in CPE could be due to the variability in the effective surface area (A_{eff}) and conductivity of the electrode surface. A_{eff} of the prepared electrodes was calculated using the Randles-Sevcik Equation (Eq 4.2) (Siswana et al., 2006).

$$I_{Pa} = (2.69 \times 10^5) n^{0.66} A_{\text{eff}} D^{0.5} \nu^{0.5} C_0 \quad (4.2)$$

where n , ν , D and C_0 are the number of electrons involved in the electrochemical reaction, scan rate in $\text{V}\cdot\text{s}^{-1}$, diffusion coefficient in $\text{cm}\cdot\text{s}^{-1}$ and bulk concentration in mole cm^{-3} of the redox probe $\text{K}_3[\text{Fe}(\text{CN})_6]$, respectively. From the plot of I_{Pa} vs. $\nu^{0.5}$ (Figure 4.10b) and equating the slope values by considering D for $\text{K}_2[\text{Fe}(\text{CN})_6]$ as $7.6 \times 10^{-6} \text{ cm}^2 \text{ s}^{-1}$, $n = 1$, A_{eff} was found to be 0.066, 0.100, 0.106, and 0.145 cm^2 , respectively for the bare GPE, AgNPs/GPE, Ag@PtNPs/GPE and PtNPs/GPE. The corresponding slopes obtained were 0.492, 0.749, 0.791, and $1.06 \times (10^{-4} \text{ A}\cdot\text{V}^{-0.5} \text{ s}^{0.5})$, respectively.

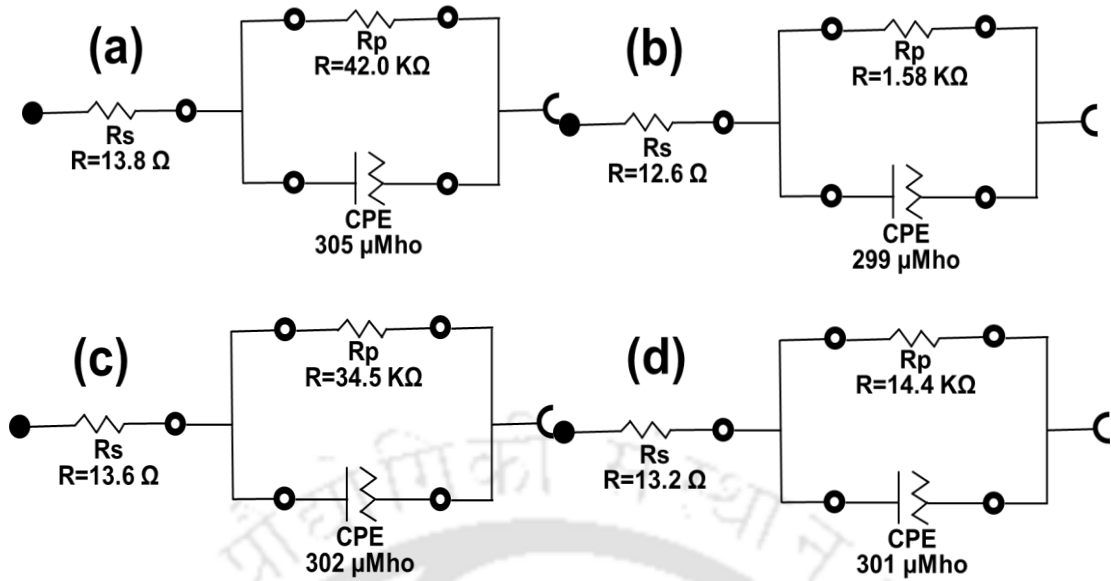


Figure 4.9: Equivalent circuit diagram for (a) GPE, (b) AgNPs/GPE, (c) PtNPs/GPE, and (d) Ag@PtNPs/GPE systems.

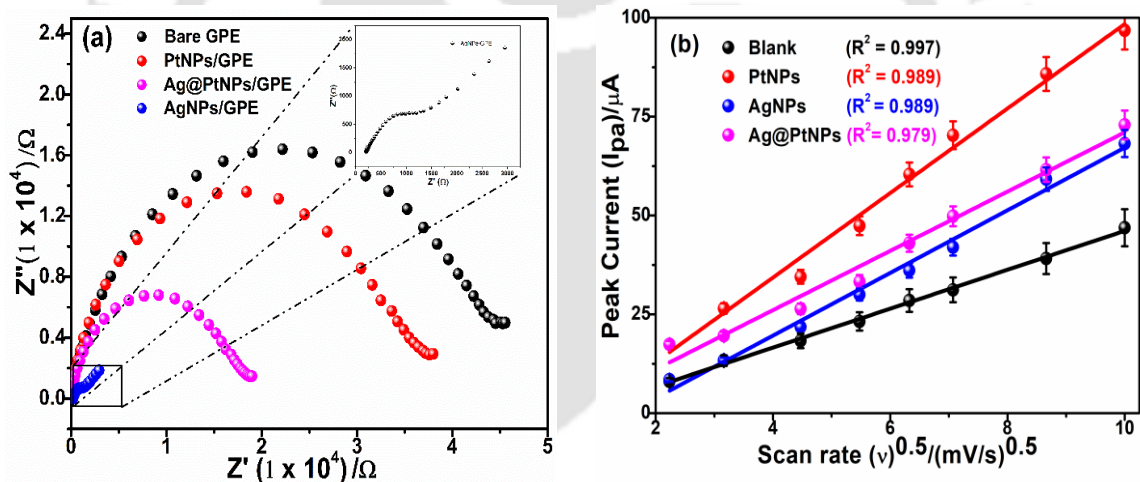


Figure 4.10: (a) EIS spectra, and (b) Peak current vs. square root of scan rate (5-100 $\text{mV}\cdot\text{s}^{-1}$) of different prepared electrodes. Reaction conditions: $\text{K}_3(\text{Fe}[\text{CN}]_6)$ 1 mM in 100 mL of 0.05M KCl at ambient temperature.

4.2.3 Pb(II) pre-concentration on electrode prior to its sensing

4.2.3.1 Determination of Pb(II) deposition potential

Deposition potential of Pb(II) is an important factor in SWASV, and it could significantly affect the sensitivity of the electrode for Pb(II) determination. The deposition potential was varied from -1.6 to -0.4 V in a buffered electrolyte (pH 5). Pb(II) was deposited at different potentials, and then it was stripped following the typical SWASV method. A distinct peak was observed at lower deposition potentials (< -1.0 V vs. Ag/AgCl) and the peaks appeared at -450 , -395 , -410 and -395 mV for the deposition potentials of

−1.0, −1.2, −1.4, and −1.6 V vs. Ag/AgCl, respectively. The peak current (I_p) of Pb(II) stripped increased gradually up to Pb(II) deposition potential of −1.2 V (Figure 4.11a). It could be anticipated that there was a decrease in Pb(II) deposition at a lower potential (< -1.2 V) due to the evolution of H_2 gas (Gumpu et al., 2017). So, a lower amount of Pb(II) deposited caused this reduction in the peak current in the stripping phase (Figure 4.11b). The shift in stripping potential towards more negative (Figure 4.11a) may be due to the underpotential deposition of Pb(II) ions that established a strong adsorbate-substrate interaction and made it difficult for the Pb(II) ions to strip from the surface (Herzog and Arrigan, 2005).

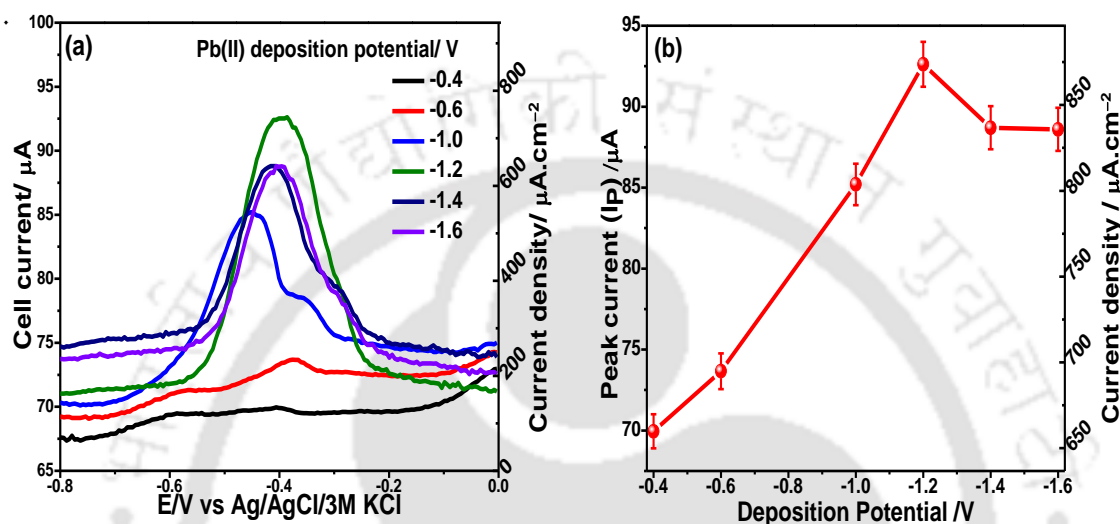


Figure 4.11: (a) Pb(II) stripping current in SWASV captured at varying deposition potential from −0.4 to −1.6 V and (b) Peak current at different deposition potentials. Deposition time 300 s and Pb(II) concentration 5 μ M in 100 mL acetate buffer (0.1 M) at pH 5.

4.2.3.2 Optimization of Pb(II) deposition time

Figure 4.12a shows that the time of Pb(II) deposition could significantly affect the stripping current. This is because a higher deposition time ($30 \text{ s} \leq t_{\text{dep}} \leq 300 \text{ s}$) allowed more Pb(II) ions to accumulate at the electrode active surface. Hence, the stripping current was increased linearly ($R^2 = 0.99$) up to 300 s (Figure 4.12b). The increase in peak current beyond 300 s levelled off either due to surface saturation or attainment of equilibrium between the metal ions at the electrode surface and solution (Herzog and Arrigan, 2005). The residual Pb(II) left in the electrolytic cell after deposition of Pb(II) on the working electrode is depicted in Figure 4.12b. It can be seen that the concentration of residual Pb(II) was decreased with deposition time with 1.85 μ M in 30 s to 1.34 μ M in 360 s. A decrease in residual Pb(II) was noted even with the decrease in steady cell current (>300 s) (Figure

4.12b) due to the formation of intermetallic compounds changing the surface property of the working electrode (Zeng et al., 2002). Therefore, the optimal deposition time of 300 s was selected for further experiments.

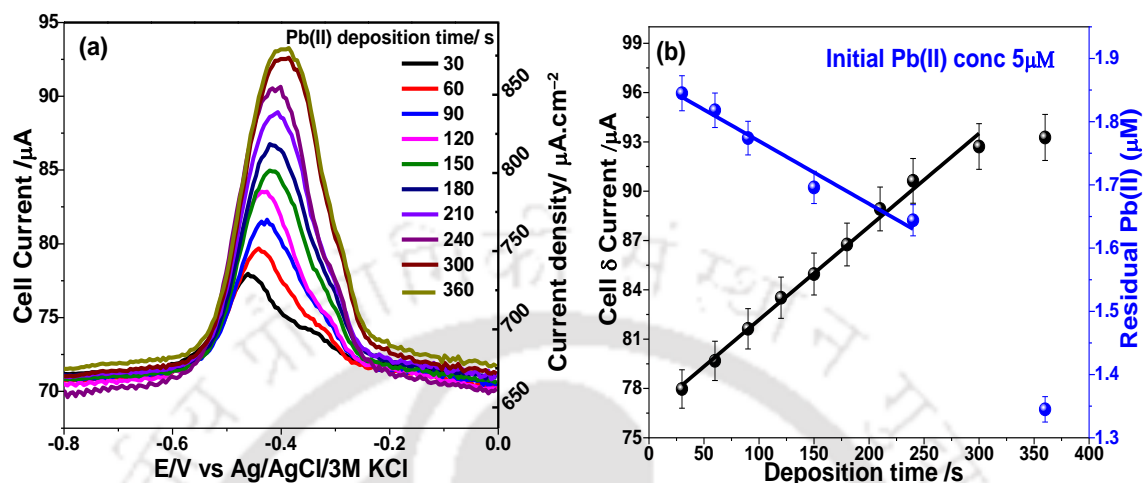


Figure 4.12: (a) Pb(II) stripping current in SWASV captured at varying deposition time from 30 to 360 s, and (b) Peak current at different deposition time and corresponding residual Pb(II) conc. In solution. Deposition potential -1.2 V, Pb(II) concentration of $5 \mu\text{M}$ in 100 mL acetate buffer at pH 5.

4.2.4 Pb(II) detection and determination by stripping from electrode surface

4.2.4.1 Optimal pH of Pb(II) sensing

The optimum pH of the electrolyte media for Pb(II) sensing was found to be 5. Further increase in the reaction pH (pH 11) showed a gradual decrease in the response current (Figure 4.13).

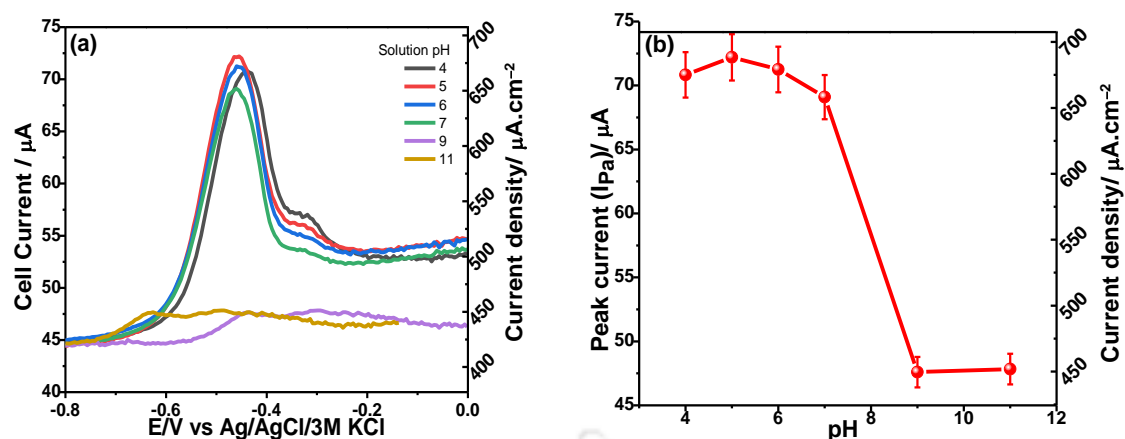


Figure 4.13: (a) SWASV of Pb(II) sensing at different pH for Ag@PtNPs/GPE (b) Variation of peak current with electrolyte media pH. Experimental conditions: Reaction volume 100 mL, Pb(II) concentration of 5 μM in acetate buffer at different pH adjusted using 1 M HCl and 1 M NaOH.

4.2.4.2 Pb(II) determination in absence of co-ions interference

The concentration of Pb(II) was varied, and the SWASV response current was recorded using AgNPs, PtNPs, and Ag@PtNPs catalysed systems. A positive peak shift was observed with the increase in Pb(II) concentration irrespective to the type of electrodes (Figures 4.14a-4.14c). For example, the peak potential of -479 mV at 0.25 μM was shifted to -389 mV at 10 μM for AgNPs/GPE. Faradaic current is the measure of the electrochemical reaction taking place at the electrode surface, and this current is itself dependant on the mass transport of Pb(II) from bulk solution to the electrode surface. At lower concentration, diffusion of Pb(II) occurs in an uninterrupted way. However, at higher concentration, the mass transport is disrupted and the system apply more potential to compensate it. Therefore, there is a peak shift as observed (Zeinu et al., 2016). The peak current followed the trend as $I_{P(\text{Ag@PtNPs/GPE})} > I_{P(\text{PtNPs/GPE})} > I_{P(\text{AgNPs/GPE})}$ at any Pb(II) concentration (1 to 10 μM). I_P was found to be 110.3, 85.1, and 14.7 μA with 10 μM Pb(II) at Ag@PtNPs/GPE, PtNPs/GPE, and AgNPs/GPE, respectively. An enhanced peak current at Ag@PtNPs/GPE could be for the complex interaction between the two electron-rich atoms that modify the surface electrical property of these nanoparticles. Moreover, the lattice strain created due to the deformities in these particles is also known to enhance the catalytic activities (Chen et al., 2015). It leads to surface trapping and densification of charge by changing the interatomic bond lengths and modifying the energy levels of the bonding electrons (Ouyang et al., 2010). The peak potential was also found to be dependent on the catalysts. In the case of 10 μM Pb(II), it appeared at -389 , -467 , and -425 mV for

the AgNPs, PtNPs, and Ag@PtNPs catalysed systems. This change in peak potentials might be for the ohmic drop (iR) of the electrolyte. This is due to the change in R_p for different catalysts (Figure 4.9) as R_s and CPE were fairly invariant for each of the modified electrodes (Figure 4.9). Whereas the increase in the concentration of Pb (II) decreased R_s , and the SWASV current was increased. So, we observe the peak shift (Britz and Brocke, 1975). However, the effect of the morphology of deposits can also affect the peak positions and stripping current of the Pb(II) (Hutton et al., 2011).

A good linearity of the SWASV response current with Pb(II) concentration was observed up to its concentration of 10 μM (Figure 4.14d). In the case of Ag@PtNPs catalysed system, two linear ranges (0.25-1 μM and 1-10 μM) were observed whereas a prolonged linear range of up to 10 μM was observed for both AgNPs and PtNPs. The transition of mass transfer to activation controlled domain appeared at 1 μM Pb(II) for the Ag@PtNPs/GPE. But, the mass transfer domain was prolonged beyond 1 μM for both AgNPs and PtNPs. So, the mass transfer resistance offered by Pb deposition went off quickly, and an early transition appeared for Ag@PtNPs than AgNPs and PtNPs. This could be due to the stripping of Pb(II) was faster at Ag@PtNPs/GPE which can be attributed to the surface geometrical roughness on Ag@PtNPs originated due to non-uniform deposition of Pt (Figures 4.4b-4.4c).

This creates mesopores on the surface, and at lower Pb(II) concentrations a faster transportation kinetics is observed attributed to the ballistic flight phenomenon (Zeinu et al., 2016). This also explains the enhanced sensitivity of Ag@PtNPs/GPE at lower Pb(II) concentrations. The factors influencing the enhancement of electrocatalytic properties of Ag@PtNPs are schematically represented in Figure 4.15. The sensitivity of the electrode was determined from the slope of the calibration line with the electroactive surface area of the electrodes. The sensitivity of Ag@PtNPs/GPE was about 4.5 and 20.20 folds higher than PtNPs/GPE and AgNPs/GPE, respectively (Table 4.1). For these sensors for the determination of Pb(II), the limit of detection (LOD) and limit of quantification (LOQ) was calculated from Eqs. (3.3) and (3.4) of Chapter 3. Where S_b is the standard deviation of the blank and m is the sensitivity of the electrode (Table 4.1). The LOD of Pb(II) of the sensors was the lowest (0.8 nM) with Ag@PtNPs/GPE followed by PtNPs/GPE (2.2 nM) and AgNPs/GPE (12.4 nM) (Table 4.1). The peak current response of Pb(II) ions for bare GPE and Nafion/GPE is compared with other NPs modified electrodes in Figure 4.16.

The storage stability of the Ag@PtNPs/GPE was studied after 90 days of its fabrication. After that Pb(II) sensing was conducted with a Pb(II) concentration of 5 μM and the response current was compared with a fresh Ag@PtNPs/GPE under identical experimental condition. There was a reduction of peak current by only 5.6% after 90 days of storage of the Ag@PtNPs/GPE at room temperature (Figure 4.17a). Repeatability of Pb(II) sensing was tested by using the same electrode in 5 different Pb(II) solutions of same concentration (5 μM). The relative standard deviation (rsd) was found to be only 1.3% (Figure 4.17b). Three different fresh Ag@PtNPs/GPEs were fabricated using the optimized protocol, and tested for the reproducibility of Pb(II) sensing. The modified electrodes also exhibited an excellent reproducibility with a rsd of 1.8% (Figure 4.17c). The above rsd values were well within the acceptable ranges.

Table 4.1. Calculated performance parameters of the electrochemical sensors for determining Pb(II) ions.

Parameters	Pb(II) determination performances		
	AgNPs/GPE	PtNPs/GPE	Ag@PtNPs/GPE
Sensitivity ($\mu\text{A}\cdot\mu\text{M}^{-1}\text{cm}^{-2}$)	15.2	66.96	307.26
SD of blank	6.3	0.0072	0.009
LOD (nM)	12.4	2.2	0.8
LOQ (nM)	40	7.2	2.6

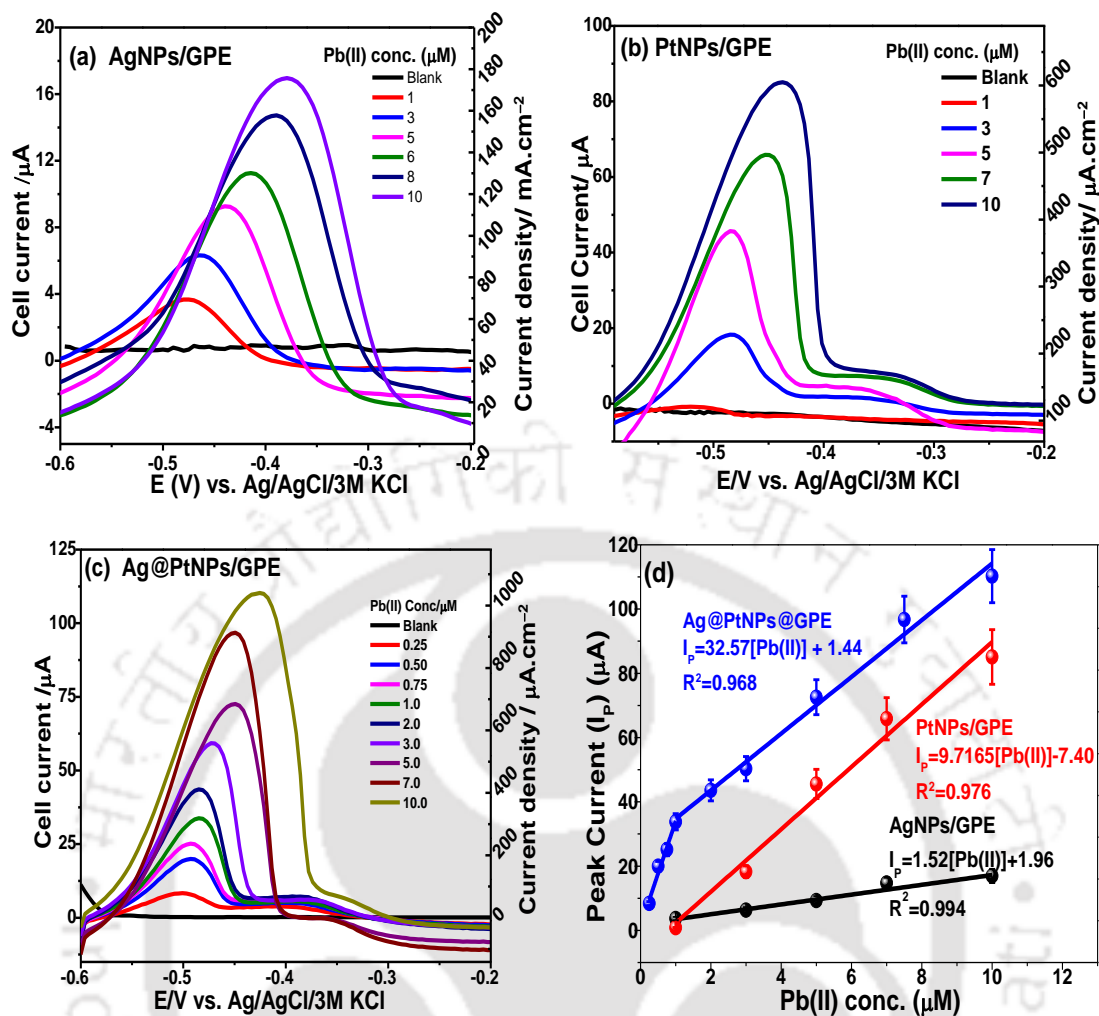


Figure 4.14: Influence of initial concentration of Pb(II) on its detection and determination in SWASV at (a) AgNPs/GPE, (b) PtNPs/GPE (c) Ag@PtNPs/GPE and (d) Variation of I_p with Pb(II) concentration in the absence co-ions. Experimental condition: Deposition potential -1.2 V, deposition time 300 s, Pb(II) concentration of 0.25 to 10 μM in 100 mL acetate buffer at pH 5.

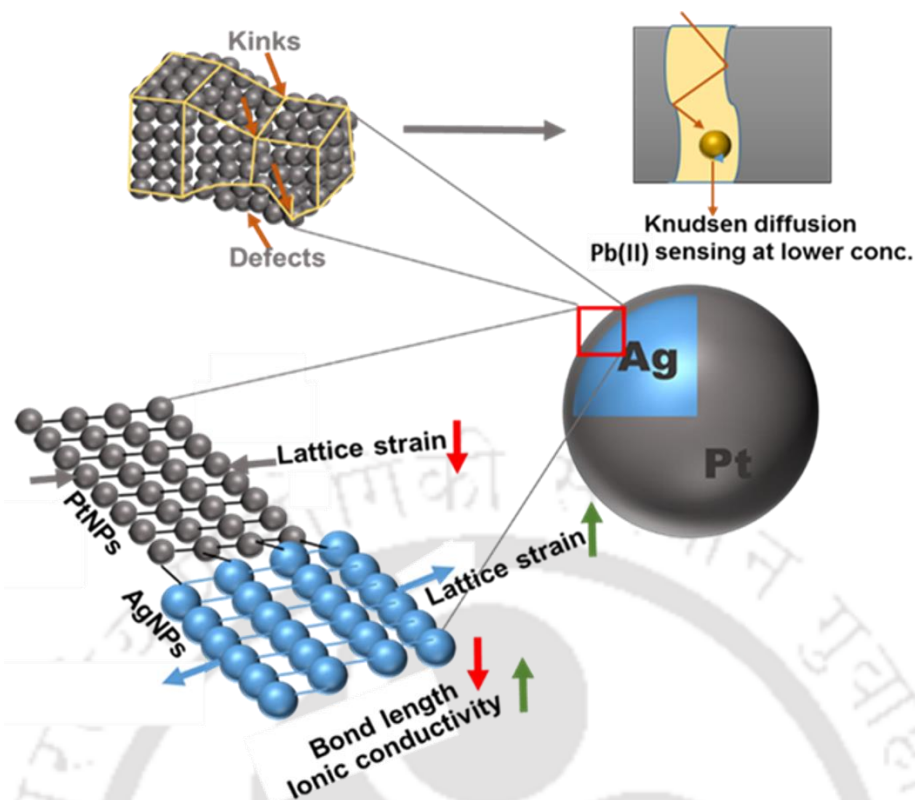


Figure 4.15: Schematic representation of the factors enhancing the electrocatalytic properties of Ag@PtNPs.

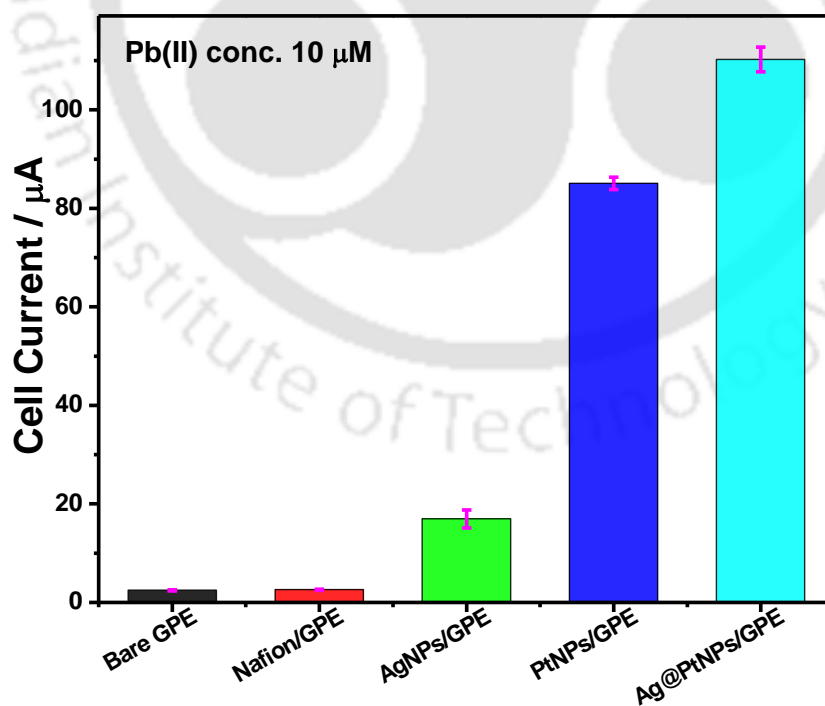


Figure 4.16: Peak current response of Pb(II) ions for different electrodes. Reaction conditions: Acetate buffer pH 5 and Pb(II) concentration 10 μM .

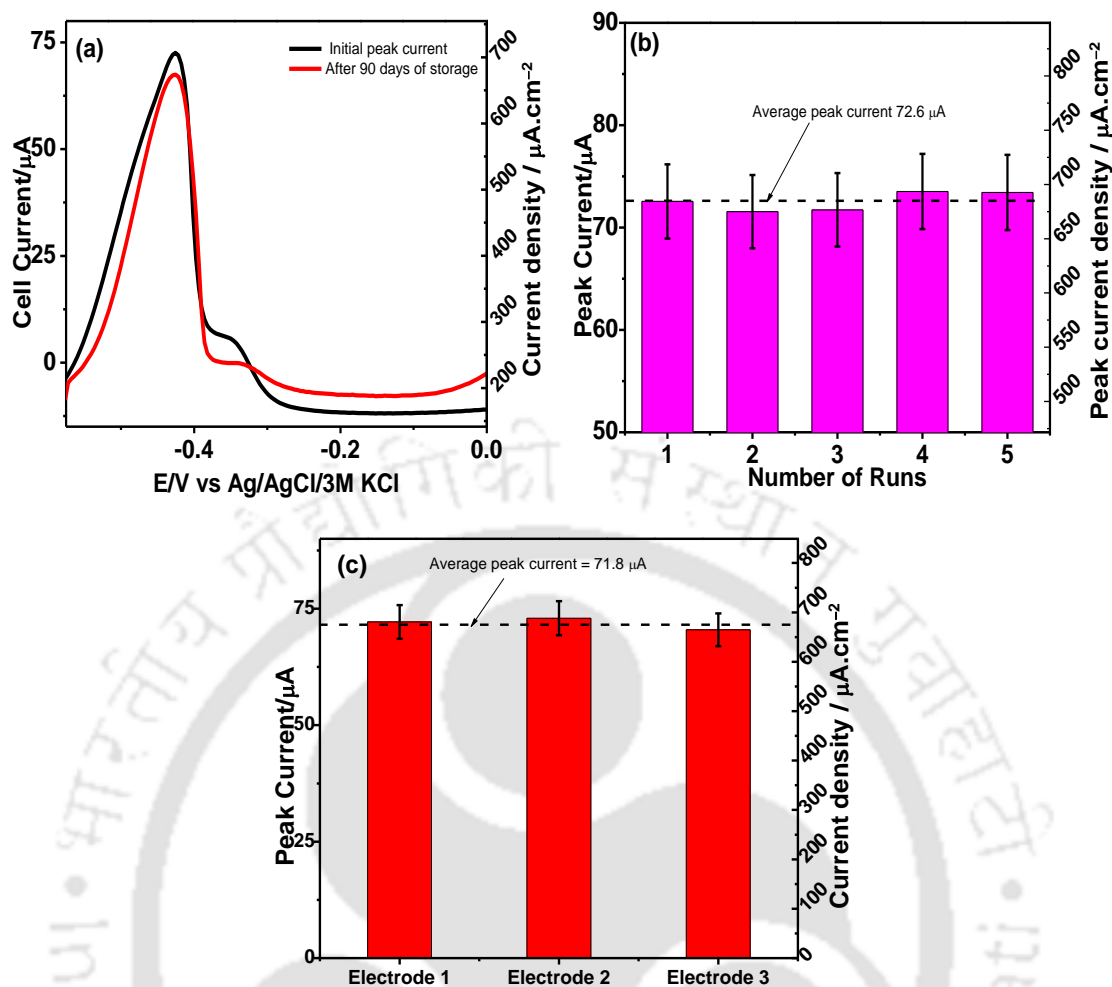


Figure 4.17: Variation of peak current of Pb(II) sensing at Ag@PtNPs/GPE at pH 5 and Pb(II) of 5 μM , (a) After 90 days of storage at room temperature, (b) Repeatability of Pb(II) sensing using the same electrode in 5 different Pb(II) solutions of same concentration (5 μM) and (c) Reproducibility of Pb(II) sensing using three different fresh Ag@PtNPs/GPE fabricated using the optimized protocol.

4.2.4.3 Co-ions interference on Pb(II) detection

It is very likely that multiple HMs is present together in the same sample, and it could interfere with the signal and selectivity during their electrochemical determination. In this study, the concentration of Pb(II) was fixed at two extreme ends of 0.25 μM (Figure 4.18a), and 1 μM in the diffusion-controlled domain (Figure 4.18b) and the concentration of Cd(II), Cu(II) and Hg(II) was varied from 0.25-10 μM in the same solution. The parametric setting was fixed at the pre-optimized values of SWASV (Figures 4.11-4.12). It was found that Pb(II) stripping current at -375 mV vs. Ag/AgCl at Ag@PtNPs/GPE was almost constant with the increase in the concentration of each of the co-HMs from 0.25 to

10, and there was a maximum 2% variation in the response current of Pb(II) (Figure 4.18c) because Ag@PtNPs catalysed a clear peak separation without any co-HMs interference. This indicates that Ag@PtNPs also could catalyse the simultaneous detection of HMs. In Table 4.2, the performance of different Pb(II) sensing systems is compared and listed up. The bio-inspired Ag@PtNPs synthesized following a simple greener route achieves comparable results in terms of LOD and detection range with complex material synthesis processes involving delicate synthesis steps and chemicals such as CNFs, BDD, etc.

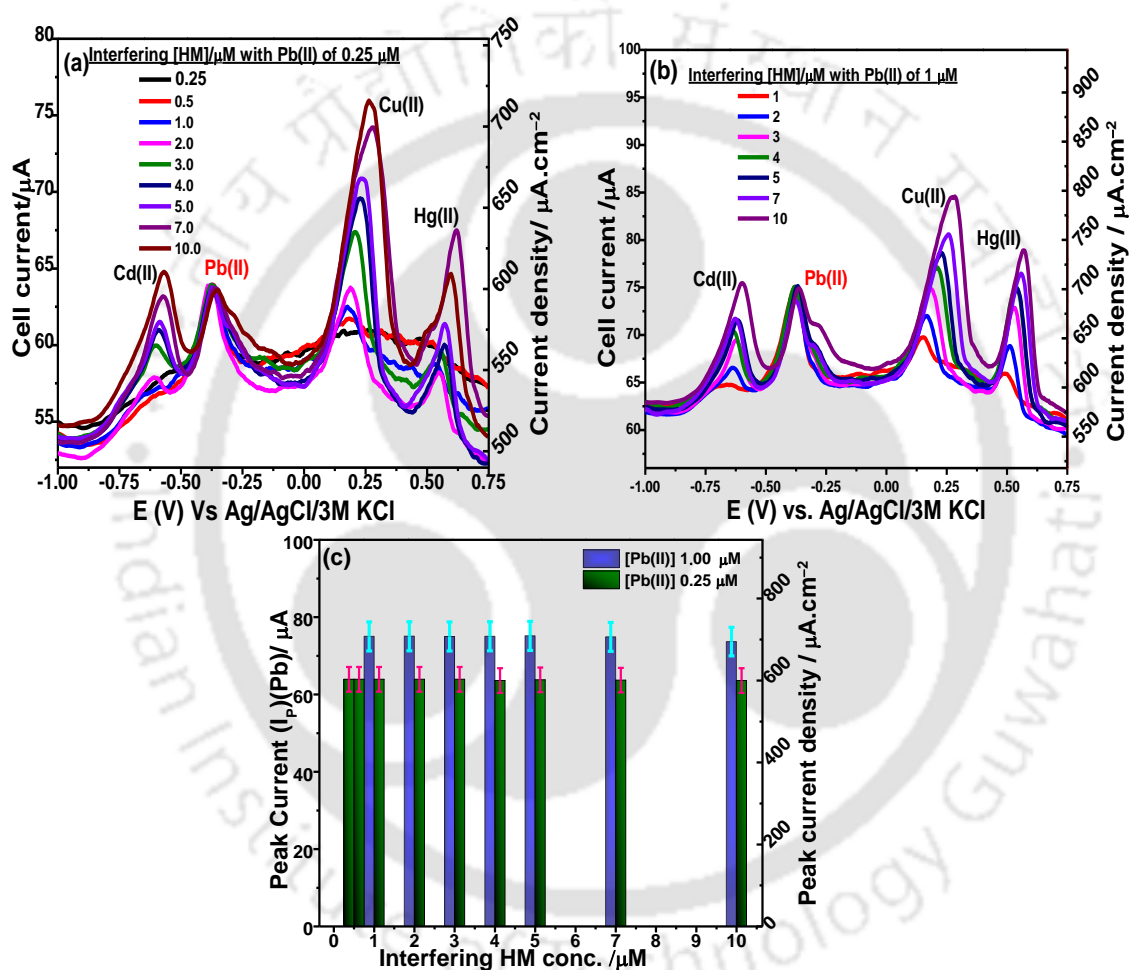


Figure 4.18: Influence of co-HM ions at different concentration on SWASV current response at fixed Pb(II) concentration. (a) Pb(II) of 0.25 μM, (b) Pb(II) of 1 μM, and (c) Peak current response at Ag@PtNPs/GPE at varying interfering HM concentration (0.25-10 μM). Experimental condition: SWASV pulse amplitude 0.025 V, frequency 15 Hz, step potential 4 mV, deposition potential -1.2 V and deposition time 300 s in 100 mL acetate buffer at pH 5.

Table 4.2. Electrochemical determination of Pb(II) in NPs catalysed system: Present work versus earlier reports.

Electrochemical platform	Technique	Supporting electrolyte	Metal system	LOD, nM	Detection range, nM	Source
SbF-CPE	Amperometry	HCl 0.01 M (pH 2)	Pb(II)	1	2-725	(Tesarova et al., 2009)
TETRAM/graphite felt electrode	LSASV	LiClO ₄ 0.1 M	Pb(II)	25	NA	(Nasraoui et al., 2010)
Thiol/clay /CPE	SWASV	HNO ₃ 0.2 M	Pb(II)	60	300-10000	(Tonlé et al., 2011)
HMDE	AGNES-SCP	KNO ₃ 0.1 M	Pb(II)	4.1	25-100	(Parat et al., 2011)
BDD	SWASV	H ₂ SO ₄ 0.1 M	Pb(II)	19.3	100- 500	(Le et al., 2012)
AuNPs/CNFs	SWASV	Acetate buffer (pH 4.5)	Pb(II), Cd(II), Cu(II)	100	100-1000	(Zhang et al., 2016)
Hydroxyapatite/ Nafion	DPV	Phosphate buffer (pH 6.8)	Pb(II), Cd(II), Cu(II)	49	NA	(Guo et al., 2017)
GO/[Ru(Bpy) ³] ²⁺	DPV	Citrate buffer (pH 6)	Pb(II), Cd(II), Hg(II), As(III)	1.41	NA	(Gumpu et al., 2017)
Ag@PtNP/GPE	SWASV	Acetate buffer (pH 5)	Pb(II)	0.8	100-10000	Present work

TETRAM: 1,4,8-tri(carbamoyl methyl) hydroiodide, LSASV: Linear sweep anode stripping voltammetry, AGNES-SCP: Absence of gradients and Nernstian equilibrium stripping-stripping chronopotentiometry, DPV: Differential pulse voltammetry, HMDE: Hanging mercury drop electrode, BDD: Boron doped diamond electrode, GO/[Ru(Bpy)³]²⁺: Ruthenium(II) bipyridine-textured graphene oxide nanocomposite.

4.2.4.4 Pb(II) determination in real sample

The performance of Ag@PtNPs/GPE was also evaluated by determining the concentration of Pb(II) in three representable environmental samples collected from local sources, i.e., river water, tap water, and sewage water. The samples were collected and were filtered through 0.45 µm filter paper to remove suspended particles from them and were used without further pretreatment. The ion chromatographs show that all these water samples are laden with multiple background anions, namely PO₄³⁻, SO₄²⁻, Cl⁻, F⁻, etc. (Figure 4.19). No Pb(II) traces were found in the tap water and river water samples at the optimized conditions of SWASV. However, traces of Pb(II) was found to be 0.48 µM at Ag@PtNPs/GPE, and the result was further verified using AAS, and the variation was only 3% (Table 4.3). For all these water samples, Pb(II) concentration of 5 µM was spiked (triplicated) and the corresponding Pb(II) was again re-determined at the Ag@PtNPs/GPE.

Pb(II) re-estimates were 100.2 (%) in tap water and 108.02 (%) in sewage water even with the presence of multiple background anions.

Table 4.3: Performance of Ag@PtNPs/GPE electrochemical sensors for Pb(II) determination from real water sample and its comparison with atomic absorption spectrophotometry (AAS).

Sample	Pb(II) added (μM)	Pb(II) by electrochemical sensor (μM)	Recovery (%)	RSD (n=3)	Pb(II) by AAS (μM)	Deviation (%)
River water	0	ND	--	--	ND	--
	5	5.36 ± 0.220	107.2	4.10	5.06 ± 0.014	5.6
Tap water	0	ND	--	--	ND	--
	5	5.01 ± 0.041	100.20	0.818	5.04 ± 0.001	0.8
Sewage water	0	0.48 ± 0.002	--	4.17	0.45 ± 0.034	6.3
	5	5.92 ± 0.466	108.02	7.87	6.08 ± 0.018	3.0

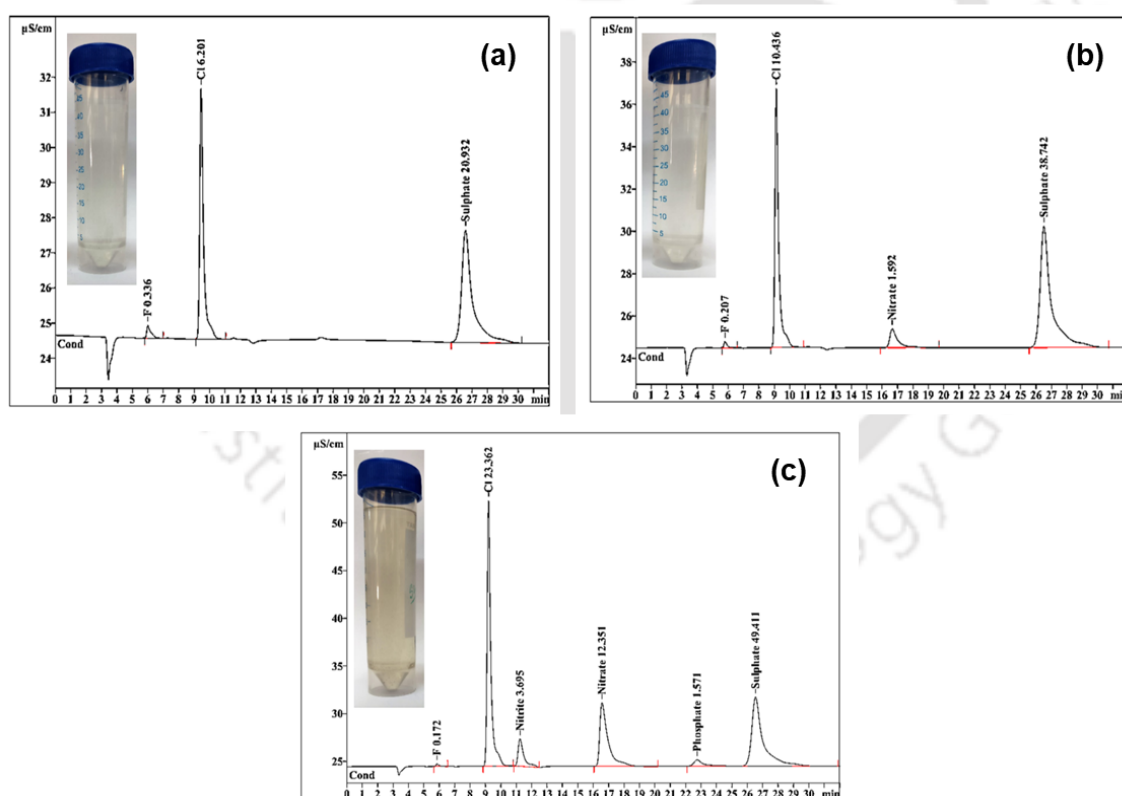


Figure 4.19: Ion chromatographs of (a) river water, (b), tap water, and (c) sewage water samples showing the anionic constituents present in the samples.

4.3 Major findings

This work was successful in devising a new bio-inspired method for the synthesis of seed-mediated Ag@PtNPs core-shell NPs synergized by the analytes present in the bio-extract of *Psidium guajava* leaves and microwave irradiation. AgNPs, PtNPs, and Ag@PtNPs of 25.5, 19.5, and 24.5 (14.5 nm core diameter and 4.55 nm shell thickness) nm were successfully decorated on graphite support electrode for the electrocatalytic Pb(II) sensing. Pb(II) deposition potential and deposition time on the Ag@PtNPs/graphite electrode for the square wave anodic stripping voltammetry were optimized as -1.2 V vs. Ag/AgCl (3 M KCl) and 300 s, and the stripping potential was found as -0.43 V vs. Ag/AgCl/3 M KCl in 0.1 M acetate buffer solution (pH 5).

The compressive lattice strain developed into Ag@PtNPs caused the enhancement of Pb(II) sensing with a sensitivity of $115.5 \mu\text{A}\cdot\mu\text{M}^{-1}\text{cm}^{-2}$ (5.3 and $34.4 \mu\text{A}\cdot\mu\text{M}^{-1}\text{cm}^{-2}$ for AgNPs and PtNPs catalysed sensors, respectively). The limit of detection was obtained as 0.8, 2.2 and 12.4 nM for the nanoparticles, respectively. Ag@PtNPs was highly selective towards different HMs, and it catalysed a distinct peak separation of Pb(II) from Cd(II), Cu(II), and Hg(II) ions (0.25-10 μM). Pb(II) present in river water, tap water and sewage water was effectively determined in the presence of background cations, anions and soluble organics. Therefore, this work provides a platform for developing bio-inspired nanoparticles based electrochemical sensors that can be applied for the detection of HM ions.

References

- Aragay, G., Merkoçi, A., 2012. Nanomaterials application in electrochemical detection of heavy metals. *Electrochim. Acta* 84, 49–61. <https://doi.org/10.1016/j.electacta.2012.04.044>
- Bäckström, M., 2003. Grassed swales for stormwater pollution control during rain and snowmelt. *Water Sci. Technol.* 48, 123–132. <https://doi.org/10.2166/wst.2003.0508>
- Bansod, B.K., Kumar, T., Thakur, R., Rana, S., Singh, I., 2017. A review on various electrochemical techniques for heavy metal ions detection with different sensing platforms. *Biosens. Bioelectron.* 94, 443–455. <https://doi.org/10.1016/j.bios.2017.03.031>
- Betts, A.J., Dowling, D.P., McConnell, M.L., Pope, C., 2005. The influence of platinum on the performance of silver-platinum anti-bacterial coatings. *Mater. Des.* 26, 217–222. <https://doi.org/10.1016/j.matdes.2004.02.006>
- Bin Hamzah, H.H., Keattch, O., Covill, D., Patel, B.A., 2018. The effects of printing orientation on the electrochemical behaviour of 3D printed acrylonitrile butadiene styrene (ABS)/carbon black electrodes. *Sci. Rep.* 8, 1–8. <https://doi.org/10.1038/s41598-018-27188-5>
- BIS, 2012. Indian Standards Drinking Water Specifications IS 10500:2012. Bur. Indian Stand. Indian Stand. Drink. Water Specif. 2, 11.
- Bose, D., Chatterjee, S., 2016. Biogenic synthesis of silver nanoparticles using guava (*Psidium guajava*) leaf extract and its antibacterial activity against *Pseudomonas aeruginosa*. *Appl. Nanosci.* 6, 895–901. <https://doi.org/10.1007/s13204-015-0496-5>
- Britz, D., Brocke, W.A., 1975. Elimination of iR-drop in electrochemical cells by the use of a current-interruption potentiostat. *J. Electroanal. Chem. Interfacial Electrochem.* 58, 301–311. [https://doi.org/10.1016/S0022-0728\(75\)80088-X](https://doi.org/10.1016/S0022-0728(75)80088-X)
- Chen, D., Li, C., Liu, H., Ye, F., Yang, J., 2015. Core-shell Au@Pd nanoparticles with enhanced catalytic activity for oxygen reduction reaction via core-shell Au@Ag/Pd constructions. *Sci. Rep.* 5, 1–9. <https://doi.org/10.1038/srep11949>
- Dao, V.D., Nang, L. Van, Kim, E.T., Lee, J.K., Choi, H.S., 2013. Pt nanoparticles immobilized on CVD-grown graphene as a transparent counter electrode material for dye-sensitized solar cells. *ChemSusChem* 6, 1316–1319. <https://doi.org/10.1002/cssc.201300353>
- Das, R.K., Golder, A.K., 2017. Co₃O₄ spinel nanoparticles decorated graphite electrode:

- Bio-mediated synthesis and electrochemical H₂O₂ sensing. *Electrochim. Acta* 251, 415–426. <https://doi.org/10.1016/j.electacta.2017.08.122>
- Esfandiari, A., Kazemeini, M., 2018. Investigating electrochemical behaviors of Ag@Pt core-shell nanoparticles supported upon different carbon materials acting as PEMFC's cathodes. *Chem. Eng. Trans.* 70, 2161–2166. <https://doi.org/10.3303/CET1870361>
- Gumpu, M.B., Veerapandian, M., Krishnan, U.M., Rayappan, J.B.B., 2017. Simultaneous electrochemical detection of Cd(II), Pb(II), As(III) and Hg(II) ions using ruthenium(II)-textured graphene oxide nanocomposite. *Talanta* 162, 574–582. <https://doi.org/10.1016/j.talanta.2016.10.076>
- Guo, Z., Li, D. di, Luo, X. ke, Li, Y. hui, Zhao, Q.N., Li, M. meng, Zhao, Y. ting, Sun, T. shuai, Ma, C., 2017. Simultaneous determination of trace Cd(II), Pb(II) and Cu(II) by differential pulse anodic stripping voltammetry using a reduced graphene oxide-chitosan/poly-L-lysine nanocomposite modified glassy carbon electrode. *J. Colloid Interface Sci.* 490, 11–22. <https://doi.org/10.1016/j.jcis.2016.11.006>
- Herzog, G., Arrigan, D.W.M., 2005. Determination of trace metals by underpotential deposition-stripping voltammetry at solid electrodes. *TrAC - Trends Anal. Chem.* 24, 208–217. <https://doi.org/10.1016/j.trac.2004.11.014>
- Hutton, L.A., Newton, M.E., Unwin, P.R., Macpherson, J. V., 2011. Factors controlling stripping voltammetry of lead at polycrystalline boron doped diamond electrodes: New insights from high-resolution microscopy. *Anal. Chem.* 83, 735–745. <https://doi.org/10.1021/ac101626s>
- Jaswal, B.B.S., Rai, P.K., Singh, T., Zorba, V., Singh, V.K., 2019. Detection and quantification of heavy metal elements in gallstones using X-ray fluorescence spectrometry, in: *X-Ray Spectrometry*. pp. 178–187. <https://doi.org/10.1002/xrs.3010>
- Khatami, M., Alijani, H., Nejad, M., Varma, R., 2018. Core@shell Nanoparticles: Greener Synthesis Using Natural Plant Products. *Appl. Sci.* 8, 411. <https://doi.org/10.3390/app8030411>
- Kobashigawa, J.M., Robles, C.A., Martínez Ricci, M.L., Carmarán, C.C., 2019. Influence of strong bases on the synthesis of silver nanoparticles (AgNPs) using the ligninolytic fungi *Trametes trogii*. *Saudi J. Biol. Sci.* 26, 1331–1337. <https://doi.org/10.1016/j.sjbs.2018.09.006>
- Lakshmanan, G., Sathiyaseelan, A., Kalaichelvan, P.T., Murugesan, K., 2018. Plant-

- mediated synthesis of silver nanoparticles using fruit extract of *Cleome viscosa* L.: Assessment of their antibacterial and anticancer activity. *Karbala Int. J. Mod. Sci.* 4, 61–68. <https://doi.org/10.1016/j.kijoms.2017.10.007>
- Le, T.S., Da Costa, P., Huguet, P., Sistas, P., Pichot, F., Silva, F., Renaud, L., Cretin, M., 2012. Upstream microelectrodialysis for heavy metals detection on boron doped diamond. *J. Electroanal. Chem.* 670, 50–55. <https://doi.org/10.1016/j.jelechem.2012.02.015>
- Li, M., Gou, H., Al-Ogaidi, I., Wu, N., 2013. Nanostructured sensors for detection of heavy metals: A review. *ACS Sustain. Chem. Eng.* 1, 713–723. <https://doi.org/10.1021/sc400019a>
- Li, Y., Wu, Y., Ong, B.S., 2005. Facile synthesis of silver nanoparticles useful for fabrication of high-conductivity elements for printed electronics. *J. Am. Chem. Soc.* 127, 3266–3267. <https://doi.org/10.1021/ja043425k>
- Liu, Jiangtao, Zhang, M., Liu, Jianbo, Zheng, J., 2016. Synthesis of Ag at Pt core-shell nanoparticles loaded onto reduced graphene oxide and investigation of its electroensing properties. *Anal. Methods* 8, 1084–1090. <https://doi.org/10.1039/c5ay02672e>
- Lu, Y., Liang, X., Niyungeko, C., Zhou, J., Xu, J., Tian, G., 2018. A review of the identification and detection of heavy metal ions in the environment by voltammetry. *Talanta* 178, 324–338. <https://doi.org/10.1016/j.talanta.2017.08.033>
- Mamuru, S.A., Ozoemena, K.I., Fukuda, T., Kobayashi, N., Nyokong, T., 2010. Studies on the heterogeneous electron transport and oxygen reduction reaction at metal (Co, Fe) octabutylsulphonylphthalocyanines supported on multi-walled carbon nanotube modified graphite electrode. *Electrochim. Acta* 55, 6367–6375. <https://doi.org/10.1016/j.electacta.2010.06.056>
- Miyakawa, M., Hiyoshi, N., Nishioka, M., Koda, H., Sato, K., Miyazawa, A., Suzuki, T.M., 2014. Continuous syntheses of Pd@Pt and Cu@Ag core-shell nanoparticles using microwave-assisted core particle formation coupled with galvanic metal displacement. *Nanoscale* 6, 8720–8725. <https://doi.org/10.1039/c4nr00118d>
- Mohammed, A.S., Kapri, A., Goel, R., 2011. Biomanagement of Metal-Contaminated Soils. <https://doi.org/10.1007/978-94-007-1914-9>
- Mouhamed, N., Cheikhou, K., Elhadji, G., Rokhy, M., Bagha, D.M., Guèye, M.C., Tzedakis, T., 2018. Determination of Lead in Water by Linear Sweep Anodic Stripping Voltammetry (LSASV) at Unmodified Carbon Paste Electrode:

- Optimization of Operating Parameters 171–186.
<https://doi.org/10.4236/ajac.2018.93015>
- Musilova, J., Arvay, J., Vollmannova, A., Toth, T., Tomas, J., 2016. Environmental Contamination by Heavy Metals in Region with Previous Mining Activity. *Bull. Environ. Contam. Toxicol.* 97, 569–575. <https://doi.org/10.1007/s00128-016-1907-3>
- Nasraoui, R., Floner, D., Geneste, F., 2010. Improvement in performance of a flow electrochemical sensor by using carbamoyl-arms polyazamacrocycle for the preconcentration of lead ions onto the electrode. *Electrochem. commun.* 12, 98–100. <https://doi.org/10.1016/j.elecom.2009.10.045>
- Ouyang, G., Zhu, W.G., Sun, C.Q., Zhu, Z.M., Liao, S.Z., 2010. Atomistic origin of lattice strain on stiffness of nanoparticles. *Phys. Chem. Chem. Phys.* 12, 1543–1549. <https://doi.org/10.1039/b919982a>
- Parat, C., Authier, L., Aguilar, D., Companys, E., Puy, J., Galceran, J., Potin-Gautier, M., 2011. Direct determination of free metal concentration by implementing stripping chronopotentiometry as the second stage of AGNES. *Analyst* 136, 4337–4343. <https://doi.org/10.1039/c1an15481h>
- Peng, Z., Wu, J., Yang, H., 2010. Synthesis and oxygen reduction electrocatalytic property of platinum hollow and platinum-on-silver nanoparticles. *Chem. Mater.* 22, 1098–1106. <https://doi.org/10.1021/cm902218j>
- Pérez-Ràfols, C., Bastos-Arrieta, J., Serrano, N., Díaz-Cruz, J.M., Ariño, C., de Pablo, J., Esteban, M., 2017. Ag nanoparticles drop-casting modification of screen-printed electrodes for the simultaneous voltammetric determination of Cu(II) and Pb(II). *Sensors (Switzerland)* 17. <https://doi.org/10.3390/s17061458>
- Qi, W.H., Huang, B.Y., Wang, M.P., Yin, Z.M., Li, J., 2009. Molecular dynamic simulation of the size- and shape-dependent lattice parameter of small Platinum nanoparticles. *J. Nanoparticle Res.* 11, 575–580. <https://doi.org/10.1007/s11051-008-9392-1>
- Ragunandan, D., Mahesh, B.D., Basavaraja, S., Balaji, S.D., Manjunath, S.Y., Venkataraman, A., 2011. Microwave-assisted rapid extracellular synthesis of stable bio-functionalized silver nanoparticles from guava (*Psidium guajava*) leaf extract. *J. Nanoparticle Res.* 13, 2021–2028. <https://doi.org/10.1007/s11051-010-9956-8>
- Salimi, A., Mamkhezri, H., Hallaj, R., Soltanian, S., 2008. Electrochemical detection of trace amount of arsenic(III) at glassy carbon electrode modified with cobalt oxide nanoparticles. *Sensors Actuators, B Chem.* 129, 246–254.

<https://doi.org/10.1016/j.snb.2007.08.017>

- Sanders, T., Liu, Y., Buchner, V., Tchounwou, P.B., 2009. Neurotoxic effects and biomarkers of lead exposure: A review. *Rev. Environ. Health* 24, 15–45. <https://doi.org/10.1515/REVEH.2009.24.1.15>
- Sayadi, M.H., Salmani, N., Heidari, A., Rezaei, M.R., 2018. Bio-synthesis of palladium nanoparticle using *Spirulina platensis* alga extract and its application as adsorbent. *Surfaces and Interfaces* 10, 136–143. <https://doi.org/10.1016/j.surfin.2018.01.002>
- Schulz, R., Bundschuh, M., Gergs, R., Brühl, C.A., Diehl, D., Entling, M.H., Fahse, L., Frör, O., Jungkunst, H.F., Lorke, A., Schäfer, R.B., Schaumann, G.E., Schwenk, K., 2015. Science of the Total Environment Review on environmental alterations propagating from aquatic to terrestrial ecosystems. *Sci. Total Environ.* 538, 246–261. <https://doi.org/10.1016/j.scitotenv.2015.08.038>
- Shao, M., Peles, A., Shoemaker, K., 2011. Electrocatalysis on platinum nanoparticles: Particle size effect on oxygen reduction reaction activity. *Nano Lett.* 11, 3714–3719. <https://doi.org/10.1021/nl2017459>
- Simpson, A., Pandey, R.R., Chusuei, C.C., Ghosh, K., Patel, R., Wanekaya, A.K., 2018. Fabrication characterization and potential applications of carbon nanoparticles in the detection of heavy metal ions in aqueous media. *Carbon N. Y.* 127, 122–130. <https://doi.org/10.1016/j.carbon.2017.10.086>
- Siswana, M.P., Ozoemena, K.I., Nyokong, T., 2006. Electrocatalysis of asulam on cobalt phthalocyanine modified multi-walled carbon nanotubes immobilized on a basal plane pyrolytic graphite electrode. *Electrochim. Acta* 52, 114–122. <https://doi.org/10.1016/j.electacta.2006.03.090>
- Tchounwou, P.B., Yedjou, C.G., Patlolla, A.K., Sutton, D.J., 2012. *Molecular, Clinical and Environmental Toxicology* 101, 1–30. <https://doi.org/10.1007/978-3-7643-8340-4>
- Tesarova, E., Baldrianova, L., Hocevar, S.B., Svancara, I., Vytras, K., Ogorevc, B., 2009. Anodic stripping voltammetric measurement of trace heavy metals at antimony film carbon paste electrode. *Electrochim. Acta* 54, 1506–1510. <https://doi.org/10.1016/j.electacta.2008.09.030>
- Thirupathi, A.R., Sidhureddy, B., Keeler, W., Chen, A., 2017. Facile one-pot synthesis of fluorinated graphene oxide for electrochemical sensing of heavy metal ions. *Electrochem. commun.* 76, 42–46. <https://doi.org/10.1016/j.elecom.2017.01.015>
- Tisdale, W.A., Held, J.T., Kortshagen, U., Reifsnnyder Hickey, D., Hunter, K.I., Mkhoyan, K.A., Greenberg, B., Dahod, N., 2018. Obtaining Structural Parameters from STEM–

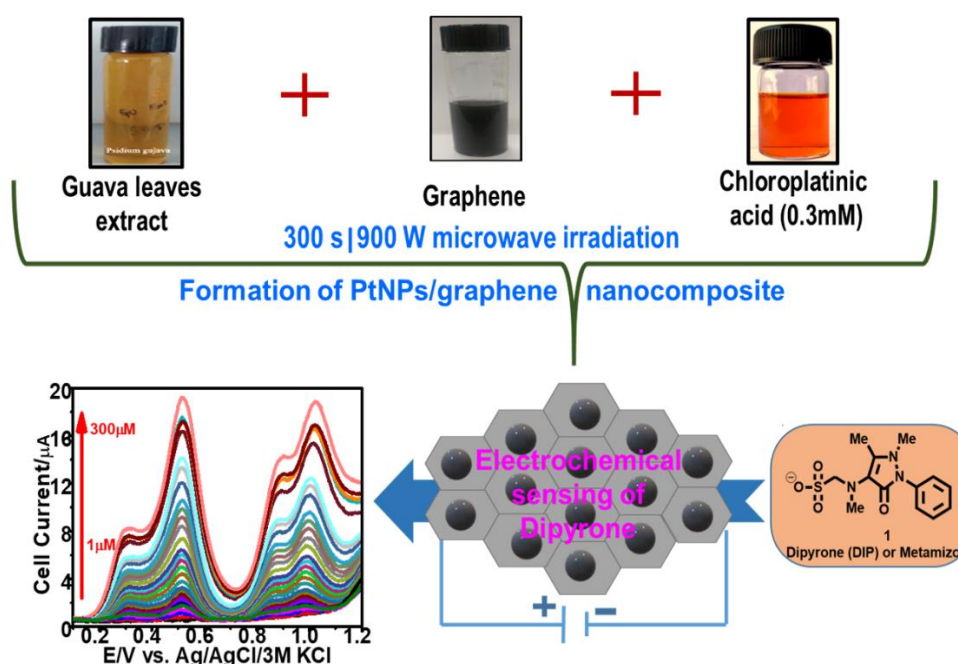
- EDX Maps of Core/Shell Nanocrystals for Optoelectronics. *ACS Appl. Nano Mater.* 1, 989–996. <https://doi.org/10.1021/acsanm.7b00398>
- Tonlé, I.K., Letaief, S., Ngameni, E., Walcarius, A., Detellier, C., 2011. Square wave voltammetric determination of lead(II) ions using a carbon paste electrode modified by a thiol-functionalized kaolinite. *Electroanalysis* 23, 245–252. <https://doi.org/10.1002/elan.201000467>
- Westsson, E., Koper, G., 2014. How to Determine the Core-Shell Nature in Bimetallic Catalyst Particles? *Catalysts* 4, 375–396. <https://doi.org/10.3390/catal4040375>
- Wu, K.-H., Lo, H.-M., Wang, J.-C., Yu, S.-Y., Yan, B.-D., 2017. Electrochemical detection of heavy metal pollutant using crosslinked chitosan/carbon nanotubes thin film electrodes. *Mater. Express* 7, 15–24. <https://doi.org/10.1166/mex.2017.1351>
- Xiao, L., Wildgoose, G.G., Compton, R.G., 2008. Sensitive electrochemical detection of arsenic (III) using gold nanoparticle modified carbon nanotubes via anodic stripping voltammetry. *Anal. Chim. Acta* 620, 44–49. <https://doi.org/10.1016/j.aca.2008.05.015>
- Xing, G., Sardar, M.R., Lin, B., Lin, J.M., 2019. Analysis of trace metals in water samples using NOBIAS chelate resins by HPLC and ICP-MS. *Talanta* 204, 50–56. <https://doi.org/10.1016/j.talanta.2019.05.041>
- Yamini, Y., Safari, M., 2018. Modified magnetic nanoparticles with catechol as a selective sorbent for magnetic solid phase extraction of ultra-trace amounts of heavy metals in water and fruit samples followed by flow injection ICP-OES. *Microchem. J.* 143, 503–511. <https://doi.org/10.1016/j.microc.2018.08.018>
- Yang, S., Wang, G., Li, G., Du, J., Qu, L., 2014. Decoration of graphene modified carbon paste electrode with flower-globular terbium hexacyanoferrate for nanomolar detection of rutin. *Electrochim. Acta* 144, 268–274. <https://doi.org/10.1016/j.electacta.2014.08.050>
- Zeinu, K.M., Hou, H., Liu, B., Yuan, X., Huang, L., Zhu, X., Hu, J., Yang, J., Liang, S., Wu, X., 2016. A novel hollow sphere bismuth oxide doped mesoporous carbon nanocomposite material derived from sustainable biomass for picomolar electrochemical detection of lead and cadmium. *J. Mater. Chem. A* 4, 13967–13979. <https://doi.org/10.1039/c6ta04881a>
- Zeng, A., Liu, E., Tan, S.N., Zhang, S., Gao, J., 2002. Stripping voltammetric analysis of heavy metals at nitrogen doped diamond-like carbon film electrodes. *Electroanalysis* 14, 1294–1298. [https://doi.org/10.1002/1521-4109\(200210\)](https://doi.org/10.1002/1521-4109(200210))

Zhang, B., Chen, J., Zhu, H., Yang, T., Zou, M., Zhang, M., Du, M., 2016. Facile and green fabrication of size-controlled AuNPs/CNFs hybrids for the highly sensitive simultaneous detection of heavy metal ions. *Electrochim. Acta* 196, 422–430. <https://doi.org/10.1016/j.electacta.2016.02.163>



CHAPTER 5

Bioinspired Synthesis of PtNPs/graphene Nanocomposites for Electrochemical Sensing of Metabolites of Dipyron



Highlights

- ◆ One-pot synthesis of Pt-decorated graphene nanocatalyst via green methodology
- ◆ Electrochemical sensor based on Pt/graphene nanocatalyst modified GCE for sensing of metabolites of dipyron
- ◆ Investigation on (electro)oxidation process of dipyron
- ◆ Electrochemical mechanism of dipyron oxidation to antipyrine proposed based on LCMS analysis
- ◆ Pt/graphene nanocatalyst tested in environmental water samples collected from supply lines and sewer lines

5.1 Background and executive motivation

Among the fastest-growing sectors, pharmaceutical industries have been one of the leading areas in the Indian economy. The boom in the pharmaceutical industry has led to increased production of pharmaceutically active compounds (PhACs) administered both for human and livestock. The generation of pharmaceutical wastes is also increased by many folds in the last decade. As a result, the concentration of PhACs in the sewer line is steadily rising over the years which in turn ends up at the sewage treatment plant (STP) and other surface water bodies (Zorita et al., 2009). The potent PhACs mostly survive the STP treatment and pose a significant threat to humans, wildlife, and aquatic ecosystems even at very minute concentrations.

Dipyrene (DIP) (also called metamizole), a pyrazolone derivative, is known to possess potent painkilling, antipyretic, and spasm-relieving properties (Teixeira and Dadamos, 2009). The drug, even at lower concentrations, may cause temporary conditions of infection of renal tissues. The drug overdose can cause transitory disturbances and inflammation of the renal tissue. Detection of DIP is crucial not only being an emerging contaminant but also for the economic perspectives minimizing its excessive loss into waste streams and monitoring the product quality. DIP also is used as the main active component of numerous drug preparations. Therefore, accurate quantification of DIP in these formulations is essential.

DIP can be determined by gas chromatography (Krokos et al., 2018), high-performance liquid chromatography (Senyuva et al., 2005), mass spectrometry (Pitarch et al., 2010), capillary electrophoresis mass spectrometry (Rajaram et al., 2015), and high-performance liquid chromatography-photochemically induced fluorimetry (Di Pietra et al., 1996). These methods though reliable, are not accessible to all due to their high-cost. Hence, it is inevitable to find low cost portable and sustainable alternatives, which do not demand costly installations. The development of reliable technology could allow us the prior and rapid detection of such pharmaceutical constituents.

Electrochemical techniques such as differential pulse voltammetry (DPV) (Pauliukaite et al., 2012a), square wave voltammetry (SWV) (Muralidharan et al., 2008), and cyclic voltammetry (CV) (de Faria et al., 2019) satisfy most of the above criteria, and they could be considered as potential tools for the highly sensitive and rapid detection of DIP.

In recent years, the use of graphene for the purpose to modify electrode surfaces has been exploited by many researchers (Chipeture et al., 2019; Martin Santos et al., 2017; Rajamani and Peter, 2018) as it could harness the gain in sensitivity, reproducibility, and specificity of an analyte in comparison with unmodified counterparts. Zhou and coworkers (Zhou et al., 2009) showed an enhanced sensitivity and a limit of detection (LoD) of 0.05 μM of H_2O_2 sensing using chemically synthesized graphene decorated glassy carbon electrodes (GCEs). In contrast, the bare graphite and GCE did not sense H_2O_2 at a low concentration of 0.05 μM . The sensitivity of H_2O_2 sensing remained unaltered even in the presence of 0.2 mM of ascorbic acid (AA), acetaminophen (APAP), dopamine (DA), and uric acid (UA). Graphene/GCE could effectively detect paracetamol by decreasing the overpotential with an increased response current as compared with bare GCE (Kang et al., 2010).

Further, platinum nanoparticles (PtNPs) are known to be applied in many catalytic reactions because of their unique properties such as resistant to oxidation at higher potentials (Berry, 1978) and superior activity, in particular for redox reactions of complex molecules (Er et al., 2017). Many researchers have shown enhanced electrocatalytic properties of PtNPs when it is supported on various carbon materials such as carbon nanofiber (Tang et al., 2004), carbon nanotube (Amatongchai et al., 2017), vulcan carbon (Odetola et al., 2017), etc. Furthermore, PtNPs/graphene nanocomposites are proven to be more effective in catalyzing the reaction in comparison to PtNPs and carbon nanostructures. There is also a decrease in the amount of catalyst required to achieve the same catalytic efficiency when PtNPs are used with the incorporation over the graphene (Higgins et al., 2016). The use of PtNPs in graphene-based transducers showed an increase in the sensitivity by two-fold magnitude towards glucose detection as compared to bare graphene electrodes (Zhang et al., 2015). TM- β -cyclodextrin/PtNPs/graphene showed a marked increase in the catalytic activity towards the electrochemical oxidation of bisphenol-A with 220 $\mu\text{A}/10 \mu\text{M}$ as compared to bare GCE and TM- β -cyclodextrin modified GCE (150 $\mu\text{A}/10 \mu\text{M}$) (Zou et al., 2017).

Therefore, it is vital to marry the PtNPs with graphene forming a PtNPs/graphene nanocomposite to test the enhancement of electrocatalytic activity for the sensing of complex DIP molecules. DIP metabolism takes about 4-6 h in the excretory system, for the elimination of its metabolites through urine (Bacil et al., 2018). Therefore, the sensing of DIP, along with its metabolic products is a prudent area of scientific studies.

In this work, we have developed a bio-inspired route for the fabrication of PtNPs decorated graphene-based sensing platform to detect metabolites of DIP present in water electrochemically. Towards this goal, *P. guajava* (guava) leaves were selected for the formation of PtNPs which are rich in antioxidants, flavonoids, and various polyphenolic compounds (Barbalho, 2012; Bose and Chatterjee, 2016; Díaz-de-Cerio et al., 2016). The use of bio-analytes also merits as stabilizing agents for the PtNPs. Microwave assisted synthesis serves a dual purpose of speeding PtNPs growth and further exfoliating thick graphene sheets to develop an effective electrocatalyst. DIP is known to show multiple oxidative pathways in a physiological environment. Hence, we focused on developing an electrochemical sensor that could determine not only DIP but also its major oxidation products. The use of bio-mediated PtNPs for the detection of DIP is nowhere reported previously to the best of our knowledge.

5.2 Results and Discussions

5.2.1 Characterization of PtNPs/graphene nanocomposites

5.2.1.1 Morphology study of PtNPs/graphene nanocomposites

Figure 5.1a shows a low magnification TEM image of the synthesized graphene sheets, which are found to be several microns in length. The graphene nanosheets were stacked on the top of each other. They are highly transparent and show great stability under the electron path of the microscope. The inset shows a characteristic hexagonal diffraction pattern of graphene sheets with a distance of 9.08 nm between two bright spots which compute out to be 0.224 nm interatomic distance corresponding to d_{100} basal plane of highly crystalline graphene sheet (Malesevic et al., 2008; Meyer et al., 2007). The high-resolution TEM image clearly shows the ordered lattices of graphene (Figure 1b). The average diameter of PtNPs nanoparticles decorated over graphene was found to be 7.75 nm (Figures 5.1c-5.1d). It can be observed that PtNPs are evenly distributed over the graphene sheet (Figure 5.1d). An individual lattice fringe of PtNPs embedded on graphene nanosheets calculated by the inverse fast fourier transform (IFFT) was found to be 0.227 nm which was from 10 consecutive fringes (Figure 5.1e) It implies a characteristic feature of Pt (111) crystal surface (Miyazawa et al., 2019). An elemental analysis was carried out to find out the local abundance of PtNPs over the graphene sheet. Figure 5.1f shows the elemental distribution of PtNPs over the graphene sheets. The red dots indicate the presence of Pt and the grey background corresponds to the graphene base. The elemental concentration of Pt

was found to be 4.63% from the EDX analysis (Figure 5.1g). The large carbon peak is attributed to the presence of carbon in the PtNPs/graphene nanocomposite.

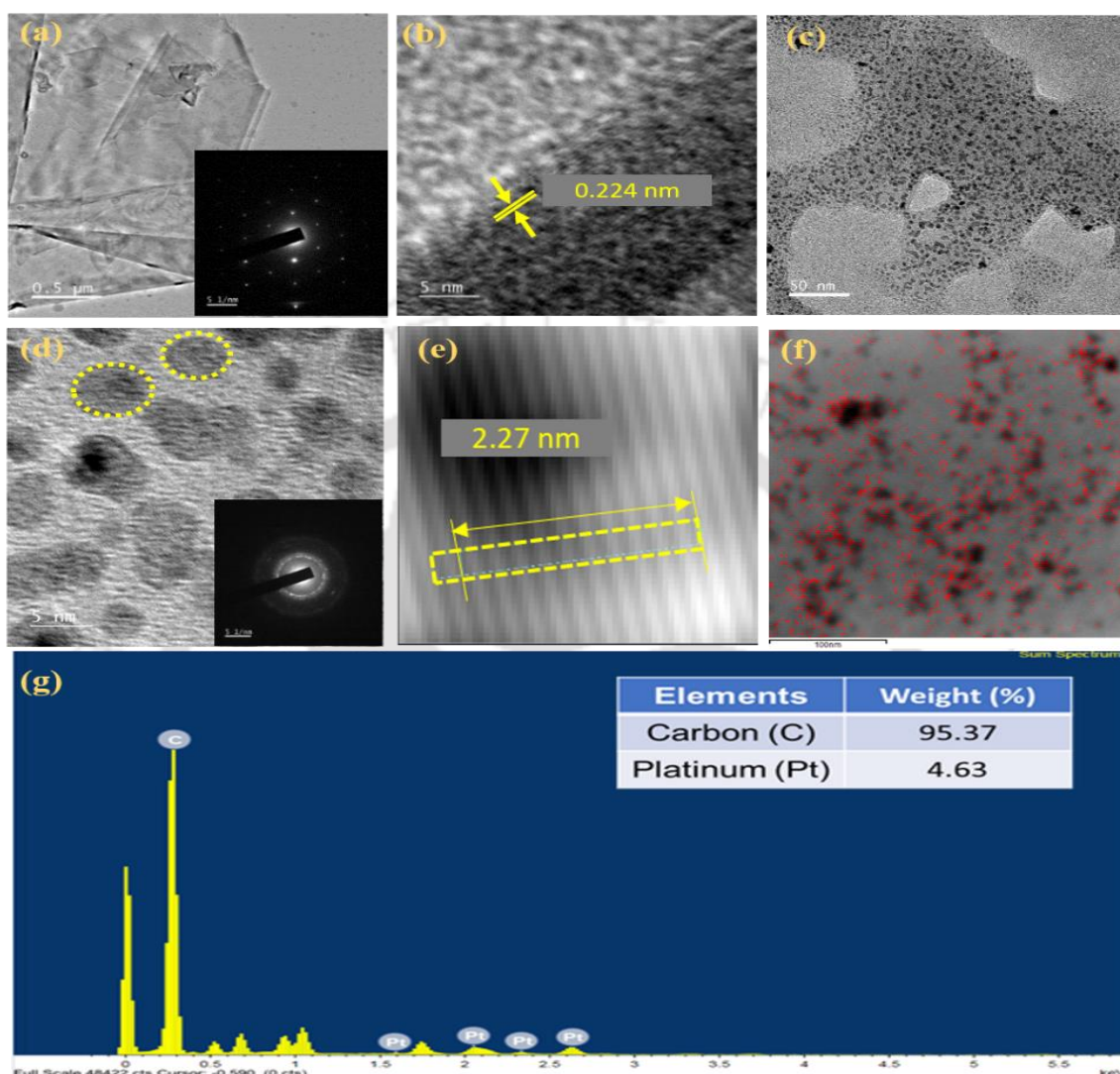


Figure 5.1: (a) TEM micrograph of graphene sheet (inset: SAED of graphene), (b) HRTEM micrograph of graphene, (c) FETEM micrograph of PtNPs, (d) HRTEM micrograph of PtNPs/graphene nanocomposite highlighted circles showing PtNPs (inset: SAED of PtNPs/graphene nanocomposite), (e) IFFT image of PtNPs on graphene sheet showing the characteristic fringe distance of 0.227 nm, (f) elemental mapping showing the distribution of Pt element on PtNPs/graphene nanocomposite, and (g) EDX spectra of PtNPs/graphene nanocomposite.

Figure 5.2 shows the FESEM images of a bare multi-layered graphene sheet and PtNPs/graphene. It shows a clean surface of pristine multilayered graphene (Figure 5.2a). The well dispersed PtNPs also can be seen (Figure 5.2b) as bright dots that confirm the

sphericity and monodispersity of the nanoparticles. Few areas on PtNPs/graphene shows a sign of minor aggregation which could be attributed to the hotspot created on the graphene surface due to the absorption of microwave by the graphene. This increased temperature promote enhanced nucleation and growth of nanoparticles in sufficient presence of precursor salt by enhancing the particle growth kinetics generating larger sized NPs over graphene (Liu et al., 2020).

The particle size distribution of PtNPs (Figure 5.3a) and PtNPs/graphene (Figure 5.3b) shows an average particle size of 3.7 and 7.7 nm, respectively. It can be seen that 60 % of PtNPs varied between 2.5 and 4.0 nm, whereas in the case of PtNPs/graphene 36 % of the particles were within 7-9 nm.

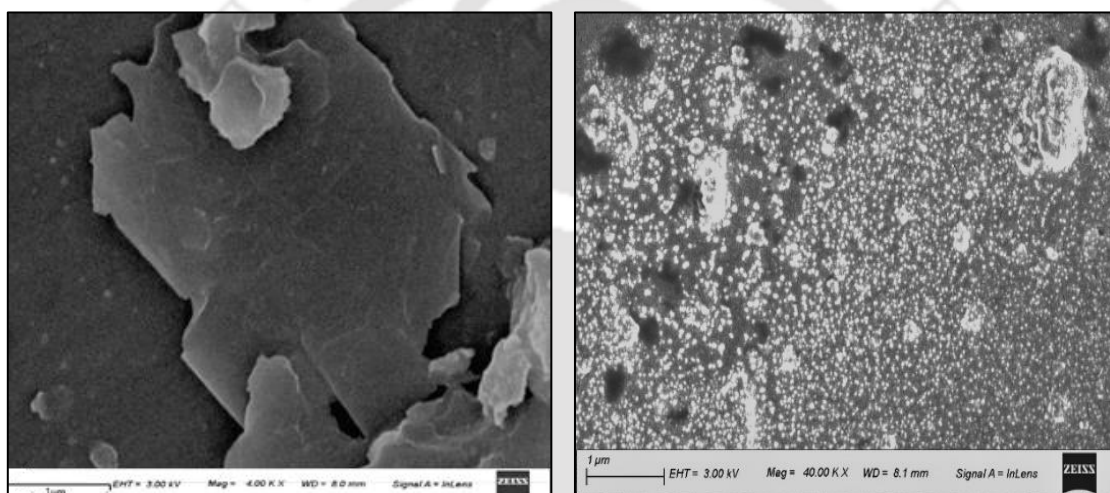


Figure 5.2: (a) FESEM image of bare graphene, and (b) FESEM image of PtNPs/graphene nanocomposites.

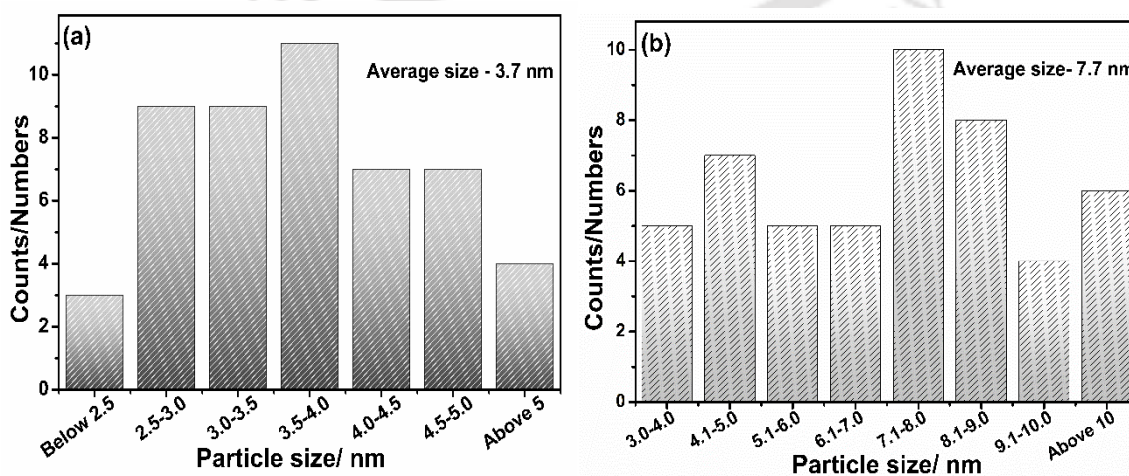


Figure 5.3: (a) Particles size distribution of PtNPs and (b) PtNPs/graphene nanocomposite.

5.2.1.2 Crystallinity analysis of PtNPs/graphene nanocomposites

XRD analysis was done to gain more knowledge on the crystallinity of the prepared nanocomposite. XRD patterns of pristine graphite, graphene nanosheets, and PtNPs/graphene nanocomposite are presented in Figure 5.4. The precursor of graphene exhibits a typical graphitic crystal structure. The peaks appeared for graphene at 26.8, 44, and 55° 2 θ angles correspond to the diffraction from (002), (100) and (004) planes of crystalline carbon (JCPDS No. 01-087-0646). The peak at around 42° 2 θ angle could be due to the interlayer defect between graphene sheets existed in some of the layered graphene sheets (Nemade and Waghuley, 2013). The diffraction peaks located at 2 θ angles of 39.8° and 46.3° in PtNPs/graphene nanocomposite are for the diffraction from the (111) and (200) crystal planes of Pt (JCPDS No. 65-2868) (Ateş et al., 2017).

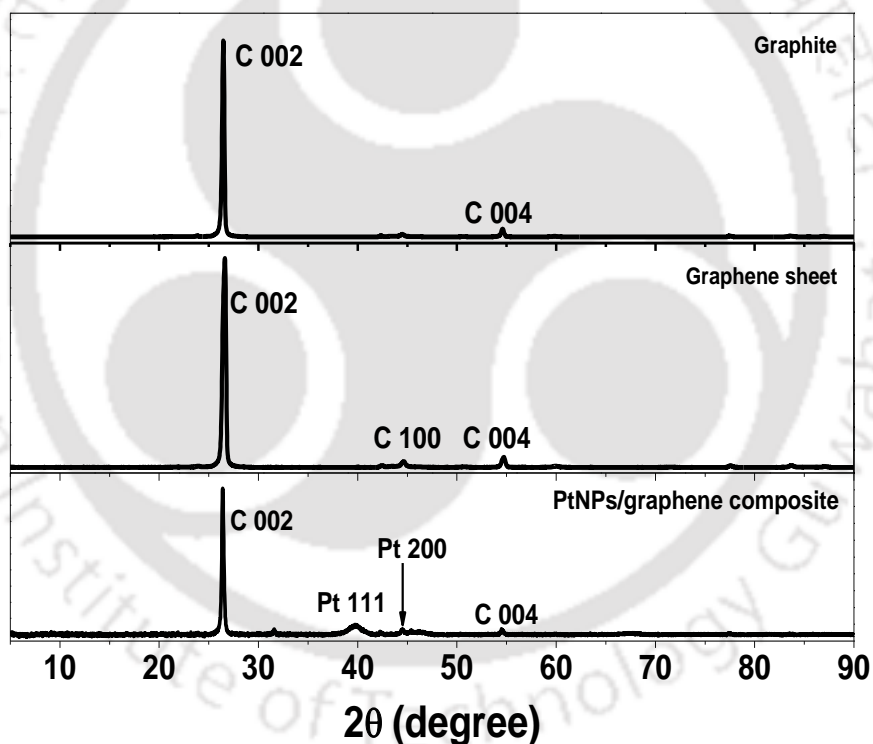


Figure 5.4: X-ray diffraction patterns of (a) bare graphite, (b) graphene nanosheet, and (c) PtNPs/graphene nanocomposite.

5.2.1.3 Raman analysis of graphene nanosheet

Figure 5.5 shows the Raman spectra of graphene nanosheets and the precursor used for its synthesis. The D, G, and 2D peaks of synthesized graphene are appeared to be quite distinct from the Raman spectra. The defects and disorders existed at the edges of the

graphene structure can be understood by the intensity of the D band identified at 1333 cm^{-1} which was absent in the case of graphite due to a complete sp^2 hybridization of carbon. However, it was present in the graphene structure because of the vibrational signals generated due to incomplete hybridization of sp^2 carbons at the edges of its structures (Malesevic et al., 2008). The G band appeared at about 1580 cm^{-1} in graphite was shifted a bit towards a higher wavenumber of 1582 cm^{-1} in the case of graphene which is a characteristic feature of some of the layered graphene nanosheets (Hernandez et al., 2008; Malesevic et al., 2008). The G-band for both the specimens was originated due to the in-plane vibrations involving the sp^2 hybridized carbon atoms. The ratio intensity of D peak (I_D) and G peak (I_G) was found to be 0.30 which indicates that there could be a stack of 6-7 graphene nanosheets (Yi et al., 2013). The decrease in the Raman shift of the 2D peak (secondary peak of D band) from 2738 to 2680 cm^{-1} is clearly indicative for the formation of graphene nanosheets (Ferrari et al., 2006). The intensity of this band is always stronger in the case of graphene as it depends on the phonon-lattice vibrational unlike the D band requires a proximity of defect to be activated. The 2D band could further split into various modes with the increase in the thickness of graphene layer as it appeared as a small hump (denoted as D') which is due to the decrease in the symmetry of graphene layers with the increase in number of layers (Graf et al., 2007; Malesevic et al., 2008).

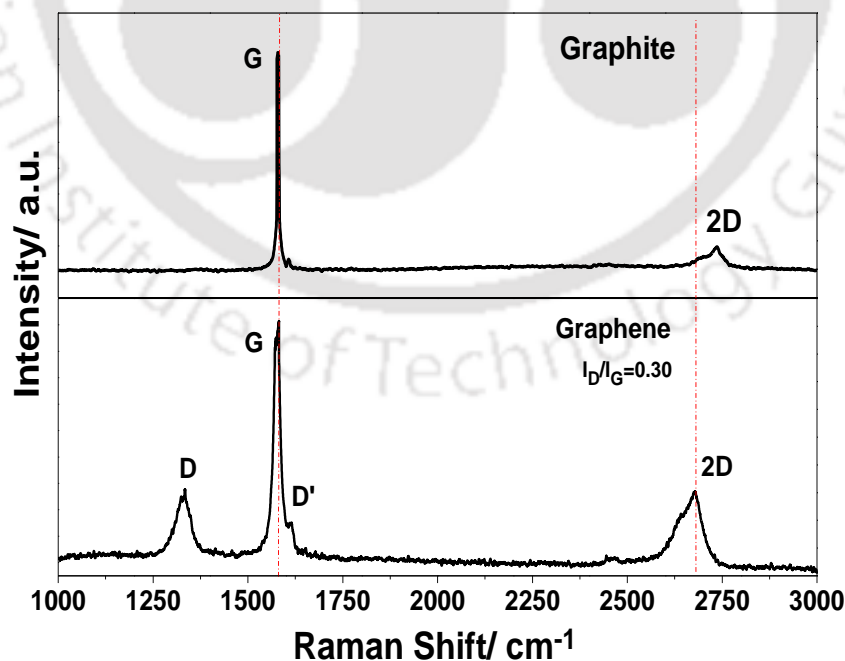


Figure 5.5: Raman spectra of bare graphite and synthesized graphene.

5.2.2 EIS of PtNPs/graphene/GCE

The EIS spectra were recorded using 0.1 mM DIP in 0.5M KCl electrolyte at pH 7 within a frequency range of 10^{-2} to 10^6 Hz. The value of charge-transfer resistance (R_p , Figure 5.6) was obtained from the Nyquist plots by simulating it based on the Randles equivalent circuits (Figures 5.7a-5.7c). It can be observed that R_p and R_s (solution resistance) were of 40.1, 32.6 and 19.9 k Ω , and 13.8, 12.6 and 10.2 Ω , respectively for bare GCE, PtNPs/GCE, and PtNPs/graphene/GCE, respectively. The corresponding constant phase elements (CPE) that arises due to the double layer capacitance were of 299, 306, and 314 μ Mho which was increased due to the presence of graphene nanosheets (Gutić et al., 2016). The PtNPs/graphene/GCE produced a semi-circle with a lower radius than that was obtained with the bare GCE. It implies a high R_p and a slow electron transfer for the bare GCE. The surface modification of GCE with PtNPs/graphene was resulted in a decrease of R_p almost by a factor of two.

From the SWV analysis (Figure 5.8), three peaks were recorded at 0.301, 0.513, and 0.991 V vs. Ag/AgCl for the PtNPs/graphene/GCE. A shoulder peak appeared at 0.87 V with the PtNPs/graphene/GCE electrode could be due to the surface adsorption reaction of the oxidation products of DIP remained from the previous steps of the reaction (Pauliukaite et al., 2010a). The peak current (at 0.5 V vs. Ag/AgCl) was about 3.8 and 1.76 times higher with PtNPs/graphene/GCE in comparison to bare GCE and PtNPs/GCE, and the peak sharpness was also very prominent in the case of PtNPs/graphene/GCE. It implies a faster electro-oxidation in the presence of PtNPs by a possible bi-functional effect between Pt and residual oxygen species present on some of the graphene layers (Li et al., 2010). The shift in the peak potential (E_p) towards a lower positive voltage in the case of PtNPs/graphene/GCE indicates that it could lower the energy required for DIP sensing reaction. Therefore, an enhancement of catalytic activity of DIP sensing at the PtNPs/graphene/GCE surface is expected.

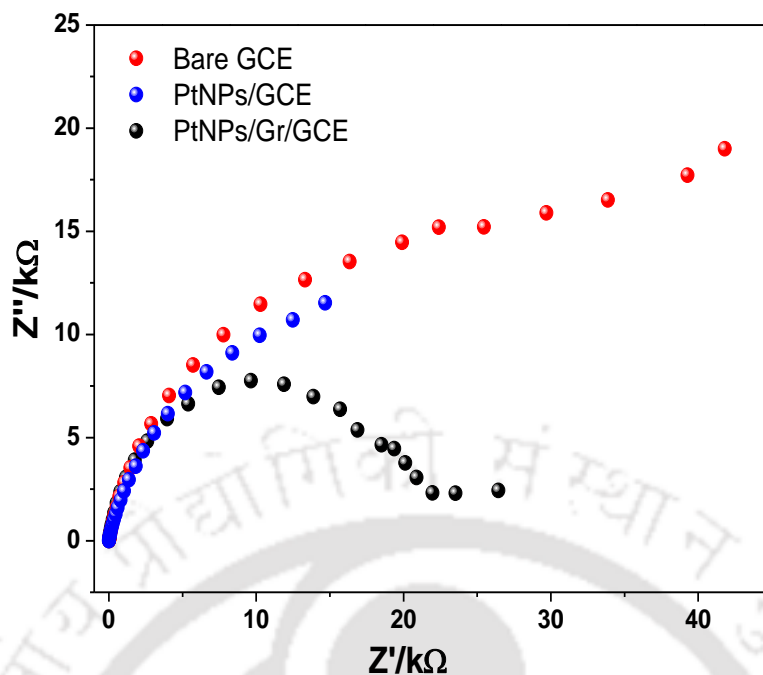


Figure 5.6: Nyquist plot with 0.1 mM DIP in 0.5 M KCl electrolyte at pH 7 within a frequency range of 10^{-2} to 10^6 Hz and 0.01 V vs. Ag/AgCl at open circuit potential.

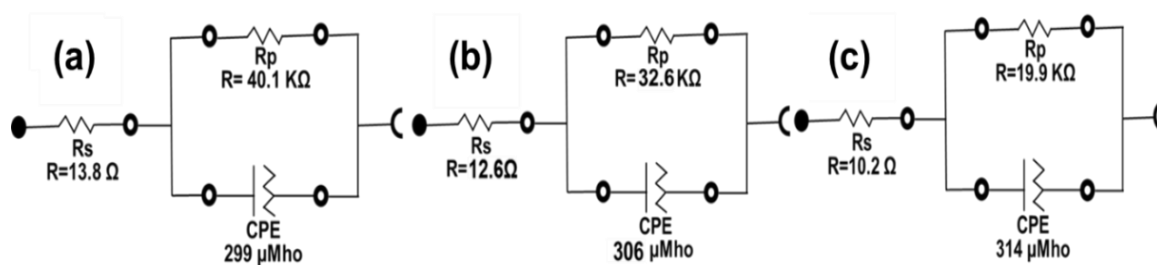


Figure 5.7: Equivalent circuit diagrams of (a) bare GCE (support), (b) PtNPs/GCE, and (c) PtNPs/graphene/GCE.

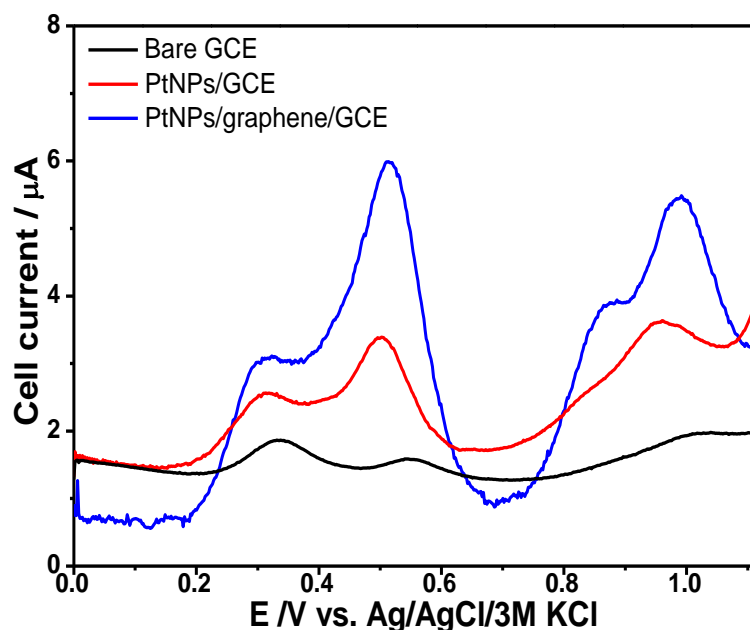


Figure 5.8: Square wave response of DIP sensed using different working electrodes. DIP concentration of 50 μM using 0.5 M KCl as supporting electrolyte. Square wave parameters: Initial potential 0.00 V and end potential 1.10 V, step potential 0.002 V, and amplitude 0.05 V vs. Ag/AgCl.

The effective active surface area (A_{eff}) of the prepared electrodes was calculated using the Randles-Sevcik Equation (Eq. 5.1).

$$I_{\text{Pa}} = (2.69 \times 10^5) n^{0.66} A_{\text{eff}} D^{0.5} \nu^{0.5} C_0 \quad (5.1)$$

Where, n is the number of electrons, ν is the scan rate in $\text{V} \cdot \text{s}^{-1}$, D is the diffusion coefficient in $\text{cm} \cdot \text{s}^{-1}$, and C_0 is the bulk concentration of the electro-analyte probe (here, $\text{Ru}[(\text{NH}_3)_6]\text{Cl}_3$) in moles. From the plot of I_{Pa} vs. $\nu^{0.5}$ (Figure 5.9), the slope of the linear fit was found to be $52.43 \mu\text{A} \cdot \text{V}^{-1/2} \cdot \text{s}^{1/2}$ ($R^2 = 0.991$) and $100.23 \mu\text{A} \cdot \text{V}^{-1/2} \cdot \text{s}^{1/2}$ ($R^2 = 0.994$), respectively for bare and PtNPs/graphene/GCE. By considering D of $8.43 \times 10^{-6} \text{cm}^2 \cdot \text{s}^{-1}$ for 1 mM $\text{Ru}[(\text{NH}_3)_6]\text{Cl}_3$ in 0.1 M KCl with $n=1$, A_{eff} was calculated to be 0.067 and 0.128cm^2 . (Wang et al., 2011) The A_{eff} of GCE was almost equivalent to the geometrical surface area of the electrode (0.070cm^2). As observed from Figures 5.9a-5.9c, the redox current response was almost doubled in the case of PtNPs/graphene/GCE as compared to bare GCE. It can also be noted that at lower scan rates (up to $50 \text{mV} \cdot \text{s}^{-1}$), the current response of both GCE and PtNPs/graphene/GCE was invariant. This could be due to the fact that $\text{Ru}[(\text{NH}_3)_6]\text{Cl}_3$, an outer sphere redox probe, acts only outside the diffusion layer. At lower scan rates ($<50 \text{mV} \cdot \text{s}^{-1}$), the thickness of the diffusion layer is much higher

than the roughness generated by the nanomaterials (Paixão, 2020). A substantial increase in the A_{eff} of 2 times was noted as compared to the unmodified GCE. Graphene allows uniform distribution of PtNPs on its surface and it increases the A_{eff} as compared to bare PtNPs (Kalambate et al., 2015).

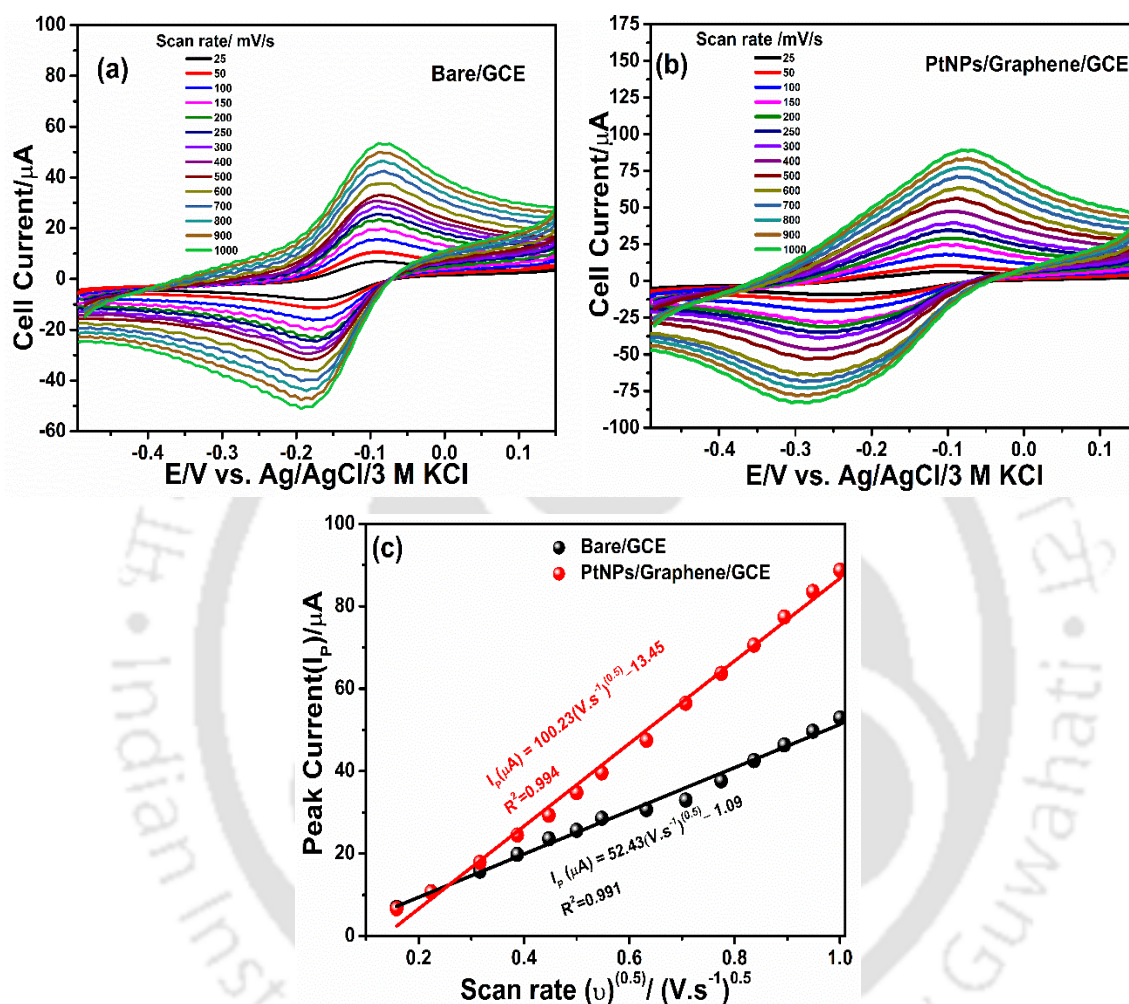


Figure 5.9: Cyclic voltammetry of (a) bare/GCE and (b) PtNPs/graphene/GCE at various scan rates from 5-200 mV.s^{-1} and (c) Peak current vs. square root of scan rate (25-1000 mV.s^{-1}) using GCE and PtNPs/graphene/GCE. Reaction conditions: 1 mM $[\text{Ru}(\text{NH}_3)_6]\text{Cl}_3$ as redox probe in 100 mL of 0.1 M KCl as supporting electrolyte at ambient temperature.

5.2.3 Electrocatalytic DIP sensing at PtNPs/graphene/GCE

5.2.3.1 Determination of electrokinetic parameters

SWV was performed using to study the effects of varying pH ranging from 3.0 to 11.0 on the sensing performance of 50 μM DIP using PtNPs/graphene/GCE. The results are shown in Figure 5.10. The highest peak current was obtained at pH 7.0 (Figure 5.10a). A shift in the potential (E_p) towards less positive values was observed with the increase in

pH from 5.0 to 9.0. It implies that the electro-oxidation of DIP is favorable in an alkaline pH. However, a drastic reduction in response current was observed at pH>7. Hence, pH 7 was taken as the optimum value for further experiments. It can be observed that the Peak 1 position at around 0.2 V vs. Ag/AgCl is highly pH-dependent, and it shifted towards a lower potential with the rise in pH. It was also found that the Peak 1 potential varied linearly with pH with a slope of 26 mV per unit pH (Figure 5.10b) which is close to the theoretical value of 30 mV per unit pH for a reaction involving 2 electrons (Siswana et al., 2006). However, the position of Peak 2 (0.55 vs. Ag/AgCl) and Peak 3 (0.9 V vs. Ag/AgCl) is found to be independent of the pH of the solution.

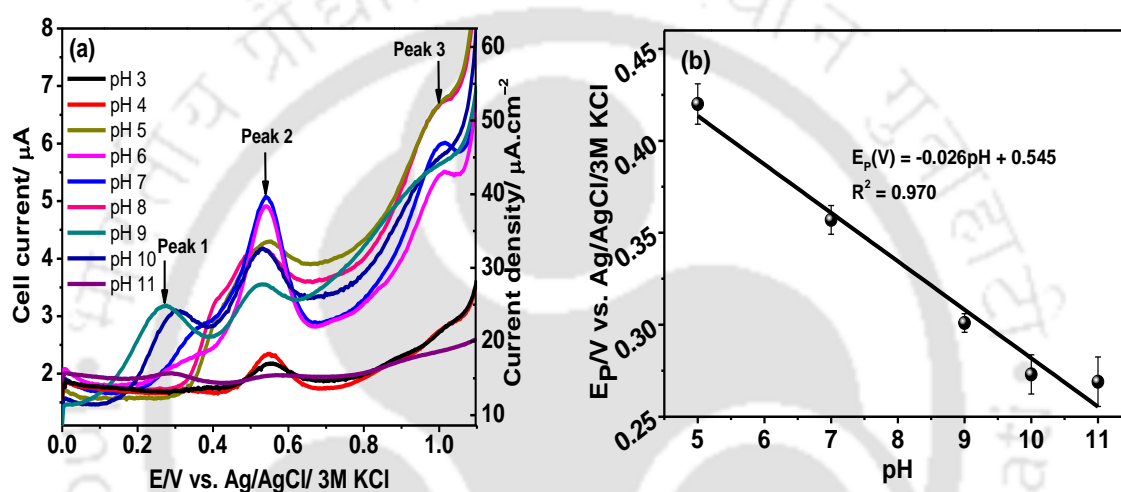


Figure 5.10: (a) Square wave response at different pH using PtNPs/graphene/GCE, and (b) E_p vs. pH (peak 1). Reaction conditions: DIP concentration of 50 μM in 0.5 M KCl supporting electrolyte. Square wave parameters: Initial potential 0.00 V, end potential 1.10 V, step potential 0.002 V, and amplitude 0.05 V vs. Ag/AgCl.

Cyclic voltammetry experiments at different scan rates (5 -200 $\text{mV}\cdot\text{s}^{-1}$) were conducted to determine the electrokinetic properties of DIP sensing (Figure 5.11a). A straight line was obtained by plotting the peak current with the square root of the scan rate (Figure 5.11b). The results show that the reaction is diffusional control (Švorc et al., 2018). Hence, Laviron equation (Eq. 3.2 of Chapter 3) for the diffusion-controlled process was used to determine the kinetic parameters (Table 5.1) (Rasappa et al., 2015).

Where, α in Eq 3.2 is the anodic charge transfer coefficient, and was calculated based on the Bard and Faulkner equation (Eq. 5.2) (Gowda and Nandibewoor, 2014).

$$\alpha = \frac{47.7}{E_p - E_{p/2}} \quad (5.2)$$

Where, E_p (V) is the anodic peak potential, and $E_{p/2}$ is the potential when current is half of the peak value. The value of αn was calculated from the slope of E_p vs. $\log v$ (Figure 5.11c), and the intercept gives the k° value. E° was obtained from the intercept of the curve of E_p vs. v ($v = 0$) (Table 5.1). These are the parameters which show the intrinsic properties of the PtNPs/graphene/GCE and different oxidation products of DIP. (Rountree et al., 2014) The decrease in the surface reaction for different oxidation products is evident from the different k° values which gives the affinity of the analyte towards the electrode interface (Table 5.1). The E° values for the reactions occurring at peak 1, peak 2 and peak 3 are respectively 0.387, 0.755 and 0.956 V vs. Ag/AgCl, and the corresponding k° values are 0.295×10^{-3} , 0.692×10^{-3} , and 0.890×10^{-3} . The positive shift in the experimental potential of peak 1 by 0.125 V, peak 2 by 0.111 V and peak 3 just by 0.029 V from the E° values implies the thermodynamic favorability of an electrochemical reaction (Elgrishi et al., 2018). This system requires more energy for the reaction to move in the forward direction due to lower k° values for peaks 1 and 2. Similarly, a sufficiently greater k° value for peak 3 gives a reaction potential close to the E° value.

Table 5.1: Electrokinetic parameters of sensing of DIP and its metabolites at different oxidation peaks using PtNPs/graphene/GCE.

Parameters	α	n	$k^\circ (10^{-3})$	E° (V)
Peak 1	0.422	$2.40 \approx 2$	0.295	0.387
Peak 2	0.588	$1.89 \approx 2$	0.692	0.755
Peak 3	0.244	$0.736 \approx 1$	0.890	0.956

Figures 5.11d and 5.11e depict the square wave voltammograms and the corresponding calibration curves of DIP sensing at the PtNPs/graphene/GCE, respectively. The voltammograms exhibited two linear ranges of DIP sensing based on its concentration, i.e., between 1-100 μM and 100-220 μM having linear relationships ($R^2 > 0.99$) as $I_p (\mu\text{A}) = 0.105 [\text{DIP}] \mu\text{M} + 0.978$ and $I_p (\mu\text{A}) = 0.057 [\text{DIP}] \mu\text{M} + 4.893$. This could be due to the rapid flux of analyte to the electrode surface at higher concentrations resulting in an accumulation of oxidation products on the electrode surface (Khalilzadeh and Borzoo, 2016). The peak at around 0.51 V (Peak 1, Figure 5.11f) is considered to develop the

calibration curve due to the reasons that this peak is independent of pH, and it acts as the rate-determining step for the whole redox system having the least k° value.

The limit of detection (LOD) and limit of quantification (LOQ) of DIP at the PtNPs/graphene/GCE was calculated using Eqs. 3.3 and 3.4 of Chapter 3, respectively.

Where, S_b is the standard deviation of the blank run (0.005) and m is the slope of the calibration curve (Figure 5.11e) containing the lowest possible detectable concentration of the analyte. LOD and LOQ were calculated as 0.142 and 0.471 μM , respectively which is a marked improvement over the LOD of 2.07 μM and 0.04 mM obtained in previous studies using epoxy-graphite composite (Pauliukaite et al., 2012b) and Ti(IV) silsesquioxane modified MCM-41 substrates (Do Carmo et al., 2019), respectively. The sensitivity of the PtNPs/graphene/GCE having A_{eff} of 0.128 cm^2 was found out from the slopes of the calibration curves (Figure 5.10 e) using Eq 3.5 of Chapter 3. It was calculated to be 0.820 $\mu\text{A} \cdot \mu\text{M}^{-1} \text{cm}^{-2}$ for the concentrations up to 100 μM and 0.445 $\mu\text{A} \cdot \mu\text{M}^{-1} \text{cm}^{-2}$ for the concentrations between 100 and 220 μM which is much greater than the sensitivity obtained (0.27 $\text{nA} \cdot \mu\text{M}^{-1}$) using graphite electrode (Baranowska et al., 2008). There was almost no increase in the current response of DIP sensing at DIP >220 μM . It might be of the surface saturation of the oxidation products. The performance parameters of DIP sensing using PtNPs/graphene/GCE and its comparison with earlier studies are provided in Table 5.2. It can be seen that the PtNPs/graphene/GCE exhibited a clear superiority of DIP sensing in comparison to the most of the studies. Silva et al. (Silva et al., 2020) showed a lower limit of DIP detection using screen-printed carbon electrodes but the sensitivity was only 0.065 $\mu\text{A} \cdot \mu\text{M}^{-1}$. Similarly, Munoz et al. (Muñoz et al., 2001) used gold electrodes extracted from compact discs for the amperometric determination of DIP and could successfully achieve an LoD of 0.1 μM and sensitivity of 0.017 $\mu\text{A} \cdot \mu\text{M}^{-1} \text{cm}^{-2}$. Nevertheless, the PtNPs/graphene/GCE worked well within a wider concentration range of DIP (1-100 μM) with an improved sensitivity of 0.820 $\mu\text{A} \cdot \mu\text{M}^{-1} \text{cm}^{-2}$.

It can be observed that the materials used for the fabrication of the sensor systems enlisted in Table 5.2 either used costly raw materials or the process of manufacture involved harsh chemicals that could potentially damage the environment. Our proposed system on the other hand exploited a bio-inspired approach of synthesizing PtNPs and PtNPs/graphene nanocomposite. The synthesized nanocomposite could successfully determine the metabolites of DIP found in natural environmental condition.

Table 5.2: Comparison between electrochemical performances of the proposed method and other studies extracted from the literature for dipyrone determination.

Working Electrode	Electrochemical techniques	Linear Range (μM)	Detection Limit (μM)	Sensitivity ($\mu\text{A}\cdot\mu\text{M}^{-1}\cdot\text{cm}^{-2}$)	Reproducibility (RSD %)	Reference
Carbon screen printed electrodes	SWV*	0.35-50	0.097	0.0652	3.1	Silva et al., 2020
Boron doped diamond	SWV	1-65	0.26	1.5	2.1	Gomes et al., 2019
Gold electrodes from compact disc	Amperometry	1-10	0.100	0.170		Muñoz et al., 2001
Glassy carbon electrode	CV*	10-100	2.97	-ND-		Bacil et al., 2018
Au screen printed electrodes	Amperometry	-ND-	5.0	-ND-		Habekost, 2018
Titanium(IV) silsesquioxane occluded in the MCM-41/ Graphite paste electrode	CV	100-900	40	0.06716		Do Carmo et al., 2019
Polythionine-carbon nanotube/ Carbon film electrode	DPV*	250-2500	15.2	1.3×10^{-3}		Ghica et al., 2015
poly (3,4-ethylenedioxythiophene) modified glassy carbon electrode	DPV	1.2-750	0.49	-ND-		Gopu et al., 2012
Reactive Blue 4 dye covalently immobilized on amine-functionalized silica	CV	49.9-440	22	0.22×10^{-3}		Martin and Teixeira, 2012
Graphite epoxy electrode modified with carbon nanotubes	DPV	50-1500	1.4	0.194		Pauliukaite et al., 2010b
Bio-inspired PtNPs/graphene/GCE	SWV	1-100	0.142	0.820	2.5	This work

*SWV: Square-wave voltammetry, CV: Cyclic voltammetry; DPV: Differential pulse voltammetry

Cyclic voltammogram recorded using 10 μM DIP in 0.5 M KCl at pH 7.0 showed three distinct oxidation peaks at 0.512, 0.759, and 927 V vs. Ag/AgCl at a scan rate of 50 $\text{mV}\cdot\text{s}^{-1}$ (red line), and a reversible reduction peak (Peak 4) at around 0.442 V vs. Ag/AgCl was also noted (Figure 5.11f). The anodic peak obtained was at 0.512 V, and the cathodic peak was obtained at 0.442 V with a ΔE_P value of 70 mV and I_{Pa}/I_{Pc} value of 1.21, and it decreases when the potential range is increased due to unavailability of the oxidation products for reduction. This implies that Peak 2 in the cyclic voltammogram (Figure 5.11f)

is the oxidation product of Peak 1. This Peak 1 also forms a reversible pair with peak 4 (black line in Figure 5.11f). The increase in the potential window converts the oxidation product (Peak 1) to further oxidations, thereby producing other products. Further, from Figure 5.11a, it can also be observed that at a scan rate above $100 \text{ mV} \cdot \text{s}^{-1}$, Peak 2 is absent, but Peak 3 is present. It indicates that Peak 3 is an oxidation product of Peak 1 and follows an independent oxidation pathway. At a higher scan rate, the reaction from Peak 1 to Peak 2 did not take place. It implies that the reaction is electrochemically less favorable than Peak 1 to Peak 3. Therefore, chronoamperometric test of DIP sensing was conducted at the oxidation potential of 0.51 V vs. Ag/AgCl at pH 7.

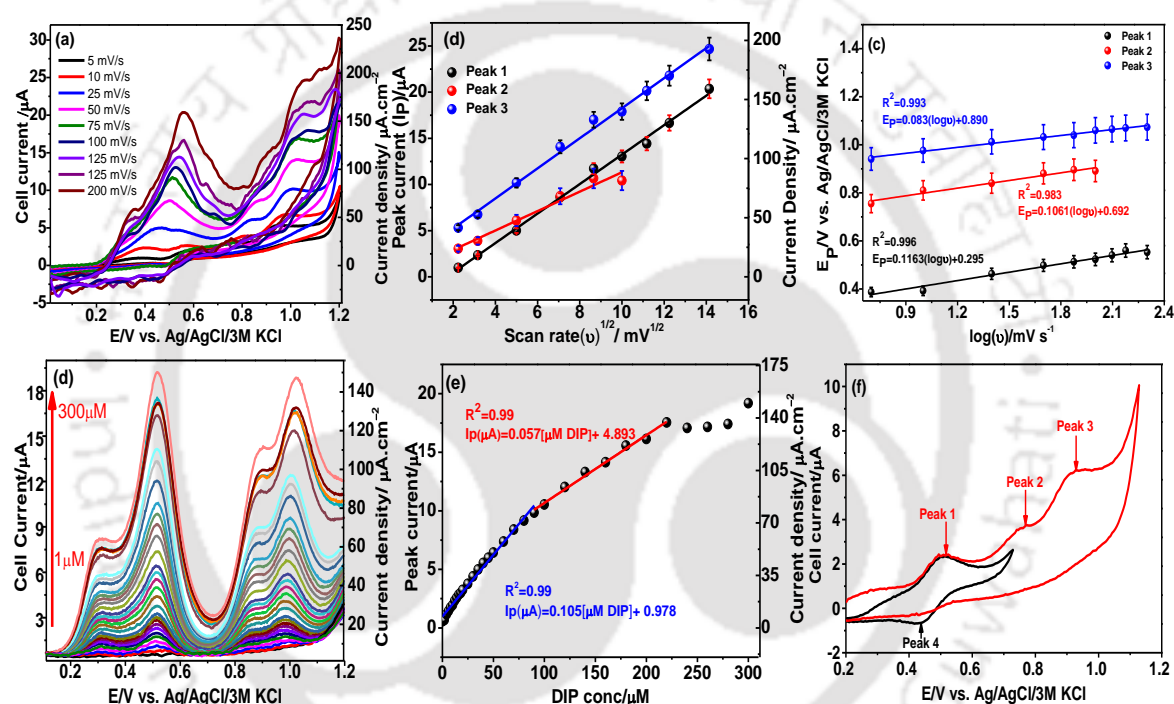


Figure 5.11: (a) Cyclic voltammogram recorded at different scan rates at PtNPs/graphene/GCE, (b) Variation of peak current (I_p) with $v^{1/2}$ (v : 5 to 200 mV·s⁻¹), (c) Variation of E_p with $\log(v)$ (v : 5 to 200 mV·s⁻¹) with 100 μM DIP in 0.5 M 100 mL KCl at pH 7, (d) SWV profile recorded with PtNPs/graphene/GCE at different DIP concentration (1 to 300 μM), (e) Calibration curve for DIP sensing, and (f) CV of DIP in a smaller electrochemical window (0.2 -0.8 V vs. Ag/AgCl) (black line) and wider electrochemical window (0.2 -1.2 V vs. Ag/AgCl) (red line) at the scan rate of 50 mV·s⁻¹.

To identify the reaction products, DIP concentration of 500 μM at pH 7 was subjected to HPLC and LC-MS analyses after 100 voltammetric cycles between 0 and 1.2 V vs. Ag/AgCl at a scan rate of 50 mV·s⁻¹ using the PtNPs/graphene/GCE. The clear and

transparent DIP solution appeared to be light yellow at the end of the reaction. DIP was detected with a retention time of 6.1 min (Figure 5.12). It disappeared after the reaction and three new peaks of the oxidation products at the retention time of 2.3, 4.3 and 17.9 min were identified in the HPLC chromatograph (Figure 5.12b).

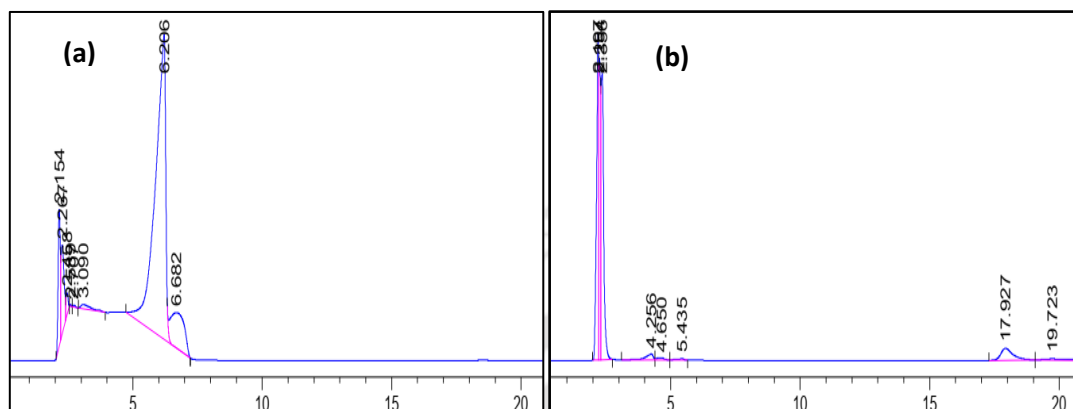


Figure 5.12: HPLC chromatograms (a) before and (b) after DIP sensing reaction. [An HPLC (Make: Agilent; 1260 Infinity II) equipped with UV detector was used for the chromatographic analysis of DIP. The detection was done at 214 nm using a UV detector.

The mass spectra recorded before and after the sensing of DIP is presented in Figure 5.13. The mass number (m/z) was compared with the literature (Giri and Golder, 2014; Habekost, 2018), and it is listed in Tables 5.3 and 5.4. DIP is quickly converted to 4-Methylaminoantipyrine (4-MAA). Therefore, the sensing of DIP essentially implies to the sensing of 4-MAA in natural environmental conditions. The mass, m/z 218.05, also supported the formation of 4-MAA. The first oxidation peak of DIP at 0.387 V vs. Ag/AgCl (Figure 5.11a) corresponds to a mechanism involving the transfer of two electrons and one proton (Figure 5.14). Thus, DIP (1) undergoes one electron oxidation at the substituted enaminic nitrogen of the pyrazolone ring to generate iminium cation radical 2 at Peak 1. Next, another one electron oxidation of radical cation 2 yielded bis-cation 3 which upon hydrolysis produces $[4\text{-DMAA}]^{2+}$ (4). As a whole the hydrolysis of DIP (1) involves 2 electron oxidation process followed by a single protonation to offer $[4\text{-MAA}]^{2+}$ (5). The mass, m/z 218.05, also supported the formation of 4-MAA. Further, demethylation of compound 5 possibly yield compound 6 $[4\text{-AA}]^{2+}$ which ultimately undergoes reduction at Peak 4 followed by condensation reaction with the produced formaldehyde to produce FAA (7). The possible mechanistic path encompassing the electrochemical process are given below. Figure 5.14a represents the overall oxidation of neutral DIP to form neutral 4-MAA, while Figure 5.14b shows the detail electrochemical paths.

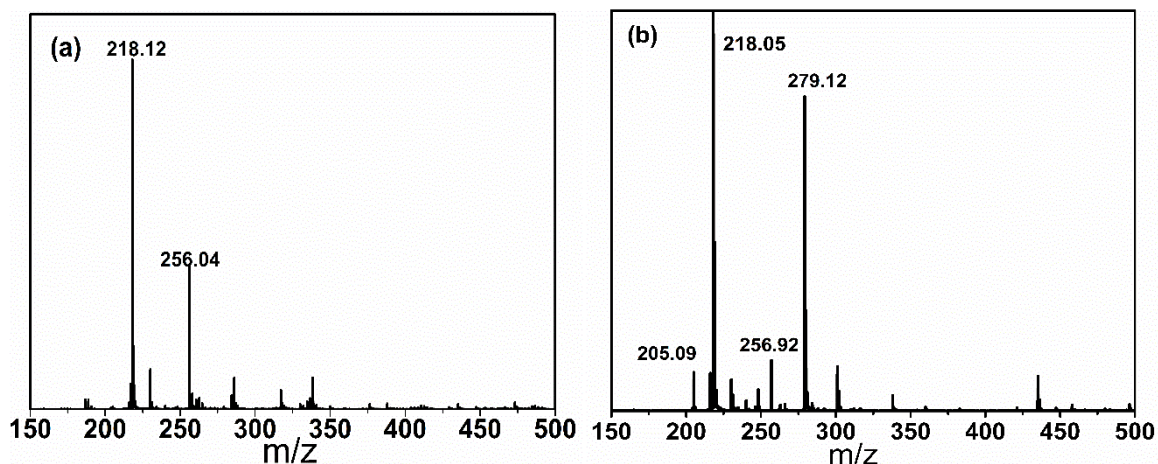


Figure 5.13: Mass spectra recorded (a) before and (b) after DIP sensing. Experimental conditions: DIP concentration 100 μ M, reaction volume 100 mL, pH 7.0 and KCl 0.5 M. Mass spectra was taken after appropriate dilution using acetonitrile.

Table 5.3: Peaks obtained from mass spectroscopy and their identification before reaction.

Product	Molecular mass	Observed molecular mass	Error/mole
$C_{12}H_{16}N_3O$ (4-MAA)	218.11	218.05	0.07
$C_{13}H_{19}N_3O_3$ (4-AAA)	279.11	279.12	0.01

Table 5.4: Peaks obtained from mass spectroscopy and their identification after reaction.

Species	Molecular mass	Observed molecular mass	Error/mole
$C_{12}H_{16}N_3O$ (4-MAA)	218.11	218.12	0.01
$C_{12}H_{13}N_3O_2$ (4-FAA)	250.07	256.9	6.03
$C_{11}H_{13}N_3O$ (4-AA)	205.11	205.09	0.02

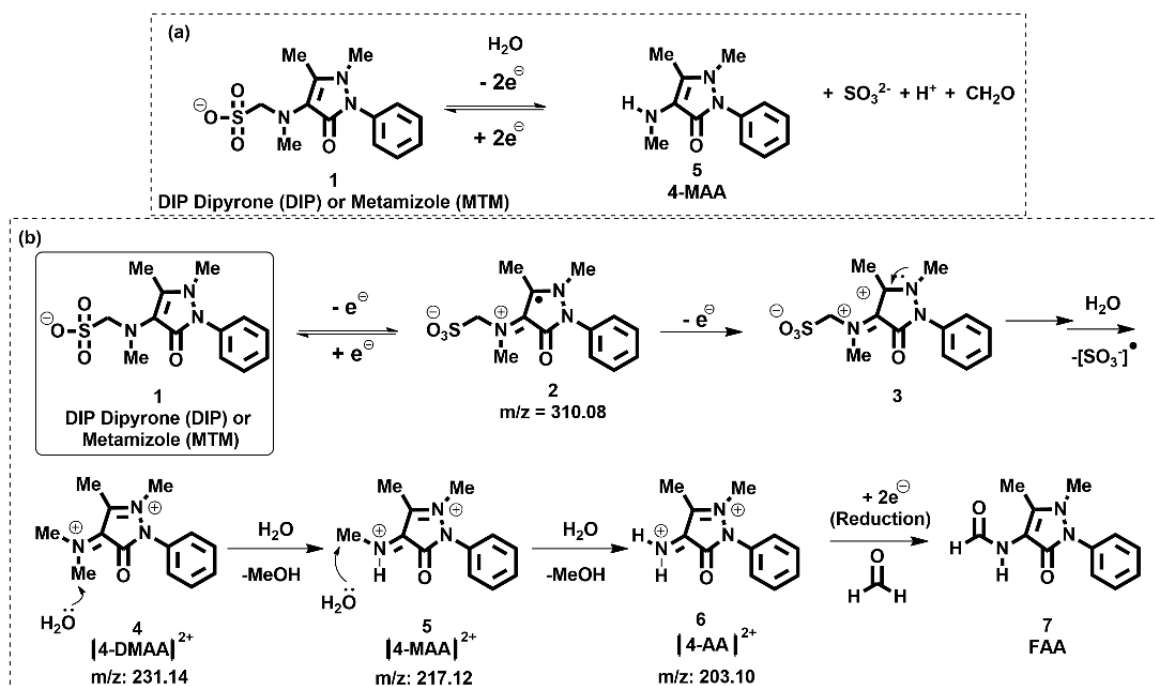


Figure 5.14: Schematic representation of the oxidation pathway of dipyrone.

5.2.3.2 Electrode stability and interference studies

In order to investigate the stability of the PtNPs/graphene/GCE, three pristine electrodes were employed for 10 individual voltammetry cycles in the presence of 15 μM DIP at the optimal condition of pH 7 with 0.5 M KCl as a supporting electrolyte (Figure 5.15). It was observed that there was no noticeable decrease in the peak current captured at 0.51 V vs. Ag/AgCl up to the 3rd cycle of the SWV runs (Figure 5.16a). After that, a gradual decrease in the peak current was observed with 20% decrease by the 10th cycle with a relative standard deviation of 8.6% (Figure 5.16a). This could be due to accumulation of stable oxidation products of DIP on the PtNPs/graphene/GCE. The experiments were triplicated and the error bar with standard deviation within 2.5% is indicative for an efficient reproducibility of DIP sensing at the PtNPs/graphene/GCE. These results are comparable with those reported earlier for electrochemical sensing of DIP using SWV (Gomes et al., 2019; Silva et al., 2020). A relative standard deviation of 6.6-8.6% was achieved for the sensing of DIP using polypyrrole-carbon nanotube modified GCE by using cyclic voltammetry (Özdokur and Koçak, 2019).

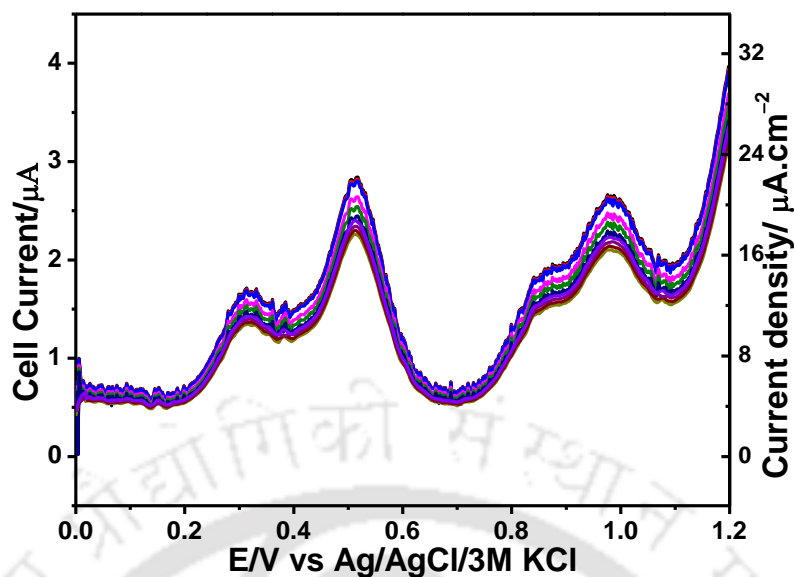


Figure 5.15: Square wave voltammetry (SWV) of PtNPs/graphene/GCE for 10 consecutive cycles using the same electrode to obtain the electrode stability. Experimental conditions: Reaction volume 100 mL, pH 7.0, KCl 0.5 M and DIP 15 μM . SWV parameters: step potential 4 mV pulse amplitude 25 mV, pulse frequency 15 Hz, scan rate of $60 \text{ mV} \cdot \text{s}^{-1}$, and scanning potential 0-1.2 V.

The chronoamperometry experiment was conducted through sequential addition of DIP, and the current response was recorded at 0.51 V vs. Ag/AgCl. A probable interference of different organic molecules, including a pharmaceutical drug on DIP sensing was done by adding 1 μM of each of the interfering molecules at an interval of 10 s. It was observed that there was no significant change in the response current due to the interferences, and the only change in the response current was noted with the addition of DIP (Figure 5.16b). The analytical results obtained by using the PtNPs/graphene/GCE is significantly better than those enlisted in Table S1 of the Supplementary Materials. Out of all the enlisted methods, SWV was found to be the most sensitive and gave better detection limits as compared to DPV and amperometry. The fabricated PtNPs/graphene nanocomposite exhibited good selectivity towards DIP in the presence of DA, UA, glucose and CIP even in concentrations twice as that of DIP. The work described by Gomes et al. showed an increased current response with simultaneous addition of AA, UA and acetaminophen during DIP sensing, and sequential addition did not show any effect on the current response (Ghica et al., 2015).

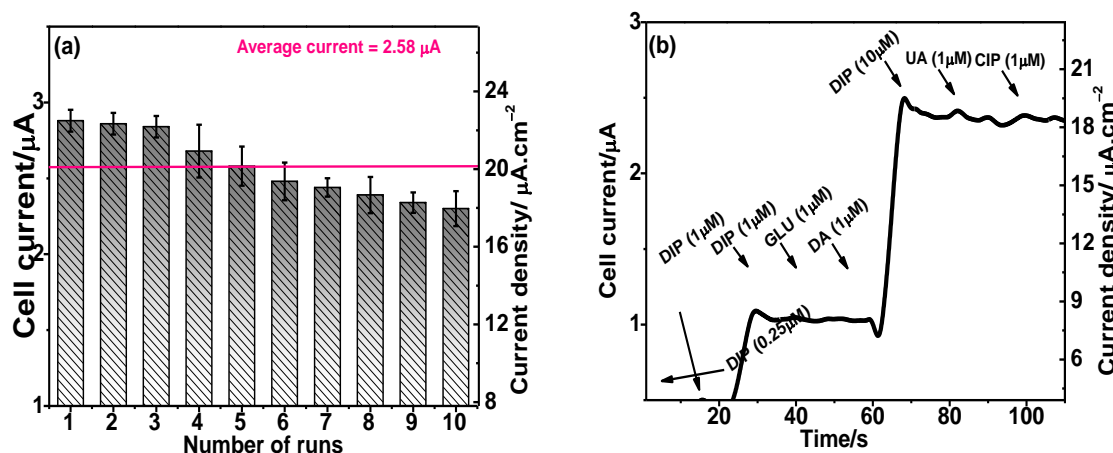


Figure 5.16: (a) Repeatability of DIP sensing using PtNPs/graphene/GCE in 10 different DIP solutions at the same concentration of 15 μM , and (b) Chronoamperometric profile showing the current response of DIP sensing in the presence of different interfering compounds (1 μM) at the set potential of 0.51 V vs. Ag/AgCl using 0.5 M KCl at pH 7.

5.2.3.3 Analysis of DIP spiked with environmental water samples

Water samples were collected from the sewage treatment plant and domestic water supply situated at IIT Guwahati Campus (India). These samples were spiked with a known concentration of DIP (Table 5.5), and the representative samples were then subjected to SWV for sensing of DIP at the PtNPs/graphene/GCE using the calibration curve obtained for the DIP concentration of 0–100 μM (Figure 5.11a). The sewage-water sample was filtered before the analysis using 0.2 μm nylon filter for the removal of suspended materials to avoid the fouling of the surface of PtNPs/graphene/GCE that could hamper the sensitivity of the sensor. The presence of organic carbon, inorganic carbon, nitrogenous compounds, and various anions in these samples are shown in Table 5.6 and Figure 5.17. The recovery of DIP concentration is shown in Table 5.5. Nearly, 100% recovery was noted in the case of both tap and sewage water samples. The relative standard deviation ranged between 0.26 and 2.09%, which is well within the acceptable limit.

The effect of the variation of DIP concentrations on its sensing at the PtNPs/graphene/GCE was also investigated in comparison with HPLC. The variation of DIP concentration in the case of tap-water was within 1.98 % and it was maximum 9 % for sewage-water samples. However, the variation was slightly more for the determination of DIP by HPLC for possible interference caused by dissolved constituents present in sewage-water samples. Whereas, DIP sensing at PtNPs/graphene/GCE was almost invariant (~100% recovery).

To mimic the natural environment condition, degradation products of DIP found in natural environment, a concentration of 0.5 μM DIP was prepared and left up to 48 h of environment exposure by keeping it in ambient conditions exposed to direct sunlight. The mass spectra were recorded at different time intervals to find the yields of degradation products of DIP (Figures 5.18a-5.18e). It was observed that 4-Methylaminoantipyrine (4-MAA, $m/z=218$) was present in all the samples. 4-MAA is the most common product that is formed in the presence of light in aqueous solution which have a half-life of 8.57 h (Burmańczuk et al., 2016). As the exposure time increased from 6 h to 48 h, products like 4-Amino antipyrine (4-AA, $m/z=203$) and Dimethylamino antipyrine (DMAA, $m/z=231$) and Formylamino antipyrine (4-FAA, $m/z=234$) were originated. Therefore, fast electrochemical sensing of DIP essentially generates oxidation products of DIP that could be found in most natural water samples (Gómez et al., 2007; Reis et al., 2013; Wiegel et al., 2004).

Table 5.5: Determination of DIP spiked in different real environmental water samples using PtNPs/graphene/GCE and HPLC.

Sample	DIP spiked (μM)	Performance of PtNPs/graphene/GCE			DIP determination using HPLC (μM)	Variation between two methods (%)
		DIP determination (μM)	Recovery (%)	RSD (%)		
Tap water	1	1.01	101.3	1.98	1.03	1.65
	10	10.02	100.15	0.68	9.87	1.44
	50	50.57	101.13	1.35	49.86	1.38
	100	99.89	99.89	0.26	98.69	1.20
Sewage water	1	0.99	99.6	2.09	1.08	7.77
	10	10.08	100.80	2.06	10.87	7.26
	50	49.93	99.86	0.50	48.26	3.34
	100	101.48	101.48	0.69	99.53	1.92

Table 5.6: Physico-chemical characterization of water samples.

Sl no.	Sample	TOC (mg.L^{-1})	TIC (mg.L^{-1})	TN (mg.L^{-1})	Anions (Refer to chromatogram Figure 5.17) (mg.L^{-1})
1	Tap Water	0.046	5.510	5.410	Cl^- , F^- , NO_3^- and SO_4^{2-}
2	Sewage water	5.620	11.890	39.730	Cl^- , F^- , NO_3^- , SO_4^{2-} and PO_4^{3-}

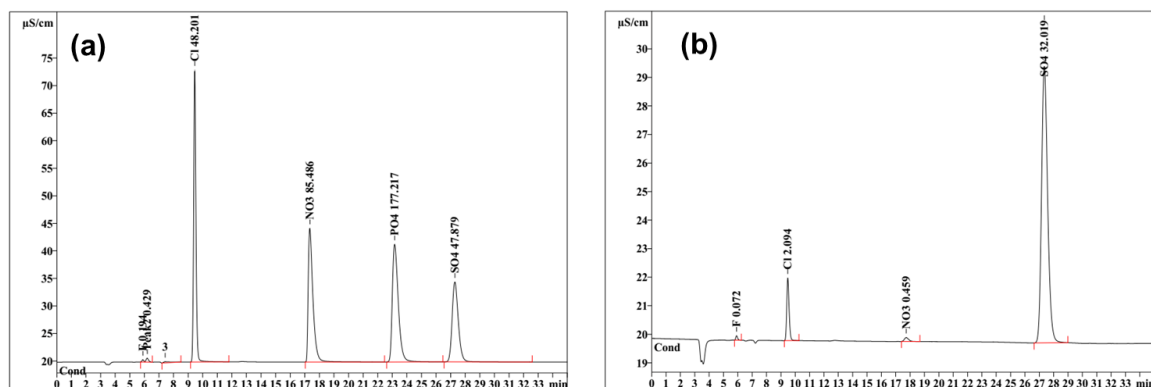


Figure 5.17: Ion-chromatograms of (a) Sewage water (filtered) and (b) Tap water used to prepare the samples spiked with DIP.

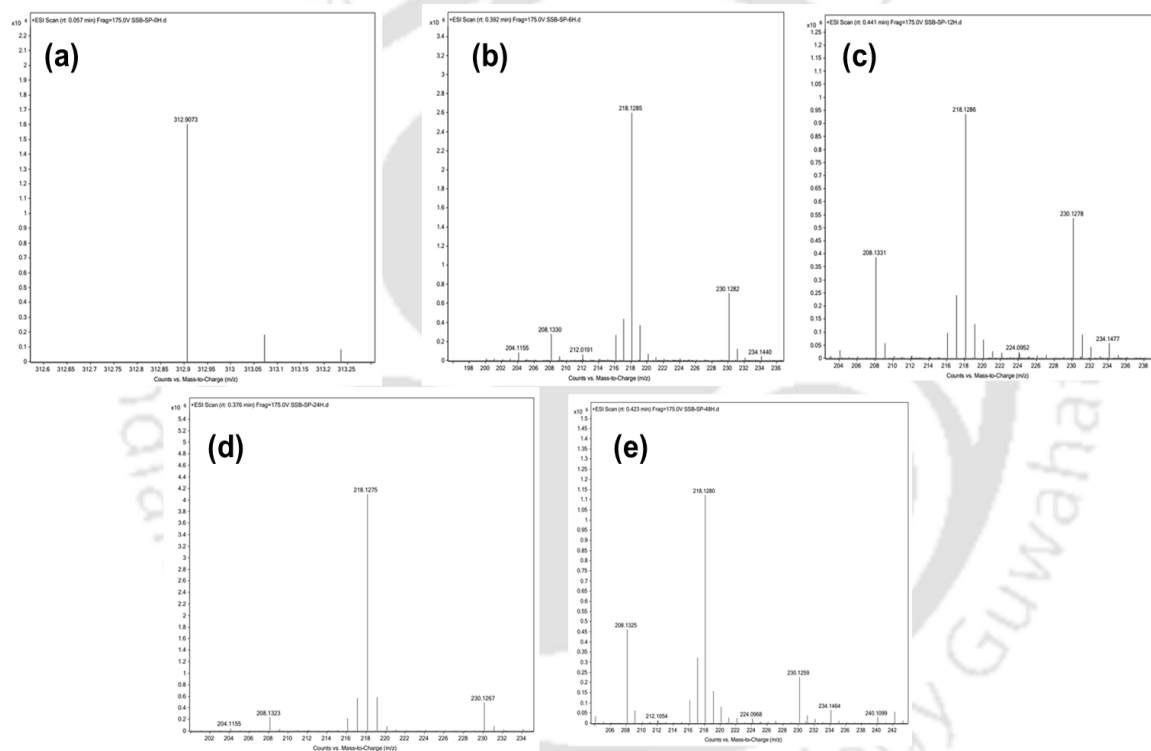


Figure 5.18: Mass spectra analysis of DIP in water exposed to environment for (A) 0 h, (B) 6 h, (C) 12 h, (D) 24 and (E) 24 h with an initial DIP concentration of 0.5 μM .

5.3 Major findings

One pot bio-inspired synthesis of PtNPs/graphene nanocomposite is successfully achieved in this study using leaves extract of *P. guajava*. However, the intrinsic variability of the composition of *P. guajava* leaves could affect the quality of nanocomposite. A mixture of acetone and water in the conjugation of sonication and microwave irradiation could successfully synthesize graphene sheets consisting of 6-7 layers. PtNPs/graphene nanocomposite was embedded on glassy carbon for an enhanced electrocatalytic sensing of DIP. The modified electrode (PtNPs/graphene/GCE) exhibited 50% fall in electrode resistance in comparison with bare GCE. The formal oxidation potential of DIP involving two electrons at the PtNPs/graphene/GCE was noted at 0.387 V vs. Ag/AgCl along with two fragmentation peaks at 0.755 and 0.956 V involving two and one electron transfer. The reaction mechanism in conjunction with the mass spectroscopy also confirmed two electrons oxidation of DIP followed by formation of two metabolic fragments. The rate constants of these reactions were determined to be 0.295×10^{-3} , 0.692×10^{-3} and $0.890 \times 10^{-3} \text{ s}^{-1}$, respectively. Two linear regimes of DIP sensing were observed at the PtNPs/graphene/GCE based on its concentration with a transition at 100 μM with a detection limit of 0.142 μM . DIP in the presence of common interferants and along its spiking with tap-water and sewage-water were conclusively determined at the PtNPs/graphene/GCE. Therefore, this work provides a platform for developing bio-inspired nanoparticles based electrochemical sensors that could be applied for the determination of pharmaceutically active compounds like DIP and help understand the mechanism involved for its sensing.

References

- Alleman, J.L., Dillon, A.C., Gennett, T., Parilla, P.A., Jones, K.M., Heben, M.J., 2010. ChemInform Abstract: A Simple and Complete Purification of Single-Walled Carbon Nanotube (SWNT) Materials. ChemInform 31, no-no. <https://doi.org/10.1002/chin.200001250>
- Amatatongchai, M., Sroysee, W., Chairam, S., Nacapricha, D., 2017. Amperometric flow injection analysis of glucose using immobilized glucose oxidase on nano-composite carbon nanotubes-platinum nanoparticles carbon paste electrode. Talanta 166, 420–427. <https://doi.org/10.1016/j.talanta.2015.11.072>
- Ateş, A.K., Er, E., Çelikkan, H., Erk, N., 2017. Reduced graphene oxide/platinum nanoparticles/nafiion nanocomposite as a novel 2D electrochemical sensor for voltammetric determination of aliskiren. New J. Chem. 41, 15320–15326. <https://doi.org/10.1039/c7nj00569e>
- Bacil, R.P., Buoro, R.M., Campos, O.S., Ramos, M.A., Sanz, C.G., Serrano, S.H.P., 2018. Electrochemical behaviour of dipyrone (metamizole) and others pyrazolones. Electrochim. Acta 273, 358–366. <https://doi.org/10.1016/j.electacta.2018.04.082>
- Baranowska, I., Markowski, P., Gerle, A., Baranowski, J., 2008. Determination of selected drugs in human urine by differential pulse voltammetry technique. Bioelectrochemistry 73, 5–10. <https://doi.org/10.1016/j.bioelechem.2008.04.022>
- Barbalho, S.M., 2012. Psidium Guajava (Guava): A Plant of Multipurpose Medicinal Applications. Med. Aromat. Plants 01, 1–6. <https://doi.org/10.4172/2167-0412.1000104>
- Berry, R.J., 1978. Study of multilayer surface oxidation of platinum by electrical resistance technique. Surf. Sci. 76, 415–442. [https://doi.org/10.1016/0039-6028\(78\)90106-1](https://doi.org/10.1016/0039-6028(78)90106-1)
- Bose, D., Chatterjee, S., 2016. Biogenic synthesis of silver nanoparticles using guava (Psidium guajava) leaf extract and its antibacterial activity against Pseudomonas aeruginosa. Appl. Nanosci. 6, 895–901. <https://doi.org/10.1007/s13204-015-0496-5>
- Burmańczuk, A., Kowalski, C., Giorgi, M., Owen, H., Grabowski, T., 2016. Pharmacokinetic investigations of the marker active metabolites 4-methylamino-antipyrine and 4-amino-antipyrine after intramuscular injection of metamizole in healthy piglets. J. Vet. Pharmacol. Ther. 39, 616–620. <https://doi.org/10.1111/jvp.12317>
- Chipeture, A.T., Apath, D., Moyo, M., 2019. Multiwalled carbon nanotubes decorated with

- bismuth (III) oxide for electrochemical detection of an antipyretic and analgesic drug paracetamol in biological samples. *J. Anal. Sci. Technol.* 5. <https://doi.org/https://doi.org/10.1186/s40543-019-0181-5>
- de Faria, L.V., Lisboa, T.P., Azevedo, G.C., Sousa, R.A., Costa Matos, M.A., Muñoz, R.A.A., Camargo Matos, R., 2019. Chemically-reduced Graphene Oxide Sensor for Dipyrone Quantification in Pharmaceutical Samples Using Amperometric Detection. *Electroanalysis* 31, 646–651. <https://doi.org/10.1002/elan.201800784>
- Di Pietra, A.M., Gatti, R., Andrisano, V., Cavrini, V., 1996. Application of high-performance liquid chromatography with diode-array detection and on-line post-column photochemical derivatization to the determination of analgesics. *J. Chromatogr. A* 729, 355–361. [https://doi.org/10.1016/0021-9673\(95\)01037-8](https://doi.org/10.1016/0021-9673(95)01037-8)
- Díaz-de-Cerio, E., Gómez-Caravaca, A.M., Verardo, V., Fernández-Gutiérrez, A., Segura-Carretero, A., 2016. Determination of guava (*Psidium guajava* L.) leaf phenolic compounds using HPLC-DAD-QTOF-MS. *J. Funct. Foods* 22, 376–388. <https://doi.org/10.1016/j.jff.2016.01.040>
- Do Carmo, D.R., Barbosa, P.F.P., Cumba, L.R., 2019. Electrochemical Behavior of Titanium (IV) Silsesquioxane Occluded in the MCM-41 Cavity and their Application in the Electro-Oxidation of Sulphite and Dipyrone Compounds. *Silicon*. <https://doi.org/10.1007/s12633-019-00215-4>
- Elgrishi, N., Rountree, K.J., McCarthy, B.D., Rountree, E.S., Eisenhart, T.T., Dempsey, J.L., 2018. A Practical Beginner's Guide to Cyclic Voltammetry. *J. Chem. Educ.* 95, 197–206. <https://doi.org/10.1021/acs.jchemed.7b00361>
- Er, E., Çelikkan, H., Erk, N., 2017. A novel electrochemical nano-platform based on graphene/platinum nanoparticles/nafion composites for the electrochemical sensing of metoprolol. *Sensors Actuators, B Chem.* 238, 779–787. <https://doi.org/10.1016/j.snb.2016.07.108>
- Ferrari, A.C., Meyer, J.C., Scardaci, V., Casiraghi, C., Lazzeri, M., Mauri, F., Piscanec, S., Jiang, D., Novoselov, K.S., Roth, S., Geim, A.K., 2006. Raman Spectrum of Graphene and Graphene Layers 187401, 1–4. <https://doi.org/10.1103/PhysRevLett.97.187401>
- Ghica, M.E., Ferreira, G.M., Brett, C.M.A., 2015. Poly(thionine)-carbon nanotube modified carbon film electrodes and application to the simultaneous determination of acetaminophen and dipyrone. *J. Solid State Electrochem.* 19, 2869–2881. <https://doi.org/10.1007/s10008-015-2926-4>

- Giri, A.S., Golder, A.K., 2014. Fenton, photo-fenton, H₂O₂ Photolysis, and TiO₂ Photocatalysis for Dipyrone Oxidation: Drug Removal, Mineralization, Biodegradability, and Degradation Mechanism. *Ind. Eng. Chem. Res.* 53, 1351–1358. <https://doi.org/10.1021/ie402279q>
- Gomes, R.N., Bezerra-Neto, J.R., Sousa, C.P., Medeiros, S.L.S., Becker, H., Soares, J.E.S., de Lima-Neto, P., Correia, A.N., 2019. Understanding the dipyrone oxidation allying electrochemical and computational approaches. *Anal. Chim. Acta* 1051, 49–57. <https://doi.org/10.1016/j.aca.2018.11.035>
- Gómez, M.J., Martínez Bueno, M.J., Lacorte, S., Fernández-Alba, A.R., Agüera, A., 2007. Pilot survey monitoring pharmaceuticals and related compounds in a sewage treatment plant located on the Mediterranean coast. *Chemosphere* 66, 993–1002. <https://doi.org/10.1016/j.chemosphere.2006.07.051>
- Gopu, G., Muralidharan, B., Vedhi, C., Manisankar, P., 2012. Determination of three analgesics in pharmaceutical and urine sample on nano poly (3, 4-ethylenedioxythiophene) modified electrode. *Ionics (Kiel)*. 18, 231–239. <https://doi.org/10.1007/s11581-011-0619-2>
- Gowda, J.I., Nandibewoor, S.T., 2014. Simultaneous electrochemical determination of 4-aminophenazone and caffeine at electrochemically pre-treated graphite pencil electrode. *Anal. Methods* 6, 5147–5154. <https://doi.org/10.1039/c4ay00467a>
- Graf, D., Molitor, F., Ensslin, K., Stampfer, C., Jungen, A., Hierold, C., Wirtz, L., 2007. Spatially resolved raman spectroscopy of single- and few-layer graphene. *Nano Lett.* 7, 238–242. <https://doi.org/10.1021/nl061702a>
- Gutić, S., Dobrota, A.S., Gavrilov, N., Baljuzović, M., Pašti, I.A., Mentus, S. V., 2016. Surface charge storage properties of selected graphene samples in pH-neutral aqueous solutions of alkali metal chlorides - particularities and universalities. *Int. J. Electrochem. Sci.* 11, 8662–8682. <https://doi.org/10.20964/2016.10.47>
- Habekost, A., 2018. The Analgesic Metamizole (Dipyrone) and Its Related Products Antipyrine, 4-Aminoantipyrine and 4-Methylaminoantipyrine. Part 1: Mass Spectrometric and Electrochemical Detection. *World J. Chem. Educ.* 6, 134–144. <https://doi.org/10.12691/wjce-6-3-6>
- Hernandez, Y., Nicolosi, V., Lotya, M., Blighe, F.M., Sun, Z., De, S., McGovern, I.T., Holland, B., Byrne, M., Gun'ko, Y.K., Boland, J.J., Niraj, P., Duesberg, G., Krishnamurthy, S., Goodhue, R., Hutchison, J., Scardaci, V., Ferrari, A.C., Coleman, J.N., 2008. High-yield production of graphene by liquid-phase exfoliation of graphite.

- Nat. Nanotechnol. 3, 563–568. <https://doi.org/10.1038/nnano.2008.215>
- Higgins, D., Zamani, P., Yu, A., Chen, Z., 2016. The application of graphene and its composites in oxygen reduction electrocatalysis: a perspective and review of recent progress. *Energy Environ. Sci.* 9, 357–390. <https://doi.org/10.1039/C5EE02474A>
- Kalambate, P.K., Sanghavi, B.J., Karna, S.P., Srivastava, A.K., 2015. Simultaneous voltammetric determination of paracetamol and domperidone based on a graphene/platinum nanoparticles/nafion composite modified glassy carbon electrode. *Sensors Actuators, B Chem.* 213, 285–294. <https://doi.org/10.1016/j.snb.2015.02.090>
- Kang, X., Wang, J., Wu, H., Liu, J., Aksay, I.A., Lin, Y., 2010. A graphene-based electrochemical sensor for sensitive detection of paracetamol. *Talanta* 81, 754–759. <https://doi.org/10.1016/j.talanta.2010.01.009>
- Khalilzadeh, M.A., Borzoo, M., 2016. ScienceDirect Green synthesis of silver nanoparticles using onion extract and their application for the preparation of a modified electrode for determination of ascorbic acid. *J. Food Drug Anal.* 24, 796–803. <https://doi.org/10.1016/j.jfda.2016.05.004>
- Krokos, A., Tsakelidou, E., Michopoulou, E., Raikos, N., Id, G.T., Gika, H., 2018. NSAIDs Determination in Human Serum by GC-MS. *Separations* 5, 5–7. <https://doi.org/10.3390/separations5030037>
- Li, Y., Gao, W., Ci, L., Wang, C., Ajayan, P.M., 2010. Catalytic performance of Pt nanoparticles on reduced graphene oxide for methanol electro-oxidation. *Carbon N. Y.* 48, 1124–1130. <https://doi.org/10.1016/j.carbon.2009.11.034>
- Liu, H., Zhang, H., Wang, J., Wei, J., 2020. Effect of temperature on the size of biosynthesized silver nanoparticle: Deep insight into microscopic kinetics analysis. *Arab. J. Chem.* 13, 1011–1019. <https://doi.org/10.1016/j.arabjc.2017.09.004>
- Malesevic, A., Vitchev, R., Schouteden, K., Volodin, A., Zhang, L., Tendeloo, G. Van, Vanhulsel, A., Haesendonck, C. Van, 2008. Synthesis of few-layer graphene via microwave plasma-enhanced chemical vapour deposition. *Nanotechnology* 19. <https://doi.org/10.1088/0957-4484/19/30/305604>
- Martin, C.S., Teixeira, M.F.S., 2012. Electrocatalytic study of an electrode modified with Reactive Blue 4 dye covalently immobilized on amine-functionalized silica 3877–3886. <https://doi.org/10.1007/s10008-012-1829-x>
- Martin Santos, A., Wong, A., Araújo Almeida, A., Fatibello-Filho, O., 2017. Simultaneous determination of paracetamol and ciprofloxacin in biological fluid samples using a

- glassy carbon electrode modified with graphene oxide and nickel oxide nanoparticles. *Talanta* 174, 610–618. <https://doi.org/10.1016/j.talanta.2017.06.040>
- Meyer, J.C., Geim, A.K., Katsnelson, M.I., Novoselov, K.S., Booth, T.J., Roth, S., 2007. The structure of suspended graphene sheets 446. <https://doi.org/10.1038/nature05545>
- Miyazawa, K., Shimomura, S., Yoshitake, M., Tanaka, Y., 2019. HRTEM structural characterization of platinum nanoparticles loaded on carbon black particles using focused ion beam milling. *Mater. Lett.* 237, 96–100. <https://doi.org/10.1016/j.matlet.2018.11.086>
- Muñoz, R.A.A., Matos, R.C., Angnes, L., 2001. Amperometric determination of dipyrone in pharmaceutical formulations with a flow cell containing gold electrodes from recordable compact discs. *J. Pharm. Sci.* 90, 1972–1977. <https://doi.org/10.1002/jps.1148>
- Muralidharan, B., Gopu, G., Vedhi, C., Manisankar, P., 2008. Voltammetric determination of analgesics using a montmorillonite modified electrode. *Appl. Clay Sci.* 42, 206–213. <https://doi.org/10.1016/j.clay.2007.11.005>
- Nemade, K.R., Waghuley, S.A., 2013. Chemiresistive gas sensing by few-layered graphene. *J. Electron. Mater.* 42, 2857–2866. <https://doi.org/10.1007/s11664-013-2699-4>
- Odetola, C., Trevani, L.N., Easton, E.B., 2017. Photo enhanced methanol electrooxidation: Further insights into Pt and TiO₂ nanoparticle contributions. *Appl. Catal. B Environ.* 210, 263–275. <https://doi.org/10.1016/j.apcatb.2017.03.027>
- Özdokur, V., Kocak, Ç.C., 2019. Voltammetric Determination of Metamizol Sodium in Pharmaceutical Tablets at Polypyrrole-Carbon Nanotube Modified Electrodes. *Erzincan Üniversitesi Fen Bilim. Enstitüsü Derg.* 12, 317–325. <https://doi.org/10.18185/erzifbed.460554>
- Paixão, T.R.L.C., 2020. Measuring Electrochemical Surface Area of Nanomaterials versus the Randles–Ševčík Equation. *ChemElectroChem* 7, 3414–3415. <https://doi.org/10.1002/celec.202000633>
- Pauliukaite, R., Emilia Ghica, M., Fatibello-Filho, O., M.A. Brett, C., 2012a. Graphite-Epoxy Electrodes Modified with Functionalised Carbon Nanotubes and Chitosan for the Rapid Electrochemical Determination of Dipyrone. *Comb. Chem. High Throughput Screen.* 13, 590–598. <https://doi.org/10.2174/1386207311004070590>
- Pauliukaite, R., Emilia Ghica, M., Fatibello-Filho, O., M.A. Brett, C., 2012b. Graphite-Epoxy Electrodes Modified with Functionalised Carbon Nanotubes and Chitosan for

- the Rapid Electrochemical Determination of Dipyrone. *Comb. Chem. High Throughput Screen.* 13, 590–598. <https://doi.org/10.2174/1386207311004070590>
- Pauliukaite, R., Emilia Ghica, M., Fatibello-Filho, O., M.A. Brett, C., 2010a. Graphite-Epoxy Electrodes Modified with Functionalised Carbon Nanotubes and Chitosan for the Rapid Electrochemical Determination of Dipyrone. *Comb. Chem. High Throughput Screen.* 13, 590–598. <https://doi.org/10.2174/1386207311004070590>
- Pauliukaite, R., Ghica, M.E., Fatibello-filho, O., Brett, C.M.A., 2010b. Graphite-Epoxy Electrodes Modified with Functionalised Carbon Nanotubes and Chitosan for the Rapid Electrochemical Determination of Dipyrone. *Graphite-Epoxy Electrodes Modified with Functionalised Carbon Nanotubes and Chitosan for the Rapid Electrochemical.* *Comb. Chem. High Throughput Screen.* 13, 590–598. <https://doi.org/10.2174/1386207311004070590>
- Pitarch, E., Portolés, T., Marín, J.M., Ibáñez, M., 2010. Analytical strategy based on the use of liquid chromatography and gas chromatography with triple-quadrupole and time-of-flight MS analyzers for investigating organic contaminants in wastewater. *Anal Bioanal Chem* 2763–2776. <https://doi.org/10.1007/s00216-010-3692-x>
- Rajamani, A.R., Peter, S.C., 2018. Novel Nanostructured Pt/CeO₂@Cu₂O Carbon-Based Electrode To Magnify the Electrochemical Detection of the Neurotransmitter Dopamine and Analgesic Paracetamol. *ACS Appl. Nano Mater.* 1, 5148–5157. <https://doi.org/10.1021/acsanm.8b01217>
- Rajaram, R., Anandhakumar, S., Mathiyarasu, J., 2015. Electrocatalytic oxidation of NADH at low overpotential using nanoporous poly(3,4)-ethylenedioxythiophene modified glassy carbon electrode. *J. Electroanal. Chem.* 746, 75–81. <https://doi.org/10.1016/j.jelechem.2015.03.028>
- Rasappa, S., Ghoshal, T., Borah, D., Senthamarikannan, R., Holmes, J.D., Morris, M.A., 2015. A Highly Efficient Sensor Platform Using Simply Manufactured Nanodot Patterned Substrates. *Sci. Rep.* 5, 1–11. <https://doi.org/10.1038/srep13270>
- Reis, R.M.H., Baio, J.A.F., Migliorini, F.L., Rocha, R.D.S., Baldan, M.R., Ferreira, N.G., Lanza, M.R.D.V., 2013. Degradation of dipyrone in an electrochemical flow-by reactor using anodes of boron-doped diamond (BDD) supported on titanium. *J. Electroanal. Chem.* 690, 89–95. <https://doi.org/10.1016/j.jelechem.2012.12.003>
- Rountree, E.S., McCarthy, B.D., Eisenhart, T.T., Dempsey, J.L., 2014. Evaluation of homogeneous electrocatalysts by cyclic voltammetry. *Inorg. Chem.* 53, 9983–10002.

<https://doi.org/10.1021/ic500658x>

- Senyuva, H.Z., Aksahin, I., Ozcan, S., 2005. Rapid , simple and accurate liquid chromatography – diode array detection validated method for the determination of dipyrone in solid and liquid dosage forms. *Anal. Chim. Acta* 547, 73–77. <https://doi.org/10.1016/j.aca.2004.12.053>
- Silva, L.R.G., dos Santos, G.F.S., Vasconcellos, M.L.S., Ferreira, R. de Q., 2020. Development of electroanalytical procedure for monitoring of metamizole in organic fertilizers (human urine and struvite) associated with portable equipment. *J. Environ. Manage.* 266, 110587. <https://doi.org/10.1016/j.jenvman.2020.110587>
- Siswana, M.P., Ozoemena, K.I., Nyokong, T., 2006. Electrocatalysis of asulam on cobalt phthalocyanine modified multi-walled carbon nanotubes immobilized on a basal plane pyrolytic graphite electrode. *Electrochim. Acta* 52, 114–122. <https://doi.org/10.1016/j.electacta.2006.03.090>
- Švorc, L., Strežová, I., Kianičková, K., Stanković, D.M., Otrisal, P., Samphao, A., 2018. An advanced approach for electrochemical sensing of ibuprofen in pharmaceuticals and human urine samples using a bare boron-doped diamond electrode. *J. Electroanal. Chem.* 822, 144–152. <https://doi.org/10.1016/j.jelechem.2018.05.026>
- Tang, H., Chen, J., Nie, L., Liu, D., Deng, W., Kuang, Y., Yao, S., 2004. High dispersion and electrocatalytic properties of platinum nanoparticles on graphitic carbon nanofibers (GCNFs). *J. Colloid Interface Sci.* 269, 26–31. [https://doi.org/10.1016/S0021-9797\(03\)00608-8](https://doi.org/10.1016/S0021-9797(03)00608-8)
- Teixeira, M.F.S., Dadamos, T.R.L., 2009. An electrochemical sensor for dipyrone determination based on nickel-salen film modified electrode. *Procedia Chem.* 1, 297–300. <https://doi.org/10.1016/j.proche.2009.07.074>
- Wang, Y., Limon-Petersen, J.G., Compton, R.G., 2011. Measurement of the diffusion coefficients of $[\text{Ru}(\text{NH}_3)_6]^{3+}$ and $[\text{Ru}(\text{NH}_3)_6]^{2+}$ in aqueous solution using microelectrode double potential step chronoamperometry. *J. Electroanal. Chem.* 652, 13–17. <https://doi.org/10.1016/j.jelechem.2010.12.011>
- Wiegel, S., Aulinger, A., Brockmeyer, R., Harms, H., Löffler, J., Reincke, H., Schmidt, R., Stachel, B., Von Tümpling, W., Wanke, A., 2004. Pharmaceuticals in the river Elbe and its tributaries. *Chemosphere* 57, 107–126. <https://doi.org/10.1016/j.chemosphere.2004.05.017>
- Yi, M., Shen, Z., Zhang, X., Ma, S., 2013. Achieving concentrated graphene dispersions in water/acetone mixtures by the strategy of tailoring Hansen solubility parameters. *J.*

Phys. D. Appl. Phys. 46. <https://doi.org/10.1088/0022-3727/46/2/025301>

Zhang, M., Liao, C., Mak, C.H., You, P., Mak, C.L., Yan, F., 2015. Highly sensitive glucose sensors based on enzyme-modified whole-graphene solution-gated transistors 1–6. <https://doi.org/10.1038/srep08311>

Zhou, M., Zhai, Y., Dong, S., 2009. Electrochemical sensing and biosensing platform based on chemically reduced graphene oxide. *Anal. Chem.* 81, 5603–5613. <https://doi.org/10.1021/ac900136z>

Zorita, S., Mårtensson, L., Mathiasson, L., 2009. Occurrence and removal of pharmaceuticals in a municipal sewage treatment system in the south of Sweden. *Sci. Total Environ.* 407, 2760–2770. <https://doi.org/10.1016/j.scitotenv.2008.12.030>

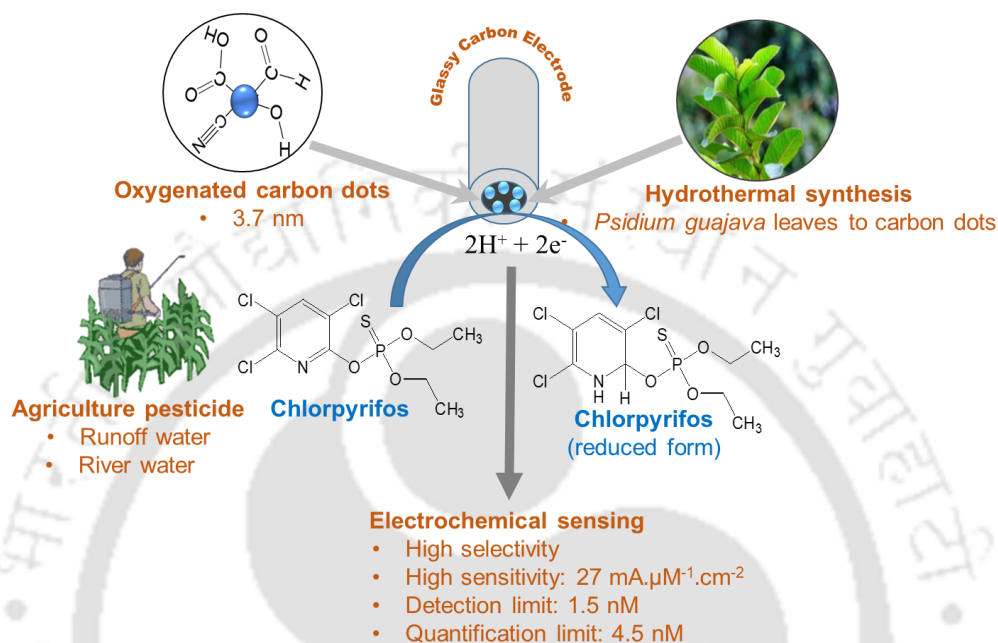
Zou, J., Liu, Z., Guo, Y., Dong, C., 2017. Electrochemical sensor for the facile detection of trace amounts of bisphenol A based on cyclodextrin-functionalized graphene/platinum nanoparticles. *Anal. Methods* 9, 134–140. <https://doi.org/10.1039/c6ay02719a>



This page is intentionally left blank

CHAPTER 6

Electrocatalytic Sensing of Chlorpyrifos using Carbon Dots Derived from Waste *Psidium Guajava* Leaves Biomass



Highlights

- ◆ Hydrothermal synthesis of carbon dots derived from waste *Psidium guajava* leaves biomass
- ◆ An electrochemical sensor based on Carbon Dots modified GCE for Chlorpyrifos sensing
- ◆ Simultaneous studies to investigate the electro-kinetics involved during the chlorpyrifos sensing at the electrode surface
- ◆ An electrochemical mechanism of Chlorpyrifos hydrogenation was proposed based on LC-MS data
- ◆ Proposed sensor was tested in agricultural samples and environmental water samples collected from river

6.1 Background and executive motivation

Pesticides are being used in agriculture to fulfil the increased demand for foods of the growing population. However, the use of pesticides is causing trouble to the environment and health as the residues of applied pesticides remain in the soil, ground and surface water, and in the air for variable periods of time. Out of 100 types of toxic organophosphate compounds, Chlorpyrifos (CHL; O,O-diethyl O-(3,5,6-trichloro-2-pyridyl) phosphorothioate) is still widely in use as an organic phosphate pesticide. Chlorpyrifos (CHL) possessing a low water solubility (1.39 mg.L^{-1}) and a high soil sorption coefficient ($271\text{-}385 \text{ L.kg}^{-1}$) (Gavrilescu, 2005; Gebremariam et al., 2012). It is highly effective in tackling the adverse effect of a broad spectrum of insect pests damaging economically important crops (Singh, 2009). However, as with other organophosphate pesticides, CHL is also known to have a toxic effect by inhibition of acetylcholinesterase enzymes' activity, which is responsible for the hydrolysis of acetylcholine, a crucial molecule in the control and transmission of neural signals in the nervous system. CHL is used in domestic and agricultural sectors to control mosquitoes, flies, insects, and pests. It is also used to control ectoparasitic infections in sheep and cattle (Mohan et al., 2004). The increased use of CHL leads to its accumulation in high concentrations in the environment, causing toxic effects on humans and animals (De Silva and Samayawardhena, 2005). CHL remains in the soil for an extended period with average $t_{1/2}$ ranging between 49.5 and 120 days depending on the soil type and could cause health hazards to humans and animals (Chai et al., 2013; Gaudet et al., 1995). CHL is a moderately toxic pesticide (Cometa et al., 2007) exhibiting long-term health effects (Ray, 1998; Richardson et al., 1993). Therefore, the detection and degradation of CHL in soil, water and the air are of great importance for solving the poisonous effect of pesticides on the environment and biological health (Albanis and Hela, 1995; Singh, 2009).

Among the various strategies, gas chromatography (Oliva et al., 1999), negative ion chemical ionization gas chromatography, mass spectrometry (Brzak et al., 1998), and high-performance liquid chromatography are well established analytical methods for the determination of CHL (Mauldin et al., 2006). However, the associated expenses could be a bar for typical laboratory installations as well as for the field applications, and it also involves a complex sample preparation process.

Therefore, it is essential to develop extremely sensitive, low-cost, sustainable, and portable devices for the analysis of organophosphate pesticides. Electroanalytical

techniques exhibit the advantage of being highly selective towards the target analyte and show good responsiveness that can be controlled or modified by tweaking the working electrode surface. They provide the feasibility of miniaturization and portability for the application in the on-field analysis.

Biomass residue is generated in the bioinspired synthesis of metal nanoparticles (Chapters 3-5). This work investigates the valorization potential of leftover biomass residue for the synthesis of nanostructured materials for electrochemical sensing applications. Therefore, the objective of this chapter is framed as “Hydrothermal synthesis of carbon dots using *Psidium guajava* leaves biomass for enhanced electrocatalytic sensing of chlorpyrifos organophosphate insecticide.”

The carbon dots (CDs), a quantum-sized carbon material, are highly hydrophilic, show good biocompatibility, and possess brilliant photoluminescence properties (Ding et al., 2018; Essner et al., 2016; Ma et al., 2017). The light-absorbing property of CDs renders them suitable for photocatalysis, energy conversion, optoelectronic devices, and chemical sensors (Luo et al., 2016). The properties of CDs like high surface area ($200\text{-}1500\text{ m}^2\cdot\text{g}^{-1}$), excellent electrical conductivity ($0.26\text{-}2.6\text{ mS}\cdot\text{m}^{-1}$), and high sorption capacity ($\sim 96\text{ mg}\cdot\text{g}^{-1}$) has been comprehended to enhance the electron transfer kinetics, reduce overpotentials, and improve electrochemical sensitivities (Asadian et al., 2019). The presence of carboxylic acid, hydroxyl, nitrile, and ketone groups on CDs helps in catalyzing various electrochemical reactions involving complex molecules. CDs increase the adsorptive properties of the working electrodes due to their enhanced π - π interactions with various complex analytes (Campuzano et al., 2019). CDs have been used in electrochemical sensing of pharmaceutical compounds like paracetamol, phenylephrine, dextromethorphan, and azathioprine (Amiri et al., 2014; Shahrokhian and Ghalkhani, 2009). In a recent study, the addition of CDs into ZrO_2 significantly increased the electrochemical signals of methyl parathion by almost 100%, with a detection limit of $0.056\text{ ng}\cdot\text{mL}^{-1}$ (Reddy et al., 2019). CDs can be produced from various low-cost materials like graphite, carbon fibres, and biomass obtained from plant materials by a ‘top-down’ approach (Lu et al., 2011; Tan et al., 2015; Zhu et al., 2015). Synthesis of CDs from such materials generally involves the use of acids to digest the larger polymers and convert the carbon precursors into carbonaceous nanomaterials. Owing to the environmental hazards associated with these methods, they are not considered as ‘green methods’.

It is previously known that proper control of the hydrothermal parameters could yield tunable size and surface functional groups of CDs (Sakdaronnarong et al., 2020).

Herein in Chapter 6, CDs were synthesized by utilizing the precursors such as citric acid, glucose, and polysaccharides present in waste *Psidium (P.) guajava* leaves in the green and facile hydrothermal method. The surface functional groups present on CDs were exploited to catalyze the electrochemical sensing of CHL on a glassy carbon electrode (GCE) decorated with CDs derived from waste *P. guajava* leaves. The sensing performance of the modified electrode (GCE/CDs) was tested for the determination of CHL present in agriculture grade pesticide and in river water, and it was then compared with High-performance liquid chromatography. The use of biomass-derived CDs for the electrochemical sensing of CHL is going to be a new study to the best of our knowledge.

6.2 Results and Discussion

6.2.1 Synthesis and characterization of CDs

6.2.1.1 Optimization of reaction temperature

The temperature has an important role in the synthesis of CDs. It helps in the breakage of various chemical bonds present in lignin, cellulose, and hemicellulose components of the leaves biomass. It also helps in the release of the volatile substances during the hydrothermal reactions that dictate the morphology and the surface properties of the synthesized CDs. The optimal temperature for the synthesis was found by varying the temperature from 160 to 200°C with a reaction time of 10 h selected based on the previous report (Wongso et al., 2020). A reaction time of 10 h could produce CDs with some crystallinity intact, known to have enhanced electrical conductivity (Pal et al., 2020). At the synthesis temperature of 160°C, aggregated biomass with the cellulose fibers was still intact as is evident from the TEM micrograph (Figure 6.1a). The formation of monodisperse CDs was obtained at a temperature of 180°C with an average particle size of 7.2 nm (Figure 6.1b). CDs size was decreased further to 200°C. Highly monodispersed CDs (polydispersity index is only 16.1%) with an average particle size of 3.7 nm were found at this temperature (Figure 6.1c). Further increase beyond 200°C could show a decrease in the yield of the synthesis of CDs (Hoekman et al., 2011; Sun et al., 2011). This could be due to the conversion of organic acids, monosaccharides, and oligosaccharides present in the leaves biomass to a form that is incapable of taking part in the CDs growth (Wang et al., 2020). Therefore, CDs synthesized at 200°C were used in the subsequent investigations.

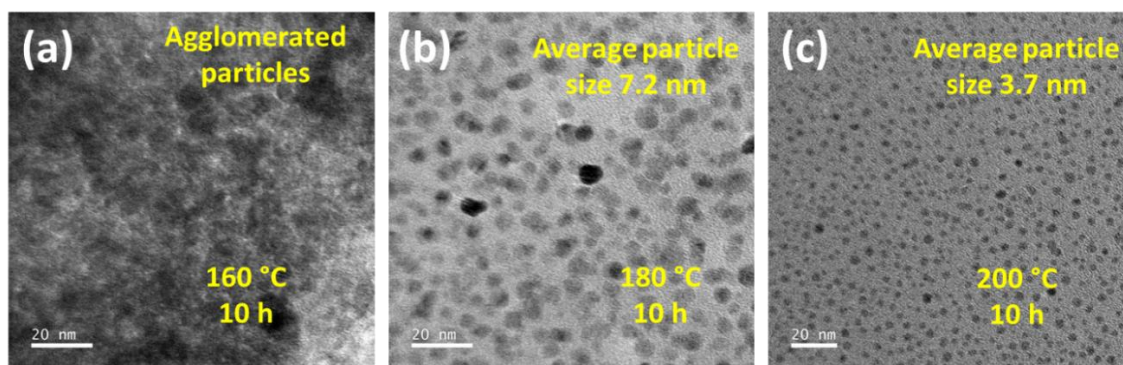


Figure 6.1: TEM micrographs of CDs formed from dried *P. guajava* leaves after a hydrothermal reaction for 10 h at different temperatures of (a) 160°C, (b) 180°C and (c) 200°C.

6.2.1.2 Physiochemical attributes of synthesized CDs

CDs show a typical excitation-dependent fluorescence property (Figure. 6.2a). An increase in the excitation wavelength from around 300 to 400 nm effectuates a redshift in the emission peak from 440 to 620 nm. The emission wavelength peak was observed at 450 nm under the excitation of 370 nm. The excitation-dependent emission behavior is attributed to the defects created due to the presence of various functional groups on the CDs surface (Huang et al., 2019; Zhao et al., 2020).

The presence of various functional groups was confirmed by conducting the FT-IR analysis of CDs (Figure. 6.2b). The strong peaks at 3422, 2923, 1384, and 1623 cm^{-1} indicate the presence of –OH groups, stretching and bending vibrations of C–H and aromatic C=C. The peaks at 1093 and 1049 cm^{-1} are related to C–N and C–O stretching vibrations. This indicates the formation of the CDs was due to the conversion of the various polymers like celluloses, hemicelluloses, lignins, and polyphenols present in *P. guajava* leaves (Zhao et al., 2020). The electrocatalytic activity of CDs is enhanced due to the increased surface defects realized by the presence of a large number of oxygen-containing functional groups (Huang et al., 2019; Yang et al., 2019).

The XRD pattern demonstrates the graphitic carbon nature of CDs with a wide peak centered at $2\theta = 22.6^\circ$ (Edison et al., 2016) and a weak peak at 43° could be attributed to the disturbance caused by the oxygen rich functional groups present on the surface contributing to C-100 peak (Liu et al., 2017).

HRTEM (Figure 6.4a) reveals clear lattice fringes of CDs with a spacing of 0.216 nm, which can be attributed to the (100) diffraction planes of sp^2 hybridized carbons equivalent to those present in graphite (Pal et al., 2020). The SAED image (Figure 6.4b)

shows very faint hexagonal electron diffraction points and a cloudy white ring indicating the amorphous nature of CDs. The particle size analysis of 50 random particles reveals a narrow particle size distribution from 1.7-4.1 nm with an average particle size of 3.7 nm (Figure 6.4c).

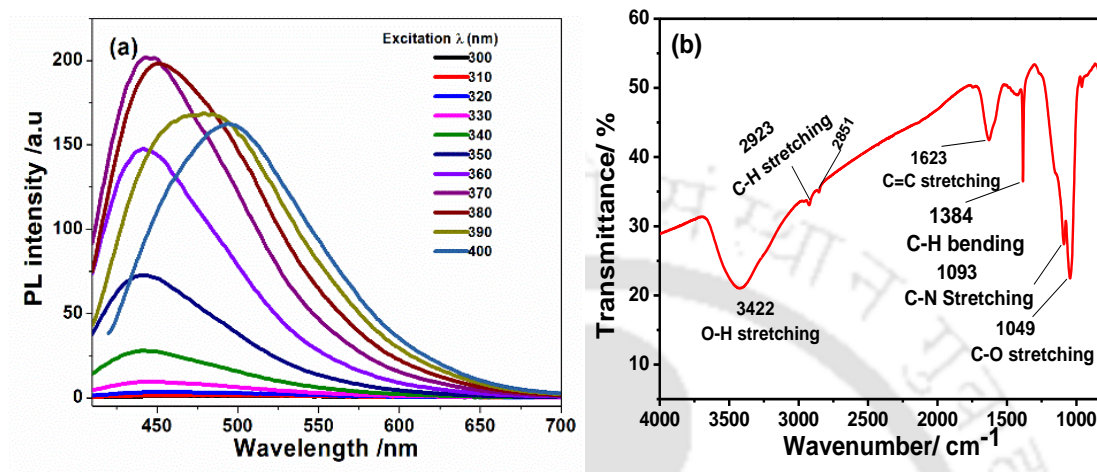


Figure 6.2: (a) Photoluminescence (PL) spectra and (b) FTIR spectra of synthesized CDs. Synthesis time 10 h and temperature 200°C.

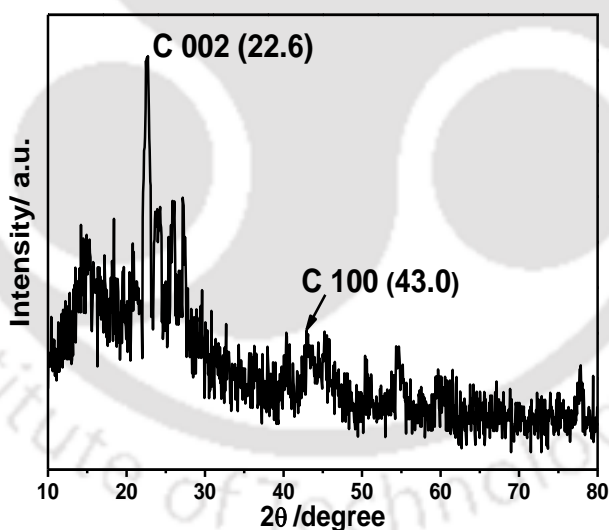


Figure 6.3: XRD pattern of synthesized CDs. Synthesis time 10 h and temperature 200°C.

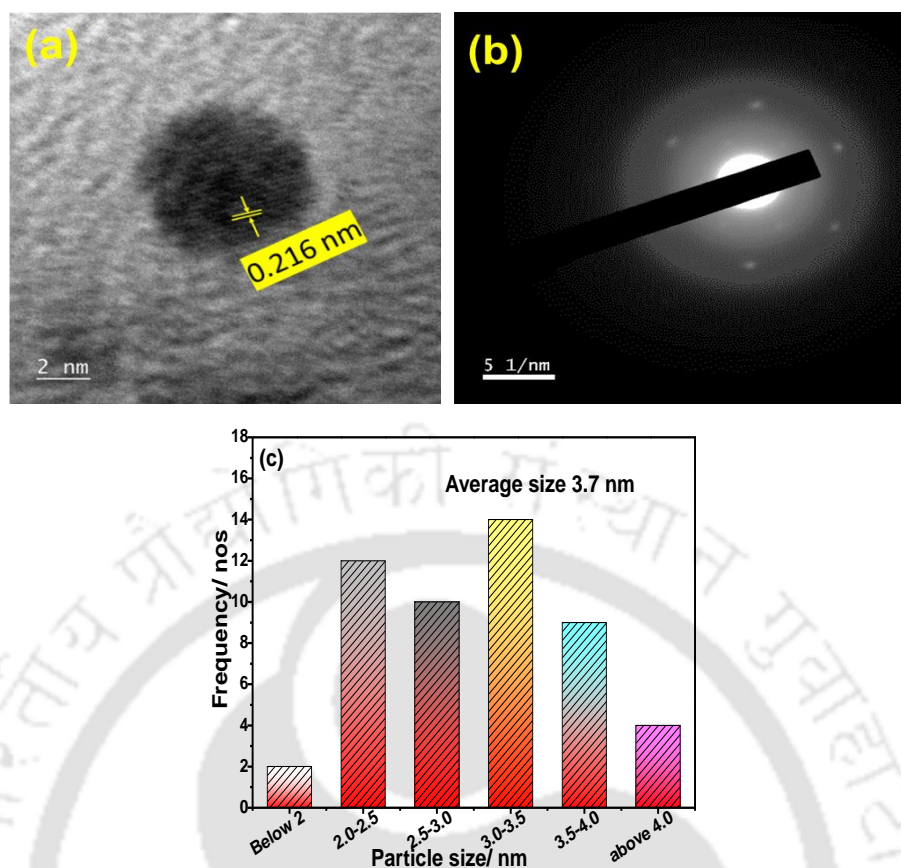


Figure 6.4: (a) HRTEM micrograph, (b) SAED, and (c) Particle size analysis of synthesized CDs. Synthesis time 10 h and temperature 200°C.

6.2.2 Characterization of working electrodes

6.2.2.1 Electroactive surface area of WE

Figures 6.5a and 6.5b show the cyclic voltammograms of bare glassy carbon electrode (GCE) and CDs/GCE at different scan rates from 5-200 $\text{mV} \cdot \text{s}^{-1}$. A pair of redox peaks at 0.14 and 0.3 V vs. Ag/AgCl for bare GCE and 0.12 and 0.3 V vs. Ag/AgCl for CDs/GCE can be observed for the redox analyte $\text{K}_2[\text{Fe}(\text{CN})_6]$. The CDs/GCE showed an increased cell current response (~ 2.5 times) compared to bare GCE, and a decrease in the reduction potential from 0.14 V in GCE to 0.12 in CDs/GCE suggests an improved surface electrokinetics.

A_{eff} of the prepared electrodes was calculated using the Randles-Sevcik equation (5.1) of chapter 5.

From the plot of I_{Pa} vs. $v^{0.5}$ (Figure 6.5c) and equating the slope values by considering D for $\text{K}_2[\text{Fe}(\text{CN})_6]$ as $7.6 \times 10^{-6} \text{ cm}^2 \cdot \text{s}^{-1}$ ($n = 1$), A_{eff} was found to be 0.157 and 0.187 cm^2 for bare GCE and CDs/GCE, respectively.

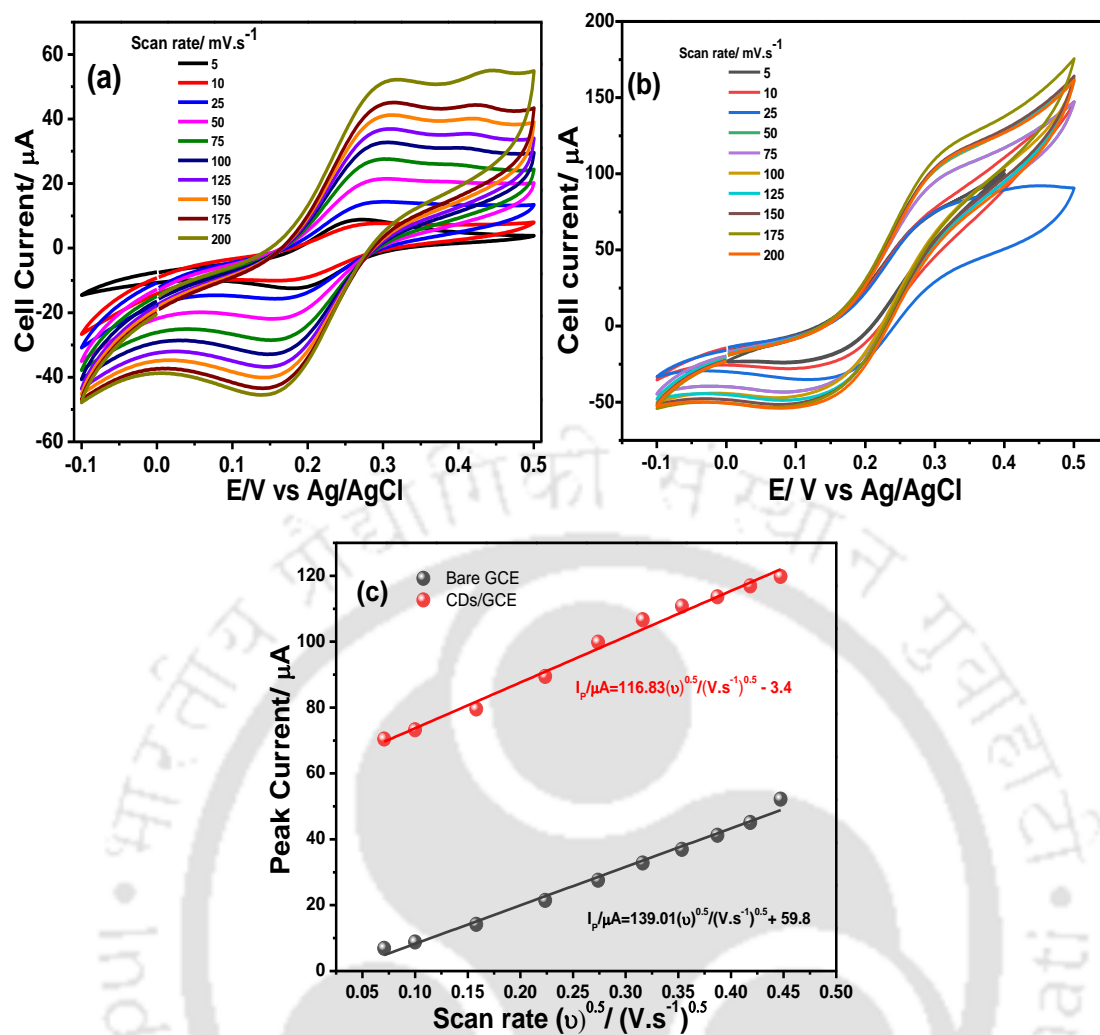


Figure 6.5: Cyclic voltammetry plots at different scan rates for (a) Bare GCE, (b) GCE/CDs and (c) Peak current vs. square root of scan rate. Reaction conditions: $K_3Fe(CN)_6$ 1 mM in 100 mL of 0.05 M KCl at ambient temperature.

6.2.2.2 Electrochemical impedance studies (EIS) of WE

EIS studies were performed using both bare GCE and GCE/CDs at the same electrochemical conditions. The Nyquist plot (1 Hz-1 MHz frequencies) shows a semicircular curve and a linear segment (Figure 6.6a). The diameter of the semicircular curve corresponds to the charge transfer resistance (R_{ct}) of the working electrode between the electrode/electrolyte interface and provides the Faradaic current of the system. The straight line at lower frequencies is due to the diffusion-controlled process at the electrode/electrolyte interface (Ghiasi et al., 2021). The equivalent circuit diagrams of bare GCE shows an R_{ct} of 3.69 K Ω (Figure 6.6b), and a decrease in R_{ct} (2.35 K Ω) (Figure 6.5c)

was observed after the modification of GCE with CDs which is indicative for an increased electron transfer kinetics (Sultan et al., 2019).

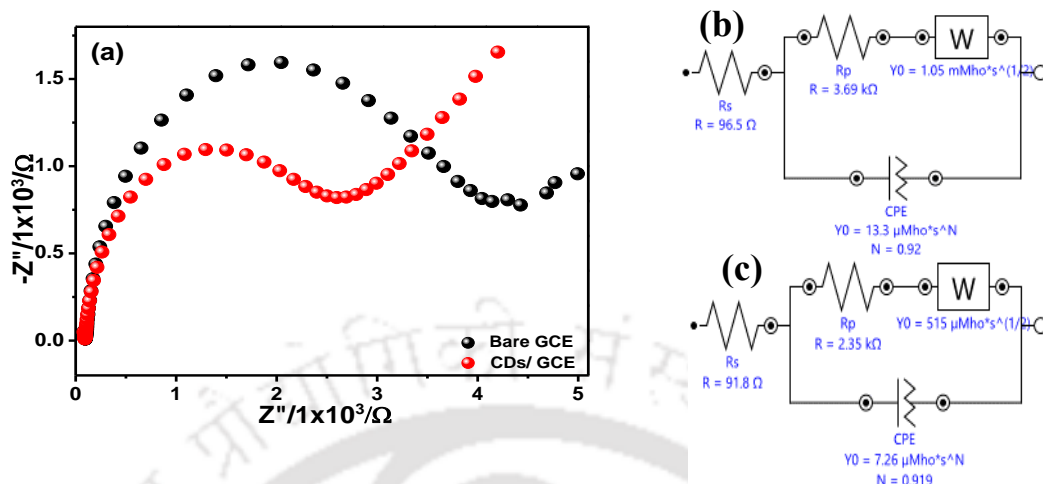


Figure 6.6: (a) Nyquist plot obtained with bare GCE and GCE/CDs in a 1 mM $K_3[Fe(CN)_6]$ solution containing 0.1 M KCl against the electrochemical circuit diagrams for (b) bare GCE, and (c) GCE/CDs.

6.2.3 Electrochemical sensing of Chlorpyrifos

6.2.3.1 Optimization of electrochemical sensing parameters

The detailed optimization experiments to determine the deposition potential and time are provided in Figures 6.7a–6.7d. It can be observed that -0.4 V and deposition time of 60 s was found optimum for the sensing of CHL.

The effects of different electrolytes (0.1 M), namely B-R buffer, KCl, and a phosphate buffer solution (PBS), on the current response of CHL was determined at the optimized pH with B-R buffer and CHL concentration of $0.50 \mu\text{M}$. The pH of the media was varied between 3 and 9 and optimized for the sensing of CHL. The concentration of CHL present in the agriculture grade sample was quantified at the optimal pH of 7 at -1.40 V vs. Ag/AgCl following the above procedure. The concentration of CHL was also determined by High-performance liquid chromatography as described in Section 2.4.2 of Chapter 2. The retention time of 8.36 min was used for the chromatographic separation. The details are provided in Figures 6.8a and 6.8b.

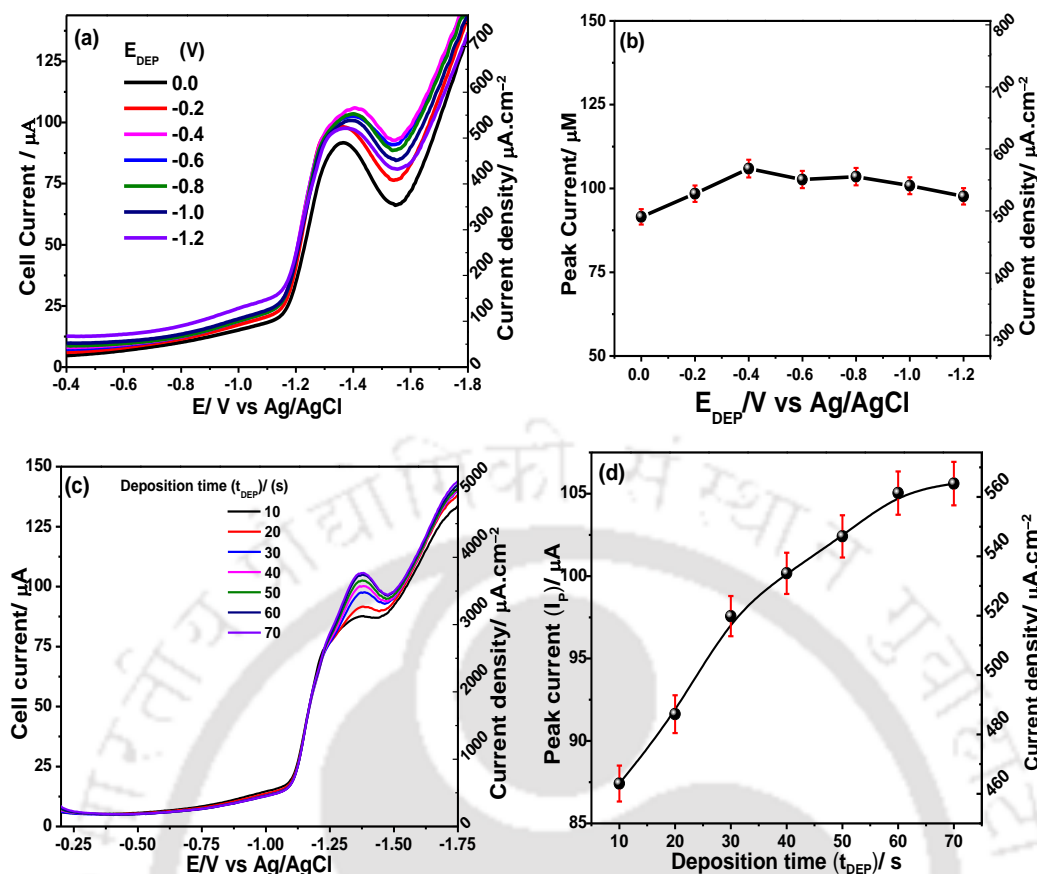


Figure 6.7: (a) Effect of deposition potential (E_{DEP}) on the square wave response of CHL, (b) Peak current vs. E_{DEP} , (c) Effect of deposition time (t_{DEP}) on the square wave response of CHL, and (d) Peak current vs. t_{DEP} . Reaction conditions: 0.5 μM CHL in B-R buffer (100 mL) at pH 7.

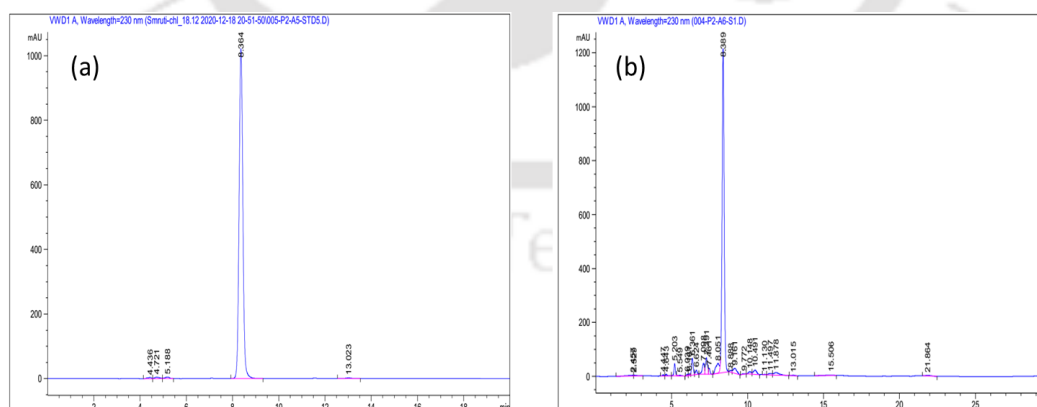


Figure 6.8: (a) HPLC chromatogram of 10 μM analytical grade (standard) CHL dissolved in ethanol, showing the retention time at 8.36 min and (b) HPLC chromatogram of 10 μM diluted (in acetonitrile) agriculture grade CHL (20% v/v) showing the presence of various additives that elute out at different retention times.

6.2.3.2 Electrochemical attributes of CHL

Square wave voltammetry was performed at optimized conditions to study the effects of varying pH ranging from 3.0 to 9 on the sensing performance of 0.50 μM CHL using GCE/CDs. Different electrolytes were tested for effective sensing of CHL. It can be seen that maximum peak intensity (-1.41 V vs. Ag/AgCl) was obtained using B-R buffer (Figure 6.9a) at pH 7. B-R buffer at pH 7 containing 40% v/v ethanol was subjected to square wave voltammetric analysis in the absence of CHL to obtain any background signals that might affect the CHL sensing. It can be noted that the presence of ethanol in the electrolyte though produces signals; they do not interfere with the response of CHL (Figure 6.9a).

B-R buffer at different pH was used to determine the best working pH for CHL sensing. It can be seen that a clear peak at pH 7 with the maximum current was found, and higher pH decreased the resulting current, and no distinct peaks were obtained (Figure 6.9b). Hence, pH 7 was selected for further experiments. A shift in the potential (E_p) towards more negative values was observed with the increase in pH, which indicates that the ability of CHL molecule to be reduced decreases with the increase in pH. It was also found that the peak potential varied linearly with pH with a slope of 46 mV per unit pH (Figure 6.9c) for a reaction involving an equal number of protons and electrons that is 2 (Gowda and Nandibewoor, 2014). It indicates an electrochemical reduction of $-\text{C}=\text{N}$ of the pyridine ring of the CHL molecule via a $2e^-$ transfer step (Figure 6.10) (Kumaravel and Chandrasekaran, 2015). This reaction is thermodynamically favoured due to the delocalization of electrons around $-\text{C}=\text{N}$ in the presence of substituted chlorine atoms in the pyridine moiety of CHL (El-Shahawi and Kamal, 1998). The reduction peak is observed at around -1.42 V vs. Ag/AgCl. At pH 7, the functional groups present on CDs tend to release their proton, and the surface becomes electron-rich (zeta potential -31.5 mV at pH 7), which attracts the CHL molecules towards the electrode surface at the δ^+ charge generated at $-\text{C}=\text{N}$, which is caused by the mesomeric effects due to the presence of the chlorine moieties in the pyridine ring. Moreover, this reaction is also augmented by applying a deposition potential E_{DEP} of -0.40 V vs. Ag/AgCl (Figure 6.7b). The mass spectra analysis of CHL before and after the sensing reaction is presented in Figures 6.11a and 6.11b. The MS spectra were analyzed using Model 6520 Accurate, Q-TOF LCMS system from Agilent Technologies, Sunnyvale, CA. It was equipped with an LC system 1200 from Agilent Technologies. The mobile phase used was acetonitrile (HPLC grade): DI water (90:10 v/v) with a flow rate of 0.3 mL.min $^{-1}$. The mass spectrometer was run with

an ESI (+) mode for the analysis of chlorpyrifos and its fragments formed during its sensing.

CHL from the aqueous electrolyte after the electrochemical reaction was separated using a standard method. Briefly, 100 mL of electrolyte solution containing 50 μM of CHL was taken in a separating funnel, and an equal 50 mL hexane was added and was shaken vigorously to form an emulsion. Intermittent venting was done to release the pressure. Then, the mixture was allowed to sit for 20 min to affect the separation of both the aqueous and organic phases. The upper hexane layer was then separated from the aqueous layer and collected in a round-bottomed flask. This step was repeated twice using fresh hexane to ensure proper extraction of CHL. The hexane was then evaporated out using a vacuum evaporator at 35°C, and the obtained residue was dissolved using acetonitrile and filtered through a 0.2 μm nylon membrane filter was subjected to LC-MS analysis.

The increase in m/z from 351.93 to 353.21 further supports the reduction of CHL molecule involving two during its electrocatalytic sensing (Figure 6.11).

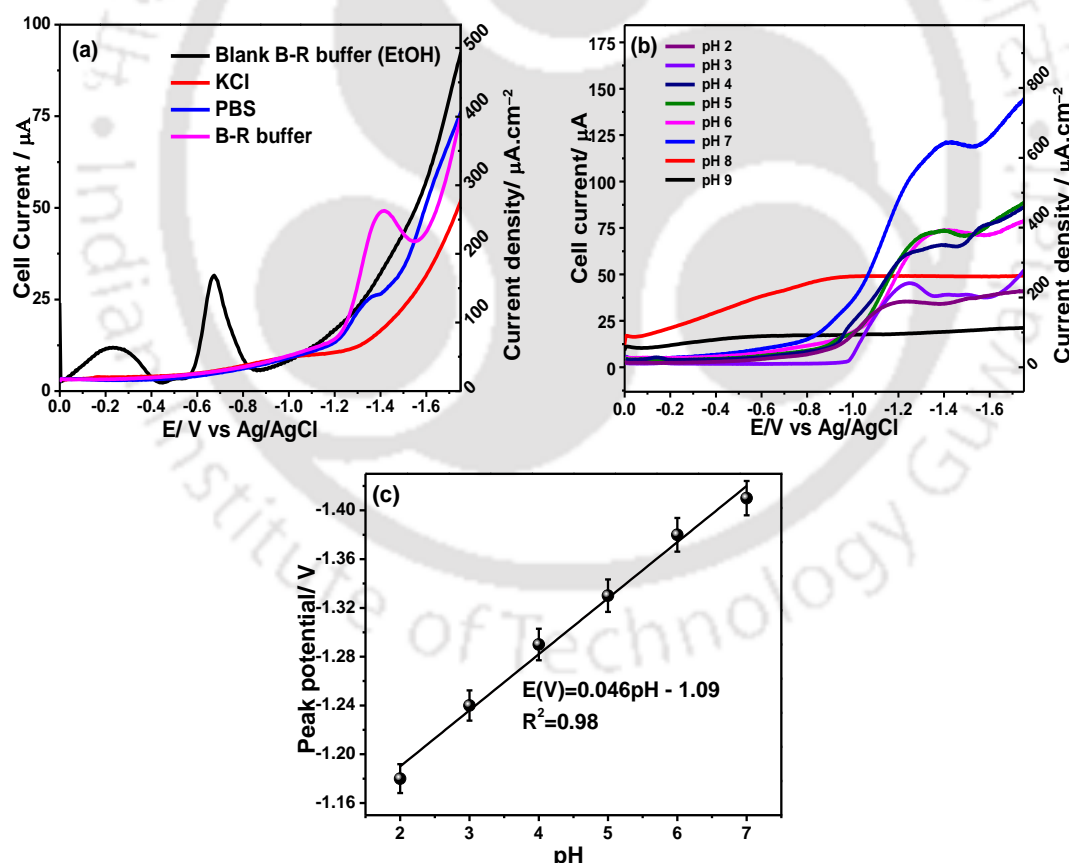


Figure 6.9: (a) SWV response recorded using GCE/CDs during electrochemical sensing of CHL (0.25 μM) with different electrolytes at pH 7, (b) Effect of pH variation on CHL sensing in B-R buffer system (0.5 μM CHL), and (c) Linear fitting of variation of peak potential as a function of pH. Reaction conditions: 0.1 M 100 mL B-R buffer, $E_{\text{DEP}} = -0.40$ V and $t_{\text{DEP}} = 60$ s.

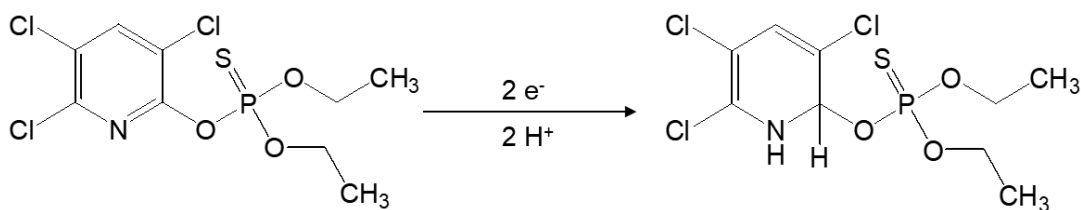


Figure 6.10: Electrochemical reduction reaction of CHL molecule at GCE/CDs.

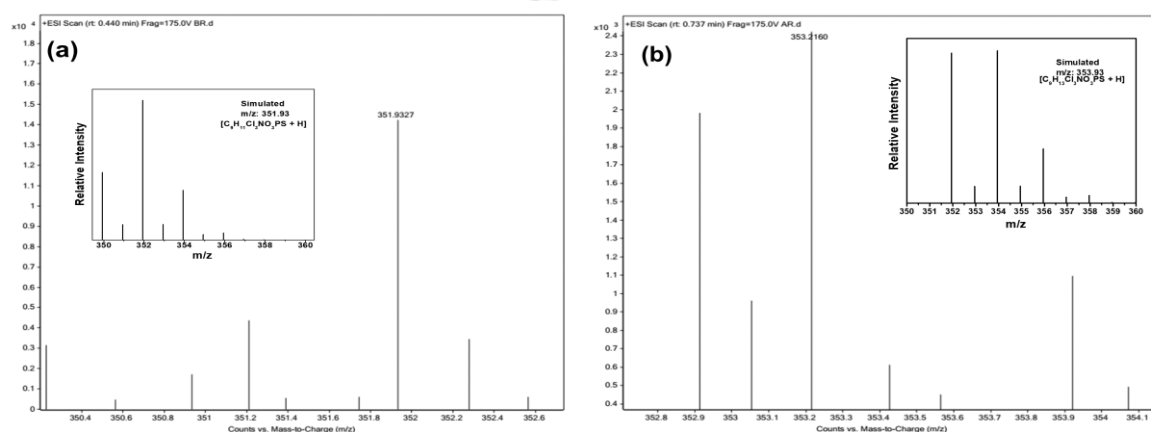


Figure 6.11: Mass spectra analysis of (a) chlorpyrifos before reaction and (b) after 20 min chronoamperometry run at -1.40 V vs. Ag/AgCl using CDs/GCE as working electrode. The insets of Figures 6.9a and 6.9b show the corresponding simulated MS spectra using m/z calculator software from Integrative Omics, PNNL, USA.

Square wave voltammetry was conducted at different scan rates (5 – 150 $\text{mV}\cdot\text{s}^{-1}$) from 0 –(-2.0) V vs. Ag/AgCl using B-R buffer as the supporting electrolyte (pH 7) at the GCE/CDs to derive the fundamental electrokinetic parameters and to understand the redox behavior of CHL sensing (Figure 6.12a). A straight line was obtained by plotting the peak current (I_p) with the square root of the scan rate (Figure 6.12b). The results show that the reaction is diffusional control (Švorc et al., 2018). Hence, the Laviron equation (Eq. 3.2 of chapter 3) for the diffusion-controlled process was used to determine the kinetic parameters.

The value of αn was calculated from the slope of E_p vs. $\log v$ (Figure 6.12c) which is 0.091 , and the intercept gives the k^0 value of $1.21 \times 10^{-3} \text{ s}^{-1}$ which shows faster electrode kinetics and a good affinity of CHL towards the modified electrode surface. E^0 of -1.34 V vs. Ag/AgCl was obtained from the intercept of the curve of E_p vs. v ($v = 0$). The Bard and Faulkner equation Eq (6.1) was used to calculate the value of α (Gowda and Nandibewoor, 2014).

$$\alpha = \frac{47.7}{E_P - E_{P/2}} \quad (6.1)$$

Where E_P (mV) is the anodic peak potential, and $E_{P/2}$ is the potential where the current is half of the peak value. It was found that the value of α is 0.2, and the number of electrons (n) involved in the reaction was calculated from the slope (Figure 6.12c) as 2.22. It matches with the results obtained from pH variation experiments (Figure 6.9c). A lower value of α indicates that the equilibrium of the reaction is more shifted towards the reactant side. This could be the reason why a large overpotential (-1.41 V) is required to facilitate the electrochemical reduction reaction (Tijani et al., 2019).

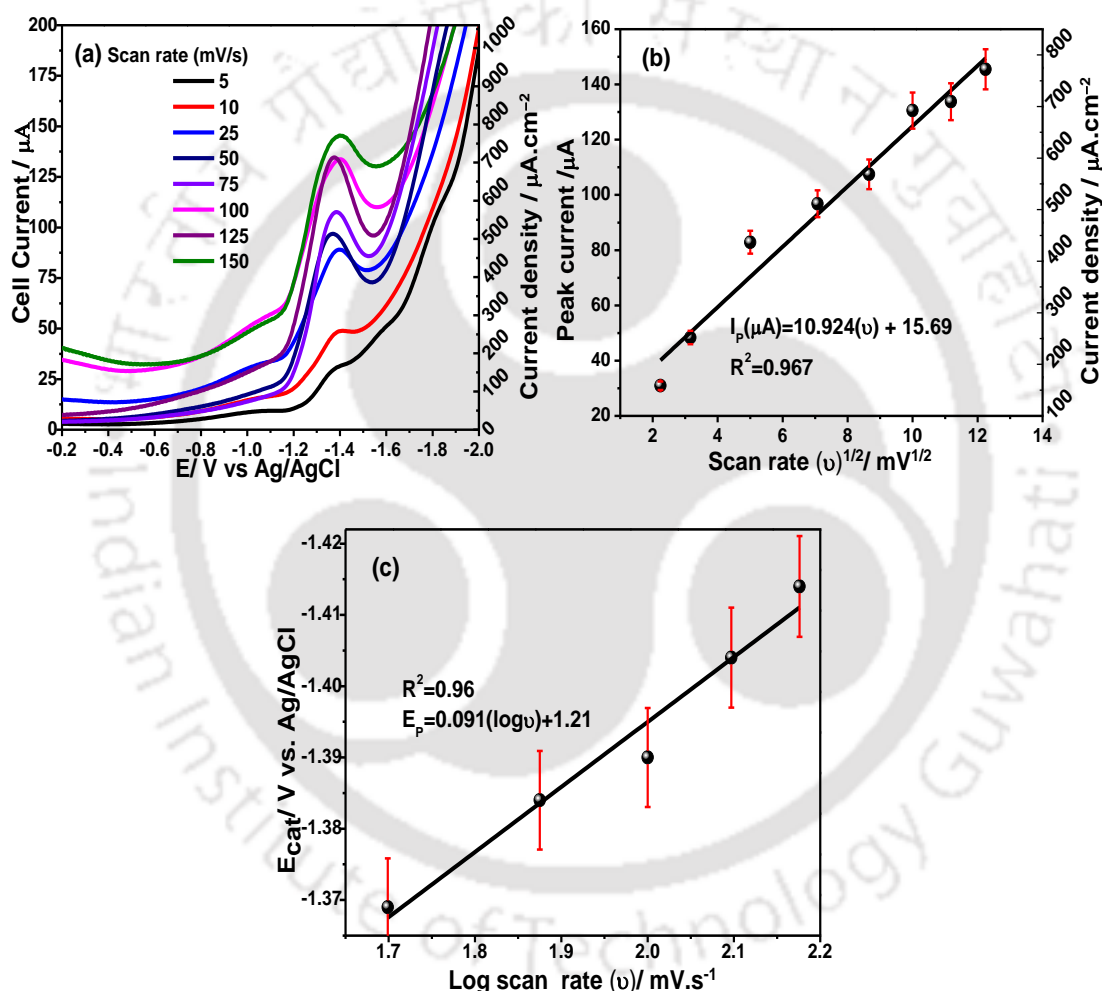


Figure 6.12: Square wave voltammograms recorded at different scan rates at GCE/CDs, (b) Variation of peak current (I_p) with $v^{1/2}$ (v : 5 to 150 $mV.s^{-1}$), and (c) Variation of E_P with $\log(v)$ (v : 5 to 150 $mV.s^{-1}$) with 0.5 μM CHL in 0.1 M 100 mL B-R buffer at pH 7, $E_{DEP} = -0.40$ V and $t_{DEP} = 60$ s.

Figures 6.13a and 6.13b depict the square wave voltammograms and the corresponding calibration curves of CHL sensing at the GCE/CDs. The voltammograms exhibited two linear ranges of CHL sensing based on its concentration, i.e., between 0.1-1

μM and 1–10 μM having linear relationships as $I_p (\mu\text{A}) = 238.93 [\text{CHL}] \mu\text{M} + 17.39$ ($R^2 = 0.998$) and $I_p (\mu\text{A}) = 28.04 [\text{CHL}] \mu\text{M} + 235.14$ ($R^2 = 0.945$). The increase in CHL concentration changes the diffusion control redox reaction to a mass transfer controlled regime, which increases the influx of CHL and enhances the reaction. It overwhelms the electrode surface resulting in an accumulation of oxidation products on the electrode surface. The limit of detection (LOD) and limit of quantification (LOQ) of CHL at the GCE/CDs was calculated using Eqs. 3.3 and 3.4 of chapter 3, respectively.

LOD and LOQ were calculated as 1.5 nM and 4.5 nM, respectively (Figure 6.13b). The sensitivity of the electrode with an electroactive surface area (A_{eff}) of 0.187 cm^2 was found to be $1.27 \text{ mA} \cdot \mu\text{M}^{-1} \cdot \text{cm}^{-2}$ (Eq. 3.5 of chapter 3). An increase in A_{eff} in the case of GCE/CDs was about 22% as compared to bare GCE due to CDs impregnation.

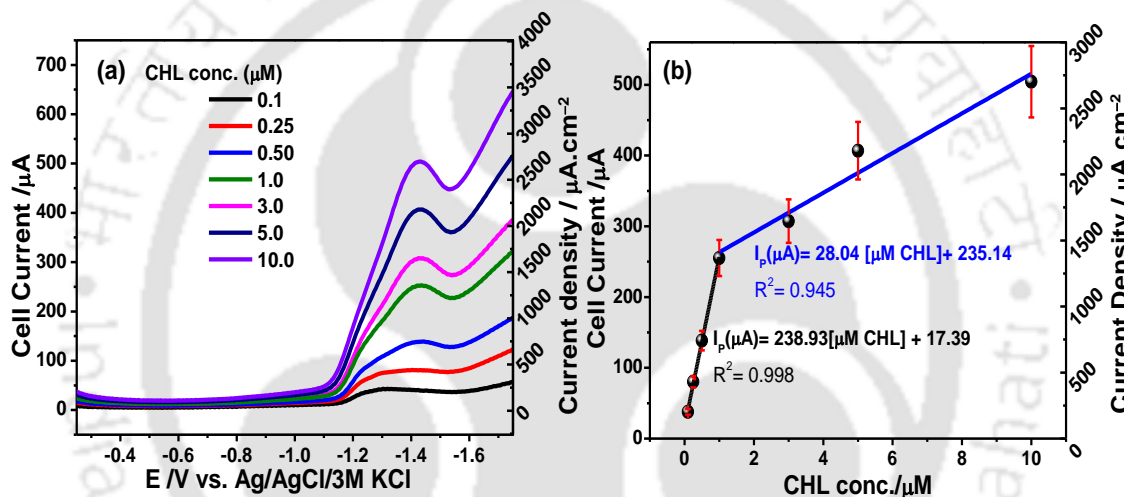


Figure 6.13: (a) Square wave voltammetric profiles recorded with CDs/GCE at different CHL concentration (0.1 to 10 μM), and (b) Calibration curve of CHL sensing. Reaction conditions: 0.1 M 100 mL B-R buffer at pH 7, scan rate $0.1 \text{ V} \cdot \text{s}^{-1}$, $E_{\text{DEP}} = -0.40 \text{ V}$ and $t_{\text{DEP}} = 60 \text{ s}$.

6.2.3.3 Repeatability and reproducibility of CHL sensing

A no. of 10 repeated tests was carried with a fixed concentration of $0.50 \mu\text{M}$ CHL to verify the repeatability of response current of CHL sensing at the GCE/CDs. The peak currents are reproducible with a relative standard deviation (RSD) of 4.77% (Figure 6.14a). The peak current decrease with respect to the initial current was 4.8% after 5 square wave voltammetric runs, which further decreased by 8.7% by the end of the 10th cycle (Figure 6.14b). This is due to the accumulation of reduced CHL on the electrode surface that could block the active recombination sites present on the surface of the CDs (Dong et al., 2019).

Further, three fresh GCE/CDs were fabricated following the same procedure in order to check the reproducibility of CHL sensing. RSD of CHL sensing was found to be within 1.17% with these three fresh GCE/CDs. It indicates that the interaction between the functional groups present on CDs and the CHL molecules didn't affect much by the method of electrode modification.

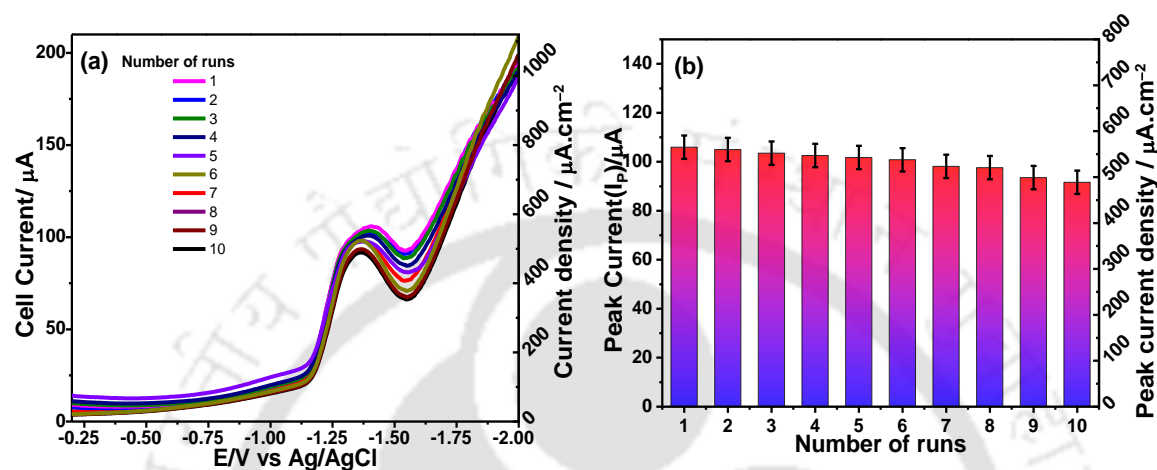


Figure 6.14: (a) SWV profile recorded with GCE/CDs, and (b) The corresponding trend in the current response in 10 consecutive sensing cycles. Reaction conditions: 0.5 μM CHL in 0.1 M 100 mL B-R buffer at pH 7, scan rate 0.1 V·s⁻¹, E_{DEP} = -0.40 V and t_{DEP} = 60 s.

6.2.3.4 Electrochemical quantification of CHL in agriculture sample

A 100 mL pack of CHL was purchased from the local market with a certified concentration of 20% (v/v). The actual concentration was determined using HPLC analysis, and it was used as a reference for the comparison with the concentration determined using the GCE/CDs. The concentration range was chosen based on the prescribed dose for on-field applications. The concentration of CHL in runoff water depends on various factors such as soil type, type of crops, application dosage, and frequency of irrigation and rainfall. The previous study suggests that the surface runoff water contains CHL in the concentration of approximately 0.5 μM, whereas the topsoil (25 cm depth) contained much higher concentrations of 0.298 mg.kg⁻¹ of soil immediately after the application of CHL (Konda and Pásztor, 2001). Figure 6.15 shows the SWV response of CHL sensing in the agriculture pesticide.

The SWV was done at a scan rate of 100 mV·s⁻¹ with an E_{DEP} and t_{DEP} of -0.40 V and 60 s, respectively. A stock solution of the agricultural grade pesticide with an equivalent CHL concentration of 1 mM was prepared in an ethanol/B-R buffer (40:60 v/v) at pH 7. In

another study, DI water was replaced by river water, and the effect of real environmental water samples on CHL sensing was tested by spiking with analytical grade CHL (Figure 6.16). The presence of 0.1, 2.0, 1.8, and 6.3 mg.L⁻¹ of fluoride, chloride, phosphate and sulphate ions in river water did not affect the sensing performance of the GCE/CDs (Figure 6.17). The maximum variation of CHL determination with respect to HPLC was 4.9%, with a low RSD of 1.08% (Table 6.1). In the case of the agriculture pesticide, the concentration of CHL quantified electrochemically using GCE/CDs showed a close agreement with HPLC (variation <5%) (Table 6.1). As stated by the manufacturer and as evident from the chromatograph (Figure 6.7b), the agriculture sample is laden with complex compounds like emulsifiers, alkyl aryl sulphonate poly-oxy ethylene ether. The presence of these complex molecules did not show any significant interference in the electrochemical detection and determination of CHL. The relative standard deviations for three consecutive preparations were found between 1.55 and 2.83%.

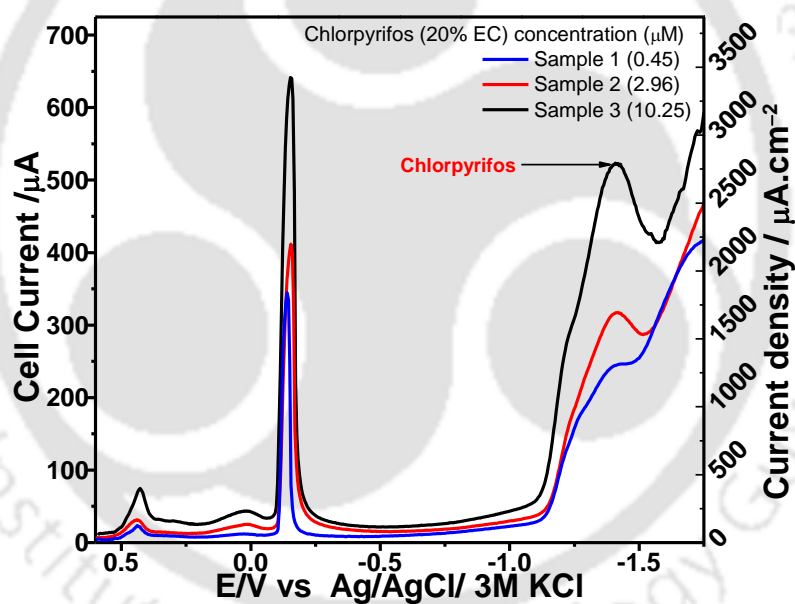


Figure 6.15: SWV analysis of commercial pesticides (20% EC) in B-R buffer (pH 7) using GCE/CDs. Reaction conditions: 0.1 M 100 mL B-R buffer at pH 7, $E_{\text{DEP}} = -0.4$ V and $t_{\text{DEP}} = 60$ s.

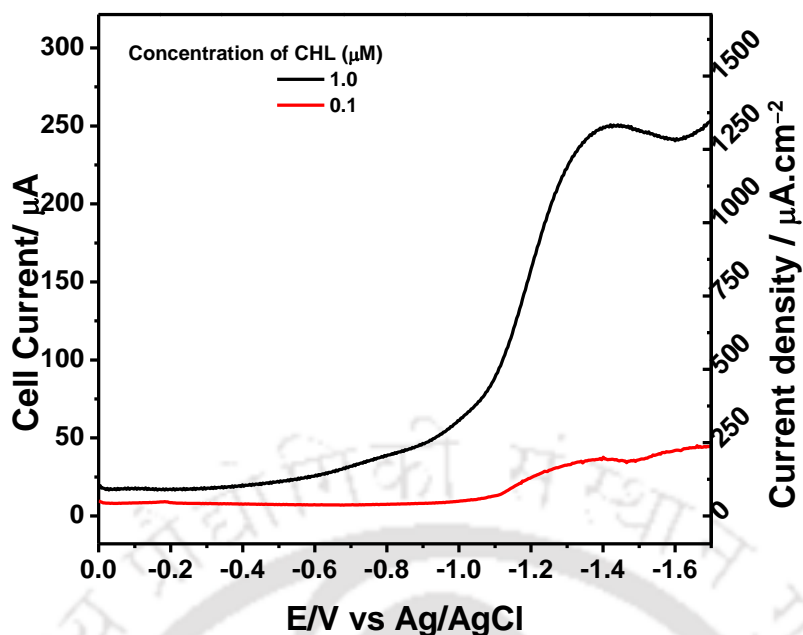


Figure 6.16: SWV analysis of CHL in river water (pH 7) using GCE/CDs. Reaction conditions: 0.1 M 100 mL B-R buffer at pH 7, $E_{DEP} = -0.4$ V and $t_{DEP} = 60$ s.

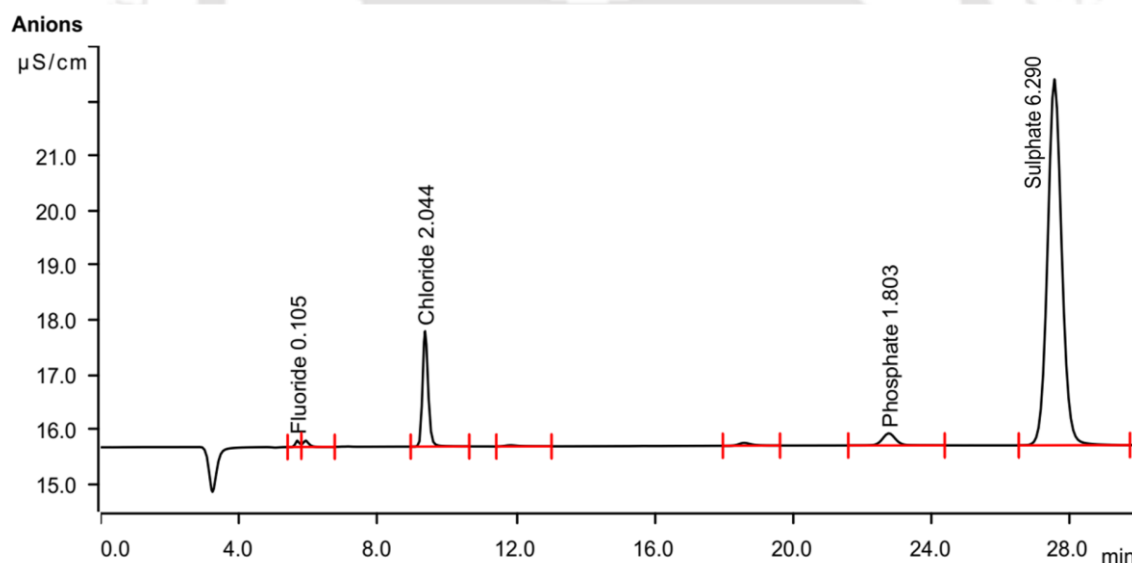


Figure 6.17: Ion Chromatography (IC) analysis of river water showing various anions present in the water sample. Operating conditions: Run time of 30 min using an eluent containing a mixture of 1.0 mM NaHCO_3 and 3.3 mM Na_2CO_3 in DI water at a flow rate of $0.7 \text{ mL}\cdot\text{min}^{-1}$. The IC column used was 6.1006.530 Metrosep A Supp 5-250 Make: Metrohm.

Table 6.1: Performance comparison for CHL determination by electrochemical sensing at GCE/CDs and by HPLC.

Sample	CHL @HPLC (μM)	GCE/CDs			Variation with respect to sensor (%)
		CHL @Sensing (μM)	Recovery (%)	RSD (%) n = 3	
Agriculture pesticide (20% v/v)	0.43	0.45	104.6	2.83	4.6
	3.1	2.96	95.48	1.68	-4.5
	9.98	10.25	102.7	1.55	2.7
River water	0.15	0.156	104.0	1.32	4.0
	1	1.049	104.9	1.08	4.9

6.3 Major findings

A simple bioinspired method devised in this study was successful in synthesizing CDs using waste *P. guajava* leaves. CDs synthesized (average size 3.7 nm) at 200°C at 10 h of hydrothermal reaction time showed good photoluminescence properties with an emission peak at 450 nm on excitation at 360 nm. CDs contained ample oxygen-containing surface functional groups on their surface, and these functional groups could act as active sites for the intermolecular interactions with CHL during electrochemical sensing.

CDs decorated GCE decreased the charge transfer resistance by about 57%. This modified electrode showed high sensitivity ($1.27 \text{ mA} \cdot \mu\text{M}^{-1} \cdot \text{cm}^{-2}$) and a low detection limit (1.5 nM) for electrochemical sensing of CHL in B-R buffer media at the optimized pH of 7 using square wave voltammetric technique. During sensing, CHL has undergone cleavage of $-\text{C}=\text{N}$ of the pyridine ring of the CHL molecule involving two protons and two electrons transfer. The repeatability of CHL sensing up to 10 cycles was limited within a relative standard deviation of 4.77%. CHL present in agriculture pesticide even in the presence of emulsifiers and additives in this sample was successfully determined at the GCE/CDs. The sensing of CHL spiked in river water was also in accordance with the concentrations determined by using HPLC.

References

- Albanis, T.A., Hela, D.G., 1995. Multi-residue pesticide analysis in environmental water samples using solid-phase extraction discs and gas chromatography with flame thermionic and mass-selective detection. *J. Chromatogr. A* 707, 283–292. [https://doi.org/10.1016/0021-9673\(95\)00334-J](https://doi.org/10.1016/0021-9673(95)00334-J)
- Amiri, M., Rezapour, F., Bezaatpour, A., 2014. Hydrophilic carbon nanoparticulates at the surface of carbon paste electrode improve determination of paracetamol, phenylephrine and dextromethorphan. *J. Electroanal. Chem.* 735, 10–18. <https://doi.org/10.1016/j.jelechem.2014.10.006>
- Asadian, E., Ghalkhani, M., Shahrokhian, S., 2019. Electrochemical sensing based on carbon nanoparticles: A review. *Sensors Actuators, B Chem.* 293, 183–209. <https://doi.org/10.1016/j.snb.2019.04.075>
- Brzak, K.A., Harms, D.W., Bartels, M.J., Nolan, R.J., 1998. Determination of chlorpyrifos, chlorpyrifos oxon, and 3,5,6-trichloro-2-pyridinol in rat and human blood. *J. Anal. Toxicol.* 22, 203–210. <https://doi.org/10.1093/jat/22.3.203>
- Campuzano, S., Yáñez-Sedeño, P., Pingarrón, J.M., 2019. Carbon dots and graphene quantum dots in electrochemical biosensing. *Nanomaterials* 9, 1–18. <https://doi.org/10.3390/nano9040634>
- Chai, L.K., Wong, M.H., Bruun Hansen, H.C., 2013. Degradation of chlorpyrifos in humid tropical soils. *J. Environ. Manage.* 125, 28–32. <https://doi.org/10.1016/j.jenvman.2013.04.005>
- Cometa, M.F., Buratti, F.M., Fortuna, S., Lorenzini, P., Volpe, M.T., Parisi, L., Testai, E., Meneguz, A., 2007. Cholinesterase inhibition and alterations of hepatic metabolism by oral acute and repeated chlorpyrifos administration to mice. *Toxicology* 234, 90–102. <https://doi.org/10.1016/j.tox.2007.02.008>
- De Silva, P.M.C.S., Samayawardhena, L.A., 2005. Effects of chlorpyrifos on reproductive performances of guppy (*Poecilia reticulata*). *Chemosphere* 58, 1293–1299. <https://doi.org/10.1016/j.chemosphere.2004.10.030>
- Ding, Z., Li, F., Wen, J., Wang, X., Sun, R., 2018. Gram-scale synthesis of single-crystalline graphene quantum dots derived from lignin biomass. *Green Chem.* 20, 1383–1390. <https://doi.org/10.1039/c7gc03218h>
- Dong, X.Y., Wang, F., Ma, J., Qiu, B.J., 2019. Preparation of an electrochemical sensor based on a Nitrogen-doped graphene modified electrode and its application for the

- detection of Methyl parathion. *Int. J. Electrochem. Sci.* 14, 11679–11679. <https://doi.org/10.20964/2019.12.02>
- Edison, T.N.J.I., Atchudan, R., Sethuraman, M.G., Shim, J.J., Lee, Y.R., 2016. Microwave assisted green synthesis of fluorescent N-doped carbon dots: Cytotoxicity and bio-imaging applications. *J. Photochem. Photobiol. B Biol.* 161, 154–161. <https://doi.org/10.1016/j.jphotobiol.2016.05.017>
- El-Shahawi, M.S., Kamal, M.M., 1998. Determination of the pesticide Chlorpyrifos by cathodic adsorptive stripping voltammetry. *Fresenius. J. Anal. Chem.* 362, 344–347. <https://doi.org/10.1007/s002160051085>
- Essner, J.B., Laber, C.H., Ravula, S., Polo-Parada, L., Baker, G.A., 2016. Pee-dots: biocompatible fluorescent carbon dots derived from the upcycling of urine. *Green Chem.* 18, 243–250. <https://doi.org/10.1039/c5gc02032h>
- Gaudet, C., Lingard, S., Cureton, P., Keenleyside, K., Smith, S., Raju, G., 1995. Canadian Environmental Quality Guidelines for mercury. *Water, Air, Soil Pollut.* 80, 1149–1159. <https://doi.org/10.1007/BF01189777>
- Gavrilescu, M., 2005. Fate of pesticides in the environment and its bioremediation. *Eng. Life Sci.* 5, 497–526. <https://doi.org/10.1002/elsc.200520098>
- Gebremariam, S.Y., Beutel, M.W., Yonge, D.R., Flury, M., Harsh, J.B., 2012. Adsorption and desorption of chlorpyrifos to soils and sediments, *Reviews of Environmental Contamination and Toxicology*. https://doi.org/10.1007/978-1-4614-1463-6_3
- Ghiasi, T., Ahmadi, S., Ahmadi, E., Babil Olyai, M.R.T., Khodadadi, Z., 2021. Novel electrochemical sensor based on modified glassy carbon electrode with graphene quantum dots, chitosan and nickel molybdate nanocomposites for diazinon and optimal design by the Taguchi method. *Microchem. J.* 160, 105628. <https://doi.org/10.1016/j.microc.2020.105628>
- Gowda, J.I., Nandibewoor, S.T., 2014. Simultaneous electrochemical determination of 4-aminophenazone and caffeine at electrochemically pre-treated graphite pencil electrode. *Anal. Methods* 6, 5147–5154. <https://doi.org/10.1039/c4ay00467a>
- He, J., Zhang, H., Zou, J., Liu, Y., Zhuang, J., Xiao, Y., Lei, B., 2016. Carbon dots-based fluorescent probe for “off-on” sensing of Hg(II) and I-. *Biosens. Bioelectron.* 79, 531–535. <https://doi.org/10.1016/j.bios.2015.12.084>
- Hoekman, S.K., Broch, A., Robbins, C., 2011. Hydrothermal carbonization (HTC) of lignocellulosic biomass. *Energy and Fuels* 25, 1802–1810.
- Huang, C., Dong, H., Su, Y., Wu, Y., Narron, R., Yong, Q., 2019. Synthesis of carbon

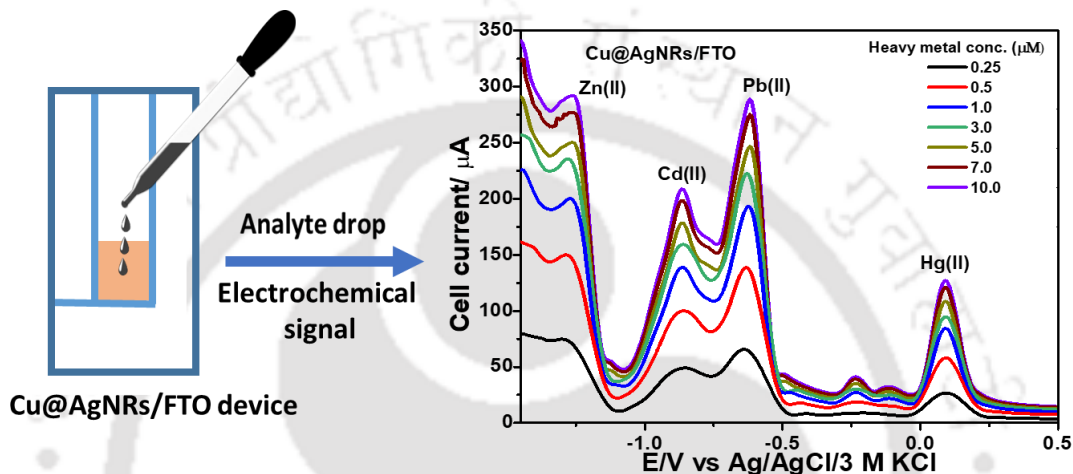
- quantum dot nanoparticles derived from byproducts in bio-refinery process for cell imaging and in vivo bioimaging. *Nanomaterials* 9. <https://doi.org/10.3390/nano9030387>
- Konda, L.N., Pásztor, Z., 2001. Environmental distribution of acetochlor, atrazine, chlorpyrifos, and propisochlor under field conditions. *J. Agric. Food Chem.* 49, 3859–3863. <https://doi.org/10.1021/jf010187t>
- Kumaravel, A., Chandrasekaran, M., 2015. Electrochemical Determination of Chlorpyrifos on a Nano-TiO₂/Cellulose Acetate Composite Modified Glassy Carbon Electrode. *J. Agric. Food Chem.* 63, 6150–6156. <https://doi.org/10.1021/acs.jafc.5b02057>
- Liu, Y., Zhou, Q., Yuan, Y., Wu, Y., 2017. Hydrothermal synthesis of fluorescent carbon dots from sodium citrate and polyacrylamide and their highly selective detection of lead and pyrophosphate. *Carbon N. Y.* 115, 550–560. <https://doi.org/10.1016/j.carbon.2017.01.035>
- Lu, J., Yeo, P.S.E., Gan, C.K., Wu, P., Loh, K.P., 2011. Transforming C₆₀ molecules into graphene quantum dots. *Nat. Nanotechnol.* 6, 247–252. <https://doi.org/10.1038/nnano.2011.30>
- Luo, Z., Qi, G., Chen, K., Zou, M., Yuwen, L., Zhang, X., Huang, W., Wang, L., 2016. Microwave-Assisted Preparation of White Fluorescent Graphene Quantum Dots as a Novel Phosphor for Enhanced White-Light-Emitting Diodes. *Adv. Funct. Mater.* 26, 2739–2744. <https://doi.org/10.1002/adfm.201505044>
- Ma, M., Hu, X., Zhang, C., Deng, C., Wang, X., 2017. The optimum parameters to synthesize bright and stable graphene quantum dots by hydrothermal method. *J. Mater. Sci. Mater. Electron.* 28, 6493–6497. <https://doi.org/10.1007/s10854-017-6337-4>
- Mauldin, R.E., Primus, T.M., Buettgenbach, T.A., Johnston, J.J., Linz, G.M., 2006. A simple HPLC method for the determination of chlorpyrifos in black oil sunflower seeds. *J. Liq. Chromatogr. Relat. Technol.* 29, 339–348. <https://doi.org/10.1080/10826070500451863>
- Mohan, S.V., Sirisha, K., Rao, N.C., Sarma, P.N., Reddy, S.J., 2004. Degradation of chlorpyrifos contaminated soil by bioslurry reactor operated in sequencing batch mode: Bioprocess monitoring. *J. Hazard. Mater.* 116, 39–48. <https://doi.org/10.1016/j.jhazmat.2004.05.037>
- Oliva, J., Navarro, S., Barba, A., Navarro, G., 1999. Determination of chlorpyrifos, penconazole, fenarimol, vinclozolin and metalaxyl in grapes, must and wine by on-

- line microextraction and gas chromatography. *J. Chromatogr. A* 833, 43–51. [https://doi.org/10.1016/S0021-9673\(98\)00860-7](https://doi.org/10.1016/S0021-9673(98)00860-7)
- Pal, A., Sk, M.P., Chattopadhyay, A., 2020. Recent advances in crystalline carbon dots for superior application potential. *Mater. Adv.* 1, 525–553. <https://doi.org/10.1039/d0ma00108b>
- Ray, D.E., 1998. Chronic effects of low level exposure to anticholinesterases - A mechanistic review. *Toxicol. Lett.* 102–103, 527–533. [https://doi.org/10.1016/S0378-4274\(98\)00260-4](https://doi.org/10.1016/S0378-4274(98)00260-4)
- ReddyPrasad, P., Naidoo, E.B., Sreedhar, N.Y., 2019. Electrochemical preparation of a novel type of C-dots/ZrO₂ nanocomposite onto glassy carbon electrode for detection of organophosphorus pesticide. *Arab. J. Chem.* 12, 2300–2309. <https://doi.org/10.1016/j.arabjc.2015.02.012>
- Richardson, R.J., Moore, T.B., Kayyali, U.S., Randall, J.C., 1993. Chlorpyrifos: Assessment of potential for delayed neurotoxicity by repeated dosing in adult hens with monitoring of brain acetylcholinesterase, brain and lymphocyte neurotoxic esterase, and plasma butyrylcholinesterase activities. *Toxicol. Sci.* 21, 89–96. <https://doi.org/10.1093/toxsci/21.1.89>
- Sakdaronnarong, C., Sangjan, A., Boonsith, S., Kim, D.C., Shin, H.S., 2020. Recent developments in synthesis and photocatalytic applications of carbon dots. *Catalysts* 10. <https://doi.org/10.3390/catal10030320>
- Shahrokhian, S., Ghalkhani, M., 2009. Electrochemical study of Azathioprine at thin carbon nanoparticle composite film electrode. *Electrochem. commun.* 11, 1425–1428. <https://doi.org/10.1016/j.elecom.2009.05.025>
- Silva, L.R.G., dos Santos, G.F.S., Vasconcellos, M.L.S., Ferreira, R. de Q., 2020. Development of electroanalytical procedure for monitoring of metamizole in organic fertilizers (human urine and struvite) associated with portable equipment. *J. Environ. Manage.* 266, 110587. <https://doi.org/10.1016/j.jenvman.2020.110587>
- Singh, B.K., 2009. Organophosphorus-degrading bacteria: Ecology and industrial applications. *Nat. Rev. Microbiol.* 7, 156–164. <https://doi.org/10.1038/nrmicro2050>
- Sultan, S., Shah, A., Khan, B., Nisar, J., Shah, M.R., Ashiq, M.N., Akhter, M.S., Shah, A.H., 2019. Calix[4]arene Derivative-Modified Glassy Carbon Electrode: A New Sensing Platform for Rapid, Simultaneous, and Picomolar Detection of Zn(II), Pb(II), As(III), and Hg(II). *ACS Omega* 4, 16860–16866. <https://doi.org/10.1021/acsomega.9b01869>

- Sun, P., Heng, M., Sun, S.H., Chen, J., 2011. Analysis of liquid and solid products from liquefaction of paulownia in hot-compressed water. *Energy Convers. Manag.* 52, 924–933. <https://doi.org/10.1016/j.enconman.2010.08.020>
- Švorc, L., Strežová, I., Kianičková, K., Stanković, D.M., Otrísal, P., Samphao, A., 2018. An advanced approach for electrochemical sensing of ibuprofen in pharmaceuticals and human urine samples using a bare boron-doped diamond electrode. *J. Electroanal. Chem.* 822, 144–152. <https://doi.org/10.1016/j.jelechem.2018.05.026>
- Tan, X., Li, Y., Li, X., Zhou, S., Fan, L., Yang, S., 2015. Electrochemical synthesis of small-sized red fluorescent graphene quantum dots as a bioimaging platform. *Chem. Commun.* 51, 2544–2546. <https://doi.org/10.1039/c4cc09332a>
- Tijani, A.S., Ghani, M.F.A., Rahim, A.H.A., Muritala, I.K., Binti Mazlan, F.A., 2019. Electrochemical characteristics of (PEM) electrolyzer under influence of charge transfer coefficient. *Int. J. Hydrogen Energy* 44, 27177–27189. <https://doi.org/10.1016/j.ijhydene.2019.08.188>
- Wang, Y., Hu, Y.-J., Hao, X., Peng, P., Shi, J.-Y., Peng, F., Sun, R.-C., 2020. Hydrothermal synthesis and applications of advanced carbonaceous materials from biomass: a review. *Adv. Compos. Hybrid Mater.* 3, 267–284. <https://doi.org/10.1007/s42114-020-00158-0>
- Wongso, V., Sambudi, N.S., Sufian, S., Isnaeni, 2020. The effect of hydrothermal conditions on photoluminescence properties of rice husk-derived silica-carbon quantum dots for methylene blue degradation. *Biomass Convers. Biorefinery.* <https://doi.org/10.1007/s13399-020-00662-9>
- Yang, F., Ma, X., Cai, W. Bin, Song, P., Xu, W., 2019. Nature of Oxygen-Containing Groups on Carbon for High-Efficiency Electrocatalytic CO₂ Reduction Reaction. *J. Am. Chem. Soc.* 141, 20451–20459. <https://doi.org/10.1021/jacs.9b11123>
- Zhao, Y., Jing, S., Peng, X., Chen, Z., Hu, Y., Zhuo, H., Sun, R., Zhong, L., 2020. Synthesizing green carbon dots with exceptionally high yield from biomass hydrothermal carbon. *Cellulose* 27, 415–428. <https://doi.org/10.1007/s10570-019>
- Zhu, C., Yang, S., Wang, G., Mo, R., He, P., Sun, J., Di, Z., Kang, Z., Yuan, N., Ding, J., Ding, G., Xie, X., 2015. A new mild, clean and highly efficient method for the preparation of graphene quantum dots without by-products. *J. Mater. Chem. B* 3, 6871–6876. <https://doi.org/10.1039/c5tb01093d>

CHAPTER 7

Fabrication of a Miniaturized Electrochemical Sensing Device using Cu and Cu@Ag Nanorods for Heavy Metals Sensing



Highlights

- ◆ Highly structured CuNRs and Cu@AgNRs formation using ascorbic acid as a reducing agent
- ◆ Miniaturized Cu@AgNRs/FTO based three-electrode sensing platform alternative to the conventional three-electrode system
- ◆ Cu@AgNRs/FTO based sensing device demonstrates nM level simultaneous detection for Zn(II), Cd(II) and Pb(II) ions
- ◆ Device reusable for 4 cycles for heavy metal sensing in the river and domestic water supply

7.1 Background and executive motivation

Environmental monitoring is one of the most critical issues that is given the highest priority by the authorities. The regulating bodies are making waste disposal parameters stricter and stricter over the period. On the other hand, rapid industrialization and extensive agricultural practices have seen an increased use of pesticides and insecticides that lead to heavy metals (HMs) contamination in water and soil (Wuana and Okieimen, 2011). These HMs end up entering into the food chain, thereby destabilizing the ecosystem. Intake of HMs more than the allowable limits could affect humans in various ways leading to reproductive disorders (Bansod et al., 2017), respiratory diseases (Oliver, 2011), and neural disorders (Sanders et al., 2009). On entering the human body, Pb(II) ions affect the nervous system and hinder their reasoning and intelligence capability (Migliorini et al., 2017). Similarly, Cd(II) ions are known to bioaccumulate in the human body and could affect the bones, kidneys, and liver. Hg(II) ions are known to be highly persistent in nature and affect humans by degenerating the kidneys and causes various cardiovascular issues (Singh et al., 2020). The source of Zn(II) in the environment is the uncontrolled disposal of industrial wastes such as metal plating industries into land and water bodies. Though a small amount of zinc is necessary as a macronutrient in human bodies, an excessive intake of Zn(II) has been shown to affect bone mass density and cause renal problems (Qu et al., 2020).

Many detection techniques such as atomic absorption spectroscopy (Gupta et al., 2010), inductively coupled plasma mass spectroscopy (Ammann, 2002), inductively coupled plasma emission spectroscopy (Ebrahimi-Najafabadi et al., 2019), and colorimetric methods (Yan et al., 2020) have been developed for the ultrasensitive detection of these heavy metal ions. However, these methods beset with high installation costs and limitations for on-field applications. Electrochemical techniques, on the other hand, are low-cost, highly sensitive, and selective towards the target analyte(s). The miniaturized systems like screen-printed electrodes have been proven to be useful for on-field applications (Aragay et al., 2011; Barton et al., 2016; Liu et al., 2019).

Further, modification of the working electrodes with nanomaterials has shown improved electrokinetic and electrocatalytic activities along with improved electrical conductivity (Cabello et al., 2017; Fang et al., 2011; Kim et al., 2016; Londono-Calderon et al., 2017). For instance, the Au@Ag core-shell nanoparticles have been used in fabricating the electrochemical sensors with enhanced Hg(II) sensing (Xu et al., 2018). Moreover, modification of the nanoparticles' surface could further enhance the

electrocatalytic response towards HMs sensing. Modifying the electrode surface with metal nanoparticles (Gong et al., 2010; Niu et al., 2015; Prakash and Shahi, 2011; Torres-Rivero et al., 2019), conductive polymers (Lo et al., 2018; Promphet et al., 2015; Yang et al., 2015; Zuo et al., 2016), ionic-liquids (Oularbi et al., 2020; Wang et al., 2017), etc. to increase the sensitivity of electrochemical sensors along with the use of specialized electrodes like boron-doped diamond electrodes (Read et al., 2014) and gold electrodes (Bernalte et al., 2020) have been reported. The successful use of fluorine-doped tin oxide (FTO) electrode is scanty for HMs sensing. FTO electrode modified with polyamide 6/chitosan electrospun nanofibers and gold nanoparticles were successful for the voltammetric sensing of Cd(II) ions (Migliorini et al., 2017). However, the potential of FTO and modified FTO as electrode materials for the concurrent sensing of HMs such as Zn(II), Cd(II), Pb(II), and Hg(II) present in water have never been explored in literature.

In the previous study (Chapter 4), it has been reported that bi-metallic Ag@Pt core-shell nanoparticles could show enhanced sensitivity towards the detection of Pb(II) ions in the presence of other HMs. In this chapter, copper-based nanocatalyst, a cheaper alternative, was synthesized in an environmentally friendly approach for simultaneous detection and quantification of HMs. Towards this goal, a miniaturized FTO-based three-electrode system is developed for in-field applications. The FTO-based miniaturized three-electrode sensing devices were decorated by Cu nanorods (CuNRs) and Cu@Ag nanorods (Cu@AgNRs) as sensing modifiers. The sensing devices (CuNRs/FTO and Cu@AgNRs/FTO) were employed for ultrasensitive electrocatalytic detection and determination of Zn(II), Cd(II), Pb(II), and Hg(II) ions present together in various environmental water samples.

7.2 Results and discussions

7.2.1 Synthesis and characterizations of CuNRs and Cu@AgNRs

7.2.1.1 Progressive formation of CuNRs and Cu@AgNRs

The bluish-green colour of the CuCl_2 solution immediately turned white as soon as the ascorbic acid (AA), polyvinylpyrrolidone (PVP), and NaCl mixture was poured into the CuCl_2 solution, which could be due to the formation of CuCl^- precipitate due to the reduction of CuCl_2 in the presence of a high concentration of AA (Figure 7.1a). As the reaction temperature increased to 80°C , the white precipitate dissolved to form a colorless solution (Figure 7.1b). This is attributed to the formation of a stable $[\text{CuCl}]^-$ complex due to the presence of the additive NaCl that supplies excessive Cl^- ions (Yokoyama et al.,

2018). Figures 7.1c-7.1g show the change in the colour of the reaction mixture at different time intervals. Figure 7.1h shows the synthesized CuNRs at the end of the reaction period.

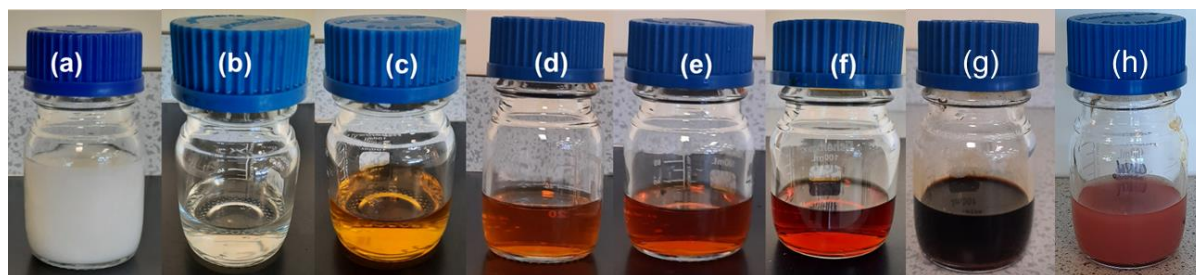


Figure 7.1: Digital photographs showing various stages of the progression of CuNRs synthesis: (a) Initial solution (60 mL), (b) 15 min, (c) 1 h, (d) 3 h, (e) 5 h, (f) 7 h, (g) 24h of reaction time, and (h) cleaned CuNRs suspended in water. Reaction conditions: CuCl₂ 0.1 M, NaCl 0.35 M, AA 1.5 M and PVP 2.4 wt%, reaction volume 30 mL, pH 3.5 and reaction temperature 80°C.

7.2.1.2 Spectral absorbance of CuNRs and Cu@AgNRs

Figure 7.2 shows the UV-vis spectroscopic analysis of the synthesized CuNRs and Cu@AgNRs dispersed in water. A distinct peak is observed at $\lambda = 592$ nm for CuNRs (black), which is indicative of the formation of copper nanowires (Liu et al., 2012). It can be observed that on reaction with Ag for 2 hours, the SPR peak due to copper is masked by the SPR peak of Ag ($\lambda = 431$ nm, red). This could be due to the deposition of Ag over the CuNRs. The deposition of Ag on CuNRs can be attributed to the galvanic displacement, which is further augmented by the presence of AA. PVP in the reaction solution helps in stabilizing the prepared Cu@AgNRs. Similar results were obtained in our previous studies on the synthesis of Ag@Pt core-shell nanoparticles where the SPR peak of the core (Ag) was masked by the deposition of Pt (shell) over it (Chapter 4).

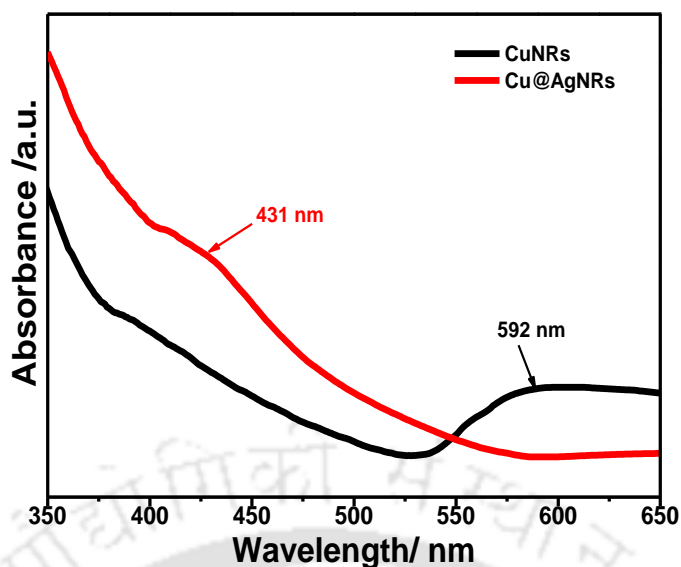


Figure 7.2: UV-vis spectroscopy analysis of the synthesized CuNRs and Cu@AgNRs. Reaction conditions CuCl_2 0.1 M, NaCl 0.35 M, AA 1.5 M and PVP 2.4 wt%, reaction volume 30 mL, pH 3.5 and reaction temperature 80°C .

7.2.1.3 Nature of crystallinity of CuNRs and Cu@AgNRs

Figures 7.3a-7.3c show the XRD analysis of CuNRs and Ag@CuNRs. The three peaks at $2\theta = 43.5^\circ$, 50.3° , and 74.1° correspond respectively to the diffraction from (111), (200) and (220) planes of face-centered cubic Cu (PDF card #00-004-0836) (Figure 7.3a), indicating that almost pure CuNRs were formed. Similarly, in the case of Cu@AgNRs (Figure 7.3b), the diffraction from (111), (200), (220), (311), and (222) planes at 38.2 , 44.2 , 64.4 , 77.5 and 81.5° 2θ angle corresponds to face-centered cubic Ag crystals (PDF card #01-077-6540), (Figure 7.3c). Few unassigned peaks (much weaker than Cu and Ag peaks) at 35.8° , 42.1° , 46.6° , 51.1° and 51.8° 2θ angle could be due to the organic substances contributed by ascorbic acid, PVP, and a trace amount of NaCl (additive) that may be present on the nanowires as reducing and stabilizing agents (Anandalakshmi et al., 2016; Arya et al., 2019).

7.2.1.4 FTIR spectra of CuNRs and Cu@AgNRs

The FTIR analysis of the synthesized CuNRs and Cu@AgNRs is presented in Figures 7.4a-7.4b. Figures 7.4a and 7.4b show similar curves, which show that the same reducing and stabilizing agents are involved in the formation of the CuNRs and Cu@AgNRs. The strong peak observed at 3450 cm^{-1} corresponds to the stretching vibration of the O-H adsorbed water group on the nanomaterial surface. C=O vibrating and

out of ring C–H bonds, respectively, give the peaks at 1680 and 1384 cm^{-1} , which could be from the carboxylic acid functional group from the AA. The C–N vibration generates a small yet important peak at around 1288 cm^{-1} , which proves the stabilization being done by PVP. The only source of the C–N bond is from the nitrogen present in the pyrrole ring in the PVP.

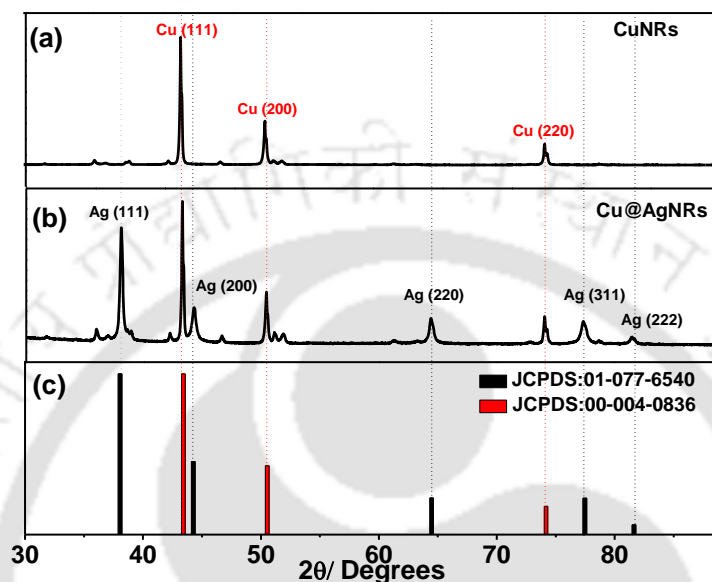


Figure 7.3: XRD analysis of the synthesized (a) CuNRs, (b) Cu@AgNRs, and (c) Corresponding JCPDS card. Reaction conditions: CuCl_2 0.1 M, NaCl 0.35 M, AA 1.5 M and PVP 2.4 wt%, reaction volume 30 mL, pH 3.5 and reaction temperature 80°C .

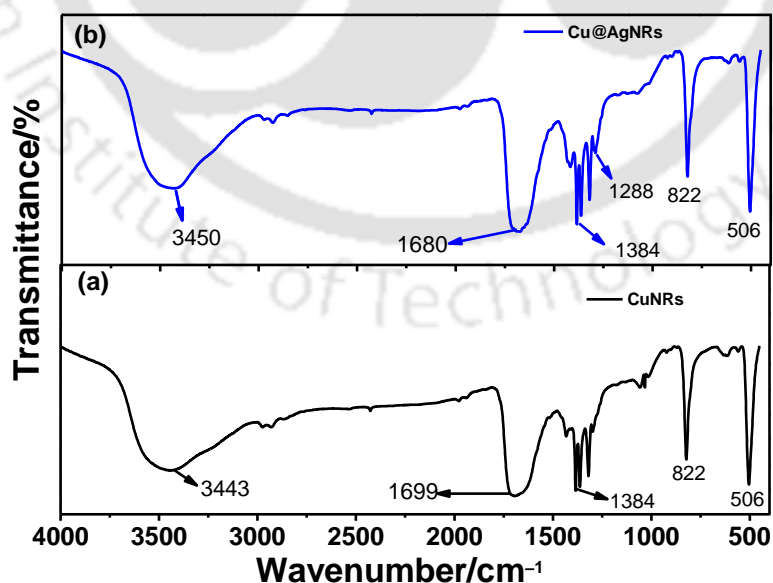


Figure 7.4: FTIR spectra of (a) CuNRs and (b) Cu@AgNRs showing various functional groups present on the nanomaterial surface.

7.2.1.5 FETEM and EDX analysis of CuNRs and Cu@AgNRs

Figure 7.5a shows a FETEM micrograph of CuNRs (average aspect ratio = 8.0). A close examination indicates that these NRs have a cyclic penta-twinned structure with five {111}-type twin boundaries arranged radially along the common {110} surface (Figure 7.6a) which is a typical phenomenon in the case of CuNRs (Lisiecki et al., 2000; Luo et al., 2016). Two sets of diffraction rings with a lattice spacing of 0.225 nm and 0.144 nm were observed, corresponding to the (111) and (220) planes of face-centered cubic Cu crystal, respectively (Figure 7.6b) (Luo et al., 2016). Figure 7.6b shows the FETEM micrograph of the synthesized Cu@AgNRs. Irregular thin layer surface deposition of Ag over the CuNRs can be seen at higher magnification (Figure 7.5c). HRTEM micrograph reveals the crystalline fringes with a lattice spacing of 0.24 nm corresponding to (111) of fcc Ag (Figure 7.5d) (Ahmad et al., 2010; Prathna et al., 2011). The elemental mapping (Figures 7.5e-7.5g) and EDX analysis show the deposition of Ag over CuNRs, and the percentage composition of Ag was 21.3 wt%, and Cu core was 78.8 wt%.

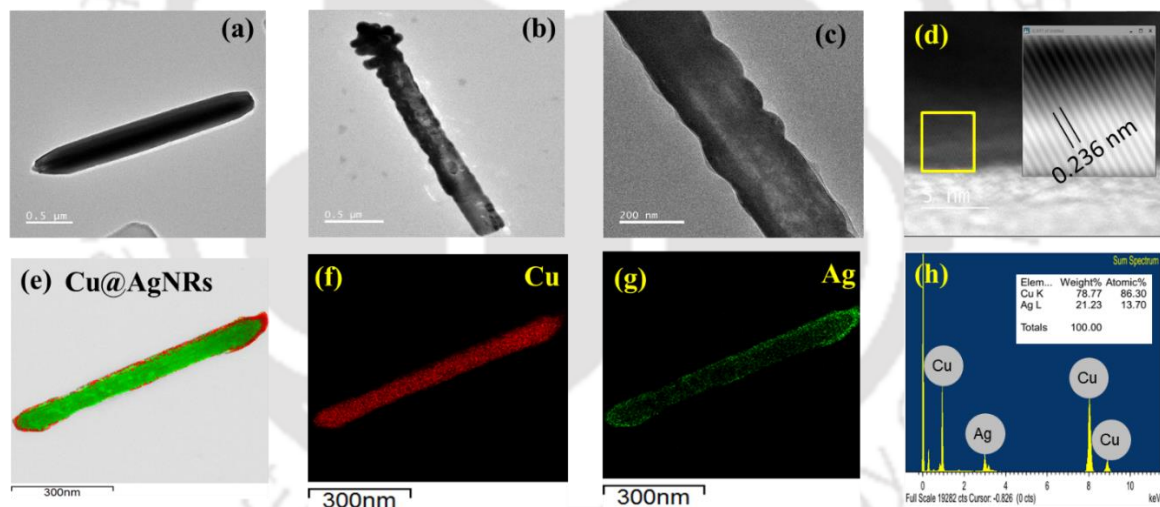


Figure 7.5: TEM micrographs of (a) CuNRs, (b and c) Cu@AgNRs, (d) HRTEM micrograph, (e) Elemental mapping, and Elemental distribution of (f) Copper, (g) Silver, and (h) EDX spectra and the elemental composition of Cu@AgNRs.

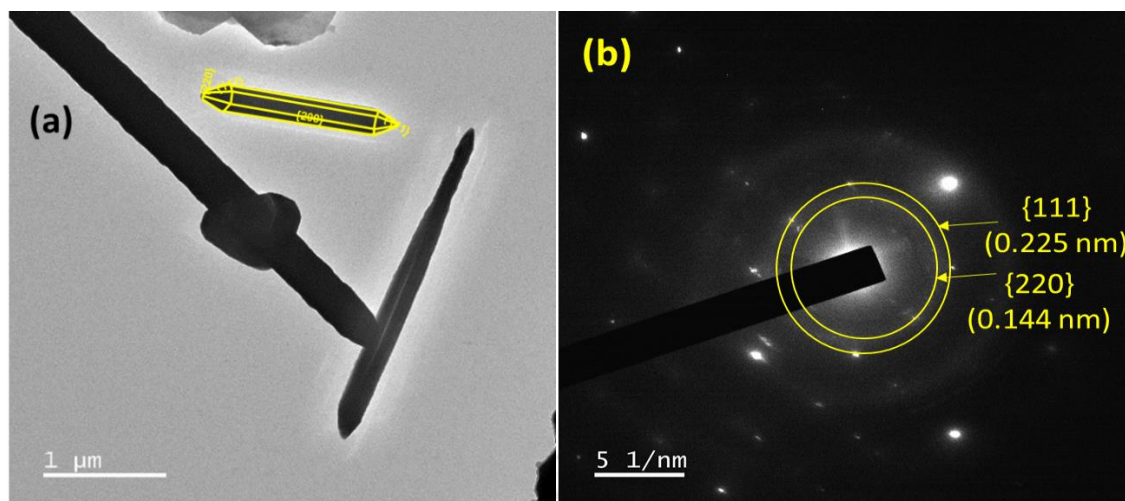


Figure 7.6: (a) FETEM micrograph of CuNRs showing the growth of various crystalline faces and (b) SAED image of CuNRs showing various diffraction rings.

7.2.2 Electrochemical characterization of the fabricated electrodes

7.2.2.1 Electrochemical impedance spectroscopy (EIS)

The obtained Nyquist plot (Figure 7.7a) shows that for the bare FTO, the electrode resistance was 3.69 KΩ and a solution resistance of 96.5 Ω (Figure 7.7b). A Warburg component that models the linear diffusion towards the electrode surface was required to complete the circuit, which shows the heterogeneity and the diffusion limitation of the electrochemical system (Macdonald and Andreas, 2014; Shi et al., 1999). The CuNRs/FTO and Cu@AgNRs/FTO show the resistance of 2.91 and 2.35 kΩ, respectively, which could be due to the increased conductivity induced by the presence of metal nanocomposites on its surface (Figures 7.7b-7.7d).

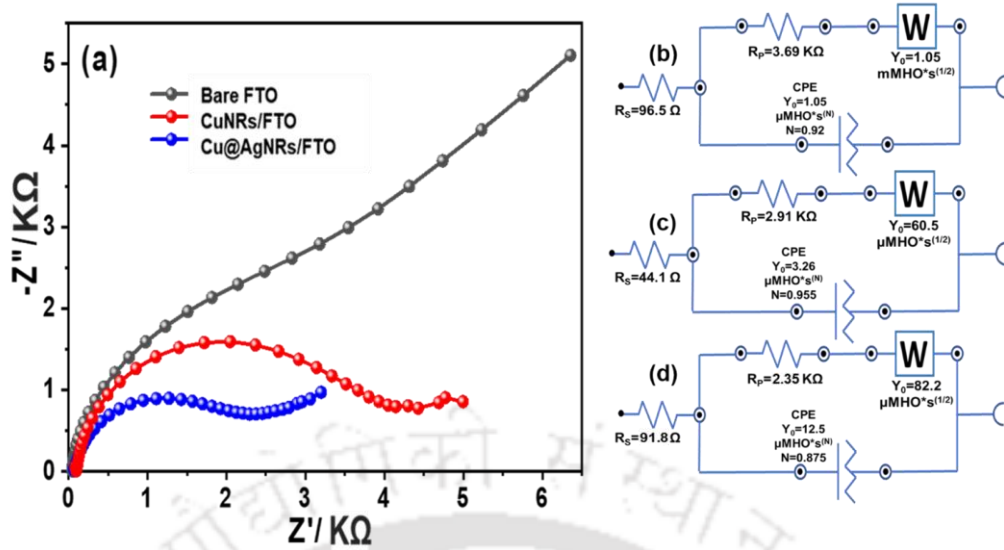


Figure 7.7 (a) Nyquist plot showing the change in resistance due to surface modifications of the FTO, (b) Bare FTO, (c) CuNRs/FTO, and (d) Cu@AgNRs/FTO showing the corresponding equivalent circuits.

7.2.2.2 Determination of electro-active surface area

The electrochemical surface area was determined by using the Randles-Sevcik relation (Eq. 4.2 of Chapter 4). The cyclic voltammograms of each electrode at varying scan rates are presented in Figures 7.8a-7.8c. It can be seen that the peak currents gradually were increased with the increase in the scan rate ($5\text{-}200\text{ mV}\cdot\text{s}^{-1}$). The peak currents obtained in the case of Cu@AgNRs/FTO is the maximum followed by CuNRs/FTO. The increase in the peak current response was about 4 times in the case of CuNRs/FTO and 5 times in the case of ACu@AgNRs/FTO. In the case of modified electrodes, the shift of the peak positions to lower potentials is indicative of an enhanced electrokinetics activity. From the plot of I_{pa} vs. $v^{0.5}$ (Figure 7.8d) and equating the slope values by considering D for $\text{K}_3(\text{Fe}[\text{CN}_6])$ as $6.67 \times 10^{-6}\text{ cm}^2\text{ s}^{-1}$ ($n = 1$) (De Lima and Maia, 2015), A_{eff} was found to be 0.026, 0.093, and 0.125 cm^2 , respectively for bare FTO, CuNRs/FTO and Cu@AgNRs/FTO. Their corresponding slope values were 0.0473, 1.671, and 2.24 ($\times 10^{-4}\cdot\text{A}\cdot\text{V}^{-0.5}\cdot\text{s}^{0.5}$).

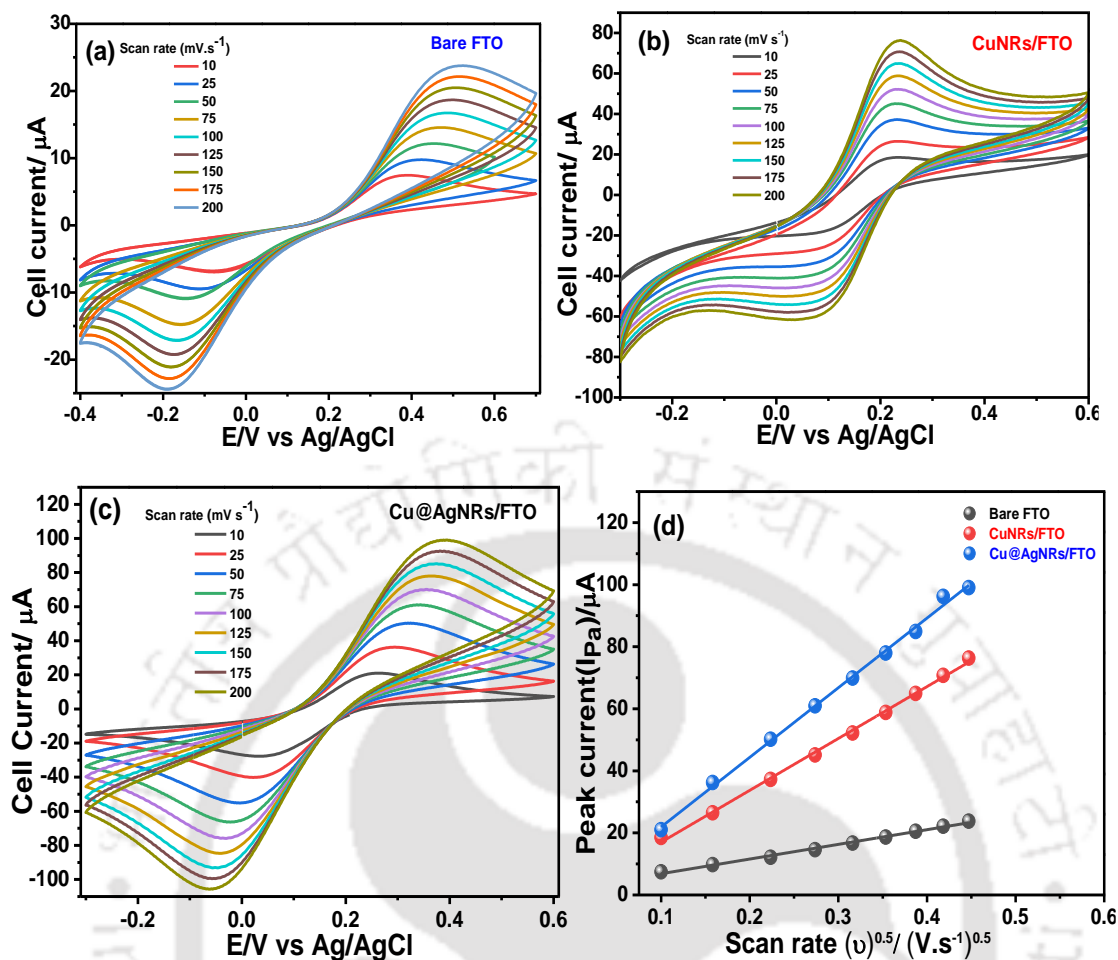


Figure 7.8: Cyclic voltammograms with different electrodes: (a) Bare FTO, (b) CuNRs/FTO and (c) Cu@AgNRs/FTO at various scan rates (10–200 $mV.s^{-1}$) and (d) Variation of peak current with square root of scan rate. Reaction conditions: $K_3(Fe[CN]_6)$ (1 mM) in 100 mL of 0.1 M KCl at ambient temperature.

7.2.3 Electrochemical sensing of HMs

7.2.3.1 CuNRs/FTO in electrochemical sensing of single HM

The square wave voltammetry method was used for the HMs sensing using CuNRs/FTO. Figures 7.9a–7.9d show the current response of Zn(II), Cd(II), Pb(II), and Hg(II) ions, respectively. It can be seen that the peak potential obtained for Zn(II), Cd(II), Pb(II), and Hg(II) were respectively at -1.3 , -0.95 , -0.50 , and 0.15 vs. $Ag/AgCl$.

Figure 7.9e shows the calibration curves at various concentrations of HMs. The limit of detection (LoD), the limit of quantification (LoQ), and the sensitivity were calculated using the Eq (3.3–3.5) of chapter 3.

The slope of the calibration curves was obtained from the corresponding linear equations depicted in Table 7.1. The LoD and LoQ for Zn(II) were calculated to be 0.005

and 0.017 μM . Similarly, for Pb(II), the LoD and LoQ were 0.007 and 0.026 μM . For Cd(II), it was respectively 0.030 and 0.099 μM . However, the least response was obtained in the case of Hg(II), and the LoD and LoQ obtained, in this case, were 0.124 and 0.414 μM , respectively. This could be due to the formation of Hg-Cu amalgams that hinder the stripping response of the sensor.

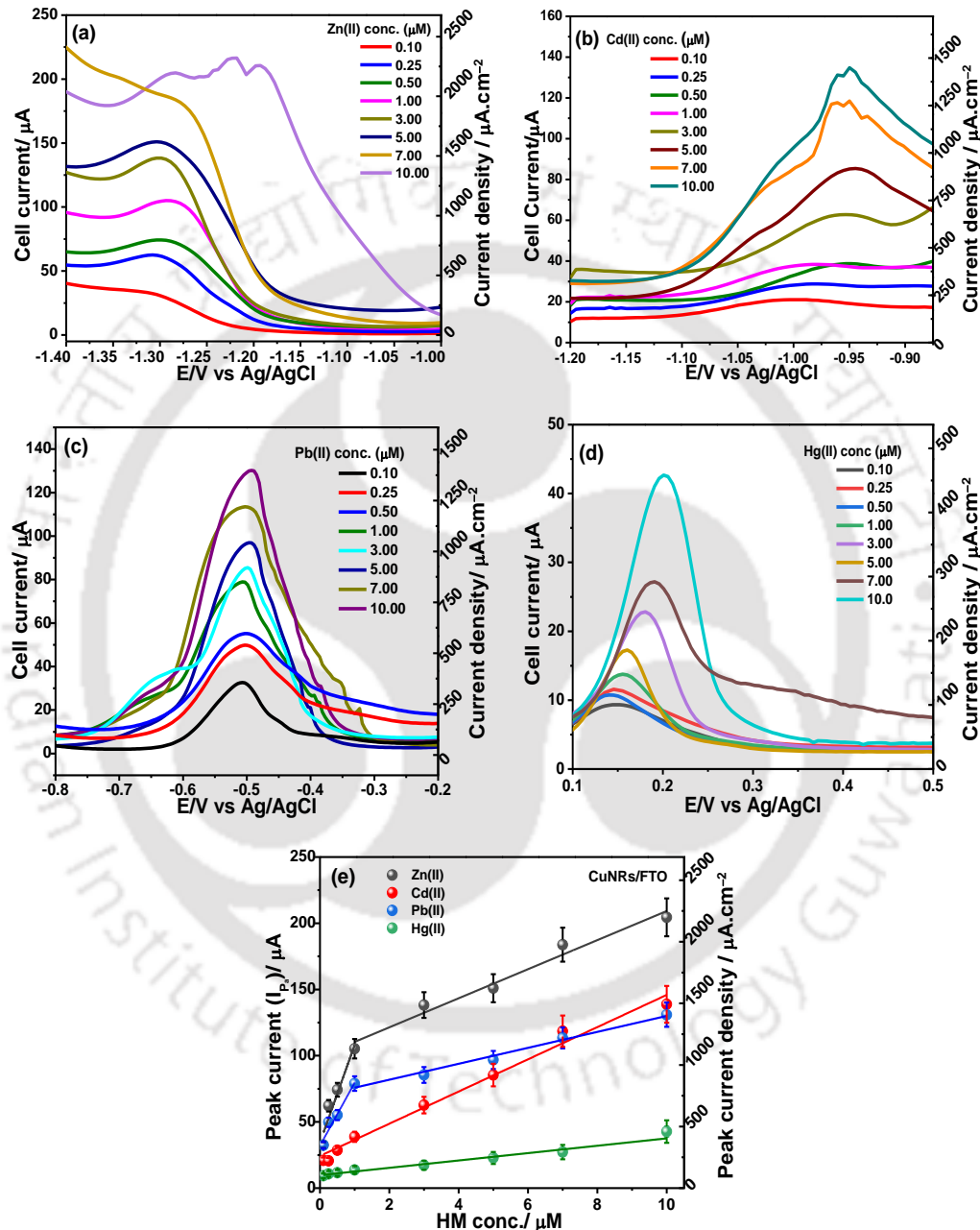


Figure 7.9: Square wave voltammograms recorded with different HM ions: (a) Zn(II), (b) Cd(II), (c) Pb(II), (d) Hg(II), and (e) Corresponding calibration curves using CuNRs/FTO based miniature device. Reaction conditions HMs concentration 0.1-10 μM in acetate buffer at pH 5. The frequency was set at 15 Hz and amplitude 0.02 V, deposition time 90 s and conditioning time 30 s.

Table 7.1: Fabricated sensor performance parameters for individual HM detection using CuNRs/FTO.

CuNRs/FTO	Sensor parameters	Zn(II)	Cd(II)	Pb(II)	Hg(II)
	Linear range (μM)	0.1-1 and 1-10			
	Linear equation	$I_{\text{pa}}(\mu\text{A}) = 73.6[\text{Zn(II)}] \mu\text{M} + 34.5$	$I_{\text{pa}}(\mu\text{A}) = 12.2[\text{Cd(II)}] \mu\text{M} + 24.3$	$I_{\text{pa}}(\mu\text{A}) = 47.4[\text{Pb(II)}] \mu\text{M} + 32.1$	$I_{\text{pa}}(\mu\text{A}) = 3.0[\text{Hg(II)}] \mu\text{M} + 9.3$
	R-squared	0.90	0.98	0.92	0.96
	LoD/LoQ (μM)	0.005/0.017	0.030/0.099	0.007/0.026	0.124/0.414
	Effective surface area (cm^2)	0.093	0.093	0.093	0.093
	Sensitivity ($\mu\text{A} \cdot \mu\text{M}^{-1} \cdot \text{cm}^{-2}$)	791.3	130.7	510.1	32.4

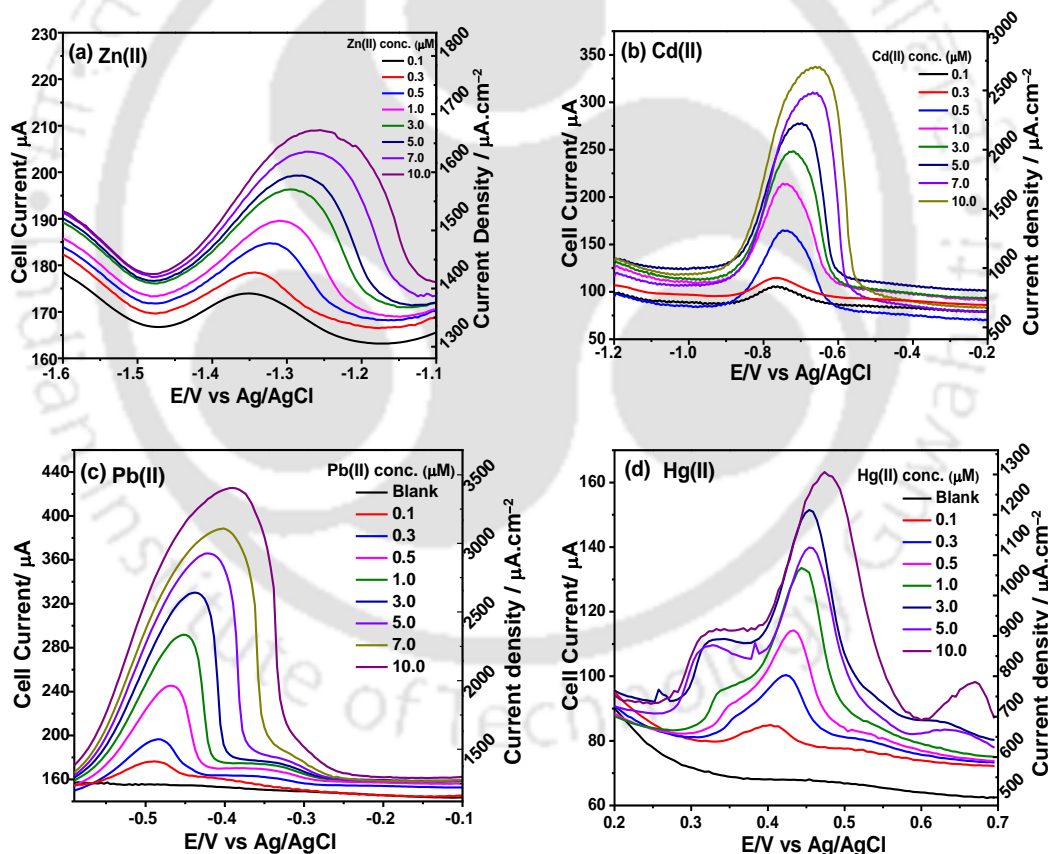
7.2.3.2 Cu@AgNRs/FTO in electrochemical sensing of single HM

The electronic effect plays an important role in explaining charge transfer efficiencies in bi-metallic nanocatalysts. From monometallic to bi-metallic nanoparticles, an additional degree of freedom is introduced that enhances their electrocatalytic catalytic characteristics. Figure 7.10 shows the individual determination of Zn(II), Pb(II), Cd(II), and Hg(II) in 0.1 M of acetate buffer at pH 5.0 against the deposition potential of -0.4 V for 90 s at Cu@AgNRs/FTO. For individual Zn(II), Pb(II), Cd(II), and Hg(II) ions, the peak potential was noted at -1.3 , -0.78 , -0.55 , and -0.4 V vs. Ag/AgCl, respectively (Figures 7.10a–7.10d). As the concentration of metal ions increases, the stripping current increased. The corresponding calibration plot of various metal ions is depicted in Figure 7.10e. Two linear ranges could be observed, which can be attributed to the change in the electrochemical reaction from diffusion-controlled at a lower concentration to surface controlled reaction at higher concentrations. Moreover, at higher concentrations, more HMs get deposited on the working electrode surface, and it becomes difficult for the system to strip all the HMs from the surface during the stripping phase of the SWASV process. Hence it shows a dip in the calibration slope at higher concentrations, thereby decreasing the sensitivity of the sensor.

The efficiency parameters for many HMs are summarized in Table 7.2. The sensitivity of Pb(II) was estimated to be approx. 1.1, 2.8, and 5.1 times higher as compared to Cd(II), Hg(II), and Zn(II). Again from Table 7.2, it can be observed that Cu@AgNRs/FTO showed improved sensing of all other HMs under consideration except for Zn(II). This could be due to the bi-metallic interactions between Ag and Zn that might have reduced the electrocatalytic activity of the sensor towards Zn(II).

Table 7.2: Fabricated sensor performance parameters for individual HM detection using Cu@AgNRs/FTO.

Cu@AgNRs/FTO	Sensor parameters	Zn(II)	Cd(II)	Pb(II)	Hg(II)
	Linear range (μM)	0.1-1 and 1-10			
	Sensitivity ($\mu\text{A} \cdot \mu\text{M}^{-1} \cdot \text{cm}^{-2}$)	791.3	130.7	510.1	32.4
	Linear range (μM)	0.1-0.5 and 0.5-10	0.1-1 and 1-10		
	Linear equation	$I_{\text{pa}}(\mu\text{A}) = 29.37[\text{Zn(II)}] \mu\text{M} + 167.8$	$I_{\text{pa}}(\mu\text{A}) = 126.1[\text{Cd(II)}] \mu\text{M} + 88.7$	$I_{\text{pa}}(\mu\text{A}) = 150.21[\text{Pb(II)}] \mu\text{M} + 111.8$	$I_{\text{pa}}(\mu\text{A}) = 52.55[\text{Hg(II)}] \mu\text{M} + 83.3$
	R-squared	0.98	0.94	0.93	0.95
	LoD/LoQ (μM)	0.009/0.03	0.003/0.010	0.001/0.003	0.005/0.16
	Effective surface area (cm^2)	0.125	0.125	0.125	0.125
	Sensitivity ($\mu\text{A} \cdot \mu\text{M}^{-1} \cdot \text{cm}^{-2}$)	234.96	1048	1200	420.4



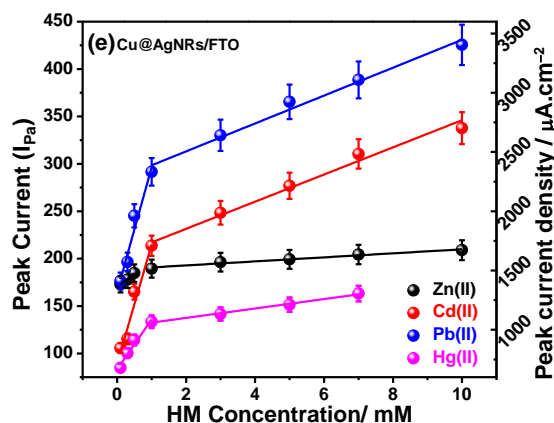


Figure 7.10. Square wave voltammograms captured with different HMs ions: (a) Zn(II), (b) Cd(II), (c) Pb(II), and (d) Hg(II) using Cu@AgNR/FTO based miniature device. Reaction conditions HMs concentration 0.1–10 μM in acetate buffer at pH 5. The frequency was set at 15 Hz and amplitude 0.02 V, deposition time 90 s, and conditioning time 30 s.

7.2.3.3 Simultaneous electrochemical sensing of HMs

Simultaneous detection and determination of Zn(II), Cd(II), Pb(II), and Hg(II) at the Bare FTO, CuNRs/FTO, and Cu@AgNR/FTO were carried out in this study, and the SWASV signals were captured simultaneously (Figure 7.11). It can be seen that blank FTO (Figure 7.11 black curve) could not produce any stripping signals for the HMs, whereas CuNRs/FTO, though could sense Cd(II), Pb(II), and Hg(II), it was unable to give any signals for Zn(II) even at high concentration (10 μM). For Cu@AgNRs/FTO, well-separated peaks were obtained. With the increase of each HMs concentration from 0.25 μM to 10 μM at a potential range of -1.4 V to +0.5 V vs. Ag/AgCl, the maximum currents gradually increased. Figures 7.12a and 7.12b show the SWASV signals for both devices. For CuNRs/FTO, the best detection for Pb(II) was possible with an extended linear range from 0.25–10 μM . However, the detection of other considered HMs was poor. The detection of Zn(II) was possible only above the concentration of 1 μM , and the detection was ceased above the concentrations of 5 μM . Similarly, the detection of Hg(II) was also very weak, with the slope of the calibration curve being 1.47. The SWASV signals and the calibration curves of the HM ions on the Cu@AgNRs/FTO device (Figures 7.12b and 7.12d) demonstrate two linear ranges between the concentrations. The linear regression equation, the corresponding linear range, linear correlation coefficient, and other performance parameters are summarized in Table 7.3. The LODs with the signal-to-noise ratio of 3 ($s/n = 3$) were found to be 0.005 μM for Zn(II), 0.003 μM for Cd(II), 0.002 μM for Pb(II) and

0.02 μM for Hg(II), respectively. The Cu@AgNRs/FTO showed well resolution peaks with a separation of 0.40, 0.25, and 0.51 V between Zn(II)-Cd(II), Cd(II)-Pb(II), and Pb(II)-Hg(II), respectively. These results indicate that the developed Cu@AgNRs/FTO-based electrochemical platform is capable of simultaneous detection of multiple HM ions with high selectivity and sensitivity.

A noticeable variation in the sensitivity of HMs sensing in the individual and simultaneous analysis was observed. In the case of CuNRs/FTO-based device, there was a reduction of 7.0, 3.0, and 2.0 times in the LoD values for Zn(II), Pb(II), and Hg(II) during simultaneous HMs detection as compared to sensing of individual HMs. However, for Cd(II), there was no change in the LoD values, but a noticeable reduction in the sensitivity from 130.75 to 104.3 $\mu\text{A}\cdot\mu\text{M}^{-1}\cdot\text{cm}^{-2}$ was observed. An overall decrease in the sensitivity was also observed in the case of other analyzed HMs. Similarly, in the case of the Cu@AgNRs/FTO based device, it can be seen that there is a decrease in LoD during the simultaneous detection of HMs by about 1.5, 2.0, and 5 times for Cd(II), Pb(II), and Hg(II), respectively. However, the sensitivity attained by Cu@AgNRs/FTO devices was much higher as compared to CuNRs/FTO devices. In the case of Zn(II), an increase in the LoD was observed for simultaneous detection of HMs as compared to individual HM detection using Cu@AgNRs/FTO. This could be due to the presence of Hg film on the working electrode surface during the deposition period (Li et al., 2017). Though a decrease in the performance was observed during the simultaneous detection of HMs (with respect to individual sensing) at the Cu@AgNRs/FTO, the peaks were well-shaped with high resolution that could be instrumental for simultaneous determination of HMs with great accuracy.

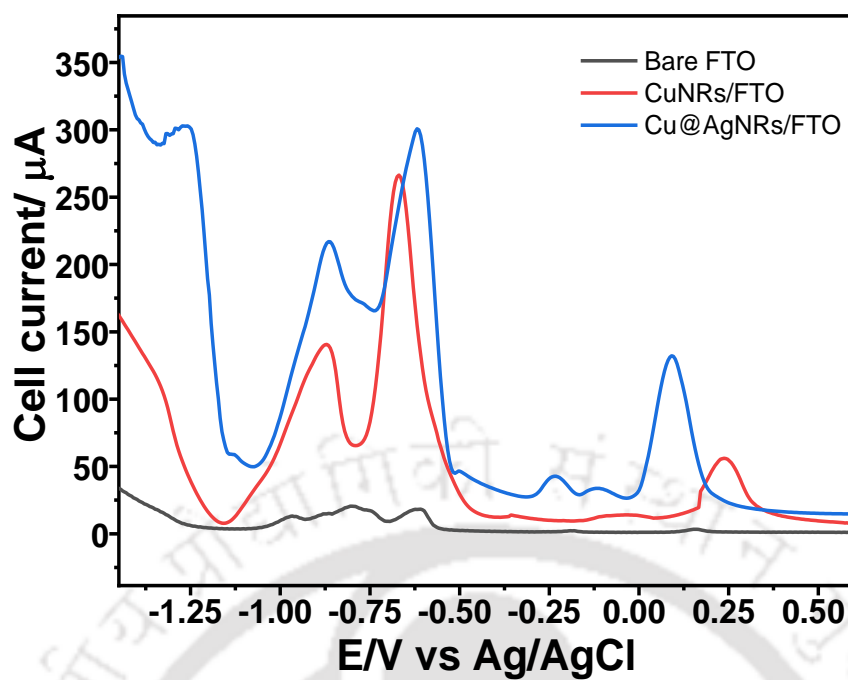


Figure 7.11: Simultaneous electrochemical sensing of Zn(II), Cd(II), Pb(II), and Hg(II) with various modified FTO based devices. Reaction conditions: HMs concentration 10 μM, in acetate buffer at pH 5.0. The frequency was set at 15 Hz and amplitude 0.02 V, deposition time 90 s, and conditioning time 30 s.

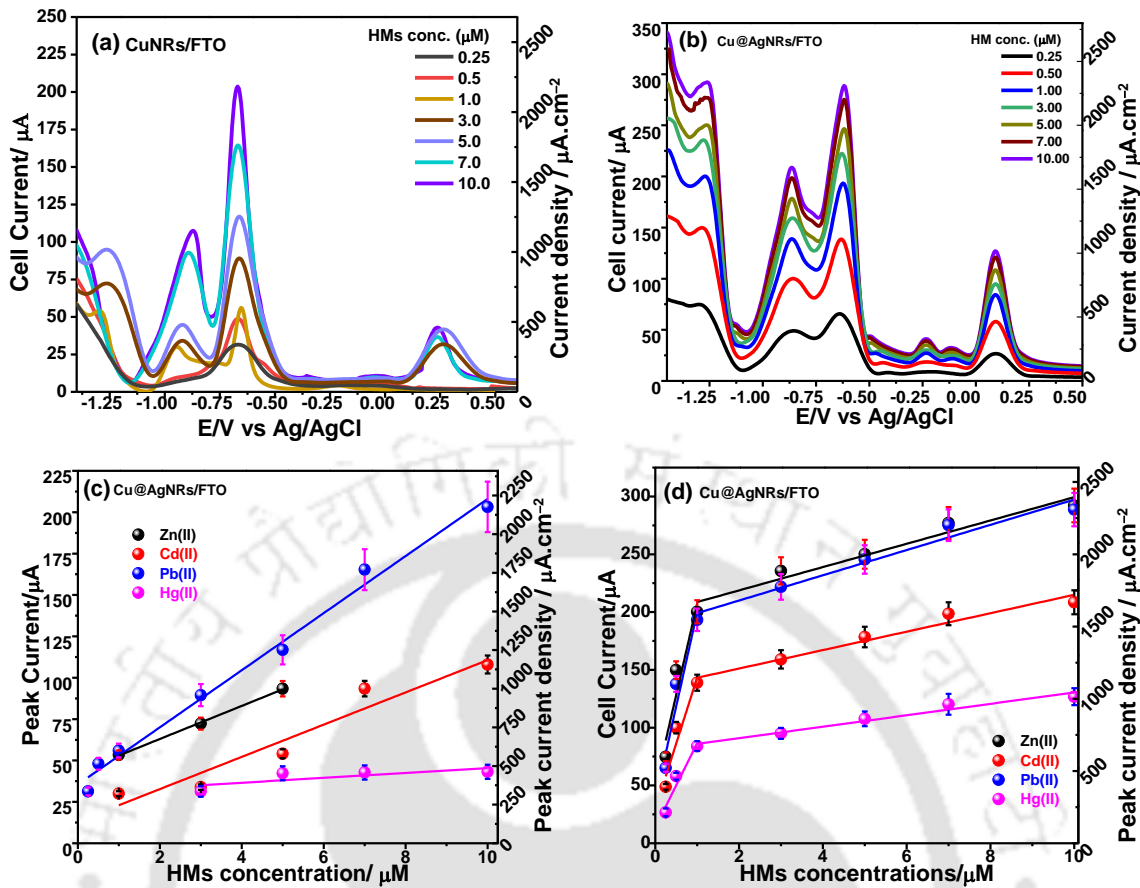


Figure 7.12: Squarewave voltammograms for simultaneous electrochemical sensing of Zn(II), Cd(II), Pb(II) and Hg(II) using (a) CuNRs/FTO and (b) Cu@AgNRs/FTO based devices, (c) Calibration curve with CuNRs/FTO, and (d) Calibration curves with Cu@AgNRs/FTO. Reaction conditions: HMs concentration 0.25-10 μM in acetate buffer at pH 5.0. The frequency was set at 15 Hz and amplitude 0.02 V, deposition time 90 s and conditioning time 30 s.

Table 7.3: Fabricated sensor performance parameters for simultaneous HMs detection.

	Sensor parameters	Zn(II)	Cd(II)	Pb(II)	Hg(II)
	CuNRs/FTO	Linear ranges (μM)	1-5	1-10	0.25 - 10
Linear equation		$I_{\text{pa}}(\mu\text{A}) = 9.99[\text{Zn(II)}] \mu\text{M} + 43.00$	$I_{\text{pa}}(\mu\text{A}) = 9.7[\text{Cd(II)}] \mu\text{M} + 13.23$	$I_{\text{pa}}(\mu\text{A}) = 17.2[\text{Pb(II)}] \mu\text{M} + 35.53$	$I_{\text{pa}}(\mu\text{A}) = 1.5[\text{Hg(II)}] \mu\text{M} + 30.64$
LoD (μM)		0.037	0.038	0.021	0.25
LoQ (μM)		0.123	0.127	0.071	0.845
Effective surface area (cm^2)		0.093	0.093	0.093	0.093
Sensitivity ($\mu\text{A} \cdot \mu\text{M}^{-1} \cdot \text{cm}^{-2}$)		107.4	104.6	185.4	15.9
Cu@AgNRs/FTO		Linear ranges (μM)	0.1-1 and 1-10		
	Linear equation	$I_{\text{pa}}(\mu\text{A}) = 29.4[\text{Zn(II)}] \mu\text{M} + 167.77$	$I_{\text{pa}}(\mu\text{A}) = 131.0[\text{Cd(II)}] \mu\text{M} + 165.5$	$I_{\text{pa}}(\mu\text{A}) = 150.2[\text{Pb(II)}] \mu\text{M} + 111.8$	$I_{\text{pa}}(\mu\text{A}) = 52.6[\text{Hg(II)}] \mu\text{M} + 83.27$
	LoD (μM)	0.005	0.003	0.002	0.025
	LoQ (μM)	0.017	0.010	0.006	0.080
	Effective surface area (cm^2)	0.125	0.125	0.125	0.125
	Sensitivity ($\mu\text{A} \cdot \mu\text{M}^{-1} \cdot \text{cm}^{-2}$)	1261.8	912.0	1297.9	583.6

7.2.3.4 Reproducibility and repeatability of fabricated devices

The reproducibility of the CuNRs/FTO and Cu@AgNRs/FTO was studied by intra-assay ($n = 3$). Relative standard deviations (RSD) with Cu@AgNRs/FTO are estimated to be Zn(II) (2.2%), Cd(II) (3.9), Pb(II) (0.98%) and Hg(II) (4.6%) far less than CuNRs/FTO Zn(II) (6.24%), Cd(II) (3.59%), Pb(II) (3.21%) and Hg(II) (7.5%). These findings demonstrate that Cu@AgNRs/FTO-based devices could minimize the detection signal differences arising from the background conditions, and it could also increase the reproducibility of the electrochemical system by minimizing the formation of oxide layers which is very important for the sensing of heavy metal ions on-the-ground application. The repeatability of the prepared devices was determined by running seven SWASV cycles using the same electrode. The SWASV signal is depicted in Figure 7.13. The peak signal responses are shown in Figure 7.14. It can be observed that there is no significant variation in the peak currents up to 4 cycles, after which there was a drastic decrease in the peak current signal in the case of both the devices. This can be attributed to the delamination of the FTO coating from the base FTO during the stripping and deposition when the counter electrode (bare FTO) acted as an anode. This was the reason why the deposition potential was limited to -0.4 V vs. Ag/AgCl to avoid the stripping of tin oxide.

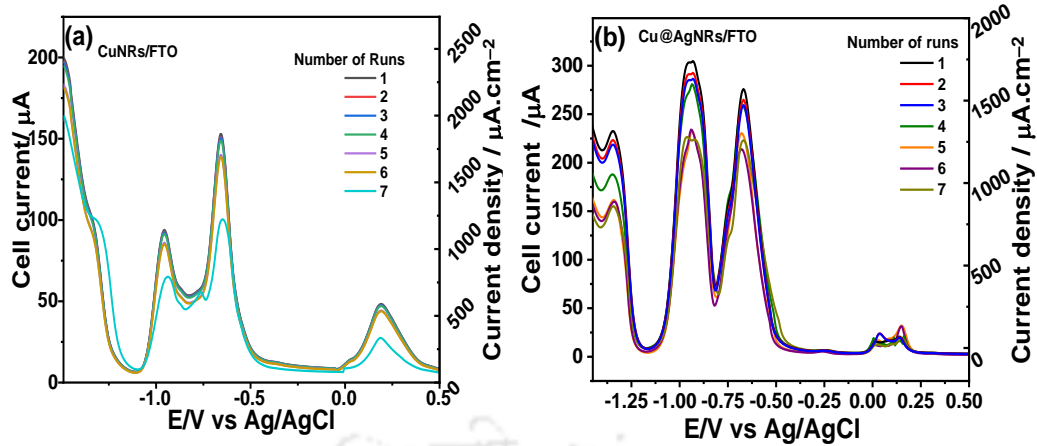


Figure 7.13: Square wave anodic stripping voltammetric profiles for simultaneous sensing of Zn(II), Cd(II), Pb(II), and Hg(II) using the fabricated miniaturized electrochemical device for seven different cycles at the (a) CuNRs/FTO and (b) Cu@AgNRs/FTO. Experimental conditions: Heavy metals concentration 10 μM , acetate buffer (pH 5.0), square wave frequency 15 Hz, amplitude 0.02 V, deposition time 90 s, deposition potential -0.5 V, and conditioning time 30 s.

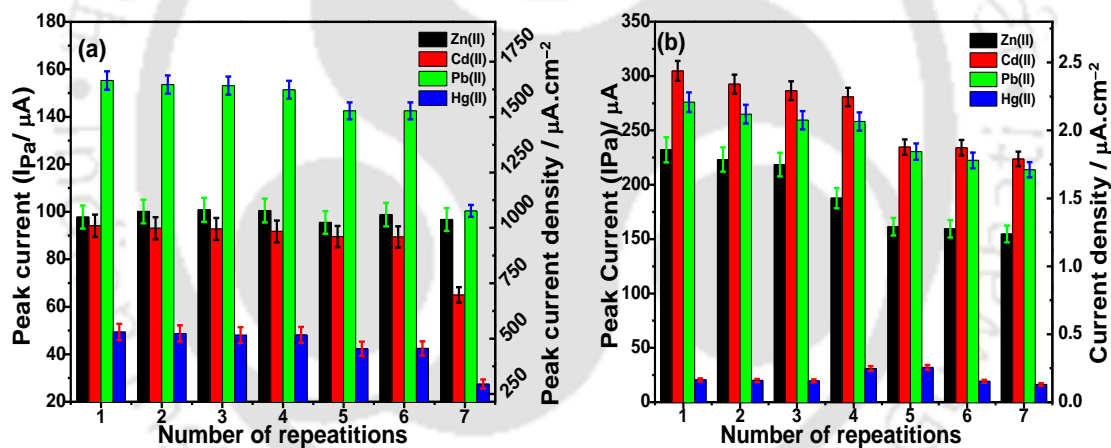


Figure 7.14: Repeatability of the peak current of sensing of heavy metal ions using (a) CuNRs/FTO and (b) Cu@AgNRs/FTO. Experimental conditions: HMs concentration 10 μM , acetate buffer (pH 5.0), square wave frequency 15 Hz, amplitude 0.02 V, deposition time 90 s, deposition potential -0.5 V, and conditioning time 30 s.

7.2.3.5 Cu@AgNRs/FTO device in environmental sample analysis

The developed Cu@AgNRs/FTO device was used for the detection of HMs present, if any, in real tap water and river water samples. The SWASV analysis for the quantification of the HMs was conducted as per the optimized parameters. In the environmental water samples, as can be seen in Figure 7.15, Zn(II), Cd(II), Pb(II), and Cu(II) stripping peaks

cannot be found. It indicates that the concentration of HMs was below the LODs of the device or that the target heavy metal ions do not occur in these samples. Therefore, the water samples were further spiked by the target HMs, and distinct and well-separated SWASV peaks were found for Zn(II), Cd(II), Pb(II), and Hg(II). The collected water samples were analyzed for their anions content, and the results are depicted in Figures 7.16a (river water)-7.16b (tap water). A very high concentration of PO_4^- ($365.65 \text{ mg}\cdot\text{L}^{-1}$) was obtained in the river water sample. Similarly, the highest concentration of Cl^- ($13.40 \text{ mg}\cdot\text{L}^{-1}$) was obtained in the tap water samples. The presence of F^- , and SO_4^- was also evident from the analysis. The tap water and river water based recovery experiment was performed using a standard supplement approach, and the results are presented in Table 7.4. The presence of interfering anions in the water sample did not show any significant adverse effects on the HMs quantification. In river water, the recovery value was obtained against a known spiked amount of HMs that were subjected for the simultaneous detection of HMs. The obtained values are 91.0–92.2, 93.9–104.9, 94.2–109.8, and 86.7–98.76% with RSD values of 3.9, 2.4, 2.1, and 5.2%, respectively. Similarly, in tap water samples, the recovery varied from 96.3–97.3, 98.7–103.3, 99.2–102.8, and 91.7–96.6%, respectively for Zn(II), Cd(II), Pb(II), and Hg(II). The RSD obtained for three replicates was 4.2, 2.2, 1.8, and 4.3%, respectively. These results clearly demonstrate that the proposed electrochemical sensors have high accuracy and reliability for sensing Zn(II), Cd(II), Pb(II), and Hg(II) in real samples.

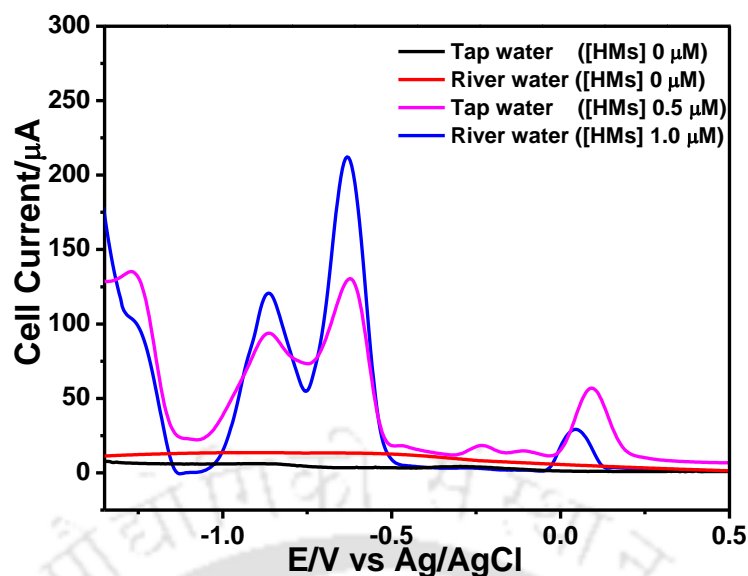


Figure 7.15: Square wave voltammetry signal for HMs in environmental water samples. Reaction conditions: The frequency was set at 15 Hz and amplitude 0.02 V, deposition time 90 s, and conditioning time 30 s at pH 5.

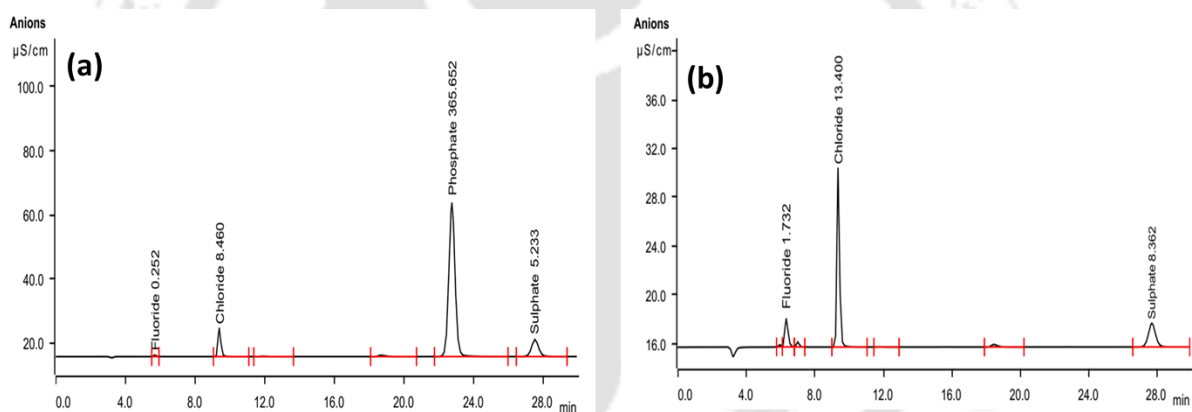


Figure 7.16: Ion-chromatographs of (a) River water and (b) Tap water used to prepare the samples spiked with HMs.

Table 7.4: Performance of Cu@AgNRs/FTO device for HMs determination from environmental water samples.

Sample	HMs (µM)	Recovery (%) obtained using Cu@AgNRs/FTO device			
		Zn(II)	Cd(II)	Pb(II)	Hg(II)
River water	0	ND	ND	ND	ND
	0.5	91.0	93.9	94.2	98.7
	1	92.2	104.9	109.8	86.7
Tap water	0	ND	ND	ND	ND
	0.5	97.3	98.8	99.2	96.6
	1	96.3	103.3	102.8	91.7

7.3 Major findings

In this work, we present an innovative and low-cost fabrication of an FTO-based miniaturized three-electrode system for the simultaneous determination of heavy metals Zn(II), Cd(II), Pb(II), and Hg(II), and this device is reusable up to 4 cycles. The devices showed an excellent analytical performance in terms of a very wide operating range spanning two linear ranges, one up to 1 μM and the other from 1 μM to 10 μM of HMs concentration. The coating of copper nanorods with silver showed enhanced sensing capabilities as compared to copper nanorods alone.

The potential of the fabricated Ag@CuNRs /FTO based devices in environmental sample analysis was demonstrated by the good reproducibility ($\text{RSD} \leq 5\%$) and the recovery values above 90% in the case of all the target HMs. Though a slight decrease in the sensitivity and other sensor performance was observed during simultaneous HMs detection, the limits were well below the permissible limits (EPA guidelines). This shows the capability of the fabricated device in the successful determination of HMs in a wide variety of environmental samples without any significant interferences. These FTO based miniaturized sensing platform could be a cheap alternative to the commercial screen-printed electrodes.

References

- Ahmad, N., Sharma, S., Alam, K., Singh, V.N., Shamsi, S.F., Mehta, B.R., Fatma, A., 2010. Colloids and Surfaces B : Biointerfaces Rapid synthesis of silver nanoparticles using dried medicinal plant of basil. *Colloids Surfaces B Biointerfaces* 81, 81–86. <https://doi.org/10.1016/j.colsurfb.2010.06.029>
- Ammann, A.A., 2002. Speciation of heavy metals in environmental water by ion chromatography coupled to ICP-MS. *Fresenius. J. Anal. Chem.* 372, 448–452. <https://doi.org/10.1007/s00216-001-1115-8>
- Anandalakshmi, K., Venugobal, J., Ramasamy, V., 2016. Characterization of silver nanoparticles by green synthesis method using *Petalium murex* leaf extract and their antibacterial activity. *Appl. Nanosci.* 6, 399–408. <https://doi.org/10.1007/s13204-015-0449-z>
- Aragay, G., Pons, J., Merkoi, A., 2011. Enhanced electrochemical detection of heavy metals at heated graphite nanoparticle-based screen-printed electrodes. *J. Mater. Chem.* 21, 4326–4331. <https://doi.org/10.1039/c0jm03751f>
- Arya, S., Prerna, Singh, A., Kour, R., 2019. Comparative study of CuO, CuO@Ag and CuO@Ag:La nanoparticles for their photosensing properties. *Mater. Res. Express* 6. <https://doi.org/10.1088/2053-1591/ab49ab>
- Bansod, B.K., Kumar, T., Thakur, R., Rana, S., Singh, I., 2017. A review on various electrochemical techniques for heavy metal ions detection with different sensing platforms. *Biosens. Bioelectron.* 94, 443–455. <https://doi.org/10.1016/j.bios.2017.03.031>
- Barton, J., García, M.B.G., Santos, D.H., Fanjul-Bolado, P., Ribotti, A., McCaul, M., Diamond, D., Magni, P., 2016. Screen-printed electrodes for environmental monitoring of heavy metal ions: a review. *Microchim. Acta* 183, 503–517. <https://doi.org/10.1007/s00604-015-1651-0>
- Bernalte, E., Arévalo, S., Pérez-Taborda, J., Wenk, J., Estrela, P., Avila, A., Di Lorenzo, M., 2020. Rapid and on-site simultaneous electrochemical detection of copper, lead and mercury in the Amazon river. *Sensors Actuators, B Chem.* 307, 127620. <https://doi.org/10.1016/j.snb.2019.127620>
- Cabello, G., Davoglio, R.A., Hartl, F.W., Marco, J.F., Pereira, E.C., Biaggio, S.R., Varela, H., Cuesta, A., 2017. Microwave-Assisted Synthesis of Pt-Au Nanoparticles with Enhanced Electrocatalytic Activity for the Oxidation of Formic Acid. *Electrochim.*

- Acta 224, 56–63. <https://doi.org/10.1016/j.electacta.2016.12.022>
- De Lima, F., Maia, G., 2015. Oxidized/reduced graphene nanoribbons facilitate charge transfer to the Fe(CN)₆³⁻/Fe(CN)₆⁴⁻ redox couple and towards oxygen reduction. *Nanoscale* 7, 6193–6207. <https://doi.org/10.1039/c5nr01123j>
- Ebrahimi-Najafabadi, H., Pasdaran, A., Rezaei Bezenjani, R., Bozorgzadeh, E., 2019. Determination of toxic heavy metals in rice samples using ultrasound assisted emulsification microextraction combined with inductively coupled plasma optical emission spectroscopy. *Food Chem.* 289, 26–32. <https://doi.org/10.1016/j.foodchem.2019.03.046>
- Fang, P.P., Duan, S., Lin, X.D., Anema, J.R., Li, J.F., Buriez, O., Ding, Y., Fan, F.R., Wu, D.Y., Ren, B., Wang, Z.L., Amatore, C., Tian, Z.Q., 2011. Tailoring Au-core Pd-shell Pt-cluster nanoparticles for enhanced electrocatalytic activity. *Chem. Sci.* 2, 531–539. <https://doi.org/10.1039/c0sc00489h>
- Gong, J., Zhou, T., Song, D., Zhang, L., 2010. Monodispersed Au nanoparticles decorated graphene as an enhanced sensing platform for ultrasensitive stripping voltammetric detection of mercury(II). *Sensors Actuators, B Chem.* 150, 491–497. <https://doi.org/10.1016/j.snb.2010.09.014>
- Gupta, S., Pandotra, P., Gupta, A.P., Dhar, J.K., Sharma, G., Ram, G., Husain, M.K., Bedi, Y.S., 2010. Volatile (As and Hg) and non-volatile (Pb and Cd) toxic heavy metals analysis in rhizome of *Zingiber officinale* collected from different locations of North Western Himalayas by Atomic Absorption Spectroscopy. *Food Chem. Toxicol.* 48, 2966–2971. <https://doi.org/10.1016/j.fct.2010.07.034>
- Kim, J., Renault, C., Nioradze, N., Arroyo-Currás, N., Leonard, K.C., Bard, A.J., 2016. Electrocatalytic Activity of Individual Pt Nanoparticles Studied by Nanoscale Scanning Electrochemical Microscopy. *J. Am. Chem. Soc.* 138, 8560–8568. <https://doi.org/10.1021/jacs.6b03980>
- Li, D., Wang, C., Zhang, H., Sun, Y., Duan, Q., Ji, J., Zhang, W., Sang, S., 2017. A highly effective copper nanoparticle coupled with RGO for electrochemical detection of heavy metal ions. *Int. J. Electrochem. Sci.* 12, 10933–10945. <https://doi.org/10.20964/2017.11.19>
- Lisiecki, I., Filankembo, A., Sack-Kongehl, H., Weiss, K., Pileni, M., 2000. Structural investigations of copper nanorods by high-resolution TEM. *Phys. Rev. B - Condens. Matter Mater. Phys.* 61, 4968–4974. <https://doi.org/10.1103/PhysRevB.61.4968>
- Liu, X., Yao, Y., Ying, Y., Ping, J., 2019. Recent advances in nanomaterial-enabled screen-

- printed electrochemical sensors for heavy metal detection. *TrAC - Trends Anal. Chem.* 115, 187–202. <https://doi.org/10.1016/j.trac.2019.03.021>
- Liu, Y.Q., Zhang, M., Wang, F.X., Pan, G.B., 2012. Facile microwave-assisted synthesis of uniform single-crystal copper nanowires with excellent electrical conductivity. *RSC Adv.* 2, 11235–11237. <https://doi.org/10.1039/c2ra21578k>
- Lo, M., Diaw, A.K.D., Gningue-Sall, D., Aaron, J.J., Oturan, M.A., Chehimi, M.M., 2018. Tracking metal ions with polypyrrole thin films adhesively bonded to diazonium-modified flexible ITO electrodes. *Environ. Sci. Pollut. Res.* 25, 20012–20022. <https://doi.org/10.1007/s11356-018-2140-x>
- Londono-Calderon, A., Campos-Roldan, C.A., González-Huerta, R.G., Hernandez-Pichardo, M.L., del Angel, P., Yacaman, M.J., 2017. Influence of the architecture of Au–Ag–Pt nanoparticles on the electrocatalytic activity for hydrogen evolution reaction. *Int. J. Hydrogen Energy* 42, 30208–30215. <https://doi.org/10.1016/j.ijhydene.2017.08.042>
- Luo, M., Ruditskiy, A., Peng, H.C., Tao, J., Figueroa-Cosme, L., He, Z., Xia, Y., 2016. Penta-Twinned Copper Nanorods: Facile Synthesis via Seed-Mediated Growth and Their Tunable Plasmonic Properties. *Adv. Funct. Mater.* 26, 1209–1216. <https://doi.org/10.1002/adfm.201504217>
- Macdonald, M.A., Andreas, H.A., 2014. Method for equivalent circuit determination for electrochemical impedance spectroscopy data of protein adsorption on solid surfaces. *Electrochim. Acta* 129, 290–299. <https://doi.org/10.1016/j.electacta.2014.02.046>
- Migliorini, F.L., Sanfelice, R.C., Pavinatto, A., Steffens, J., Steffens, C., Correa, D.S., 2017. Voltammetric cadmium(II) sensor based on a fluorine doped tin oxide electrode modified with polyamide 6/chitosan electrospun nanofibers and gold nanoparticles. *Microchim. Acta* 184, 1077–1084. <https://doi.org/10.1007/s00604-017-2082-x>
- Niu, P., Fernández-Sánchez, C., Gich, M., Ayora, C., Roig, A., 2015. Electroanalytical assessment of heavy metals in waters with bismuth nanoparticle-porous carbon paste electrodes. *Electrochim. Acta* 165, 155–161. <https://doi.org/10.1016/j.electacta.2015.03.001>
- Oliver, J., 2011. *Bio-management of Metal-Contaminated Soils, Climate Change 2013 - The Physical Science Basis, Environmental Pollution.* Springer Netherlands, Dordrecht. <https://doi.org/10.1007/978-94-007-1914-9>
- Oularbi, L., Turmine, M., Salih, F.E., El Rhazi, M., 2020. Ionic liquid/carbon nanofibers/bismuth particles novel hybrid nanocomposite for voltammetric sensing of

- heavy metals. *J. Environ. Chem. Eng.* 8, 103774. <https://doi.org/10.1016/j.jece.2020.103774>
- Prakash, S., Shahi, V.K., 2011. Improved sensitive detection of Pb²⁺ and Cd²⁺ in water samples at electrodeposited silver nanonuts on a glassy carbon electrode. *Anal. Methods* 3, 2134–2139. <https://doi.org/10.1039/c1ay05265a>
- Prathna, T.C., Chandrasekaran, N., Mukherjee, A., 2011. Colloids and Surfaces A : Physicochemical and Engineering Aspects Studies on aggregation behaviour of silver nanoparticles in aqueous matrices : Effect of surface functionalization and matrix composition. *Colloids Surfaces A Physicochem. Eng. Asp.* 390, 216–224. <https://doi.org/10.1016/j.colsurfa.2011.09.047>
- Promphet, N., Rattanarat, P., Rangkupan, R., Chailapakul, O., Rodthongkum, N., 2015. An electrochemical sensor based on graphene/polyaniline/polystyrene nanoporous fibers modified electrode for simultaneous determination of lead and cadmium. *Sensors Actuators, B Chem.* 207, 526–534. <https://doi.org/10.1016/j.snb.2014.10.126>
- Qu, X., Yang, H., Yu, Z., Jia, B., Qiao, H., Zheng, Y., Dai, K., 2020. Serum zinc levels and multiple health outcomes: Implications for zinc-based biomaterials. *Bioact. Mater.* 5, 410–422. <https://doi.org/10.1016/j.bioactmat.2020.03.006>
- Read, T.L., Bitziou, E., Joseph, M.B., Macpherson, J. V., 2014. In situ control of local ph using a boron doped diamond ring disk electrode: Optimizing heavy metal (mercury) detection. *Anal. Chem.* 86, 367–371. <https://doi.org/10.1021/ac403519p>
- Sanders, T., Liu, Y., Buchner, V., Tchounwou, P.B., 2009. Neurotoxic effects and biomarkers of lead exposure: A review. *Rev. Environ. Health* 24, 15–45. <https://doi.org/10.1515/REVEH.2009.24.1.15>
- Shi, M., Chen, Z., Sun, J., 1999. Determination of chloride diffusivity in concrete by AC impedance spectroscopy. *Cem. Concr. Res.* 29, 1111–1115.
- Singh, S., Numan, A., Zhan, Y., Singh, V., Van Hung, T., Nam, N.D., 2020. A novel highly efficient and ultrasensitive electrochemical detection of toxic mercury (II) ions in canned tuna fish and tap water based on a copper metal-organic framework. *J. Hazard. Mater.* 399, 123042. <https://doi.org/10.1016/j.jhazmat.2020.123042>
- Torres-Rivero, K., Torralba-Cadena, L., Espriu-Gascon, A., Casas, I., Bastos-Arrieta, J., Florido, A., 2019. Strategies for surface modification with ag-shaped nanoparticles: Electrocatalytic enhancement of screen-printed electrodes for the detection of heavy metals. *Sensors (Switzerland)* 19, 1–14. <https://doi.org/10.3390/s19194249>
- Wang, H., Zhao, G., Zhang, Z., Yi, Y., Wang, Z., Liu, G., 2017. A portable electrochemical

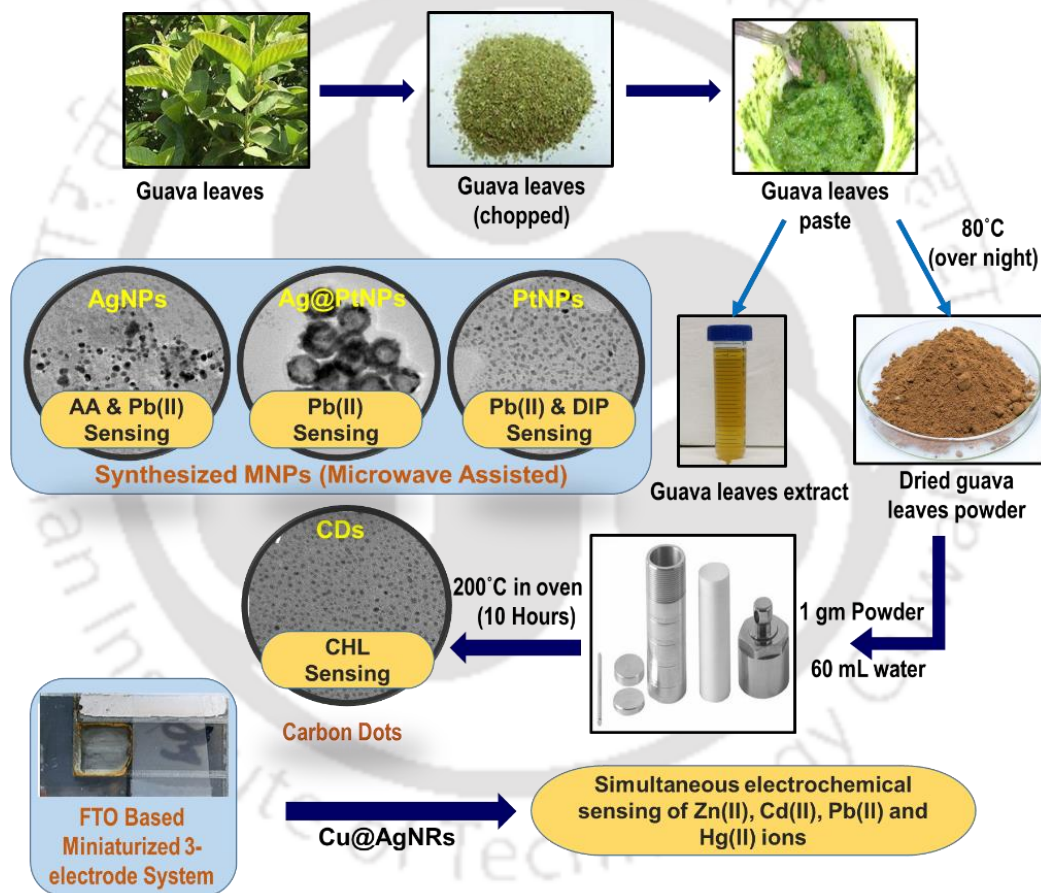
- workstation using disposable screen-printed carbon electrode decorated with multiwall carbon nanotube-ionic liquid and bismuth film for Cd(II) and Pb(II) determination. *Int. J. Electrochem. Sci.* 12, 4702–4713. <https://doi.org/10.20964/2017.06.73>
- Wuana, R.A., Okieimen, F.E., 2011. Heavy Metals in Contaminated Soils: A Review of Sources, Chemistry, Risks and Best Available Strategies for Remediation. *ISRN Ecol.* 2011, 1–20. <https://doi.org/10.5402/2011/402647>
- Xu, A., Chao, L., Xiao, H., Sui, Y., Liu, J., Xie, Q., Yao, S., 2018. Ultrasensitive electrochemical sensing of Hg²⁺ based on thymine-Hg²⁺-thymine interaction and signal amplification of alkaline phosphatase catalyzed silver deposition. *Biosens. Bioelectron.* 104, 95–101. <https://doi.org/10.1016/j.bios.2018.01.005>
- Yan, Z., Yuan, H., Zhao, Q., Xing, L., Zheng, X., Wang, W., Zhao, Y., Yu, Y., Hu, L., Yao, W., 2020. Recent developments of nanoenzyme-based colorimetric sensors for heavy metal detection and the interaction mechanism. *Analyst* 145, 3173–3183. <https://doi.org/10.1039/d0an00339e>
- Yang, Y., Kang, M., Fang, S., Wang, M., He, L., Zhao, J., Zhang, H., Zhang, Z., 2015. Electrochemical biosensor based on three-dimensional reduced graphene oxide and polyaniline nanocomposite for selective detection of mercury ions. *Sensors Actuators, B Chem.* 214, 63–69. <https://doi.org/10.1016/j.snb.2015.02.127>
- Yokoyama, S., Motomiya, K., Jeyadevan, B., Tohji, K., 2018. Environmentally friendly synthesis and formation mechanism of copper nanowires with controlled aspect ratios from aqueous solution with ascorbic acid. *J. Colloid Interface Sci.* 531, 109–118. <https://doi.org/10.1016/j.jcis.2018.07.036>
- Zuo, Y., Xu, J., Zhu, X., Duan, X., Lu, L., Gao, Y., Xing, H., Yang, T., Ye, G., Yu, Y., 2016. Poly(3,4-ethylenedioxythiophene) nanorods/graphene oxide nanocomposite as a new electrode material for the selective electrochemical detection of mercury (II). *Synth. Met.* 220, 14–19. <https://doi.org/10.1016/j.synthmet.2016.05.022>



CHAPTER 8

Conclusions and Scopes for Future Studies

This chapter outlines the salient outcomes of the overall doctoral work. The suggestions and recommendations of future work direction are also provided based on the experience of the present study.



8.1 Overall conclusions

In the course of this thesis, I worked on the bioinspired synthesis of various spherical and tailor-made nanoparticles using reducing and capping agents present in the leaves extract of the *Psidium guajava* (guava) plant. These bioinspired synthesized nanoparticles were used in the modification of graphite paste electrodes (GPEs) and glassy carbon electrodes (GCEs) by drop-casting method for electrochemical sensing of different organic analytes like ascorbic acid, dipyrone (drug), chlorpyrifos (an organophosphate pesticide), and inorganic analytes (heavy metal ions). The fabrication of a miniaturized three-electrode system was also successful for the electrochemical sensing of heavy metal ions.

The mass spectra analysis of the bio-extract revealed the presence of various antioxidants and polyphenols like ascorbic acid, quercetin, chlorogenic acid, caffeic acid, naringenin, and rutin. These components could successfully reduce metal precursors like silver nitrate and chloroplatinic acid to produce stable silver, platinum, and tailor-made bimetallic core-shell Ag@Pt nanoparticles. The biomass residue generated during bio-extract preparation was also used for the synthesis of carbon dots for electrocatalytic sensing of chlorpyrifos.

❖ Microwave-assisted synthesis of silver nanoparticles and ascorbic acid sensing

One-pot synthesis of silver nanoparticles was carried out by using the analytes present in the aqueous extract of *Psidium guajava* leaves, where the synthesis reaction was synergised by microwave. The sluggishness of the bioinspired process was tackled by the use of microwave-assisted synthesis of nanoparticles and synthesis was possible within 90 s, which would otherwise take hours to complete without it. The bioinspired synthesis of metal nanoparticles was found to be pH dependant and an optimum pH of 9.5 was found as the sweet spot for the synthesis of the nanoparticles without any contamination of silver oxides. A highly selective and sensitive electrochemical sensor was successfully developed for the sensing of ascorbic acid using the modified GPE with the silver nanoparticles. This electrokinetic behaviour of the modified electrode was successfully implemented to quantify ascorbic acid contents in the biological entities, namely, *S. edule* and *Z. mauritiana*. The developed sensing platform showed high selectivity towards ascorbic acid even in the presence of dopamine and uric acid.

❖ **Bioinspired synthesis of Ag@Pt core-shell nanoparticles for Pb(II) sensing**

A methodology of nanoparticle washing was developed that would inhibit particle aggregation and help in the controlled removal of the capping agents (without hampering the zeta potential) which would enhance the positively charged platinum ions to get deposited on the Ag nanoparticles core to form a highly structured core-shell nanoparticle. This microwave-assisted bioinspired synthesis of Ag@Pt core-shell nanoparticles was introduced by using bio-extracts from *Psidium guajava* leaves. The porous platinum shell enhanced the Pb(II) adsorption on the working electrode and the synergistic effects of both silver and platinum present in the Ag@Pt nanoparticles improved the sensitivity of the electrode towards Pb(II) ions. It was hypothesized that the lattice strain induced due to the inconsistencies in the lattice spaces of silver and platinum at the heterojunction enhanced the electrochemical sensitivity of the electrode. The square wave anode stripping voltammetry was used successfully to quantify Pb(II) present in sewage water, river water, and domestic tap water. Hence, this electrochemical sensor could be a low-cost and convenient alternative that could provide very accurate quantification of Pb(II) in a plethora of environmental water samples.

❖ **PtNPs/graphene nanocomposites for sensing of metabolites of dipyrone**

The successful synthesis of high-quality 6-7 layers thick graphene in the presence of acetone, controlled ultra-sonication (40 Hz/ 4 h), and microwave irradiation (700 W/ 3 min) was developed that could act as an alternative green method to the well-known Hummer's or modified hummers method. One-pot bioinspired synthesis of PtNPs decorated graphene nanocomposites was achieved that showed very high sensitivity towards sensing of the metabolites of dipyrone. The detailed mass spectral analysis and electrokinetic studies could establish a mechanism of the formation of the oxygenates of dipyrone. A highly selective electrochemical sensor based on the PtNPs/graphene nanocomposite was developed which could successfully sense the metabolites of dipyrone in spiked environmental water samples with ~100% recovery results.

❖ **Bioinspired carbon dots for electrocatalytic sensing of chlorpyrifos**

This study aimed at utilizing the guava leaves biomass wastes generated after the bio-extract separation. The hydrothermal synthesis of the leaves biomass powder at 200°C for 10 h could produce carbon dots of 3.7 nm size. These carbon dots possessed various functional groups like carboxylic acid, hydroxyl, and amine groups on their surface that

could successfully capture chlorpyrifos (an organophosphate pesticide) and electrocatalyze its reduction reaction. This electrochemical sensor could effectively quantify chlorpyrifos in agricultural formulations that are generally applied in various agricultural fields to control pests. The sensor system provides an alternative sustainable approach towards environmental monitoring of chlorpyrifos and opens an avenue to direct research for developing more sustainable bioinspired electrochemical sensors to monitor pesticides, insecticides, and fertilizers.

❖ **Miniaturized electrochemical sensing device for simultaneous heavy metal sensing**

A portable electrochemical sensing device that can be applied for on-field monitoring of heavy metal ions was successfully developed using a fluorine-doped tin oxide (FTO) based three-electrode system. Silver-coated copper nanorods (Cu@AgNRs) synthesized in an environmentally friendly method showed improved sensing capabilities compared to copper nanorods (CuNRs) modified FTOs. The Cu@AgNRs modified FTOs could successfully quantify Pb(II), Zn(II), Cd(II), and Hg(II) both in single metal systems and in mixed metal systems with the detection limits in the nM range. These devices showed repeatability of up to 4 cycles thus providing an alternative to the conventional screen-printed electrodes that are normally single-use devices and generate a lot of plastic solid wastes.

8.2 Scopes for future studies

- ❖ Work has now been done on the bioinspired synthesis of nanomaterials using crude bio-extracts, but the specific functionality of the individual phytochemical is yet to be determined.
- ❖ More work needs to devote in developing new selective and sensitive recognition layers, but the integration of these developed sensors with a user-friendly and mobile potentiostat device is at its nascent stage and more work can be focused on this aspect.
- ❖ Different nanocatalysts are specific towards a particular group of analytes. The researches can be focused in developing a universal electrocatalytic system that could simultaneously detect varied groups of analytes.
- ❖ Commercially available portable screen-printed electrodes are generally single-use devices, though this work presents a miniature device that shows repeatability of up to 4 cycles; more focuses and researches should be devoted towards the development of reusable miniature devices.

Annexure-I: Selection of bio-extract for the synthesis of metal nanoparticles

The source of bioextract was chosen considering factors like availability, economic importance, growth characteristics, reducing substance contents, etc. Three group of plants have been chosen i.e., one is a shrub (*S. trilobata*), second is a fern (*D. esculentum*) and third is a group of two higher plants, *Z. maritima* and *P. guajava*. They were expected to be rich in reducing substances. The availability of these plants and their potential implications are summarized in Figure A1. The leaves of the plants are used as the source of reducing agent for the biosynthesis of nanoparticles. The leaves were collected at the particular time of the year right before the fruiting season to avoid the seasonal variations in the bio-components in the leaves extract. The leaves extract were stored in deep freeze for upto 3 months without affecting the reducing capability of the extracts. Quirectin a very strong anti-oxidant is abundantly found in the leaves of *D. esculentum* (*J. Agri. Food. Chem.*, 2008, 49, 3106–3112.) and *P. guajava* (*J. Ethnopharmacol.*, 2001, 117, 1, 1–27). Among other important groups of compounds that help in reduction of metal ions are flavonoids, saponins, terpenoic acid, oleanolic acid, ascorbic acid and other organic acids are found in the selected sources (Figure A2).

To establish the formation of AgNPs, the absorbance was taken using UV-vis spectrophotometer that shows characteristic peak for AgNPs. In this experiment, the extract concentration was varied with a precursor concentration of 1 mM. The characteristic peaks at about 420 nm for AgNPs can be evidenced from Figure A2. At higher leaves concentration upto water to leaves ratio of 50, the intensity of the characteristic peak for the formation AgNPs was increased irrespective to the type of the leaves. After that there is a decrease in the peak intensity due to higher particle size which was resulted from the reduction in surface plasmon effect of AgNPs. So, the water to leaves ratio of 50 was considered for the further experiments. Figure A3 gives the pictorial images of control bio-extract, and after reaction which shows the characteristic brown colour for the formation of AgNPs. Further evaluation of Figure A2 shows *P. guajava* shows comparatively faster synthesis of the AgNPs and was chosen as a source for the bio-extract for further experiments.



Spagneticola trilobata (*S. trilobata*)

Common names: Creeping daisy, Trailing Daisy or Wadelia. It is a perennial creeper, known to have many medicinal properties. Native to wet tropical regions of the world including India & Bangladesh (Wu et al., 2013).



Psidium guajava (*P. guajava*)

Common name: Guava. It is widely found all over the world and is a good source of antioxidants and other minerals. The leaves contain ascorbic acid, guavanoic acid, tannins, β -sitosterol, flavonoids, triterpenoids and volatile oil that act as good reducing agents (Kullu et al., 2013).



Ziziphus maritima (*Z. maritima*)

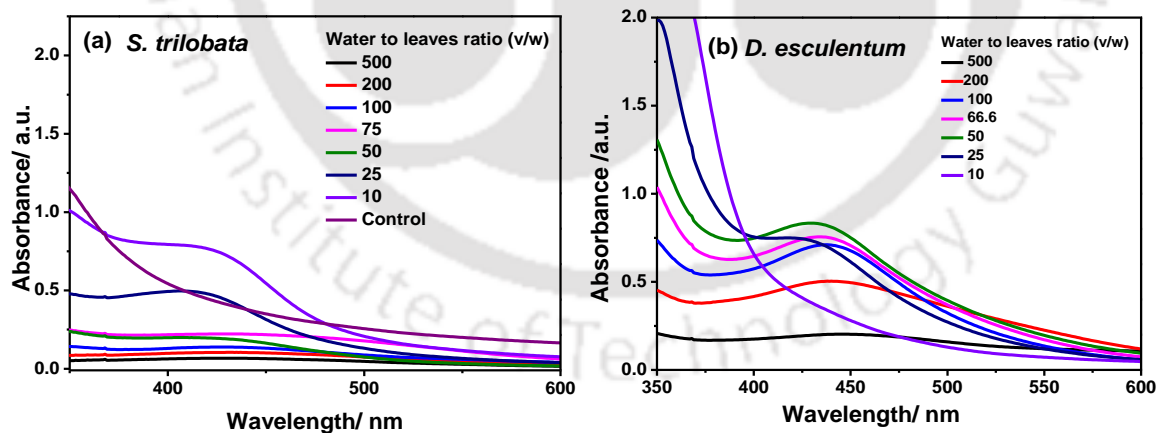
Common name: Jujube. The leaves of the plant are a great source of ascorbic acid. It is a tropical deciduous plant. It is also known for its many medicinal applications. The leaves contain many organic acids and flavonoids (Abalaka et al., 2010).



Diplozium esculentum (*D. esculentum*)

This plant is commonly found in India, mostly, in damp places and along the streams. It is known to have immunosuppressing capability and also used as vegetables in some places in India. It is basically an evergreen and available throughout the year (Kaushik et al., 2011).

Figure A1: Studied sources of bio-extracts.



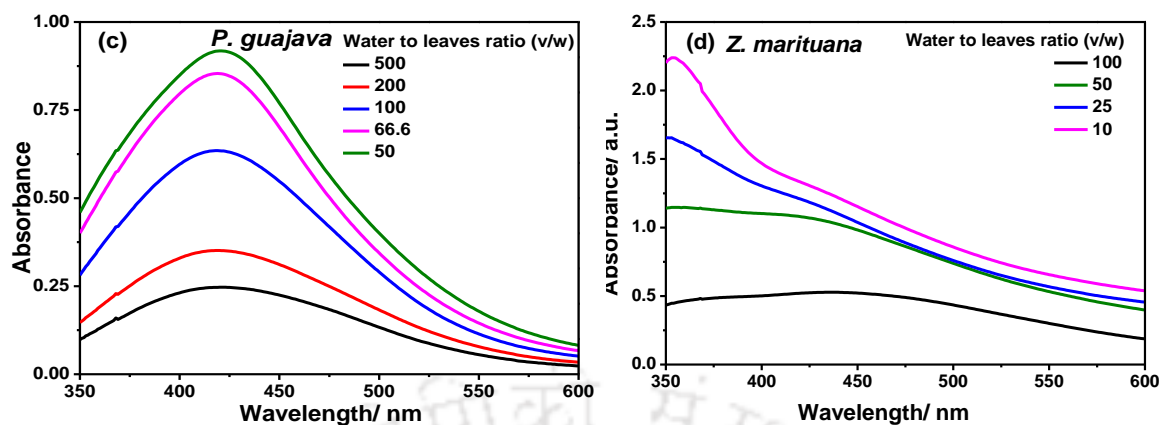


Figure A2: UV-vis spectra for AgNPs synthesized using different leaf extracts at varying water to leaves ratio (mL/g) after 48 h of reaction. Experimental condition: Reaction volume 100 mL, initial Ag^+ concentration 1 mM, pH natural, stirring 150 rpm and temperature $25 \pm 5^\circ\text{C}$.

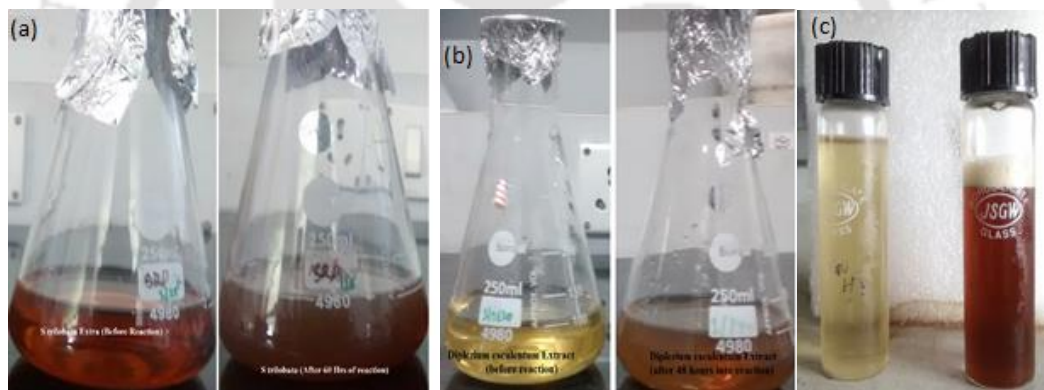


Figure A3: Images showing the change in colour before and after 48 h of reaction. (a) *S. trilobata* (natural pH of 6.4), (b) *D. esculentum* (natural pH of 6.8) and, (c) *P. guajava* (natural pH of 5.8) extracts. Experimental condition: water to leaves ratio (v/w) 50 mL/g, reaction volume 100 mL, initial Ag^+ concentration 1 mM, stirring 150 rpm and temperature $25 \pm 5^\circ\text{C}$.



RESEARCH OUTCOMES

Scholarship

Commonwealth Split-Site Scholarship- 2019, 1st Oct 2019 – 30th Sept 2020, Department of Pure and Applied Chemistry, University of Strathclyde, Glasgow, Scotland, UK

Journal Publications (incorporated in the thesis)

1. **S.R. Dash**, S.S. Bag and A.K. Golder, (2018), *Synergized AgNPs formation using microwave in a bio-mediated route: Studies on particle aggregation and electrocatalytic sensing of ascorbic acid from biological entities*, **J. Electroanal. Chem.** **827**, 181–92. [10.1016/j.jelechem.2018.09.023](https://doi.org/10.1016/j.jelechem.2018.09.023).
2. **S.R. Dash**, S.S. Bag and A.K. Golder, *Synthesis of highly structured spherical Ag@Pt core-shell NPs using bio-analytes for electrocatalytic Pb(II) sensing*, **Sensors Actuators, B Chem.** **314** (2020) 128062. doi:[10.1016/j.snb.2020.128062](https://doi.org/10.1016/j.snb.2020.128062).
3. **S.R. Dash**, S.S. Bag and A.K. Golder, *Bio-inspired Synthesis of PtNPs/Graphene Nanocomposite for Electrocatalytic Sensing of Dipyrone and its Metabolites*, **Analytica Chimica Acta** **1167**, (2021) 338562. <https://doi.org/10.1016/j.aca.2021.338562>
4. **S.R. Dash**, S.S. Bag and A.K. Golder, *Electrocatalytic sensing of chlorpyrifos using carbon dots derived from waste Psidium guajava leaves biomass (Under Review)*
5. **S.R. Dash**, S.S. Bag, A.K. Golder and A. Ivaturi, *Fabrication of a miniaturized electrochemical sensing device using Cu and Cu@Ag nanorods for heavy metal sensing (Communicated)*
6. **S.R. Dash**, A.K. Golder and A. Ivaturi, *Signal enhancement in electrochemical sensors for detection of heavy metal ions in water: Strategies and recent developments (Review article under preparation)*

International Conferences and Workshops

1. **S.R. Dash**, S.S. Bag and A.K. Golder, (2020), *Electrocatalytic Determination of Cd(II) using Bio-inspired AgNPs and PtNPs modified sensing platforms*, One Day Workshop DST-UKIERI on “Recent Advances in Water Contaminants Detection and Remediation”, Department of Pure and Applied chemistry, University of Strathclyde, Glasgow, UK.
2. **S.R. Dash**, S.S. Bag and A.K. Golder, (2019), *AgNPs and PtNPs formed in a bio-mediated route for electrocatalytic Cd(II) determination*, “iSAEST-12”, Twelfth International Symposium on Advances in Electrochemical Science and Technology, Chennai, India.
3. **S.R. Dash**, S.S. Bag and A.K. Golder, (2018), *A bio-inspired approach for the synthesis of Ag@Pt (core-shell) nanoparticles for the electrochemical sensing of heavy metals*, One Day Workshop DST-UKIERI on “Recent Advances on Bio-inspired Nanomaterials for Environmental Applications”, IIT Guwahati, India.

National Conferences

1. **S.R. Dash**, S.S. Bag and A.K. Golder (2015), *Synthesis and antibacterial effect of nanoparticles –A mini review*, “CHEMCON 2015”; Indian Chemical Engineering Congress, 68th Annual Session of Indian Institute of Chemical Engineers, IIT Guwahati, India.
2. **S.R. Dash**, S.S. Bag and A.K. Golder (2017), *Application of biosynthesized silver nanoparticles in developing electrochemical sensors and biosensors*, Research conclave 2017, Indian Institute of Technology, Guwahati, India.
3. **S.R. Dash**, S.S. Bag and A.K. Golder, (2017), *Biosynthesis of silver nanoparticles and their application in electrochemical sensing of ascorbic acid*, “Reflux 2017”, Department of Chemical Engineering, Indian Institute of Technology, Guwahati, India.
4. **S.R. Dash**, S.S. Bag and A.K. Golder, (2018), *Bio-inspired silver nanoparticles as platform for the optical sensing of Cu (II) ion in water samples*, “AEPS-2018”, Centre for the Environment, Indian Institute of Technology, Guwahati, India.



Smruti Ranjan Dash

Research Scholar

Centre for the Environment,
Indian Institute of Technology Guwahati, Guwahati, Assam, 781039 India

✉ d.smruti@iitg.ac.in

✉ dash.sr111@gmail.com ☎ +91 7503702440



📖 ACADEMICS.....

Ph.D. Sept 2021	Environment Indian Institute of Technology Guwahati, Guwahati, India Principal Courses Undertaken: <ul style="list-style-type: none">• Industrial Wastewater Pollution Control• Catalysts and Adsorbents• Energy Resources• Bioprocess Engineering
M.E. May 2012 CGPA 8.62/10	Environmental Engineering Government College of Technology, Coimbatore, India Principal Courses Undertaken: <ul style="list-style-type: none">• Primary and Secondary treatment of Wastewater• Remote Sensing & Geographic Information System• Environmental Impact Assessment• Solid Waste Management• Cleaner Production• Water Treatment and Supply
B.Tech May 2009 Marks-79.64%	Biotechnology Institute of Advance Studies and Education University, Rajasthan, India Principal Courses Undertaken: <ul style="list-style-type: none">• Environmental Biotechnology• Biochemistry, Immunology• Principles of Molecular Genetics• Bio-separation & Downstream Process• Fermentation Technology and Bioprocess Engineering
Intermediate May 2005 Marks-64.4%	Science Dharanidhar Junior College, Keonjhar, Odisha, India Subjects studied: <ul style="list-style-type: none">• Physics• Chemistry• Biology• Mathematics
High school May 2003 Marks-76%	Greenfield School, Palaspanga, Odisha, India Subjects studied: <ul style="list-style-type: none">• English• Science• Mathematics• Social Science• Sanskrit

📖 Awards and Scholarships.....

2019	Commonwealth Split-site Scholarship-2019 Commonwealth Commission U.K. 1 st Oct 2019-30 th Sept 2020
2019	IELTS (Band Score 7)
2014	Ministry of Education (Former MHRD), Institute Fellowship, IIT Guwahati Dec-2014-Oct 2019
2010	GATE 2010 May 2010-May 2012

PUBLICATIONS

1. **S.R. Dash**, S.S. Bag and A.K. Golder, Bio-inspired Synthesis of PtNPs/Graphene Nanocomposite for Electrocatalytic Sensing of Dipyrone and its Metabolites, *Analytica Chimica Acta* 1167, 338562 <https://doi.org/10.1016/j.aca.2021.338562>.
2. **S.R. Dash**, S.S. Bag and A.K. Golder, Synthesis of highly structured spherical Ag@Pt core-shell N.P.s using bio-analytes for electrocatalytic Pb(II) sensing, *Sensors Actuators, B Chem.* 314 (2020) 128062. <https://doi.org/10.1016/j.snb.2020.128062>.
3. **S.R. Dash**, S.S. Bag and A.K. Golder, (2018), Synergized AgNPs formation using microwave in a bio-mediated route: Studies on particle aggregation and electrocatalytic sensing of ascorbic acid from biological entities, *J. Electroanal. Chem.* 827, 181–92. <https://doi.org/10.1016/j.jelechem.2018.09.023>.
4. A. Kannan, **S.R. Dash**, S. Jayanthi, R Rateesh Kumar, (2013), Performance of anaerobic sequencing batch reactor for biomethane and biohydrogen recovery from distillery wastewater, *Indian J. Environ. Prot.* 33(10), 816-28.
5. **S.R. Dash**, S.S. Bag and A.K. Golder, Electrocatalytic sensing of chlorpyrifos using carbon dots derived from waste Psidium guajava leaves biomass (**Under Review**)
6. **S.R. Dash**, S.S. Bag, A.K. Golder and A. Ivaturi, Fabrication of a miniaturized electrochemical sensing device using Cu and Cu@Ag nanorods for heavy metal sensing (**Under Review**)

CONFERENCES

1. **One Day Workshop DST-UKIERI on “Recent Advances in Water Contaminants Detection and Remediation” Department of Pure and Applied Chemistry, University of Strathclyde, Glasgow, UK.**
S.R. Dash, S.S. Bag and A.K. Golder, (2020), Electrocatalytic Determination of Cd(II) using Bio-inspired AgNPs and PtNPs modified sensing platforms.
2. **“iSAEST-12”, Twelfth International Symposium on Advances in Electrochemical Science and Technology, Chennai, India.**
S.R. Dash, S.S. Bag and A.K. Golder, (2019), AgNPs and PtNPs formed in a bio-mediated route for electrocatalytic Cd(II) determination.
3. **One Day Workshop DST-UKIERI on “Recent Advances on Bio-inspired Nanomaterials for Environmental Applications”, IIT Guwahati, India.**
S.R. Dash, S.S. Bag and A.K. Golder, (2018), A bio-inspired approach for the synthesis of Ag@Pt (core-shell) nanoparticles for the electrochemical sensing of heavy metals.
4. **“AEPS-2018”, Centre for the Environment, Indian Institute of Technology, Guwahati, India.**
S.R. Dash, S.S. Bag and A.K. Golder, (2018), Bio-inspired silver nanoparticles as platform for the optical sensing of Cu (II) ion in water samples.
5. **“Research conclave 2017”, Indian Institute of Technology, Guwahati, India.**
S.R. Dash, S.S. Bag and A.K. Golder (2017), Application of biosynthesized silver nanoparticles in developing electrochemical sensors and biosensors,
6. **“Reflux 2017”, Department of Chemical Engineering, Indian Institute of Technology, Guwahati, India.**
S.R. Dash, S.S. Bag and A.K. Golder, (2017), Biosynthesis of silver nanoparticles and their application in electrochemical sensing of ascorbic acid.
7. **“CHEMCON 2015”; Indian Chemical Engineering Congress, 68th Annual Session of Indian Institute of Chemical Engineers, IIT Guwahati, India.**
S.R. Dash, S.S. Bag and A.K. Golder (2015), Synthesis and antibacterial effect of nanoparticles –A mini review.

8. **National Conference on “CIVIL 2020” Department of Civil Engineering, Karpagam Engg. College, Coimbatore, India.**
S.R. Dash, A. Kannan and S. Jayanthi (2013), Hydrogen production from distillery wastewater using Anaerobic Sequential Batch Reactor.
9. **National Conference on “Environmental Challenges towards Sustainability -2012” department of Civil Engineering, Government college of technology, Coimbatore, India.**
S.R. Dash, A. Kannan and S. Jayanthi (2012), Optimization of pH for efficient production of biohydrogen from distillery wastewater using ASBR.

☪ LANGUAGES.....

- Hindi
- English
- Oriya

- Biological wastewater treatment

☪ HOBBIES.....

- Wildlife Photography

☪ RESEARCH INTERESTS.....

- Electrochemical Sensors
- Electroanalysis
- Emerging pollutant sensing and removal
- Domestic & industrial wastewater treatment

☪ VOLUNTEERSHIPS.....

- Volunteered at IIT Guwahati ‘CHEMCON 2015’
- I volunteered in WILDLIFE CENSUS 2011, Coimbatore Forest range conducted by Coimbatore forest division, Tamil Nadu.

☪ WORK EXPERIENCE.....

RESEARCH ASSISTANT (16/02/2009 -19/02/2010), Crest Biotech Pvt. Ltd., New Delhi

My job responsibility was to analyze all raw materials used for alcohol fermentation and assist in R&D to develop new technologies for our clients to increase their alcohol productivity in distilleries and maintain the yeast cultures in the lab.

SENIOR ENGINEER (06/08/2012 -30/09/2014), Larsen & Toubro Limited, New Delhi

My job responsibility at L&T construction was complete supply chain management and coordinating with the construction planning team to procure material for construction projects. Independently handled the procurement of material for two mega residential projects worth ₹1000 crore of value.

☪ PROFICIENCIES.....

Technical Expertise

- UV-Visible Spectrophotometer, Microwave reactor
- Atomic Absorption Spectroscopy
- HPLC, GC and Ion Chromatography

- XRD, FTIR, TEM and SEM Analytical Techniques
- All Electroanalytical techniques
- Metals, antibiotics & pesticide detection
- Molecular tools & techniques

Software Packages

- Lightroom,
- Microsoft office 2003-2019
- ImageJ, Nova 2.1.5
- Origin
- ChemDraw

PROJECTS

Commonwealth Scholarship Cu and Cu@Ag Nanorods based Miniaturized Electrochemical Heavy Metal Sensors

A portable electrochemical sensing device that can be applied for on-field monitoring of heavy metal ions was successfully developed using a fluorine-doped tin oxide based three-electrode system. Silver-coated copper nanorods (Cu@Ag) synthesized in an environmentally friendly method showed improved sensing capabilities than copper nanorods modified FTOs. The Silver-coated copper nanorods modified FTOs could successfully quantify Pb(II), Zn(II), Cd(II), and Hg(II) both in single metal systems and in mixed metal matrices with the detection limits in the nanomolar range. These devices showed repeatability of up to 4 cycles, thus providing an alternative to the conventional screen-printed electrodes that are typically single-use devices and generate a lot of plastic wastes.

Ph.D. Bioinspired Engineering of Nanomaterials for Electrocatalytic Sensing of Heavy Metals and Organic Analytes

In my PhD, I worked on the bioinspired synthesis of various spherical and tailor-made nanoparticles using reducing and capping agents present in the leaves extract of the *Psidium guajava* (guava) plant. These bioinspired synthesized nanoparticles were used in the modification of graphite paste electrodes (GPEs) and glassy carbon electrodes (GCEs) by drop-casting method for electrochemical sensing of different organic analytes like ascorbic acid, dipyrone (drug), chlorpyrifos (an organophosphate pesticide), and inorganic analytes (heavy metal ions). The fabrication of a miniaturized three-electrode system was also successful for the electrochemical sensing of heavy metal ions. The mass spectra analysis of the bio-extract revealed the presence of various antioxidants and polyphenols like ascorbic acid, quercetin, chlorogenic acid, caffeic acid, naringenin, and rutin. These components could successfully reduce metal precursors like silver nitrate and chloroplatinic acid to produce stable silver, platinum, and tailor-made bimetallic core-shell Ag@Pt nanoparticles. The biomass residue generated during bio-extract preparation was also used to synthesize carbon dots for electrocatalytic sensing of chlorpyrifos.

M.E. Anaerobic Biphasic Process for The Recovery of Hydrogen and Methane from Distillery Wastewater Using AnSBR

The objective of this project was to produce cleaner fuels in the form of Hydrogen and Methane gas from distillery wastewater and studying the treatment efficiency of the process. Dark fermentation was implemented in anaerobic bioreactors using enriched biological sludge obtained from distillery wastewater treatment plants. The segregation of the acidogenesis and the methanogenesis phases of the anaerobic fermentation process in two separate AnSBR in series resulted in enhanced biofuels production and improved the COD reduction of the wastewater.

B.Tech Ethyl Alcohol Fermentation Based on Starch Grains

The objective of this project was to develop process parameters to enhance alcohol production in grain-based distilleries with minimizing the energy required for the process. The rice grain powders were first subjected to Jet cooking, followed by liquefaction and saccharification of the grains using thermostable α -amylase and glucoamylase. These saccharified grains were then fermented using Yeast to generate ethanol. It was found that the jet cooking at high temperatures resulted in the formation of non-fermentable sugars that hampered the efficiency of alcohol production, whereas bypassing the jet cooking increased the alcohol production by 20%.

Name	Smruti Ranjan Dash
Father's Name	Madan Mohan Dash
Gender	Male
Age	32
Date of Birth	1 ST JUNE, 1988
Nationality	Indian
Permanent Address	At/po: Salapada, PS: Ghasipura, Anandpur, Keonjhar Odisha – 758020 India

BIOGRAPHICAL INFORMATION

“ REFERENCES

Dr. Animes Kumar Golder

*Professor, Department of Chemical Engineering
Indian Institute of Technology Guwahati, Assam,
India 781039*

✉ animes@iitg.ac.in

Dr. Subhendu Sekhar Bag

*Professor, Department of Chemistry
Indian Institute of Technology Guwahati, Assam,
India 781039*

✉ ssbag75@iitg.ac.in

I declare that all the information furnished above is correct.

Date: 15th Sept 2021

Place: IIT Guwahati

Smruti Ranjan Dash